Considerations for Automated NDE Applications

Charles Norman MacLeod

Department of Electronic and Electrical Engineering

University of Strathclyde

A thesis submitted for the degree of

Doctor of Philosophy

Acknowledgements

Abstract

To ensure that infrastructure owners, operators and planners have sufficient information readily available to them regarding the state and condition of their asset, numerous advances and developments have been demonstrated in the field of Non Destructive Evaluation (NDE). The process of detailed imaging and examination of structures and components in a sensitive, safe and inherently non-intrusive manner has numerous advantages in operational, financial and safety terms.

Only by delivering NDE sensors directly to all points of interest on a structure, can the desired coverage of the structure or component be undertaken. This vision has driven research and developments in the area of automated collection of NDE data.

This thesis identifies and addresses key challenges and technical boundaries currently preventing wider industrial uptake of automated NDE. This has been accomplished through novel research and developments in key areas related to platform kinematics and dynamics, localisation and registration to the structure under inspection, path planning and physical NDE sensing. These advances provide a unified framework to both establish and progress remote automated NDE forward for future commercial deployment.

A contribution to knowledge was presented on the positional performance characteristics of a custom rotary wing aerial inspection platform after a series of hover tests within a tracking volume. An additional contribution was presented on the results of a comprehensive evaluation of a laser based positioning sensor operating under a wide range of engineering materials, along with the development

of a novel distance correction algorithm. A new custom approach for robotic NDE path planning was researched and developed based on conventional CAD/CAM machining, while utilising a novel custom agile ultrasonic thickness mapping crawler to highlight proof of principle. Both of these approaches provide an additional contribution to knowledge, both individually in their respective fields and also together in highlighting the unique advantages of their combined approach. Finally a new NDE sensor concept based on the vibrissae of rodents such as rats and mice, for both surface roughness and surface profiling measurement, was adapted and investigated for NDE sensing applications. The results document a contribution to knowledge in the area with discrimination down to 14 micrometre Roughness Average presented.

Contents

List of Figures

List of Abbreviations

ADC	Analogue to Digital Convertor
ADM	Absolute Distance Metre
AGC	Automatic Gain control Circuit
AIFM	Absolute Interferometer
AMCW	Amplitude Modulated Continuous Wave
APD	Avalanche Photodiode
API	Application Programming Interface
ASA	Aerial Sensing Agent
A-Scan	Amplitude Scan
ASIC	Application Specific Integrated Circuit
AUT	Automated Ultrasonic Thickness
BIOTACT	BIOmimetic Technology for vibrissal Active Touch
BRL	Bristol Robotics Laboratory
CAD	Computer Aided Drawing
CAM	Computer Aided Manufacturing
CC3D	Copter Control 3D
CCRJ	Corner Cube Reflector Jig
CIA	Contact-Induced Asymmetry
CNC	Computer Numeric Control
CPP	Coverage Path Planning
C-Space	Configuration Space
CUE	Centre for Ultrasonic Engineering
DLL	Dynamic Linked Library

DLP	Data Light Processing
DOF	Degree of Freedom
EC	Eddy Current
EEE	Electronic & Electrical Engineering
EMATs	Electromagnetic Acoustic Transducers
EPSRC	Engineering and Physical Science Research Council
ESC	Electronic Speed Controllers
FIRST	Facility for Innovation and Research in Structural Testing
FPGA	Field Programmable Gate Array
GPS	Global Positioning Systems
GUI	Graphical User Interface
IFM	Interferometer
ILW	Intermediate Level Waste
IMU	Inertial Measurement Unit
IR	Infrared
LAT	Laser Absolute Tracker
LED	Light Emitting Diode
LRF	Laser Range Finder
MDF	Medium Density Fibreboard
MFL	Magnetic Flux Leakage
NC	Numeric Control
ND	Not Detected
NDE	Non Destructive Evaluation
NDEvR	NDE Research Association
NRP	Number of Rejected Measured Points
NS	Not Scanned

NVP	Number of Valid Measured Points
PC	Personal Computer
PD	Proportional-Derivative
PID	Proportional Integral Derivative
PIG	Pipeline Inspection Gauge
PMMA	Poly(methyl methacrylate)
POD	Probability of Detection
PSD	Power Spectral Density
PVC	Polyvinyl Chloride
RCNDE	Research Centre in Non-Destructive Evaluation
RCP	Rapid Cessation of Protraction
RMS	Root Mean Square
RMSE	Root Mean Square Error
ROV	Remote Operated underwater Vehicles
RRR	Red Ring Reflector
RSA	Remote Sensing Agents
SCIP	Scanning sensor Command Interface Protocol
SDK	Software Development Kit
SLAM	Simultaneous Localization and Mapping
SMR	Spherically Mounted Reflector
SPI	Serial Peripheral Interface
SSD	Sensor to Surface Distance
TBR	Tooling Ball Reflector
TOF	Time of Flight
UAV	Unmanned Aerial Vehicles
VMCS	VICON Motion Capture System

VMP	Valid Measurement Probability
VTOL	Vertical Take-Off and Landing
XML	Extensible Markup Language

Chapter 1

Introduction

1.1 Non-Destructive Evaluation

With a concerted and growing emphasis on human safety [1] and the environment [2], greater information is required on the current state and condition of the world's infrastructure. Higher operational demands such as greater working loads and longer working lifetimes [3], coupled to reduced capital investment in replacement designs has exerted greater strain and stress on numerous components, critically affecting their condition and safe working lifetime [4].

To ensure that infrastructure owners, operators and planners have sufficient information readily available to them regarding the state and condition of their asset, numerous advances and developments have been demonstrated in the field of Non-Destructive Evaluation (NDE). The process of detailed imaging and examination of structures and components in a sensitive, safe and inherently non-intrusive manner has numerous advantages in not only operational, but also in financial and safety terms. Quantitative information and results on the condition of the parts under test, allow suitably skilled personnel to make decisions on remaining lifetime and required replacement, ensuring maximum asset value, usage and safety.

Several NDE techniques have been researched, developed and commercially deployed to non-invasively inspect structures and components under test and these are not limited to ultrasonic, electromagnetic, radiographic and visual methods.

Ultrasonic methods utilise mechanical vibrations, with a frequency greater than 20,000 kHz, to propagate through liquids, solids and air [5]. Piezoelectric materials can be exploited to generate mechanical vibration energy from electrical pulse energy. In the context of NDE, when such waves are transmitted and propagated into a component under test, any reflected or scattered wave energy can be detected and utilised to determine information on the component structure. Signal processing techniques such as those based on time of flight between the transmitted and received waves can be employed to determine locations of areas which feature change in acoustic impedance, where reflections can occur. These would include the back wall of any component and areas of discontinuities or breaks, allowing such a technique to assess the condition of the component under test. [5]

Magnetic methods operate on the principle of detection and measurement of distortions and changes in the field of magnetised ferromagnetic materials. In the context of NDE, surface-breaking and subsurface flaws generate local magnetic flux leakage fields which when detected can infer areas, or locations, of concern within a component. [6]. Radiographic methods rely on the transmission and processing of electromagnetic radiating waves, commonly known as X-Rays to internally inspect components under test. The specific wavelengths used (10 nm – 10 x10^{-4} nm) are able to penetrate materials, with partial absorption [7] and in an NDE context, when

detected on the underside of components, provide knowledge of the internal structure. With reference to NDE, areas of defects provide zones of lower absorption within a component, therefore allowing greater radiating energy to pass through the path from the source to the detector [7]

Many serious defects, from a strength view, are often surface-breaking [6] and therefore visual methods offer the potential for their detection. Visual techniques by their own nature rely on optical inspection methods and can be utilised to also infer information on surface profile, roughness and texture [6].

The UK Research Centre in Non-Destructive Evaluation (RCNDE) of which the Centre for Ultrasonic Engineering (CUE) is a founding member, comprises six university partners (Imperial College, Strathclyde, Warwick, Nottingham, Bristol and Manchester) and sixteen major end user companies (including Airbus, Rolls Royce, Shell, BP, Sellafield Ltd, National Nuclear Laboratory, E.ON, RWE npower and Network Rail) communally representing a large range of industrial sectors [8]. These industrial members are collectively represented by a not-for-profit company, NDE Research Association (NDEvR) and have together developed both a 5,10 and 20 year vision for NDE requirements and priority research topics to deliver the vision. [9]

1.2   Automated Non-Destructive Evaluation

Numerous areas requiring attention and detailed surveying on large scale structures such as those found in the energy and transport sectors are in areas often not only very difficult to access, but also often hazardous to human beings [10]. This situation

along with the requirements for greater inspection accuracy and efficiency has underpinned a research and development drive to automate the collection of NDE sensor data [11]. Only by delivering NDE sensors to all points of interest within a structure, can full extensive coverage of the assembly be undertaken. Automation of NDE sensing procedures improves accuracy by reducing human error [12], which can often be categorised as the weakest link in the NDE supply chain [13]. Additionally task efficiency and completion times can potentially be further improved through automation of the task by employing a swarm of fully autonomous intelligent sensing systems. Furthermore automated processing of the collected NDE sensor data can be undertaken to fundamentally aid defect detection and recognition, when especially dealing with large sensor datasets [14].

It is worth noting that NDEvR members are united in their desire for enhanced defect detection, characterisation and improved reliability through automation. This fundamentally will address human factors and add value through "design for NDE" at build stage. [9]. Over the past eight years the CUE has established research into Reconfigurable Systems for Automated and Remote NDE, investigating core concepts and developments to enable reliable remote inspection.

Previous research has focussed on mobile crawler [15-16] and pipe crawler delivery platforms [10], localisation strategies and approaches through novel visual [17] and Bayesian methods [18], along with multi sensor (Ultrasonic, Visual, Eddy Current (EC) and Magnetic Flux Leakage (MFL)) implementation and data processing [19-22].

With regards to automated collection of NDE, NDEvR members have indicated their desire for as high a specification and performance, as feasibly possible, in terms of positional and path accuracy, miniaturisation, sensing resolution and payload and runtime capacity. Fundamentally these desires drive and promote research in the field of automated NDE.

They have indicated however, that for mobile NDE to be a credible, widely adopted technique for general applications of a non-specialised nature, positional requirements in terms of point accuracy of 1 mm or smaller are required. This allows sufficient confidence to be had when analysing acquired sensor data and its reference to specific features within the component or structure. Additionally such accuracy allows inspections to be repeatable and therefore allow methods such as rate of change comparisons to be undertaken. They have also indicated that, for mobile NDE applications, access ports being no larger than 250 mm in diameter should be considered when investigating platform mechanics and deployment mechanisms. These overarching desires have fundamentally driven and continue to drive the above mentioned localisation research within CUE.

Additionally for the purpose of this thesis it is worth mentioning that the typical range of defects being considered and therefore being desired to be identified, are larger than 1mm. This would include areas such as corrosion thickness loss of large steel structures in the order of a millimetre and larger, utilising techniques such as ultrasonic thickness mapping. Additionally swelling and bulging highlighted by abnormal shape or contour, of items such as tanks and drums, of a millimetre and

larger along with surface-breaking cracks of width 1 mm or larger are also regarded as significant areas of interest, with techniques such as visual or metrological sensing modalities capable of identifying such features.

Therefore to address the above aims and goals, this thesis has identified that automated and remote NDE requires a number of key elements and strategies in order to deliver the performance required and hence offer credible solutions to real life problems. These six elements and their respective position within an automated NDE flow chain are shown below in Figure 1.1.
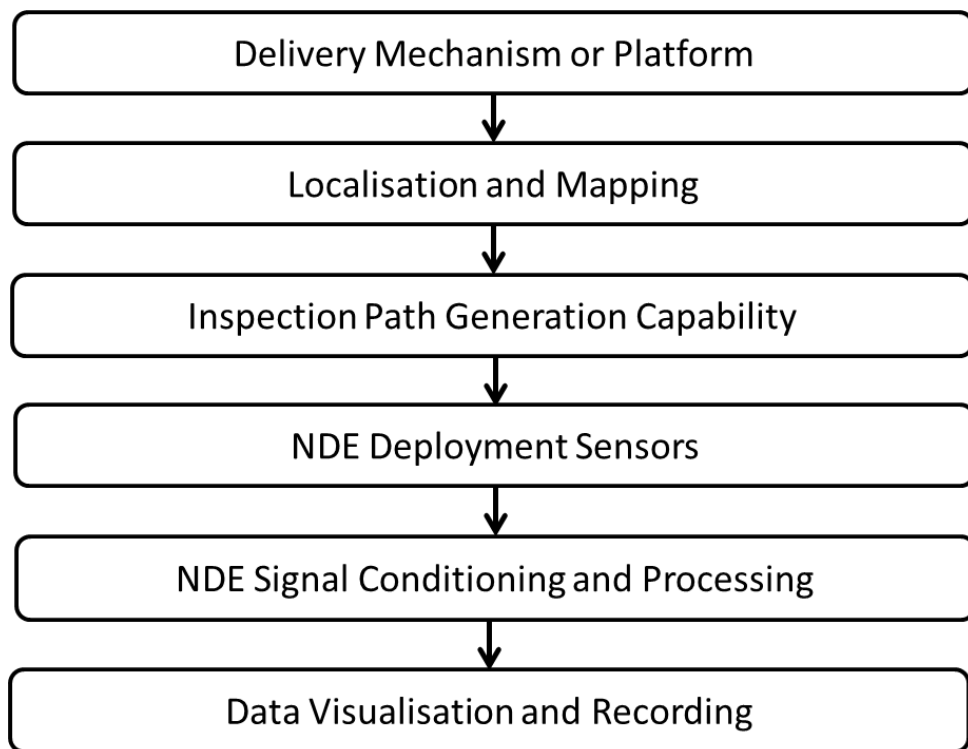
Figure 1.1 Automated remote NDE key elements

Each element is then individually detailed and discussed below.

1.2.1 Delivery mechanism or platform:

This consists of a suitable propulsion mechanism with sufficient payload capacity, power, runtime, processing power and communication protocols for successful deployment and retrieval. The delivery mechanism must be suitable for the inspection and possess the ability to account for access constraints and obstacles while also being capable of reaching each desired measurement point safely and efficiently.

1.2.2 Localisation and mapping:

The pose of the NDE platform is required to be known for both navigation and forward path planning in order to reach and deploy an NDE sensor at desired points of interest. The localisation of the system within a volume is of further importance in NDE applications due to the additional requirement of finding the true position of potential defect locations. Furthermore to perform inspections with confidence and undertake repeatable measurements requires increased positional awareness.

It must be further noted that traditional NDE techniques require critical control of distance from the sensor to the surface under inspection, commonly known as stand-off or lift-off, to ensure maximum sensor efficiency and performance [23]. Therefore accurate information and knowledge of inspection system position is a significant challenge facing the successful practical deployment of autonomous NDE systems.

When operating an autonomous inspection platform it must be capable of determining a collision free path from the start to end location. To correctly and accurately define such a path, a comprehensive map of the environment under question is required. If such a map is not available beforehand, the platform must acquire it live through a variety of sensor measurements. Accurate mapping is only therefore possible with accurate localisation, as any mapping sensor information is relative to the measurement point [24]. Therefore a technique which has received considerable research focus is that of Simultaneous Localization and Mapping (SLAM) [25].

1.2.3 Inspection path generation capability:

Software based algorithms are required to produce the necessary waypoints and paths for travel of the delivery platform and associated sensors to the points of interest. Path planning strategies must account for desired area and volume coverage while also ensuring obstacle avoidance. Additionally they must consider and ensure both safe access and exit of the complete system.

1.2.4 NDE deployment sensors:

The particular NDE sensor, or sensors, to be deployed must be suitable for not only the desired material and degradation inspection required but also the platform motion constraints. Therefore the imaging and defect localisation sensors are highly application specific, from not only a pure NDE perspective but also in relation to the specified automated approach being taken.

The exact choice of all sensors (mapping and NDE) is strongly influenced by the material and area under inspection including local conditions such as geometry, environment and inspection requirements.

1.2.5 NDE signal conditioning and processing:

It is necessary to undertake signal conditioning and processing of raw NDE sensor data to ensure meaningful signal extraction. Where possible pre-processing on the platform can mitigate data transfer issues and noise, albeit at the expense of power consumption, space and payload capacity

1.2.6 Data visualisation and recording:

Effective NDE sensor data visualisation is an important tool in assisting human interpretation and understanding of complex structural components. Large volumes of NDE data require to be carefully analysed to increase successful probability of detection (POD). Correct spatial alignment and registration of NDE data relative to a part or component is of critical importance especially when considering items and locations such as joints and seams. Accurate position referenced data storage and recording ensures that auditable results are available for not only future reference occurrences but also monitoring purposes with comparison of multiple inspection datasets.

1.3   Aims of this Thesis

Previous research within the field of automated NDE has highlighted the challenges of access, position estimation, obstacle avoidance and sensor suitability on practical industrial deployments. This body of work investigates and addresses potential solutions to each area in turn with practical deployment conditions and scenarios driving the fundamental research. Therefore the aims and objectives of this thesis were to understand and quantify the constraints to remote mobile,(both wheeled and aerial) NDE inspection, specifically addressing issues with relation to localisation, mapping, path planning and sensing.   Weaknesses and opportunities for improvement in each of the six key elements of automated NDE, discussed above, were to be identified, discussed, researched and developed to further improve the realisation of remote NDE

1.4   Contributions to Knowledge

This thesis presents a number of unique and novel, industry focused contributions to the fields of automated and remote NDE. These are:

- The development of a novel ultrasonic thickness mapping agile crawler. The three wheeled design incorporates an actively controlled rear wheel probe sensor, allowing for versatile steering and accurate dead reckoning of the platform. This is the first time such an arrangement has been deployed.

- The qualification of positional performance of a custom designed aerial platform to address the suitability of current and future localisation and NDE sensor approaches. Such pose data has wide ranging consequences on parameters such as NDE sensor design and path planning strategies. Multiple platform designs were critically evaluated to ascertain the optimum system

design for automated practical NDE inspections. A suitable high performance embodiment of the preferred platform motion system was designed and then constructed with a clear view to analyse the positional performance using state-of-the-art photogrammetry motion tracking equipment.

- The characterisation of distance accuracy of a standard mobile platform laser range finder when deployed against common industrial samples. The effect of small variations in delivery platform pose, as typically encountered under practical deployment scenarios, was investigated. An additional contribution was made with the development of a novel adaptive compensation algorithm, highlighting improved distance estimation when dealing with challenging specularly reflective surfaces such as stainless steels.

- A unique machining based coverage path planning strategy for use with mobile NDE inspection platforms. The performance and advantages of such a strategy, in terms of coverage rate, obstacle avoidance and simplicity, were evaluated and discussed after undertaking a mock thickness inspection.

- The adaption and characterisation of a new surface roughness and profiling sensor, based on the vibrissae of rodents such as rats and mice, for NDE applications. Research highlighted the sensor is highly suited to automated NDE deployment, with particular insensitivity to positional sensor-surface stand-off

1.5   Thesis Structure

The remainder of this thesis is structured as follows, Chapter 2 provides an overview of current research and industrial deployment of surface contact automated and remote NDE platforms for industrial inspection tasks. Chapter 3 then introduces a

new novel ultrasonic thickness mapping platform for areas of limited access, large surface area and featuring obstacles. This novel platform is used later in Chapter 6 to demonstrate the advanced new path planning approach developed in this thesis.

Chapter 4 reviews the state of the art in robotic aerial based inspection. Although often employed for surveying applications, the use of aerial platforms in NDE is limited due to fundamental performance constraints. This chapter reviews the fundamental flight geometries and identifies a preferred platform for NDE. This platform is then characterised for NDE applications by quantifying the pose error when undertaking a series of indoor flight manoeuvres.

The error in distance measurement, when deploying a common optical laser based range scanner from a mobile platform in an industrial environment is characterised in Chapter 5. The sensor is commonly deployed from both surface and aerial robotic platforms, therefore the dynamic performance under such conditions with industrial surfaces was evaluated. Additionally a strategy was identified and instigated to correct for range error, based on *a priori* training data and material identification.

Chapter 6 introduces a new machining based path planning strategy, for full area converge and obstacle avoidance, for mobile NDE delivery platforms. Applicable to both wheeled and aerial platforms, this chapter addresses what is a major current weakness in robotic automated inspection. Using the wheeled inspection platform described in Chapter 3, a full area NDE thickness inspection has been evaluated and the error in sample thickness and measured position quantified.

A new approach to physical NDE sensing for robotic deployment in the form of a tactile sensor is introduced in Chapter 7. Having identified the challenges associated with traditional NDE sensor deployment on robotic platforms, this chapter provides an entirely new approach that bypasses these challenges. Using a whisker based sensor developed by Bristol Robotics Laboratory, the sensor is quantified for use in NDE measurements for both surface roughness characterisation, and surface form measurement. It is demonstrated that such a sensor may have an important role to play in future autonomous robotic NDE deployments.

Chapter 8 provides an overall summary, conclusions and suggestions for future work. In addition there exists three appendices providing additional info with appendix A being a thorough overview and description of key enabling measurement technologies, systems and procedures which were utilised throughout this thesis. Appendix B provides additional graphical information of data gathered and analysed in Chapter 4, while appendix C provides additional graphical and statistical information of data gathered and analysed in Chapter 5.

1.6   Publications Arising from this Thesis

1.6.1   Journal Paper

MacLeod, C.N., Pierce, S.G, Sullivan, J.C.., Pipe, A., Dobie, G. and Summan, R., 'An active whisking based remotely deployable NDE sensor', Sensors Journal IEEE, vol. 13, no. 11, pp. 4320-4328, Nov. 2013.

1.6.2   Conference Papers

Pierce, S.G., MacLeod, C.N., Dobie G. and Summan R., 'Path Planning & Measurement Registration for Robotic Structural asset Monitoring', 7th European Workshop on Structural Health Monitoring & 2nd European Conference of the Prognostics and Health Management (PHM) Society, pp. 2258-2265, Nantes, 2014.

MacLeod, C.N., Pierce, S.G., Summan, R., Dobie, G., Sullivan, J. C., Pipe, A. and Cao, J., 'Remotely deployable aerial inspection using tactile sensors', 40th Annual Review of Progress in Quantitative Nondestructive Evaluation, pp. 1873-1880, Baltimore, Maryland, USA, 2013

Dobie, G., Galbraith, W., MacLeod, C.N., Summan, R., Pierce, S.G. and Gachagan, A., 'Automatic ultrasonic robotic array', 40th Annual Review of Progress in Quantitative Nondestructive Evaluation, pp. 1881-1888, Baltimore, Maryland, USA, 2013.

Pierce, S.G., Dobie, G., Summan, R. and MacLeod, C.N., 'Reconfigurable robotic platforms for structural non-destructive evaluation', 1st International Conference on Through Life Engineering Services TESConf, Cranfield, 2012.

MacLeod, C.N., Pierce, S.G., Sullivan, J.C. and Pipe, A., 'Remotely deployable autonomous surface inspection and characterisation using active whisker sensors', 6th European Workshop on Structural Health Monitoring & 1st European Conference of the Prognostics and Health Management (PHM) Society, pp. 392-399, 2012.

Pierce, S.G., Punzo, G., Dobie, G., Summan, R., MacLeod, C.N., McInnes, C., Biggs, J., Macdonald, M. and Bennet, D.J., 'Reconfigurable robotic platforms for structural health monitoring', 6th European Workshop on Structural Health Monitoring & 1st European Conference of the Prognostics and Health Management (PHM) Society, pp. 1187-1194, 2012.

1.7   Additional Publications by the Author

1.7.1   Journal Papers

Summan, R., Pierce, S.G., Dobie, G., Hensman, J. and MacLeod, C.N., 'Practical constraints on real time Bayesian filtering for NDE applications', Mechanical Systems and Signal Processing, vol. 42, issue 1-2, pp. 181-193, 2014.

Dobie, G., Summan, R., MacLeod, C.N. and Pierce, S.G., 'Visual odometry and image mosaicing for NDE'. NDT and E International, vol. 57, pp. 17-25, 2013

1.7.2 Conference Papers

MacLeod, C.N., Pierce, S.G., Morozov, M., Summan, R., Dobie, G. I. , McCubbin, P., McCubbin, C., Dearie, S. and Munro, G., 'Automated Metrology and NDE Measurements for Increased Throughput in Aerospace Component Manufacture', 41st Annual Review of Progress in Quantitative Nondestructive Evaluation, Boise, Idaho, USA, 2014.

Summan, R., Dobie, G., Guarato, F., MacLeod, C.N., Marshall, S., Pierce, S. G. and Forrester, C., 'Image Mosaicing for Automated Pipe Scanning', 41st Annual Review of Progress in Quantitative Nondestructive Evaluation, Boise, Idaho, USA, 2014.

Clark, R., Punzo, G., Macdonald, M., Dobie, G., Summan, R., Macleod, C.N. and Pierce, S.G., '3D Model Generation Using an Airborne Swarm', 41st Annual Review of Progress in Quantitative Nondestructive Evaluation, Boise, Idaho, USA, 2014.

Brown, R., Pierce, S.G., Dziewierz, J., Jackson, J., Lardner, T., MacLeod, C.N., Morozov, M., Collison, I. and Dutton, B., 'Automated Full Matrix Capture for Industrial Processes', 41st Annual Review of Progress in Quantitative Nondestructive Evaluation, Boise, Idaho, USA, 2014.

Clark, R., Punzo, G., Macdonald, M., Dobie, G., Summan, R., Macleod, C.N. and Pierce, S.G., 'Autonomous Swarm Testbed with Multiple Quadcopters', Proceedings of the 1st World Congress on Unmanned Systems Engineering, 2014.

Ahmed, K.E, Ju, X., Whitters, C.J., Pierce, S.G., MacLeod, C.N., 'Calibratation of 3D Scanners for Quantification of Tooth Wear', 46th meeting of the Continental European Division of the International Association for Dental Research organized together with NOF, Florence, 2013.

Chapter 2

Robotic Inspection

2.1   Delivery Mechanisms

The fundamental requirement for autonomous NDE systems has driven research and development in robotic delivery mechanisms for NDE applications [10,16]. Robotic systems have seen continued rise in adoption in both traditional areas (military, space, manufacturing, energy) [26-31] and new areas such as home and consumer markets [32-34] due to their advantages in terms of task efficiency, cost, safety and performance [35-36].

In 1400BC the regarded first example of an automated mechanical system, namely a water clock, was developed by the Babylonians [37], while through the subsequent centuries saw greater developments in watchmaking [37] and android (resembling human appearance) systems. Additionally a distinct strand of development in industrial machinery from the 18th century gave rise to mechanical assisted fabrication, with the developments of lathe turning machines [38]. It was then also that the wildly accepted term 'Robot' was first introduced by Russian writer Karel Čapek for his word 'Robota' implying subordinate labour [39]. Research advances coupled to commercial demand and requirements in the 20th century led to the widespread adoption of Numeric Control (NC) machinery into the industrial sectors

such as manufacturing and hazardous material handling [40-41]. The later developments of electronics, integrated circuits, computer systems and software gave rise to the adoption of Computer Numeric Control (CNC) control systems for industrial robotic systems [42]. Continued research was and still is being undertaken in understanding and developing the intelligent connection between perception and action with a sustained drive in areas such as sensing, artificial intelligence (AI) and control methodologies [43-44].

2.2 NDE Delivery Mechanisms

Automated NDE sensor deployment and inspection has been researched and undertaken from a number of delivery mechanisms not limited to manipulator, pick and place, mobile crawler and mobile aerial designs [45-48]. Each mechanism possesses its own inherent advantages and disadvantages with respect to sensor deployment and therefore careful application specific selection is required to achieve desired overall inspection performance.

2.3 NDE Industrial Manipulators

Industrial manipulator designs are of particular interest and suitability when considering NDE deployment for inspections which are of a constrained and repetitive nature, as their fixed base limits mobility. Equally this fundamental design aids to improve overall positional accuracy and repeatability.

Devices featuring low (< 3) degrees of freedom have been utilised in multiple automated NDE scenarios. Cartesian (X-Y) 2D scanners are typically used for

immersion scanning of components featuring planar geometry at the point of manufacture (Figure 2.1). Circular pipe weld inspection is undertaken using scanner collars which allow translation around and across the pipe (Figure 2.2). Thickness mapping of long circular structures can be undertaken using collar devices which feature an extra degree of freedom to permit motion along the entire component (Figure 2.3).
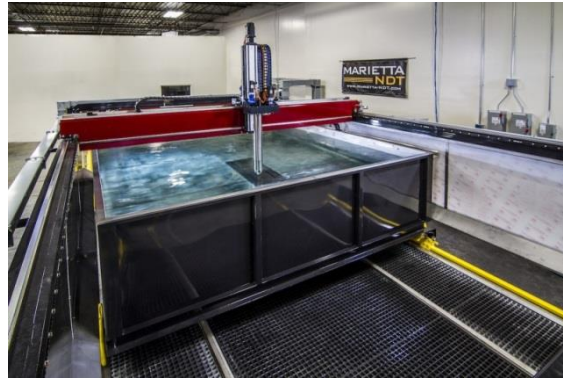
Figure 2.1 Marietta NDT X-Y ultrasonic scanner [49]
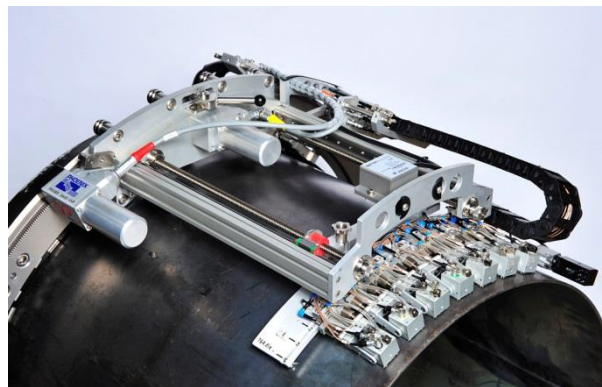
Figure 2.2 Phoenix ISL Dual-axis motorised weld scanner [50]
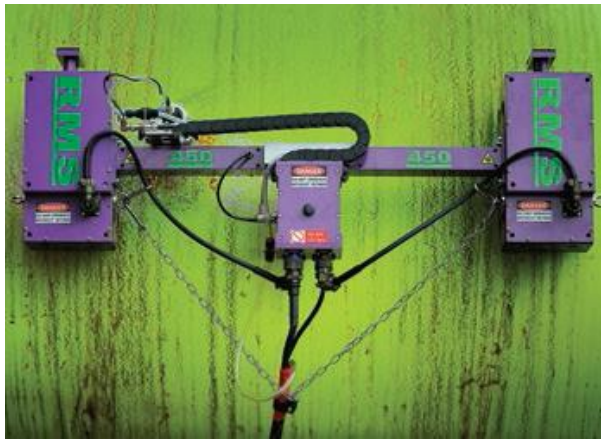
Figure 2.3 Silverwing NDT RMS2 Corrosion Mapping System [46]

Although offering solutions to dedicated bespoke applications further degree of freedom manipulator based solutions are required to fully inspect increasingly complex components and structures. Recent advances in full six Degree Of Freedom (D.O.F.) manipulators, traditionally developed through manufacturing applications, has seen an increased drive and potential for NDE scanning of modern complex shaped components such as those utilised in the aerospace industry [45,51].

Research in this area has seen the development of systems such as the Genesis Systems NSpect Robotic Non-Destructive Inspection cell, shown in Figure 2.4, performing "part to process", or "process to part" ultrasonic inspection using either an immersion tank scan, or recirculating water couplant [45]. Similar NDE specific research developments have been recently undertaken at both TWI [51] and USL [52]. Additionally Airbus Nantes and EADS Innovation Works have developed a similar immersion phased array surface adaptive imaging system and are further adapting this to include laser generated ultrasound [53].

Figure 2.4 Genesis NSpect NDT scanning system [45]

Within the FIRST laboratory there exists a pair of floor mounted six axis robot positioning manipulators (KUKA KR5 HW), capable of general purpose positioning or following pre-generated toolpaths. Each device is capable of carrying a five kilogram payload to a point in a 3D volume with ± 40 μm repeatability, with a maximum reach of 1423mm [54]. Such a system can be used for direct automated NDE deployment or testing and benchmarking novel sensor applications and devices within a constraint environment (Figure 2.5).
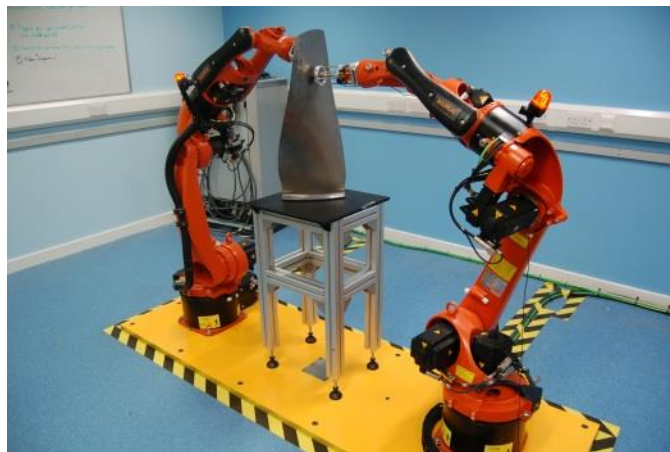
Figure 2.5 FIRST Laboratory KUKA KR5 ARC HW

2.4   Mobile Robots

Inspections which are of a more complex remote access challenge often require the use of mobile robotic platforms to provide the required flexibility and movement to reach the desired location. These mobile robotic systems require the necessary actuation to provide movement within the environment. This environment can be on land, submerged or airborne and each application requires a relevant movement mechanism [55-58]. Locomotion is the term that describes this technique and can be provided by techniques such as wheels, tracks, legs and propellers [59].

One of the most developed and used industrial mobile robotic inspection systems is that of Pipeline Inspection Gauges (PIG), which travel through on or off-line pipelines. Initially designed for abrasive cleaning purposes in a specific sized pipe, these bullet shaped devices relied on positive hydrostatic pressure in a liquid filled line for locomotion [60]. Over the years imaging sensors have been deployed on more intelligent designs which can also include some form of relative and absolute positioning systems [61]. Locomotion techniques have evolved to include compressed air or gas, while adopting hybrid propulsion mechanisms to adapt to complex and changing shaped pipework [62].

In addition Remote Operated underwater Vehicles (ROV) have been utilised for imaging and inspection explorations since first introduced by the Royal navy in the 1950s [63]. The tethered mobile ROV once deployed underwater utilises propellers and pumps for locomotion and mobility purposes while buoyancy vessels are water or air filled depending on the depth of submersion required. These ROV platforms

can feature manipulator arms, illumination sources and many visual sensors for both manual guidance ability and imaging areas of concern [64].Researchers in Robert Gordon University have investigated the fusion of multiple NDE sensor data, both ultrasonic and Eddy Current (EC) acquired from an underwater ROV when undertaking a practical weld inspection [65]. Additional developments have been documented in the detection of deep water pipe flange bolt cracking, through a top surface pilot controlled ROV with fourteen ultrasonic sensors [66]. Research and development has been undertaken in the robotic inspection of girth welds, using visual and ultrasonic means, from ROV platforms in fifty metre deep Danish waters [67]. Ultrasonic transducers were utilised for both inspection and fine localisation when attempting to locate and scan the weld profile. While additionally inspection, using visual sensors, of the bottom surface of boiling water nuclear reactors has been demonstrated through the deployment of a custom, manually controlled, miniature 6 D.O.F ROV [68].

A mobile platform design which has seen sustained adoption and deployment from an NDE perspective, in primarily thickness mapping applications, is that of the wheeled crawler. Typically utilising two or more motor powered wheels for locomotion purposes these devices often utilise ferromagnetic traction in the form of permanent magnet equipped wheels [69].

2.5   Review of Commercial NDE Mobile Inspection Robots

2.5.1   Silverwing NDT – Scorpion

Silverwing NDT's Scorpion is a manually controlled, wired, magnetic traction crawler to perform thickness mapping of the surface in above ground ferromagnetic storage tank inspections [69]. Featuring an encoder and a patented dry coupled single element wheel probe, amplitude scans (A-Scans) and B-Scans of the material under inspection are possible. Due to the four wheeled nature of the design, slippage of the tyres must occur when undertaking rotation movements resulting in challenging positional control. The open loop control of motor speed by simple operator push button drive voltage adjustment, results in variations between individual drive speeds causing a subsequent reduction in positional and path control. Furthermore the drag forces associated with the armoured umbilical cable when traversing, especially in horizontal directions, results in poor path control.

Figure 2.6 Silverwing NDT Scorpion [69]

2.5.2   JIREH - TriPod

Similarly to Silverwing's Scorpion the TriPod is a manually controlled vertical crawler, with magnetic traction. This device features a visual camera and a wet-coupled UT thickness probe [70]. This coupling requirement requires constant pumping of couplant gel or water from the base station to smear over the inspection area, giving only discrete single point measurements. This couplant requirement presents real challenges in areas of documented water shortages. Additionally such a

technique naturally reduces the coefficient friction of the surface and therefore has the potential to reduce path and positional control.

Figure 2.7 JIREH TriPod [70]

2.5.3 Helical Robots

Helical robots develop and sell a range of sized wireless crawlers [71]. These crawlers feature mecanum wheeled traction to allow the crawler to drive in two axes orthogonally [72]. Such a technique has the potential for faster scanning as no turning motions are required. However much greater control is required of the individual drive speeds to ensure the uniformity required for straight line motions [72]. The magnetic traction system only allows the crawler to climb ferromagnetic surfaces. The Crawler is only equipped with a basic pan/tilt camera for manual Visual NDE and features no on-board intelligence or automation capability [71].

Figure 2.8 Helical Robots HR-MP20T [71]

2.5.4 Technitest NDT

The Technitest CETA, is a three wheeled wired magnetic traction crawler with an offset drive wheel design. This permits successful traction over weld beads and rivets whilst retaining adhesion to the surface. In a similar manner to Silverwing's Scorpion the CETA offers a dry coupled single element wheel probe providing A& B Scans of the material under inspection [73]. The open loop nature of the passive third wheel has the potential for increased positional and path uncertainty, especially when considering external disturbances to the rear wheel [16]

Figure 2.9 Technitest NDT Ceta [73]

2.5.5 Alstom Inspection Robots

Alstom have a dedicated inspection R&D department developing one-off bespoke scanning products for a wide range of industries. They have generic base crawlers

which feature some basic intelligence and wireless capability. They have experience in the deployment of traditional NDE sensors such as ultrasonic, eddy current, thermography and x-ray. Currently no devices feature extensive automation capabilities along with complex 3D shape NDE data visualisation or positioning strategies. [74]

Figure 2.10 Alstom Inspection Robots [74]

2.5.6   Phoenix Inspection Systems.

Phoenix Inspection System offer a range of standard and bespoke NDE scanning solutions traditionally featuring fixed x-y scanning systems. They have recently launched a wired magnetic traction crawler with wheel encoder odometry This device is very similar to the Jireh Tripod and can be deployed with ultrasonic irrigations probes for component inspection [75].

Figure 2.11 Phoenix ISL MagBug [75]

2.6 Commercial NDE Mobile Platform Inadequacies

As has been shown above the currently available commercial platforms have well documented inadequacies when considering the theme of automated NDE. Many of those available feature no automation capability and require constant manual intervention and control. There exists clear areas of required research in areas not limited to platform mechanics, motion control and pose localisation. Additionally as shown by the availability of only visual and single element ultrasonic sensors, extensive research is required on NDE sensing modalities which can provide quantifiable meaningful information to inspection scenarios such as internal weld imaging and near surface defects. These sensors which should explore new methodologies and develop on established ultrasonic and electromagnetic array designs critically require adaption to ensure suitability for automated approaches.

2.7   Mobile Platform Research

Mobile robotic platforms feature strongly in both general and NDE research work for their flexibility and capability to offer very adaptable positioning solutions. Traditionally research in the area has been funded primarily through governmental and collaborative sources and has investigated specific areas not limited to adhesion, locomotion, localisation and control [76 – 81].

London South Bank University have a well accomplished automated NDE research group with research developments in novel traction delivery platform mechanisms, underwater weld inspection and cylindrical pipe climbing robots (Figures 2.12 a,b & c) [82 – 84]. Researchers at Imperial College London have investigated the suitability of mecanum wheels for NDE applications. They have defined metrics related to motion accuracy, motion precision and oscillations of the platform relative to the surface. This work has shown their high suitability, with suitably designed platform mechanics and control strategies, to planar surfaces, however the system performance has been shown to decrease with increased surface curvature [72].
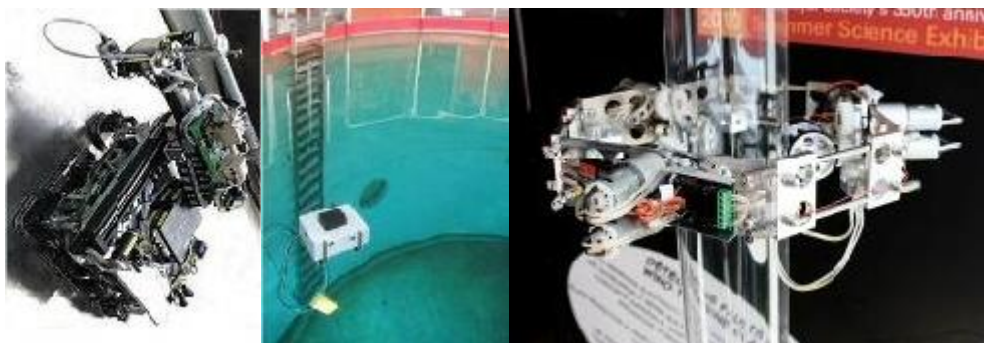
Figure 2.12 South Bank University – a) ROBAIR [76], b) FPSO [77], c) RING [78]

Researchers at COPPE-Federal University in. Rio de Janeiro have investigated the use of mobile robotic platforms for the underwater inspection of ship hulls [85]. The developed system, featuring ferromagnetic traction, utilises eight single element ultrasonic transducers and the surrounding seawater as the couplant mechanism. Specifically investigated was the simulation and verification in the resultant change in the probability of detection (POD) of defects measured by overlapping sensor ultrasonic beams [85].

Researchers at ETH Zurich in conjunction with ALSTOM have developed the "Magnebike", a compact magnetic wheeled inspection robot with high mobility for inspection of complex environment [86-87] (Figure 2.13). Primary research has focussed on the novel delivery mechanism and localisation of the platform prior to undertaking NDE inspection. The novel five actuator design for five separate degrees of freedom (two wheels, two lifters and a steering unit) allowed verification of the claimed high mobility of the compact robot on complex paths. This included confirmation of the platforms ability to successfully handle longitudinal, and circumferential paths, many complex and concave obstacles all without any inclination to gravity [88]
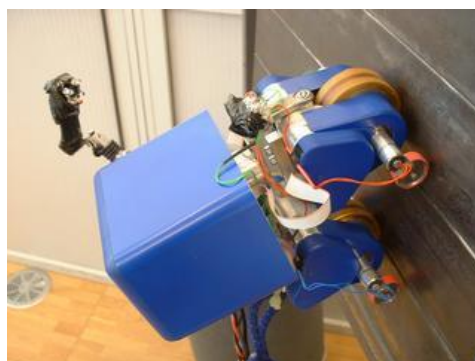
Figure 2.13 ETH Zurich Magnebike [79]

Similarly White et al [89] has developed and quantified the positional accuracy of a tethered suction based platform for manufacturing and inspection of aerospace components. Researchers at Carnegie Mellon, Pennsylvania [90] have developed the Explorer range of visual and eddy current inspection devices for complex and high pressure pipelines shown in Figure 2.14. These designs have been shown to be deployable in both low pressure (< 125 PSI) and high pressure (> 500 PSI) live pipelines featuring long lengths (> 300 m) and multi-angle bends. Furthermore they have also researched the concept of live oil filled storage tank inspection through remotely deployable visual and ultrasonic methods. The system featured acoustic sensors for localisation and has been shown to be capable of performing a mock tank inspection submerged in 25 °C water for over ten hours [91].

Figure 2.14 Carnegie Mellon Pipe Inspection Device [90]

2.8 CUE RSA

Remote Sensing Agents (RSA) capable of remotely accessing challenging structures and then undertaking detailed NDE, using a variety of specialised sensors and payloads, have been developed within the Centre for Ultrasonic Engineering at the University of Strathclyde. Two distinct robotic delivery design methodologies having

been investigated, namely magnetic traction robotic crawlers, that can transverse over ferromagnetic and level to gravity surfaces, and a pipe crawler platform system that negotiates itself along lengths of complex intertwined pipework [15,16,19].

Significant developments have been made in the development of both hardware and software control systems for all necessary tasks associated with remote automated NDE inspection.

The current state of the art RSAs developed feature a fleet of ruggedised three wheeled crawlers capable of performing physical inspection tasks using a variety of NDE sensor payloads. Utilising magnetic wheels these crawlers are able to adhere to ferromagnetic surfaces and allow inspection of components in a loosely constrained 3D environment (Figure 2.15).

Figure 2.15 Remote Sensing Agents (RSA)

The current RSAs are of a differential drive wheel design with a passive rear wheel roller mechanism. Measuring approximately 175 x 124 x 85 mm and weighing 1.5 kg these aluminium chassis and body products allow payload carrying capacity of approximately 2 kg.
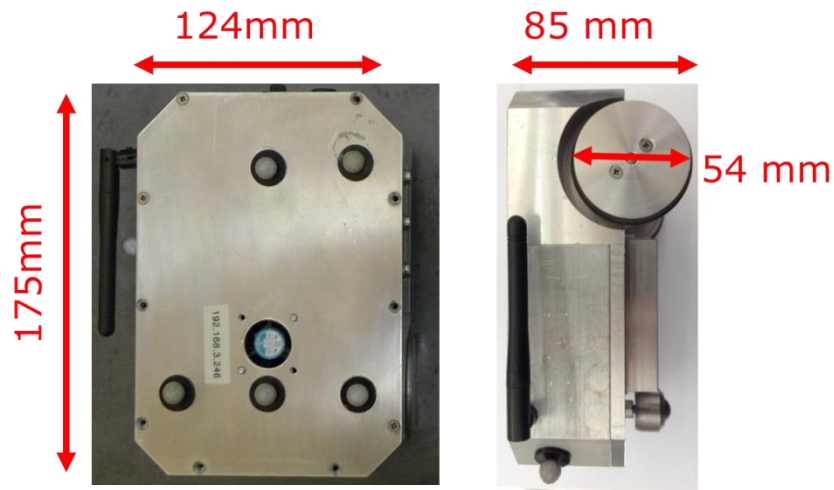
Figure 2.16 RSA Dimensions (Plan and Elevation)

The current platform utilises a core electronic structure, shown in Figure 2.17, to implement all the necessary functions required to deploy the device in an autonomous NDE inspection environment. The hardware consists of a Linux embedded general purpose processor (GPP) [92] to perform the high level and computationally heavy functions, while a 16 bit microcontroller [93] performs low level functions such as drive and motor control. Integrated motor optical encoders provide odometry information while an Inertial Measurement Unit (IMU) [94] provides both a three axis accelerometer and gyroscope respectively. The platform communicates to a host controller machine through a standard IEEE 802.11g wireless communication channel. Three cell lithium polymer batteries provide the required power to supply the demands of the system and current configuration allows for approximately four hours runtime. Manually tuned Proportional Integral and Derivative (PID) controllers are used to regulate and control wheel speeds.

The developed platform possesses the necessary flexibility and range of features to allow a variety of both mapping and imaging sensors systems to be utilised and implemented accordingly.
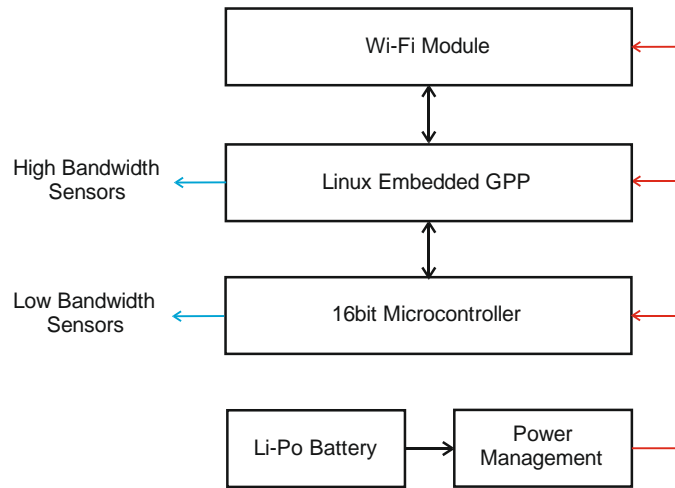
Figure 2.17 **RSA System Structure**

2.9   RSA GUI

A custom proprietary C++ Personal Computer (PC) Graphical User Interface (GUI) has been developed within CUE for full control of the RSA fleet. The GUI features a 3D visual world representation, where structural asset Computer Aided Drawing (CAD) models can be imported, displayed and the position of the robot relative to the sample visualised. Path trajectories can be manually selected across the sample and subsequent NDE results can be displayed and visualised relative to the sample. All RSA parameters including raw NDE results are logged and can be visualised live if desired. The core code features data fusion of visual and MFL NDE data results for enhanced visualisation and recording. Full movement control of single or multiple RSAs can be achieved through a number of input strategies such as manual wheel

speed control, joystick controller, surface point and click and basic 2D rectangular raster scanning as highlighted in Figure 2.18.
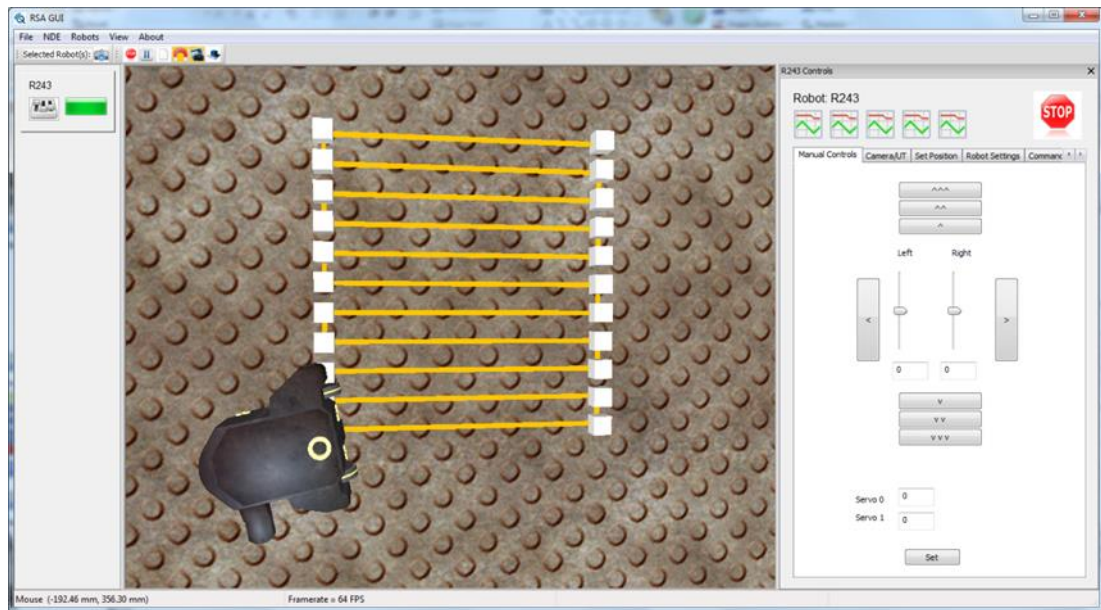
Figure 2.18 RSA GUI – Manually Defined Waypoint Raster Scan

2.10 Conclusion

This chapter identified the key fundamental desirables for the successful deployment of automated NDE approaches. Delivery mechanism designs and their importance and advantages were considered along with the relevant state of the art in their respective fields. An overview was provided on the current state of manipulator and remote crawler automated NDE platforms, in existing industrial usage, to provide some context to the reader.

Additionally the current state of the art CUE RSA platform was discussed, highlighting the flexible and powerful nature of the miniature platform.

Requirements for future automated NDE platform research were identified in areas not limited to platform mechanics, platform motion control, sensors suitable for automated robotic deployment and overall system automation in both collection and processing terms. Specifically this would include novel platform mechanic and traction solutions for increased agility for manoeuvring across and over obstacles, while working within volumes of a non-ferromagnetic nature. Improved motion control is desired to deploy sensors across surfaces with greater path velocity and position accuracy. NDE sensors which are more suitable to automated NDE robotic delivery, in areas not limited to lift-off sensitivity, pose misalignment, couplant demands and robustness, are required to be investigated and developed for increased commercial adoption. Further research is required for greater on-board system intelligence in order to improve automation ability, in both collection and processing of acquired data, to minimise human requirements and increase automatic defect analysis ability and robustness.

Chapter 3

Remote Ultrasonic Mapping

3.1   Automated Thickness Mapping RSA

A novel agile crawler was designed and developed to specifically investigate the feasibility of constrained access remote ultrasonic mapping. The Automated Ultrasonic Thickness (AUT) RSA is a three wheel robotic crawler featuring the novel step of a single element ultrasonic wheel probe fitted as an active rear wheel and is shown in Figures 3.1 and 3.2. The novel combination of an active steering control mechanism and integrated ultrasonic wheel probe presents a unique contribution to knowledge. This particular implementation allows for versatile steering and accurate dead reckoning of the platform, which is not feasible with industrial four wheeled designs due to their requirement of slippage when turning [95]. These unique characteristics permit the platform an additional degree of mobility when compared against present crawler inspection platforms.
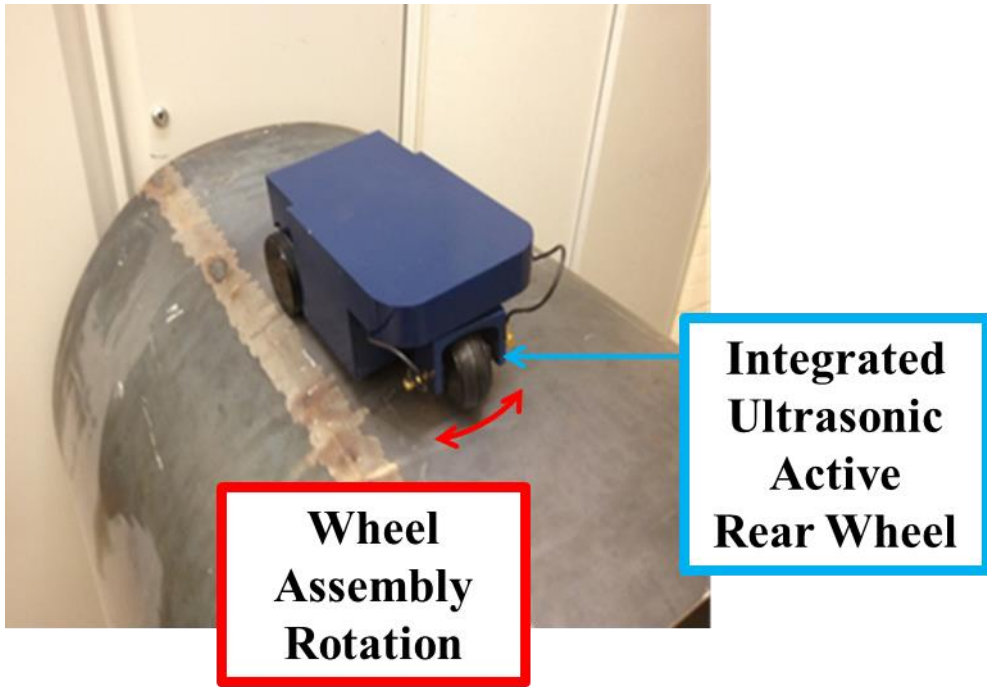
Figure 3.1 AUT RSA
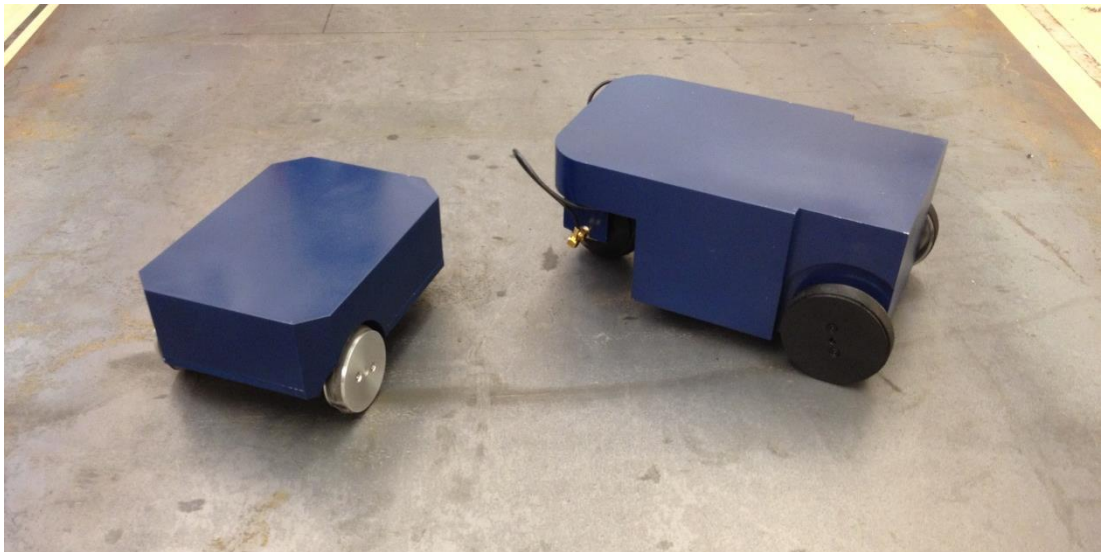
Figure 3.2 RSA & AUT RSA

3.2 Silverwing NDT Wheel Probe

The Silverwing NDT wheel probe is 5 MHz split crystal dry coupled sensor with a bandwidth of approximately 1 MHz. Featuring no liquid filled region it consists of two solid acoustically matched rubber tyres rotating around the transducer housing for transmit and receive signals respectively [96]. An exploded image of the transducer is shown below in Figures 3.3 and 3.4.
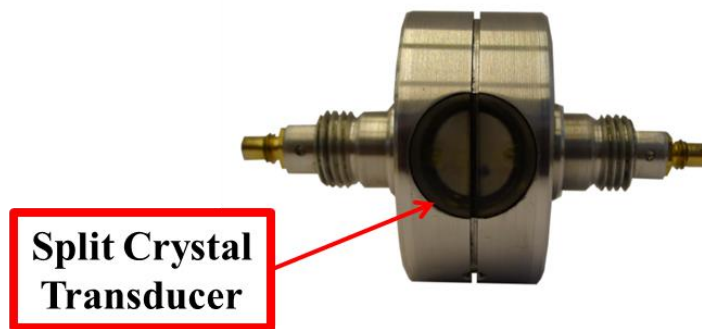
Figure 3.3 Silverwing NDT wheel probe transducer
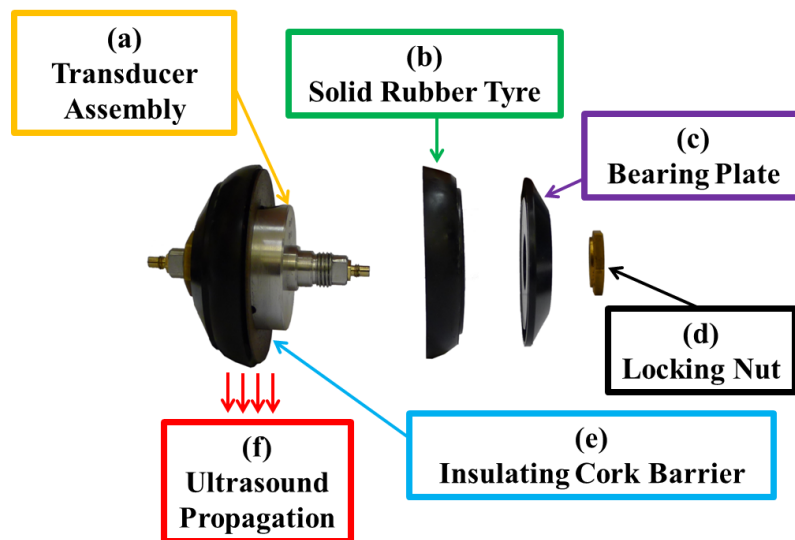
Figure 3.4 Silverwing NDT wheel probe structure

The transmitted compressional wave inaugurates with excitation of the transducer elements, which then propagates through the well matched impedance tyre. Ensuring appropriate contact or couplant between the tyre and sample surface, through either compressive downward force or fine misting, ensures a portion of the wave energy propagates through to the sample. A percentage of this wave energy is then reflected back from any discontinuities within the sample or the ultimate back wall. This reflected wave then travels through the sample and tyre, ultimately exciting the piezoelectric receiver producing an appropriate signal. This procedure is illustrated below in Figure 3.5.
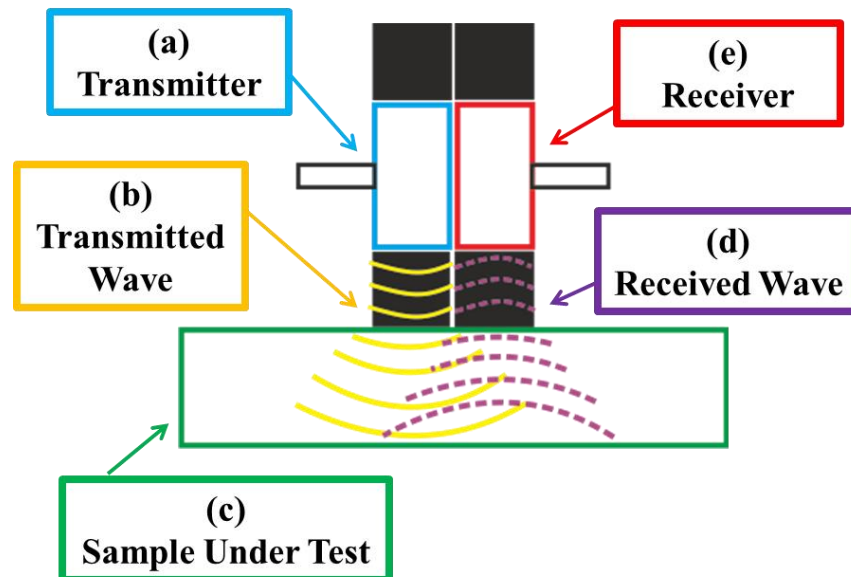
Figure 3.5 Silverwing wheel probe wave propagation illustration

3.3 AUT RSA

The inclusion of the active rear wheel probe required some necessary bespoke technical solutions to be developed. These can be separated into their core disciplines, namely mechanical, electrical and software. Where possible continued

use was made of suitable parts and systems utilised on the current RSA to aid commonality and reduce wastage.

3.4 AUT RSA Mechanical Components

The mechanical requirement to implement an actively driven rear wheel necessitated the design and construction of a complete new chassis. Fundamentally this required to not only be able to rotate the rear wheel along its perpendicular axis rigidly, but to also measure this rotation for control and ultimately overall position estimate purposes. In keeping with the theme of demonstrating miniature inspection platforms for asset management the mechanism and overall design was required to be not substantially larger than the standard RSA. Through various discussions with BP, Shell and Doosan Babcock NDT personnel, it was felt that a maximum height of 100mm should be sought to aid with clearance and access in typical industrial confined environments. With this constraint in mind a dual driven worm drive arrangement was designed and constructed to offer the desired low profile and expected torque requirements. An incremental optical encoder, similar to that found in the standard RSA gearbox, was incorporated into the drive arrangement to measure rotation angle change. Due to nature of the encoder, the active back wheel mechanism required calibration before first use to ensure the desired home position.

The final rear wheel mechanism is shown below in Figure 3.6, highlighting the individual components.
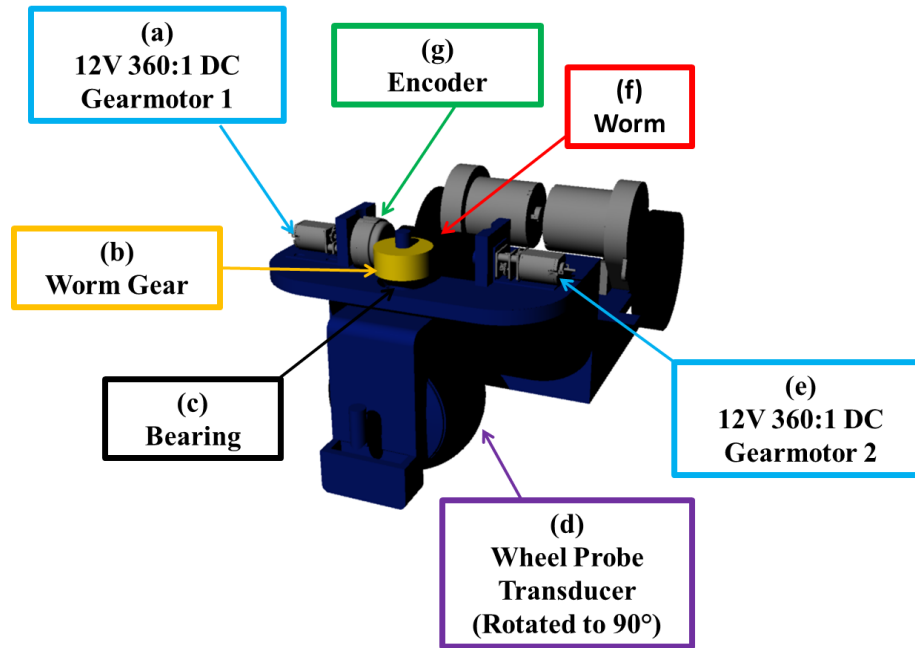
Figure 3.6 AUT RSA mechanical structure

An additional second bearing was also included in the covering case in an attempt to ensure the axis of rotation of the mechanism remained perpendicular to the robot chassis. This was required to retain normal incidence of the ultrasonic transducer to the surface and ensure correct operation. Therefore it must be noted that the design only allowed the ultrasonic waves to be transmitted perpendicular to the surface when both the front and rear wheels were considered to be coplanar.

The reference home angle of the active rear wheel transducer assembly, relative to the chassis platform, was defined as shown below in Figure 3.7. Additionally the rotation convention utilised is also illustrated.
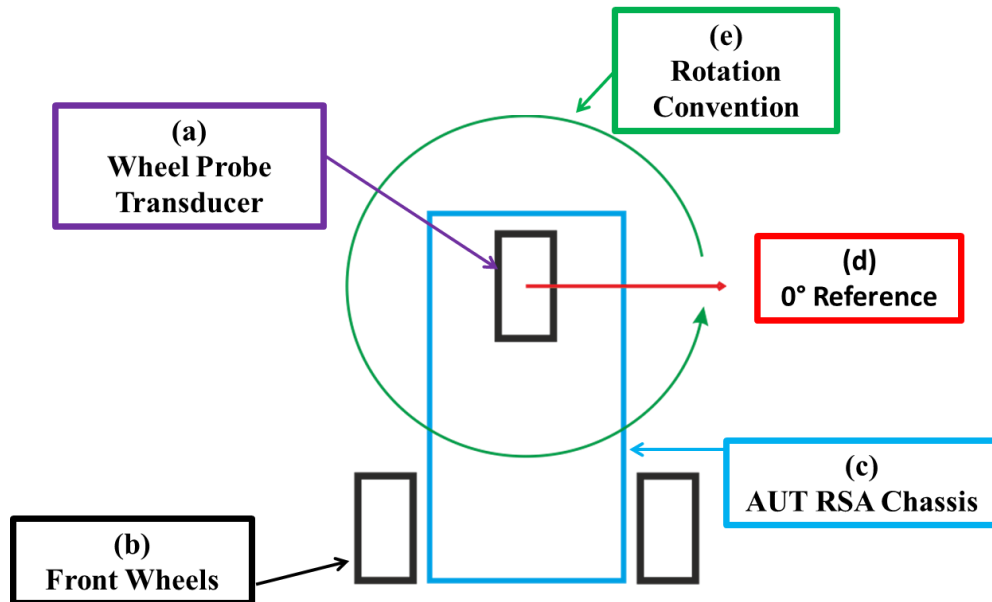
Figure 3.7 AUT RSA Rear Wheel Assembly Rotation Reference and Convention (Plan View)

The front wheels' radii were increased to match the rear wheel probe radius to aid chassis simplicity. Additionally the motors were uprated from the standard RSA model, while still retaining the standard gearbox. Neodymium (NeFeB) ring magnets were inserted inside the hubs of the front wheels and could be attached to the active back wheel housing if required. Furthermore a larger single piece case was manufactured to house, enclose and protect all necessary components as shown in Figure 3.8.
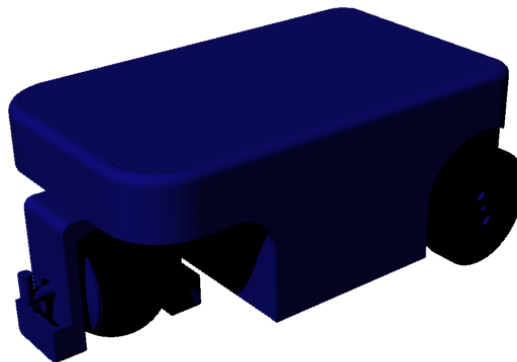
Figure 3.8 AUT RSA assembly

3.5 AUT RSA Electrical Systems

The electrical component changes can be further divided into motor drive electronics and ultrasonic drive and acquisition electronics.

3.5.1 Motor Drive Electronics

The actively driven rear wheel mechanism necessitated the inclusion of a third motor drive channel in the standard CUE RSA drive electronics platform. The dual motor drive design was driven from a single H-bridge channel with one motor wired polar opposite to the first. This ensured that each motor rotated in the same direction while maintaining simple drive structure. The necessary third encoder data channel was also routed to suitable microcontroller inputs.

3.5.2 Ultrasonic Drive and Acquisition Electronics.

Due to the split nature of the transducer the drive and receive electronics could be simply de-coupled and separated from each other.

3.5.2.1 Drive Electronics.

The drive electronics consisted of a single channel high voltage square wave pulser. A step-up boost DC-DC convertor provided a 110V drive excitation voltage which was switched across the transducer by means of a MOSFET, driven by TTL logic signal. The schematic is shown below in Figure 3.9.
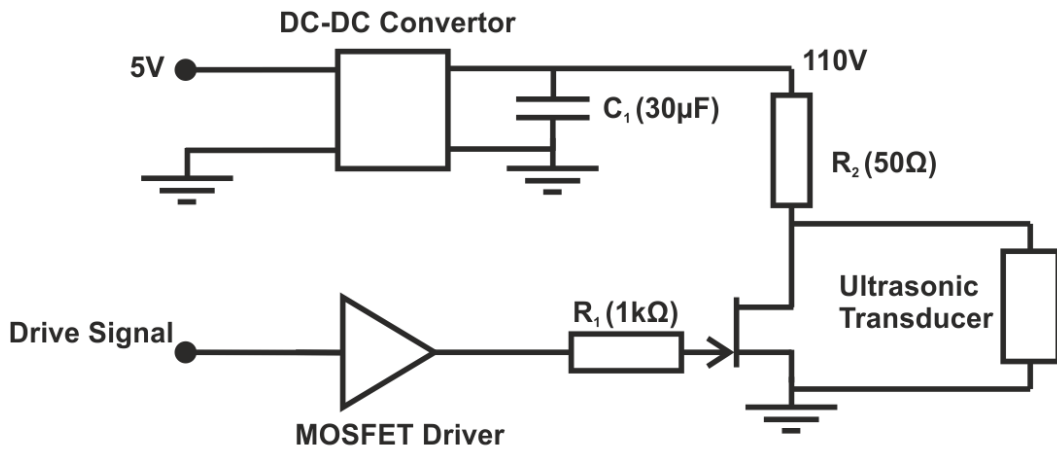
Figure 3.9 **Ultrasonic drive electronic schematic**

3.5.3 Acquisition Electronics

The acquisition electronics consisted of a single channel low-noise pre amplifier coupled to a high speed Field Programmable Gate Array (FPGA) Analogue to Digital Convertor (ADC). A USB connection is then established with the GPP, which then buffered and transferred the raw data to the host computer as shown in Figure 3.10.

Figure 3.10 AUT Ultrasonic acquisition structure

3.5.3.1 Pre-Amplifier system

The discrete pre-amplifier consisted of a single Analog Devices 8085 Integrated Circuit voltage feedback amplifier with a gain of 30. Biasing was provided by additional resistors R_2, R_3 and R_4.
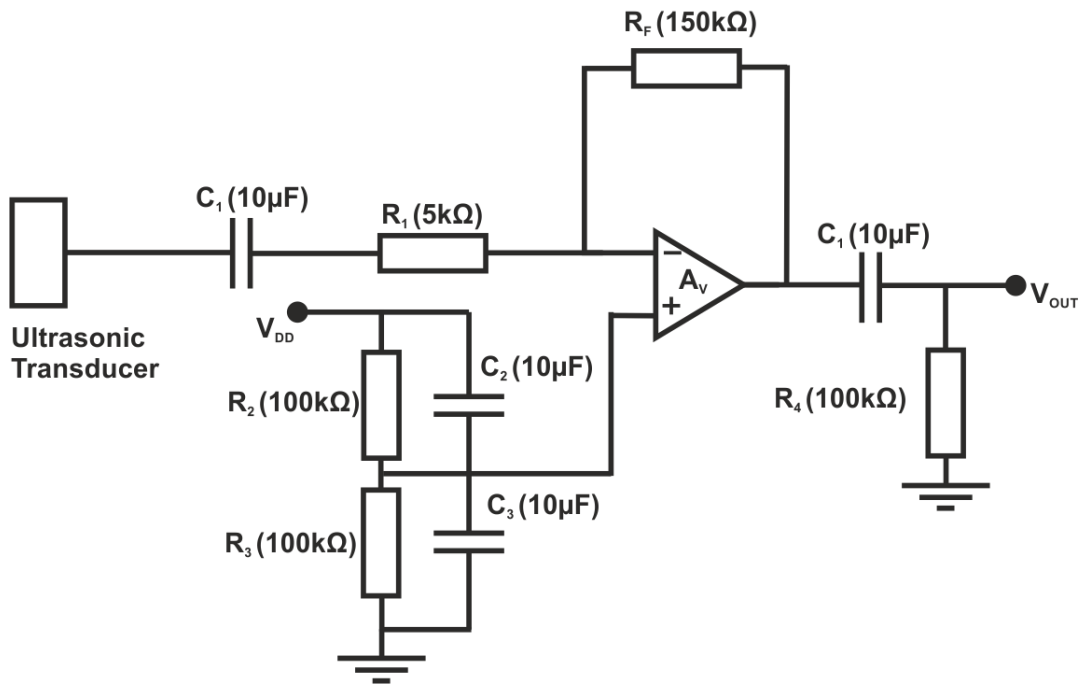
Figure 3.11 AUT RSA Ultrasonic pre-amplifier schematic

3.5.3.2 FPGA ADC system

The FPGA ADC system consisted of a KNJN Saxo-Q board, featuring an Altera EP2C5 core and four 8bit 200Msps ADCs [97]. This system uses USB for power and communication purposes. FPGA data acquisition software was written in Verilog [98] and currently supports sampling rates of up to 75MHz. Additionally a digital line out was utilised to trigger the digital drive firing signal circuitry.
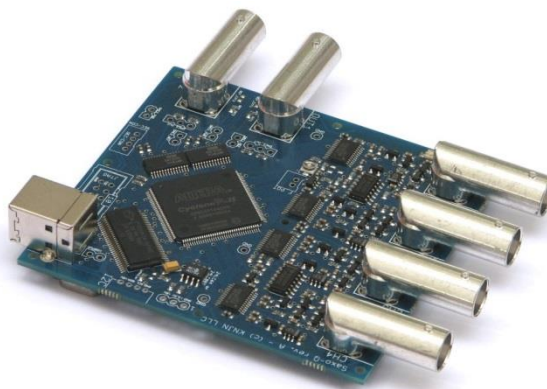
Figure 3.12 KNJN Saxo-Q [97]

3.6 AUT RSA Ultrasonic System Sample Performance

The AUT RSA ultrasonic system performance, including the combination of wheel probe, drive and receive electronics, was evaluated when transmitting into a laboratory calibration steel block of thickness 52 mm. The resultant ADC receive signal is shown below:
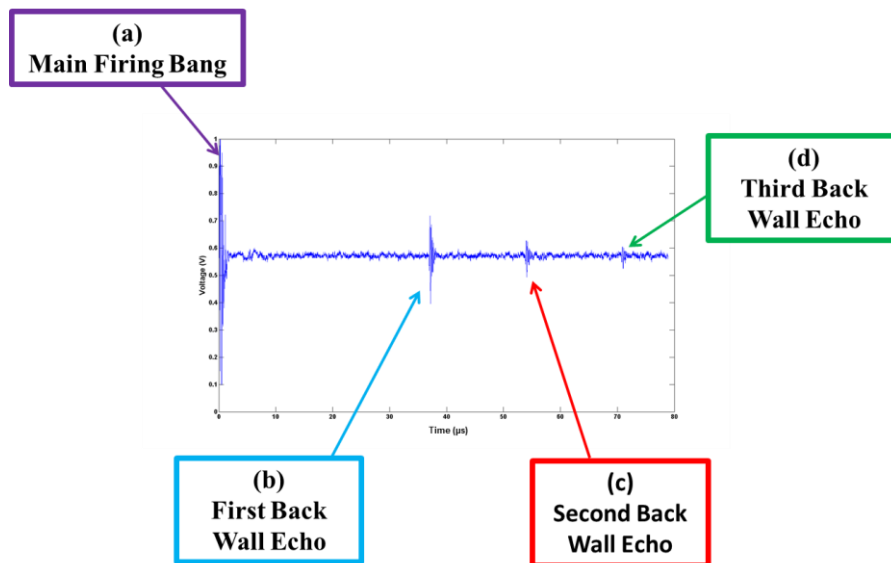
Figure 3.13 AUT RSA Sample Ultrasonic Acquisition

The thickness of the steel sample was evaluated, by determination of the time between the first and second back wall echo and knowledge of the standard speed of sound in steel being 6100 m/s [99]. The calculated thickness of the steel block was determined to be 51.58 mm with the Signal to Noise Ratio (SNR) being evaluated as 21.8 dB.

3.7 AUT RSA Software

The core software built upon the standard RSA suite, while implementing some minor additional changes to ensure correct operation of the AUT RSA.

3.6.1 Microcontroller

The microcontroller code was changed to incorporate the necessary low level commands to drive and control the active rear wheel based on the desired position and measured signals. Fundamentally the active rear wheel angle, defined as shown above in Figure 3.7, must match the motion of the front two wheels when undertaking non-uniform speed manoeuvres such as turns and arcs. Variations between the front drive wheel rotation speeds result in the robot following an arc trajectory, while knowing the offset of the central back wheel the resultant angle of the rear wheel can be calculated.

Additionally logic was incorporated to ensure that no forward wheel motion was undertaken when the rear wheel is rotating to a desired angle to match a distinct change in forward motion paths.

3.6.2 Embedded General Purpose Processor

The software on the embedded processor was altered to incorporate the necessary communication protocol and buffering required for the correct operation of the USB FPGA triggering and acquisition system. Furthermore the acquired raw UT signals were then relayed back to the RSA GUI host computer for further processing.

3.6.3 RSA GUI

The RSA GUI was modified to incorporate commands for single or repeat UT triggering. Plotting of the raw amplitude scans was available with the corresponding Hilbert transformed data [100]. With the correct input selection of the approximate speed of sound in the material the thickness of the material under inspection could be

estimated. All thickness mapping data could then be exported with corresponding known position data.

3.6.4 RSA API

The CUE RSAs feature an Application Programming Interface (API) simplifying the interface to the robotic platform into a small set of commands that can run from any programming language (C, C++, C#, Matlab, Labview etc.), removing the complexity of robot management, communications and integration of global positioning systems from the developer. [101]. Developers can access the API through a Dynamic Linked Library (DLL) in Microsoft Windows. The system structure is highlighted in Figure 3.14.
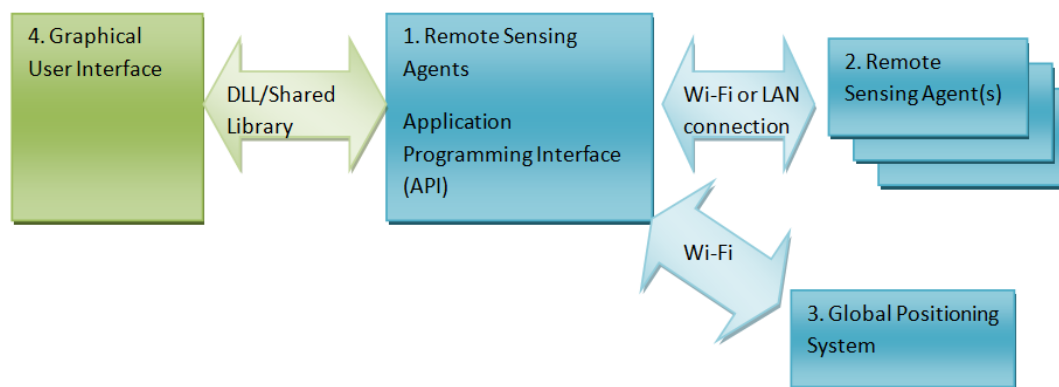
Figure 3.14 RSA API Structure [101]

Previous work has developed a suite of MATLAB commands that can access the API and control basic functions of the RSA [102]. This allows the RSAs to be both simulated and controlled from the MATLAB development environment.

3.6.5 RSA GUI Desired Coordinate Control

It was desired to add functionality to enable the AUT RSA to drive to defined points in planar space. A custom Extensible Markup Language (XML) encoding format was developed which delivered the required functionality.

50

Five variables are required to be transmitted with each set of desired coordinates and are shown below in Table 3.1.

Command	Structure	Description
X	Float	Desired X coordinate.
Y	Float	Desired Y coordinate.
θ	Float	Desired Theta angle for turn motions.
StopAtEnd	Boolean (1 = true)	Stop after reaching desired coordinates.
TurnOnSpotToFaceTarget	Boolean (1 = true)	Turn to face desired coordinates before moving in straight line motion.

Table 3.1 AUT RSA XML Commands

3.8   Conclusion

A novel differential drive robot platform incorporating an actively driven rear ultrasonic wheel probe was presented and discussed. Envisaged for constrained access remote ultrasonic mapping, the core mechanical, electrical and software design methodologies required to enable such a system were thoroughly discussed.

The AUT RSA platform is utilised later in Chapter 6 to highlight the combined benefits of both such a versatile platform and automated path planning strategies. The positioning and path accuracy, along with the Ultrasonic NDE measurement

system are evaluated and characterised under industrial sample conditions to quantify the platform performance.

The fundamental design permits autonomous mobile NDE research to be investigated with a platform which inherently is capable of undertaking a common manual inspection task.

Chapter 4

Aerial NDE

4.1 Aerial NDE

To offer additional practical solutions to common industry specific inspection requirements, further flexibility is required in terms of manoeuvrability, capability and accessibility from the current research theme of automated NDE using robotic vehicles. The introduction of an aerial platform allows many inspection tasks to be researched by fundamentally not constraining the inspection to surfaces of ferromagnetic material or level to gravity. Such a platform will readily allow the inspection of complex structures not only constructed from ferromagnetic metal but also common composite materials, in true three dimensional space.

Such dimensional flexibility undoubtedly offers significant advantages and movement options when considered in the context of not only inspection platforms, but also general robotic vehicles; however this flexibility comes at the cost of losing fixed known constraints in all planes. Such constraints found in other robotic platforms are the coordinate frames with respect to the surface to which it is attached, allowing points of end effectors in free space to be known relative to a fixed reference point. Aerial vehicles by their very nature are unconstrained in all of the primary parameters, notably vertical thrust generating lift, roll, pitch and yaw. These four variables allow the platform to move to any definite point in free space limited

only by the work volume and application specific designs of various platforms. In the context of inspection systems this lack of rigidity results in not only positional uncertainty in the normal X-Y plane but also in the Z axis.

The research interest and commercial usage of Unmanned Aerial Vehicles (UAV) has undergone buoyant growth in activity over the past decade. This progression can be attributed to many indirect factors, however key to this surge is the ever increasing view and viable use of such devices to provide remote controllable data acquisition platforms in areas often inaccessible and dangerous to human beings. Proven developments and improvements in sensor technologies, smart data processing techniques and power control systems have allowed credible aerial platforms to be developed and deliver the required performance to become commercially viable.

Growing attention has been given to low altitude aerial vehicles within the military, commercial and research communities over the past number of years. Such designs have been utilised to primarily investigate and research surveillance and mapping requirements in outdoor environments [103]. Within this context a variety of aerial vehicle designs have been utilised, equipped with sensing apparatus such as basic cameras, thermal, multi and hyperspectral imaging equipment, Radar and Lidar devices [104-105]. Such visual based sensor designs are traditionally employed due to their operation being minimally affected by the aforementioned pose uncertainty.

A number of organisations across the world offer aerial photography for a variety of purposes including inspection of overhead power lines [106] and flare stacks [106] while achieving high temporal and spatial resolution, using low cost and rapid

response equipment [108]. In outdoor situations large high payload capacity vehicles can be utilised that are able to hover within a volume of two hundred percent of its base volume without fear of collision [109]. Furthermore the widespread availability and satisfactory accuracy of current Global Positioning Systems (GPS) allow such platforms to be constrained to operate along waypoints and within applicable boundaries.

To operate such aerial platforms in indoor environments or confined outdoor volumes satisfactorily and safely requires a systematic re-evaluation of design, technology and implementation protocol. In such environments numerous constraints are imposed on aerial motion, notably the reduction in safe flying volume, entrance and exit accesses and the lack of a general positioning system. The solution to these problems requires research and development in system design, control, dynamic modelling, and range and motion sensing [109].

A robotic platform designed from the outset for automated aerial inspection activities necessitates a very distinct and specific specification and set of desirables, unique to the tasks and applications. This research has established a base of fundamental desirables specific to automated NDE.

4.2   Automated Aerial NDE Platform Desirables

1. **At all times feature stable controlled movement ensuring human and structural safety.**

   Critical to ensuring successful deployment of any NDE inspection technique is the ability to undertake the task involved with maximum safety, with

procedures in place to ensure no risk of injury or damage to humans, the environment or structures.

2. **Possess a level of hovering capability, to the minimum required by the specific sensor being deployed.**

   Due to the finite sampling time required for the majority of current NDE measurement techniques, the inspection platform must consequently ensure disturbances are minimised during inspection, by primarily ensuring minimal deviation in the six degrees of freedom of the platform.

3. **Have accurate knowledge of position and local environment in both indoor and outdoor situations.**

   Fundamentally required for robot path planning, collision avoidance and when considering NDE applications, the true location of any measured defects or areas of concern.

4. **Possess intelligent condition monitoring of on-board electro-mechanical components and high performance control algorithms.**

   Such control systems will ensure safe reliable operation, while safeguarding swift action in the unlikely event of a fault being developed.

5. **Be small enough in size for the given inspection task and access constraints, while featuring excellent manoeuvrability to allow for use in confined environments.**

   The resultant size of any aerial platform performing NDE inspection is application specific, dependant on parameters such as work volume, payload, runtime and access area.

6. **Be reliable, robust and possess adequate redundancy.**

   The platform must be capable of withstanding the minimum requirements found in typical inspection environments, while also ensuring reasonable component failure and damage will not compromise the integrity, execution and safety of the inspection.

7. **Feature advanced power efficient devices and features to ensure lengthy run times.**

   Optimisation of the energy efficiency of all electrical and mechanical components will ensure minimum energy usage, therefore maximising inspection and platform runtime.

8. **Payload capacity for transport of sensors and wheeled crawlers.**

   To maximise NDE leverage the platform must be capable of deploying a reasonable number of sensor technologies to maximise information through multiple sensor data fusion, in a similar manner to the current RSA platforms. Furthermore the option of transporting and deploying the RSA platforms at convenient locations in an inspection task would be a beneficial albeit application specific task.

Due to the demanding and somewhat conflicting desirables, a review of traditional and developed platform designs was initiated to gauge the performance and limitations of each design.

The principal requirements for any successful aerial vehicle are [110]:

To generate vertical upward motion the lift force must exceed the aerial vehicle's weight and be capable of being controlled. The propulsive thrust in a forward flight direction must be equal, or exceed the aerial vehicle's drag and be capable of being controlled. Additionally there must be control forces and moments, which are capable of altering the aerial vehicle's attitude in pitch, roll and yaw.

4.3 Balloon Based Vehicles

Aerial vehicles based around an envelope airbag filled with a less dense gas than air are considered the most simple in terms of set-up and design. These non-rigid, semi rigid and rigid designs date back to pre-1900 where extensive use was made of this type of aerial vehicle until the Hindenburg disaster of 1937 [111]. A number of independent actuators control the position of the vehicle by applying forces in the desired direction, whereupon a lighter than air gas such as helium fills the hollow structure. Recent research programs designing and utilising such designs have done so in both indoor and outdoor environments with a variety of measurement applications [112]. It has been shown that a modern large scale balloon structure of dimensions (1.1 x 0.6 x 0.6 m) giving a volume of the order of 0.4 m^3 is only capable of carrying 100 g payload while also requiring a typical manoeuvre and turning area of 25 m^2 in one plane [113]. As such these designs require a voluminous balloon structure to carry substantial payload as their lifting ability is directly related to the resultant air pressure surrounding them [111]. The low rate of change of the critical movement parameters in such a design has obvious control advantages; however this is obviously at the expense of manoeuvrability as stated above. Such a design features very poor external disturbance rejection from the effects of increasing wind

speed when flown in an outdoor environment. Under hover conditions such designs require little power to ensure the correct position of the vehicle is maintained within acceptable tolerances, giving extended run times in the order of hours as the lifting action of the gas is inherently and potentially of infinite duration. The disadvantages can nevertheless be accepted in specific applications where a large volume occupied with predominately free still air is available and large flight times are required.

4.4   Fixed Wing Aircraft

Fixed wing aircraft by their very nature utilise one or more fixed wings to generate the necessary lift force when travelling forward through air. Further mechanical linkages such as ailerons and stabilisers control the roll, pitch and yaw of the aircraft. While possessing excellent endurance characteristics, as demonstrated when operating in gliding mode, their fundamental design means they are unable to hover without secondary propulsion devices [114]. Such designs are not used traditionally in enclosed confined spaces due to their requirement for large take-off and landing areas if not modified again with specific secondary powertrain components.

4.5   Biologically Inspired

Insects and birds are classed as the most efficient flyers in the environment, with leading dynamics, manoeuvrability, speed and agility [115]. Furthermore their pronounced ability to handle large varying surrounding conditions such as wind turbulence ensures that much research has been undertaken in understanding their flight dynamics and methods of propulsion.

The normal method of mechanical actuation in such species is that of the flapping wing design, which using a number of complex unsteady aerodynamic phenomena allows the insects to produce lift and thrust forces several times their original size [116]. Additionally such designs exhibit the greatest potential for miniaturisation over other aerial platform designs; however there exists limited understanding of the aerodynamic effects at low Reynolds numbers. Many practical designs have been developed over a number of years [115-117], however they currently are far inferior to standard developed conventional aerial flight designs, when comparing payload, robustness and overall control.

4.6   Rotary Wing Aircraft

Rotary wing aircraft or rotorcraft feature one or more rotor blades configured in a specific arrangement whereupon rotation of the blades produces the required lift and movement forces. This design allows forward flight to be sustained at far lower velocities than possible with fixed wing aircraft, in fact being reduced to nil to allow the rotary wing aircraft to hover and feature vertical take-off and landing (VTOL). Through development and innovation many rotary wing aircraft configurations exist today each with their own merits and drawbacks, however they are all still governed by the same fundamental blade theory. The main rotary wing configurations are the conventional helicopter design, tandem, the coaxial model and evolutions of a quadrotor.

4.6.1   Conventional Helicopter

Conventional helicopter designs feature a single main rotor coupled to a smaller tail rotor. The rotation of the main rotor provides the required thrust and control in the

vertical plane. Furthermore adjusting and tilting the plane of action of the main rotor will allow control of the fore, aft and lateral movements while also controlling both pitch and roll. Yaw control is achieved through the horizontal force generated in the vertical plane by a smaller tail rotor as shown in Figure 4.1.

Vertical Flight

Direction of Motion
Thrust Vectors

Longitudinal Flight

Thrust Vectors
Direction of Motion

Lateral Flight

Direction of Motion
Thrust Vectors

Yaw Control

Rotor Rotation
Tail Rotor Thrust Vector
Main Rotor Thrust Vector
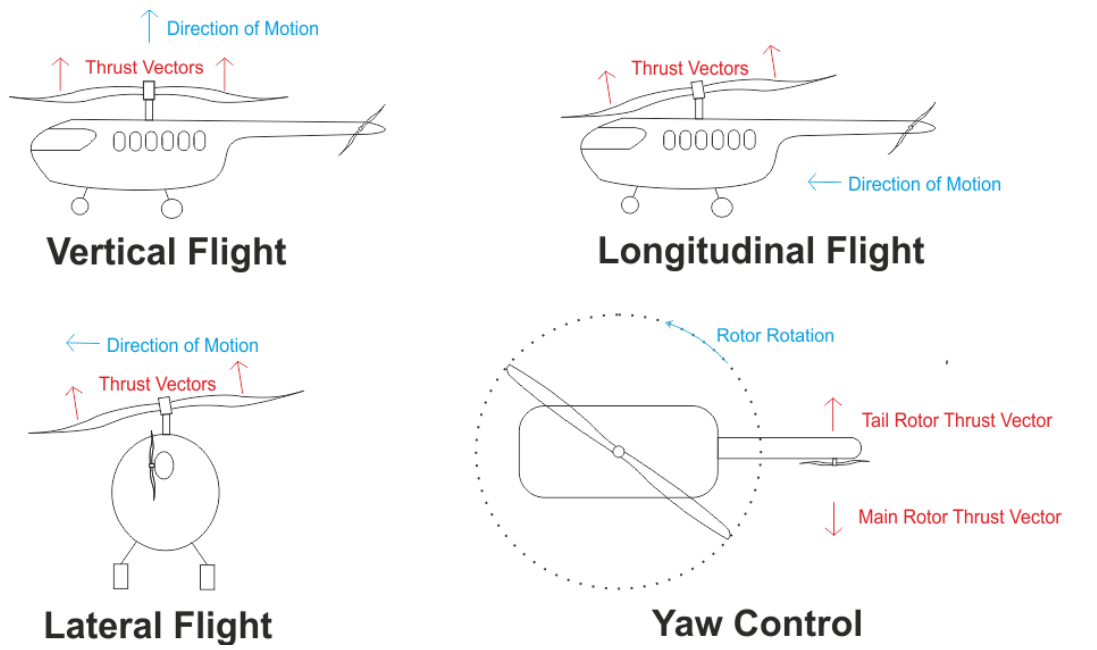
Figure 4.1 Conventional Helicopter Flight

4.6.2 Tandem Configuration

The tandem configuration features two main rotors located at opposite ends of the main chassis body. Vertical thrust and control is provided by both rotors simultaneously, while tilting the plane of action of each rotor controls movement in both roll, longitudinal and lateral directions. Differential control of both thrust and rotor tilt of each rotor controls the aircrafts pitch and yaw movements.

The rear rotor blades are mounted higher than the front blades to ensure that they rotate in as undisturbed air as possible to give satisfactory lifting performance. This however can give rise to undesirable effects when undertaking manoeuvres at slow

speeds and low altitudes as the aircraft can enter a nose up attitude, due to the rear motor sinking into the downwash of the front rotor blades [110].

4.6.3 Coaxial Configuration

The coaxial configuration features two rotor blades mounted vertically on the same axle. Vertical lift and control is again provided by the combined thrust of both rotor blades, while longitudinal, lateral, pitch and roll control is provided by tilting the plane of action of both blades. Yaw control is provided by differential rotor torques which can result in the undesirable effect of autorotation when descending [110]. Autorotation is the effect of lift forces altering their direction of rotation and then forcing the air to rotate the rotor instead, resulting in yaw control reversal.

4.6.4 Quadrotor Configuration

The quadrotor and its evolutions feature four or more rotor blades organised symmetrically along a parallel plane. Control of the vertical lift and movement is a result of the combined thrust of all rotors, while differential thrust between the front and rear rotors produce a pitch torque enabling longitudinal translation motion, similarly differential thrust between the left and right rotors produce a roll torque enabling lateral translation motion [118].
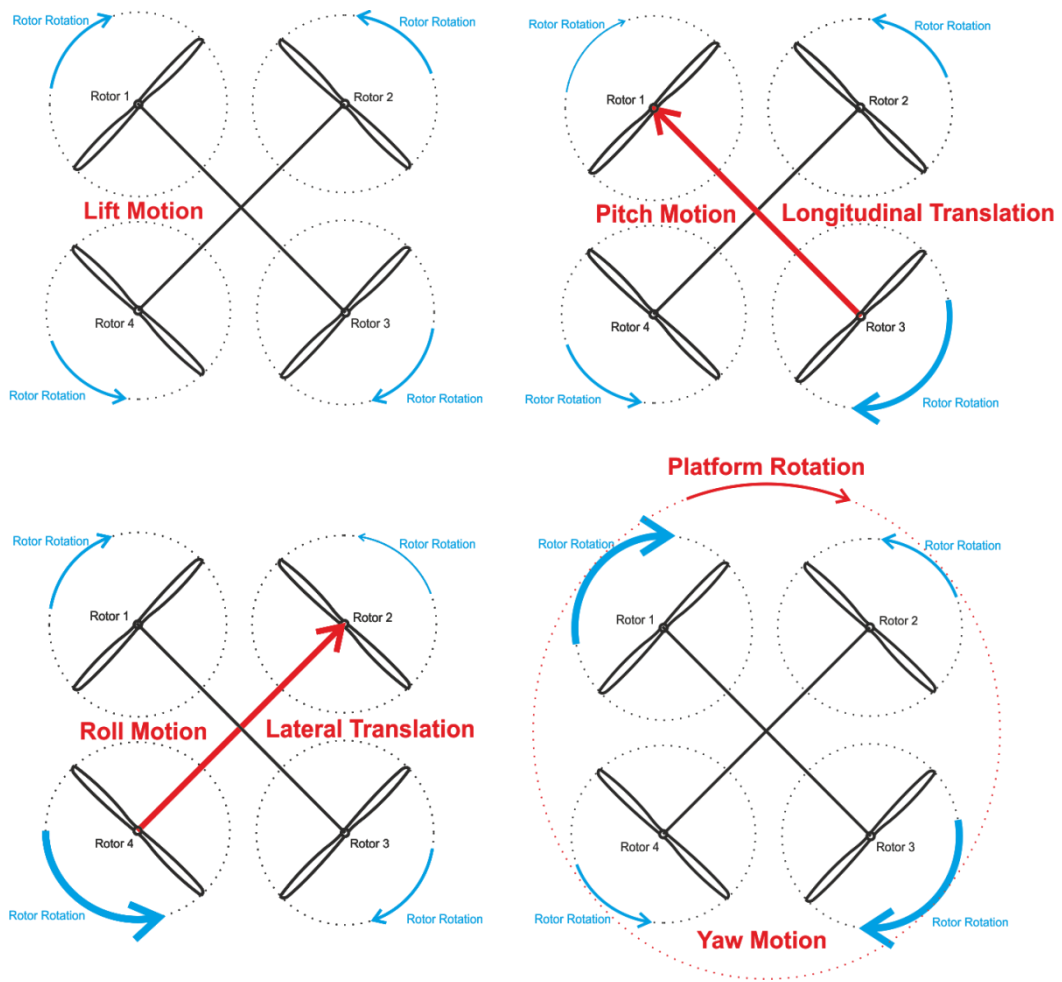
Figure 4.2 Quadrotor Flight Modes

Separate rotors spinning in opposite directions allow such designs to control aircraft yaw angle. While all blades rotating at the same velocity sum the reactive yaw torque to zero, changes in the speed of one of the clockwise or anticlockwise set of rotors will force the aircraft to rotate in the direction of the induced torque. This is illustrated in Figure 4.2.

4.7 Platform Comparison

When reviewing the desirables for a suitable aerial platform for NDE applications discussed in Section 4.2, a weighting factor was given to each of the key differing features, based on the author's perception of their importance to the overall strategy. For each desirable feature, a score based on the mechanism detailed below in Table 4.1 was awarded to the platform of highest ability judged by the author. For direct numerical comparisons all other platforms were allocated a mark in proportion to these bounds based on their own technical performance. The results of this scoring procedure are shown below in Table 4.2.

Score	Definition
0	Not compliant – Does not possess ability in respect of the specification desired.
1	Inadequate - Does not meet desired minimum specification in any area.
2	Below Acceptable - Does not meet minimum desired specification in all areas.
3	Acceptable – Adheres to minimum desired specification.
4	Good – Above minimum desired specification.
5	Excellent -No improvement required.

Table 4.1 Aerial Platform Scoring Mechanism

	Weighting	Fixed Wing Aircraft	Rotary Wing Helicopter	Rotary Wing Multiple Rotor	Balloon Based	Insect Inspired
Stationary Hover Flight	3	1	4	5	4	2
Low Speed Flight	3	1	4	5	5	3
VTOL	3	0	5	5	4	3
Reliability, Robustness and Redundancy	3	4	2	4	2	2
Indoor Usage	3	1	4	5	2	3
Safe Manoeuvrability	2	2	4	4	1	4
Endurance	2	4	2	2	5	2
Power Cost	1	3	2	2	5	3
Control Cost	1	3	2	3	5	2
Payload Capacity	1	5	3	3	1	1
Miniaturization	1	3	4	4	1	5
TOTAL		56	80	96	75	62

Table 4.2 Aerial Platform Comparison Matrix

From Table 4.2 it became clear that only a multiple rotor - rotary wing aircraft such as the quadrotor design could satisfy all the requirements and perform to the minimum desired standard. The Rotary Wing Multiple Rotor design features a number of advantages over conventional rotary wing aircraft, primarily negating the need for complex rotor actuation mechanical control linkages. The application of four or more thrust forces acting at a distance away from the centre of gravity can yield far more stable hovering capability than that found in conventional helicopter deigns, where one thrust force acts through the centre of gravity [119]. Furthermore the diameter of each individual rotor is considerably lower than that for an equivalent payload capacity conventional helicopter design, which lowers the stored kinetic

energy in each propeller in-flight mitigating the risk posed by such designs if involved in collisions [120].

Requirements such as safe and stable hover can be maximised through the usage of such rotary wing based designs, while redundancy can be achieved through the introduction of multiple similar function rotors. Payload capacity is greater than that of traditional helicopter designs of a similar area footprint [119], however due to the requirement of multiple rotors, such a footprint becomes reasonably large due to the constraints of the design. Multiple rotors require large energy requirements and hence endurance and run-time capabilities are reduced accordingly.

4.8   Rotary Wing Platform Modelling

To accurately allow a detailed understanding to be obtained of rotary wing multiple rotor aircraft, a complete mathematical model was developed from first principals.

The forces generated by gravity, inertia and air drag oppose platform motion, while the gravitational forces acting on the mass of the platform oppose vertical motion delivered by the thrust lift force from the rotating propellers. All lift forces can be assumed to be attributed to the rotating propellers, as both the horizontal velocity of the platform is low and the lack of considerable surface area on the platform to facilitate aerodynamic lift [109].

Inertial forces oppose both linear and rotary accelerations of the platform, assisting with the overall stability of the aerial platform. The mass of each motor located at the end of a solid lever from the centre of the platform generate inertia forces which resist pitch and roll angular accelerations. Furthermore further acceleration in both

pitch and roll can be contained by ensuring that the centre of gravity of the platform coincides with the aerodynamic pivot centre of the platform.

Air drag forces on the platform provide damping to both linear and rotational motion. Air drag forces are proportional to platform velocity, and can be neglected except for those in opposition to the rotation of the rotors, providing damping to rotor velocity and assisting disturbance rejection [109].

When considering fixed wing aircraft the lift or drag coefficients are based on the forward flight and wing area, however when considering rotary wing aircraft these assumptions are not applicable. Zero forward velocity in hover renders an infinite condition; therefore the rotor tip speed and complete swept rotor disc area are considered [110]. Thrust force is induced when a rotating propeller pushes air in the perpendicular direction to its plane of rotation. The airflow produces thrust to push the platform in reaction to the air drag force on the rotating propellers [109].

The thrust force (F_T) produced per rotary wing rotor is defined as;

$$F_T = \frac{1}{2}\rho A C_T r^2 \Omega^2 = K_T \Omega^2 \tag{4.1}$$

where ρ is the density of the air, A is the swept rotor disc area, C_T is the thrust coefficient, r is the blade radius, Ω is the angular velocity of the propeller and K_T is the thrust force factor.

Similarly the drag force (F_D), which acts parallel to the direction of blade motion;

$$F_D = \frac{1}{2}\rho A C_D r^2 \Omega^2 = K_D \Omega^2 \tag{4.2}$$

where C_D is the drag coefficient and K_D is the drag force factor.
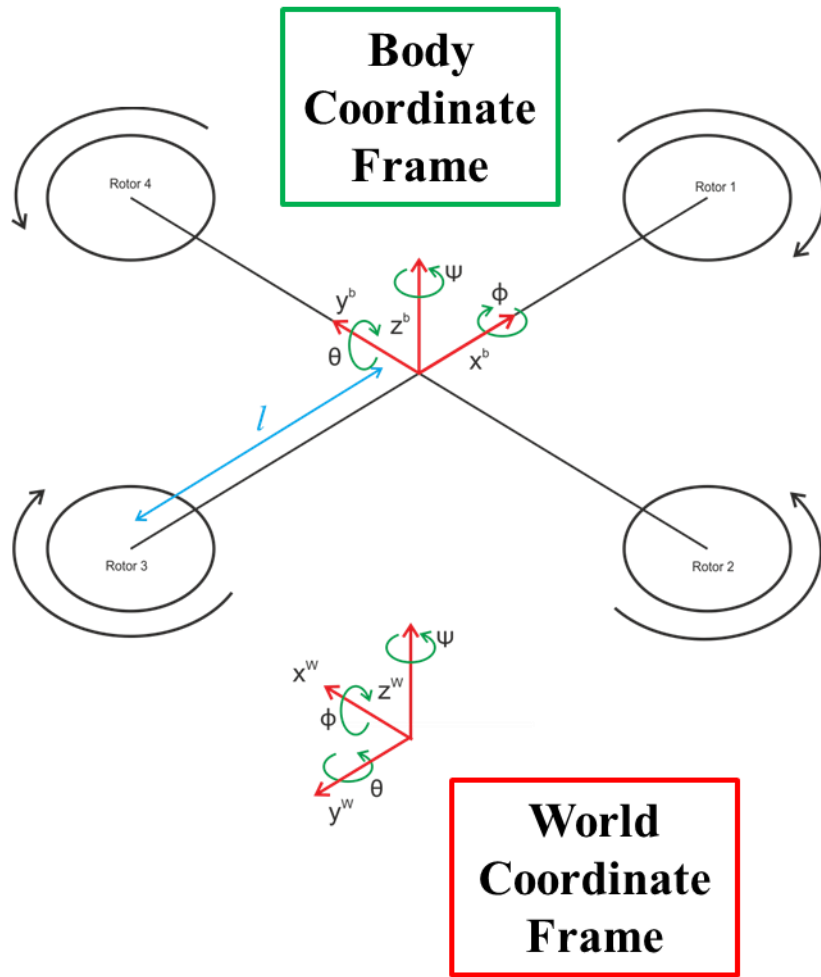
Figure 4.3 Quadrotor Configuration

Consider the rotary wing aircraft shown in Figure 4.3, with local body frame, expressed relative to the fixed world frame. The fundamental equations of motion relating to the aircraft can be developed with respect to the body coordinate frame, which coincide with the centre of mass of the vehicle. The dynamics of a rigid body under body force $f^b \in \mathbb{R}^3$ and torque $\tau^b \in \mathbb{R}^3$, when applied at the centre of mass of the vehicle, specified with respect to the body coordinate frame, is given by the following Newton-Euler form [121-122].

$$\begin{bmatrix} mI_{3\times3} & 0 \\ 0 & M \end{bmatrix} \begin{bmatrix} \dot{v}^b \\ \dot{\omega}^b \end{bmatrix} + \begin{bmatrix} \omega^b \times mv^b \\ \omega^b \times M\omega^b \end{bmatrix} = \begin{bmatrix} f^b \\ \tau^b \end{bmatrix} \qquad (4.3)$$

where $v^b \in \mathbb{R}^3$ is the body velocity vector, $\omega^b \in \mathbb{R}^3$ is the body angular velocity vector, $m \in \mathbb{R}$ specifies the mass, $I \in \mathbb{R}^{3\times3}$ is an identity matrix and , $M \in \mathbb{R}^{3\times3}$ is an inertial matrix

In order to compute the translational dynamics it is necessary to evaluate the forces acting on the body f^b. In the inertial frame, the centrifugal force (ω^b x mv^b) is nullified [123] and therefore:

$$f^b = \omega^b \times mv^b + mI_{3x3}\dot{v}^b = f^a + R_{WB}^T f^g \qquad (4.4)$$

where f^a is defined as the thrust forces acting on the airframe body, R_{WB} is the rotational matrix mapping the body frame to the world frame and f^g defines the acceleration due to gravity, expressed in the world frame.

Neglecting translational motion horizontal drag forces, f_a at hover is defined by;

$$f^a = \begin{bmatrix} f_x^a \\ f_y^a \\ f_z^a \end{bmatrix} = \begin{bmatrix} 0 \\ 0 \\ \sum_{i=1}^{4} F_{T\,i} \end{bmatrix} \qquad (4.5)$$

R_{WB} is given by;

$$R_{WB} = R_\psi R_\theta R_\phi = \begin{bmatrix} \cos\psi & -\sin\psi & 0 \\ \sin\psi & \cos\psi & 0 \\ 0 & 0 & 1 \end{bmatrix} \begin{bmatrix} \cos\theta & 0 & \sin\theta \\ 0 & 1 & 0 \\ -\sin\theta & 0 & \cos\theta \end{bmatrix} \begin{bmatrix} 1 & 0 & 0 \\ 0 & \cos\phi & -\sin\phi \\ 0 & \sin\phi & \cos\phi \end{bmatrix} \quad (4.6)$$

and f^g is defined as:

$$f^g = \begin{bmatrix} 0 \\ 0 \\ -mg \end{bmatrix} \qquad (4.7)$$

To express the acceleration of the platform in the world coordinate frame (F^W), the transformation of forces between the body-fixed frame and the world coordinate frame is given by;

$$\begin{bmatrix} F_x^W \\ F_y^W \\ F_z^W \end{bmatrix} = m \begin{bmatrix} \ddot{x} \\ \ddot{y} \\ \ddot{z} \end{bmatrix} = R_{WB}f^b = R_{WB}f^a + f^g \qquad (4.8)$$

Giving;

$$\ddot{x} = \frac{(cos\psi \sin\theta \cos\phi + \sin\psi \sin\theta)u_1}{m} \qquad (4.9)$$

$$\ddot{y} = \frac{(\sin\psi \sin\theta \cos\phi - \cos\psi \sin\phi)u_1}{m} \qquad (4.10)$$

$$\ddot{z} = -g + \frac{(\cos\phi \cos\theta)u_1}{m} \qquad (4.11)$$

where;

$$u_1 = K_T \sum_{i=1}^{4} \Omega_i^2 \qquad (4.12)$$

Similarly in order to compute the rotational dynamics of the platform, it is necessary to evaluate the torque moments on the platform.

$$\tau^b = \omega^b \times M\omega^b + M\dot{\omega}^b = \omega^b \times M\omega^b + \tau_a \qquad (4.13)$$

By inspection of Figure 4.3, τ_a is the torque applied on the airframe body along an axis, fundamentally being the difference in torque generated by each propeller on the other axis.

$$\tau_a = \begin{bmatrix} lK_T(\Omega_4^2 - \Omega_2^2) \\ lK_T(\Omega_3^2 - \Omega_1^2) \\ K_D(\Omega_2^2 + \Omega_4^2 - \Omega_1^2 - \Omega_3^2) \end{bmatrix} = \begin{bmatrix} lu_2 \\ lu_3 \\ u_4 \end{bmatrix} \tag{4.14}$$

where l is the length from the propeller centre to the platform pivot centre, in this case the centre of mass.

The cross product of $(\omega^b \times M\omega^b)$ is determined by:

$$\omega^b \times M\omega^b = \begin{bmatrix} \omega_x \\ \omega_y \\ \omega_z \end{bmatrix} \times \begin{bmatrix} M_{xx}\omega_x \\ M_{yy}\omega_y \\ M_{zz}\omega_z \end{bmatrix} = \begin{bmatrix} \omega_y\omega_z(M_{zz} - M_{yy}) \\ \omega_x\omega_z(M_{xx} - M_{zz}) \\ \omega_x\omega_y(M_{yy} - M_{xx}) \end{bmatrix} \tag{4.15}$$

Defining that:

$$\begin{bmatrix} \omega_x \\ \omega_y \\ \omega_z \end{bmatrix} = \begin{bmatrix} \dot{\phi} \\ \dot{\theta} \\ \dot{\psi} \end{bmatrix} \tag{4.16}$$

Therefore:

$$\tau^b = \begin{bmatrix} M_{xx}\ddot{\phi} \\ M_{yy}\ddot{\theta} \\ M_{zz}\ddot{\psi} \end{bmatrix} = \begin{bmatrix} \dot{\phi}\dot{\theta}(M_{zz} - M_{yy}) + lu_2 \\ \dot{\phi}\dot{\psi}(M_{xx} - M_{zz}) + lu_3 \\ \dot{\phi}\dot{\theta}(M_{yy} - M_{xx}) + u_4 \end{bmatrix} \tag{4.17}$$

Therefore the rotational dynamics of the platform are given by;

$$\ddot{\phi} = \left(\frac{M_{yy} - M_{zz}}{M_{xx}}\right)\dot{\theta}\dot{\psi} + \frac{l}{M_{xx}}u_2 \tag{4.18}$$

$$\ddot{\theta} = \left(\frac{M_{zz} - M_{xx}}{M_{yy}}\right)\dot{\psi}\dot{\phi} + \frac{l}{M_{yy}}u_3 \qquad (4.19)$$

$$\ddot{\psi} = \left(\frac{M_{xx} - M_{yy}}{M_{zz}}\right)\dot{\phi}\dot{\theta} + \frac{u_4}{M_{zz}} \qquad (4.20)$$

Equations 4.9-4.11 and 4.18-4.20 can therefore be utilised to appropriately model the translational and rotational dynamics of a basic fixed pitch rotary wing platform. These fundamental governing equations allow simulation and evaluation of design parameters such as blade area, motor thrust and frame design to be verified. It must be noted that although the above equations have been derived, no modelling or simulation was undertaken to ascertain flight performance and stability of such a design.

4.9 NDE Specific Aerial Platform Design

When considering the documented restricted access port diameter dimension (250 mm), introduced in Chapter 1 for access to confined volumes requiring inspection, the design of a novel bespoke platform primarily for automated aerial NDE was initialised. The desirable platform elements introduced in 4.2 were to be at all-times considered and ultimately define the overall platform specification. Rotary wing aircraft featuring eight or more rotors configured in certain arrangements feature inherent true redundancy ensuring continuous operation in the event of a motor or rotor failure, by having backup motor rotor combinations for each key function. As shown in Section 4.8, increases in motor power, rotor diameter and motor rotor combinations can allow the designer and operator to carry larger payloads by increased vertical force.

Due to Equation 4.1 it is clear that any decrease in blade radius r_{rotor} will cause a decrease in thrust due to the effective power four relationship from the radius r and area A terms. Therefore large scale reductions in blade radius were discouraged and efforts made to ensure maximisation of this parameter. Furthermore to ensure a feasible trade-off between the proportions of the platform and the potential payload, it was decided that the vehicle would not require to be operational while travelling through such a confined access port. This decision allowed for the integration and use of standard commercially available rotary wing propellers, reducing not only upfront capital cost, but also the substantial labour hours incurred in the complex development of custom propellers.

Again due to the complex blade theory and implementation of propellers operating in the wake of another propeller fixed above it, it was decided that all propellers should be reasonably free from turbulent disturbances from other nearby operational propellers. Therefore the design of fitting two propellers on the same vertical axis mounted with one above and the other below two separate motors was rejected.

Therefore when considering suitable designs which met all the required specifications and criteria, a narrow H-shaped structure was conceived which when fitted with standard eight inch propellers would be 230mm wide in shutdown mode, but still capable of carrying a substantial payload. This is illustrated in Figure 4.4.
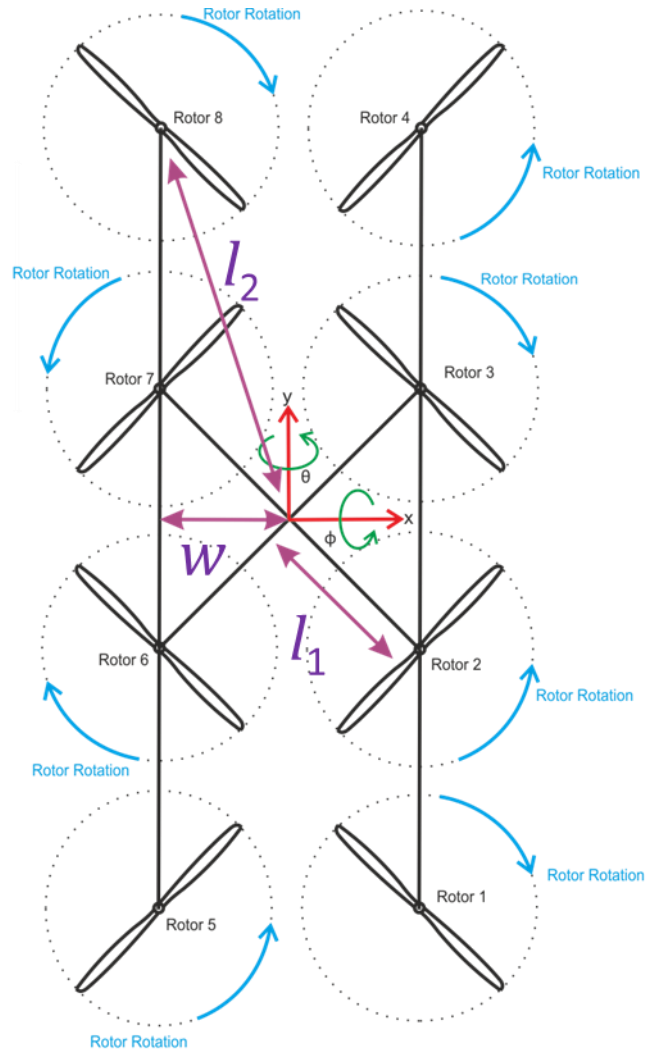
Figure 4.4 Bespoke Aerial Platform

The complete dynamic model was analysed and developed from first principals, following the same procedure as found in 4.8. The six independent equations of motion are given below:

$$\ddot{x} = \frac{(cos\psi \sin\theta \cos\phi + \sin\psi \sin\theta)u_1}{m}$$

(4.21)

$$\ddot{y} = \frac{(\sin\psi \sin\theta \cos\phi - \cos\psi \sin\phi)u_1}{m}$$

(4.22)

$$\ddot{z} = -g + \frac{(\cos\phi \cos\theta)u_1}{m}$$

(4.23)

The rotational dynamics are again computed as show in 4.8 and based on the distances from the respective rotor centre to the platform pivot centre.

$$\ddot{\phi} = \left(\frac{M_{yy}-M_{zz}}{M_{xx}}\right)\dot{\theta}\dot{\psi} + \frac{l_1}{M_{xx}}u_{2A} + \frac{l_2}{M_{xx}}u_{2B} \tag{4.24}$$

$$\ddot{\theta} = \left(\frac{M_{zz}-M_{xx}}{M_{yy}}\right)\dot{\psi}\dot{\phi} + \frac{w}{M_{yy}}u_3 \tag{4.25}$$

$$\ddot{\psi} = \left(\frac{M_{xx}-M_{yy}}{M_{zz}}\right)\dot{\phi}\dot{\theta} + \frac{u_4}{M_{zz}} \tag{4.26}$$

Where:

$$u_1 = K_T \sum_{i=1}^{8} \Omega_i^2 \tag{4.27}$$

$$u_{2A} = \left((\Omega_7^2 + \Omega_2^2) - (\Omega_6^2 + \Omega_3^2)\right) \tag{4.28}$$

$$u_{2B} = \left((\Omega_8^2 + \Omega_1^2) - (\Omega_5^2 + \Omega_4^2)\right) \tag{4.29}$$

$$u_3 = K_T\left((\Omega_5^2 + \Omega_6^2 + \Omega_7^2 + \Omega_8^2) - (\Omega_1^2 + \Omega_2^2 + \Omega_3^2 + \Omega_4^2)\right) \tag{4.30}$$

$$u_4 = K_D\left((\Omega_2^2 + \Omega_4^2 + \Omega_6^2 + \Omega_8^2) - (\Omega_1^2 + \Omega_3^2 + \Omega_5^2 + \Omega_7^2)\right) \tag{4.31}$$

Again equations 4.21-4.26 can therefore be utilised to appropriately model the translational and rotational dynamics of the custom fixed pitch rotary wing platform. With such a unique design comprehensive modelling and simulation of the overall platform dynamics and stability would be worthwhile. With such an undertaking design parameters such as blade area, motor thrust and frame design, with respect to optimum platform length and width could be identified.

Due to the extensive resourcing and time required to sufficiently simulate and optimise the custom bespoke platform design, it was decided to review commercially available fixed pitch rotor platforms with a view to ascertaining their suitability and performance for initial automated aerial NDE investigations.

4.10 Commercial Aerial Platforms

A detailed review was undertaken on commercial multi-rotor platforms to ascertain their capability and performance with a view to accelerate aerial based NDE research on proven platforms.

A conservative specification was imposed on the required payload capability to ensure future expansion and capacity. Mounting specific machine vision photographic equipment ($\approx$ 300-350 g) [124] and a laser range finding unit ($\approx$ 160 g) [125] on the platform to perform 3D mapping, sensing and inspection, would require a minimum of 500 g of payload capacity. To comfortably accommodate these required components and an element of expansion, a minimum payload capacity of 600 g was considered desirable while also ensuring reasonable performance in other areas such as flight time, purchase cost and manoeuvrability.

4.10.1 Draganfly Innovations

The Draganfly X6 [126] and X8 [127] are six and eight rotor configurations of the rotary winged aircraft respectively. These designs feature two rotors mounted in the same axis of rotation, each separately driven by a motor above and below the other respectively.

The X8 platform has recently been developed and released featuring redundancy and a payload capacity of 1 kg. This state of the art commercial system features Draganfly specific on-board stabilization software and control systems, with the capability for numerous third party optical sensors. The device itself spans a width of 1060 mm while being 320 mm high.

Figure 4.5 Draganfly X8 [127]

4.10.2 Ascending Technologies

Ascending Technologies are a German company that focuses on producing high performance aerial vehicles for commercial and research use. The minimum required payload (>500g) discussed above, discounts all but two of the research platforms. Their Pelican platform [128] is a four rotor design capable of carrying a payload of 500g and runs for 25 minutes unloaded.

The Pelican (651 x 651 x 188 mm) utilises an Intel atom processor for all on-board processing and as such would require new specific software to be developed from that developed on the Linux based RSA system. Ascending Technologies specific software can be used to control the platform along a series of predefined waypoints; however any modifications to this would require software modifications through a

supplied Software Development Kit (SDK). The Pelican is currently utilised as the preferred platform at numerous academic institutions for aerial based research [129-130].
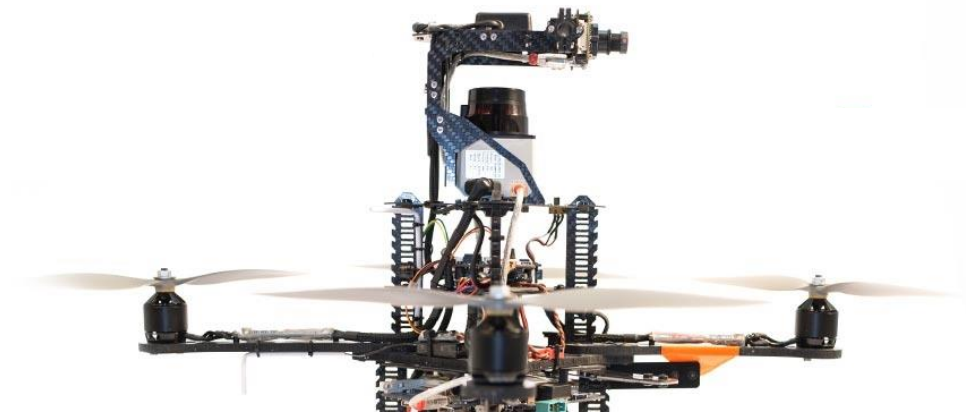
Figure 4.6 Ascending Technologies Pelican [128]

The Firefly is a newly developed platform with six rotors featuring a patented redundant propulsion system which allows controlled flight even with the loss of one rotor. Featuring a payload capacity of 600 g and wind load capacity of 10 m/s it further benefits from a frame in frame concept to decouple the IMU sensor and payloads from the vibration inducing motors [131]. This mechanism allows improved stability and payload dynamic performance, while only being 665 mm wide and 165 mm high. Furthermore the platform can be fully programmed via its on-board ARM microcontroller and a dedicated Intel based CPU for higher computational tasks.

Figure 4.7 Ascending Technologies Firefly [131]

The Falcon 8 is Ascending Technologies only commercial platform [120], commonly selected for aerial photography applications. This novel v-shaped design can fly outdoor in winds of up to 10m/s and features an uninterrupted field of view for typical optical sensors. This eight rotor deign can lift 500 g payload for 18 minutes, while being 770 x 820 x 125 mm in size and is currently utilised for industrial flare stack and power line inspection [48].

Figure 4.8 Ascending Technologies Falcon 8 [132]

4.10.3 Microdrone

Microdrone is another German company that specialise in the design and production of high quality aerial platforms. They currently produce two quad-rotor based designs with varying payload capability. One such design only carries an insufficient 200g while the more suitable design is capable of lifting 3000 g [133]. However this

impressive lifting potential is achieved through the use of large diameter rotors, and therefore a substantial frame volume of 2052 x 1880 x 360 mm. This very specific vehicle with impressive lifting capability features lengthy run times ($\approx$ 45 minutes) and inherently is ideally only suitable for outdoor use.

Figure 4.9 Microdrone Aerial Platform [134]

4.10.4 Mikrokopter

MikroKopter is a modular multi-rotor system, with the capability of designing, building and operating unique aerial platforms from 4 to 12 motors [135]. This open source system has a very large and growing internet community which actively contribute to both software and hardware. They currently sell a wide range of components to allow construction of a number of generic kits, while also having the option of designing and developing customisable and application specific platforms. Quad, hex and octo rotor configurations are available each with a highly varied lifting capability and run time depending on the power and drivetrain component

selection. The eight rotor set, approximately 780 mm wide and deep with a height of 400 mm, features inherent redundancy and a lifting capability of 1 kg while also being capable of running 25 minutes unladen [136].

Figure 4.10 MikroKopter Okto-Kopter [136]

4.10.4.1 Mikrokopter Okto-Copter

The core of the Okto-copter electronic platform [136] is an Atmel 8bit microcontroller to perform all necessary control functions. A 6 D.O.F. IMU containing a 3 axis gyroscope and accelerometer provide the necessary tilt, acceleration and rotational sensing capabilities. The mechanical actuators used within the design are ten inch fixed pitch propellers coupled to eight brushless DC motors, offering greater efficiency, power to weight ratio and longer lifetime than traditional brushed DC motors. The design principal utilises a fixed armature with permanent magnets attached to a freely rotating outer structure. There is no mechanical commutator, instead the function is provided through electronic means using eight 8bit motor controllers, outputting a tri-phase signal based on the rotor's position acquired through back-electromotive force measurement [136]. High

capacity lithium polymer batteries provide the power to satisfy the requirements of the system. The system structure is illustrated in Figure 4.11.
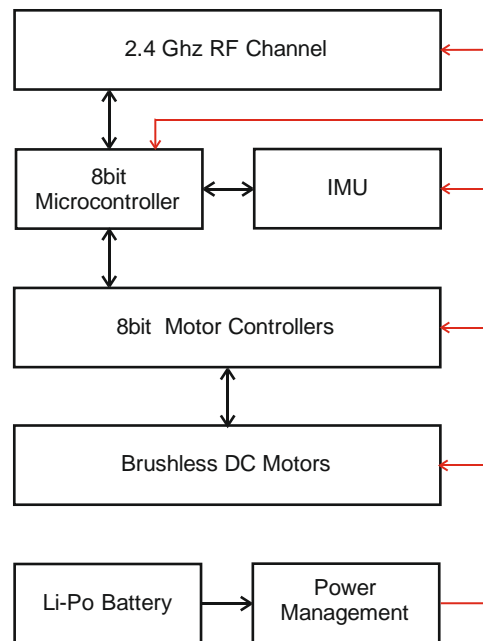
Figure 4.11 MikroKopter Okto-Kopter Electronic System

4.11 Platform Considerations

As shown above there exists many commercial fixed pitch multi-rotor platforms with the required payload capability specified in Section 4.10. The increasing range of commercial platforms currently available highlights the overall trend in the market with respect to increased use and deployment of such systems as shown in [106,107].

The above commercial platforms were assessed in terms of their specification and performance, with respect to the aerial NDE platform desirables documented in Section 4.2 and in particular on those that were deemed measurable given the information freely available.

Using the aerial platform scoring mechanism introduced in Table 4.1 each platform
was ranked with respect to the specification desirable as noted in column 1 of Table
4.3

	Draganfly X8	Ascending Technologies Pelican	Ascending Technologies Firefly	Ascending Technologies Falcon 8	Microdrone md4-3000	Mikrokopter Okto-Copter
Payload Capacity (Highest desired)	4	3	3	3	5	4
Dimensions (Smallest desired)	3	5	4	3	1	3
Redundancy	5	0	5	5	0	5
Indoor Usage (Recommended)	2	4	4	2	2	2
Outdoor Usage (Recommended)	5	1	1	5	5	1
Endurance (Longest run-times desired)	3	3	3	3	5	3
Open architecture (Open desired)	3	5	5	3	5	3
On-board processing power (Greatest desired)	3	3	5	3	3	2
Inspection sensing modalities	3	3	3	3	3	3
Localisation strategies (Highest accuracy desired)	2	3	3	2	2	2
Path planning strategies (Coverage desired)	2	2	2	2	2	2
On board electro-mechanical component monitoring	3	3	3	3	3	2
Cost (5 = Lowest)	2	4	3	2	2	5
TOTAL	40	39	44	39	38	37

Table 4.3 Commercial Aerial Platform Comparison

As shown in Table 4.3, although platforms exist which feature strong performance in
areas such as payload capacity, redundancy and indoor and outdoor usage
characteristics, no commercial platform possess exceptional performance in areas
such as localisation, path planning and inspection sensing modalities.

It is worth mentioning that all of the platforms above have support for non-contact
visual sensing systems such as DSLR cameras, however no solution exits for contact

based measurement sensor deployment from such platforms. Additionally no clear quantifiable measurement data exists, or is provided, with respect to platform position and path accuracy, which will ultimately dictate the feasibility and concept of surface contact based aerial NDE sensing.

Therefore the focus of this body of work is to ultimately characterise and quantify these positional parameters for currently available flight technology systems and therefore not focus directly on platform mechanics and designs. There exists clear opportunity for research in not only the NDE sensing domain but also in novel platform systems for improved flight performance and control. Ongoing research in areas such as platform designs[137], platform localisation [138] and control strategies [139] have been documented and continue to be undertaken. As shown in [131] novel designs can reduce power consumption requirements while still featuring redundancy, while the introduction of ducting systems, surrounding the rotors, offers potential for reduced turbulent flow and ultimately higher positional stability [140].

4.12 CUE Aerial Sensing Agent (ASA)

Given the desire to quantify the positional accuracy of such multi-rotor platform deigns, for potential automated NDE tasks, it was necessary to obtain a platform to deploy and characterise. Given the budget financial constraints and relatively high recommended retail price of commercial systems, the skillset of personnel involved in the project and the ultimate desire for an open and flexible system architecture, for future research tasks, a decision was made to specify and then construct a multi-rotor device.

For simplicity and given the ample volumetric space of the laboratory, a four rotor fixed pitch configuration, high performance, platform was designed and the necessary components specified for research purposes in the field of aerial NDE.

In collaboration with an Electronic & Electrical Engineering (EEE) undergraduate individual project [141] the integration and control of the specific high performance aerial aircraft hardware was undertaken. The platform is shown below in Figure 4.12.

Figure 4.12 CUE Aerial Sensing Agent (ASA) [141]

4.11.1 CUE ASA System Architecture

This quad-rotor specification features four 10x45 composite propellers each driven by a brushless motor similar to those utilised in the commercial Microkopter platform [142]. These were driven by corresponding high update rate 40A Electronic Speed Controllers (ESC) [143].

Power is provided by a four serially connected lithium polymer cells, giving a 2200 mA/h 14.8 V battery and allowing an approximate 20 minutes runtime with a

payload capacity of 650 g. The quad-rotor computational processing, control and stabilization was undertaken by an Openpilot Copter Control 3D (CC3D) platform running an STM32 32-bit microcontroller running at 90 MIPs with 128 KB Flash and 20 KB RAM [144].

The current UoS RSA electronic system platform discussed in Section 2.7 was utilised for communication and NDE data acquisition purposes. Control and operational information is passed through Serial Peripheral Interfaces (SPI) from the UoS RSA system to the on-board flight control system (CC3D) of the aerial platform.

A custom C# external GUI has been implemented to allow the operator to enter desired flight and inspection parameters such as position, pose and scan paths, while also allowing digital graphical visualisation of the position information within a limited 2D world to be recorded. The GUI is capable of accessing live VICON object motion data through a standard TCP/IP link. The Wi-Fi protocol is utilised for communication between the host computer running the GUI and the aerial platform.

The system structure and architecture is shown below in Figure 4.13.
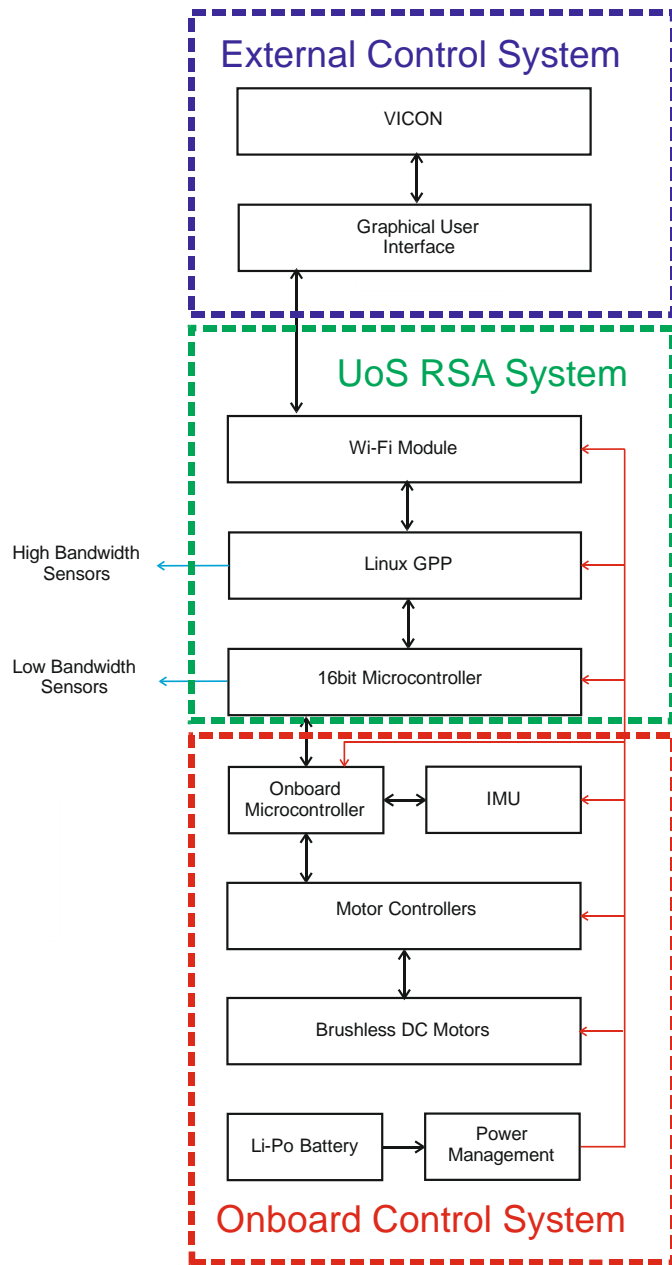
Figure 4.13 CUE ASA System Structure

4.13 Visual Aerial NDE

Visual methods of surface examination can be critical in detecting many serious structural strength defects along with more common structural issues such as weld defects [6]. Such systems if deployed correctly to the point of interest can provide a rapid surface scanning solution.

The positional freedom and uncertainty of aerial platforms result in visual sensing being the favoured technique for aerial inspection - either by analysis of high resolution stills or post processing of stitched images [145-146]. However it must be noted that visual inspection methods possess inherent drawbacks and practical limitations such as variation of lighting and conditions, spurious reflections and intensive data processing [147-148].

When considering aerial NDE, visual methods are important for not only traditional inspection applications but also for position estimation and localisation approaches. Research work undertaken in CUE has highlighted this approach, albeit on the RSA platform and showed significant potential as an on-board absolute positioning strategy [17].

4.12.1 Vision System

After a detailed review a machine grade vision camera compatible with the current electronic and software system was selected [149]. One of the key features of the chosen device is its global shutter function, which ensures each pixel is receiving light for the exact same amount of time, reducing the presence of artefacts and

motion blur. Furthermore the use of larger higher sensitivity pixels allows the device to perform well in extremely low light conditions, with reduced digital noise.

To optimise the current electronic and software system, while also ensuring maximum performance of the visual camera system, it was decided to make use of the on-board Digital Signal Processor of the OMAP system [150]. This device, while physically present, is not supported in the standard software distribution, therefore seriously limiting its ease of potential usage. Therefore to enable the specialised hardware, extensive tools and libraries were sourced, acquired and utilised to ensure the device was set-up and functional on commencement of sensor development (Figure 4.14).
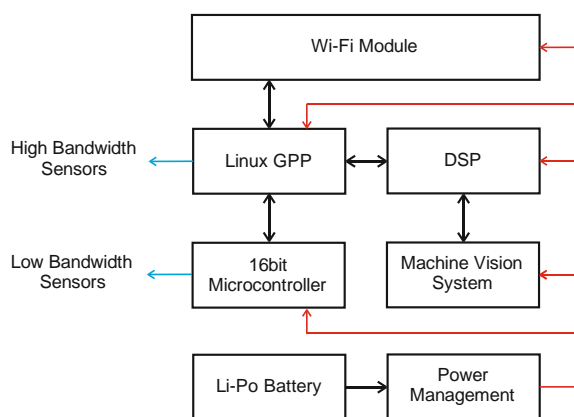
Figure 4.14 OMAP Based Vision System Structure

4.14 Closed Loop Position Control

4.13.1 Platform Closed Loop Control Strategy

By acknowledging that primary human control is undesirable when operating specialised automation equipment such as an aerial NDE platform, it becomes

necessary to apply closed loop intelligent control systems to control platform pose. Human control can be affected by a number of issues, such as motivation, tiredness and concentration, all which have a detrimental effect on task safety and quality [151-152]. Furthermore intelligent automation control systems can offer reaction times that are far shorter than available from humans, offering finer positional accuracy and therefore stability [153].

A closed loop positional strategy was developed for both platform position(X,Y,Z) and platform orientation (Ψ,θ,ϕ). The overall control methodology and strategy implemented is shown below in Figure 4.15.
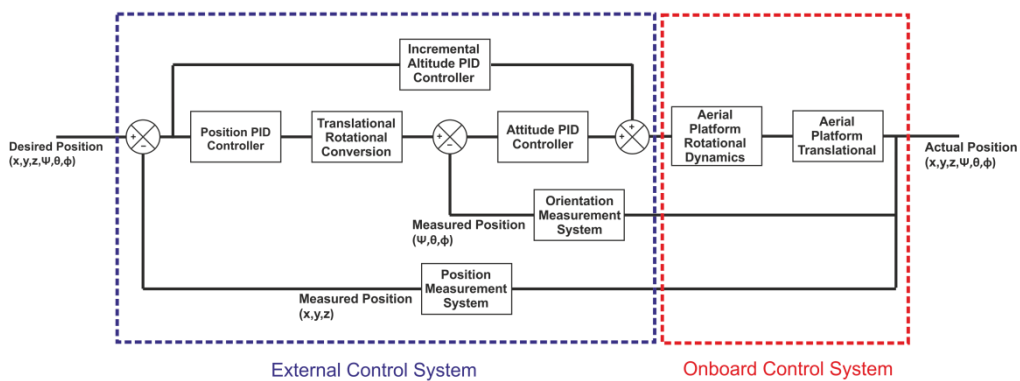
Figure 4.15 Closed Loop Positional Control Structure

The control system implemented is that of a cascaded multi-loop type where the first controller base output is the reference set-point for the attitude difference calculation. The error in attitude is the second PID controller input which controls the overall attitude of the platform. Through attitude motion, the platform translational motion varies, which when measured provides the necessary negative feedback. Desired coordinate position and pose values are the reference inputs to the negative feedback control system.

Through such a control strategy the 6 DOF pose of the platform can be controlled and specified, through the indirect updating of individual overall thrust, roll, pitch and yaw values.

Due to their robust performance and functional simplicity PID controllers were chosen and implemented within the overall control strategy [154]. The controller action is derived by considering the magnitude of the output to input error, its accumulation (integral) and its rate of change (derivative). The controller is tuned by altering the effect of each of these components through three gains *KP*, *KI* and *KD*.

Altitude and therefore position in the Z-axis is controlled through a parallel single control loop. The error in Z position, derived from the reference and actual measured position, is the input of a single PID controller which updates the gas input of the platform to simply alter and control the altitude. An incremental PID controller is selected as the effect of vertical thrust does not accumulate.

The measurement system measurand could be either the 6 D.O.F. information being measured by a system such as the VICON Motion Capture System (VMCS) (Appendix A.2) or 3 D.O.F. positional data being captured by a device such as the Laser Absolute Tracker (LAT) (Appendix A.3) along with the platform's on-board inertial sensors providing the orientation angle information.

4.15 Platform Closed Loop Control Development

Bespoke C# software was developed to implement the closed loop control methodology presented in Section 4.13.1 and highlighted in Figure 4.16. Initially the

6 D.O.F. platform pose information was acquired and provided by the VMCS tracking system for simplicity reasons.

Desired waypoint commands can be loaded singly or in a serial fashion for multiple desired positions. A scan path can then be defined using a number of consecutive discrete waypoints.

Due to logistical and performance considerations the CUE ASA platform was chosen to initially be deployed under the closed loop control methodology strategy.

All PID controllers were manually tuned to ensure a satisfactory response speed and minimum overshoot when travelling along a path to a desired waypoint.

4.16 System Specific Performance

4.15.1 Hover Stability

As discussed in Section 4.2 a credible aerial NDE platform must possess a satisfactory level of hovering capability to account for the finite sampling time required for accurate NDE sensor measurement. Therefore a hover stability test was undertaken to analyse the platform performance and stability, coupled to its ability to reject unwanted external disturbances.

The user selectable X-Y origin was approximately set offset to the centre of the measurement volume frame as shown below in plan view in Figure 4.16. This convention was continued for all subsequent aerial investigation
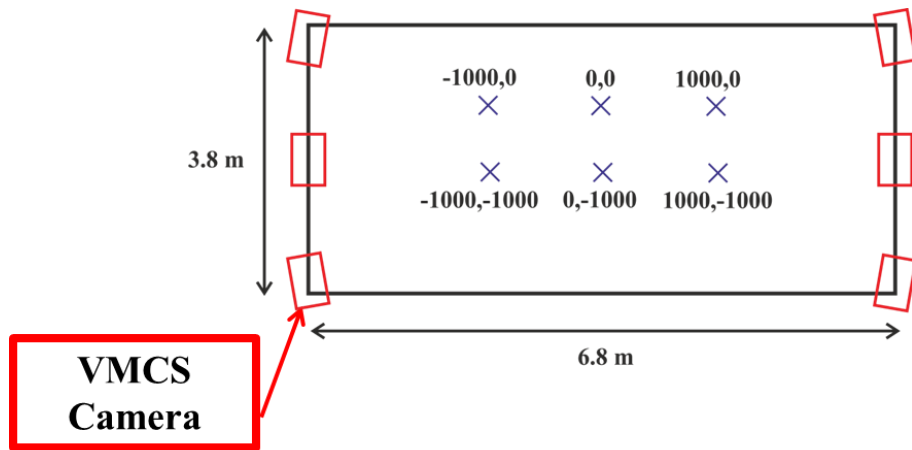
Figure 4.16 Origin Setting within Measurement Volume

The root mean square error (RMSE) of each position parameter are shown below in Table 4.4 when undertaking a hover test at desired coordinates (0,0,1000) mm for 300 seconds. This time is measured to begin from the first moment the Cartesian position of the platform passes through the desired position. The choice of hover time (300 seconds) was arbitrary to highlight long term platform stability.

Position Parameter	Root Mean Square Error
X	10.03 mm
Y	7.56 mm
Z	14.41 mm
Roll (Ψ)	0.33 °
Pitch (θ)	0.52 °
Yaw (Φ)	1.28 °

Table 4.4 CUE ASA 300 Second Hover Performance

4.15.2 Positional Performance

To characterise and ascertain the positional accuracy performance of the aerial vehicle when undertaking an indoor NDE inspection, a series of hover tests were undertaken at six distinct locations throughout the VMCS measurement volume.

4.15.2.1   500 mm Altitude Flight

The six locations are shown in Figure 4.18 in reference to the measurement volume, whereupon a 15 second hover was undertaken at a plane of desired height 500mm. Similar to the above hover test the time was measured to begin from the first moment the Cartesian position of the platform passed through the desired position. The choice of shorter hover time (15 seconds) was chosen to replicate the time to undertake a typical NDE measurement.

The mean pose of the platform through this 15 second duration is recorded in Table 4.5 along with the resultant XYZ 3D distance to the desired location. Table 4.5 therefore records the systematic error of the platform.

The mean error for all position parameters (X,Y,Z), is calculated and shown in Table 4.6, along with the standard deviation for each axis. Additionally the RMSE distance to the mean platform pose is shown alongside in Table 4.6.

Similarly the mean and standard deviation for platform orientation parameters (Ψ,θ,ϕ) is shown in Table 4.7.

Desired Position (x,y,z) (mm)	Mean Pose						Mean Position XYZ Error (mm)
(Ψ & θ & $\Phi = 0^\circ$)	X (mm)	Y (mm)	Z (mm)	Ψ ($^\circ$)	Θ ($^\circ$)	Φ ($^\circ$)	
0,0,500	+5.65	-2.06	483.94	-0.58	+0.17	-0.92	17.15
1000,0,500	1012.50	-1.95	483.85	-0.85	-0.18	-0.60	20.52
1000,-1000,500	1018.02	-1004.61	484.22	-1.08	+0.45	-0.99	24.39
0,-1000,500	+14.90	-1002.90	485.39	-0.95	+0.34	-0.63	21.07
-1000,-1000,500	-990.05	-1001.93	485.96	-0.76	+0.22	-0.43	17.32
-1000,0,500	-994.33	-1.78	484.74	-0.58	+0.17	-1.24	16.38

Table 4.5 CUE ASA 15 Second Hover Mean Pose

Desired Position (x,y,z) (mm)	Mean Error (mm)			Standard Deviation (mm)			RMSE (mm)
(Ψ & θ & $\Phi = 0$)	X	Y	Z	X	Y	Z	
0,0,500	+5.65	-2.06	-16.06	2.49	5.81	3.80	7.38
1000,0,500	+12.50	-1.95	-16.15	3.02	5.43	3.27	7.02
1000,-1000,500	+18.02	-4.61	-15.78	2.74	2.27	2.94	4.62
0,-1000,500	+14.90	-2.90	-14.61	2.38	1.93	3.19	4.42
-1000,-1000,500	+9.95	-1.93	-14.04	3.37	5.20	3.85	7.29
-1000,0,500	+5.67	-1.78	-15.26	3.29	5.45	4.21	7.63

Table 4.6 CUE ASA 15 Second Hover Position Performance

Desired Position (x,y,z) (mm)	Mean Error (°)			Standard Deviation (°)		
(Ψ & θ & Φ = 0)	Ψ	Θ	Φ	Ψ	Θ	Φ
0,0,500	-0.58	+0.17	-0.92	0.18	0.38	0.50
1000,0,500	-0.85	-0.18	-0.60	0.18	0.35	0.99
1000,-1000,500	-1.08	+0.45	-0.99	0.19	0.16	1.17
0,-1000,500	-0.95	+0.34	-0.63	0.17	0.18	0.63
-1000,-1000,500	-0.76	+0.22	-0.43	0.22	0.33	0.95
-1000,0,500	-0.58	+0.17	-1.24	0.21	0.33	1.13

Table 4.7 CUE ASA 15 Second Hover Orientation Performance

The covariance matrix of position distribution, measured from the mean pose, at each location was calculated to highlight the variation in terms of platform position. The diagonal element represents variance and the off-diagonal terms are cross covariance between components comprising the position vector.

$$Cov_{(0,0,500)} = \begin{bmatrix} 6.21 & 1.19 & 0.28 \\ 1.19 & 33.85 & 1.06 \\ 0.28 & 1.06 & 14.46 \end{bmatrix}$$

$$Cov_{(1000,0,500)} = \begin{bmatrix} 9.13 & -3.43 & 0.48 \\ -3.43 & 29.54 & 5.93 \\ 0.48 & 5.93 & 10.71 \end{bmatrix}$$

$$Cov_{(1000,-1000,500)} = \begin{bmatrix} 7.52 & -1.95 & -0.45 \\ -1.95 & 5.17 & -0.79 \\ -0.45 & -0.79 & 8.66 \end{bmatrix}$$

$$Cov_{(0,-1000,500)} = \begin{bmatrix} 5.66 & 0.62 & 1.57 \\ 0.62 & 3.73 & -0.92 \\ 1.57 & -0.92 & 10.17 \end{bmatrix}$$

$$Cov_{(-1000,-1000,500)} = \begin{bmatrix} 11.34 & 3.66 & 2.09 \\ 3.66 & 27.09 & 5.98 \\ 2.09 & 5.98 & 14.83 \end{bmatrix}$$

$$Cov_{(-1000,0,500)} = \begin{bmatrix} 10.82 & 2.68 & -1.06 \\ 2.68 & 29.71 & -1.77 \\ -1.06 & -1.77 & 17.74 \end{bmatrix}$$

Ellipsoid representations highlighting the distribution at each desired location were produced and are located in Appendix B.1. An example is shown below in Figure 4.17 for a desired position of 0,0,500. Additionally the distribution ellipsoids, for each hover location, are shown in the X-Y, X-Z and Y-Z planes respectively (Appendix B.1). The length of each ellipsoid axes is equal to the square of the standard deviations highlighted in Table 4.4. The colour gradient of the ellipsoid is relative to the Z Axis value. Such a visualisation tool rapidly highlights the variation in axis distribution.
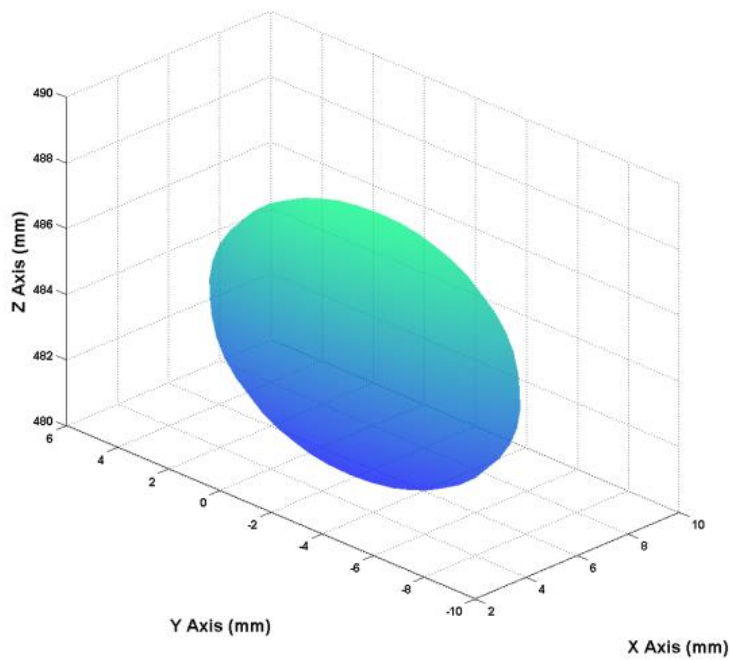
Figure 4.17 CUE ASA Position Error Distribution at Desired Position 0,0,500.

4.15.2.2   1500 mm Altitude Flight

An additional six hover position accuracy investigations were undertaken at similar 2D Cartesian locations but at a greater vertical altitude of 1500 mm. Similarly a 15 second hover time was measured at each location.

Again the mean pose of the platform through this 15 second duration is recorded in Table 4.8 along with the resultant XYZ 3D distance to the desired location. Table 4.8 therefore records the systematic error of the platform.

The mean error for all position parameters (X,Y,Z), is also calculated and shown in Table 4.9, along with the standard deviation for each axis. Additionally the RMSE distance to the mean platform pose is shown alongside in Table 4.9.

Similarly the mean and standard deviation for platform orientation parameters (Ψ,θ,ϕ) is shown in Table 4.10.

Desired Position (x,y,z) (mm) (Ψ & θ & Φ = 0)	Mean Position						Mean Position XYZ Error (mm)
	X (mm)	Y (mm)	Z (mm)	Ψ (°)	Θ (°)	Φ (°)	
0,0,1500	11.40	-1.69	1485.43	-0.83	0.27	-0.94	18.62
1000,0,1500	1012.54	-1.22	1484.65	-0.85	0.21	-0.74	19.92
1000,-1000,1500	1017.18	-1001.55	1481.38	-1.01	0.23	-0.65	23.35
0,-1000,1500	15.83	-1002.58	1484.94	-0.98	0.36	-0.90	19.27
-1000,-1000,1500	-985.05	-1003.56	1484.34	-0.94	0.40	-0.83	22.00
-1000,0,1500	-986.52	-1.90	1484.62	-0.90	0.24	-0.63	20.89

Table 4.8 CUE ASA 15 Second Hover Mean Pose

Desired Position (x,y,z) (mm)	Mean Error (mm)			Standard Deviation (mm)			RMSE (mm)
(Ψ & θ & Φ = 0)	X	Y	Z	X	Y	Z	
0,0,1500	+11.40	-1.69	-14.62	6.37	4.53	4.94	9.25
1000,0,1500	+12.53	-1.22	-15.44	3.87	4.89	5.83	8.54
1000,-1000,1500	+17.24	-1.63	-15.66	5.98	3.86	4.29	8.31
0,-1000,1500	+15.83	-2.65	-10.67	3.91	2.65	3.51	5.88
-1000,-1000,1500	-14.95	-3.68	-15.72	7.90	2.86	3.37	9.06
-1000,0,1500	-13.95	-1.90	-15.43	5.87	4.60	4.16	8.54

Table 4.9 CUE ASA 15 Second Hover Position Performance

Desired Position (x,y,z) (mm)	Mean Error (°)			Standard Deviation (°)		
(Ψ & θ & Φ = 0)	Ψ	Θ	Φ	Ψ	Θ	Φ
0,0,1500	-0.83	0.27	-0.94	0.28	0.29	0.76
1000,0,1500	-0.85	0.21	-0.74	0.21	0.33	0.79
1000,-1000,1500	-1.01	0.23	-0.65	0.27	0.27	0.61
0,-1000,1500	-0.98	0.36	-0.90	0.18	0.19	0.78
-1000,-1000,1500	-0.94	0.40	-0.83	0.37	0.19	1.08
-1000,0,1500	-0.90	0.24	-0.63	0.29	0.32	1.15

Table 4.10 CUE ASA 15 Second Hover Orientation Performance

The covariance matrix of position distribution, measured from the mean pose, at each

location was calculated to highlight the variation in terms of platform position.

$$Cov_{(0,0,1500)} = \begin{bmatrix} 40.68 & -3.01 & -0.52 \\ -3.01 & 20.60 & 2.99 \\ -0.52 & 2.99 & 24.43 \end{bmatrix}$$

$$Cov_{(1000,0,1500)} = \begin{bmatrix} 15.12 & 5.94 & 4.59 \\ 5.94 & 23.91 & -9.58 \\ 4.59 & -9.58 & 34.01 \end{bmatrix}$$

$$Cov_{(1000,-1000,1500)} = \begin{bmatrix} 35.86 & -0.78 & -0.32 \\ -0.78 & 14.93 & 6.91 \\ -0.32 & 6.91 & 18.28 \end{bmatrix}$$

$$Cov_{(0,-1000,1500)} = \begin{bmatrix} 15.30 & -2.58 & -0.06 \\ -2.58 & 7.03 & -0.86 \\ -0.06 & -0.86 & 12.34 \end{bmatrix}$$

$$Cov_{(-1000,-1000,1500)} = \begin{bmatrix} 62.58 & -7.95 & -1.26 \\ -7.95 & 8.22 & -1.44 \\ -1.26 & -1.44 & 11.36 \end{bmatrix}$$

$$Cov_{(-1000,0,1500)} = \begin{bmatrix} 34.53 & 0.14 & -0.62 \\ 0.14 & 21.17 & 0.58 \\ -0.62 & 0.58 & 17.36 \end{bmatrix}$$

An ellipsoid representation highlighting this error is shown, for each hover location

in Appendix B.2. Additionally the distribution ellipsoids, for each hover location, are

shown in the X-Y, X-Z and Y-Z planes respectively (Appendix B.2). Again the

length of each ellipsoid axes is equal to the square of the standard deviations

highlighted in Table 4.7.

4.17 CUE ASA Positional Accuracy Discussion

It is clear that significant positional inaccuracy, in the order of millimetres, exists when deploying fixed pitch rotor wing aircraft for NDE purposes.

The errors presented in Tables 4.5 - 4.10 highlight the challenge of deploying traditional NDE sensors to point of interest within a structure, with respect to sensor-surface distance and lift-off.

It is shown that significant systematic error exists in the mean pose of the platform, with reference to the desired, at all six locations and both vertical altitudes (Tables 4.5-4.10). It is intuitive that increased integral gain and further tuning on the closed loop pose controller should reduce this error. It is worth noting that no claim is made to the full optimisation of the PID controllers used primarily in the closed loop positional control strategy. As stated the controllers were manually tuned to a point deemed reasonable and satisfactory, in terms of response and minimum overshoot, at a number of discrete locations, however the validity and purity of these tunings must be considered.

Nonetheless the pose control ability of the CUE ASA is quantified when hovering around the mean position, with an average mean XYZ error at an altitude of 500 mm of 5.95 mm and 7.51 at 1500 mm. This increased positional variation distribution is also documented with increased platform pose parameter standard deviation at the greater vertical altitude (Tables 4.6,4.7,4.9,4.10). This is further highlighted in the diagonals of each covariance matrix and ellipsoid distribution plots for the increased altitude tests.

From a sensor deployment perspective it is worth considering the angular orientation error presented in Tables 4.7 and 4.10, particularity that of the Yaw angle. This angle is of critical importance when considering the requirement of traditional NDE sensors in remaining perpendicular to the surface under inspection. Highlighted in the literature is that traditional NDE sensors (contact UT, EC, MFL) do not currently possess the level of stand or lift-off sensitivity to be deployed from such a position uncertain platform. This necessitates the requirement for new research in the field of lift-off insensitive NDE sensors for such automated platform deployment. Preliminary work in this area is presented later in Chapter 7.

A critical consideration when assessing the validity and accuracy of this position measurement, is the systematic measurement error. In tandem with this body of work, researchers at CUE have identified variation in measurement accuracy across the VMCS measurement volume [155]. In line with the outcomes of [155] the accuracy of the VMCS system was verified using a custom calibration procedure, referenced to absolute optical interferometry.

As all VMCS camera central focus points are focussed to approximately the central region of the ground plane of the measurement volume, it has been proven that tracking accuracy is reduced as you drift away from the central region. This accounts for greater error in measurement of increased radius from the measurement volume centre not only in a 2D context but also with increased vertical altitude. This coupled to high variability in the initial human driven calibration routine and operational drift in the position of the cameras due to thermal expansion of the mounting frame results in variability and non-uniform measurement performance across the volume [155].

A correlation exists with respect to this accuracy variation and platform pose accuracy, as generally increased vertical altitude and distance from the measurement volume centre highlight increased pose distribution as shown in Tables 4.5, 4.6, 4.8, 4.9.

Going forward significant developments could be undertaken to further improve the performance of such aerial vehicles. As stated the suitability and performance of the position controllers could be further investigated and assessed, with new control methodologies considered.

Increased update rate IMUs, platform controllers and speed controllers should further enhance the positional performance through greater sensory information and reduced interpolation cycle. Additionally mechanical improvements in terms of blade aerodynamics and ducting could be considered to reduce turbulent air flow around the rotor.

Further work should also investigate the deployment of on-board positioning and localisation strategies to remove the need for fixed world systems such as the VMCS system. Such strategies highlight position and localisation accuracies of far lesser accuracy than found with fixed world systems such as the VMCS, which then naturally reduce platform stability even further. This will further dictate the choice of suitable NDE sensor. This approach will ultimately be required for full autonomous deployment in unknown environments.

This body of work has accurately quantified and characterised the positional performance of an aerial platform design which is seeing increased industrial and

research deployment. Such quantification provides numeric information to both highlight the suitability and applicability of traditional NDE sensors and determine the need for future lift-off insensitive NDE sensors for autonomous platforms. As stated earlier, the feasibility of such a sensor is presented and discussed in Chapter 7.

4.18 Aerial Visual Inspection

A mock visual inspection was undertaken, using the CUE ASA, of the laboratory rear wall to highlight proof of principal. As discussed in Section 4.12 aerial deployed visual NDE based methods can provide useful information regarding a surface or structure from a large surface stand-off distance. Using the CUE ASA and the image processing system described in Section 4.12.1 a simple rectangular raster scan path was executed to capture a large section of the surface. Using the same VMCS origin as utilised in Section 4.15.1 the following waypoints were selected to compose the path (Table 4.11).

Desired X (mm)	Desired Y (mm)	Desired Z (mm)
1000	-500	500
-1000	-500	500
-1000	-500	750
1000	-500	750
1000	-500	1000
-1000	-500	1000
-1000	-500	1250
1000	-500	1250
1000	-500	1500
-1000	-500	1500

Table 4.11 CUE ASA Aerial Inspection Path Waypoints

A 640 by 480 pixel photograph was repeatedly triggered at a frequency of 2Hz with the CUE ASAs desired translational velocity set at 0.25 m/s. A selection of individual images are shown below (Figure 4.18), showing minimal motion blur and tearing.
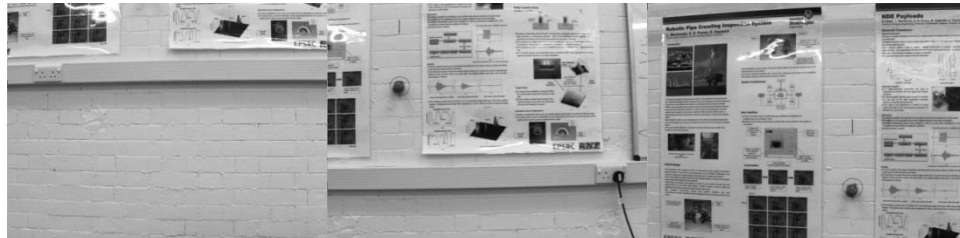
Figure 4.18 Individual Aerial Visual Inspection Images

All 206 images acquired during the mock inspection scan were then stitched together using the commercially developed PTGui (Graphical User Interface for Panorama Tools) [156] to create an overall panoramic image of the full rear wall surface (Figure 4.19). Typically image stitching, which aligns and overlaps individual images, is performed by dedicated image registration [17, 157] and fusion techniques [158].
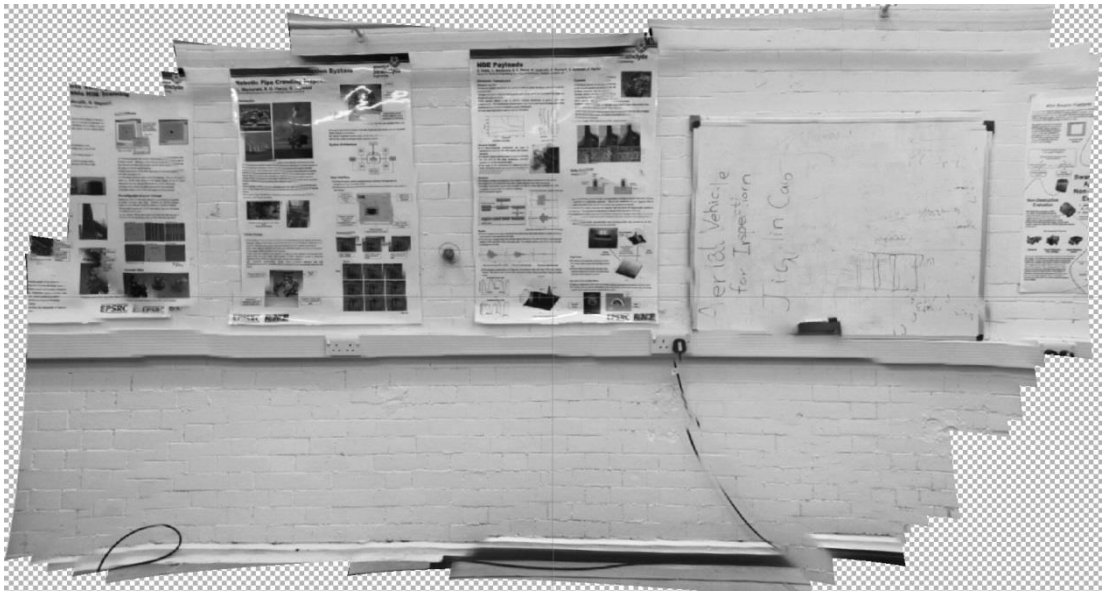
Figure 4.19 Aerial Visual Inspection Panoramic Result
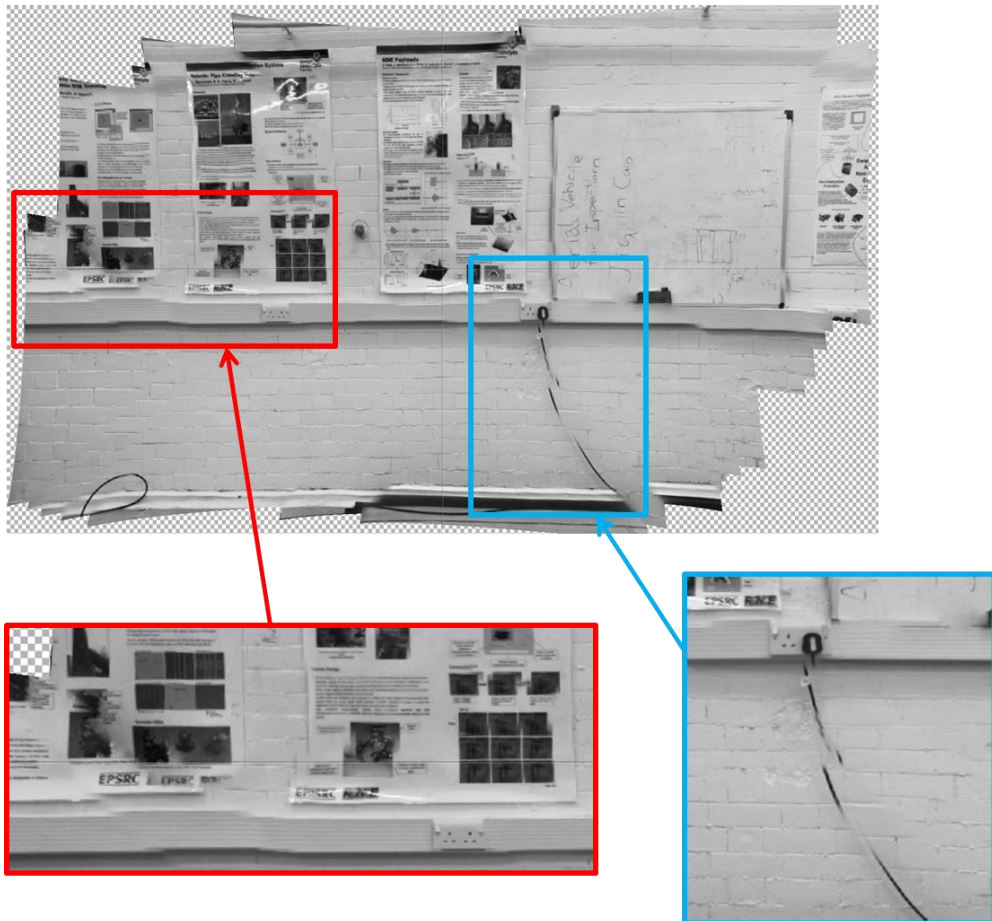
Figure 4.20 Aerial Visual Inspection Close-Up

It is clear from Figure 4.20 that areas of the overall image panorama exist where the stitching was sub-optimal and hence produced errors. On investigation it became apparent that false feature matches were often the cause of these, particularly in areas of little or self-similar features, such as the lower level repetitive painted brickwork. Additionally areas of little overlap between subsequent images were identified to be the cause of the further image alignment errors.

However the overall purpose of the inspection was to highlight the feasibility and give a sense of the performance available from a visual based aerial NDE inspection platform, with positional uncertainty as highlighted in Section 4.16.

Figure 4.21 positively highlights the overall performance of the concept, while there is clear evidence of further work being required in improving the overall visual NDE inspection tool chain. This should consist of two strands of improving first the quality in terms of resolution, clarity and focus of the individual images and secondly the image mosaicing and stitching algorithms to deal with self-similar and few feature surfaces found in typical industrial environments.

Improvements in the position and motion control of aerial platforms, such as those discussed in Section 4.16 will naturally improve the first of these while improvements in machine vision camera resolution and sensitivity will also greatly assist these shortcomings. NDE specific and targeted research will be required to be undertaken to improve, customise or develop new image processing feature extractors to yield the required performance on typical sparse feature industrial surfaces.

4.19 Conclusion

In this chapter the benefits and approaches to implementing aerial based NDE have been introduced. A review was undertaken discussing the merits and designs of multiple aerial delivery mechanisms with an NDE specification and metric system introduced. The high suitability of fixed pitch rotary winged aircraft in addressing aerial NDE challenges was presented along with a review of current commercial platforms and deployment applications. The CUE ASA platform was presented along with initial approaches to implementing closed loop positional control.

The main contribution to knowledge of this chapter was in the characterisation and quantification of positional performance and accuracy of a custom aerial platform at locations throughout a reference measurement volume. RMSE errors as low as 4.42 mm were measured, when undertaking a 15 second hover, highlighting the challenge of deploying standard ultrasonic and electromagnetic NDE sensors which require careful control of surface lift-off.

Due to the insensitivity to lift-off of visual sensors and to highlight automated aerial NDE potential, a mock visual inspection was undertaken on an indoor laboratory surface. This investigation highlighted the basic performance available from such a deployment concept, when utilising standard image processing tools, with areas of future research focus discussed.

Chapter 5

Characterisation of Laser Scanner for Localisation and Mapping

5.1 NDE Based Localisation and Mapping

The integration of NDE techniques and robotic inspection platforms present significant positional requirements in terms of path planning, obstacle avoidance and defect localisation and quantification. When considering path planning and obstacle avoidance, incorrect and inaccurate robot or object positions can result in potentially catastrophic results. The increased positional uncertainty accentuates the problems of remote structural inspection from two perspectives. Firstly, the location of a defect in the structure is important, with increased positional uncertainty leading to increased error in detection of defect locations. Secondly, and more importantly is that many NDE modalities require a carefully controlled stand-off distance from the surface for accurate defect detection and sizing [159-161]. Therefore accurate sensory positional information remains critical to safety, performance and accuracy when considering practical remotely deployable NDE. A further challenge of NDE based localisation is that the typical environments into which platforms are deployed differ substantially, in terms of core materials and surfaces, to those discussed in localisation literature [162]. Materials such as carbon and stainless steels, aluminium, concrete and certain

plastics are commonly utilised in dark, damp, humid, high temperature and potentially radioactive conditions [163].

CUE has undertaken a sustained drive in researching robotic positioning strategies for NDE applications [17]. Due to the aforementioned pronounced requirements of remote NDE systems, standard commonly developed strategies lacked the necessary performance and accuracy to sufficiently deliver meaningful data [18]. Positioning strategies can be evaluated and separated into being either relative or absolute systems.

Absolute pose as its name suggests is the localisation of an object within a working envelope referenced to specific coordinates and therefore is independent of all previous poses. Relative pose, also known as dead reckoning, is a measured pose within a volume relative to other previous poses. Uncertainty in previous measurements gives rise to further uncertainty in the current measurement. Relative systems although providing good short term accuracy are prone to increased error in the longer term due to environmental and systematic influences [164]. Examples of relative measurement systems include odometry (Wheel encoders, Visual, Acoustic, LIDAR) and Inertial Measurement Units (IMU) giving ultimate position information. Examples of absolute measurement systems include photogrammetry, beacon based range sensing (Acoustic, Laser, Visual), Global Positioning Systems (GPS) and IMUs providing orientation information.

When operated in areas with zero or limited *a priori* knowledge of the structure, robotic vehicles must rely on on-board sensors to determine pose. Range sensing of distance to nearby objects is a well-established method utilised in robotic applications for obstacle avoidance and mapping [165-167]. Signal processing techniques and algorithms such as Simultaneous Localisation and Mapping (SLAM) [24] utilise such sensor data to develop 2D and 3D models of the surroundings. From these models maps can be constructed, on and off-line, to generate path plans, to firstly reach the region of interest and secondly to scan and inspect the desired area.

SLAM results in the robot both acquiring and building a map of its environment while also simultaneously localising itself relative to the acquired map [24]. SLAM is inherently more challenging than individual localisation and mapping [168]. In purely localisation, the map is known *a priori* and therefore knowledge of the environment can assist in determining the position of the robot [169]. In a traditional purely mapping scenario, the pose of the robot is known allowing all mapping point data to be referenced to the known position [25]. Pose collectively defines the global position and orientation of the object within a volume. When both criteria are unknown the measurement challenge is considerable and typically requires fusion techniques from multiple sensors to best estimate both the pose of the acquiring robot and the surrounding environmental features [18].

Range sensing for robotic scanning applications has been investigated utilising ultrasonic [170], visual [171,172], and laser based sensing modalities [173]. Although being commonplace in research and deployment applications, significant

uncertainty, with regards to sensor accuracy and performance, still exists. This thesis chapter focuses on the characterisation of a common miniature robotic optical laser range finding module. This is relevant as the sensor is both the largest and currently the highest performance module that the present fleet of the CUE RSA, AUT RSA and CUE ASA could perceivably carry.

This thesis chapter presents the results of detailed experimental comparisons, in terms of distance measurement error, accurately referenced to a high accuracy laser tracker (Appendix A) to variation in surface material properties and range finder orientation. Furthermore a real-time strategy for identification of potentially erroneous range measurements is described. Additionally a novel and new framework for material identification and range error correction is presented based on acquired characterisation and calibration data.

5.2   Laser Based Localisation and Mapping

Of all such technologies laser based mapping has undergone the greatest research, development and deployment based on metrics of performance, accuracy, ease of operation and complexity [174-175]. Single point range estimation can be undertaken by the reflection of a transmitted beam from an object placed within the line of sight of the emitted beam. 2D plane scanning can then be developed by the movement of such a single beam in a planar manner. This can be acquired by pure translation of both the transmit and receive system, or by simple rotational scanning of both

components. The latter has been the most widely adopted due to the reduced footprint and working volume requirements inherent in such a design.

3D scanning can be further achieved through movement of such a 2D system in the final axis. Traditionally this has been undertaken by gravitational or actuated pitching motions which produce a volumetric range scan [176].

Robotic research has investigated 2D laser based range scanning for applications such as object tracking [177], obstacle avoidance [178-180], mapping [181-182], localisation [183-184] and feature extraction [185-186].

5.3   Laser Based Range Measurement

5.3.1   Time of Flight Measurement

Traditional Laser Range Finders (LRF) utilise either Time of Flight (TOF) or Amplitude Modulated Continuous Wave (AMCW) phase shift to determine the distance to objects [187]. The former as its name suggests measures the time of flight of an emitted pulse to return and from knowledge of the speed of light can determine the distance to the reflecting object.

$$L_{SS} = \frac{vt}{2} \qquad\qquad (5.1)$$

where:

L_{SS} is the sensor to surface distance in mm.

v is the speed of light in mm/s

t is the time difference between the transmitted and returned optical beam (s)

The principle is graphically illustrated in Figure 5.1. A LRF, commonly employed in robotic applications, which utilises such a technique, is that of the SICK LMS200 [188] and its newer successor the LMS500. The device performance and accuracy has been thoroughly characterised in [189]. The LMS500 features a measurement range of 0 to 80 m with systematic error of ±35 mm for ranges of up to 20 m. The large size (160 X 155 X 185 mm) and weight (3.7 kg) of the sensor result in it being only suitable for relatively large robotic delivery platforms.
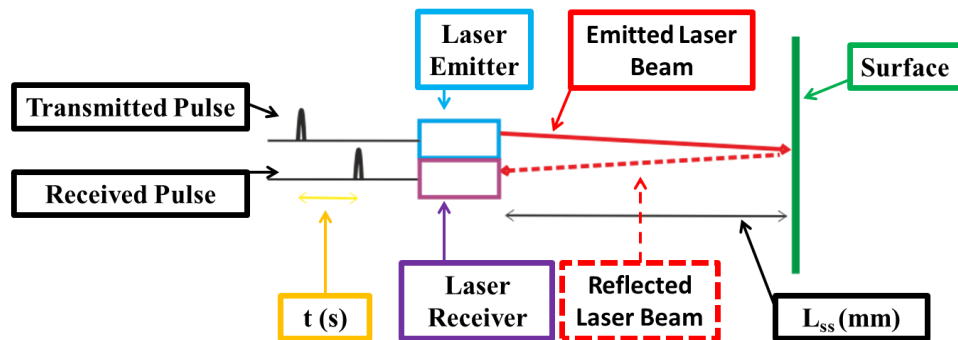
Figure 5.1 Time Of Flight (ToF) Principle

5.3.2 Phase Shift Measurement

AMCW phase shift measurement as its name suggests utilises the phase difference between the transmitted and object reflected beam to calculate the sensor to surface distance (SSD) [190].

$$L_{SS} = \frac{\phi v}{4\pi f} \qquad\qquad (5.2)$$

Where:

L_{SS} is the sensor to surface distance in mm.

ϕ is the phase difference in radians.

v is the speed of light in mm/s

f is the modulation frequency in Hz.

It is clear from Equation 5.2 that higher SSD precision can be achieved with increased modulation frequency. A challenge associated with phase measurement is the task of dealing with and detecting cyclic changes greater than one period with a single wave strategy [190]. Thus typically alternate modulation frequencies are deployed on the transmitted output wave to circumvent this challenge [190].

One such sensor that utilises AMCW phase measurement and commonly deployed in positional range measurement applications for miniature autonomous robotic systems is that of the Hokuyo URG-04LX (Figure 4.2). This is due to its small form factor (50x50x70mm), low mass (170g) and specification [190].

5.4   Hokuyo URG-04LX.

Developed specifically for robot platform navigation applications, a 785nm Class 1 laser scans a maximum 240° sweep angle, with an angular resolution of 360/1024°, and a quoted maximum range of 4095mm. Accuracy is quoted as ±10mm at range distances of up to 1000mm and rising to ±2% of the total distance for the remainder

of the range scale. Two alternate modulation frequencies (46.55 and 53.2 MHz) are employed on transmitted light beams, while two ADC sample the received optical beam for subsequent digital phase difference measurement [190].

Figure 5.2 HOKUYO URG-04lX [191]

A simplified scanner model is shown below in Figure 5.3. The infrared laser projects downward to an inclined mirror mounted on an optically encoded rotary stage, resulting in a horizontal output beam. The returning beam is focussed on to another inclined mirror and converted to a vertical beam for reception on the horizontal faced photodiode. A brushless motor rotates the rotary stage, with position feedback provided by the optical odometery. An Application Specific Integrated Circuit (ASIC) features two ADC, motor position measurement control electronics and frequency specific clock and timing signals necessary for operation. RS232 and USB communication buses are available and offer the potential of real time data transmission and capture. A proprietary Hokuyo ASCII based communication protocol was developed codenamed Scanning sensor Command Interface Protocol (SCIP) to allow control of sensor operation and features such as resolution, sweep angle and operation.
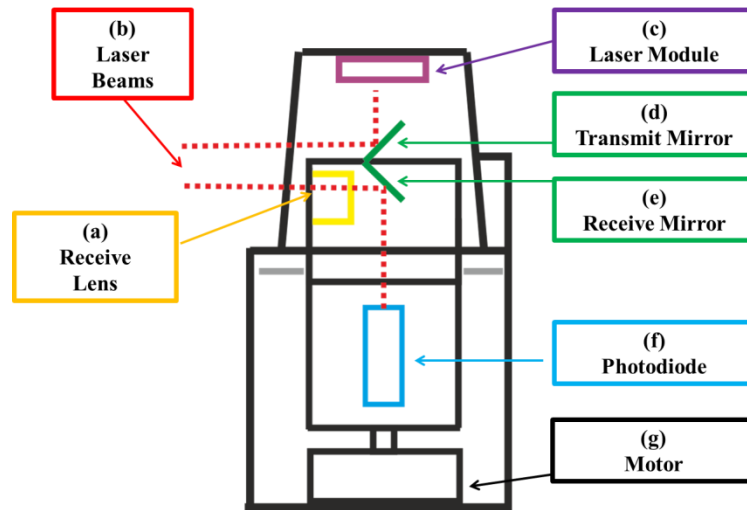
Figure 5.3 HOKUYO URG-04LX Structure

This sensor has been utilised on a variety of wheeled, crawler and aerial platforms [192-195]. The author, system developers and adopters have both documented and experienced measurement errors when dealing with glossy reflective surfaces[162, 176,190,196-197], due to the effects of specular reflection and saturation of the photodiode [190].

5.5 Material Reflection

Specular reflection (ϱ_r) is reflection without diffusion in accordance with the laws of optical reflection as in a mirror, where the angle of reflection equals the angle of incidence for a planar boundary. Diffuse reflection (ϱ_d) is defined as reflection, on the macroscopic level, where there is no specular reflection. Reflectivity (ϱ_∞) is the reflectance of a layer of the material of such a thickness that there is no change of reflectance with increase in thickness. Reflectance (ϱ_e) is defined as the ratio of the reflected flux to the incident flux in the given conditions [198].

$$\varrho_e = \varrho_r + \varrho_d \tag{5.3}$$

Gloss is the mode of appearance by which reflected light from objects is perceived as superimposed on the surface due to the directionally selective properties of that surface [198]. The gloss of a surface is dependent on the illumination and the surface properties, namely the material itself, its surface topography, its degree of transparency and its substrate [199]. Specular gloss is defined as the gloss observed or measured at the specular angle, which itself is defined as the angle with respect to the normal.

Therefore specular reflection, where the angle of reflection is equal to the angle of incidence, is proportional to the gloss of the surface under question. Conversely diffuse reflection is inversely proportional to the gloss of the surface. Increasing the gloss of a surface will therefore decrease the diffuse reflectivity, while at the same time increase the specular reflectivity until the overall reflectivity is fully specular as found with a pure mirror.

Accurate information and knowledge of surface condition and properties, prior to and during LRF scans is challenging. As the optical intensity of the transmitted laser remains approximately constant due to the fixed input power, the effect of SSD and surface local conditions affect the intensity of the reflected laser beam.

Therefore parameters of the received optical signal are a function of the local surface condition and can therefore be used to infer information regarding the surface such as roughness, gloss and base material.

5.6   Received Signal Measurement

Recent developments with respect to firmware and communication protocol (SCIP 2.0) have allowed operators of the Hokuyo URG-04LX to measure and monitor a number of additional received signal parameters such as the received optical intensity and gain controller values [200]. Received optical intensity is related to the reflected optical intensity after removing the effects of distance and inclination [197].

As discussed in [190], due to saturation of the Avalanche Photodiode (APD) during operation, particularly with highly reflective surfaces, an Automatic Gain control Circuit (AGC) is inbuilt in the sensor. Only consistent or unmodified received signal intensity data permits discrimination and calculation of parameters such as surface material. Work undertaken to establish the transfer function of the AGC determined the relationship was nonlinear due to the conversion from the original received optical power to the modified gain controlled received intensity as a voltage output from the 10 bit A-D convertor of the AGC.

The original unmodified received optical luminous intensity (I_r) is given by [197]:

$$I_r = \frac{1023 \times \sqrt{I_O}}{V_a} \qquad (5.4)$$

Where:

I_o is the AGC modified received luminous intensity

V_a is the AGC voltage.

When undertaking LRF surface scans it is possible to have rejected or zero range data measurement points at a particular scan point due to excessively low or excessively high reflected light, each with their own specific error code [185]. With this capability, previous research by [192, 197] have highlighted material identification strategies and the ability to offer a confidence metric on the distance accuracy of measured surfaces. However much of this previous work relating to the operation, use and characterisation of the Hokuyo URG-04LX and other similar laser range scanners, has focussed on single beam analysis, where the remaining sweep angle scanning potential is neglected [162,176,196]. This simplistic approach is too limited in practice due to the potential large volume of data available when fully utilising a sweeping laser range scanner.

Furthermore considering the widespread use of materials such as carbon and stainless steels, aluminium, concrete and certain plastics, all with widely varying surface reflectance characteristics, it is essential to further evaluate performance operating with these real surfaces.

5.7   Experimental Motivation

To fully characterise the LRF for NDE deployment, it was clear that a full sweeping scan, with variation in material surfaces such as those found in a practical inspection

scenario had to be considered. The materials selected, based on their use in industrial environments, were sheets of aluminium, black carbon steel, stainless steel, portland cement concrete, plywood, polyvinyl chloride (PVC), Poly(methyl methacrylate) (PMMA) also known as acrylic glass or perspex and white paper symbolising matte surfaces such as plasterboard.

Many of the typical industrial surfaces, to which an automated NDE system would be deployed, are of large area, such as those consisting of multiple sheets of standard steel plate (2000 x 1000 mm) or mass poured concrete sections (> 5000 mm wide). Therefore a large as possible surface scan was desired to analyse the system performance across a large sweeping angle to mimic that of a typical automated NDE inspection. A sample area of 800 mm width was selected on the basis of being both acceptable in terms of scanning angle at larger distances, while also being practically manageable. Due to the practicalities of undertaking a portland cement concrete inspection a pre-cast slab was selected with a limited sample surface width of 700mm.

Chapter 4 highlighted that Aerial NDE inspection platforms experience some deviations in pitch, roll and yaw angles while undertaking hover or sensor acquisition manoeuvres while also featuring deviations in actual Cartesian positions. From practical experience this is also correct when dealing with the surface constrained RSA platforms, albeit to a lesser extent. With this information the effects of angle and distance changes on the LRF performance and accuracy had to be analysed.

Prior knowledge on typical pose variations and practical scanning limitations, when deploying mobile NDE inspection platforms, resulted in the desired maximum angular deviation to be considered in each axis to be chosen as ± 4°, with 2° increments giving five distinct angular orientations per position. To further enhance the reality of the work, in relation to similar practical inspection experiences, it was desired to vary each angle systematically in turn so as to analyse the effects of rotation changes in all three axes.

5.8 Experimental Concept

The Hokuyo URG-04LX LRF was mounted on the end joint of an industrial KUKA KR5-HW 6 DOF positioner (6DOFPOS) [54]. This approach allowed for controlled movement and repeatable scanning positions, not only in traditional 3 DOF (x,y,z) positions but also in roll (C), pitch (B) and yaw (A) orientation angles within its defined work envelope. The KUKA end effector pose was remotely controlled with custom code implemented through the KUKA Robot Sensor Interface [201], providing bi-directional pose information every 12 ms. Therefore the desired pose could be transmitted from a remote computer and the actual pose as measured from the internal encoders received by the external computer.

A manual linear rail allowed movement of the material sample along the X-axis direction of the 6DOFPOS with a maximum sensor to surface distance (SSD), shown in Figures as L_{SS}, of approximately 4 m, matching the specified detection range of the LRF. This is illustrated below in Figures 5.4 and 5.5.
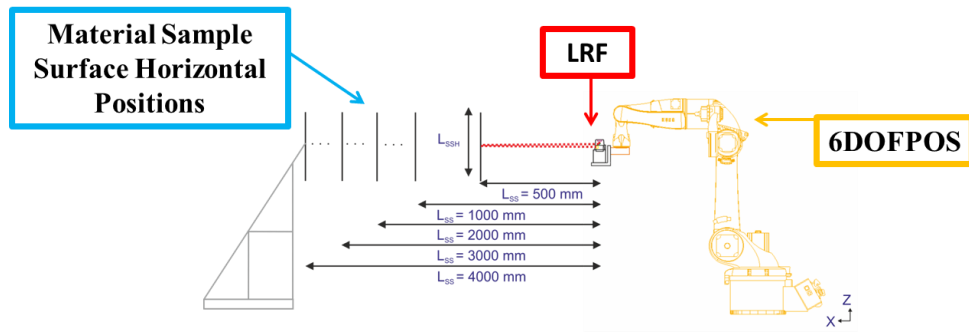
Figure 5.4 Experimental Set-Up [53]
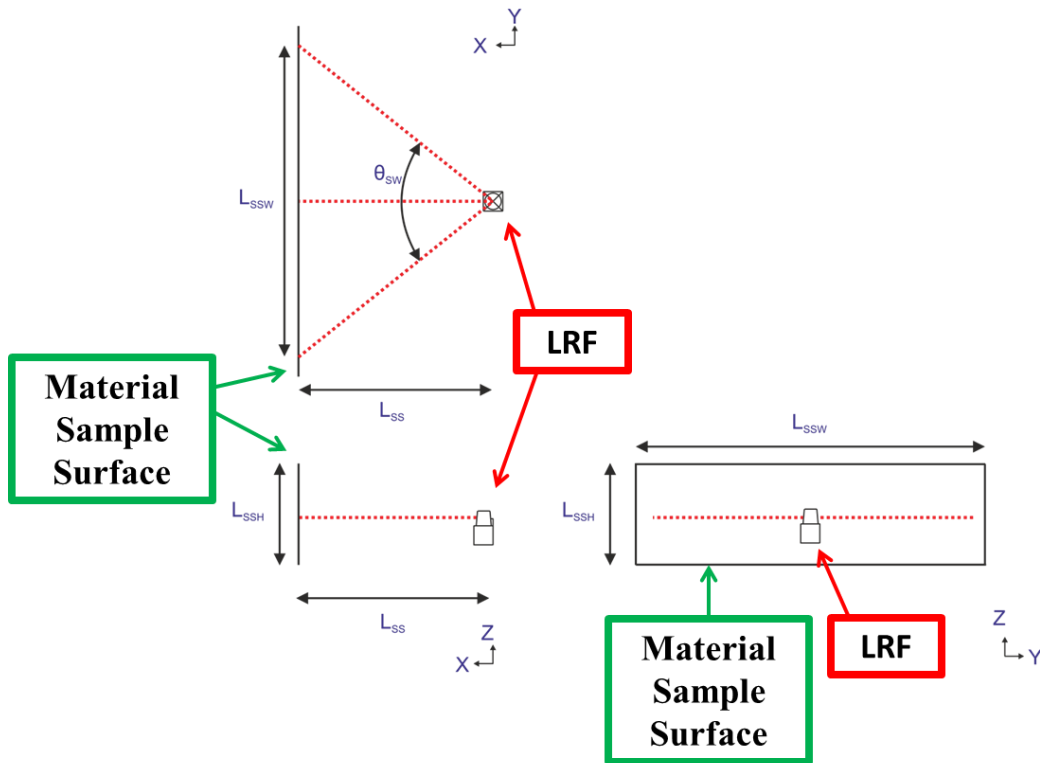
Figure 5.5 **LRF Surface Scanning Convention**

The following parameters are utilised to define the LRF surface scanning convention:

- L_{SS} Sensor to Surface Distance (SSD) (mm).

- L_{SSH} Surface vertical height (mm).

- L_{SSW} Surface horizontal width (mm).

- θ_{SW} Angular sweep window (°).

A metrology based Leica Laser Absolute Tracker (LAT) (Appendix A.3) utilising an interferometer measurement system, which can measure the 3 DOF position of a retro reflector in free space to accuracies of ±0.2µm + 0.15µm/m, was employed to offer measurement accuracy capability for both distance and alignment tasks.

A Corner Cube Reflector Jig (CCRJ) was produced which when substituted with the LRF on the end of the 6DOFPOS, had its reflector centre vertical height matched to the midpoint height between the LRF transmit mirror and LRF receive lens. This is illustrated in Figure 5.6. A simplification assumption was made that this point matched both the transmit and receive beam exit and entry point. This allowed the LRF position in free space to be estimated in the XYZ plane of the positioner.
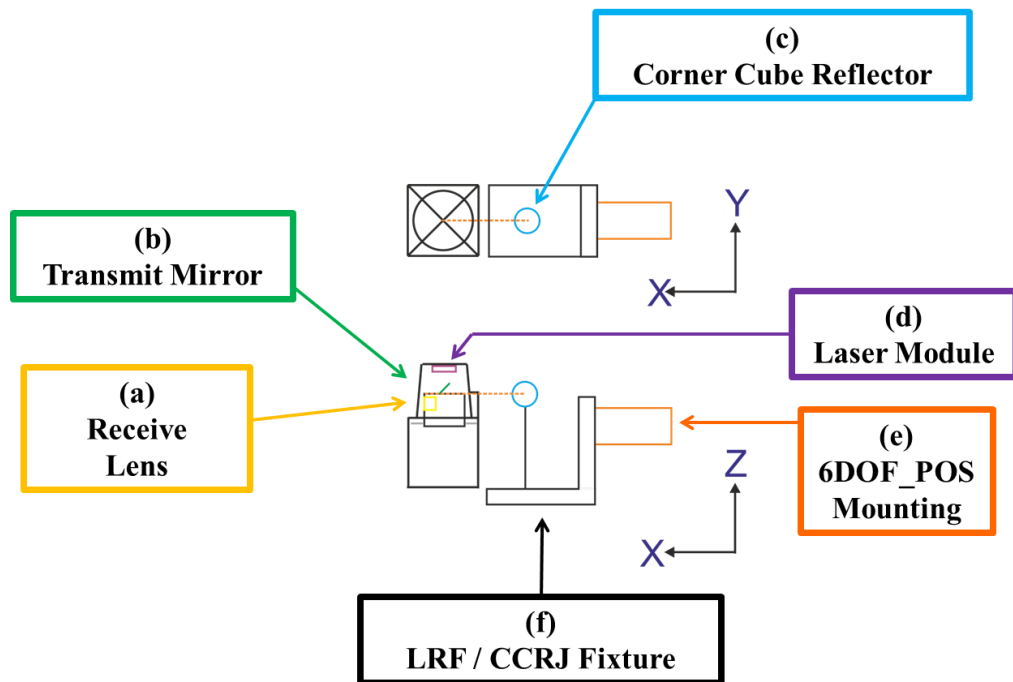
Figure 5.6 CCRJ Arrangement

Five different SSD distances were investigated, of nominal values 500, 1000, 2000, 3000, 4000 mm. These were selected to best represent the typical range of industrial stand-off distances compatible with the Hokuyo sensor.

By utilising the LAT the rail was aligned normal to the positioner Y- axis along the full range. Secondly the SSD was measured accurately, by direct measurement of 3 points on the sample surface to give the surface plane, and its normal distance between it and the nominal zero angle orientation pose of the CCRJ. The actual measured SSD were then obtained to be 532.0, 1020.4, 2001.1, 2993.9 and 3994.2 mm using a reference aluminium sheet of thickness of 2 mm.

A refinement was added to deal with the varying thickness of different sample surface materials. After simple mean thickness measurement of the sample using the LAT, the CCRJ was employed to adjust the home X axis position of the 6DOFPOS accordingly to account for any offset. This process allows all measurement samples to be at accordingly similar SSD.

As the SSD increased, along with the sample scan area width remaining constant, the scanning sweep angle was reduced to ensure only the sample surface was being scanned. The scan angles and corresponding number of sweep points were reduced as the SSD increased, with this indicated in the following table (Table 5.1) for all materials.

SSD (mm)	Sweep Angle (°)	Potential Sweep Points	Actual Sweep Points	Sweep Angle (°) (Concrete)	Sweep Points (Concrete)	Actual Sweep Points (Concrete)
532.00	73.88	210.15	209	66.68	189.67	189
1020.44	42.80	121.76	121	37.86	107.69	107
2001.15	22.61	64.30	63	19.84	56.46	55
2993.93	15.22	43.29	43	13.34	37.93	37
3994.22	11.42	32.53	31	10.016	28.49	27

Table 5.1 LRF Scanning Parameters

The actual number of sweep points per distance was reduced to an odd number, to ensure there was a single normal beam with an even number of points both clockwise (right) and anti-clockwise (left) of it.

So as to ensure the LRF swept laser points remained within range on the sample surface, it was clear that deviations in the yaw and pitch angles, required corrective deviations in the Y and Z axes respectively. This ensured that the central normal LRF beam remained positioned in the same point on the sample surface throughout all angular movements. Measurements undertaken at increased SSD therefore featured increased Y and Z travel from the nominal centre to ensure the central perpendicular beam was reflected from the same point on the surface (Figure 5.7).

It must be noted that the scanned points remained constant throughout and as such the scanned sample width deviated from the original of 800 mm during material scans depending on the rotation angle. To ensure consistency and surface coverage

during scans at large angular deviations, it was deemed to include an additional 100 mm of material sample width after calculation of the worst case surface beam width due to the change in beam ray length at large sweep angles.
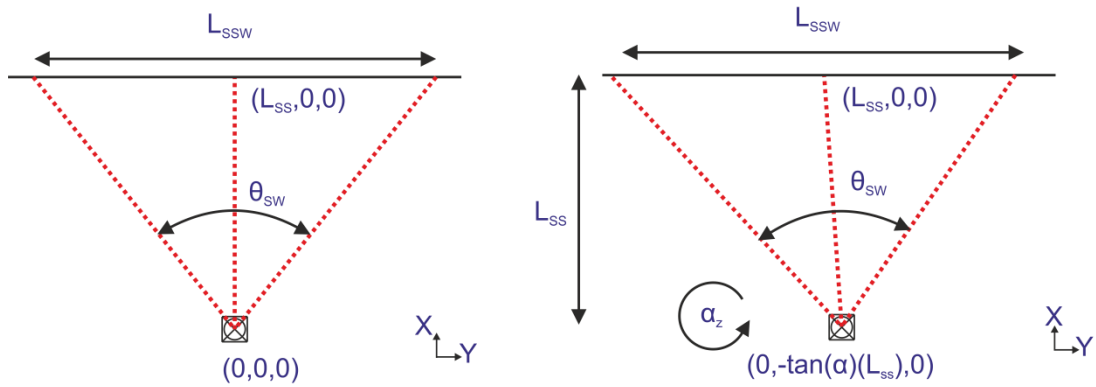
Figure 5.7 LRF Scanning Pose Adjustment

Therefore considering each angle orientation (A, B & C) and five possible values (-4, -2, 0, 2 & 4) resulted in a total number of 125 discrete measurement poses spaced between 25 separate Cartesian positions.

As the Hokuyo sensor could only output one measurement parameter at a time, if it is desired to maintain the lowest minimum angular spacing, a number of measurements are undertaken at each discrete pose in a sequential fashion due to limitations within the sensor. The overall measurement strategy is illustrated in Figure 5.8, noting that received intensity and AGC values were acquired for both modulation frequencies. Furthermore ten scans were undertake of each parameter to evaluate noise and variation in the data measurement
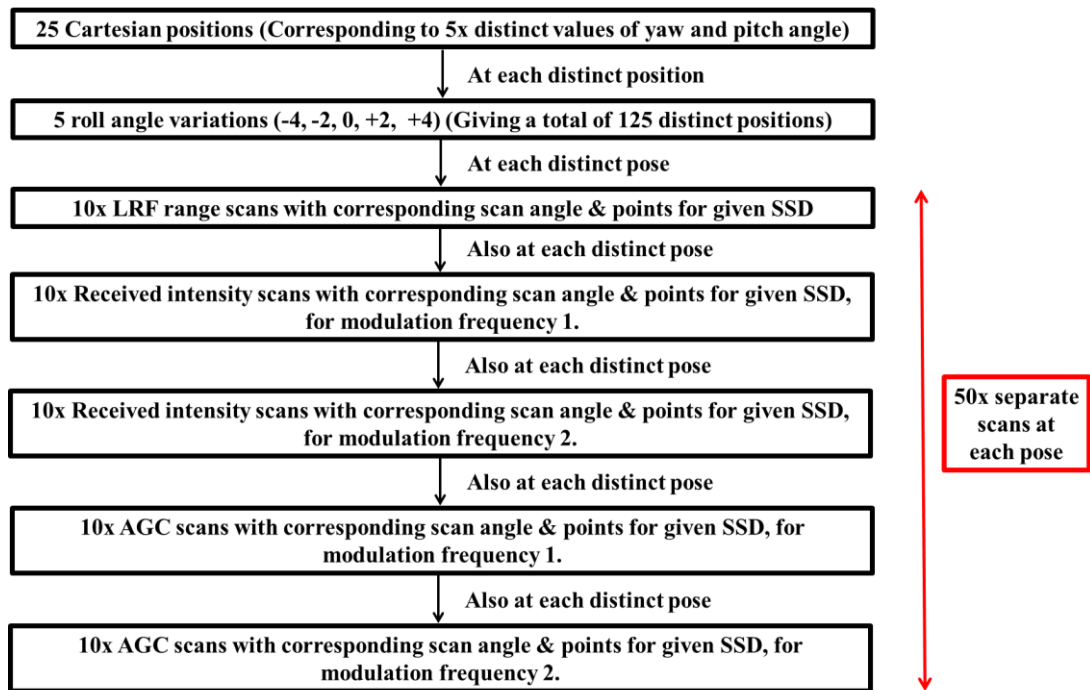
Figure 5.8 LRF Scanning Procedure

Therefore a total of 50 separate scans were undertaken at each distinct pose. After reviewing the separate modulation frequency received intensity and AGC values, and noting the minimal variation existing between each of the corresponding sets, a decision was taken to average both. Therefore the final measurement output at each pose location is summarised in Figure 5.9:
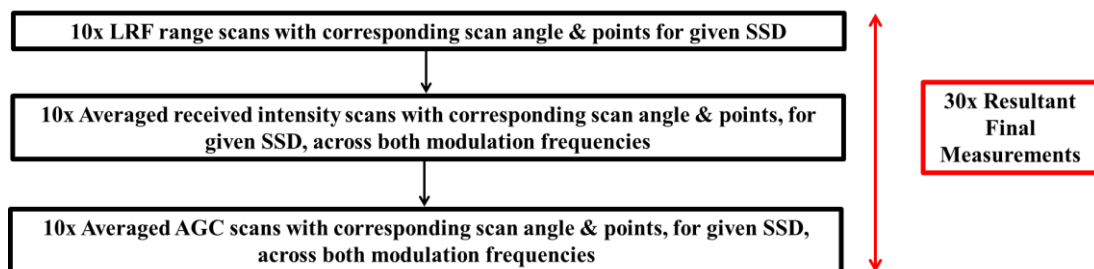
Figure 5.9 LRF Scanning Procedure

128

It must be noted that as per [160, 180] the LRF was operating for a minimum of 90 minutes prior to any measurement or scanning. This reduced any potential drift effects present in the measurement data, due to a perceived increase in internal operating temperature [180]. Additionally all measurement scans were undertaken in normal indoor laboratory ambient lighting conditions.

5.9 LRF Sample Measurement Data

To highlight the form and characteristics of the raw LRF measurement data, mean received intensity, AGC gain, range data and the corresponding calculated restored intensity, are shown below (Figure 5.10) for a paper surface at nominal 1000 mm SSD and zero orientation angle. The mean range data is outputted and presented in polar form and therefore has not been transformed into the 2D Cartesian form traditionally displayed. The fairly stable and consistent data values, of each parameter, across the sample surface.
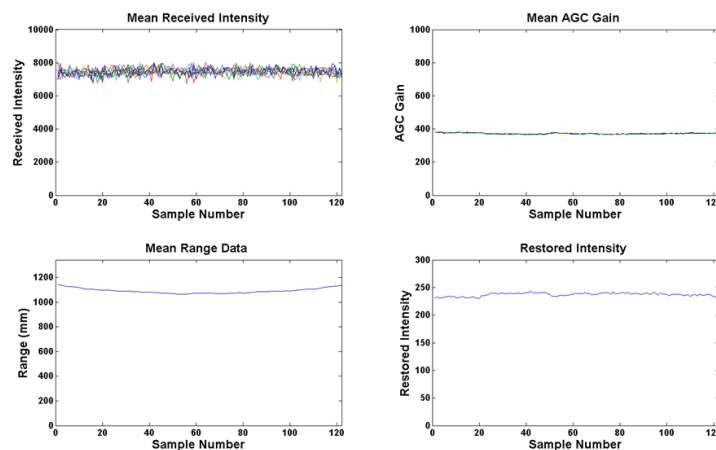
Figure 5.10 LRF Output Data for Paper Surface at nominal 1000 mm SSD

The same output parameters for a specular reflective aluminium surface are shown below in Figure 5.11. Again this was measured at nominal 1000 mm SSD and zero orientation angles. It is clear that significant change in raw measurement data is visible as the LRF sweeps radially across the sample. A large peak in received intensity, around the LRF to surface central perpendicular beam, is accompanied with a corresponding large unanticipated positive distance change in measured range data due to the aforementioned APD saturation [190]. Additionally low restored intensity values are obtained at the outer areas of the sample surface as expected due to the specular nature of the reflection.
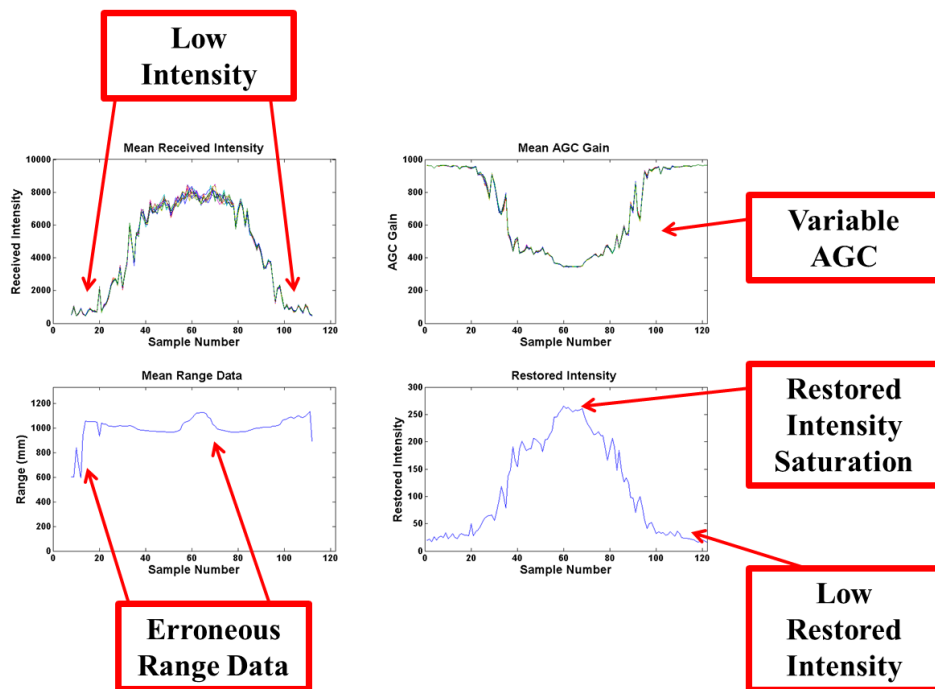
Figure 5.11 LRF Output Data for Aluminium Surface at nominal 1000 mm SSD

Such deviations in range and intensity measured parameters are visible across different materials to various degrees of extent. The following work begins to

characterise and quantify the error associated with these variations across a number of sample surfaces.

5.10 LRF Data Processing

In order to evaluate the error in the range data captured by the LRF, this data firstly had to be transformed into a common global coordinate frame. As the LAT provided the absolute ground truth positioning system, it was decided that all measurements would be with respect to the frame of reference of the LAT. The 3 D.O.F. Cartesian position of the CCRJ at the each of the 25 distinct measurement locations, where the five orientations angles are manipulated, were measured and recorded by the LAT.

The remaining 3 D.O.F. orientation angles of the CCRJ and hence LRF transmit and receive locations were measured by the KUKA manipulator and then coordinate transformed, using a least squares fitting method, into the frame of reference of the LAT using the known 3 D.O.F. Cartesian position data [202].

As discussed above, the surface plane, made up from three distinct measurement points, were recorded in the frame of the LAT.

A final coordinate transform was used to transform the LRF measurement data into the frame of reference of the LAT. This was undertaken to align the 3D points set into the global coordinate system through knowledge of the LRF – LAT transformation matrices (25 such matrices corresponding to 25 end effector

positions) recorded previously. This process allowed all measurement data to be recorded and analysed with respect to the measured surface plane.

5.11 LRF Characterisation and Performance Validation

Given the volume of data collected (125 separate range scans, each of up to 209 points of intensity and AGC values) a strategy for processing the data was formulated.

It is worth noting the large volume of measurement data recorded during the complete study. As discussed, at each separate material distance trial, 125 separate range scans, each nominally consisting of a minimum of 31 to a maximum of 209 distinct points, are measured along with their corresponding intensity and AGC values. Simple analysis of such data, bearing in mind the large number of varying parameters, is not easily practical and required some compromise to aid overall understating.

Firstly, an overall 3D representation of every range scan was produced in the frame of reference of the LAT, showing the generated surface plane and transmit and receive points of the LRF. This is a useful visual tool to aid visualisation and understanding of the overall process. An example of this is shown below (Figure 5.12) for a calibration white paper sheet sample at nominal 1000 mm SSD.
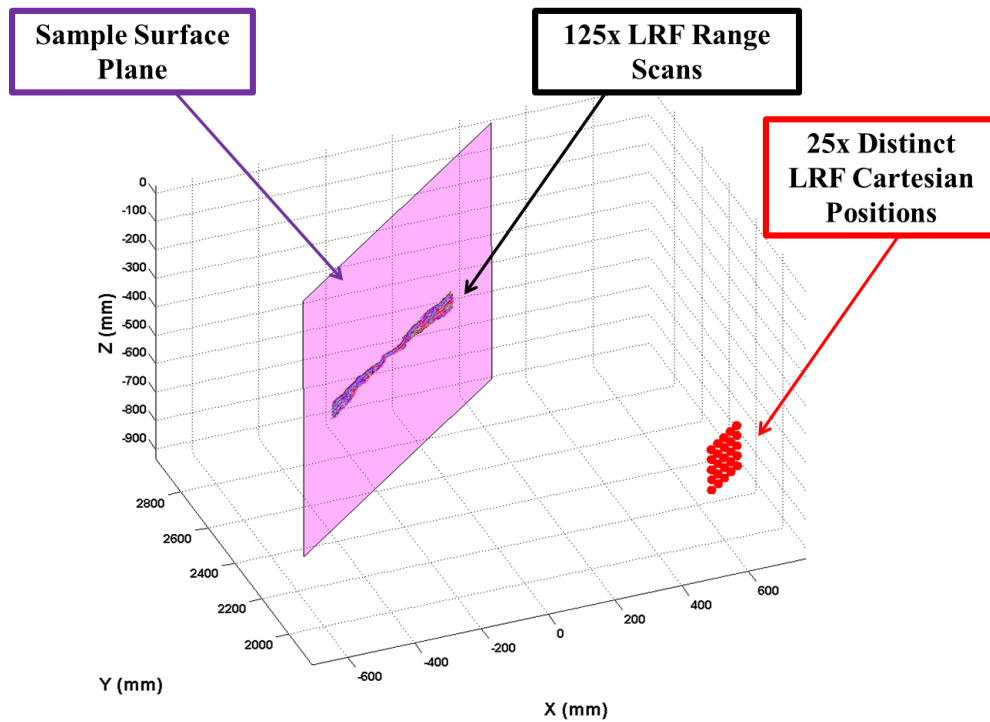
Figure 5.12 3D LRF Data Visualisation in frame of reference of LAT

5.10.1 Distance Error Quantification

The distance error was calculated for each individual scan point as the shortest perpendicular distance between the point and the sample surface. Therefore for each scan, a number of error measurements were recorded corresponding to the number of individual scan points specified in the acquisition.

The Root Mean Square Error (RMSE) of the LRF range dataset with respect to the material surface was computed to generate a single error value for each range measurement. These RMSE values were then used to generate surface plots allowing identification of trends in the data.

The 125 distinct pose angles of the LRF, as its rotated around the yaw (A), pitch (B) and roll (C) orientations of the end effector of the 6DOFPOS is illustrated in Figure 5.13, highlighting uniform raster scanning in the angle space.
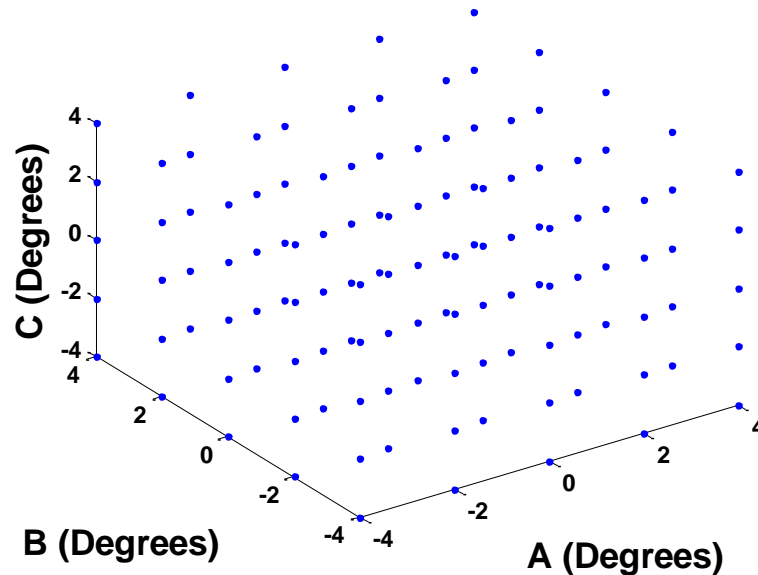
Figure 5.13 Complete Scanning Pose Locations

Given the three independent orientation variables, the error data may be viewed from three perspectives namely AB, AC and BC. Due to the design of the orientation sweep, for a fixed AB/AC/BC pair there exists multiple data points corresponding to variation in the remaining angle of the LRF. At each location exists five RMSE range error measurements corresponding to the five distinct angle values of the final third orientation angle.

To gain an understanding of the trend of the error data, the mean value of the column of five RMSE errors for each angle pair of the independent axes was calculated.

Such a plot is shown below (Figure 5.14) for AB orientation perspective for a calibration white paper sheet sample at nominal 1000 mm SSD with the blue markers highlighting the individual RMSE errors and the red markers the mean of each column.
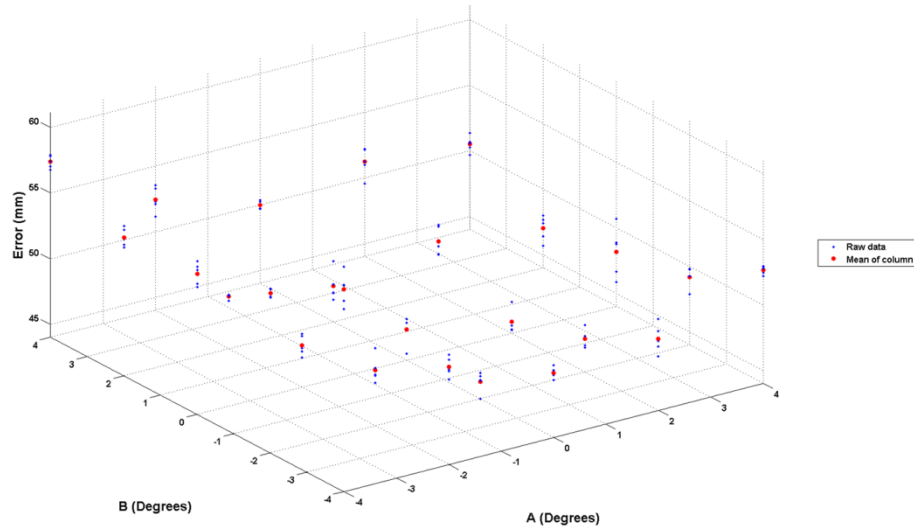
Figure 5.14 Two Angle Orientation Error Visualisation

The calculation of this mean enables a surface to be plotted along both axes.

Such a plot is shown below (Figure 5.15) for AB orientation perspective for a calibration white paper sheet sample at nominal 1000 mm SSD
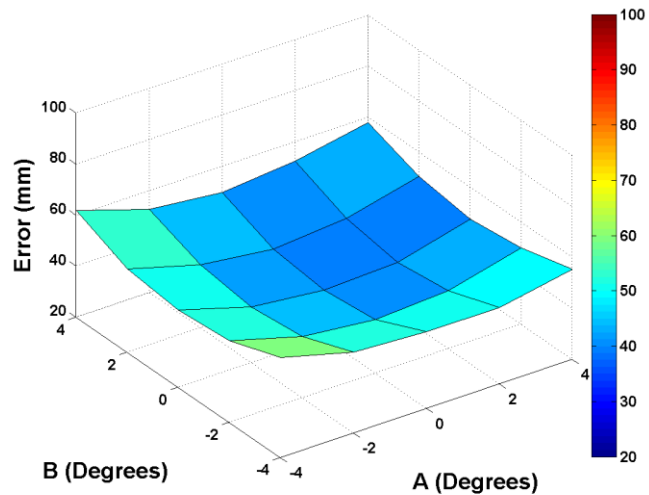
Figure 5.15 Two Angle Orientation Error Surface Plot

The mean error, with respect to both orientation axes, across this surface plot can then be calculated along with its corresponding standard deviation.

5.10.2 Restored Intensity Quantification

Using Equation 5.4 the restored intensity for each scan across the whole scanning window can be calculated. Calculation of the area under this curve yields a single value to describe the intensity of the reflected scan. Similarly at each angle pair, on the independent axes, there exist five restored intensity area measurements, each corresponding to the five distinct angle values of the remaining orientation angle. A surface plot can be generated based on the mean of these five distinct values at each angle perspective location.

Such a plot is shown for AB orientation perspective for a calibration white paper sheet sample at nominal 1000 mm SSD and is shown in Figure 5.16.
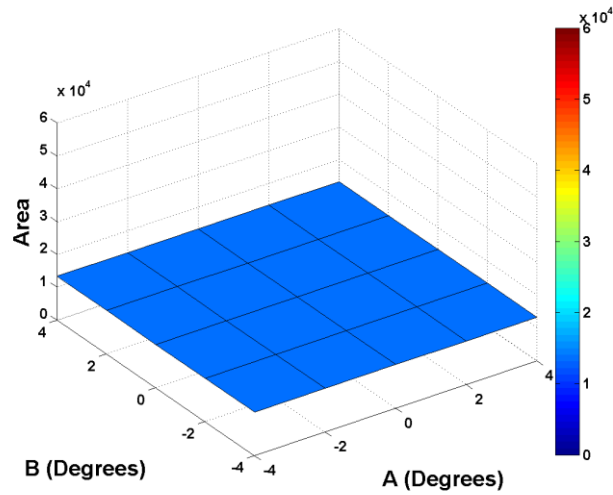
Figure 5.16 LRF Restored Intensity Area Surface Plot

5.10.3 Scan Point Rejection Quantification

As discussed above, rejected measurement points, based on low or high reflected intensity are easily quantified and logged at any particular scan point and hence complete scan window. Additionally for the purposes of this characterisation study, points outwith ±10 % of the nominal SSD are classed as bad measurement points and hence are also rejected. This is a purely subjective value based on the empirical evidence of the sensors performance and overall desired acceptable performance level.

Similarly the percentage of points rejected per scan window can be calculated and then shown as above with respect to two angle perspectives. The mean percentage rejection per two orientation angle location can then be computed and a similar surface trend plot produced.

5.10.4 Bad Measurement Rejection Prediction

As discussed above, points exist which are classified as rejected or bad measurement points as they fall outwith a specified tolerance (±10 % of SSD) and do not produce a corresponding intensity based error code. From study of measured parameters, range, received intensity and AGC, it became clear, from observation, that large variation in received intensity between each subsequent scan correspond to points within the range data that fall outwith the specified tolerance. This is shown below (Figure 5.17) for aluminium sheet sample at nominal 3000 mm SSD.
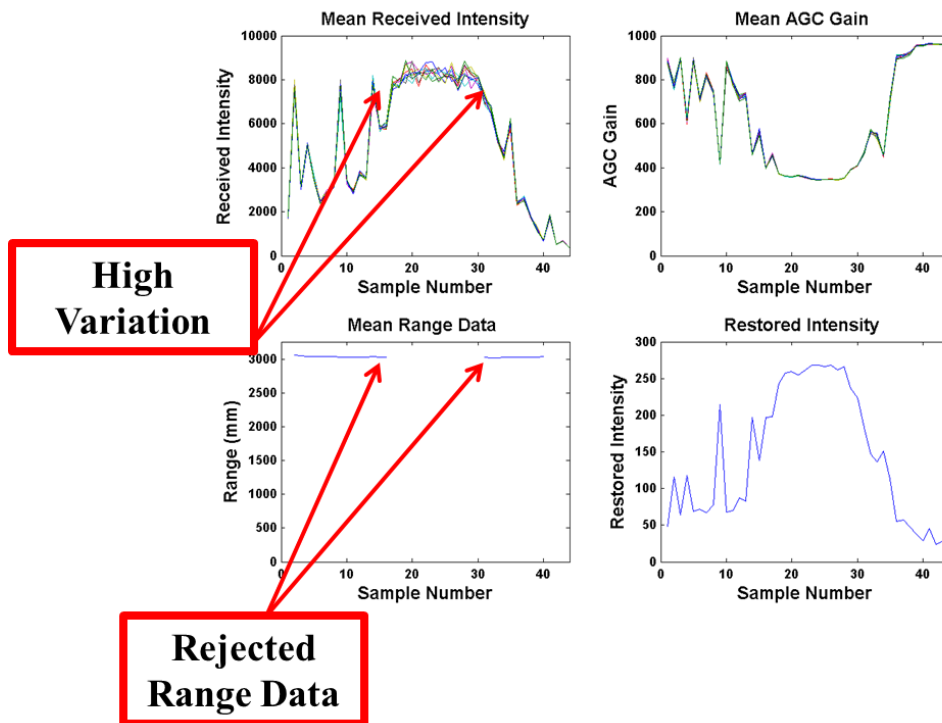
Figure 5.17 LRF Rejected Range Data Points

It was found that low received intensity values of below 2000 presented problems for the sensor and often resulted in rejected range data, with corresponding high AGC gain. Often these low intensity values produced a corresponding error code however

no specific value was identified to a represent a low received intensity error. This is shown in Figure 5.18 for aluminium sheet sample at nominal 500 mm SSD.
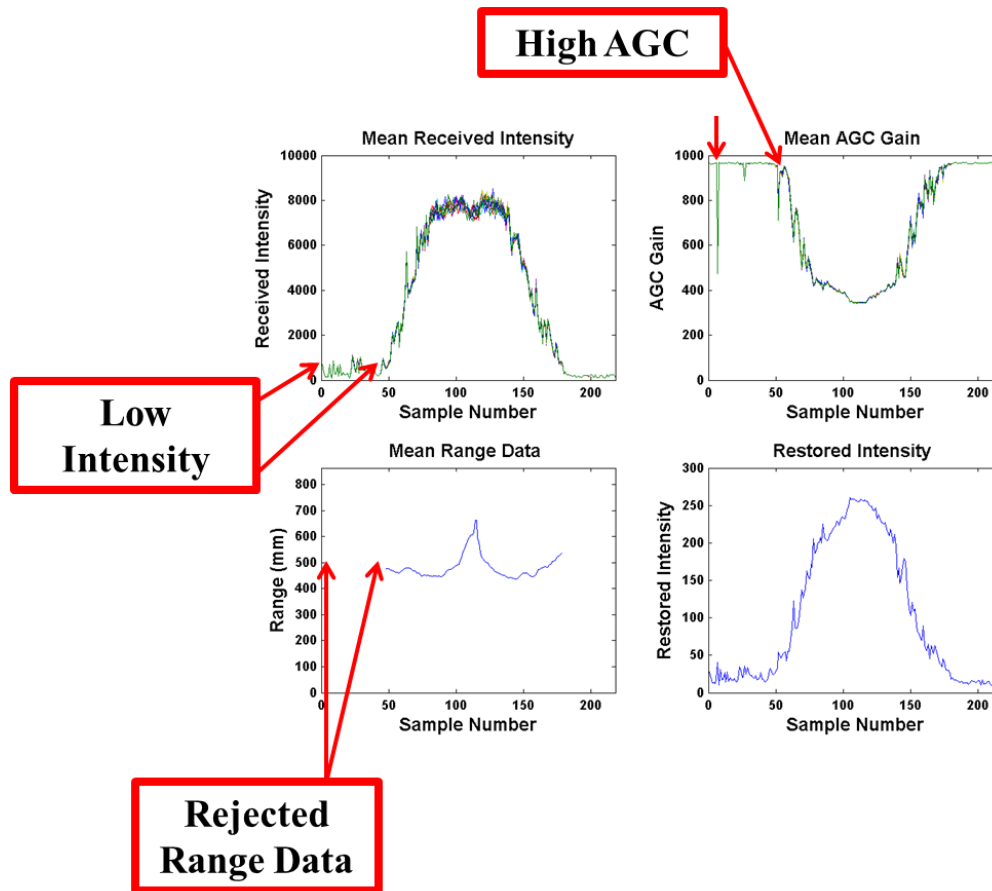
Figure 5.18 LRF Rejected Range Data Points

Similarly received intensity data greater than 8000 often produced erroneous range data but again did not always produce the according high intensity error message.

To evaluate the probability of bad or rejected measurement data based on received intensity variation, the following procedures were undertaken. The standard deviation of restored intensity data from each of the individual ten mean values sampled at each pose location was calculated. Concurrently the range data from each corresponding sample point was classified as a valid or rejected point. Again, a

139

rejected measurement is one that is outwith ±10 % of the nominal SSD. Furthermore any scan point which produced an according error message (for either low or high intensity) was also removed from the resultant dataset for evaluation.

Therefore the validity of all measurement points across a full scan can be plotted against the received intensity standard deviation. This is shown in Figure 5.19 for aluminium sheet sample at nominal 3000 mm SSD.
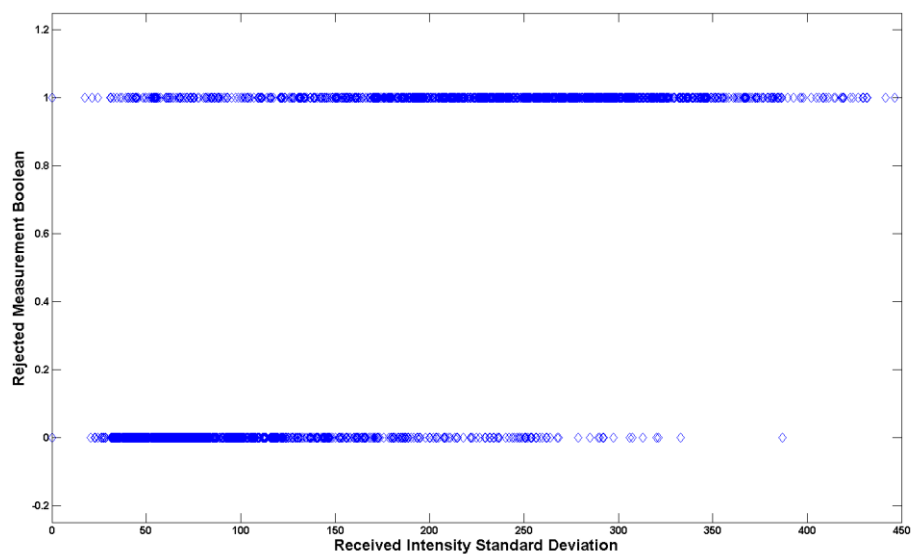
Figure 5.19 Received Intensity Standard Deviation against LRF Range Measurement Validity

As shown higher received intensity standard deviation features a greater density of rejected measurements.

The data is further divided by binning all data within bins of incremental width of standard deviation 10. The width was chosen arbitrarily on the basis of dividing the

large deviation scale into smaller datasets. Across each bin the validity of range measurement, in a range of zero to one, is calculated by:

$$VMP = \frac{NVP}{NVP+NRP}$$ (5.5)

Where:

VMP   Valid Measurement Probability

NVP   Number of Valid Measured Points

NRP   Number of Rejected Measured Points

Therefore within each bin a validity measurement probability value was calculated and could then be plotted accordingly for the whole range. This is shown in Figure 5.20 for aluminium sheet sample at nominal 3000 mm SSD.
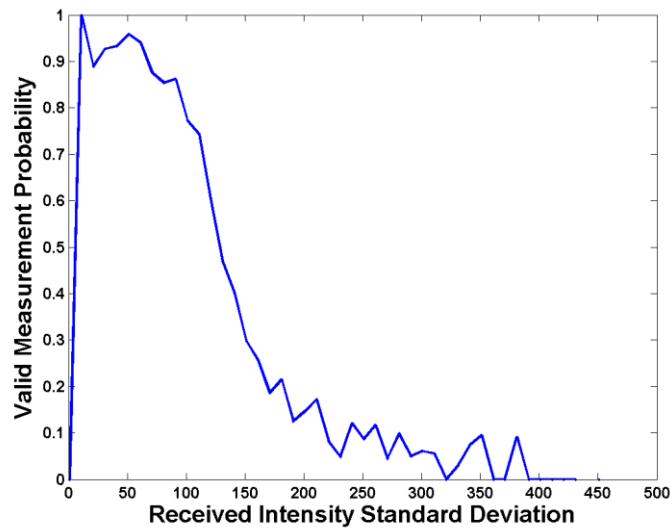
Figure 5.20 LRF Range Validity as a function of Received Intensity Standard Deviation

5.10.5 Overall Distance Error Quantification

It would be beneficial to simply highlight the magnitude and polarity of the distance error of all scans across the complete angular orientation window. A normal distribution histogram was introduced to represent and encompass the range distance from the LRF to each individual scan point in the complete measurement scan. This was plotted against the true SSD as measured by the LAT. Such a plot is shown below in Figure 5.21.
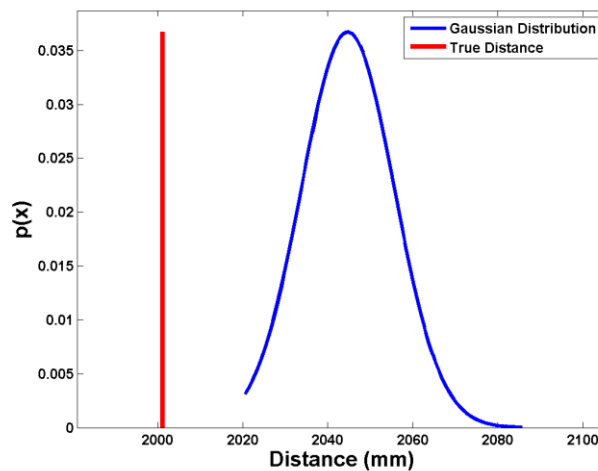
Figure 5.21 LRF Distance Measurement

5.10.6 Range Data Stability

As per [174,194] the variation in measurement range data can be evaluated. As ten samples were acquired at each measurement pose location, the distribution of distance error, with respect to the LAT measured SSD, could be evaluated. A simple normal distribution histogram was then established to represent the data. Such a plot is shown below in Figure 5.22 for the nominal 0, 0, 0 (A, B, C) pose location for calibration white paper sheet sample at nominal 1000 mm SSD.
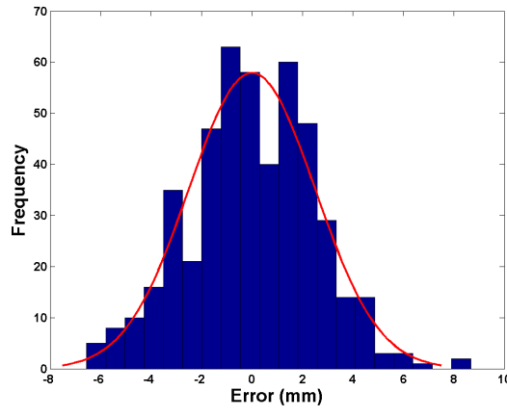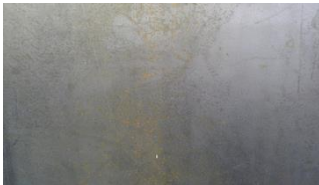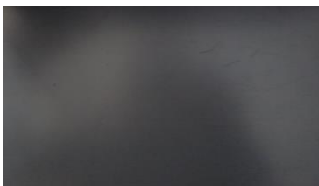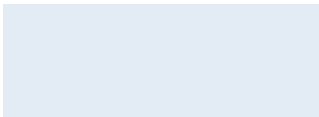
Figure 5.22 LRF Range Data Variation

5.12 Sample Scanning

The test surfaces investigated featured the properties documented in Table 5.2 and were scanned in that order. The data processing and visualisation techniques discussed in Section 5.10 were then all applied and recorded for full interpretation.

The full suite of data and plots generated are shown for the first two samples to highlight the variation in sensor performance when scanning matte or glossy surfaces. All other samples feature a shortened data recording policy, with the full suite of plots available and recorded in Appendix C. Additionally all surfaces feature a specific individual discussion to highlight the characteristics and performance recorded when laser scanning such surfaces.

Material	Sample Surface	Description
Paper		Type: White coated woven paper Media Weight:120g/m2 Area Dimension: 900 x 600 mm
Aluminium		Type: Aluminium Sheet Thickness: 3 mm Alloy:1050 Standard: EN 485 Area Dimension: 900 x 600 mm
Steel		Type: Cold Reduced Steel Sheet Thickness: 1 mm Standard: BS EN 10131 Area Dimension: 900 x 600 mm
Stainless Steel		Type: Cold Rolled Stainless Steel Sheet Thickness: 2 mm Specification:1.4301 2B Standard: BS EN 10088-4 Area Dimension: 900 x 600 mm
Concrete		Type: Standard Finish British Standard Paving Thickness: 50 mm Standard: BS EN 1339 Area Dimension: 700 x 600 mm
PVC		Type: Polyvinyl Chloride (PVC) Sheet Thickness: 10 mm Standard:ASTM-D-1784-99 Class: Class 12454-B (Type 1 Grade 1) Area Dimension: 900 x 600 mm
Wood		Type: Structural Hardwood Plywood Sheet Thickness: 18 mm Standard:EN13986, BS EN 636-2, BS EN 314 Area Dimension: 900 x 600 mm
Perspex		Type: Clear Cast Perspex Sheet Thickness: 6 mm Standard:ISO7823-1 Area Dimension: 900 x 600 mm

Table 5.2 Test Sample Surface Information Reference

5.13 Paper Surfaces

In a similar manner to [162,176, 190], scans were undertaken on white paper as this is the material surface to which the sensor performance is characterised by the manufacturer.

When considering the range finder's performance when scanning white paper, it is shown in Figures 5.23-5.25 that the lowest RMSE mean error was found at the shortest distance of 500 mm. At this distance minimal change in error was found when varying any of the orientation angles through the chosen range as highlighted in Figures 5.23-5.25. Furthermore at this distance the nominal distance recorded by the laser range finder was consistently greater than the actual physical sensor to surface distance giving a positive distance error.

As nominal sensor to surface distance increased to 1000 mm, the RMSE mean error also increased across the orientation angles, with a particular nonlinear trend beginning to be discernible in yaw (A) and pitch (B) orientations. This is further emphasised and visible with increased nonlinearity present at greater nominal ranges. Such a nonlinear effect was not evident for roll (C) rotations as highlighted in Figure 5.25 with only such variation seen in the single alternate angle Figures 5.23, 5.24. The standard deviation of the distance error increased with increasing SSD.

No nonlinear trend was witnessed on any restored intensity area surface plots where the overall mean intensity decreased as the SSD increased, as expected. The intensity

reduced to approximately 5% of the 500 mm SSD value at 4000 mm SSD. Generally the standard deviation of the restored intensity area decreased with increasing SSD. No rejected measurement points were recorded when scanning the paper surface and as such no percentage rejection or validity measurement probability plots are shown as the latter is always a Boolean one.

It is clear from Figure 5.30 that although all nominal distance errors were positive, significant systematic offset error appears to exist for all measurements poses. The histograms for the acquired measurement range, at zero orientation angles, highlight the normal distribution centred on nominal zero error for all paper sensor to surface distance measurements.

Distance Error viewed from AB Angle

(a)

(b)

(c)

(d)

(e)
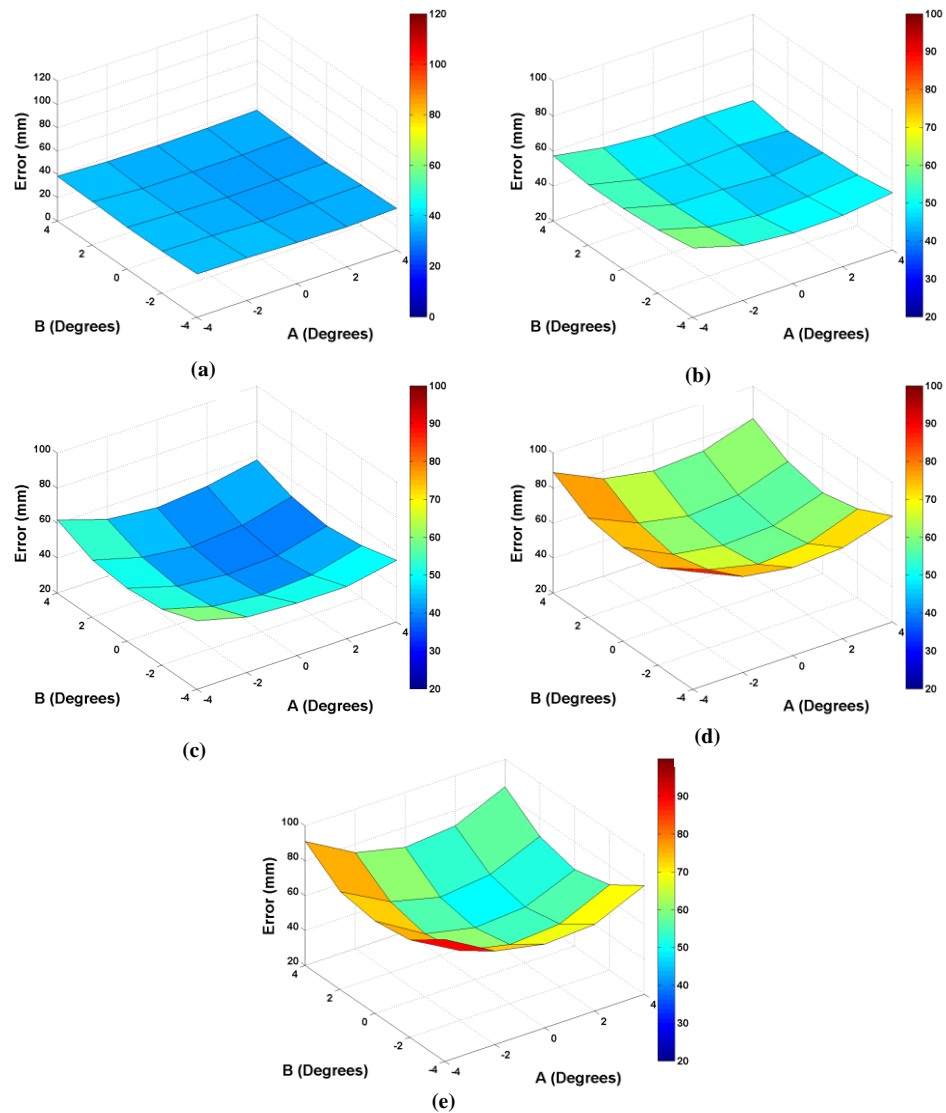
Figure 5.23 AB Angle LRF RMSE Mean Error, (a) – Nominal SSD 500 mm, (b) – Nominal SSD 1000 mm, (c) – Nominal SSD 2000 mm, (d) – Nominal SSD 3000 mm, (e) – Nominal SSD 4000 mm (All other plots follow this labelling convention) (Paper)

Nominal SSD (mm)	RMSE Mean (mm)	Distance Error (AB) Standard Deviation (mm)
500	35.25	1.50
1000	50.21	3.87
2000	48.80	6.20
3000	69.70	9.22
4000	68.02	11.62

Table 5.3 AB Angle LRF Distance Error Statistical Performance (Paper)

Distance Error viewed from AC Angle

(a)

(b)

(c)

(d)

(e)
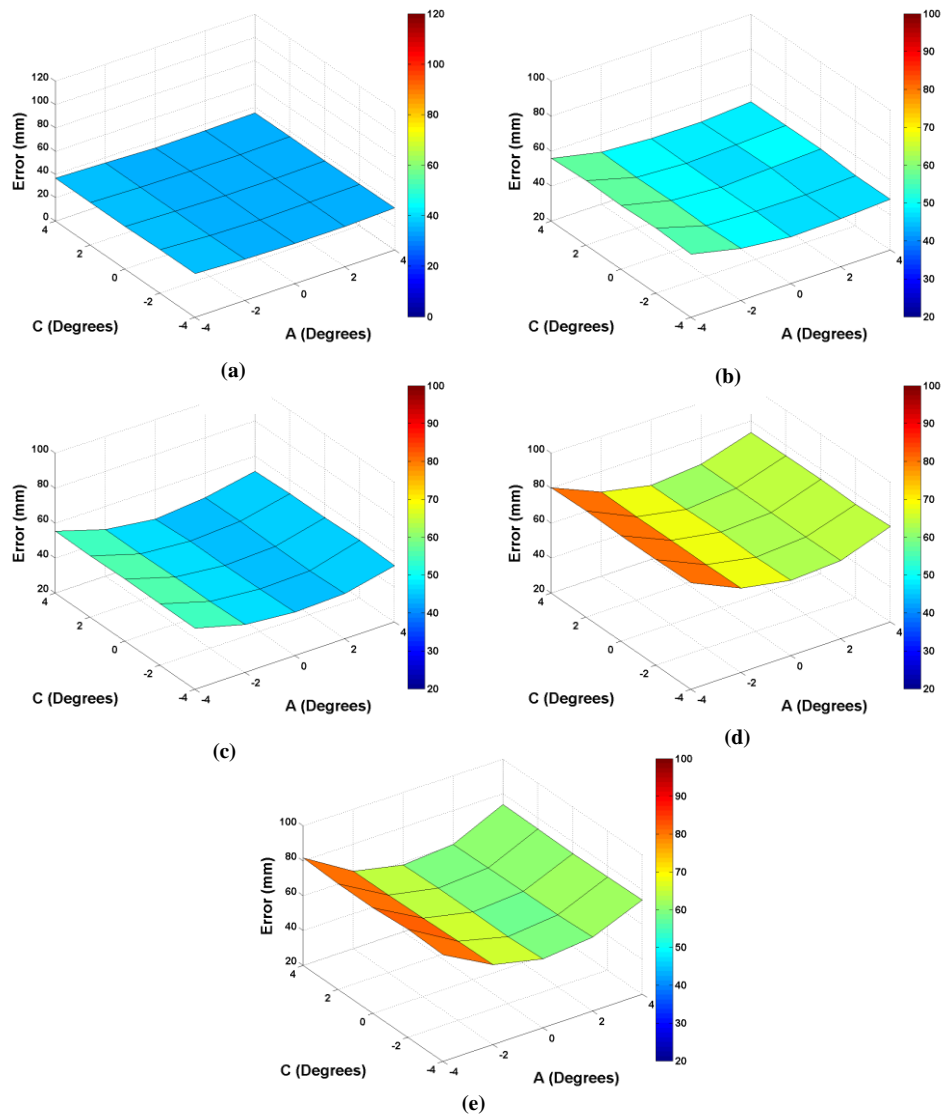
Figure 5.24 AC Angle LRF RMSE Mean Error (Paper)

Nominal SSD (mm)	RMSE Mean (mm)	Distance Error (AC) Standard Deviation (mm)
500	35.25	1.05
1000	50.21	3.35
2000	48.80	4.29
3000	69.70	6.64
4000	68.02	8.49

Table 5.4 AC Angle LRF Distance Error Statistical Performance (Paper)

148

Distance Error viewed from BC Angle

(a)

(b)

(c)

(d)

(e)
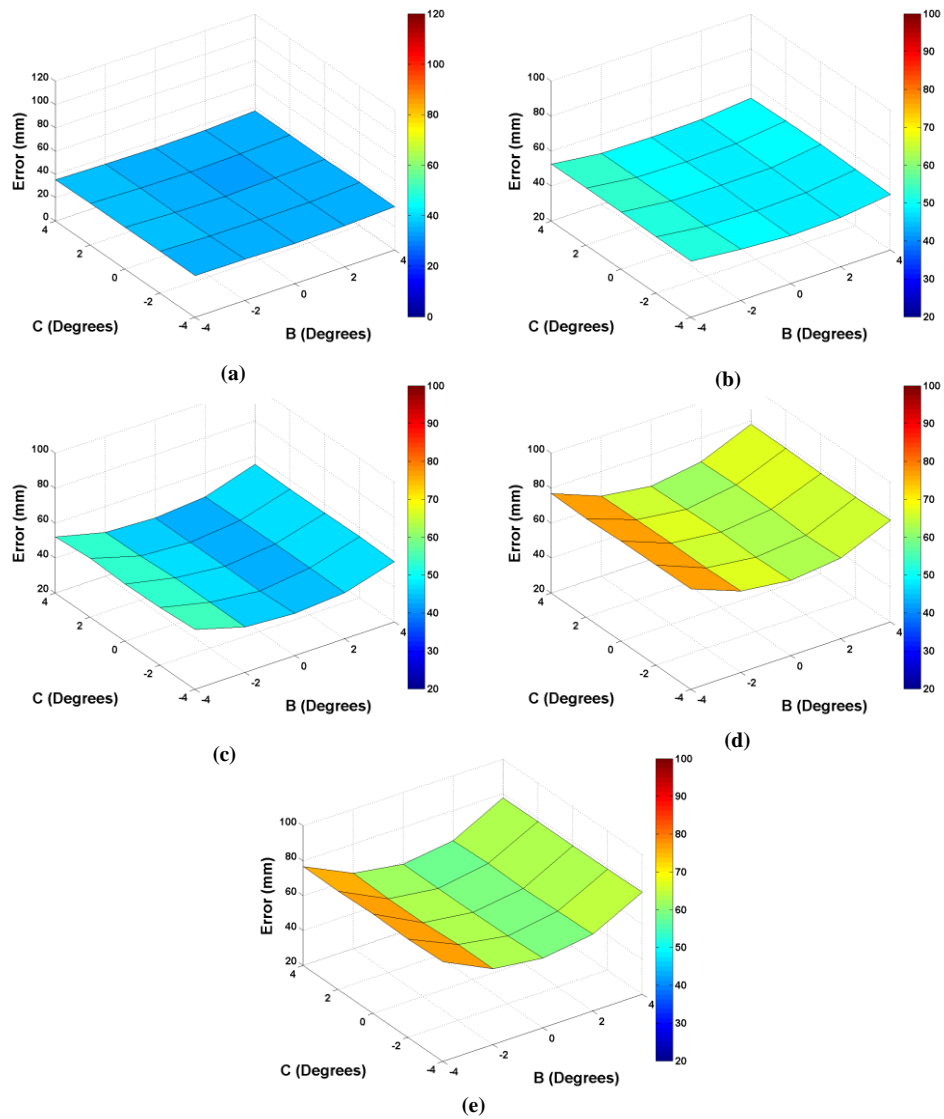
Figure 5.25 BC Angle LRF RMSE Mean Error (Paper)

Nominal SSD (mm)	RMSE Mean (mm)	Distance Error (BC) Standard Deviation (mm)
500	35.25	1.05
1000	50.21	1.87
2000	48.80	4.49
3000	69.70	6.40
4000	68.02	7.95

Table 5.5 BC Angle LRF Distance Error Statistical Performance (Paper)

Restored Intensity viewed from AB Angle

(a)

(b)

(c)

(d)

(e)
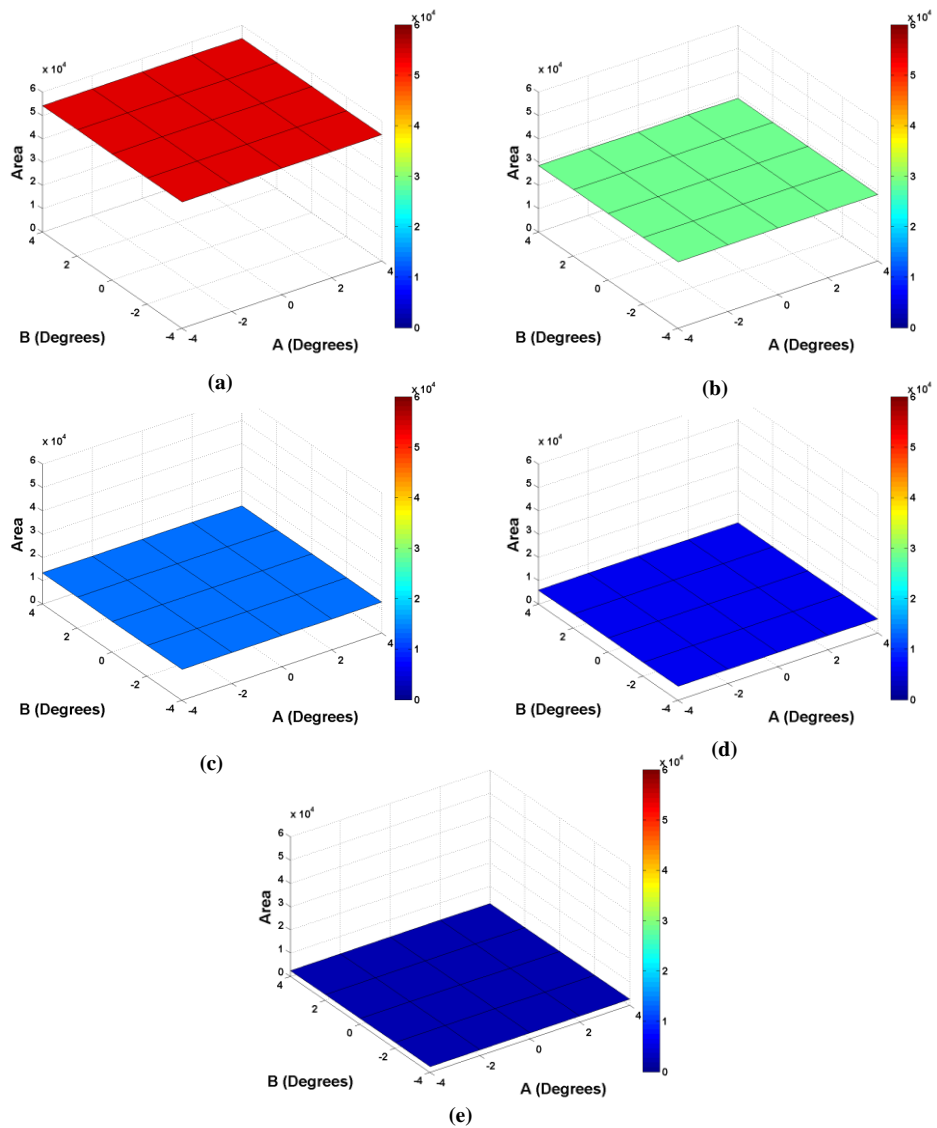
Figure 5.26 AB Angle LRF Restored Intensity Area (Paper)

Nominal SSD (mm)	Restored Intensity Area Mean	Restored Intensity Area (AB) Standard Deviation
500	54242.80	52.45
1000	28571.00	46.88
2000	13292.80	52.78
3000	6015.19	50.05
4000	2531.76	32.26

Table 5.6 AB Angle LRF Restored Intensity Area Statistical Performance (Paper)

Restored Intensity viewed from AC Angle

(a)

(b)

(c)

(d)

(e)
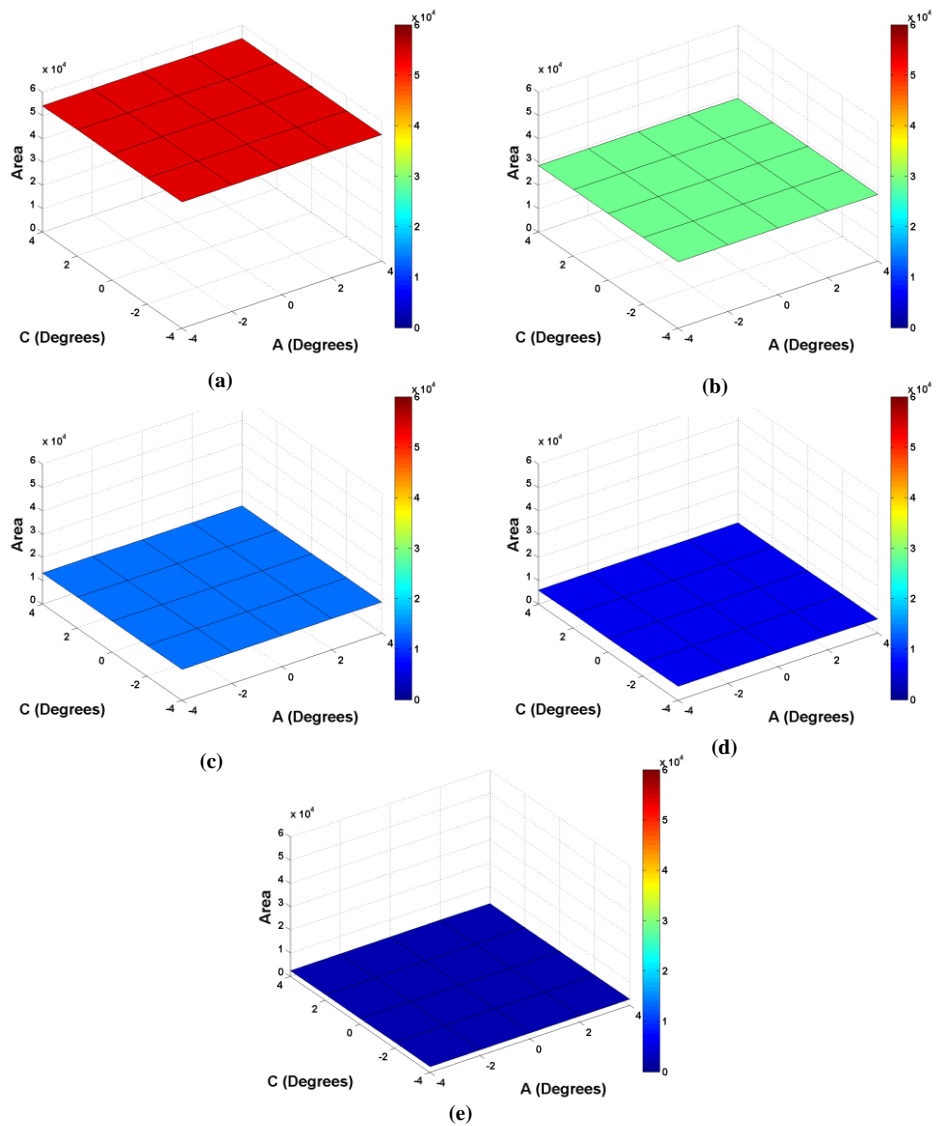
Figure 5.27 AC Angle LRF Restored Intensity Area (Paper)

Nominal SSD (mm)	Restored Intensity Area Mean	Restored Intensity Area (AC) Standard Deviation
500	54242.80	41.11
1000	28571.00	31.92
2000	13292.80	27.68
3000	6015.19	36.87
4000	2531.76	28.43

Table 5.7 AC Angle LRF Restored Intensity Area Statistical Performance (Paper)

Restored Intensity viewed from BC Angle

(a)

(b)

(c)

(d)

(e)
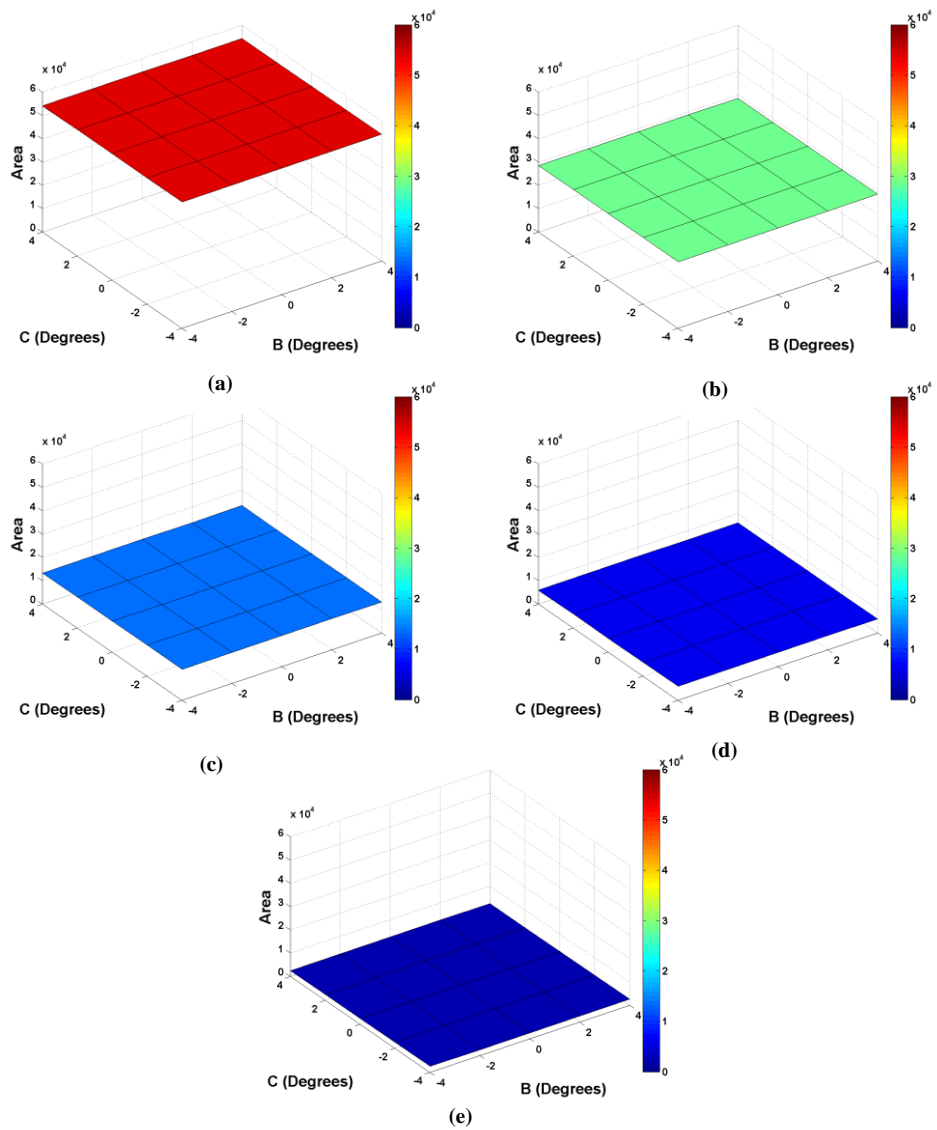
Figure 5.28 BC Angle LRF Restored Intensity Area (Paper)

SSD (mm)	Restored Intensity Area Mean	Restored Intensity Area (BC) Standard Deviation
500	54242.80	27.90
1000	28571.00	26.74
2000	13292.80	37.43
3000	6015.19	34.27
4000	2531.76	22.96

Table 5.8 BC Angle LRF Restored Intensity Area Statistical Performance (Paper)

Scan Plan View
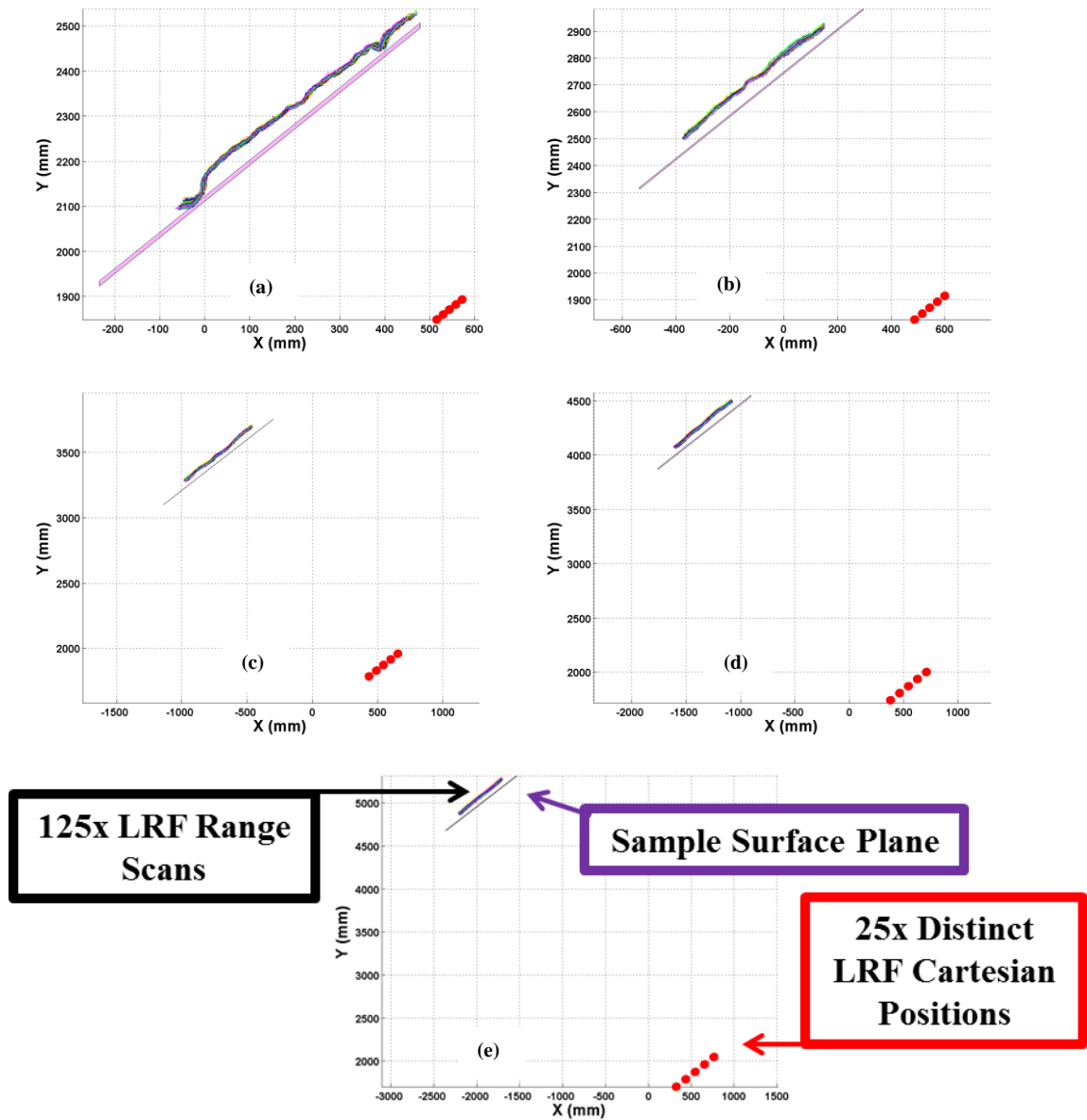
Figure 5.29 LRF Scan Plan View, (a) – Nominal SSD 500 mm, (b) – Nominal SSD 1000 mm, (c) – Nominal SSD 2000 mm, (d) – Nominal SSD 3000 mm, (e) – Nominal SSD 4000 mm (All other scan plots follow this labelling convention) (Paper)

Distance Error
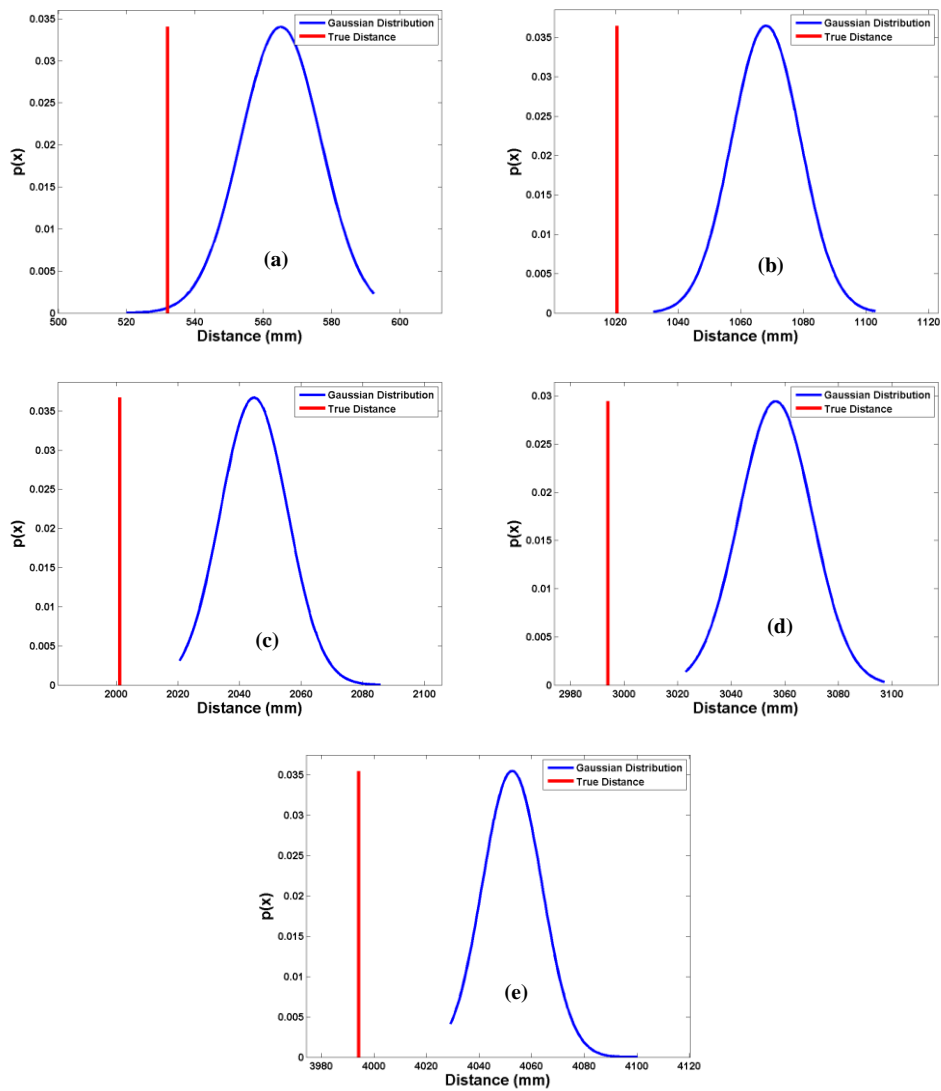
Figure 5.30 LRF Distance Error (Paper)

Distance (mm)	Distance Error Mean (mm)	Distance Error Standard Deviation (mm)	Distance Error Minimum (mm)	Distance Error Max (mm)
500	33.12	11.72	-12.01	60.29
1000	47.61	10.93	11.61	82.48
2000	43.56	10.87	19.44	84.59
3000	62.61	13.55	29.11	103.18
4000	58.33	11.25	35.01	106.00

Table 5.9 LRF Distance Error Statistical Performance (Paper)

Single Shot Histogram
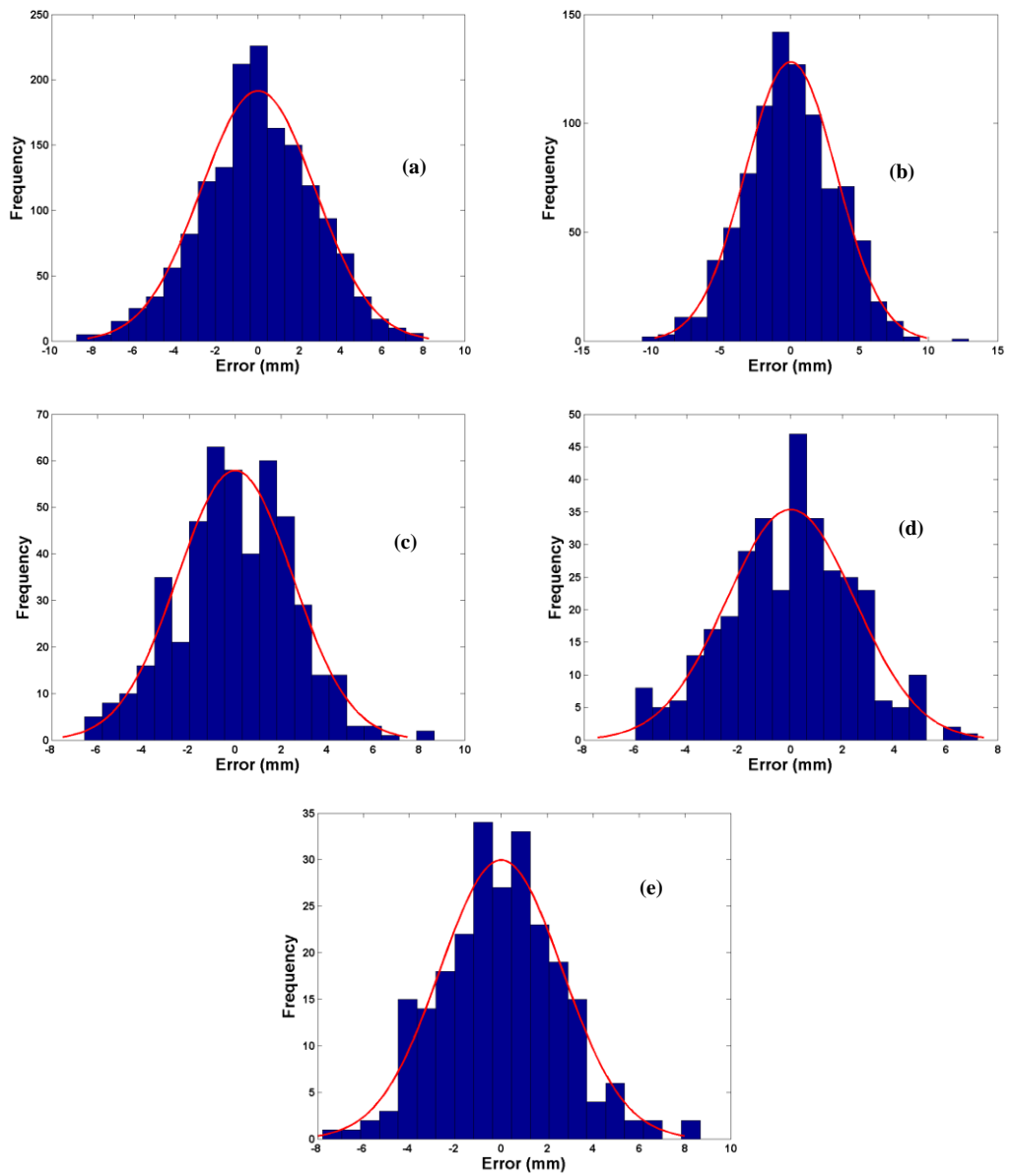
Figure 5.31 LRF Range Data Variation (Paper)

5.14 Aluminium Surfaces

It is evident from Figures 5.32-40 that significant error can be present when scanning aluminium surfaces with the URG-04LX laser ranger scanner.

In Figures 5.32-34 the lowest error occurred at an SSD of nominal 1000 mm, but these plots highlight the overall RMSE mean error, removing any polarity information. The nonlinear sensitivity to yaw (A) and pitch (B) motions is further emphasised by the aluminium surface conditions. Standard deviation of the distance error increased with increasing SSD. Figure 5.39 indicates significant errors were present, especially from laser scan beams located close to the central zero degree beam, at distances of 500, 1000 and 2000 mm nominal SSD.

Due to the angle of incidence of such beams with respect to the surface, strongest specular reflection was present at these angles and hence returned beam intensity was greatest. This high intensity was considered to cause saturation of the APD [174] and prevent correct distance measurement.

The highly specular nature of the surface resulted in the overall restored intensity area measurements being considerably lower at low (< 3000 mm) SSD scans when compared to that of white paper. At higher SSDs (> 3000 mm) the mean restored intensity area measurement was found to be greater than that of similarly measured paper. It is worth noting that across all SSDs, the standard deviation of the restored intensity area surface plots was considerably higher when compared to its equivalent paper counterparts.

Figures 5.35-37 highlight that measurement failure points occurred through all SSDs with the percentage failure decreasing at SSDs of 1000 and 2000 mm from their higher initial (SSD 500 mm) value before again increasing with increased SSDs. Concurrently with increasing SSD, occurs a significant increase in percentage rejection standard deviation, with a similar trend of no apparent dominant effect of roll (C) orientation.

Figure 5.38 highlights that with increased (> 3000 mm) SSD the probability of a valid measurement decreased rapidly with increased received intensity standard deviation. Additionally the figures demonstrate that small received intensity standard deviation values can account for both valid and rejected range measurement data.

Figure 5.40 shows the overall distance error polarity and magnitude changes as the SSD increased. This clearly identifies a systematic offset which varies as a function of distance for aluminium surfaces.

Distance Error viewed from AB Angle

(a)

(b)

(c)

(d)

(e)
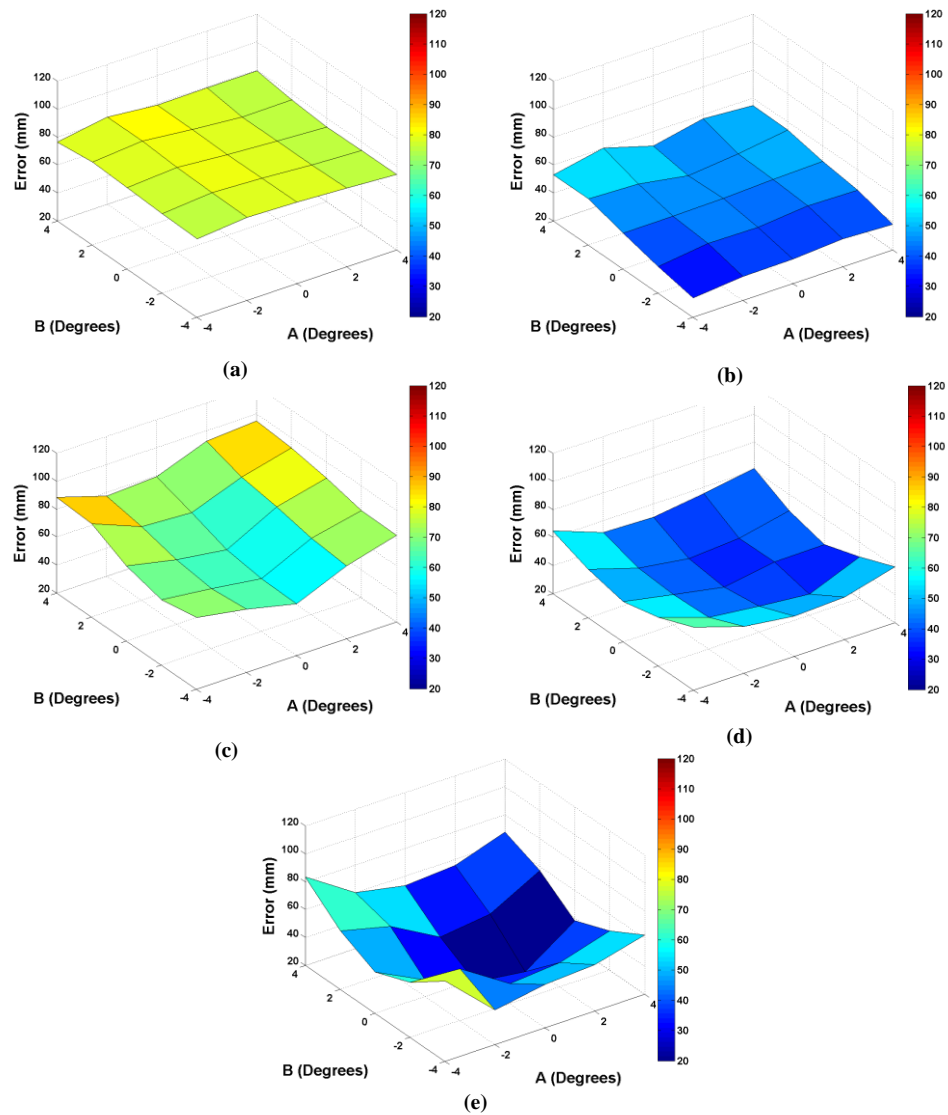
Figure 5.32 AB Angle LRF RMSE Mean Error (Aluminium)

Nominal SSD (mm)	RMSE Mean (mm)	Distance Error (AB) Standard Deviation (mm)
500	77.67	2.44
1000	46.72	6.74
2000	76.09	11.20
3000	48.57	8.72
4000	49.67	16.39

Table 5.10 AB Angle LRF Distance Error Statistical Performance (Aluminium)

158

Distance Error viewed from AC

(a)

(b)

(c)

(d)

(e)
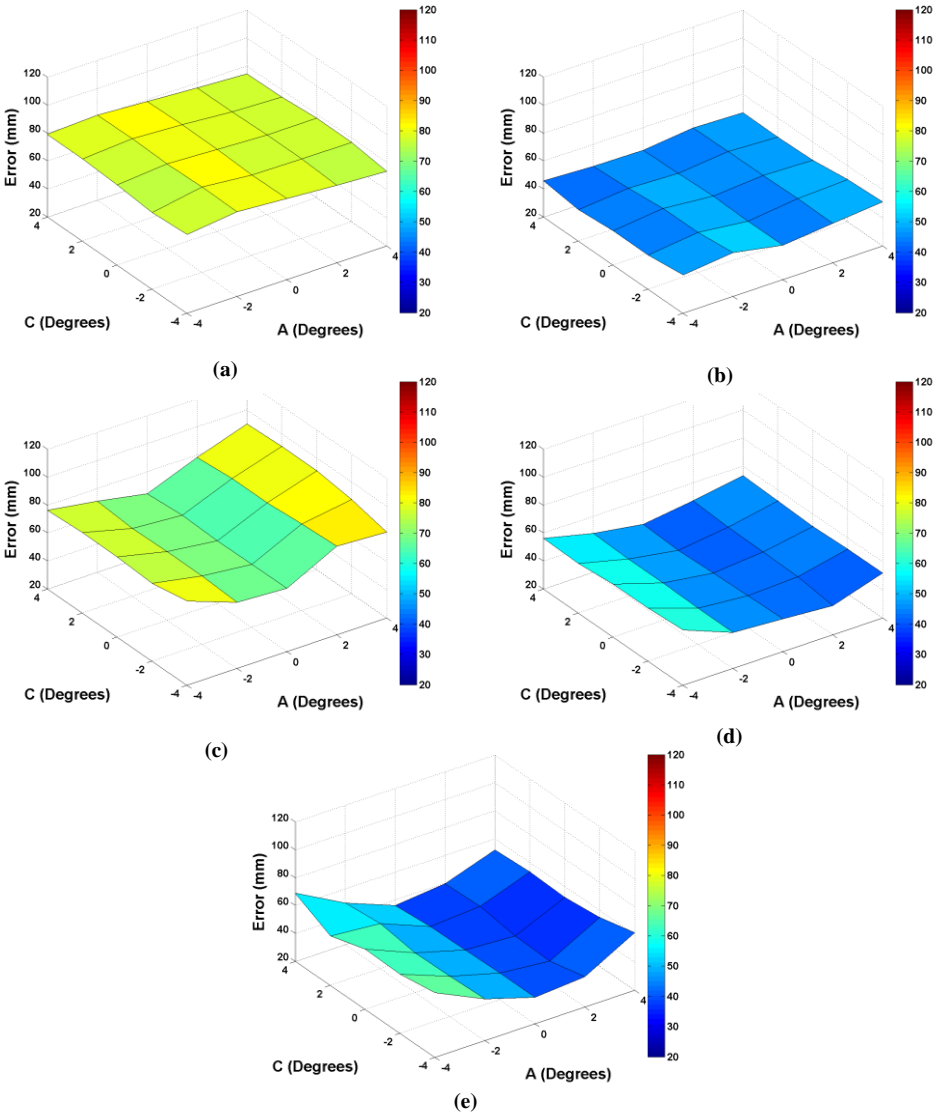
Figure 5.33 AC Angle LRF RMSE Mean Error (Aluminium)

Nominal SSD (mm)	RMSE Mean (mm)	Distance Error (AC) Standard Deviation (mm)
500	77.67	2.21
1000	46.72	2.40
2000	76.09	8.71
3000	48.57	5.81
4000	49.67	10.15

Table 5.11 AC Angle LRF Distance Error Statistical Performance (Aluminium)

159

Distance Error viewed from BC

(a) (b) (c) (d) (e)
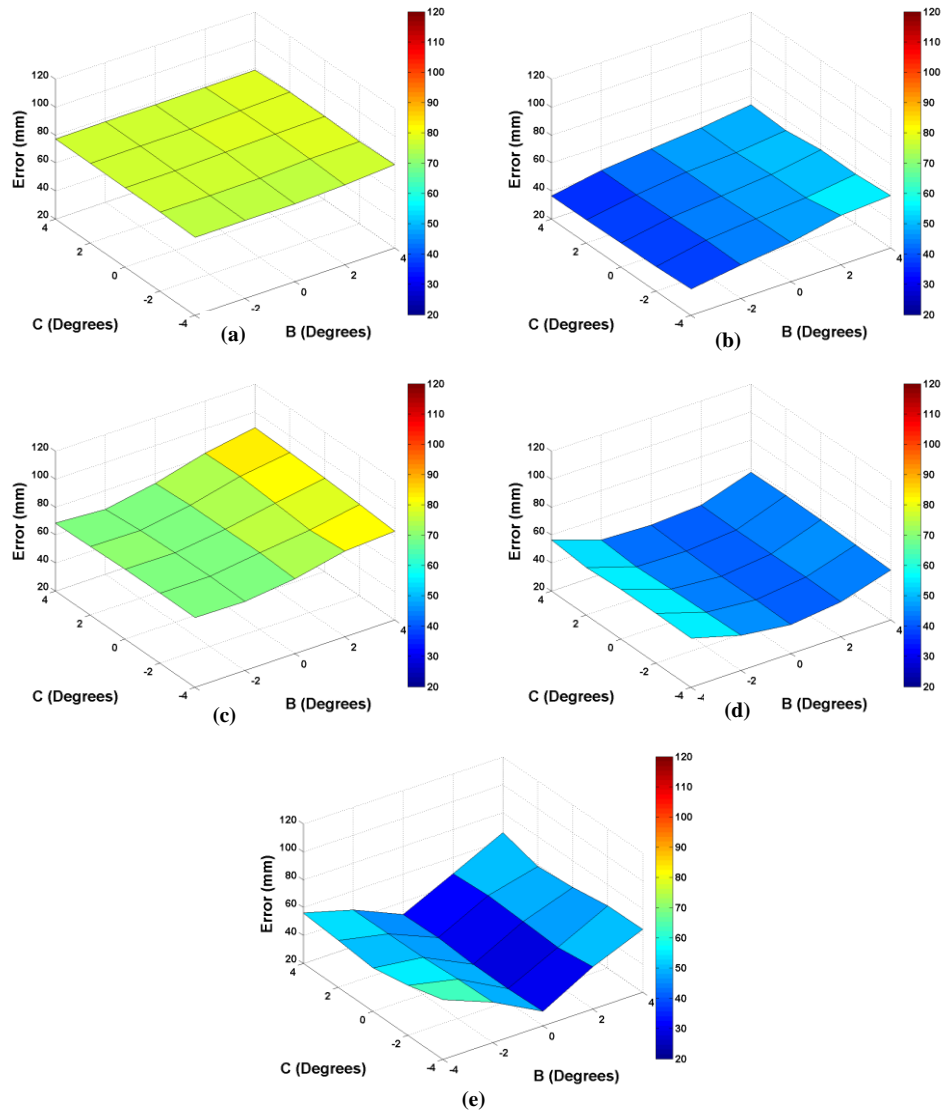
Figure 5.34 BC Angle LRF RMSE Mean Error (Aluminium)

SSD (mm)	RMSE Mean (mm)	Distance Error (BC) Standard Deviation (mm)
500	77.67	1.25
1000	46.72	6.35
2000	76.09	7.18
3000	48.57	6.41
4000	49.67	11.34

Table 5.12 BC Angle LRF Distance Error Statistical Performance (Aluminium)

Restored Intensity

Nominal SSD (mm)	Restored Intensity Area Mean	Restored Intensity Area Standard Deviation		
		(AB)	(AC)	(BC)
500	21711.60	674.53	305.49	622.21
1000	13152.60	885.58	483.97	759.49
2000	7005.02	977.18	549.00	828.84
3000	5148.29	901.62	813.15	416.91
4000	3948.78	1061.31	810.00	676.48

Table 5.13 LRF Restored Intensity Area Statistical Performance (Aluminium)

All Restored Intensity Area Plots are shown in the Appendix C, Figures C.2-5.

Percentage Rejections viewed from AB Angle

(a)

(b)

(c)

(d)

(e)
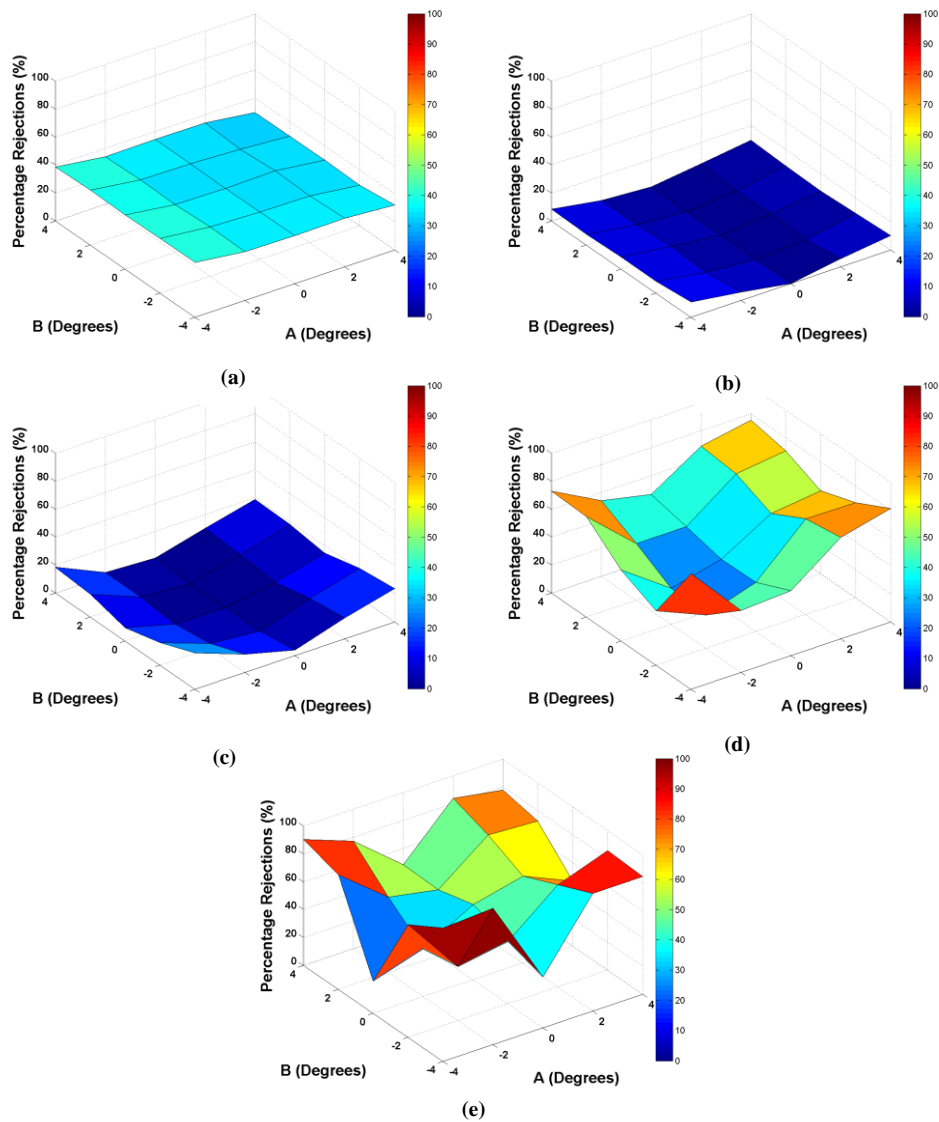
Figure 5.35 AB Angle LRF Percentage Rejections (Aluminium)

Nominal SSD (mm)	Percentage Rejection Mean	Percentage Rejection (AB) Standard Deviation
500	34.32	2.95
1000	5.11	6.65
2000	10.46	8.18
3000	55.85	17.46
4000	65.99	21.51

Table 5.14 AB Angle LRF Percentage Rejection Statistical Performance (Aluminium)

Percentage Rejections viewed from AC Angle

(a)

(b)

(c)

(d)

(e)
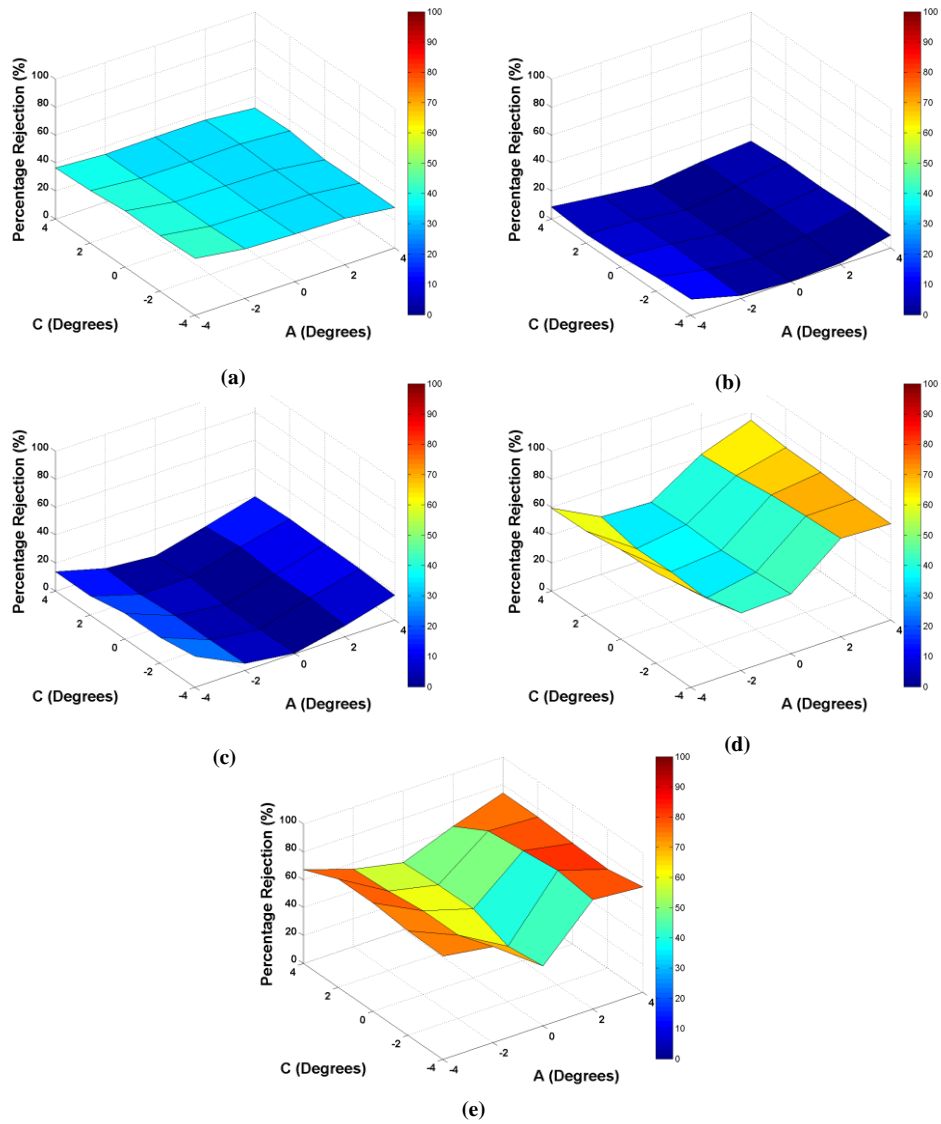
Figure 5.36 AC Angle LRF Percentage Rejections (Aluminium)

Nominal SSD (mm)	Percentage Rejection Mean	Percentage Rejection (AC) Standard Deviation
500	34.32	3.07
1000	5.11	3.70
2000	10.46	7.48
3000	55.85	14.40
4000	65.99	12.52

Table 5.15 AC Angle LRF Percentage Rejection Statistical Performance (Aluminium)

Percentage Rejections viewed from BC Angle

(a)

(b)

(c)

(d)

(e)
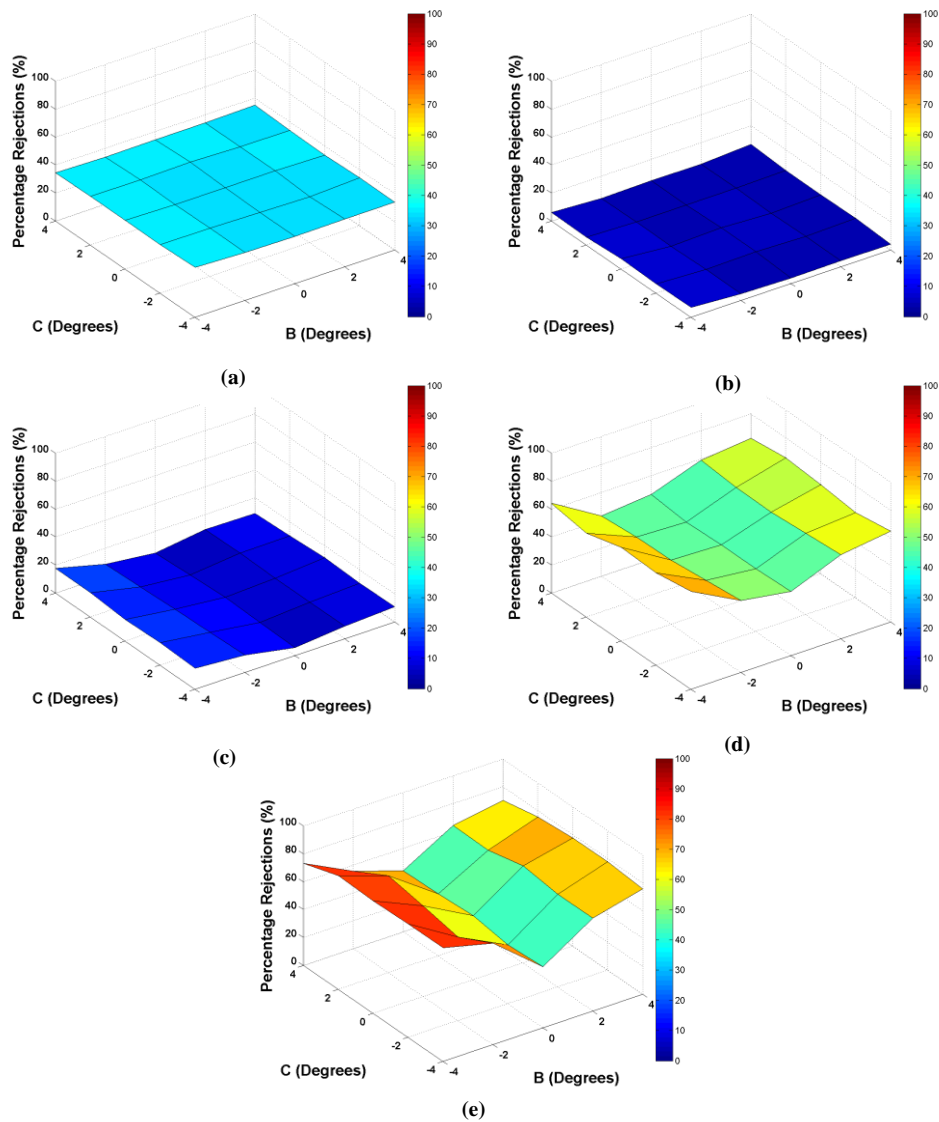
Figure 5.37 BC Angle LRF Percentage Rejections (Aluminium)

Nominal SSD (mm)	Percentage Rejection Mean	Percentage Rejection (BC) Standard Deviation
500	34.32	0.58
1000	5.11	0.98
2000	10.46	3.54
3000	55.85	8.84
4000	65.99	13.10

Table 5.16 BC Angle LRF Percentage Rejection Statistical Performance (Aluminium)

Valid Measurement Probability
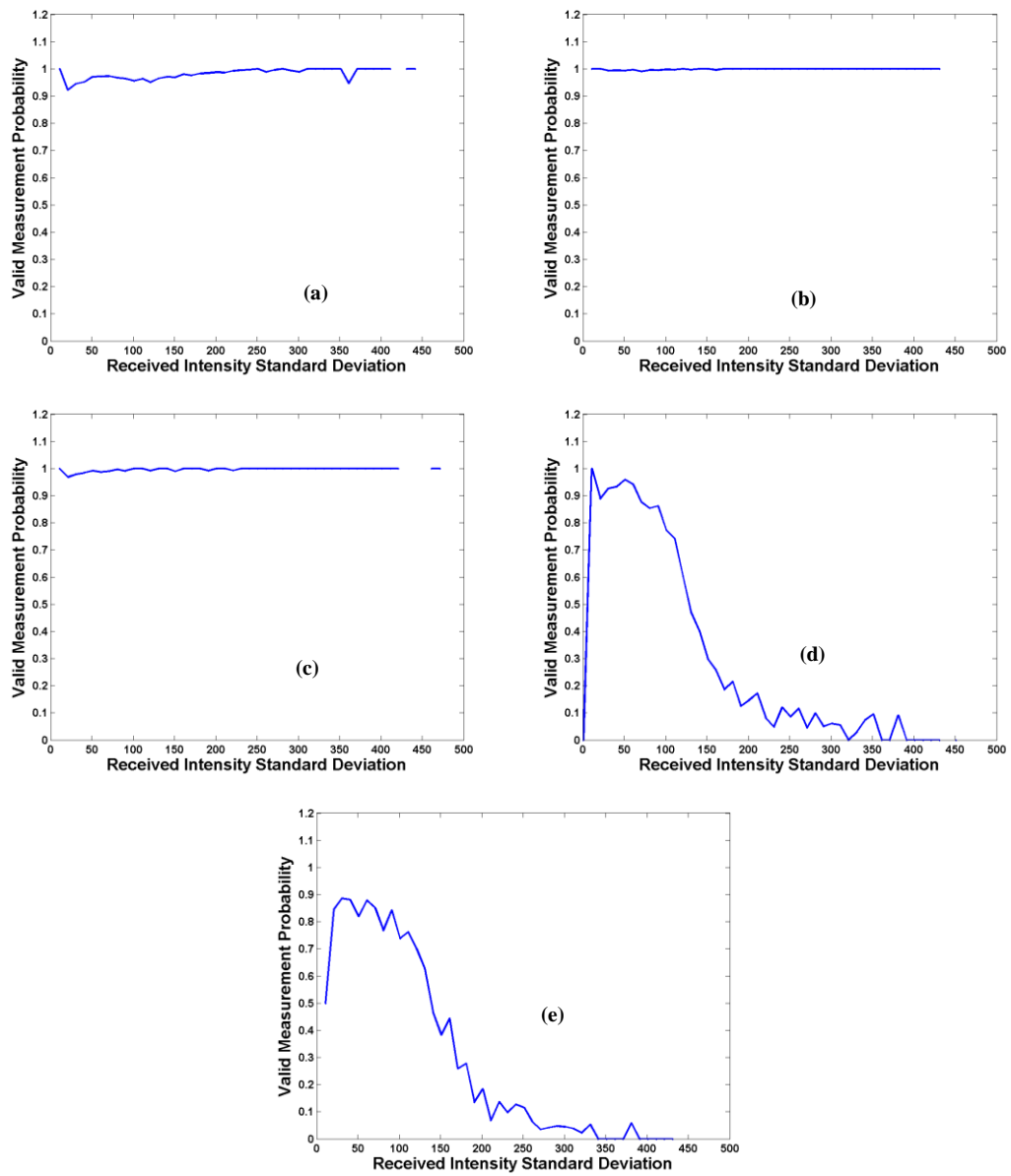
Figure 5.38 LRF Range Validity as a function of Received Intensity Standard Deviation (Aluminium)

Scan Plan View
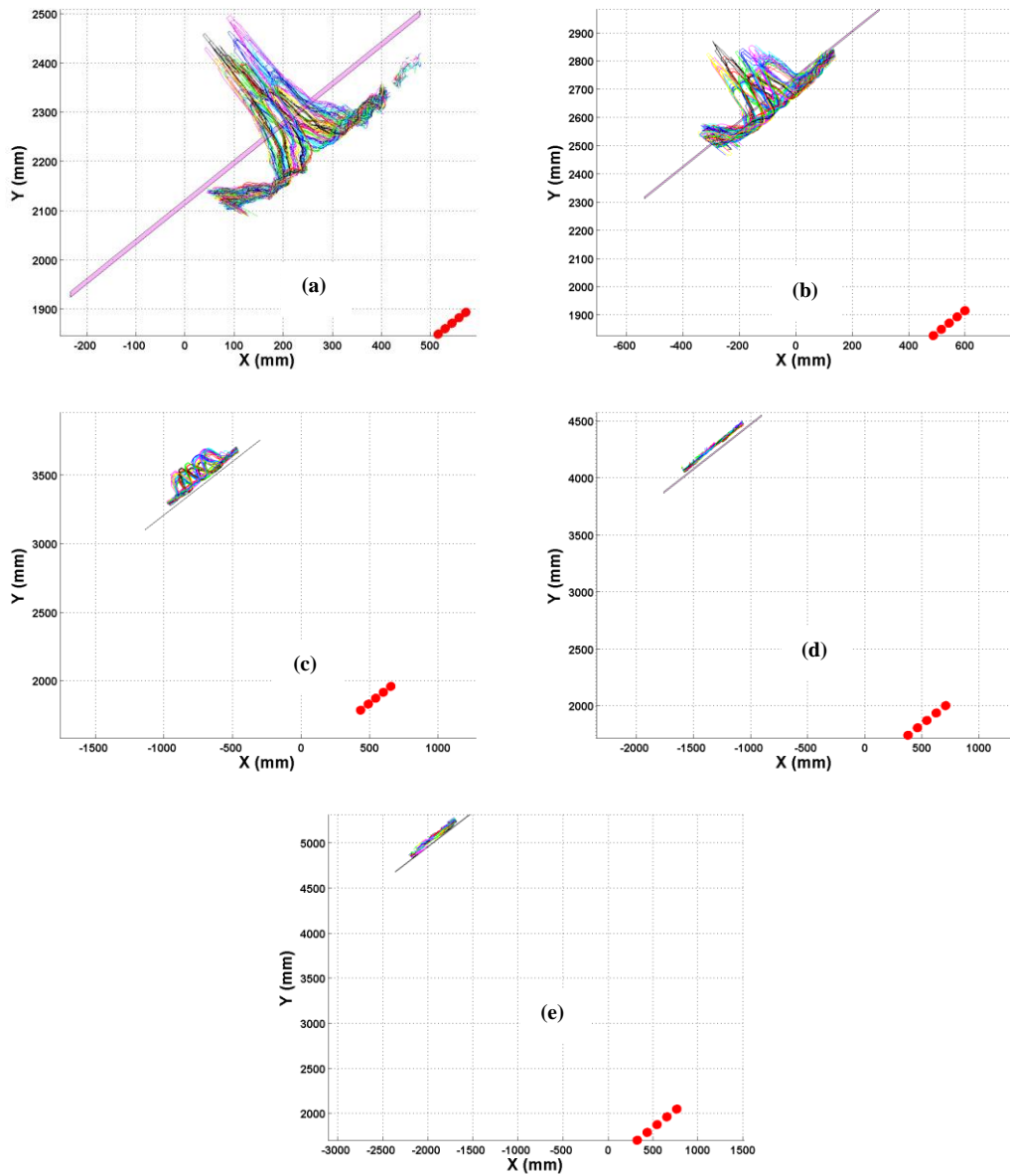
Figure 5.39 LRF Scan Plan View (Aluminium)

Distance Error
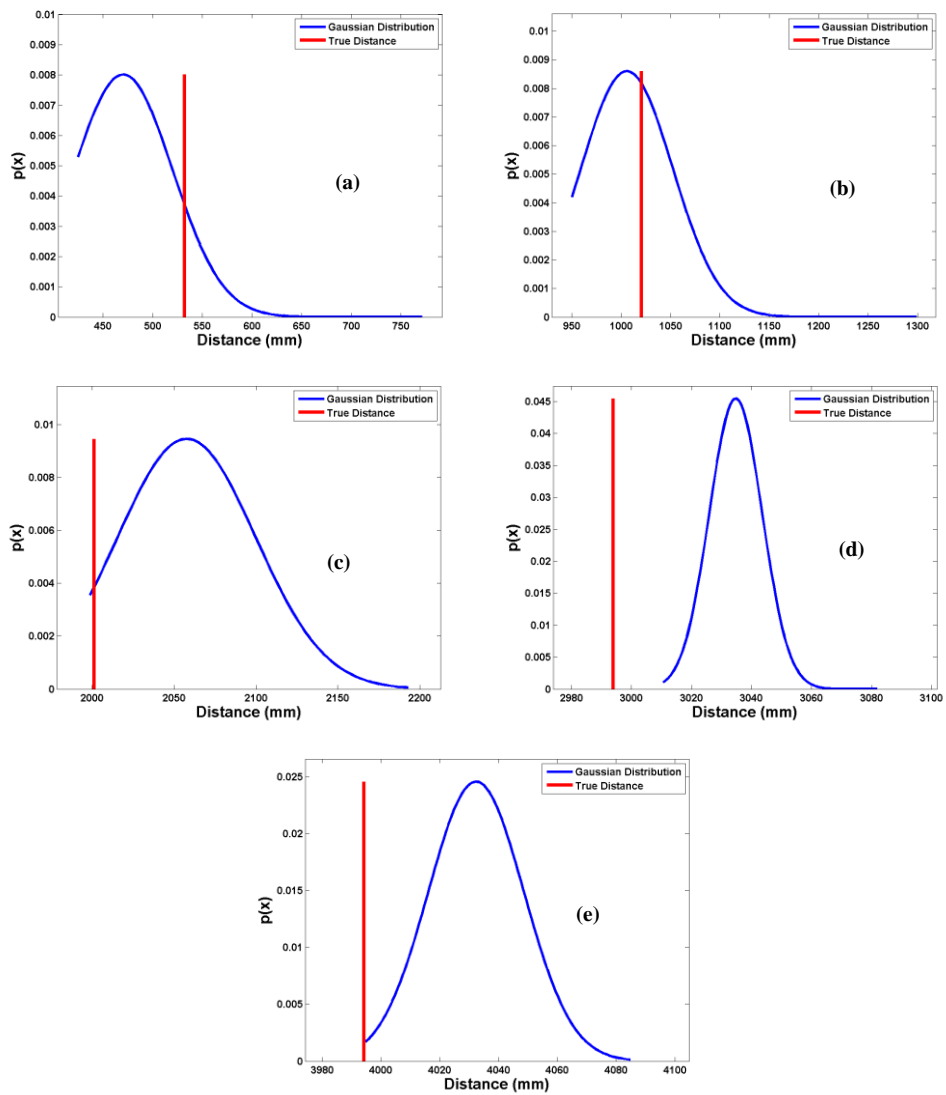
Figure 5.40 LRF Distance Error (Aluminium)

Nominal SSD (mm)	Distance Error Mean (mm)	Distance Error Standard Deviation (mm)	Distance Error Minimum (mm)	Distance Error Max (mm)
500	-72.49	28.58	-106.98	42.87
1000	-30.44	21.42	-70.24	29.50
2000	56.55	42.17	-2.414	191.80
3000	40.80	8.77	16.68	87.88
4000	38.10	16.23	0.59	90.50

Table 5.17 LRF Distance Error Statistical Performance (Aluminium)

5.15 Steel Surfaces

Similarities in ranging performance to those identified in Section 5.14 for the aluminium sample were noted. These included similar data trends in terms of polarity and magnitude of distance error as a function of SSD (Figure C.18). Similarly large distance errors were recorded at the central angle laser beams (Figure C.17). However, overall the magnitude of errors and probability of erroneous errors were reduced when compared to aluminium.

When considering the orientation angle variation similar nonlinearity was present in the Yaw (A) and Pitch (B) angles but to a much greater degree than present on the aluminium data. It is clear from Appendix C, Figures C.7-.9 that when considering steel, that this nonlinearity has both a negative and positive effect to the nominal zero angle value, with negative effects being visible on both the 500 and 1000 mm SSD. Again increased SSD yielded a greater standard deviation on the mean RMSE.

With regards to restored intensity, steel behaved in a similar manner to white paper, with a decrease of restored intensity area mean with increasing SSD. The actual values were lower however at each range distance, albeit with increased standard deviation when directly compared to paper.

When considering rejected measurement points, only at nominal SSDs of 500, 3000 and 4000 did this actually occur, while also highlighting both increased AB angle nonlinearity effect and standard deviation with increased SSD.

Figures C.13-16 highlight that although displaying percentage rejection at three distinct SSDs, the majority of these occurring at the larger (3000 & 4000 mm) ranges arise due to too low sensitivity and yield an according error message. At an SSD of 500 mm, lower standard deviations can yield rejected measurement data points, while the probability increased again with increased deviation.

RMSE Mean Distance Error

Nominal SSD (mm)	RMSE Mean (mm)	Distance Error Standard Deviation (mm)		
		(AB)	(AC)	(BC)
500	55.47	0.82	0.77	0.57
1000	33.82	2.48	1.95	1.64
2000	26.00	5.29	4.25	3.26
3000	48.17	9.74	7.10	6.66
4000	50.72	13.35	9.60	9.22

Table 5.18 Orientation Angle LRF Distance Error Statistical Performance (Steel)

Restored Intensity

Nominal SSD (mm)	Restored Intensity Area Mean	Restored Intensity Area Standard Deviation		
		(AB)	(AC)	(BC)
500	33386.10	235.28	137.04	225.07
1000	19118.80	357.68	187.67	335.59
2000	7650.40	579.15	219.34	527.66
3000	3114.57	520.29	116.14	506.83
4000	1456.78	280.03	128.58	246.34

Table 5.19 Orientation Angle LRF Restored Intensity Area Statistical Performance (Steel)

Percentage Rejection

Nominal SSD (mm)	Percentage Rejection Mean	Percentage Rejection Standard Deviation		
		(AB)	(AC)	(BC)
500	30.47	3.32	3.68	1.75
1000	0	0	0	0
2000	0	0	0	0
3000	6.55	8.55	8.18	2.14
4000	28.33	15.99	15.38	4.34

Table 5.20 Orientation Angle LRF Percentage Rejection Statistical Performance (Steel)

Distance Error

Nominal SSD (mm)	Distance Error Mean (mm)	Distance Error Standard Deviation (mm)	Distance Error Minimum (mm)	Distance Error Max (mm)
500	-47.84	24.66	-81.98	21.10
1000	-29.75	21.95	-75.19	32.29
2000	19.58	14.08	-12.14	72.35
3000	38.95	10.98	9.92	79.94
4000	35.57	13.75	5.32	82.20

Table 5.21 LRF Distance Error Statistical Performance (Steel)

All plots are shown in the Appendix C, Figures C.7 - 19.

5.16 Stainless Steel Surfaces

As with the steel and aluminium surfaces, stainless steel exhibited similar characteristic behaviour with respect to nominal distance error and orientation angle error. Figure C.32 highlights that the shift from negative to positive nominal distance error occurred between 500 and 1000 mm nominal SSD, therefore confirming its occurrence at a reduced SSD to that of aluminium and steel.

Additionally the Gaussian bell curve type profile produced when scanning aluminium was again apparent in Figure C.31 albeit more pronounced and lower in variation. This is highlighted with much higher mean RMSE values and lower standard deviation values when directly compared to aluminium. (Appendix C, Figures C.20-22. Table 5.22). Figures C.20-22 demonstrate that a reduced level of distance error nonlinearity was present with yaw and pitch orientation angles changes, when compared to aluminium and steel. With regards to restored intensity area, the values are very similar to that of its carbon steel counterpart but with a much increased standard deviation (Table 5.23).

The percentage rejection plots (Appendix C, Figures C.27-29) highlight that rejected measurements were only found at larger SSDs (>3000 mm) but as Appendix C, Figure C.30 show these rejections were also not accompanied by a corresponding error code. As found with aluminium increased received intensity standard deviation yields rejected measurement range data points.

RMSE Mean Distance Error

Nominal SSD (mm)	RMSE Mean (mm)	Distance Error Standard Deviation (mm)		
		(AB)	(AC)	(BC)
500	37.37	0.75	0.65	0.69
1000	42.78	2.26	2.02	1.03
2000	89.82	4.93	3.26	3.70
3000	94.92	9.44	7.09	6.24
4000	94.04	11.06	7.88	7.73

Table 5.22 Orientation Angle LRF Distance Error Statistical Performance (Stainless Steel)

Restored Intensity

Nominal SSD (mm)	Restored Intensity Area Mean	Restored Intensity Area Standard Deviation		
		(AB)	(AC)	(BC)
500	33313.70	309.88	527.45	569.78
1000	18262.50	240.53	252.61	268.38
2000	8230.51	281.82	273.67	102.55
3000	4469.79	259.41	252.37	57.79
4000	2722.75	606.80	604.66	43.12

Table 5.23 Orientation Angle LRF Restored Intensity Area Statistical Performance (Stainless Steel)

Rejected Percentage

Nominal SSD (mm)	Percentage Rejection Mean	Percentage Rejection Standard Deviation		
		(AB)	(AC)	(BC)
500	0	0	0	0
1000	0	0	0	0
2000	0	0	0	0
3000	28.50	15.05	15.15	1.91
4000	42.10	20.25	20.17	2.13

Table 5.24 Orientation Angle LRF Percentage Rejection Statistical Performance (Stainless Steel)

Distance Error

Nominal SSD (mm)	Distance Error Mean (mm)	Distance Error Standard Deviation (mm)	Distance Error Minimum (mm)	Distance Error Max (mm)
500	-12.37	36.46	-79.52	119.89
1000	24.94	34.41	-28.38	143.51
2000	80.79	27.09	34.67	169.04
3000	86.83	10.72	57.03	135.68
4000	80.04	15.08	41.00	123.96

Table 5.25 LRF Distance Error Statistical Performance (Stainless Steel)

All plots are shown in the Appendix C, Figures C.20 - 33.

5.17 Concrete Surfaces

Figures C.35-47 reveal that matte industrial surfaces such as concrete pose a significant challenge in terms of accurate distance measurement to the LRF. Figure C.46 shows that the polarity of measurement distance error switched from positive to negative for the 1000 SSD measurement, while then returning to a positive error for subsequent greater SSD readings. When considering the mean RMSE plots (Appendix C, Figures C.35-37) the performance was very similar to that of white paper with slightly increased values. However in a similar fashion to the previously discussed metallic materials nonlinear effects in measurement error are found in both the yaw and pitch angles.

Again similar to white paper, the restored intensity mean and standard deviation followed a similar trend to that of paper, albeit at lower mean and higher standard deviation values (Appendix C, C.38-40 & Table 5.27). Appendix C, Figures C.41-44 highlight the rejected measurement points found when scanning concrete surfaces at an SSD of 4000 mm were all the result of low returned intensity.

RMSE Mean Distance Error

Nominal SSD (mm)	RMSE Mean (mm)	Distance Error Standard Deviation (mm)		
		(AB)	(AC)	(BC)
500	20.80	1.60	1.43	0.83
1000	55.98	11.12	2.10	11.00
2000	65.28	7.92	6.05	5.17
3000	88.00	7.60	5.37	5.37
4000	90.73	15.22	11.65	9.60

Table 5.26 Orientation Angle LRF Distance Error Statistical Performance (Concrete)

Restored Intensity

Nominal SSD (mm)	Restored Intensity Area Mean	Restored Intensity Area Standard Deviation		
		(AB)	(AC)	(BC)
500	43928.30	80.58	65.15	55.81
1000	35525.50	339.05	627.52	920.51
2000	7214.63	338.96	142.72	300.69
3000	2339.84	153.12	45.59	142.13
4000	1068.24	84.46	41.65	65.37

Table 5.27 Orientation Angle LRF Restored Intensity Area Statistical Performance (Concrete)

Percentage Rejection

Nominal SSD (mm)	Percentage Rejection Mean	Percentage Rejection Standard Deviation		
		(AB)	(AC)	(BC)
500	0	0	0	0
1000	0	0	0	0
2000	0	0	0	0
3000	0	0	0	0
4000	6.59	11.04	8.84	5.21

Table 5.28 Orientation Angle LRF Percentage Rejection Statistical Performance (Concrete)

Distance Error

Nominal SSD (mm)	Distance Error Mean (mm)	Distance Error Standard Deviation (mm)	Distance Error Minimum (mm)	Distance Error Max (mm)
500	18.77	7.22	-2.28	42.88
1000	-57.99	14.49	-103.45	-8.06
2000	59.87	11.84	37.28	94.29
3000	80.85	6.42	63.72	108.29
4000	79.76	14.19	54.25	127.61

Table 5.29 LRF Distance Error Statistical Performance (Concrete)

All plots are shown in the Appendix C, Figures C.35 - 47.

174

5.18 PVC Surfaces

When scanning PVC surfaces using the LRF, large distance errors were measured at beams close to the normal incidence beam, in a similar manner to that found for the metallic surfaces as shown in Figure C.59. However Figures C.49-51 and Table 5.30 highlight the reduced mean RMSE and standard deviation at low (< 1000 mm) SSDs compared to all other materials but then increase substantially for increased SSDs.

Figures C.53-55 and Table 5.31 highlight the relatively high restored intensity area, compared to metallic surfaces, at low SSD which decreases substantially at increased SSDs (> 1000 mm). Appendix C, Figures C.55-58 highlight that all the rejected measurement points recorded at SSDs of 3000 and 4000 were all due to low intensity conditions further confirmed by the restored intensity area reduction mentioned above.

Again a shift in measurement distance polarity error and magnitude was seen with increasing SSD (Appendix C, Figure C.60). Again similar to all other scanned materials, nonlinear effects were observed when rotating in both Yaw and Pitch orientations.

RMSE Mean Distance Error

Nominal SSD (mm)	RMSE Mean (mm)	Distance Error Standard Deviation (mm)		
		(AB)	(AC)	(BC)
500	31.96	1.83	0.865	1.62
1000	30.82	2.91	2.59	1.36
2000	76.62	6.75	4.74	4.82
3000	100.12	8.11	6.23	4.91
4000	76.67	14.80	9.69	10.90

Table 5.30 Orientation Angle LRF Distance Error Statistical Performance (PVC)

Restored Intensity

Nominal SSD (mm)	Restored Intensity Area Mean	Restored Intensity Area Standard Deviation		
		(AB)	(AC)	(BC)
500	40537.00	348.92	221.28	210.52
1000	17990.60	409.25	184.89	357.49
2000	5973.49	577.54	72.12	565.80
3000	2289.70	349.64	103.22	332.63
4000	1118.19	204.11	110.27	164.41

Table 5.31 Orientation Angle LRF Restored Intensity Area Statistical Performance (PVC)

Percentage Rejection

Nominal SSD (mm)	Percentage Rejection Mean	Percentage Rejection Standard Deviation		
		(AB)	(AC)	(BC)
500	0	0	0	0
1000	0	0	0	0
2000	0	0	0	0
3000	23.91	18.07	17.40	3.79
4000	49.84	20.52	18.27	7.73

Table 5.32 Orientation Angle LRF Percentage Rejection Statistical Performance (PVC)

Distance Error

Nominal SSD (mm)	Distance Error Mean (mm)	Distance Error Standard Deviation (mm)	Distance Error Minimum (mm)	Distance Error Max (mm)
500	-21.08	25.73	-65.37	58.10
1000	24.00	20.03	-17.93	73.63
2000	71.49	12.70	13.15	117.97
3000	89.12	9.08	63.22	119.45
4000	61.33	13.71	28.94	101.61

Table 5.33 LRF Distance Error Statistical Performance (PVC)

All plots are shown in the Appendix C, Figures C.49-61.

5.19 Wood Surfaces

It is clear from the measurement data (Appendix C, Figures C.63-71) that wood behaved in a very similar manner to white paper when scanned with the LRF, with respect to the general trends observed previously. However wood surfaces highlighted greater mean RMSE, restored intensity area mean, standard deviations and distance error mean when compared to the white paper surfaces (Appendix E, Figures C.63-71 & Tables 5.34-36). Additionally similar to all others scanned materials nonlinear effects were visible with respect to mean RMSE, when rotating in both Yaw and Pitch orientations (Appendix C, Figures C.63-65).

RMSE Mean Distance Error

Nominal SSD (mm)	RMSE Mean (mm)	Distance Error Standard Deviation (mm)		
		(AB)	(AC)	(BC)
500	57.13	1.26	1.13	0.62
1000	70.91	2.31	2.22	0.70
2000	83.18	4.67	4.57	1.35
3000	95.99	11.05	6.7	8.76
4000	99.32	11.38	8.46	7.61

Table 5.34 Orientation Angle LRF Distance Error Statistical Performance (Wood)

Restored Intensity

Nominal SSD (mm)	Restored Intensity Area Mean	Restored Intensity Area Standard Deviation		
		(AB)	(AC)	(BC)
500	53777.7	352.39	338.19	96.10
1000	28556.5	270.43	207.42	173.71
2000	13463.4	243.44	100.76	212.37
3000	6258.85	427.11	79.38	411.88
4000	2324.02	182.23	30.40	178.02

Table 5.35 Orientation Angle LRF Restored Intensity Area Statistical Performance (Wood)

Distance Error

Nominal SSD (mm)	Distance Error Mean (mm)	Distance Error Standard Deviation (mm)	Distance Error Minimum (mm)	Distance Error Max (mm)
500	55.89	10.94	13.53	91.64
1000	68.47	10.32	39.92	100.79
2000	78.17	12.11	52.40	119.22
3000	88.82	13.95	55.51	132.81
4000	89.78	10.53	61.90	128.16

Table 5.36 LRF Distance Error Statistical Performance (Wood)

All plots are shown in the Appendix C, Figures C.63-71.

5.20 Poly(methyl methacrylate) (PMMA) Perspex Surfaces

The high light transmission properties of the Perspex surface present a highly challenging surface on which to perform optical based laser range scanning. After reviewing the raw data it was not possible or credible to perform any error based or accuracy characterisation on the materials.

The scan plan view for a SSD of 500 mm is shown below (Figure 5.41), highlighting the raw range data, with clear large scale error, recorded by the LRF.
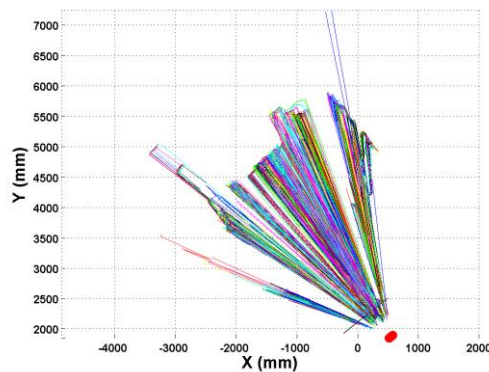
Figure 5.41 PVC Scan Plan View

5.21 Laser Based Surface Scanning Conclusion

This chapter focused on the characterisation of range estimation of a common miniature robotic optical laser range finding module. This is relevant as the sensor is both the largest and currently the highest performance module that the present fleet of the CUE RSA, AUT RSA and CUE ASA could perceivably carry.

A thorough study of the performance of the Hokuyo URG-04LX and a characterisation of the system error when scanning various commonly found industrial materials was undertaken. Specifically the study investigated the effects of small orientation angle changes of the LRF, in a similar manner to which it would experience when being deployed on a CUE RSA or ASA.

A detailed process of error measurement and visualisation has been undertaken which specially addresses the large volume of data generated by such a study. A number of parameters, not limited to traditional range data but also received and restored intensity and AGC gain, have been evaluated across the study. This work highlights that significant range distance errors are introduced when optically laser scanning common industrial materials. The specular reflective nature of some materials, such as aluminium, stainless steel and PVC, results in large deviation in range data from the true value, with mean RMSE errors as high as 100.12 mm recorded. It is worth noting that the surface roughness of each sample was not quantified, due to practical constraints, or modified from its original manufactured form and therefore relevant manufacturing specification.

Therefore a procedure for evaluating the performance of other and future laser range sensors, while operating under similar industrial conditions has been established. As shown in this chapter, this encompasses parameters such as sensor orientation angle, surface material and reflectivity.

Through the discussion of laser scanning each material it has become clear that, for at least the surfaces sampled in this study, it is possible to identify the surface being scanned based on parameters evaluated and discussed throughout this study. With this signature knowledge, determination of surface would allow correction factors to be developed to improve the LRF performance and in turn remove any distance mapping measurements.

5.22 LRF Surface Identification

As has been shown above, glossy samples have a negative impact on the performance and accuracy of the LRF, due to an increase in specular reflection, coupled to a greater intensity of reflected light saturating the APD. These effects have a detrimental effect on the pose estimation performance of any system deploying such an LRF for ranging purposes.

As found in [192] and through observation of the measured datasets, there existed a relationship between the restored optical luminous intensity (I_r), across the swept angle range, and the sample surface. Therefore through analysis of the restored intensity a broad appreciation of the sample surface can be determined [203-205].It is worth noting that for the purposes of this study the overall sample surface parameter being identified consists of the combined effect of surface gloss, surface texture, often defined by surface roughness, and surface colour [206]. Given the variation in each of these parameters, especially surface colour, across the seven materials sampled, a valid assumption and approximation can be made that basic material identification can be therefore achieved.

For simplicity and an initial undertaking, only the zero orientation datasets (A=B=C=0°) were considered. A polynomial was selected to best fit all restored intensity curves for every material, at each SSD. Through inspection of the data it was established a fifth order polynomial sufficiently captured the overall curve trends, where y represents the amplitude of the restored intensity and x represent the scan point number.

$$y = ax^5 + bx^4 + cx^3 + dx^2 + ex + f \qquad\qquad (5.5)$$

This is shown below in Figure 5.42 for a sample surface of aluminium, where the blue points represent the raw measured restored intensity amplitude corresponding to a particular scan point, each joined together to give the overall blue trace representing the full scanned intensity curve. The red trace highlights the polynomial fitted curve. Additionally recorded, for aluminium, in Table 5.37 is the polynomial coefficient values at each separate SSD.
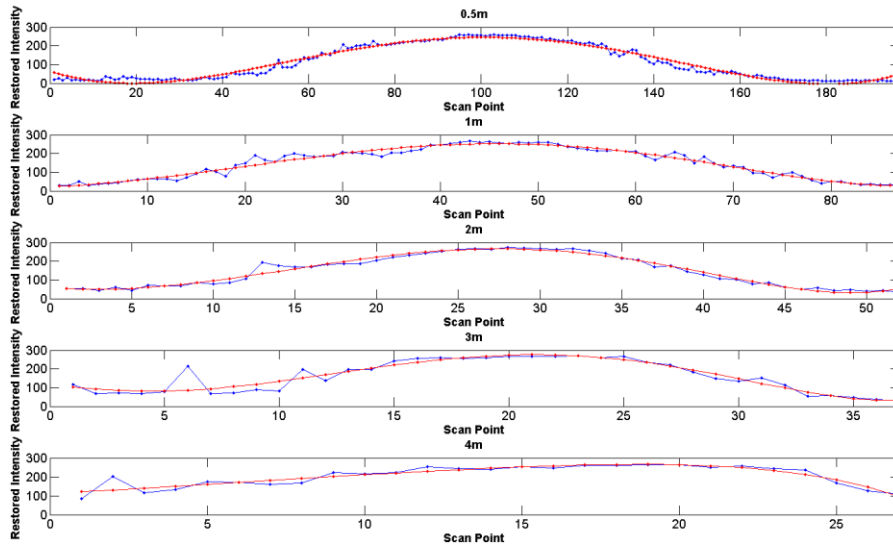
Figure 5.42 Restored Intensity Curve Fitting (Aluminium)

All other sample surface material plots and coefficient tables are located in Appendix

Figures C.72 - 77 and Tables C.51 – 56.

Material Surface				Aluminium		
Nominal SSD (mm)	Polynomial Coefficient					
	a	b	c	d	e	f
500	0	0	-0.0020	0.2531	-7.5872	65.8840
1000	0	0	-0.0032	0.2454	2.0515	22.7918
2000	0	-0.0007	-0.0142	1.2082	-6.3912	59.4969
3000	0.0001	-0.0042	0.0042	2.3714	-19.3419	120.7386
4000	-0.0001	0.0050	-0.1034	0.9669	6.4854	113.7436

Table 5.37 Aluminium Surface Curve Fitting Coefficients (Aluminium)

The polynomial coefficients for all materials were then plotted alongside each other

accordingly for each SSD.

183
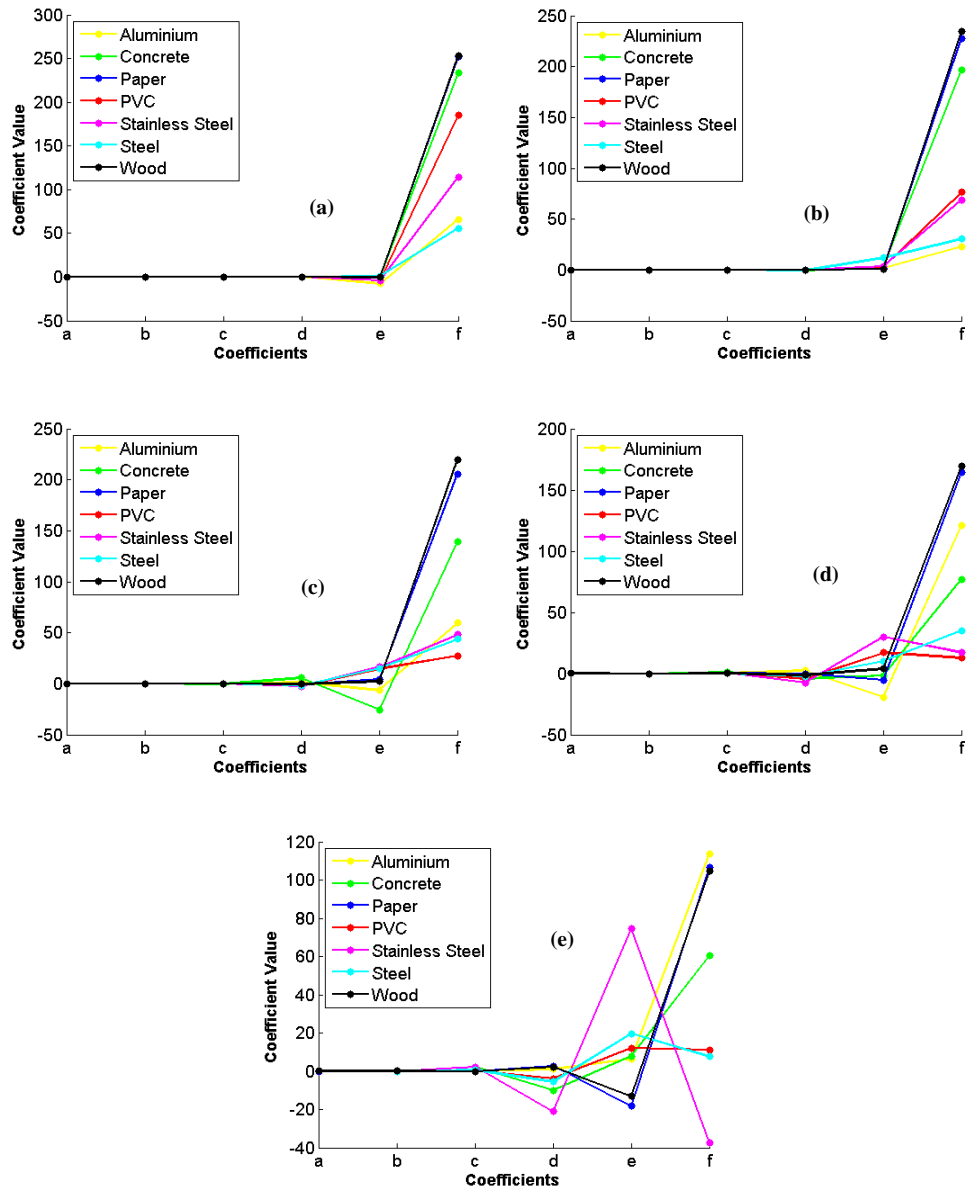
Figure 5.43 Restored Intensity Polynomial Coefficients (a) – Nominal SSD 500 mm, (b) – Nominal SSD 1000 mm, (c) – Nominal SSD 2000 mm, (d) – Nominal SSD 3000 mm, (e) – Nominal SSD 4000 mm (Aluminium)

From Figure 5.43 it is clear that discrimination and identification of the surface based on the restored intensity of the LRF is feasible, due to the variation in coefficient value with material.

For classification to occur, similar coefficients are computed for a scanned surface received intensity profile. These coefficients are subsequently compared on a per-coefficient basis, in terms of Euclidean distance, to the coefficients previously computed for each material. The surface classification is achieved through that with the greatest consensus in terms of total minimum Euclidean distance.

5.23 LRF Range Calibration

With knowledge of the material, it is then conceivable that correction factors can be applied to calibrate the LRF for range accuracy, when scanning challenging surfaces. This is a further development of the material agnostic calibration methods presented previously [162,176,196,207,208]. Such a strategy could be established using reference calibration data acquired in a similar manner to the above body of work, across many sample surfaces and ranges, while estimating correction parameters related to correction factors based on material surface, range and sweep angle point. Such a technique would ultimately establish calibration factors for each scan point, which could then be applied to future measured points based on the current estimation of material surface identification and range.

Such a technique and procedure was established for the Hokuyo LRF to correct for the errors identified and documented previously in this chapter. The calibration procedure accounts and compensates for artefacts and errors documented previously when scanning common industrial surface materials. An assumption was made that the scanned environment could be viewed to be composed of linear segments

between scanned points. Only range data acquired perpendicular to the material surface, with zero degree roll, pitch and yaw orientation angles, collected during the sensor characterisation phase was utilised. This simplification was introduced for practical and computational reasons.

Using the range data previously acquired at each of the five specific SSD distances, for each material, a curve fitting procedure (fifth order Gaussian) was applied to the perpendicular range data (Shown for Aluminium at nominal 1000 mm SSD - Figure 5.44). A Gaussian based fitting approximation curve was chosen on the basis of suitability, with respect to lowest fitting error. The resultant range scale mapping of the fitted curve to the true range measured by the LAT was determined at each distinct scan point. Following this procedure, a correction curve corresponding to each LAT measured SSD, for each material, was generated. This allowed a resultant correction curve, per scan point and material to be stored for further online operation.
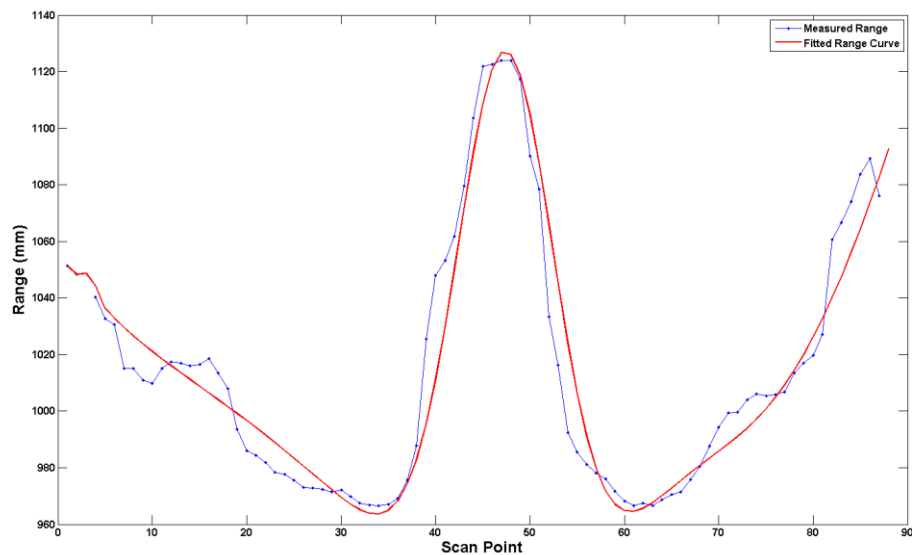
Figure 5.44 LRF Range Curve Fitting (Aluminium)

Correction curves for true distances lying between those recorded using the Leica were obtained via linear interpolation, for simplicity, between each of the five distinct LAT measured SSD distances.

During online operation, the mean range of the received range measurement was computed. This distance was used to generate the corresponding correction curve, located on a point between the five nominal SSD distances (Figure 5.45). This is an obvious approximation as the true range distance may not correspond to the mean range. This assumption was made due to the calibration algorithm requiring a range measurement estimation.
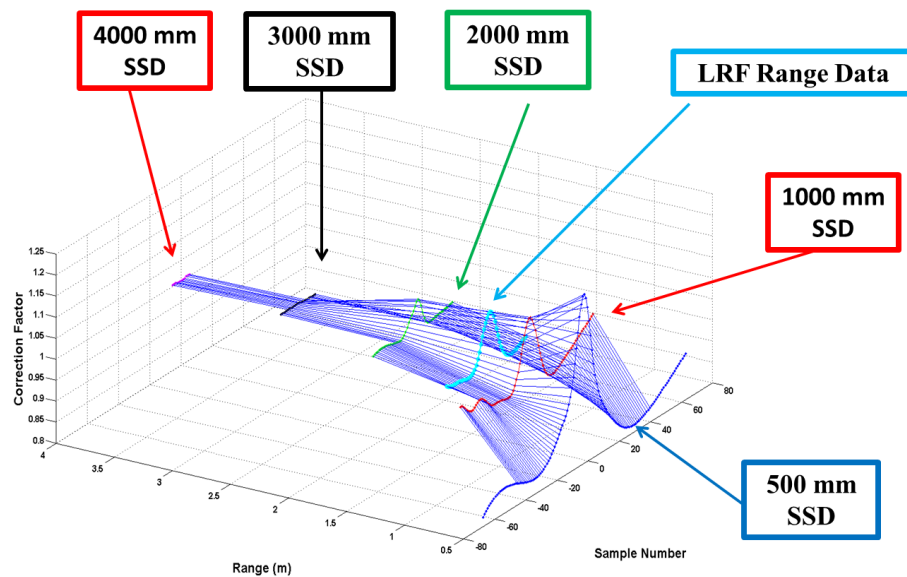
Figure 5.45 Scan Point Correction Factor Curve (Aluminium)

The corresponding correction scaling factor per scan point, based on the acquired mean range data, can then be applied to the received range measurement data to correct for and reduce the overall distance error.

The calibration and correction procedure was then applied to the previously acquired datasets, with different SSDs and materials. The RMSE across the complete scan window at each nominal SSD, for the zero orientation angle pose, for each material, is recorded in Table 5.38 (Uncorrected) and Table 5.39 (Corrected). Highlighted is the overall reduction in RMSE with the corrected calibration procedure.

| Nominal SSD (mm) | RMSE (mm) | | | | | | |
| | Material | | | | | | |
	Paper	Aluminium	Steel	Stainless Steel	Concrete	PVC	Wood
500	45.34	X_{OB}	X_{OB}	37.92	26.00	23.65	68.36
1000	53.42	49.98	25.91	50.91	50.68	37.05	74.39
2000	41.77	84.95	22.86	91.26	50.60	72.34	79.11
3000	62.32	X_{NVD}	35.58	83.21	76.53	86.22	83.78
4000	X_{OB}	X_{OB}	X_{OB}	X_{OB}	X_{OB}	X_{OB}	X_{OB}

Table 5.38 Uncorrected LRF Range RMSE

| Nominal SSD (mm) | RMSE (mm) | | | | | | |
| | Material | | | | | | |
	Paper	Aluminium	Steel	Stainless Steel	Concrete	PVC	Wood
500	12.17	X_{OB}	X_{OB}	9.93	11.79	11.69	14.13
1000	7.64	19.16	24.20	6.29	12.40	5.96	8.73
2000	5.93	6.69	7.09	6.39	1.65	6.74	5.46
3000	5.78	X_{NVD}	3.89	7.59	2.87	5.89	5.48
4000	X_{OB}	X_{OB}	X_{OB}	X_{OB}	X_{OB}	X_{OB}	X_{OB}

Table 5.39 Corrected LRF Range RMSE

where:

X_{OB} is defined as a dataset where mean range measurement is out with the minimum (532.00) and maximum (3994.22) SSD distance, yielding the correction inoperable.

X_{NVD} is defined as a dataset which contains no valid data to perform a corresponding scaling correction factor. This was found to occur when high intensity points, with corresponding error code, were detected and constitute the complete correction window, allowing no scaling correction data to be generated.

5.24 Test Sample

To highlight successful proof of principal a separate test sample was scanned and measured to ascertain the calibration correction algorithm performance. The aluminium sample surface was scanned at an LAT measured SSD of 1295.23 mm. After correct classification of surface material, the correction algorithm was applied and its result is shown in Figure 5.46. RMSE of the original and corrected range measurement data is shown in Table 5.40.
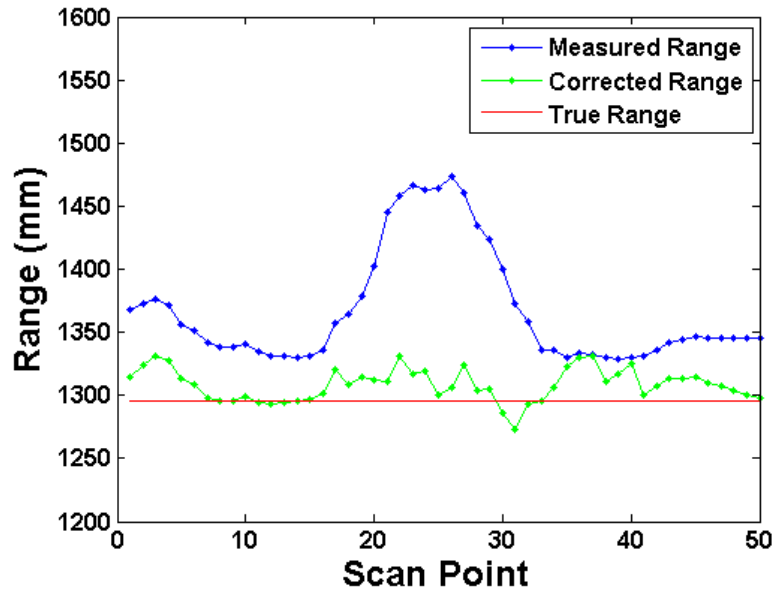
Figure 5.46 Corrected LRF Range Data

SSD	Original Range Measurement RMSE (mm)	Corrected Range Measurement RMSE (mm)
1295.23	83.87	18.03

Table 5.40 Corrected LRF Range RMSE

As shown by Figure 5.46 and the reduced RMSE (Table 5.40), such an approach further improves the performance and accuracy of the optical based LRF sensor. This has clear benefits to any automated NDE system, deploying such an LRF for pose estimation, albeit based on *a priori* calibration data.

5.25 Material Identification and Calibration Conclusion

The knowledge regarding the effectiveness and robustness of the above material classification and correction algorithms is limited, due to the limited volume of surfaces sampled at various ranges. Future work should analyse and characterise the

suitability and performance of such a material classification strategy, with particular emphasis on the number of correct classifications across the material spectrum. Further testing is required in fully assessing the suitability of such a range correction algorithm across the complete working range of the LRF sensor. Furthermore future work should also establish the effects, to each strategy, of variation in material surfaces out with those analysed and complex geometries.

The material identification and range correction algorithms developed have highlighted proof of principal in addressing the errors found after thorough characterisation of the LRF. These strategies provide the benchmark ground framework for future research focus in further improving LRF performance for automated NDE systems.

This section has proposed a novel computationally inexpensive algorithm for range correction in industrial scenarios. It makes the assumption that the contour extracted by the LRF is composed of linear segments between scan points. In such man-made, recti-linear environments this is not a very restrictive assumption. The correction algorithm was shown to reduce the RMSE error associated with range estimation on a planar aluminium surface from 83.87 mm to 18.03 mm. It is envisioned that the proposed technique will be researched and developed further to handle incidence angles other than the normal, while also assessing the robustness of the solution.

Chapter 6

Automated NDE Path Planning

6.1   Path Planning

Coverage Path Planning (CPP) is the procedure of determining a path that passes over all points of an area or volume while avoiding obstacles [209]. Example robotic applications that require such a planning strategy include vacuum cleaning robots, painting robots, underwater imaging systems, demining robots, lawn mowers, agricultural robots and window cleaners [210-220]. Cao et al [216] defined a set of criteria and requirements for robotic systems undertaking CPP operations in 2D environments.

1. The robot must move through all the points in the target area covering it completely to ensure desired area and point coverage.

2. The robot must fill the region without overlapping paths, to ensure minimum runtime and aid overall efficiency.

3. Continuous and sequential operation without any repetition of path is desired to both aid overall efficiency and reduce platform accelerations and decelerations.

4. The robot must avoid all obstacles

5. Simple motion trajectories (e.g. straight lines or circles) should be used for simplicity and control.

6. An "optimal" path is desired under available conditions, while still satisfying all of the above criteria.

In complex scenarios it is often challenging to satisfy all the above criteria, especially number 5, [209] and often priority consideration is required. CPP algorithms can be classified as heuristic or complete depending on whether or not they provably guarantee complete coverage of the free space [209]. Additionally independently they can be classified as either off or or-line. Choset et al [221] stated that off-line programming requires *a priori* knowledge of the environment and relies on the environment remaining static throughout the operation window. On-line programming algorithms differ in that they do not require such *a priori* knowledge and utilise real-time sensor measurements to profile the environment and produce path planning strategies based on the acquired information.

6.1.1 Advantages of off-line programming [222]:

1. Robot programming can occur without stopping or disturbing the intended task. Robots can be programmed prior to deployment and remain in service while being re-programmed for a new task. Therefore robot programming can be carried out in parallel with service, shortening downtime.

2. The programming efforts are relocated from a robot operator to a simulator/engineer.

3. Reduction in safety risks. The robot programmer does not have to be present in the working volume during programming activities.

4. Robot programs can be first tested using simulation tools. This allows engineers to anticipate and predict the robot behaviour and optimize the process accordingly.

6.1.2 Disadvantages of off-line programming tools:

1. Relatively high initial investment required in software and training.

2. The calibration process requires stringent procedures and controls. A poor calibration process can lead to severe inaccuracies during operation.

3. *A priori* environmental and robot information is required in advance of deployment. Accurate environment and platform modelling is therefore critical in off-line robot simulators as inconsistencies and incomplete modelling hinder safe and successful deployment. Changes in the environment from when the knowledge was acquired or changes to the platform kinematics or dynamics must be continually relayed back to the simulator [223-224].

Automation of path planning can yield benefits in terms of production, efficiency, and safety. Automated area coverage path planning for spray painting applications has received considerable research and industrial focus [225-226]. Traditional human operator taught paths for industrial 6 D.O.F. robots are inefficient in terms of workflow, throughput and material usage. This procedure not only exposes the operator to hostile environments but its output quality is highly dependent on variable industry skill levels [225-229]. CPP for industrial component inspection has

recently undergone significant research in high value manufacturing applications, especially in aerospace, with a variety of NDE sensors being deployed [45,230-238].

CPP for crawler devices has also recently attracted research interest in areas such as material handling and logistics [239], vacuum cleaners [240], agriculture [241], demining [215] and inspection [45,230-244]. Traditional path planning algorithms for such platforms has focussed on Configuration Space (C-Space) representations such as Voronoi diagram [245], regular & occupancy grids, generalised cones [246], quad-tree [247] and vertex graphs [248]. Additionally CPP for Aerial platforms has received attention for opportunities in surveillance [249], agriculture [250] and disaster and emergency management [251].

Although sharing similarities to other industrial robotic applications coverage path planning strategies, automated inspection coverage path planning is highly challenging insofar that many NDE applications require scanning of features that would normally be classed as obstacles in traditional robotics. Examples of such objects would include weld joints of items such as pipe risers and side walls. This subtle distinction must be considered, as robotic positioning and path planning algorithms must not just register and ultimately safely avoid such an object, by typically moving as far as possible away from the object, but register and carefully approach such objects to allow traditional NDE sensors to be deployed with minimal sensor-surface distance. It must also be noted that a small as possible stand-off distance must be consistent, along or around an object, while also being repeatable to allow code compliant correct inspection strategies to be deployed at regular intervals.

This latter point ensures operators are able to confidently monitor rate of change of inspected structures.

Therefore object or obstacle avoidance strategies are of similar or greater significance as they must not only recognise dangerous obstacles, but also be intelligent in determining them as surfaces/features requiring inspection, or in fact just obstacles requiring complete avoidance. Therefore objects can be grouped into those that require fine-controlled contact of an appropriately posed sensor, or those requiring complete non-contact.

One critical exception to traditional object avoidance strategies and of significance to automated NDE systems is when deploying contact based traction platforms. Crawler platforms such as wheeled or gripper clamps, deploying traditional ferromagnetic/friction strategies or more advanced approaches such as vacuum devices, use objects for successful manoeuvring. Therefore additionally object or obstacle avoidance strategies must also consider the platform propulsion technique and its surface requirements when deciding courses of action.

It is therefore logical that all parts of an automated NDE system, except contact based inspection/localisation sensors and traction devices, should always avoid contact to nearby objects throughout the inspection process. This is highly applicable in deployment strategies of tight space or confined access, en route to the desired inspection points.

6.2   NDE Path Planning Related Parameters

Path or motion planning is a key component in the realisation of autonomous robotic systems [252]. From a robotic perspective path planning is the method and approach to progress to a defined goal or location. Interlinked and conflicting parameters such as obstacle avoidance, travelling velocity, completion time and robustness define the overall strategy and technique. These will be discussed in greater detail in the following section, highlighting the key parameters of NDE path planning.

6.3.1   Platform

The chosen or desired inspection deployment platform naturally dictates the optimum path planning strategy to be investigated. Full 6 D.O.F. platforms (aerial, fixed arm) can manoeuvre to positions along paths that surface traction platforms (crawlers) cannot achieve. This additional freedom allows greater flexibility dealing with challenging access constraints albeit at the expense of simplified obstacle avoidance.

6.3.2   Area & geometry to be inspected & imaged

The area, point or object requiring inspection again naturally dictates the path planning strategy. For example simple flat rectangular geometries would typically require traditional parallel raster scanning techniques, while spiral geometries would require circular loop paths. Complex shaped surfaces naturally require complex spline type paths with parallel non-equal distance paths.

6.3.3 NDE sensor deployment

In terms of path planning, of critical importance is the sensor active aperture or sensor footprint. The sensor choice and area to be inspected are closely interlinked insofar that they directly dictate the number of imaging passes required to completely satisfy the coverage requirements. Sensor resolution is directly controlled through sensor design fundamentals and relates to the window and minimum sampling area of the sensor.

6.3.4 NDE path pattern

The NDE path pattern is directly dictated by parameters such as inspection speed and desired resolution. Firstly the fixed sampling time of traditional NDE sensors defines the maximum motion velocity directly limiting the overall inspection time. Path resolution is dictated by the largest spacing increment between subsequent waypoints (Figure 6.1).
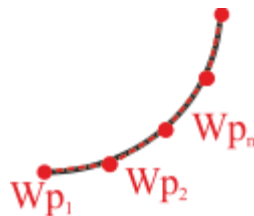
Figure 6.1 Arc Interpolation

Measurement resolution is fundamentally limited by the maximum sensor and path resolution. Additionally overall inspection time is directly controlled by the motion velocity and measurement spacing along the desired path.

6.3.5   Robot & Sensor Positioning Strategies

The accuracy and repeatability of the platform and sensor positioning system ultimately limit the maximum inspection coverage rate as inaccuracies would yield to greater required path overlap and multiple sweeps. Additionally the initial tolerance of any acquired surface/object metrology information can again directly affect the coverage rate as multiple incremental sweeps may be required to image the desired feature.

6.3.6   Material

The material under inspection can influence the path planning strategy in two distinct manners:

1. The delivery platform may use a particular method of traction (i.e. magnetic) and restrict its movement to surfaces that comply and suit such constraints.

2. The material itself may dictate the pose of the sensor directly to very specific values or ranges. This is often required in photogrammetry applications when reflectance scattering properties of the sample dictate the angle of optical rays. [253]

6.3   NDE & Machining Path Planning Parallels

There are many similar aims and goals between automated NDE inspection and traditional manufacturing machining path planning. Both have a desire to fully cover large areas/surfaces of both planar and complex geometry in the most efficient manner. Both scenarios could feature one or more edge boundaries and areas/volumes that are to be left untouched. Additionally each situation can require a

singular path around distinct components of both simple (square, circular etc.) and complex (spline path etc.) nature.

The automation of traditional machine tools, such as milling machines and lathes, began with the advent of NC by MIT researchers in 1952 [254]. NC offered electronic control of mechanical actuators, through commands encoded on a storage medium. The advent of computer technology establishing Computer Numeric Control (CNC) allowed the advent of far more complex multi-axis machining tool paths to be generated efficiently and safely [255]. The late 1980's saw a great rise in the volume of published research in CNC path planning and generation from a variety of specialised areas such as manufacturing, electrical, mathematics and software [256]. This volume of work led to a large influx of specialised and area-specific research which did not cross disciplinary boundaries and therefore had little or no industrial uptake [256].

The individual concepts in manufacturing milling path planning are now considered along with the corresponding NDE concept.

6.4.1   Manufacturing process planning

This considers the overall process and the consequences of undertaking milling operations at specific stages. In an NDE context an example scenario would be when undertaking a storage vessel inspection, which would likely require draining, prepared accordingly and then inspected prior to painting.

6.4.2 Machine tool and controller hardware design kinematics.

This considers the physical capabilities and potential range of movements which can be achieved or required by the machine tool. In an automated NDE context this specifically relates to the deployment platform design and its degrees of freedom, its controllers and positioning feedback strategies

6.4.3 Cutting force estimates and modelling

In traditional machining operations the cutting force is highly dependent on the material, cutting tool, throughput and machine rigidity. Correct modelling allows operators to specify maximum safe permissible cutting force for maximum throughput feed rates. NDE sensors traditionally operate under a finite range of load pressures and therefore safe and correct sensor measurement requires control and application specific adjustment to the inspection scenario.

6.4.4 Path generation

Manufacturing operations require the movement of the cutter across the complete areas and features requiring machining for the task to be completed efficiently. Similarly NDE sensors require to be scanned across areas and features requiring inspection in a repeatable and precise fashion.

6.4.5 Machining simulation and verification

To confidently allow operators to proceed with and visualise future machining operations, simulation of the tool cutter with respect to the machined part is typically performed. This ensures the final part is as manufactured with no errors, produced by

stray cutting operations, while also allowing the operator to plan the physical process around items such as fixturing and cycle time. In potential automated NDE applications, simulations offer the operator the opportunity to ensure compliance with the required feature coverage while also ensuring no collisions with the sample or surroundings.

6.4   Machining and NDE Coverage Path Planning

For the purposes of this body of work the author has identified a similarity between traditional milling manufacturing operations and that of a desired automated NDE inspection. Specifically strong similarities exist within the area of path planning where perpendicular movement of an end-effector across large potentially complex shaped surfaces and features is a shared common goal.

6.5   Traditional Machining: Pocket milling

In typical negative machining operations a pocket is defined as an area with defined borders in which material should be removed. It must be noted that the borders can be defined inside or outside the part denoting a closed or open pocket respectively [257].

6.5.1   Closed Pocket

As shown in Figure 6.2 (a) all tool paths are located within internal borders. A single sweep of the complete border path defines the overall shape, while multiple parallel varying length raster paths remove the remaining internal material. It must be noted that such paths are not limited to planar 2D surfaces and can be easily applied to

complex shaped geometries. A typical remote NDE application in which a similar tool path could be deployed would be that of the internal mapping of an Oil and Gas Storage tank floor. The complete floor region would be located within walls which define the edge and boundary of the scanning area.

6.5.2   Closed Pocket with Island

This path is similar to the closed pocket described above, with multiple parallel varying length raster paths, except that one or more island areas are left un-machined (Figure 6.2 (b)). Again as with the closed pocket tool-path a typical remote NDE application in which a similar tool path could be deployed would be that of the internal mapping of an Oil and Gas Storage vessel floor with one or more protruding obstacles such as pipes and flanges.

6.5.3   Open Pocket with Bounds

An open pocket (Figure 6.2 (c)) is similar to the closed pocket described above, with multiple parallel varying length raster paths to remove internal material, except that one or more boundaries are on the edge or outside of the part. A typical remote NDE application in which a similar tool path could be deployed would be when performing normal incidence ultrasonic imaging of composite aerospace components within stringer edged bounds.

6.5.4   Completely Open Pocket

This path is similar to the open pocket described above, with multiple parallel varying length raster paths, except that all boundaries are on the edge or outside of the part (Figure 6.2 (d)). A typical remote NDE application in which a similar tool

path could be deployed would be when performing ultrasonic imaging of composite aerospace components on the outer mould line.

6.5.5   Open Pocket with Island

Again this approach is similar to the completely open pocket except with one or more un-machined islands (Figure 6.2 (e)). A typical remote NDE application in which a similar tool path could be deployed would be when performing ultrasonic imaging of composite aerospace components on the outer mould line with protruding external fixating components.
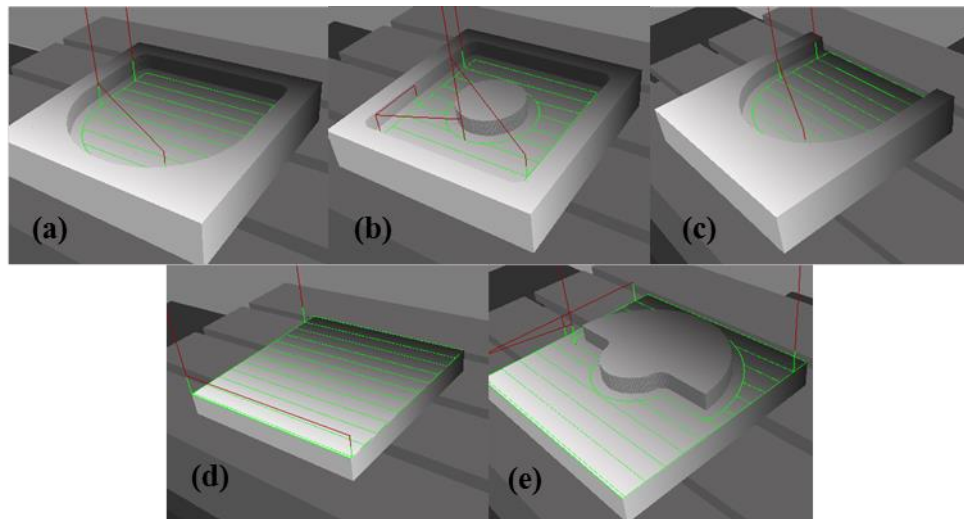
Figure 6.2 (a)-Closed Pocket Machining, (b)-Closed Pocket with Island Machining, (c)- Open Pocket with Bounds Machining, (d)-Completely Open Pocket Machining, (e)-Open Pocket with Island Machining [257]

6.6   Numeric Control

The industrial standard for machine tool operation through Computer Aided Manufacturing (CAM) techniques is that of G-Code [258]. G-Code is a standardised high level NC language that is accepted by all standard CNC machine tools. Standard

movements such as straight line interpolation and arc are permitted with control of plunge and feed-rate along with spindle speed. These basic functions allow a variety of operations to be undertaken and correspondingly a range of machining functions to be performed (Table 6.1).

CODE	Description	Example Structure
G00	Rapid Traverse Motion (x,y,z)	N10 G00 X5.00 Y10.00 Z 20.00
G01	Linear Interpolation Motion (x,y,z)	N20 G01 X5.00 Y10.00 Z 20.00
G02	Clockwise (CW) Interpolation Motion (X (Arc starting X Point), Y (Arc starting Y Point), I (Relative X distance to arc centre), J (Relative Y distance to arc centre),	N30 G02 X10.00 Y10.00 I5.00 J5.00
G03	Counter Clockwise (CCW) Interpolation Motion	N40 G03 X10.00 Y10.00 I5.00 J5.00
G04	Dwell for a specified time (F (Seconds))	N50 G04 F10
G20	Imperial programming selection	N50 G20
G21	Metric programming selection	N60 G21
G28	Return to machine zero (x,y,z)	N70 G20 X0 Y0 Z0
G54	Work coordinate system 1 (x,y,z)	N90 G54 X20 Y20 Z20
G90	Absolute programming selection	N80 G90
G91	Relative programming selection	N80 G91

Table 6.1 Numeric Control G-Codes

Additional auxiliary functions are prefixed by other command letters (Table 6.2).

Variable Address	Description	Example
N	Line or block number. Indicates the line number, usually in increments of 10.	N10 N20
T	Tool select (T (Tool Number))	N10 T03
S	Spindle speed (S (revolutions per minute))	N20 S3000
M	Miscellaneous Functions	

Table 6.2 Numeric Control Auxiliary Functions

Codes prefixed with the letter M denote start and end positions of particular programs (Table 6.3).

CODE	Description	Example Structure
M00	Program Stop	N10 M00
M02	Program End	N20 M02
M03	Spindle on clockwise	N30 M03
M04	Spindle on counter-clockwise	N30 M04
M30	Program end and reset	N40 M30

Table 6.3 Numeric Control M-Codes

Additional g-code functions have been added to the standard protocol through the years which allow more complex explicit functions to be specified depending on the application.

6.7   Post-Processors

A post-processor is a tool that translates output statements from a robot simulator to a target robot language, for deployment of off-line path planning programming algorithms [223]. Figure 6.3 illustrates the flowchart involved in this whole process. Firstly the complete robot, work volume, tasks and therefore paths are all generated and simulated before optionally being displayed to the operator. Using this data and the *a priori* knowledge of the robot kinematics and dynamics, a post processor can be utilised to translate the simulated data to that required by the target robot system for eventual deployment. Calibration can occur on real movement actions by correcting the simulator parameters if required.
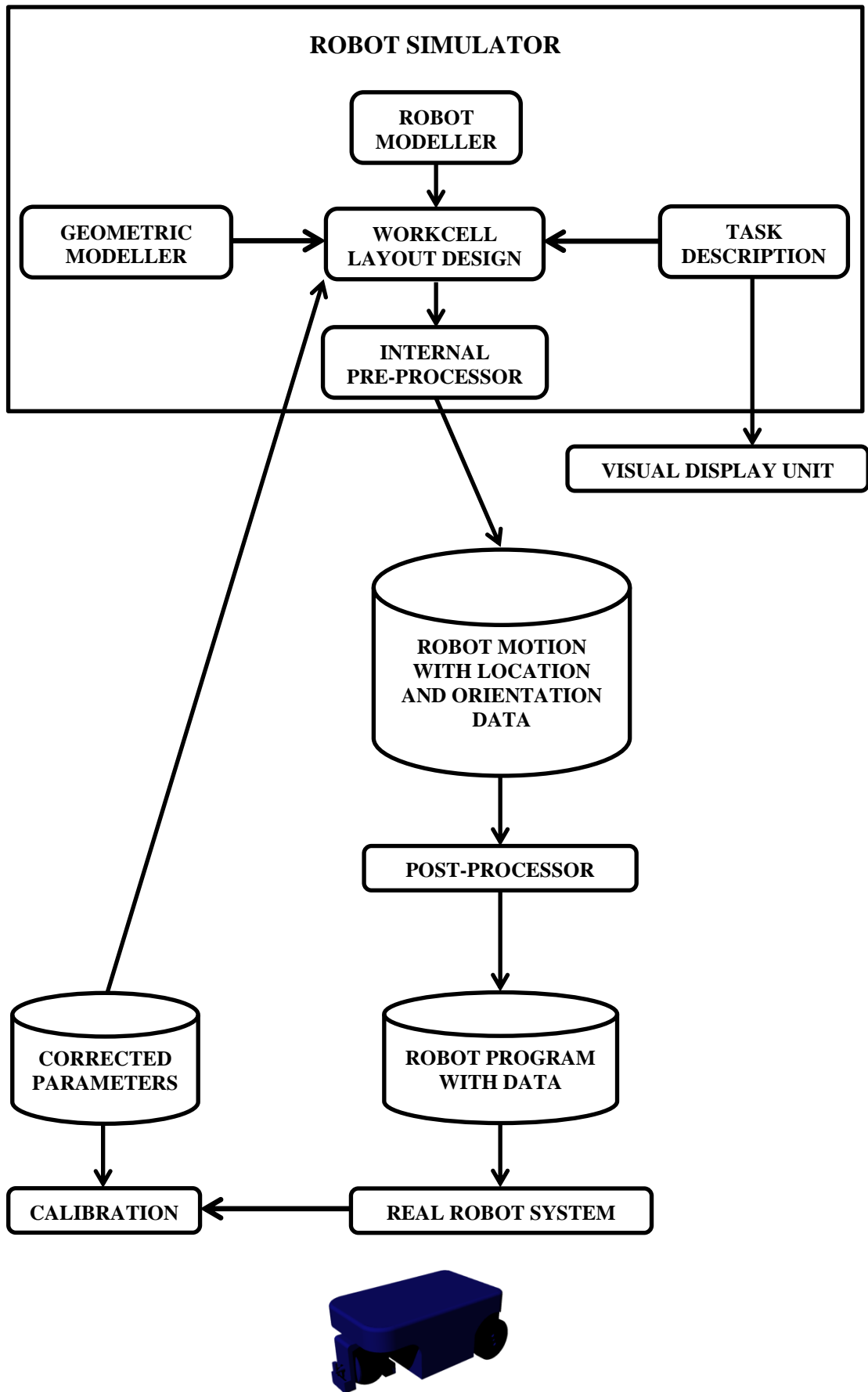
Figure 6.3 Robot Programming Structure [223]

Traditionally robot kinematics are either described or measured in end-effector Cartesian coordinates or individual drive/manipulator movements [223].

Post processors can be categorised as system-dependent, application dependent or generic [223]. System dependant post-processors translate robot simulation commands into a specific robot language, traditionally applicable to a certain manufacturer or system protocol [224]. Application dependant post-processors are made for a specific application with custom sequences. Generic post-processors are theoretically capable of translating multiple simulator commands into languages for multiple robot controllers [223].

A system-dependent post processor and associated tool-chain has been developed for the CUE AUT RSA to allow CPP algorithms to be simulated and deployed in NDE inspection scenarios.

6.8   Computer Aided Drawing & Manufacture

The Mastercam X6 CAD/CAM package has been utilised throughout this body of work due to it being the CUE preferred CAM package [243]. The CUE licensed package has support for all three milling options, those being:

Mill, Level 1:

Includes Mill Entry, plus surface creation, many additional toolpaths (for all construction and tool planes), highfeed machining, toolpath editor, toolpath transforms and stock definition [259].

Mill, Level 2:

Includes Mill, Level 1, plus additional toolpaths, toolpath projection, surface rough and finish machining, surface pocketing, containment boundaries and check surfaces [259].

Mill, Level 3:

Includes Mill, Level 2, plus 5-axis wireframe toolpaths, more powerful surface rough and finish machining and multi-axis toolpaths [259].

6.9   Tool Design

A custom machine tool was designed to simulate the AUT RSA dimensions when undertaking an inspection operation (Table 6.4).

Index	Machine Tool Parameter (mm)	AUT RSA Parameter
1	Cutter Diameter	UT Wheel Probe Nominal Contact Area Diameter (20 mm)
2	Flute Size	UT Wheel Probe Diameter (65 mm)
3	Shoulder Size	Wheel Probe Wheel Arch Nominal Height to Ground (73 mm)
4	Overall Height	AUT RSA Height (105 mm)
5	Shank Diameter	AUT RSA Working Envelope Diameter (460 mm)
6	Holder Diameter	AUT RSA Working Envelope Diameter (460 mm)
7	Holder Height	Holder Not Utilised - Nominal (1 mm)

Table 6.4 Tool Parameters
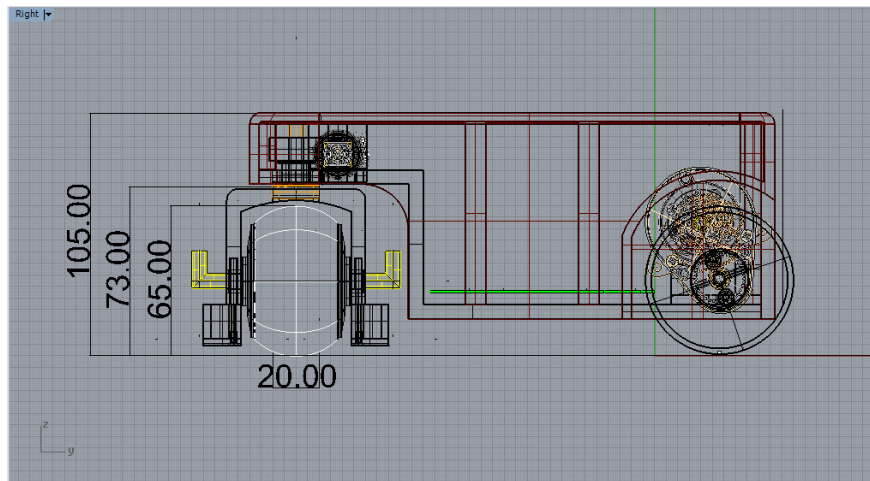
Figure 6.4 AUT RSA Dimensions

The working envelope of the AUT RSA was represented as a cylinder of diameter 460 mm. This was calculated from the turning centre origin between the drive wheels to the safe outer maximum limit of extension of any part of the platform. This includes the whole case, the active back wheel when turned ninety degrees to the normal and all associated connectors.
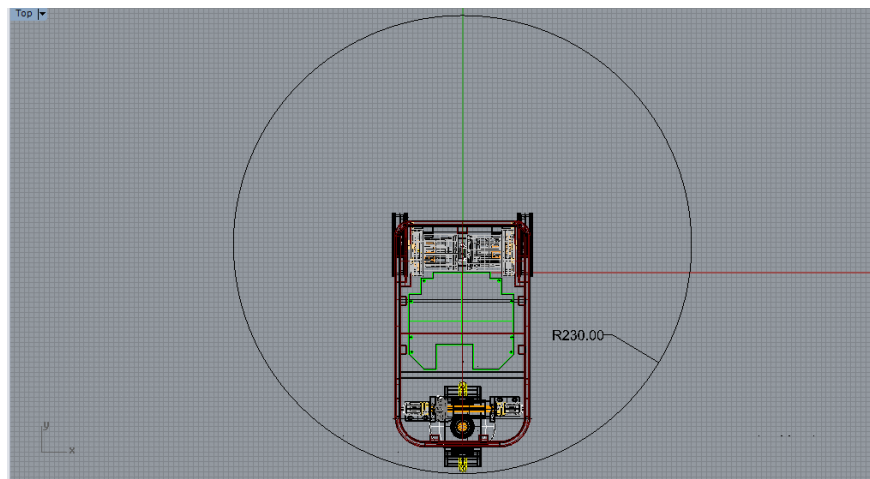
Figure 6.5 AUT RSA Working Envelope
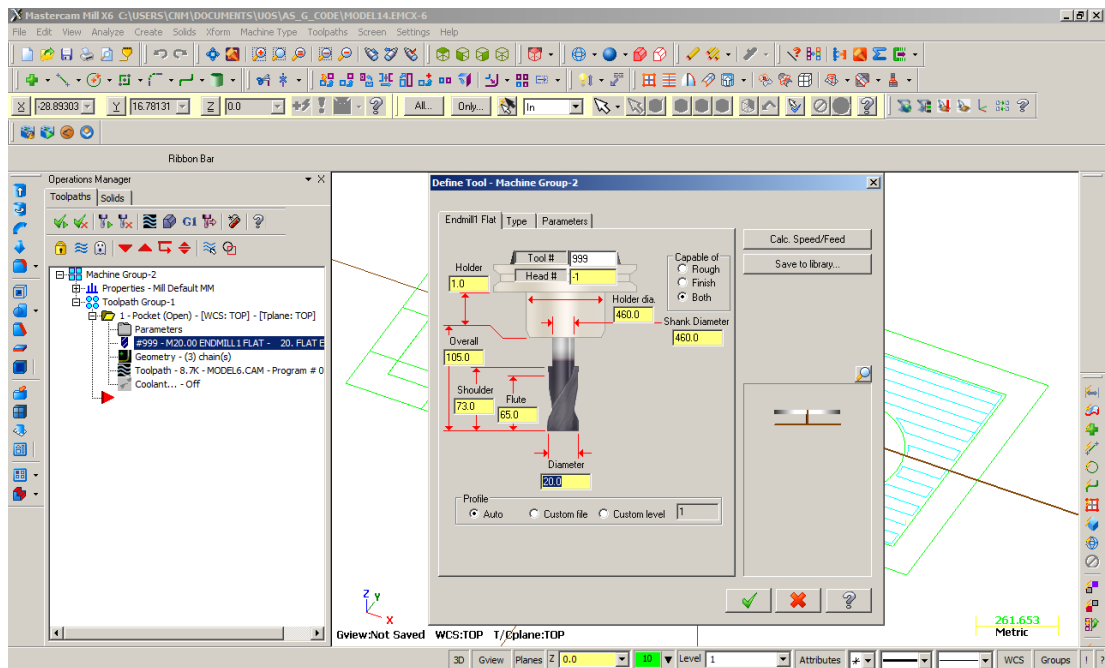
Figure 6.6 AUT RSA Custom Tool

Auxiliary tool functions were specific to correspond to additional AUT RSA functions (Table 6.5).

Machine Tool Parameter	AUT RSA Parameter
Feed Rate (mm per minute)	RSA scanning speed (mm/s)
Retract Rate (mm per minute)	RSA travelling speed (mm/s)
Spindle Speed (revolutions per minute)	RSA UT acquisition frequency (Hz)

Table 6. 5 Auxiliary Tool Parameters

In milling machining operations, feed rate is the feed of the tool in relation to the work piece, in distance per time-unit, related to the feed per tooth and number of teeth in the cutter [260]. Spindle speed is the number of revolutions the milling tool on the spindle makes per minute [260]. Retract rate is the speed at which the machine tool withdraws from the work piece and undergoes rapid motion [260].

In 2D milling commands Mastercam features no intelligent tapered cutter or tool holder collision protection by adaption to the tool end point path trajectory. It is a requirement of the operator to ensure no collisions or gouging occurs by reviewing the generated path motion simulation. Due to the rear swing nature of the active back wheel of the AUT RSA, the full working envelope of the RSA can be defined with a radius of 230mm from the turning centre of the RSA. As shown in Figure 6.10 the actual working envelope at any particular instance of time will consist of a partial section of the full envelope defined by the current pose of the platform. Therefore to ensure no collisions with objects or obstacles located in the sample geometry an additional 230 mm of clearance following the contours of each island is specified.

6.10 CUE RSA Post-Processor

A custom post processor was developed to interface with Mastercam X6 and export the necessary numeric code in a format suitable for driving the AUT RSA. The CUE RSA post-processor was based on that of the Southwestern Industries Inc. ProtoTRAK SMX post-processor for two key reasons:

Firstly the EEE Department Mechanical workshop operates an XYZ Machine Tools SMX 3500 bed mill, featuring a ProtoTRAK SMX controller [261]. This machine, in which the author has experience of programming, was utilised to construct all mechanical parts for the AUT RSA including chassis, case and motor supports.

Secondly the output format is of a straightforward and simplistic nature, when compared to other post processor outputs and contains no superfluous comments.

Therefore the ProtoTRAK SMX post processor was adapted to export only the limited number of basic function G Codes discussed above in Table 6.1. Additionally for further simplicity only block numbers beginning at 100 and increasing by 10 with each new line are exported. Furthermore a delimiting space was inserted between the block number and subsequent informative code for user processing reasons.

6.11 MATLAB RSA Parser

A MATLAB based parser was implemented to accept the post-processed numeric control output and convert this into suitable commands, in the appropriate XML structure format as discussed in Section 3.6.5, for driving the RSAs to desired locations.

6.12.1 Straight Line Motion (G00, G01)

When dealing with straight line motion the parser simply outputs the desired commands as shown in Table 6.6.

Command	Structure	Value
X	Float	Desired X coordinate.
Y	Float	Desired Y coordinate.
θ	Float	0
StopAtEnd	Boolean (1 = true)	1
TurnOnSpotToFaceTarget	Boolean (1 = true)	1

Table 6.6 AUT RSA Straight Line Motion Commands

The "StopAtEnd" Boolean toggles if the RSA should physically stop the motors after reaching a desired waypoint. The "TurnOnSpotToFaceTarget" Boolean defines if the RSA should rotate on the spot to the desired pose for attempting a straight line motion to the desired waypoint, or adjust its pose continually on an arc movement.

6.12.2 Arc Motions (G02, G03)

When dealing with arc motions, it must be remembered that all arcs are fundamentally represented by a finite number of straight line sections. Correspondingly the parser first requires the operator to specify the maximum length of any arc divided straight line estimates. Each arc is then divided into the corresponding number of straight line interpolations from the start point to the desired end location. Therefore one line of the inputted numeric code containing G02 or G03 codes can result in a number of desired X and Y coordinates depending on the desired resolution of the path. When dealing with arc motions the parser outputs a number of the following commands shown in Table 6.7 in a serial fashion.

Command	Structure	Value
X	Float	Desired interpolated X coordinate.
Y	Float	Desired interpolated Y coordinate.
θ	Float	0
StopAtEnd	Boolean (1 = true)	0
TurnOnSpotToFaceTarget	Boolean (1 = true)	1

Table 6.7 AUT RSA ARC Motion Commands

The "StopAtEnd" Boolean is set to false so as not to stop at each interpolated point and avoid the ramp up and down phase of the motors when passing through such points.

215

6.12.3 Speed Commands

All speed related and acquisition rate commands discussed in Table 6.5 are exported in an accompanying text file which is read in by the GUI and processed accordingly.

6.12.4 Visual Simulation and Export

Once all necessary waypoints are computed for the entire process they are then plotted for visual examination by the operator. An estimate of the time required by an RSA to complete such an inspection is given. If content the operator can then select to simulate the RSA path visually, in real or accelerated time, making use of the aforementioned MATLAB API command interface. Additionally the operator then selects to export the waypoint and additional required motion commands in the necessary XML format for reading by the RSA GUI.

6.12 Example Scanning Application

Large steel plates are utilised in many industrial structures not limited to oil and gas storage tanks, ship hulls and wind turbine towers. Due to environment and local conditions these plates are often subject to corrosion and as such gradually face loss of thickness from their original manufactured size. To conform with appropriate legislation and ensure integrity, thickness mapping is undertaken at appropriate locations across the plated structure.

Thickness mapping of steel plates is a challenging inspection, when considering full area coverage due to logistics such as structure features/obstructions, robotic logistics and environmental conditions.

State of the art inspection systems currently undertake single line measurements, traditionally of the simplest pass with minimal obstructions and do not naturally lend themselves to full-scale mapping [69]. Furthermore wired systems are limited in their overall reach and deployment suitability when considering umbilical dynamics, mass and tangle free operation.

The AUT RSA platform featuring magnetic traction and wireless operation significantly widens the scope and potential of automated full area coverage thickness mapping.

A sub-scale sample was fabricated to simulate a realistic application area for the AUT RSA, including obstructions and simulated defects.

A 2000 x 1000 mm Carbon Steel (S275) plate of nominal 10 mm thickness was selected to mimic a traditional plated floor. Two obstructions were affixed to the plate to mimic typical industrial obstacles protruding through the floor. These obstacles are listed in Table 6.8. Seven flat bottom holes of 25 mm diameter and six similar holes of 10 mm diameter were machined into the plate at various locations and varying depths to simulate localised loss of thickness. These artificial defects are described in Table 6.9. A plan of the sample is shown below in Figure 6.7.
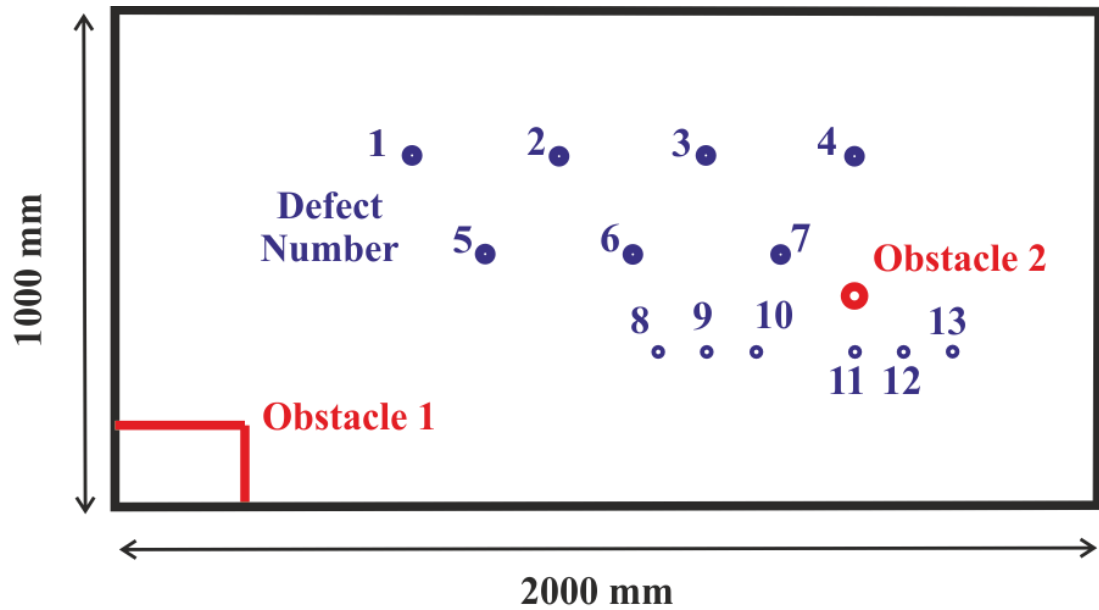
Figure 6.7 Industrial Sample

10 mm thick Medium Density Fibreboard (MDF) robot travel run-offs, 300 mm wide, were positioned around the sample to ensure the platform height and orientation remained consistent in the event of any part of the RSA requiring to travel out with the steel sample area.

Obstacle Number	Description	Industrial Representation
1	Rectangular box of width 270 mm and breadth 170 mm, centred at (-865,-415)	Pipe Duct
2	40mm Diameter Cylinder centred at (500,-75)	Pipe Riser

Table 6.8 Industrial Sample Obstacle Information

Defect Number	Diameter (mm)	Actual Location(x,y) (mm)	Actual Plate Thickness (mm)
1	25	-400,210	8.25
2	25	-100,210	6.08
3	25	200,210	3.85
4	25	500,210	1.66
5	25	-250,10	6.20
6	25	50,10	3.74
7	25	350,10	0.80
8	10	100,-190	9.12
9	10	200, -190	7.87
10	10	300, -190	5.87
11	10	500, -190	3.99
12	10	600, -190	1.96
13	10	700, -190	1.12

Table 6.9 Industrial Sample Artificial Defect Information

Thickness information was acquired by 100 reference micrometre inspections equally spaced around the outside perimeter of the sample. The results of this scan are listed in Table 6.10.

Parameter	Value
Mean Thickness	9.98 mm
Minimum Thickness	9.73 mm
Maximum Thickness	10.21 mm
Thickness Standard Deviation	0.15 mm

Table 6.10 Industrial Sample Thickness Information

6.13 Industrial Sample Reference Inspection

A reference ultrasonic NDE inspection of the industrial sample was undertaken to define a suitable and credible benchmark for the subsequent AUT RSA inspection. Normal incidence ultrasonic thickness mapping was undertaken using a GE Roto-Array wheel probe [262] and Olympus Omniscan MX2 PA controller [263].
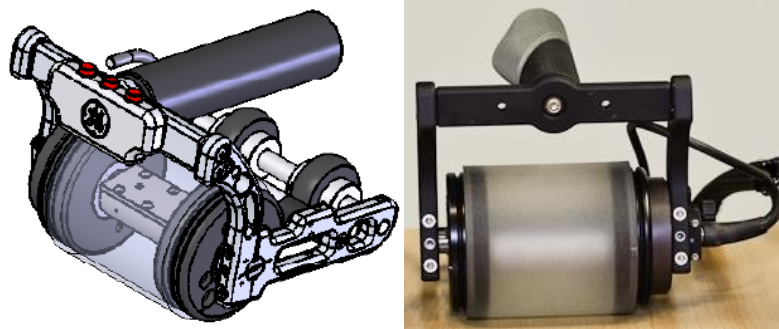

Figure 6.8 GE Roto-Array

Figure 6.9 Olympus Omniscan MX2

The wheel probe utilised featured an internal 5 MHz 64 element linear ultrasonic array enclosed in a liquid filled tyre. The specification of the wheel probe is shown below in Table 6.11.

Parameter	Value
Element Count	64
Frequency	5 MHz
Pitch	0.8 mm
Elevation	6.4 mm
Kerf	0.09 mm
Nominal Delay Path (Array face to outside of tyre) = Phasor Probe Offset Value	28.2 mm
Nominal Liquid Delay Velocity	1509 m/s

Table 6.11 GE Roto-Array Specification

The Omniscan featured a 16:64 phased array module with 16 individual pulser/receiver channels and the potential to drive a maximum of 64 elements at 115 Volts. The reference thickness map of the sample (2000 x 1000 mm) is shown below in Figure 6.10 highlighting the nominal 10 mm thickness and varying depth defects. The colour of any area is indicative of the thickness of the material as measured ultrasonically.
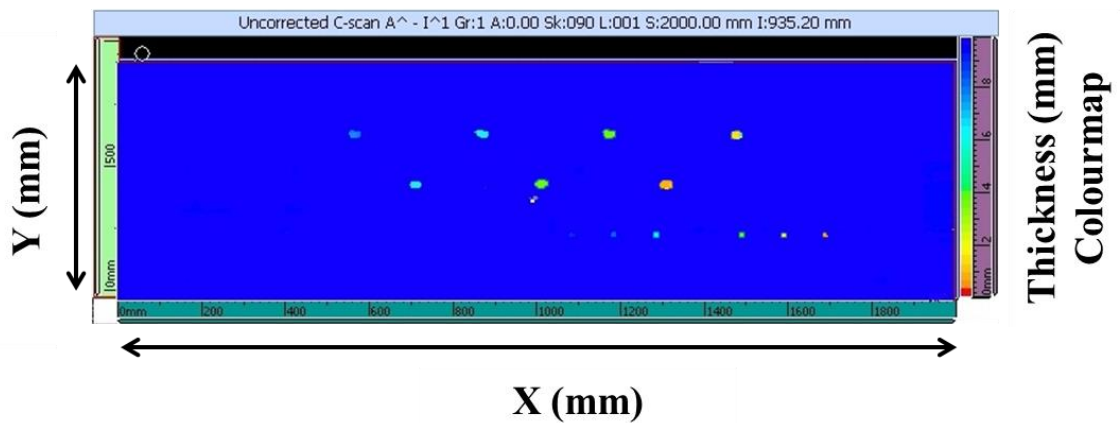
Figure 6.10 Reference Industrial Thickness Map

When compared against Figure 6.7 it is clear that all seven 25 mm diameter artificial defect flat bottomed holes are located along with the six 10 mm diameter similar holes. Additionally a further defect present within the sample is located nearby to defect 6. The Amplitude Scan (A-Scan), showing the amplitude of the transmit and receive signals, and Sector Scan (S-Scan), showing a cross sectional view of the sample derived from multiple A-Scans, are shown below (Figure 6.11) for the approximate centre of this apparent defect.
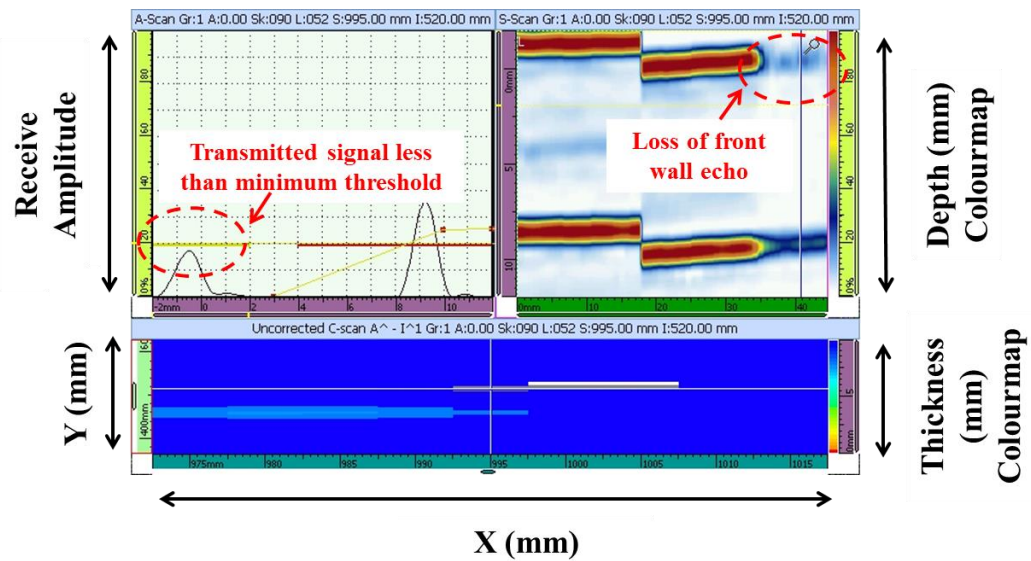
Figure 6.11 Identified Defect A & S- Scans

From the A and S-Scans it is clear that loss of transmission into the material is responsible for this apparent false call. This is very evident from the loss of the front wall echo as shown in the S-Scan.

6.14 Measurement Strategy

To sufficiently highlight proof of principal and implementation in NDE thickness mapping and inspection terms, a suitable measurement strategy had to be devised. A raster scan, with consistent spacing, across the sample and avoiding the riser

obstructions was deemed to sufficiently highlight the unique benefits of this novel approach, especially when considering large scale structures.

The CAD model of the industrial sample was imported into Mastercam X6 to generate the appropriate numeric control output based on standard machining operations. The 2000 x 1000 mm sample area was sub-sampled to 1600 x 800 mm to allow a sufficient safety margin for the robot as it travels along its desired paths.
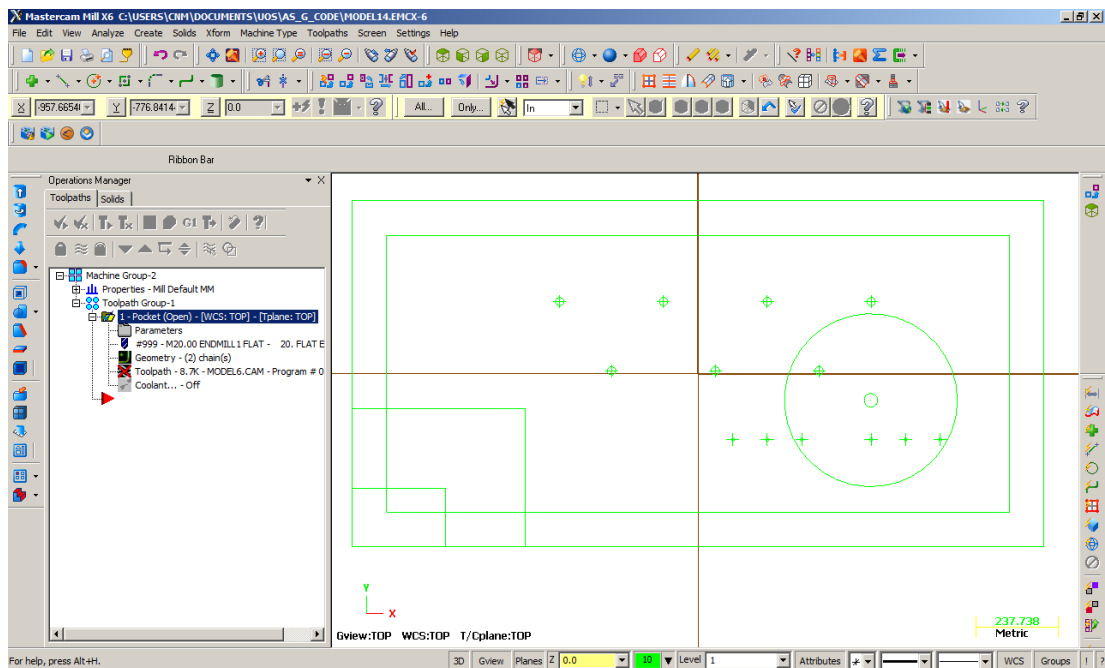
Figure 6.12 Industrial Sample CAM Environment

An open pocket with multiple island operations was selected as the sample was a plate with no sides, while each riser represented an island obstruction not requiring inspection. The UT Window/Desired Stepover parameter defined by the cutter diameter setting was selected to be 50 mm, this being a compromise between the minimum required to ensure complete full area thickness mapping (10 mm) and a

justifiable value which would be deemed practically suitable in terms of coverage and task completion time, whilst still being scalable to the full value.

Speed and rate parameters were set as shown in Table 6.12.

Machine Tool Parameter	AUT RSA Parameter
Feed Rate (mm per minute)	RSA scanning speed (25 mm/s)
Retract Rate (mm per minute)	RSA travelling speed (50 mm/s)
Spindle Speed (revolutions per minute)	RSA UT acquisition frequency (10 Hz)

Table 6.12 AUT RSA Scan Parameters

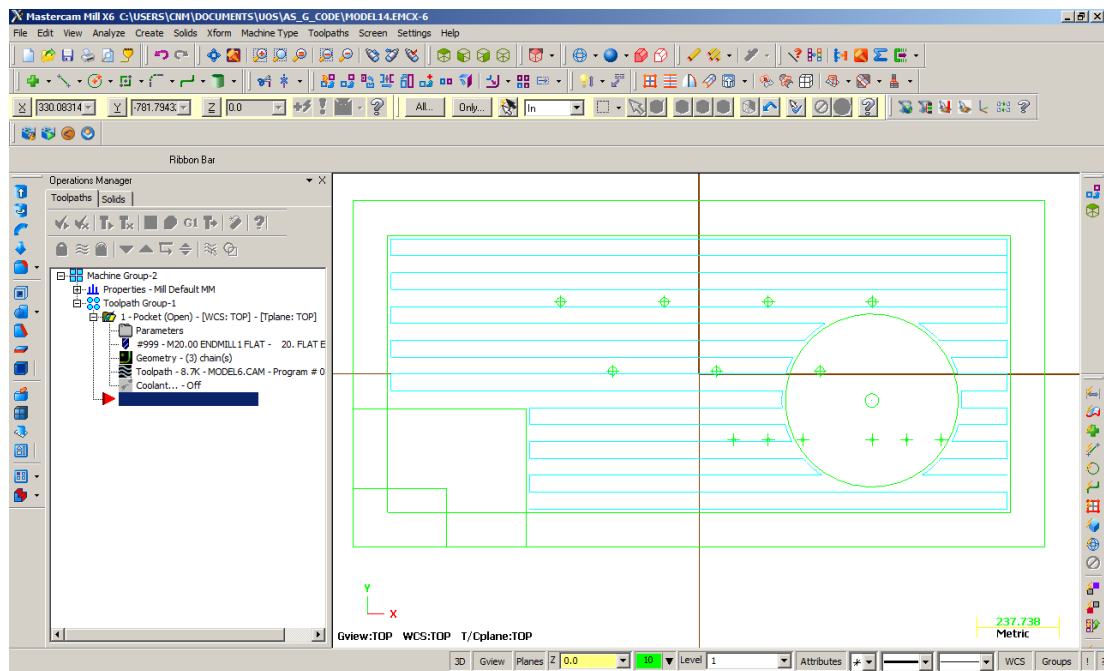The generated path is shown below in Figure 6.13.

Figure 6.13 Industrial Sample Scan Generated Path

224

The operator is then advised to simulate the operation to ensure no collisions or gouging. Snap shots of the simulation are shown below in Figure 6.14.
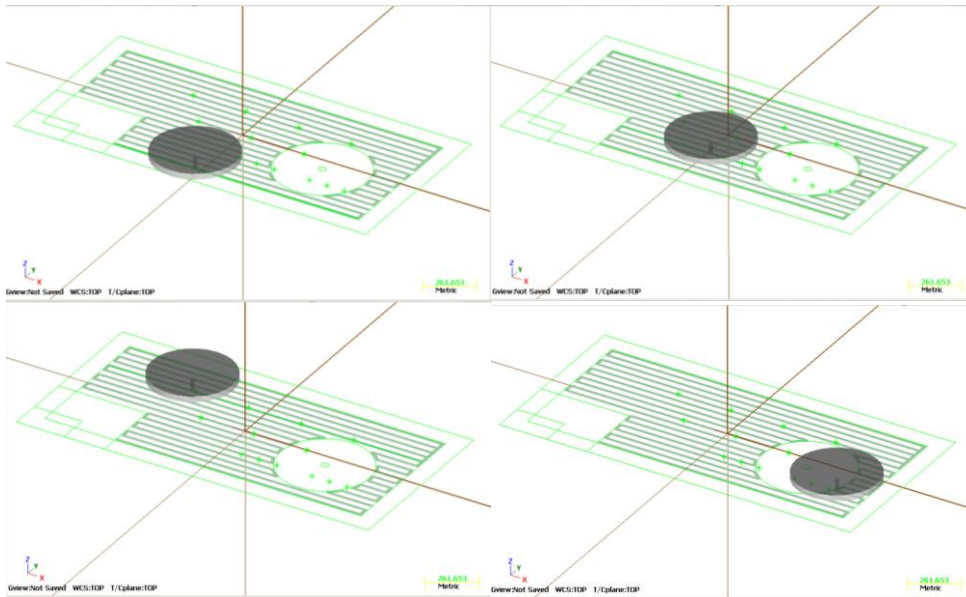
Figure 6.14 Path Simulation

The output was then exported through the custom CUE RSA post-processor to give the appropriate NC output.

The developed MATLAB parser then imported the NC file and the operator was requested to specify the minimum arc interpolation distance. A value of 10 mm was selected based on both knowledge of typical applications which normally involve large diameter components and also experience that the RSAs are not accurate in undertaking small distance straight line motions due to the ramp-up start phase of the two motors.

The desired waypoints are then computed and displayed for the operator, while offering the capacity to simulate the robot undertaking the path. Once satisfied the operator exports the waypoints in the desired XML format.

The desired path XML file is read into the RSA GUI and the coordinates plotted on the visual display (Figure 6.15).
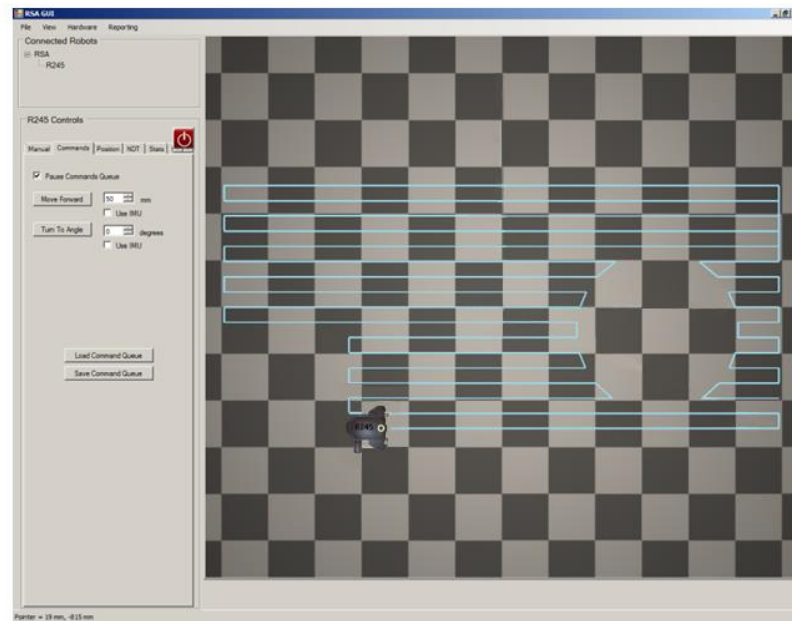
Figure 6.15 RSA GUI Path

6.15 CUE AUT RSA Thickness mapping

All captured ultrasonic A-Scan datasets were loaded within MATLAB and the corresponding thickness of the material calculated using successive back-wall echos. Sixteen times averaging was applied when sampling the raw ultrasonic data to reduce noise to an acceptable value and be deemed immaterial in affecting further calculations. Due to the compressive nature of the wheel probe design and the variation in sound propagation through the rubber tyre and sample, accurate

226

calculation of the thickness of the sample based on conventional time of flight information between the transmitted pulse and the first back-wall echo return was deemed unsuitable. Three successive back-wall echos are utilised in the calculation for averaging purposes. The method and formula utilised is shown below in Figure 6.16 and Equation 6.1 respectively:
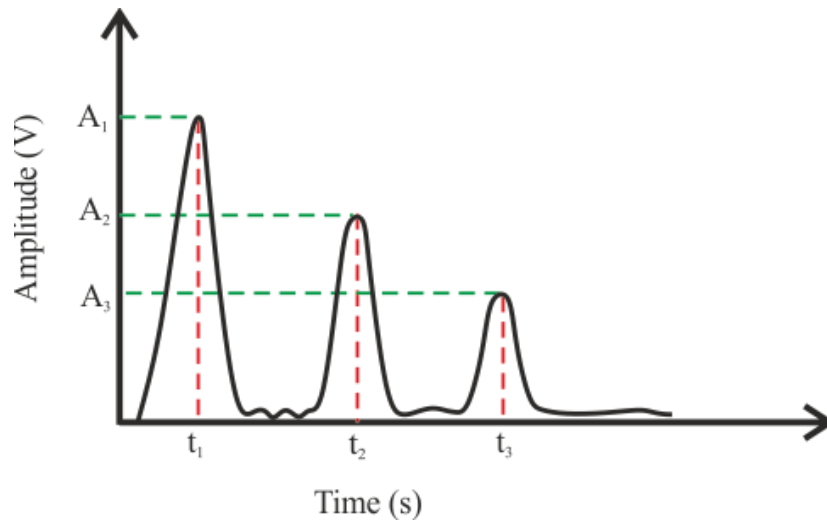
Figure 6.16 Back Wall Echo Thickness Measurement

v_c =*Speed of sound in material (mm/s).*

A_1 =*1st back wall echo amplitude (V).*

t_1 =*1st back wall echo time (s).*

A_2 =*2nd back wall echo amplitude (V).*

t_2 =*2nd back wall echo time (s).*

A_3 =*3rd back wall echo amplitude (V).*

t_3 =*3rd back wall echo time (s).*

m_t =*Material thickness (mm)*

$$m_t = \left(\frac{v_c \times (t_3 - t_1)}{4}\right) \times 1000 \qquad (6.1)$$

Additionally due to the dry-coupled nature of the wheel probe, small local variations in coupling between the tyre and surface yield corresponding changes in back wall echo amplitude, with poorly coupled instances yielding reduced amplitudes. The minimum peak detection amplitude of each back wall echo must therefore take into consideration the coupling environment and the effect this has on respective signals. As the receive acquisition process begins shortly after the firing pulse, the largest peak in the acquired captured data should logically correspond to the first back wall echo. Due to the attenuative nature of traditional materials successive back wall echos will have correspondingly reduced amplitudes. Therefore the peak detection algorithms utilised take into account the varying amplitude of the first echo and detect both the second and third maxima based on the former.

Each ultrasonic acquisition was both time-stamped and position-stamped. As shown in Appendix A.2 the position of the RSA as measured by VICON, and correspondingly logged, was that of the centre of turning rotation, namely the central point of the drive wheels axis. As the ultrasonic wheel probe was located at the rear of the platform, displaced in one axis along the length of the robot, the position related to the point of actual ultrasonic measurement followed an arc movement centred on the RSA centre of rotation. A 2D coordinate transform was utilised to calculate the correct point of ultrasonic measurement and is shown below:

Ψ_{RSA} =Yaw angle of RSA as measured by VICON (°).

D_{TTC} =Distance along axis of transducer to turning centre of RSA (mm).

RSA_{TCx} = RSA turning centre position in X axis as measured by VICON (mm).

RSA_{TCy} = RSA turning centre position in Y axis as measured by VICON (mm).

$$UT\_Meas\_Pos_x = (D_{TTC} \times \cos \Psi_{RSA}) + RSA_{TCx} \qquad (6.2)$$

$$UT\_Meas\_Pos_y = (D_{TTC} \times \sin \Psi_{RSA}) + RSA_{TCy} \qquad (6.3)$$

All ultrasonic measurements were converted into a corresponding thickness value at their correct position of capture.

6.16 AUT RSA Calibration

The performance of the thickness mapping ability of the AUT RSA system was evaluated on a single straight line path on a 10mm thick calibration sample plate 2000 mm long and 300 mm wide. A reference thickness measurement was taken ten times along the same path using a calibrated micrometre. The result of this calibration is shown in Table 6.13.

Parameter	Micrometer Value	AUT RSA Value	Error
Mean Thickness	9.98 mm	9.61 mm	-0.37 mm
Minimum Thickness	9.73 mm	8.86 mm	-0.87 mm
Maximum Thickness	10.21 mm	10.12 mm	-0.09 mm
Thickness Standard Deviation	0.15 mm	0.35 mm	0.2 mm

Table 6.13 AUT RSA Calibration Information

6.17 CUE AUT RSA Acquisition

The summarised investigation procedure was;

1. Import desired CAD geometry to be inspected into Mastercam.

2. Select AUT RSA cutter model and define raster step-over distance.

3. Generate path trajectory, selecting each obstacle object as a chain boundary.

4. Generate milling path operations.

5. Validate path operations to ensure no collisions or gouging.

6. Post-process path operations through custom CUE RSA post-processor

7. Generate XML RSA waypoints by loading post-processed path operations through the MATLAB RSA parser.

8. Correctly set-up and calibrate VICON motion capture system, as discussed in Appendix A.2 and align origin to that utilised in Mastercam CAD environment.

9. Place the AUT RSA at an appropriate location on the sample geometry to be inspected, ideally locating the turning point close to the starting waypoint location.

10. Activate and power the AUT RSA.

11. Launch the RSA GUI and create a new project to generate a connection between the GUI and the AUT RSA.

12. Activate repeat UT acquisition on the AUT RSA.

13. Load the desired waypoint coordinate data into the GUI.

14. Deploy the AUT RSA for the inspection.

Once the investigation is complete:

1. De-activate and power down the AUT RSA.

2. Load all project data log files into MATLAB for post-processing.

3. Enter the speed of sound for the appropriate material under inspection.

4. Thickness map of the surface to be inspected will be generated.

6.18 NDE Results

The thickness map produced from the numeric control driven AUT RSA scan is show below in Figure 6.17. Critically the result highlights the successful nature of the generated and travelled paths in avoiding both obstacle one and two. As discussed in Section 6.13 the run out areas outwith the steel sample area, shown by the outer red lines at 2000 x 1000 mm, were of MDF at a similar height of 10 mm. The scan was undertaken in a timeframe of 15 minutes.
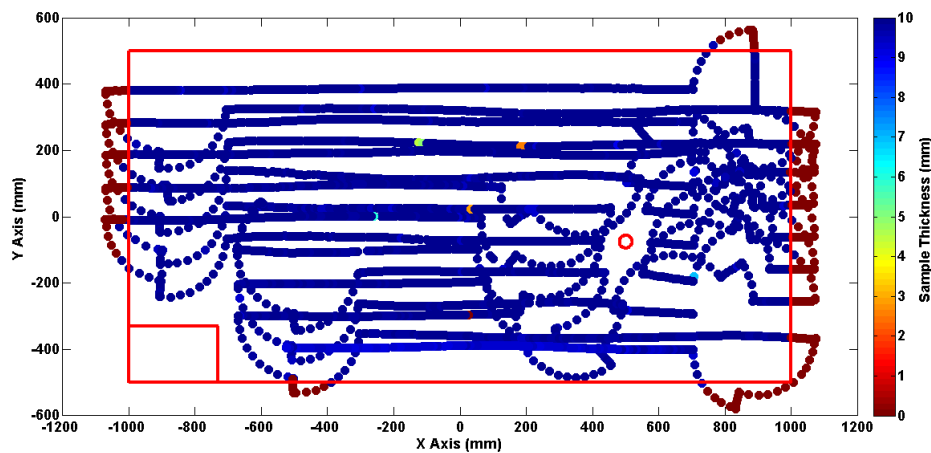

Figure 6.17 AUT RSA Thickness Map

The ultrasonic thickness map with superimposed defect outlines highlighting their location and size is shown in Figure 6.18. From this plot it is clear that defects 8, 9

231

and 10 were not scanned, while defect 1 is not fully scanned as both path trajectories do not pass through close to the defect centreline.
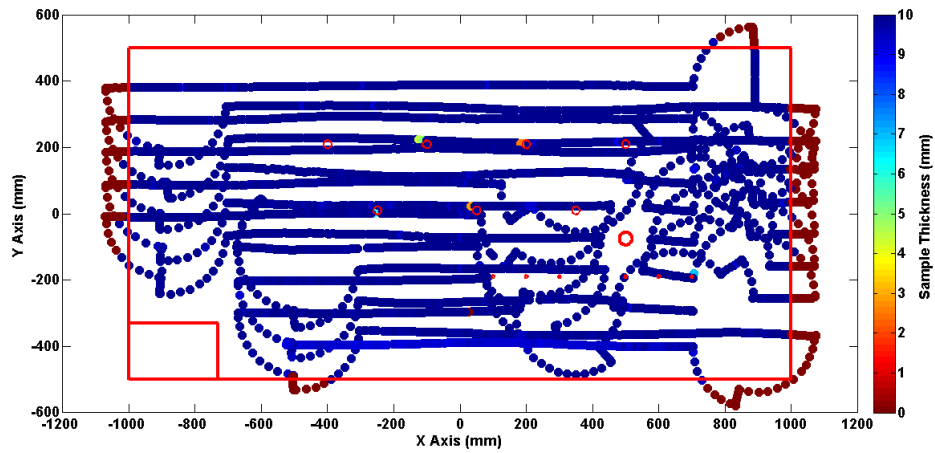
Figure 6.18 AUT RSA Thickness Map with Overlaid Defects

To clearly visually identify potential defects all measurements with a recorded plate thickness lower than the minimum value obtained on the nominally similar calibration plate (8.86 mm), are flagged and recorded as locations of potential loss of material. The result of this thresholding is shown below (Figure 6.19), overlaid with superimposed defect outlines and numbers highlighting their location and size.

Figure 6.19 AUT RSA Located Defects

As expected defects 4 and 7 were Not Detected (ND) due to the low nominal remaining plate thickness and the damping characteristics of the transducer. Similarly 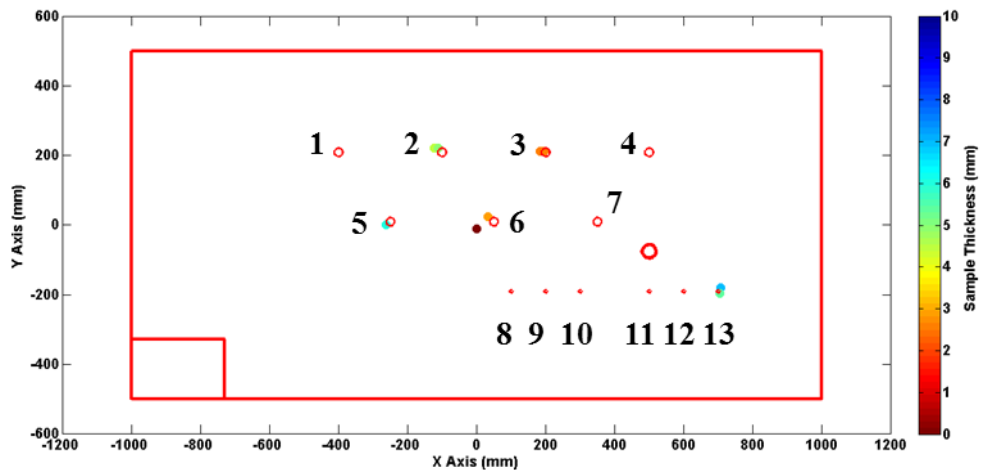defects 11 and 12 were not recovered due to the thin plate thickness and their challenging smaller diameter, when considering the transducer pitch size. Additionally defects 8, 9 and 10 were Not Scanned (NS) as previously discussed. Defect 1 was in fact not recovered due to the previously discussed path trajectory to which the transducer followed. Defects 2, 3 and 13 were all detected twice at neighbouring sample locations indicating that the AUT RSA transducer trajectory passed through the defect for more than one sample interval. This was most likely achieved by travelling through close to the defect centreline to maximise the defect area visible by the transducer. Defect 13 was the only 1 of 6 10 mm diameter holes located.

Additionally one non-artificial defect was also located close to the plate origin, as previously highlighted by the reference ultrasonic thickness inspection discussed in Section 6.14. Similarly, after reviewing the AUT RSA A-Scan information this was due to loss of transmission. On investigation of the physical steel plate, an adhesive film was present on the surface in the area identified by both ultrasonic scans therefore not allowing the ultrasonic wave to propagate through to the sample and cause loss of transmission.

The AUT RSA defect results are recorded in Table 6.14. The location of a measured defect is defined as the centre point of the transducer as calculated from platform turning centre position as measured by VICON. The X and Y error is calculated

from the mean X and Y measured location when a defect is located by multiple successive measurements. Similarly when considering measured plate thickness the mean value is taken in instances of multiple successive measured plate thickness measurements.

Defect Number	Diameter (mm)	Actual Location(x,y) (mm)	Measured Locations(x,y) (mm)	Error (x,y) (mm)	Actual Plate Thickness (mm)	Measured Plate Thickness (mm)	Plate Thickness Error
1	25	-400,210	ND	N/A	8.25	ND	N/A
2	25	-100,210	-124.4,223.2 -112.3,222.7	- 18.35,13.0	6.08	4.64	-1.44
3	25	200,210	182.7,213.2 194.8,213.3	11.25, 3.3	3.85	2.57	-1.28
4	25	500,210	ND	N/A	1.66	ND	N/A
5	25	-250,10	-262.4,1.2	-12.4,-8.8	6.20	5.99	-0.21
6	25	50,10	32.2,23.5	17.8,13.5	3.74	2.82	-0.92
7	25	350,10	ND	N/A	0.80	ND	N/A
8	10	100,-190	NS	N/A	9.12	NS	N/A
9	10	200, -190	NS	N/A	7.87	NS	N/A
10	10	300, -190	NS	N/A	5.87	NS	N/A
11	10	500, -190	ND	N/A	3.99	ND	N/A
12	10	600, -190	NS	N/A	1.96	NS	N/A
13	10	700, -190	707.2,-181.3 704.3,-195.4	5.75,1.7	1.12	6.54	5.42

Table 6.14 AUT RSA Scan Defect Information

6.19 Scan Path Accuracy

The desired (red) and travelled (blue) path of the turning point of the AUT RSA is shown below in Figure 6.20.
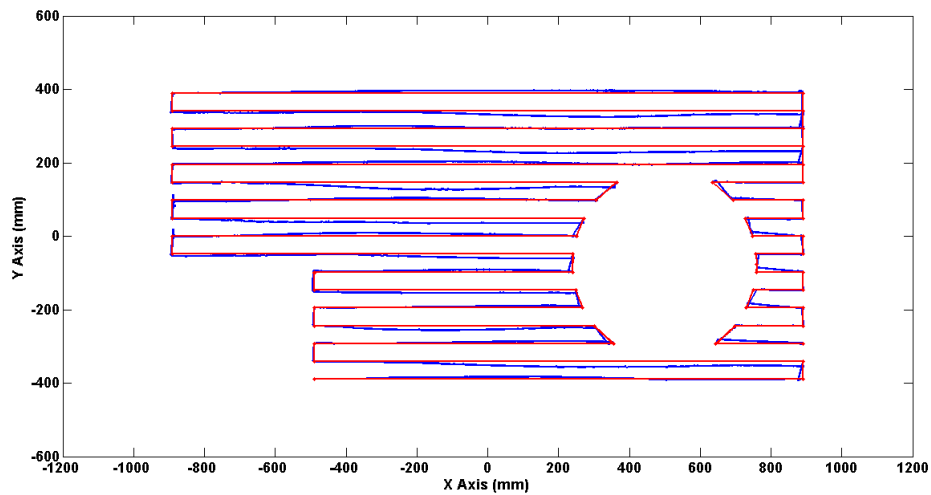
Figure 6.20 AUT RSA Path Accuracy

In order to characterise the performance of the AUT RSA and quantify the overall path error for the scan, both the desired and actual paths were mathematically compared. It must be remembered, as discussed in Section 6.12.2, that all desired motions are straight line linear paths between the start and the corresponding desired straight line end waypoint. Therefore no position information is readily available for locations between the start and end waypoint of such straight line motions.

This must be compared to the actual measured positional information as computed by the VICON motion capture system, which as discussed in Appendix A.2 produces a 6 D.O.F. pose estimate at a frequency of 100 Hz. The frequency to which the RSA GUI can acquire VICON measurement data is 50 Hz as indicated by successive timestamps. Therefore when travelling between a start and end waypoint, for a particular motion, the AUT RSA desired path knowledge consists of only two waypoints, while its actual path knowledge is far denser and updated to the RSA GUI

at 50 Hz increments. Therefore to credibly quantify the error a suitable path accuracy measurement strategy was developed:

1. The actual measured path start waypoint (MP_S) is defined as the nearest VICON desired positional measurement to the desired path start waypoint (DWP_1).

2. Similarly the actual measured path end waypoint (MP_E) is defined as the nearest VICON desired positional measurement to the desired path end waypoint (DWP_2).

3. Due to the linear motion between desired start and end waypoints a straight line equation can be obtained to describe the gradient and offset parameters of the desired path.

4. For each actual measured point ($MP_{1...N}$), the error magnitude ($PE_{1...N}$) is defined as the perpendicular, from the desired path, distance between an unknown point along the path intersecting with an actual measured point. This is illustrated in Figure 6.21.

5. The path error from the desired trajectory at each measured point along the actual scan can then therefore be quantified.

Figure 6.21 Path Error

The path error at each measured point along the path is shown in green in Figure 6.22, with a subset region illustrated in Figure 6.23.
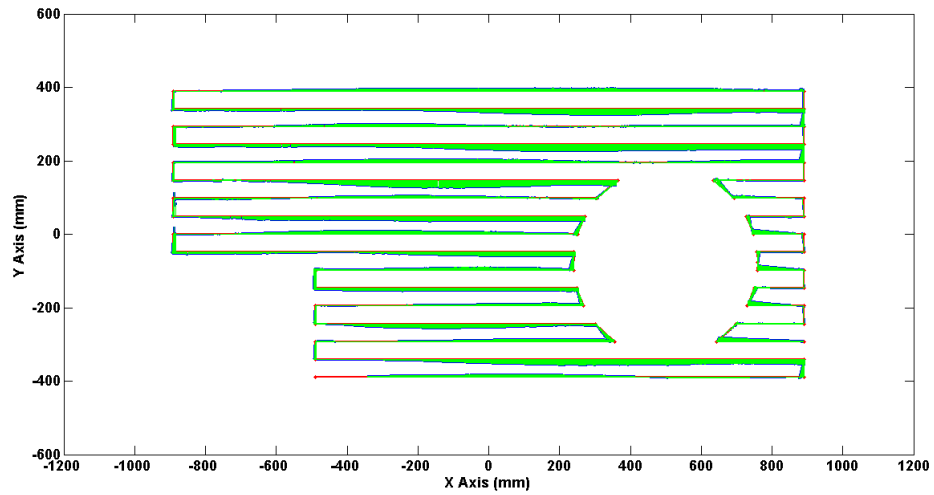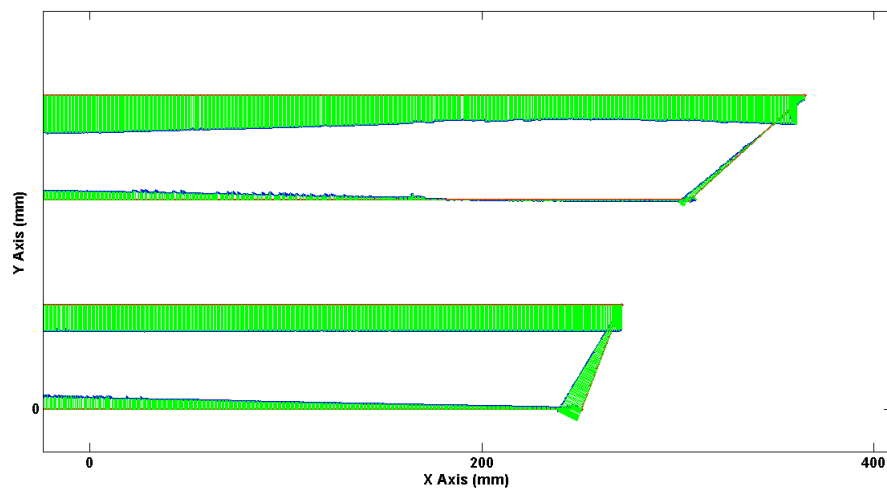

Figure 6.22 AUT RSA Path Error

Figure 6.23 AUT RSA Path Error

The corresponding statistical information on the path accuracy is shown in Table 6.15.

Parameter	Value
Max Path Error (Positive)	+13.48 mm
Max Path Error (Negative)	-19.38 mm
Mean Path Error (Absolute)	4.41 mm
RMS Error	6.14 mm
Path Error Standard Deviation	6.10 mm

Table 6.15 AUT RSA Path Accuracy

The histogram highlighting the distribution of path error distance is shown below in Figure 6.24. A 1 mm bin width was selected based on the documented consensus of desired minimum 1 mm position accuracy of mobile NDE applications, discussed in Chapter 1.
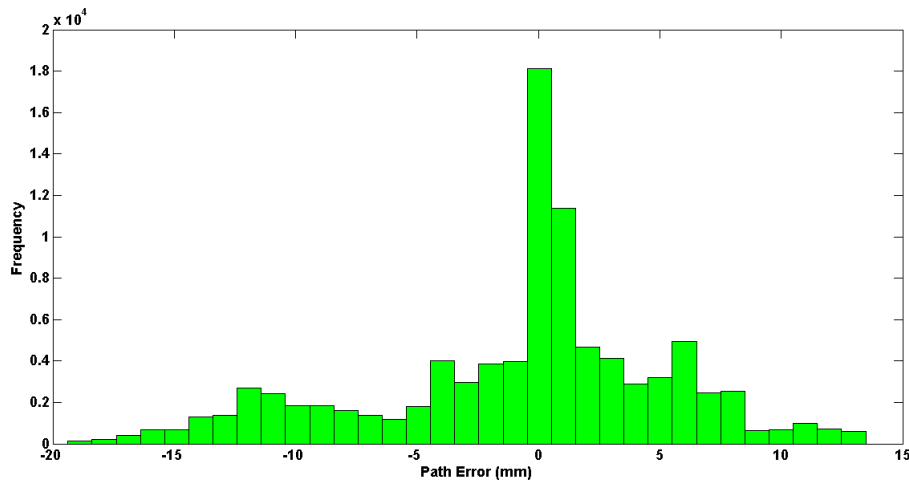

Figure 6.24 AUT RSA Path Error Histogram

Figure 6.28 highlights a first mode in the distribution of path error located around negative 12 mm, which after analysis of the data and Figure 6.26, it became clear that this can be attributed to the error associated in travelling long horizontal (X-

Axis) straight paths. Two modes in distribution are located at both positive 5 mm and negative 5 mm which again after analysis were found to occur on the short step over paths interlinking the long horizontal paths. The final and dominant path error mode, located around 0 to 1 mm, was attributed to the general dominant positional accuracy of the system, when considering effects such as platform mechanics and control system performance.

6.20 Discussion

This section has introduced a new CPP strategy for automated NDE inspection scenarios. Specifically highlighted are the approach, development and evaluation of an obstacle avoiding plate thickness mapping system.

From a path planning perspective, the trial scans positively highlight the ability of the strategy to avoid obstacles and provide the operator with the ability to achieve large area inspection coverage. Although not highlighting full scanning coverage, due to logistical constraints, it is not inconceivable to logically conclude that a reduced step over distance to match the transducer aperture would achieve this.

From an NDE perspective as highlighted in Table 6.14, the AUT RSA when driven from numeric code operations locates a number of artificial defects present within the sample. Reasons for not locating and recovering all defects are put forward including five of the six 10 mm diameter defects (8,9,10,11,12) and one 25 mm defect (1) not being scanned, along with one 25 mm defect (7) being too deep. A number of these non-detections were expected prior to the trialling of the system due

to knowledge of the system specification and performance limitations. Located defect positional accuracy is somewhat poor when considering the accuracy of the VICON position feedback ground truth system. Additionally as shown in Section 6.20 the actual path accuracy is also somewhat poor, with large deviations experienced on both short and long sections.

Defect positional accuracy for the AUT RSA broadly relies on two key factors:

1. The pitch of the Ultrasonic Transducer. A smaller pitch will give a much reduced measurement aperture, albeit still centred at the same point as a larger pitched device. Additionally the smaller pitch would allow smaller defects such as the 10 mm diameter flat bottomed holes to be detected.

2. The positional accuracy of the centre of the active back wheel mechanism, where the ultrasound transducer is located. Fundamentally this depends on the platform path accuracy which is dependent on a number of factors:

    a. The accuracy and rigidity to which the AUT RSA platform was designed and manufactured to ensure all axes remain true during inspection. It is considered that this is not an issue of concern for the current AUT RSA platform.

    b. The accuracy to which the VICON object was defined with respect to the turning centre of the platform. It must be remembered that the active back wheel position is derived indirectly based on turning centre measurements. The procedure for defining the turning centre is discussed in Appendix A.2.1 and was followed. It is considered that this step was performed sufficiently well, however further changes

could be incorporated. A precisely manufactured guide, with pre-located VICON targets at suitable locations, could be utilised to locate the turning centre with greater accuracy.

c. The accuracy to which the zero degree angle of the active back wheel mechanism is first set and maintained. The wrong alignment of the back wheel significantly impedes the ability of the platform to follow straight lines with constant yaw angle errors present forcing the AUT RSA sideways. Due to slippage and encoder resolution visible small degree (< 3 °) errors were apparent by the end of the scan. Re-design of the complete back wheel mechanism and uprating of the encoders would be required to alleviate or reduce any error due to this phenomena.

d. The operation and performance of the AUT RSA 2D move commands. As can be seen in Figures 6.22 and 6.23, clear waypoint overshoot and then pose launch angle errors are present within the system. It is believed that significant gains could be achieved by overhauling and tightening the tolerance of the 2D move commands. It must be noted that due to logistical constraints this option was not felt to be achievable in the available timescale.

e. The operation and performance of the AUT RSA heading controller which controls the platform position and pose along a path to its desired waypoint destination. It must be noted that the Proportional and Derivative controller parameters were manually updated prior to the final scans in an attempt to optimise performance sufficiently. It is

considered that an AUT RSA system model, incorporating noise and uncertainty in the active back wheel mechanism angle, would have to be developed to fully understand and realise the appropriate design and implementation of a suitable heading controller. The current PD controller, although not fully ideal for the task, was deemed to be sufficiently optimised and tuned given the circumstances.

    f. The accuracy of the VICON motion tracking system and its resolution in deciphering small pose changes when the platform is travelling along a motion path. The accuracy of the system has been characterised in [140] and the guidelines suggested to improve accuracy reliability followed.

With respect to the ultrasonic measurement the ultrasonic thickness accuracy is a function of:

1. The ability of the transducer to generate true signals representing received reflector reflections. This relates specifically to the characteristics of the transducer in relation to the sample nominal thickness.. As previously discussed the current AUT RSA wheel probe transducer is traditionally utilised in nominally thicker ($\approx$ 25 mm) applications. The un-damped nature of the transducer results in significant error in measured thickness of thin plate, as indicted by the measurement of defect 13. Additionally due to the nominal dry coupled nature of the wheel probe, saturation of the receiver amplifier can occur at points of reduced acoustical impedance, most notably arising due to seepage of tyre friction reducing oil after servicing. Such

saturation can yield error in the thickness mapping measurement due to the aforementioned dependence on signal amplitude.

2. The ability and performance of the thickness extraction algorithms. Specifically this relates to the intelligence in extracting the necessary back wall echos and de-computing the time differences. It must be noted that ultrasonic thickness mapping accuracy was not the focus of the body of work and as such the procedures utilised are deemed sufficiently suitable but not optimised.

6.21 Conclusion

The logic and thought behind a manufacturing driven path trajectory strategy for NDE applications was presented, yielding benefits in coverage, simulation and obstacle avoidance. The similarities between traditional machining operations and inspection scenario requirements in terms of path step-over, tool collision avoidance and the tool/sensor remaining perpendicular to the surface were highlighted and discussed. A successful strategy was developed to deploy the AUT RSA platform on a mock industrial thickness mapping inspection scenario and the steps required to undertake this highlighted and documented. The results of the inspection were presented and analysed with respect to the true data. Explanations were provided to clarify the discrepancies and errors found in both defect location and depth. Additionally the path accuracy of the AUT RSA over the whole sample was analysed and proposals put forward to address its performance limitations.

This section critically highlights the benefits, in terms of area coverage, obstacle avoidance and reduced path overlap, of adopting such a novel machining based path planning strategy for NDE inspections. These advantages were highlighted by the successful deployment of the AUT RSA on a mock inspection task. Furthermore this approach is not fundamentally limited to crawler platforms and can be scaled up to aerial platforms by including the Z-Axis components of the CAM generated numeric code. Therefore it can be conceived that the foundations to a scalable flexible obstacle avoiding path planning strategy for NDE applications is presented. This establishes the basis of an approach to using CAD/CAM programming to provide mobile robot path planning strategies. Therefore a universal control and path planning methodology is now possible for different NDE robot platform modalities.

Chapter 7

Tactile Sensing

7.1 Tactile Sensing

Conventional NDE sensor deployment commonly involves ultrasonic, eddy current, thermography, radiography and visual sensing modalities. For a number of practical reasons, such as lift-off sensitivity and susceptibility to surface features such as obstructions and liquids, these techniques do not yield themselves to be highly suitable for automated applications. A new technique based on the sense of touch, inspired by rodent facial whiskers, was investigated for its suitability to NDE applications. It is clear that surface, and possibly sub-surface, measurement information can be meaningfully extracted while providing conformance and compliance to end-effector and sample surface changes.

Animals such as rodents, seals and shrews detect proximity to nearby objects, along with their shape and texture, using their facial whiskers (vibrissae). The discrimination capability of these animals is quite remarkable: blindfolded rats are able to reliably perform rough-smooth discriminations that would be challenging for human fingertips [264]. Seals are able to detect and follow the hydrodynamic trail left by travelling fish utilising their whiskers [265], while pygmy shrews are able to identify, follow and apprehend local prey insects [266].

Whisking, the active oscillatory motion imparted to the facial whiskers by opposing pairs of intrinsic and extrinsic muscles, is a characteristic of the exploratory behaviour of the animal. This process of brushing and sweeping the end tapered whisker tip across the surface in a back and forth manner induces vibrations along the shaft that are transduced into neural signals by mechanoreceptors in the whisker follicle, providing the corresponding vibration pattern neural encodings to allow surface information to be measured [254,267-268]. From a neural processing perspective, signals instigated in the afferent cells of the trigeminal nerve are relayed to processing stations in the brainstem, midbrain, cerebellum, and forebrain, before being passed to further brain areas involved in memory, spatial mapping and decision making [269]. This process is illustrated in Figure 7.1.
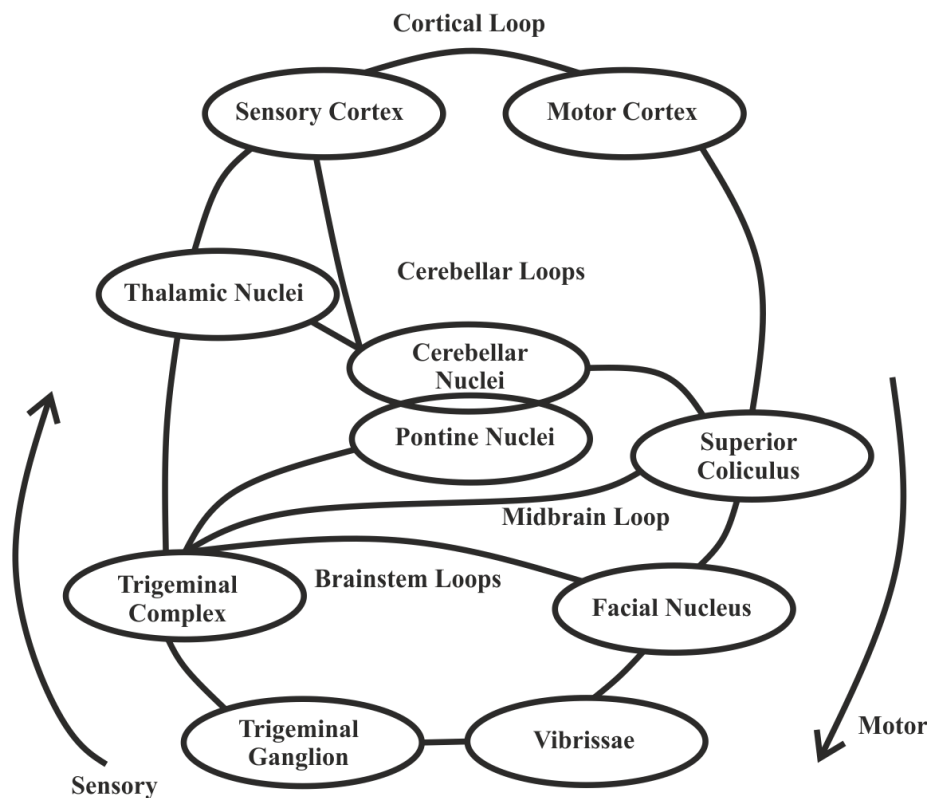

Figure 7.1 Rodent Whisker Sensory Structure [270]

This active whisking process of purposeful control and the seeking of information must therefore possess some benefit to the animal, namely the ability to control the direction of large area scans and also the velocity and duration of surface contact. It has been suggested that therefore such animals actively whisk their vibrissae to achieve greater sensory information in a similar manner to humans who adjust their fingertips movement when exploring surfaces [269]. Additionally it has been concluded that these whisker movements are actively controlled so as to increase the likelihood of environmental contacts while constraining such interactions to minimal surface force [269]. This is complemented by the delicate sensory transducers being located some distance away from the point of surface contact to avoid undue contact force.

Actuated artificial whiskers based on the facial whiskers of such animals and mice can therefore potentially provide a new degree of sensory information, with potential applications in robotics, automated systems, surveillance and emergency support.

Through the BIOmimetic Technology for vibrissal ACtive Touch (BIOTACT) European Union FP7 project, researchers at Bristol Robotics Laboratory (BRL) have undertaken a long-term European wide collaboration with biologist and engineers, to further understand the operation of vibrissae systems and their potential use and application in automated engineering systems [271]. In investigating biomimetic sensing they have focussed their research on the manner in which vibrissae endowed animals physically acquire sensory information regarding their surroundings. One main outcome of this collaboration is the development of modular fully controllable

artificial active whisking sensors as shown in Figure 7.2. Such artificial active whisking sensor modules allow investigating of the effects of active whisking strategies on performance of tasks such as shape classification and texture discrimination.
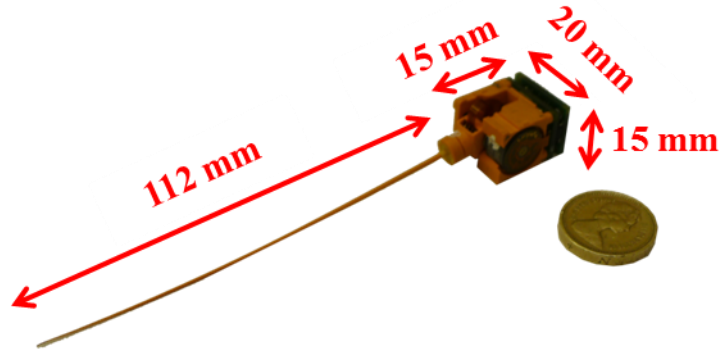

Figure 7.2 Artificial Whisker Module

7.2 Whisking Robots

Actuated whiskers were primarily investigated to gain a greater insight into the vibrissal sensorimotor system of rodents such as rats and mice, however considerable potential exists for adapting the artificial whisker sensors for use, for example, in navigational and proximal sensing applications for autonomous robotic vehicles in conditions of poor visibility [269, 271-273]. Recent work has focussed on tactile based uncertain contact pose texture classification and Simultaneous Location and Mapping strategies for robotic systems [274-275].

Figure 7.3 Tactile Based SLAM [274]

7.3 Tactile NDE

The potential NDE applications of such a sensor lie primarily in the capability for monitoring surface roughness and local profile geometry. This is particularly relevant given the continued large scale use of hot-rolled steel in industrial structures, due to its high strength to weight ratio, consistency and flexible design. Such a material requires extensive and substantial protection systems to reduce susceptibility to corrosion. The unstable iron-oxide mill scale, produced on the surface of steel after the hot rolling process, reacts with moisture in the environment resulting in corrosion of the steel. Throughout this process mill scale is removed from the steel leaving an irregular corroded surface behind. The rate and quantity of corrosion is dependent on many factors, primarily the length of time exposed to a wet environment, resulting in chemical, electro-chemical or microbiological reactions [276]. Studies have shown a direct correlation between the surface roughness and the amount of corrosion degradation and loss of material in carbon steel [277]. An

increase in corrosion material loss leads to an increase in the roughness of the sample under inspection [277].

The performance and durability of protective coatings and products applied to industrial metal surfaces are significantly affected by the state of the material immediately prior to application [278]. The primary factors influencing performance are the presence of rust, mill scale, surface containments and the surface profile [279]. The profile of a specimen under question is the foundation to which all objective surface assessments are made, allowing all standard surface roughness parameters to be then mathematically computed from the data [280].

The conventional method of determining the surface profile of a sample is through the use of a stylus based contact system [280]. By measuring the deviations of a small stylus following the peak and troughs of a sample, a two-dimensional outline of the surface profile can be obtained. A simpler method makes use of a depth gauge to average a series of deviations of the valleys of the surface, measured respectively to the peaks on which the device rests. Numerous optical methods exist based on techniques such as interferometry, Schmaltz optical sectioning and confocal microscopy. The traditional referenced British standard [281] on determining sample surface texture utilises a comparator panel with four sections of defined standard roughness characteristics [276]. A manual operator makes a visual and tactile comparison and classifies the sample surface as Fine, Medium or Coarse, dependant on its similarity to the referenced segments.

Modern surface profilometers are limited in practicality and flexibility when considering automated large scale industrial scanning. Firstly many of the devices based on contact and non-contact methods are fixed installation products which are naturally unsuitable for remote deployment (Figure 7.4). Secondly the presence of highly irregular surface profiles, results in large scale peak to trough deviations often in the tens of millimetres. Many modern stylus based surface profile and roughness measurement devices (Figure 7.5) sacrifice vertical axis travel for greater sensing resolution [282], when coupled with vertical travel ranges in the hundreds of micrometre range are then therefore completely unsuitable for practical full scale industrial surface scanning. Furthermore loose or flaking surface particles inhibit the operation and reliability of such precision mechanisms, rendering the device unusable. Again optical methods are limited and vulnerable to the surface condition, reflectivity and colour when performing roughness inspection [280,283].

Figure 7.4 Mitutoyo 178-544-2, 200 mm measuring range, 800 x 651 x 1200 mm volume [284].

Figure 7.5 Mitutoyo 178-561-02E, 17 mm measuring range, 174 x 66 x 58 mm volume [285].

Therefore a surface inspection and roughness measurement system for rapid large scale automated scanning must feature wide vertical axis travel, coupled with sufficient resolution and repeatability, along with the ability to accommodate the presence of practical surface features.

This body of work presents initial findings on the suitability and applicability of utilising vibrissae based tactile sensing for automated NDE applications. It is proposed that the tactile and compliant nature of the active whisker sensor results in the technique being:

Insensitive to stand-off distance – The separation between the sensor and surface is not critical compared to traditional sensors.

Simple, inexpensive and robust - Sensing electronics are far away from surface contact thus reducing wear and damage.

A rapid surface scanner - Dense arrays of whisker shafts would allow the area coverage per unit time to scale linearly with the number of whiskers.

Compliant with large profile changes and surface contaminants – This is an important characteristic for real industrial inspection of curved surfaces, areas of corrosion and regions of artefacts such as weld beads, rivets, liquids and flaking paint.

7.4 Artificial Whisking Module

The whisker shafts were produced using composite material and Data Light Processing (DLP) rapid-prototyping technology to achieve fine taper tip sizes coupled with sufficient strength and toughness to withstand repeated impact against surfaces. Smaller tip sizes allow for greater surface sensing resolution along with reduced impact on sensing performances if tip breakages occur.

The whisker shaft was actively swept back and forth using an integrated three-phase brushless geared DC motor and its corresponding protraction angle (θ) with respect to the module normal measured to 14 bit resolution using a non-contact Hall-effect sensor. Real time drive signal generation and closed loop Proportional-Derivative (PD) control is provided by the integrated 16bit digital signal microcontroller, allowing for whisking frequencies comparable to that of real rat vibrissae. Furthermore the orthogonal axes deflection (X^{awm}, Y^{awm})(Figure 7.6) of the whisker shaft base, located within a polyurethane filled dashpot housing, are again measured to 14 bit resolution using a non-contact Hall-effect sensor (Figure 7.6). This is achieved through the addition of a magnet attached to the base of the whisker shaft. All three measured properties (θ, X^{awm}, Y^{awm}) are transferred, at 2 KHz sampling rate, to a host Personal Computer (PC) via an external FPGA . Each individual whisker

module weighs approximately 8 g while being 20 x 15 x 15 mm in size. Figure 7.6 details the coordinate alignment convention of the whisker module, specifically the X^{awm} and Y^{awm} of the deflection sensor and the protraction angle (θ) being defined as positive rotation around that same X^{awm} axis.
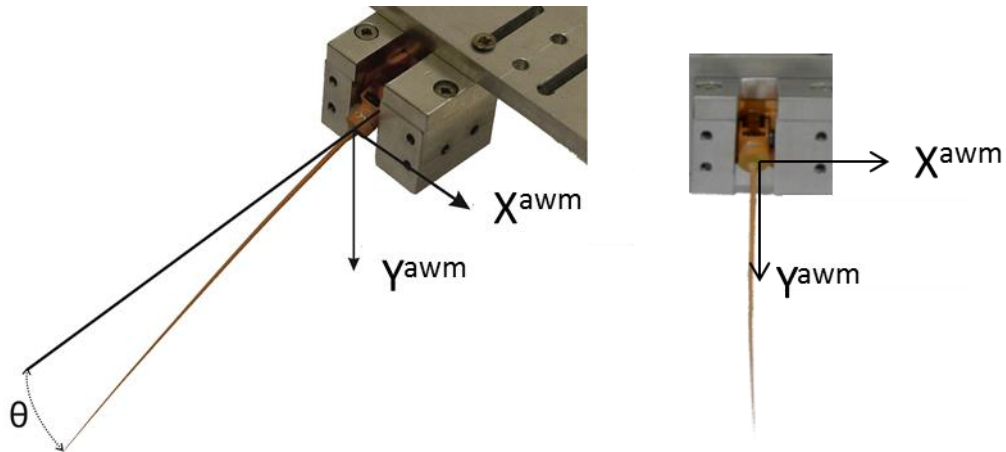
Figure 7.6 Whisker module with established coordinate conventions

The active whisker sensor is also fully compatible and integrated with the existing RSA electronic and software platform by transferring all sensor data directly from the on-board microcontroller through a dedicated Serial Peripheral Interface (SPI) bus.
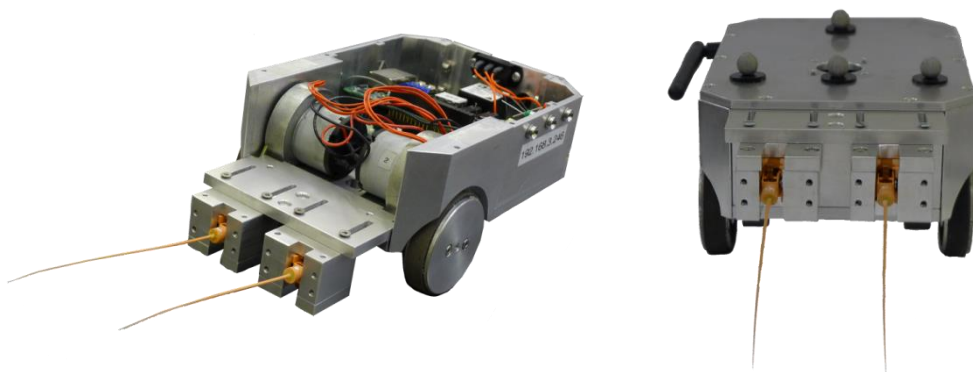
Figure 7.7 Tactile Sensing RSA

7.5　Whisking Drive Signals

Previous research has focussed on the particulars and importance of motor control in the whisking motion [255]. Two methods were investigated namely: Rapid Cessation of Protraction (RCP) - a feedback technique where sensory signals resulting from whisker-environment contact are used to regulate the same contact, and Contact-Induced Asymmetry (CIA) is an example of feed-forward control, with sensory signals resulting from whisk contact utilised to regulate subsequent whisk contacts.

In this work the drive signal for motor control was a fixed-amplitude, fixed-frequency sinusoidal signal with no control performed on sensory information from whisker-environment contact.

7.6　Whisker Inspired NDE Application – Experimental Arrangement

To accurately characterise and evaluate the performance of such an active sensing system for NDE applications, the whisker module was mounted on a fixed Cartesian scanner arm, allowing controlled and repeatable scans of test surfaces to be performed.
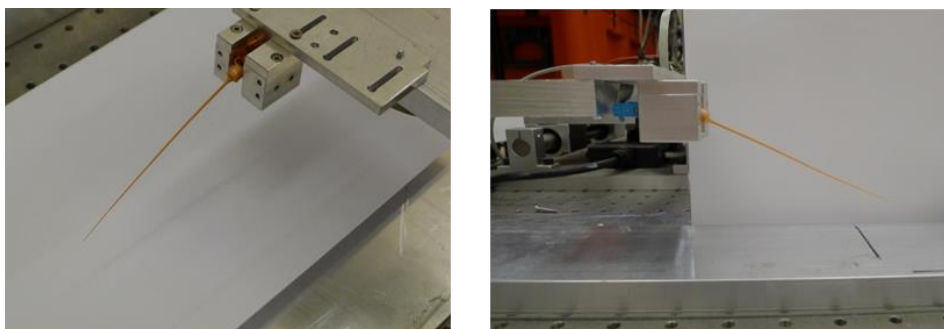

Figure 7.8 Experimental Set-Up

Using a calibrated three dimensional Laser Tracker (LAT) system [Appendix A.3] the scanning arm and ground truth reference measurement surface were both levelled to gravity. The VMCS T160 based 6 D.O.F. tracking system was utilised to acquire real time 100 Hz positional information of the whisker module [Appendix A.2]. The scanner, VMCS and whisker module control were integrated together in the MATLAB programming environment, allowing for a complete closed loop scanning system to be implemented and operated.

The whisking frequency (f_w) was selected as 1.8 Hz. This is slower than the typical whisking frequency of rats (Dominant frequency 8 Hz), however the 112 mm long whisker used throughout this work is longer than that of a typical rodent. This frequency was selected arbitrarily and limited testing has shown that this is not critical in achieving successful texture classification [271].

In this work each whisking process is defined as five seconds of eight complete cycle whisks (Figure 7.9 a). A free space whisk is defined as an unperturbed whisk where the sensor does not make physical surface contact; correspondingly a perturbed whisk references a surface contacting whisk. The surface contact area of each whisk cycle corresponds to a trough in the measured θ angle, with the corresponding mean of the complete eight troughs computed to derive the average θ angle per process. The saturation and clipping effect witnessed on each upper peak is due to the damping and resistance to whisk motion caused by the flexible printed circuit board connection of the orthogonal deflection Hall-effect sensor.

Both relative orthogonal whisk X^{awm} and Y^{awm} axis displacement components (Figure 7.9 b & c) are obtained through baseline subtraction of the relative reference unperturbed free space whisk displacement. The Power Spectral Density (PSD) of the data is computed and the resultant mean total energy per whisk process, given by the average integral of the PSD whisk cycle curves. Therefore for each complete whisk process, a relative mean angle value along with the mean energy for both orthogonal X^{awm} and Y^{awm} axis components is computed.
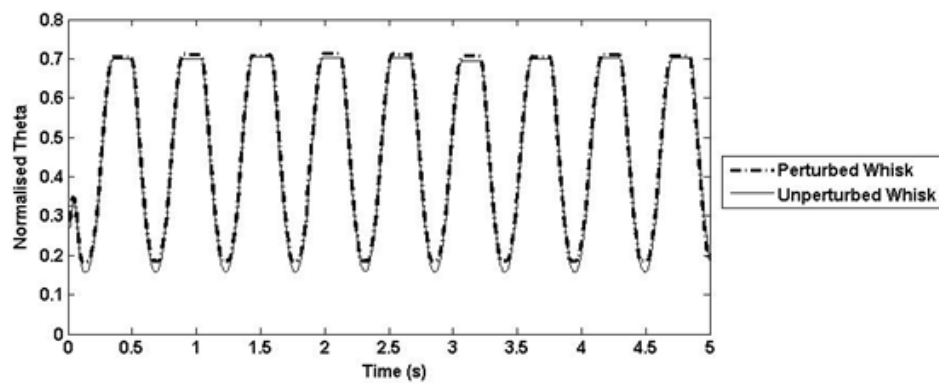
(a) Whisker protraction angle.
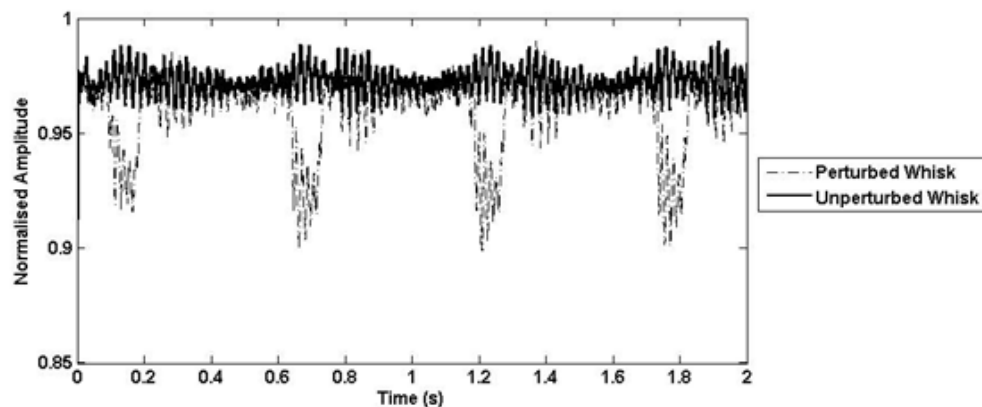
(b) Whisker X^{awm} axis deflection.
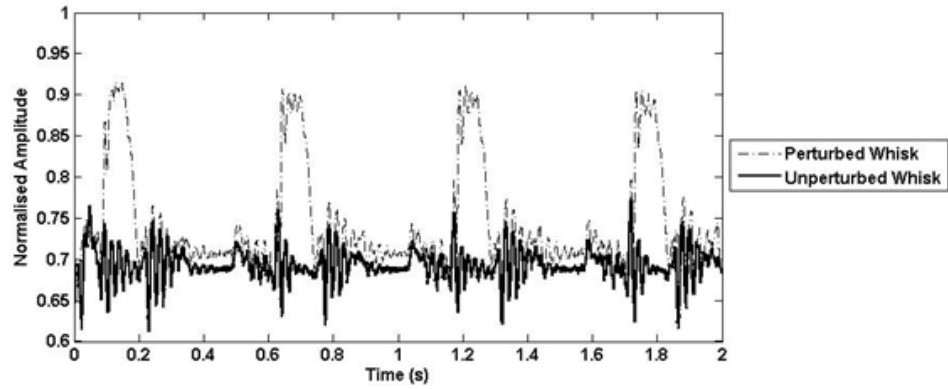
(c) Whisker Y^{awm} axis deflection.

Figure 7.9 Perturbed and unperturbed whisking module sensor outputs

7.7 Whisker Shaft Deformation

7.7.1 Shaft Deformation

The flexible and compliant nature of the composite based whisker shaft results in bending and plastic deformation of the structure on contact with reduced vertical displaced surfaces. If the vertical height between the whisker module shaft centre and the surface under inspection decreases, coupled with the driving whisk amplitude remaining constant, the shaft undergoes bending on contact with the surface.. This outcome causes an error in the measured protraction angle of the whisker shaft, when referenced to the normal surface inspection point at the shaft tip. This process is illustrated in Figure 7.10 with respect to the world coordinate frame and the vertical displacement denoted as Z^w.
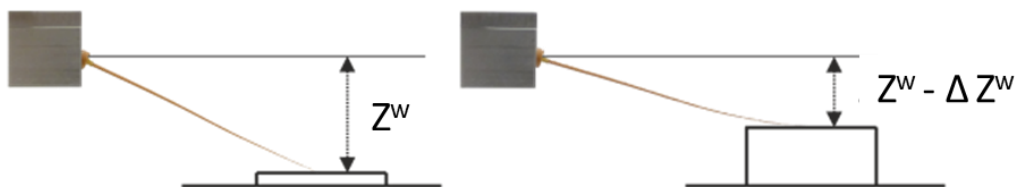

Figure 7.10 Reduction in vertical displacement between module shaft centre and surface under inspection.

To characterise the non-rigid nature of the shaft, a test sample was designed and produced to allow the protraction angle of the whisker to sweep through a range of controlled discrete levels, while monitoring its corresponding output. The maximum to minimum vertical distance under inspection was chosen as 15mm in an attempt to recreate a realistic range found in an industrial situation. This range was further divided in to fourteen 1mm stepped increments each of 20mm depth and width and ten 0.1mm increments of similar shape (Figure 7.11). The test sample was produced from aluminium and manufactured using traditional milling removal.
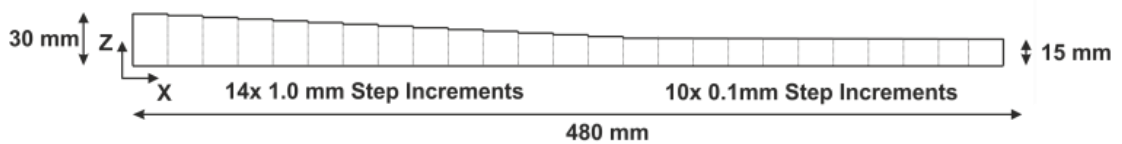
Figure 7.11 Whisker deformation test piece sample.

The step height of each increment was measured using the LAT to confirm its dimension specification after manufacture. The vertical height of 75 mm between the whisker module shaft centre and the surface under question was chosen as it offered the minimum distance possible between the scanner arm and ground truth measurement surface. This along with the known whisker shaft length (112mm) were both utilised in the characterisation of the whisker shaft. Furthermore this height was then referenced as the zero nominal module-surface stand-off distance.

259

7.7.2   Ideal Rigid Shaft

A solid rigid cylinder of the same length as the whisker was simulated to rotate from the same vertical centre point as the current module. The simulated protraction angle was recorded at each point of the simulated shaft coming into contact with each step of the test sample, while also ensuring that no bending of the ideal shaft occurred. The experimental principle is illustrated below in Figure 7.12. The simulated ideal protraction angle across the steps was plotted against the measured whisker θ angle after both being normalised to remove scaling factors (Fig. 7.13).
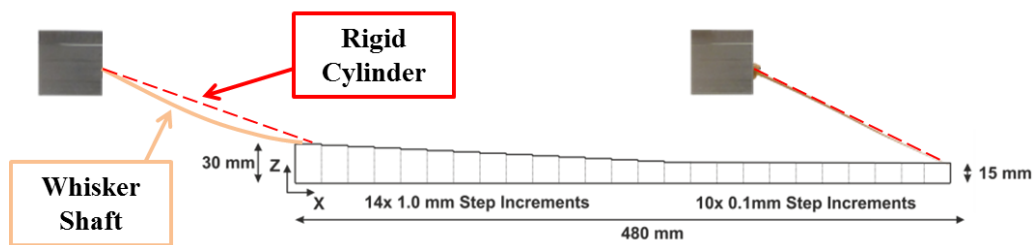
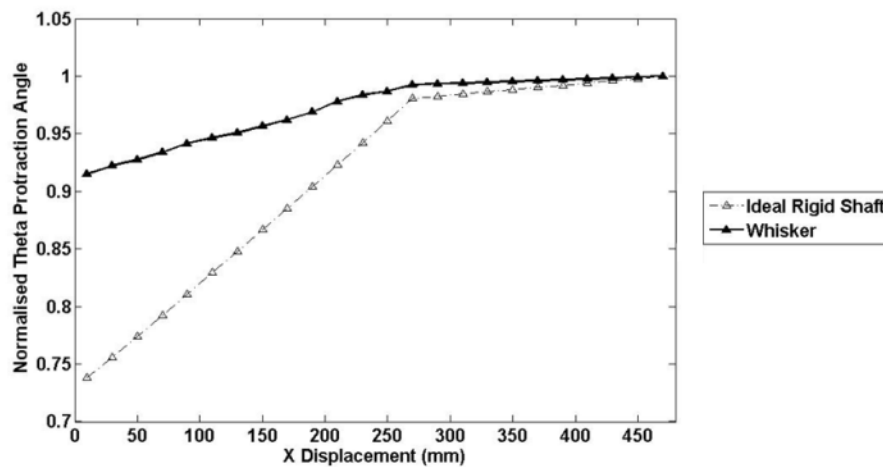**Figure 7.12 Whisker and rigid shaft bending experiment principle.**

Figure 7.13 Whisker shaft protraction angle (solid line) and ideal shaft protraction angle (dashed line).

As expected when the vertical height from whisker module centre point to sample surface is reduced the real whisker shaft measures a greater protraction angle, caused by the shaft no longer being rigid and therefore bending, allowing far greater tip surface area coverage.

7.7.3   Non-Rigid Shaft Compensation

A correction factor across the measured vertical height range was established to compensate for the bending influence of the shaft. The multiplication factors between the real whisker and the ideal rigid shaft protraction angles were computed and are shown plotted below (Fig. 7.14) against the rotational protraction angle of the whisker shaft.
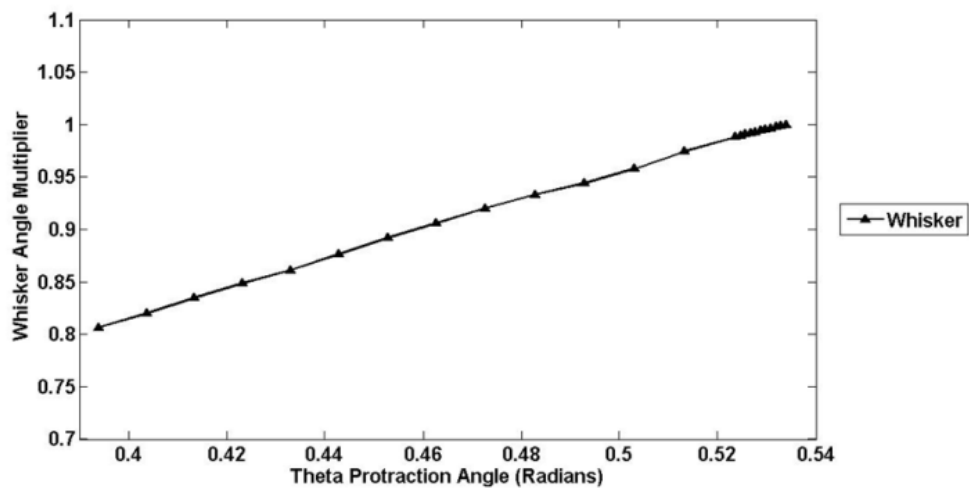

Figure 7.14 Whisker module protraction angle multiplier.

A linear straight line fit was selected to sufficiently fit the multiplier data points. The coefficients are shown in Equation 7.1:

$$y = 1.381x + 0.264 \qquad\qquad (7.1)$$

where x is the theta protraction angle in radians and y is the whisker angle multiplier. The mean and standard deviation of the residuals were found to be 0.0067 and 0.0014 respectively and deemed to be satisfactory.

7.8   Whisker Based Surface Roughness Characterisation

7.8.1   Constant Mean Vertical Height Sample

Five samples of similar area, namely 20 by 60 mm, controlled commercial grade abrasive paper were selected ranging from P240 to P80 ISO grit designation. A test piece was configured with the samples arranged in order of decreasing grit size and 20 mm wide aluminium spacing between each sample, giving a total length of 220 mm. Using the Laser Tracker the mean maximum deviation of peaks in the vertical axis from a referenced plane, defined as the underside base of the backing paper, of each sample was measured over a length of 60 mm. Each sample was then indented by its corresponding height value into an aluminium block of 15 mm depth through milling removal, resulting in a constant mean vertical height of 15 mm for all the samples. Such a technique permits discrimination of surface roughness and surface vertical offset.
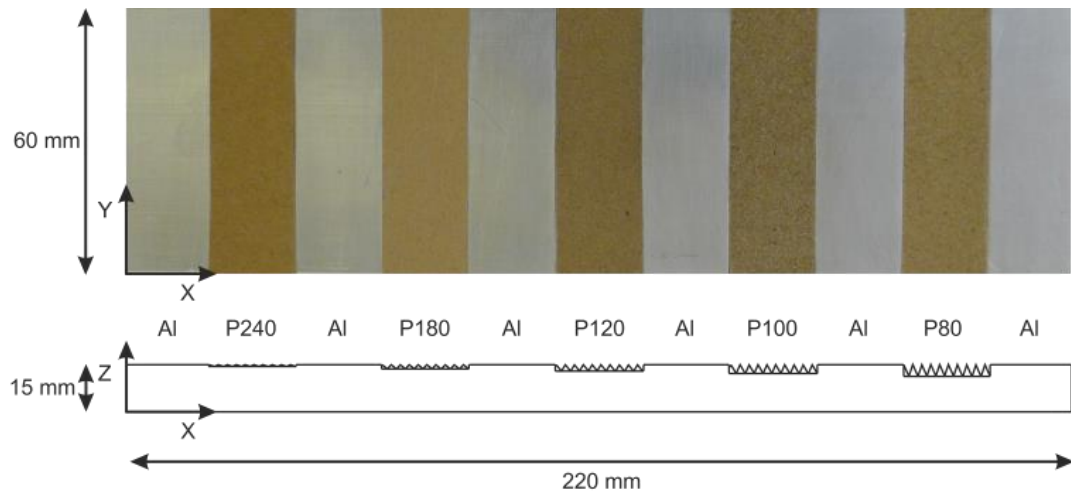
Figure 7.15 Indented surface roughness test piece sample.

A standard method of quantifying one feature of surface texture is Roughness Average (R_a), with others detailing Root Mean Square (RMS) and maximum or minimum values [280]. R_a is the arithmetic mean value of the departure of the profile (y) from a centre line throughout the sampling length [280].

$$R_a = \frac{1}{n}\sum_{i=1}^{n}|y_i| \qquad (7.2)$$

Using a calibrated surface roughness meter the R_a value of each sample was measured five times across the range of area, with the results shown in Table 7.1. The measuring system utilised a 5 μm stylus with a 5 mm traverse length and 0.8 mm cut off, which defines the wavelength filter value.

ISO Grade	P240	P180	P120	P100	P80
R_a (μm)	14.66	17.66	24.06	27.06	59.72
R_a (μm)	14.27	15.22	22.73	32.34	51.30
R_a (μm)	12.80	15.40	20.18	34.78	54.68
R_a (μm)	13.67	14.62	20.67	29.55	48.55
R_a (μm)	13.11	20.67	26.93	30.48	50.28
Mean R_a (μm)	13.70	16.71	22.91	30.84	52.91
Standard Deviation (μm)	0.78	2.49	2.74	2.91	4.42

Table 7.1 Indented Test Piece Sample Roughness Data

7.8.2 Tactile Surface Roughness Measurement

A line scan of 220mm length and 1mm step size was undertaken across all five samples and six aluminium segments, with a single whisking process at each point. The direction of travel was from left (P240) to right (P80), with reducing ISO Grade. The scan was undertaken ten times to ascertain measurement variation and the normalised amplitude standard deviation measured as 0.013, which was deemed satisfactory. A moving average filter, with span of five whisking processes was utilised to smooth the raw X^{awm} and Y^{awm} axis energy data, which was then normalised to the respective peak energy amplitude value (Fig. 7.16 & 7.17). The R_a data was normalised from the mean values shown in Table 7.1.
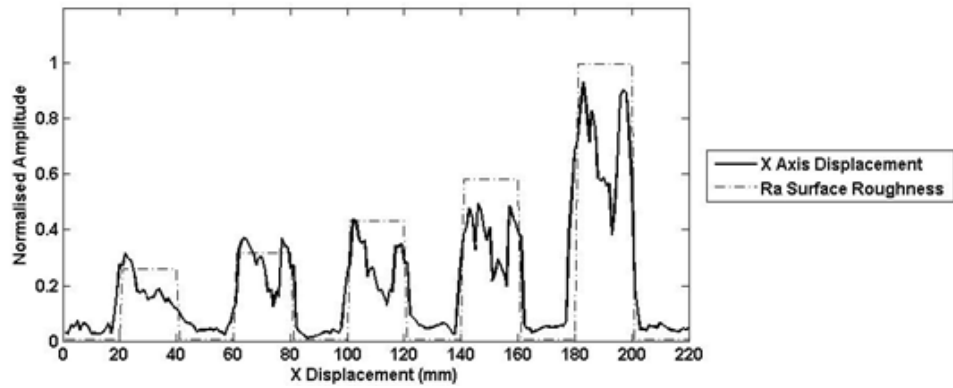
Figure 7.16 Indented surface roughness test piece sample whisker module X^{awm} axis deflection energy (solid line) and Roughness Average (Ra))(dashed line).
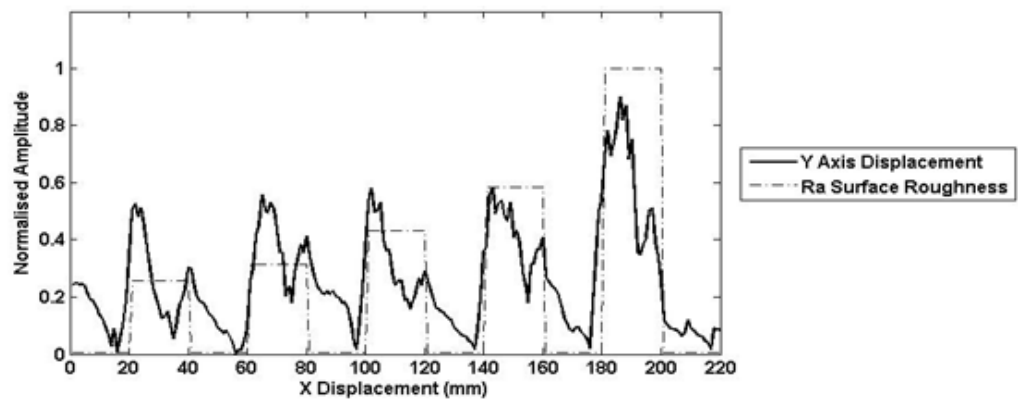

Figure 7.17 Indented surface roughness test piece sample whisker module Y^{awm} axis deflection energy (solid line) and Roughness Average (Ra) (dashed line).

Note that the R_a data is a single value mean over the sample width as measured by the surface roughness meter, whereas the X^{awm} and Y^{awm} axis displacements of the whisking sensor are the instantaneous values as a function of position. In relation to Figures 7.15 and 7.16, we expect the *mean* of the X^{awm} and Y^{awm} axis whisker displacements in each sample width window to be proportional to the corresponding mean R_a value.

The mean surface roughness amplitude across each abrasive paper sample width was plotted against the mean R_a value of each sample. A third order polynomial fit was then applied to each data set (Figures 7.18 & 7.19).
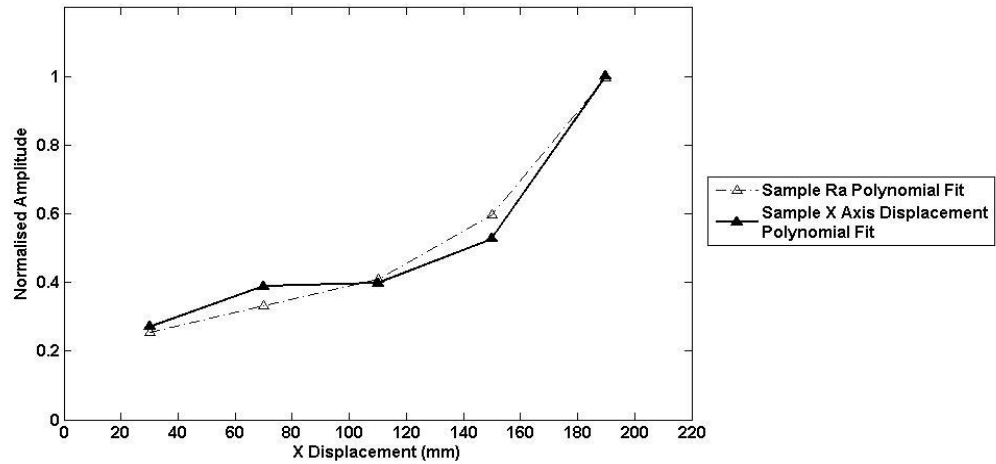

Figure 7.18 Mean Indented Sample X$^{\text{awm}}$ Axis Amplitude
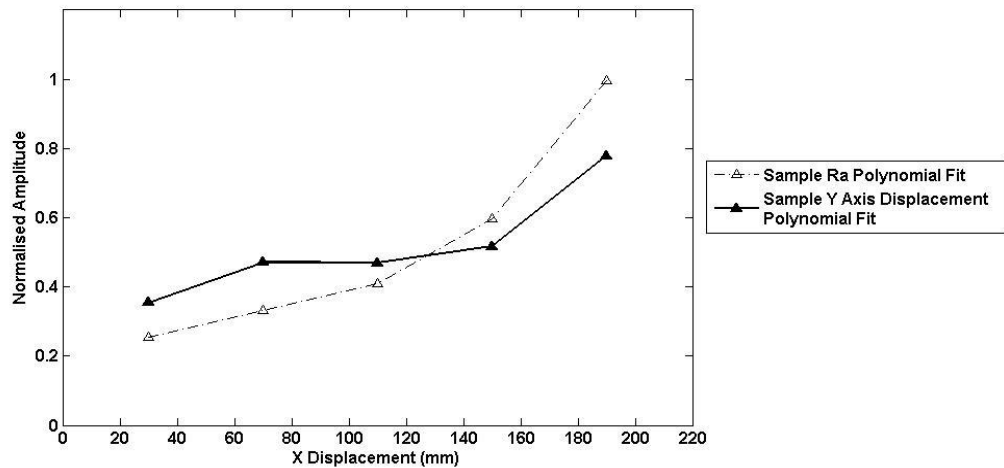
The correlation coefficient (r_x) between the five sampled mean indented X$^{\text{awm}}$ axis amplitudes (X) and the five corresponding mean R_a data values (R_a), measured across the width of each distinct sample, was computed using (7.3) and found to be 0.988.

$$r_x = \frac{\sum_N (X_N - \bar{X})(R_{a_N} - \overline{R_a})}{\sqrt{\left(\sum_N (X_N - \bar{X})^2\right)\left(\sum_N (R_{a_N} - \overline{R_a})^2\right)}} \qquad (7.3)$$

Where N defines the appropriate abrasive sample index, ranging from the lower bound of 1 (ISO P240) to the upper bound of 5 (ISO P80). $\bar{x}$ defines the mean of all

five X^{awm} mean values, while $\overline{R_a}$ defines the mean of the five R_a data values measured across the width of each distinct sample.

When similarly considering the Y^{awm} Axis:

Figure 7.19 Mean Indented Sample Y^{awm} Axis Amplitude

Similarly the correlation coefficient (r_y) between the five sampled mean indented Y^{awm} axis amplitudes and the five corresponding mean R_a data values, measured across the width of each distinct sample, was found to be 0.973.

Taking the individual mean X^{awm} and Y^{awm} axis displacement amplitudes across each abrasive paper sample and plotting against the mean R_a value, for that corresponding sample, yields a monotonically increasing relationship as shown in (Figure 7.20). It can be seen that the sensitivity of the device, in terms of both the X^{awm} and Y^{awm} axis displacement, is non-linear throughout the sampled surface roughness range.
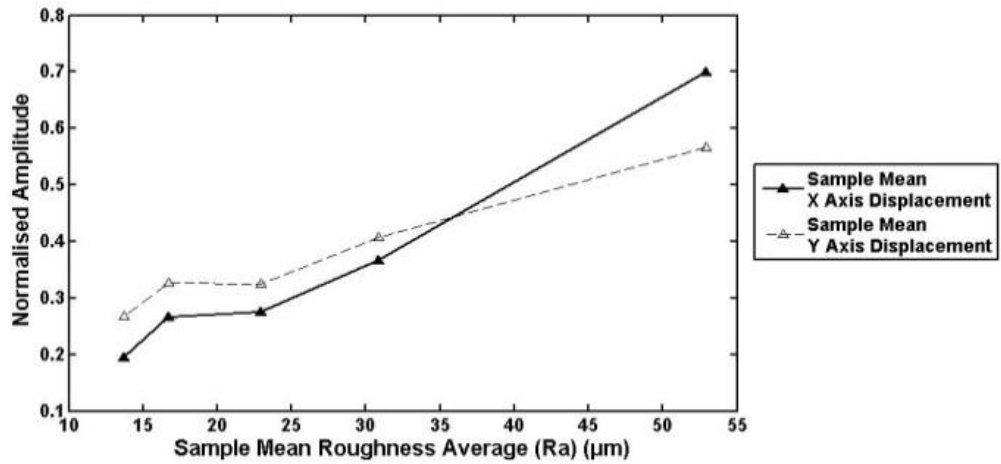
Figure 7.20 Mean indented X^{awm} axis deflection energy (solid line) and mean indented Y^{awm} axis deflection energy (dashed line).

7.8.3 Sensor Surface Lift-off

The test piece scan was re-undertaken at a number of sensor-surface lift-off positions in the vertical axis from the surface plane. The nominal sensor-surface distance, defined as the vertical height between the whisker module shaft centre and the surface under inspection, was referenced as zero lift-off. The amplitude of the driving signal remained constant. The results are shown in Table 7.2.

Nominal Sensor–Surface Lift-Off (mm)	X Axis Correlation Coefficient & (Percentage error from zero lift-off)	Y Axis Correlation Coefficient & (Percentage error from zero lift-off)
0	0.988	0.973
1.5	0.986 (0.20 %)	0.971 (0.21 %)
3	0.976 (1.22 %)	0.966 (0.72 %)
6	0.953 (3.54 %)	0.946 (2.77 %)

Table 7.2 Module lift-off X & Y axis surface roughness correlation

In comparison at similar lift-off values (1.5 & 3 mm) a conventional differential eddy current probe's peak amplitude decreases to 34% and 19% of the zero lift-off value respectively [23]. Again similar lift-off variations result in significant changes (>1 µs) to ultrasonic arrival times when using Electromagnetic Acoustic Transducers (EMATs) [159].

7.8.4   Protraction Angle Surface Profiling

A single line scan of 220mm length was performed across all five samples and adjacent six segments of aluminium, with a corresponding step size of 1mm. The protraction angle as measured across the length of the sample is plotted in Figure 7.21.
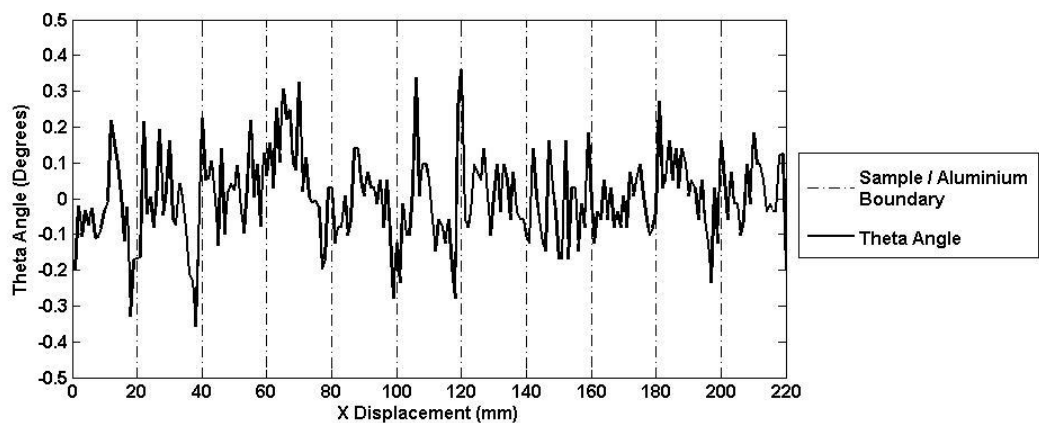

Figure 7.21 Indented Sample Whisker Protraction Angle

The theta angle zero value is defined as the mean theta protraction angle value obtained when whisking along a 220mm long 15mm deep aluminium block with no artificial sample indentation.

7.8.5   Non - Constant Mean Vertical Height Sample

A further test was conducted using a second test piece with five similar ISO abrasive paper samples un-indented into a 15mm deep aluminium block, resulting in a non-constant mean vertical height (Figure 7.22).
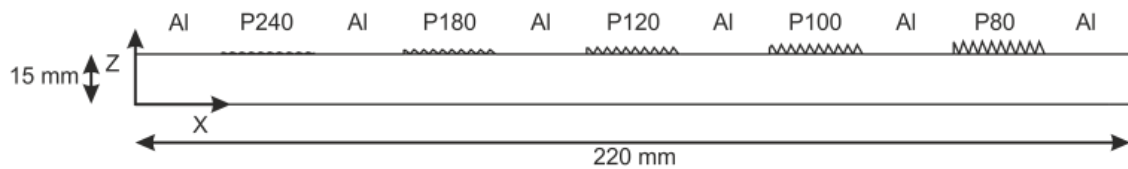

Figure 7.22 Un-Indented surface roughness test piece sample.

The protraction angle as measured across the length of the sample and each sample width is plotted in Figure 7.23.
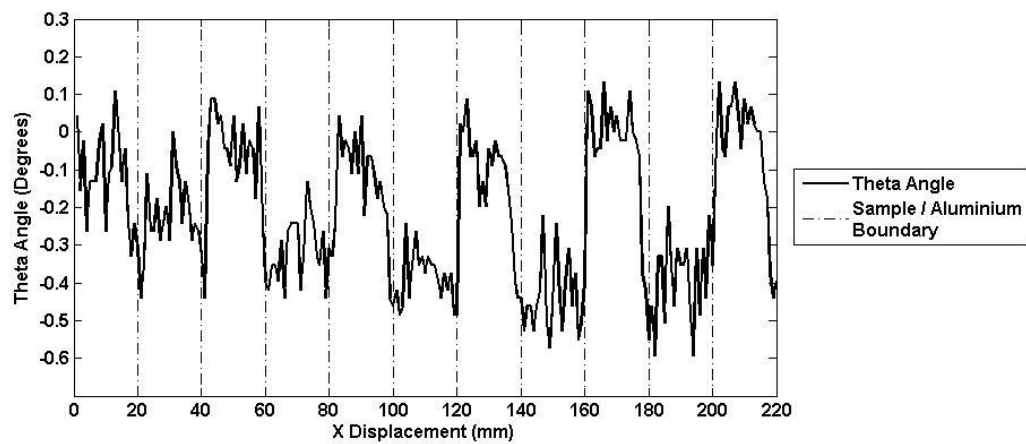

Figure 7.23 Un-indented Sample Whisker Protraction Angle

The mean protraction angle as measured across each abrasive sample in a 20 mm window, corresponding to the width of each sample, was taken and plotted against the mean vertical height of each sample measured previously (Figure 7.24). Again a

270

third order polynomial fit was applied to each data set, based on acceptable fitting error, whereupon the correlation coefficient was found to be -0.942. The negative sign confirms that with increasing sample vertical height, the whisker protraction angle in fact decreases. This is due to the shortened arc length travel required to sample surface contact.
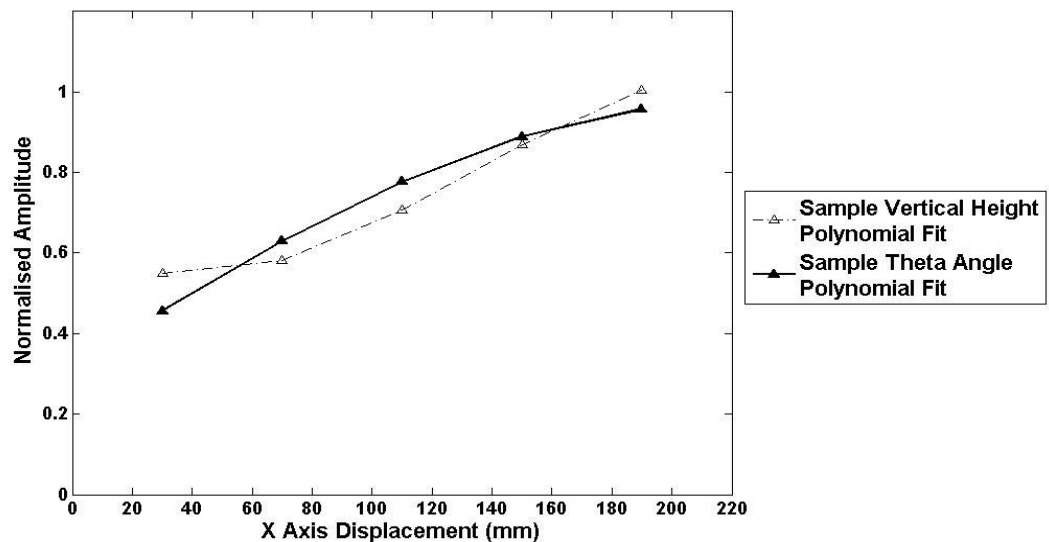

Figure 7.24 Mean protraction angle (solid line) and sample mean vertical height (dashed line).

7.9   Artificial Defect Quantification

7.9.1   Artificial Defect Test Piece Specimen

Having quantified the sensor response to surfaces with known roughness values, an additional test was undertaken to evaluate the sensor performance with larger area surface defects. Accordingly an artificial defect test sample was developed consisting of a solid aluminium piece and four circular flat bottomed holes of 14 mm diameter and depths of 0.4, 0.6, 0.8 and 1.0 mm from the non-milled sample surface (Figure

7.25). The depth, shape and magnitude were all chosen arbitrarily in an attempt to simulate an area of localised surface corrosion.
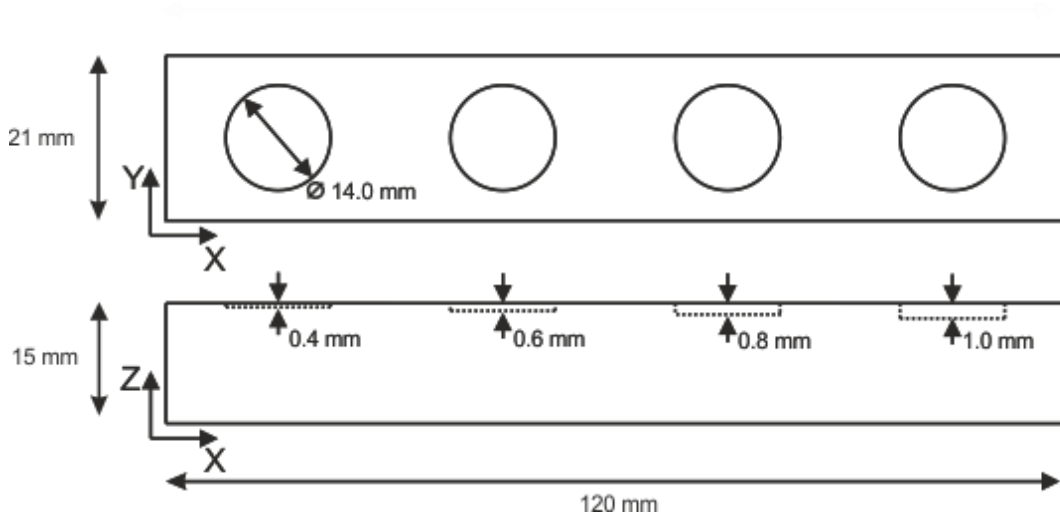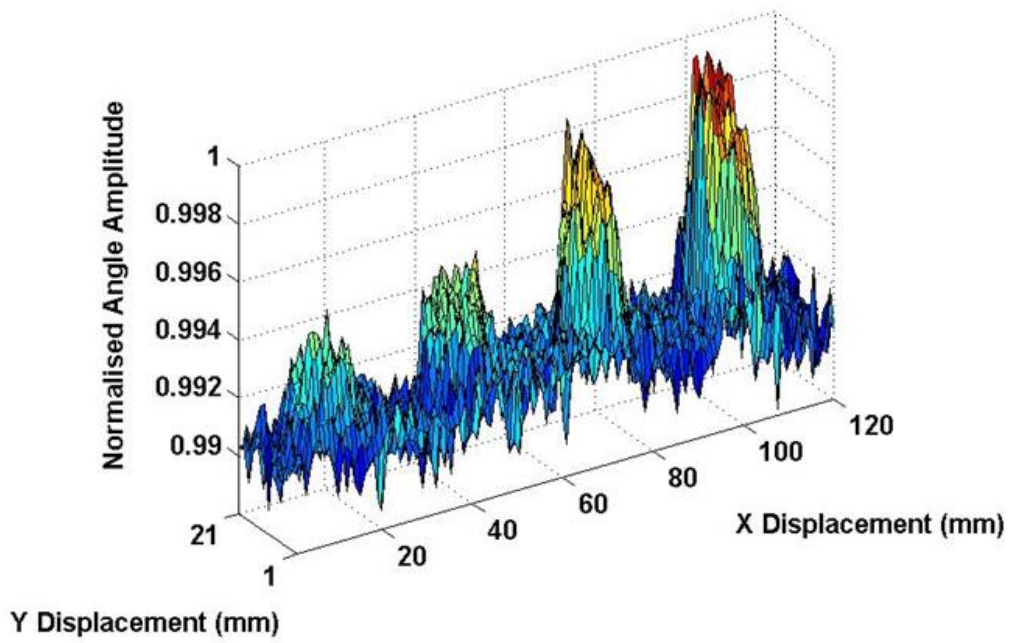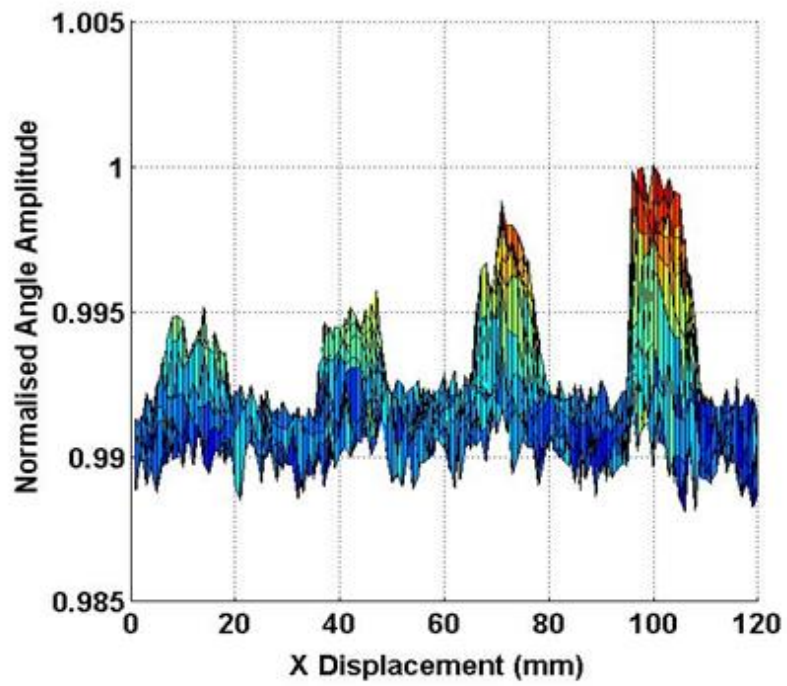

Figure 7.25 Artificial defect test piece sample.

7.9.2 Whisker Inspired Surface Scanning

A raster scan was performed on the full surface area of the test sample with 1mm resolution in both the X and Y axis of the world coordinate frame. At each measurement point one complete whisking process was undertaken. The unfiltered raw data is shown in below in Figure 7.26.

(b) Unfiltered raw whisker module 3D surface scan.

(b) Side profile of unfiltered raw whisker module 3D surface scan.

Figure 7.26 Unfiltered raw whisker module 3D surface scan of artificial defect test piece sample.

A Gaussian 3 by 3 filter array of standard deviation 1 was then applied to smooth the raw data and its result shown below (Figure 7.27)
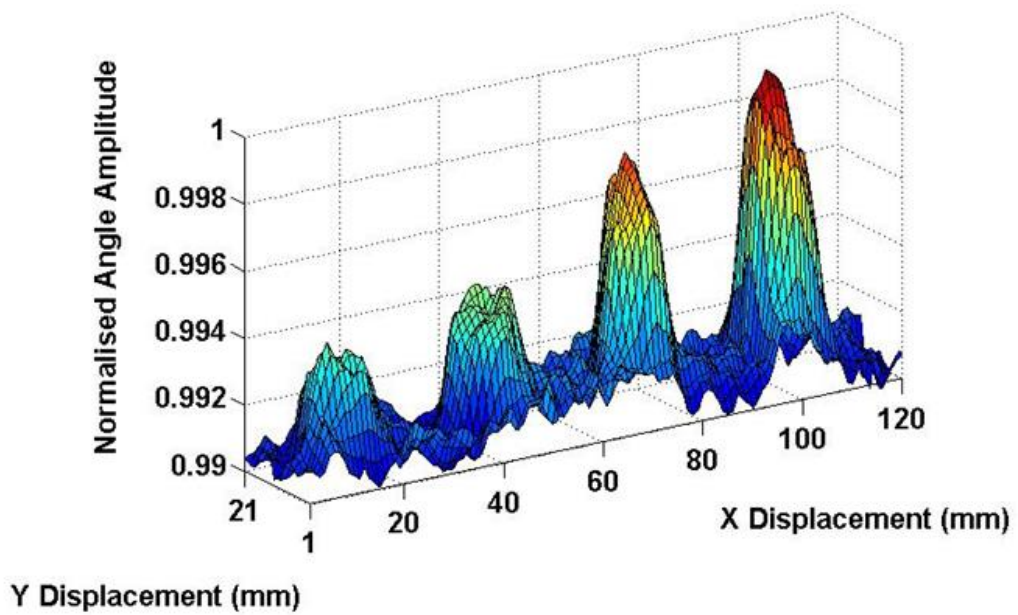
Figure 7.27 Gaussian filtered whisker module 3D surface scan of artificial defect test piece sample.

7.9.1   CAD Model Sub-Sampling

To characterise the surface mapping performance of the whisker module the 3D Computer Aided Drawing (CAD) model of the artificial circular pit test sample was registered as the reference model for correlation purposes. In order to take account of the finite resolution (1 by 1 mm) of the whisker module scan, the CAD model was sub-sampled to the corresponding resolution across the whole sample area.
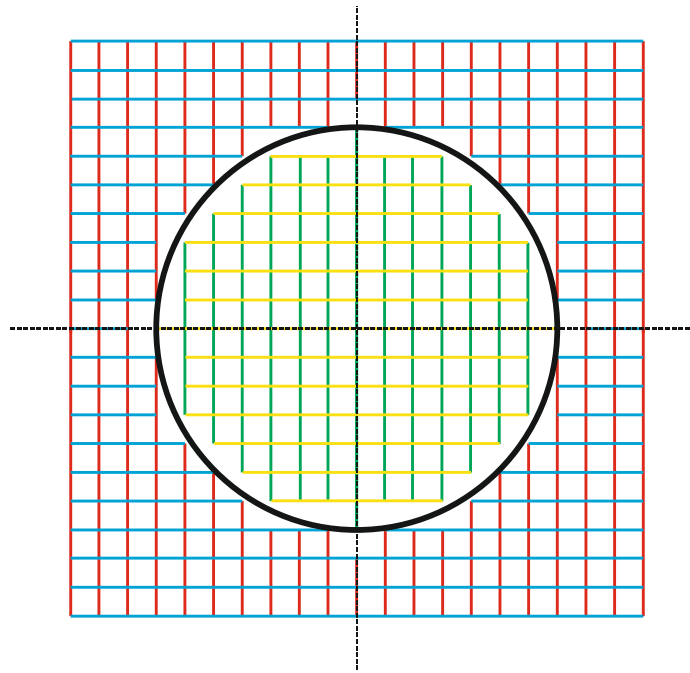
Figure 7.28 Sub-sampled CAD

Again using a rigid rod model, the corresponding protraction angles for the non-milled surface and adjacent circular defects were calculated and utilised as the ideal protraction angle at each point in the sub-sampled CAD model.

7.9.2 Whisker Inspired Surface Scanning Performance

Using the principle of the correlation algorithm detailed in Equation 7.3, the raw unfiltered data protraction angle values were compared against the sub-sampled ideal model values, with the result being 0.8039, corrected for shaft deformation. Similarly the filtered data protraction values were then compared against the ideal model, with the result being 0.8523.

The rotational protraction angle standard deviation measured across the un-milled defect free surface was found to be 0.039 degrees for the filtered data sets. The vertical perpendicular to the surface standard deviation (Y_σ) was found to be 0.24 mm under the nominal un-milled defect free surface level for the filtered data, when computed from the circular arc of the known whisker shaft. As expected the vertical perpendicular to the surface standard deviation above the nominal surface is greater due to the circular nature of the arc of whisker rotation. This is shown in Figure 7.29 where the vertical uncertainty is a result of the angular deviation at the rotational point of the whisker shaft base. Table 7.3 summarises the whisker module performance.
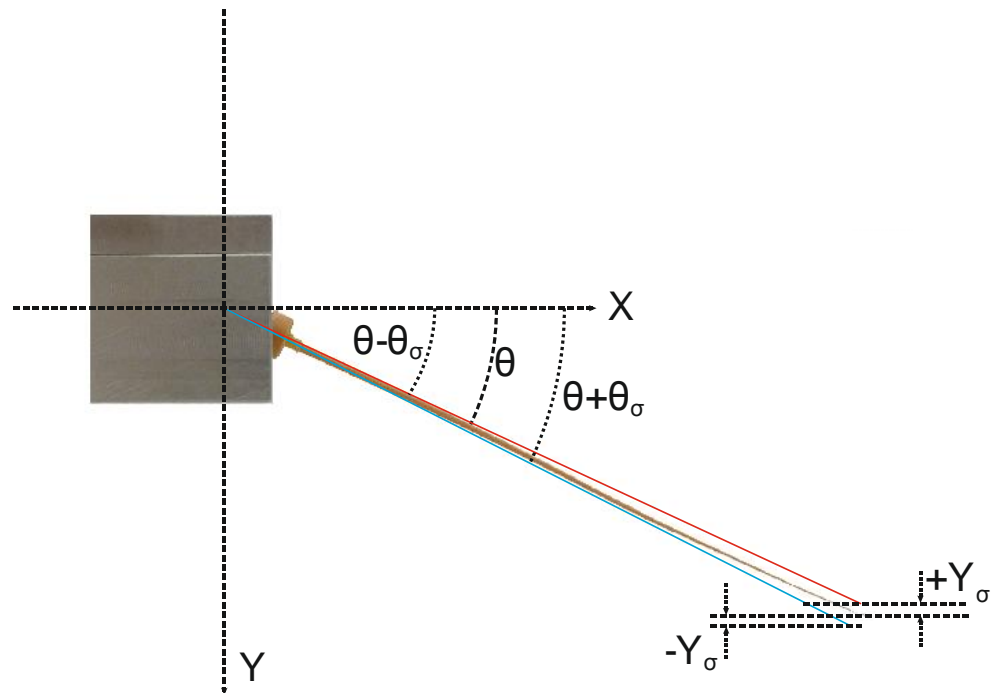
Figure 7.29 Side profile of whisker module highlighting angular and vertical standard deviation.

	Deformation Corrected Correlation	Angular Standard Deviation (σ)	Vertical Height Standard Deviation (σ)
Raw Data	0.8039	0.050°	-0.31mm, +0.34mm
Filtered Data	0.8523	0.039°	-0.24mm, +0.27mm

Table 7.3 Whisker Module Performance

7.10 Discussion

This section introduces a new tactile based surface profiling sensor, based on biologically inspired vibrissae, for automated NDE inspection scenarios. Specifically highlighted and characterised is the sensor's performance for monitoring surface roughness and profile.

Section 7.8 introduced the experimental methodology and subsequent results of surface roughness measurement utilising the whisker sensor. From Figures 7.16 and 7.17 it is clear that the sensor is most sensitive to large changes in surface roughness average, as witnessed at each side of the abrasive sample boundary. Additionally it is visible that across both X^{awm} and Y^{awm} deflection energy scans a minima oscillation is measured across each abrasive sample width. Future work should ascertain if this is directly linked to the oscillatory nature of the whisking sensor, by initially performing a similar scan over a much large width (> 20 mm) abrasive sample. Such a test would also sufficiently characterise the sensors ability in measuring continuous

277

surface roughness against measurement of variation in surface roughness. Further exploratory research would also include the investigation of effects in surface roughness measurement to direction of travel. With a reversal scan strategy being instigated across the sample documented in Section 7.8, it is envisaged a mirror response, to those shown in Figures 7.16 and 7.17, would be witnessed across each abrasive sample. Research should also be undertaken to identify the reasons behind the gradual decay in Y^{awm} Axis amplitude when departing an abrasive sample and travelling across the aluminium surface, with initial examination pointing to whisking motion along that axis being a contributing factor.

This novel sensor shows promise in measuring surface profile, as indicated by the results documented in Table 7.3 and Section 7.8.5, by indirect measurement of whisker displacement within a dashpot. The high correlation documented in Section 7.8.5 (-0.942) and result of Table 7.3 highlight the ability of the sensor in detecting profile changes above a measured noise floor of 240 μm.

Mathematical modelling of the artificial whisking sensor could further enlighten areas of performance limitation and aid greater understanding of the overall operation of the device when sampling certain surface geometries. One such area would be the movement of the whisker within the elastic dashpot according to various surface contacts across the length of the whisker shaft.

With respect to surface roughness measurement performance:

1. The effect of the length of the shaft on surface roughness measurement accuracy and performance is to some degree unknown, with initial hypotheses indicting that longer shafts will average local surface profile changes due to the extended surface contact length and area.

2. The effect of whisking frequency and number of whisks per surface point are not fully characterised or understood. For automated application increased whisking frequency and lower whisks per surface point would obviously be highly beneficial in terms of surface coverage rates. However initial trials with higher whisking frequencies ($\approx$ 8 Hz) highlighted substantially increased measurement noise and hence lower surface roughness sensitivity. It was considered that the current 2 Hz value demonstrates a suitable compromise between frequency and sensitivity performance. Regarding the number of whisks per contact point the current value of eight was chosen to provide a compromise between measurement acquisition speed and performance. Initial trials with reduced whisk counts highlighted the variance in single measurements and that therefore this should necessitate further exploratory research.

With respect to surface profiling performance it is highlighted in Figure 7.28 that the angular protraction angle resolution and whisker length directly control the actual surface profiling performance and resolution. Therefore:

1. The protraction angle measurement resolution is directly related to the minimum rotational resolution of the Hall Effect sensor. It must be remembered that the high 14 bit resolution of this device is across the full 360 degrees of rotation and therefore somewhat unused due to the limited rotational sweep and arc of the whisker. It is considered that this rotational performance is at the reasonable limit of performance currently available and further focus should lay elsewhere

2. From a rotational based surface profiling measurement perspective it is clear that a short as possible whisker shaft will yield lower minimum detectable deviations. However as stated above the effect of whisker length for surface roughness measurement is inconclusive and therefore further work should focus on optimisation of the length.

7.11 Conclusion

This body of work has introduced a novel sensor for NDE based on the biological vibrissae of rodents. It has been shown that an active whisking sensor can accurately quantify the surface roughness of various sample surfaces of increasing roughness average (R_a) in the range 14-53 micrometre, with correlation to standard measurement techniques in the range of 0.97-0.99. The sensitivity of the sensor, in this roughness range, was evaluated and highlighted a non-linear but monotonic response.

It was demonstrated that the device is largely insensitive to sensor-surface lift-off distances producing an error of only 1.22% when comparing a three to a zero

millimetre lift-off. This insensitivity to lift-off is a major advantage for the whisking sensor over conventional eddy current, ultrasonic, and magnetic flux leakage probes where lift-off distances must be controlled to a fraction of a millimetre to avoid erroneous defect indications.

A surface scan of a test sample with artificial defects, to simulate surface pitting, was undertaken and analysed against an ideal CAD model to highlight the sensor applicability for detecting profile changes. It was shown that the sensor could detect 14 mm diameter flat bottomed holes with depths ranging from 0.4 to 1.0 mm.

The ability of the whisker module sensor to detect small changes in surface roughness and surface profile, while possessing little sensitivity to lift-off will enable the sensor to be employed in a variety of positional uncertain automated NDE inspection scenarios. These inspections can relate to the mapping and measurement of corrosion mechanisms associated with surface roughness, local profile and sharp boundary change detection related to surface breaking cracks.

Chapter 8

Conclusion

8.1 General Overview

A thorough and extensive body of work has been presented, discussing firstly the current state of the art and secondly the contribution to the field of remote automated NDE. The challenges in terms of access constraints, localisation, motion planning and sensing have all been comprehensively introduced and discussed for remote NDE applications.

It is clear that automation of NDE and delivery of NDE via robotic platforms has great potential for applications across many industrial measurements tasks. However serious technology barriers exist that insofar only limited application, or highly bespoke and specialised, robotic inspection products exist.

This thesis has addressed a number of these technology barriers and provides incremental improvements in some areas with additional radical new and novel approaches to others.

Firstly, wheeled robotic platforms were considered with regard to access, dynamics and manoeuvrability. The novel AUT RSA platform, with integrated ultrasonic thickness measurement, was introduced and presented to highlight the potential remote ultrasonic mapping benefits with respect to area coverage, remote access and

obstacle avoidance. The advantages and performance of this platform were demonstrated later in Chapter 6 when utilised to demonstrate the feasibility of a novel path planning strategy. The path accuracy was evaluated and found to be within a bound of -19.38 to +13.48 mm with a mean of 4.41 mm, when undertaking a complex obstacle avoidance area coverage path across an area of $2m^2$. These results highlight the unattractive performance of such a platform, when considering potential NDE inspection tasks such as weld bead following, even under laboratory tracking conditions. Practical steps to further improve these within the laboratory, such as control loop optimisation, were suggested and considered realistic and feasible to adopt.

When considering future real inspection deployment the requirement for further optimisation and complementary improving strategies, drawn from inspiration within the conventional robotics and sensing communities is clear. Without such work such positional and path accuracy presents a problem in moving forward to true automated NDE measurement.

The feasibility of undertaking quantitative aerial based NDE was comprehensibly evaluated and the key requirements of such a platform identified. Considering a fixed pitch rotary wing aircraft specifically for NDE, the CUE ASA platform's positional performance was critically quantified when undertaking various indoor manoeuvres, in a precision 6 D.O.F measurement cell, to establish the constraints on real NDE imposed by flight dynamics. Root Mean Square Errors, with respect to desired 3D position, as low as 4.42 mm were measured across a 15 second hover window, quantifiably highlighting the current positional performance and accuracy of such platforms. This level of positional accuracy is clearly below the level required for

many high accuracy NDE inspections, especially when considering the deployment of traditional lift-off sensitive NDE sensors and in view of these being obtained under controlled laboratory conditions. These results emphasise the real requirement and availability of suitable position insensitive NDE sensors and highlights and enforces the current commercial approach of deploying position insensitive optical sensing modalities from such aerial platforms.

One approach, considered within CUE, to improve the overall inspection performance of large scale structures such as wind turbines, oil, gas and nuclear structures is that of a hybrid aerial and wheeled crawler approach. The aerial platform would provide an overall coarse visual map, model and inspection, which then could be utilised to infer and dictate the areas of potential greater inspection interest to be undertaken with traditional NDE sensors deployed from a wheeled crawler. Such an approach would benefit from the advantages of both delivery approaches while still providing the asset operator with a large range of relevant NDE inspection measurement data.

Given that the positional accuracy of both the wheeled and aerial platform have been identified and shown to be lower than desirable under precision laboratory tracking conditions, critically highlights the requirement for highly accurate position information in real field inspections. Local positional and mapping sensor performance and accuracy are therefore deemed critical to addressing and meeting positional accuracy requirements.

Given that optical laser based range-finding exhibits an often central role to robotics, its applications to NDE measurement, through critical robot positioning and potential

surface characterisation, has been considered in detail. An extensive study of operation at various angles and separations from a range of real engineering surfaces has been undertaken. It was found that errors ranged across the sample surfaces to a maximum of 191.80 mm. Metrics were established to ascertain the validity of range measurements, based on received intensity data, when dealing with specular reflective surfaces. Additionally the foundation of a calibration and correction algorithm, for such instances, was introduced based on measured range, intensity and *a priori* characterisation data. Using this novel approach it has been demonstrated that it is possible to reduce range errors in an example application from a RMSE error of 83.87 mm to 18.03 mm.

As stated above the real world positional accuracy of non-ideal wheeled and aerial delivery platforms are critically governed by the performance of the on-board positioning and localisation sensors. This work has highlighted the inaccuracies typically associated with such strategies and in particular a common laser range finder. This is further exacerbated when dealing with challenging industrial surfaces and therefore degrades the overall position accuracy potential of aforementioned delivery platforms. This naturally therefore then has a direct impact on the applicability and performance of any deployed NDE sensor, further limiting the options to only those with increased positional insensitivity such as optical. The novel correction strategy developed and presented attempts to reduce this positional error and therefore any requirement on sensor position sensitivity to a level as close to that measured in the precision laboratory environment. Clearly great care needs to be taken in interpreting such local on-board laser range data, underlying the

increased requirement for the approach of multi position sensor fusion for accurate NDE inspection as shown in [18].

Any real NDE system, whether wheeled or aerial requires some degree of forward path planning if an approach avoiding direct human piloting is to be adopted. This path planning, and how it relates to the position of the platform relative to the structure, is central to making meaningful quantitative NDE measurements, positionally referenced to the structure. Modern world industrial structures traditionally are built as per technical drawings, more commonly now available in various 2D and 3D CAD formats. This feature directly allows structure specific coverage path planning approaches to be developed to locate and inspect areas of precise interest. A new machining based path planning strategy for mobile NDE inspection platforms, including both wheeled and aerial, was developed and presented. This approach has clear benefits for NDE applications in terms of area coverage, feature inspection and obstacle avoidance.

To highlight these clear benefits a real ultrasonic thickness scan was undertaken utilising the aforementioned AUT RSA platform highlighting the clear remote NDE advantages of such a path planning technique. Two obstacles were successfully avoided while undertaking a number of user defined parallel raster scan UT measurements.

Ultrasonic plate thickness measurement errors in the range -1.44 mm to + 5.42 mm were found and the reasons for these discussed. The un-damped nature of the transducer coupled to the thin thickness of the sample plate (10 mm), especially at artificial defect locations can be readily explained, justified and corrected if required.

Although the performance of the ultrasonic thickness mapping is less than desirable and currently unsuitable for current similar thickness industrial plate mapping, the purpose of the platform was to highlight the manoeuvrability of such a novel design with an integrated ultrasonic wheel probe. Insofar this has been clearly demonstrated and justifiable reasons for its performance limitations discussed.

Older and organic structures which feature no technical drawing CAD information would benefit from a first pass SLAM exploratory scan, acquiring data from sensors such as the characterised and optimised LRF, for an initial coarse map construction as described in Chapter 5 and in [24]. Therefore detailed coverage path planning as the proposed machining based strategy could then be deployed building on the previous acquired data. Such an approach directly suits the aforementioned hybrid aerial and wheeled crawler approach for large structures such as wind turbines and oil, gas and nuclear structures.

Conversely structures which feature original build drawings but have featured extensive ad-hoc modifications could initially deploy an inspection platform based on trajectories from the proposed CAD/CAM approach and then utilise SLAM approaches [24], again using sensors such as the characterised and optimised LRF, to update the technical drawing information freely, this in turn updating the machining based full area coverage inspection path. This would then therefore close the inspection path loop, by first updating the CAD model and providing the asset operator with greater quantitative metrological information while also optimising the scan parameters for the actual structure. Only with such an approach would full area coverage and obstacle avoidance be realistically and credibly possible.

Finally a new biologically inspired NDE sensor was introduced. The sensor was developed by researchers at the Bristol Robotics Laboratory and adapted for NDE applications such as surface roughness and profile monitoring. The performance of the evaluated tactile sensor highlighted positive behaviour with respect to measuring surface roughness in the range of 14 to 53 µm, with correlation values of 0.988 being found when compared to a standard surface roughness meter. Additionally a key finding with respect to lift-off sensitivity was identified in that a correlation of minimum 94.6 % to the zero lift-off situation, being observed with increased stand-off up to 6 mm.

Such lift-off sensitivity is highly suited and congruous to the previously discussed wheeled and aerial delivery platforms, with respect to their cited position uncertainty. This sensor critically highlights a new NDE approach for both measurement of local macroscopic surface shape and local microscopic surface roughness from autonomous platforms, which possesses little sensitivity to lift-off. The sensor itself further suits practical NDE deployment by having all sensing electronics far away from the point of contact and featuring low cost polymer whisking strands.

Additionally such a sensor can be critically utilised to provide not only NDE measurements but also structure relevant position data as shown in [274], ideally being fused with other sensors such as the LRF to provide a best estimate of current location in real inspection scenarios. Therefore such a new sensor can provide NDE measurements while also improving the position information, itself dictating the coverage rate, area and obstacle avoidance performance and efficiency.

As the sensor itself does not provide true internal imaging capabilities, this instrument will not directly replace or compete with traditional well established ultrasonic and magnetic approaches, but critically complement and in turn theoretically increase their applicability to automated systems. With the aforementioned lift-off insensitive surface measurement capable of both NDE and position localisation, it is possible that delivery platform could be adapted and more finely controlled to ensure surface and feature tracking, with improved positional uncertainty, suitable for such traditional NDE sensing modalities. Such an approach would yield the most advantageous and beneficial automated NDE system, featuring both detailed and accurate internal and surface measurement information. Such applications could include wind turbine blades, where surface and internal damage are equally of critical importance for dynamic and structural reasons respectively. Additional areas could be those of ship and submarine hulls, where paint loss and material thickness are both of utmost importance.

Overall this thesis identifies and addresses significant challenges associated with remote automated NDE, with substantial developments being introduced and evaluated in the fields of platform mechanics, localisation, path planning and sensing. Key advances and findings have been researched, proven and developed to enhance the applicability and potential of automated solutions to industrial NDE challenges.

It must be made clear that all approaches are not individually fully optimised or capable of immediate practical inspection deployment. As discussed above many of the approaches require further developments in other complimentary areas. One such area is platform performance where development in multi-sensor deployment and

fusion strategies will yield far greater control and accuracy performance. The new path planning strategy, which delivers clear aforementioned benefits, would itself be further suited to practical deployment with live map correction strategies, as discussed, made up from accurate measurement information from localisation sensors such as the LRF.

Clearly no single approach is suitable with respect to actual practical deployment and all areas require much greater attention, research and development to enable the future goal of increased automated NDE for structural inspection.

8.2   Future Work

A number of key areas of future work in respective fields and areas have been documented throughout the thesis, with a general summary of these below.

The novel thickness mapping AUT RSA clearly requires far greater point and path position accuracy and control. This should be achieved by further optimisation and development of the on-board control strategies, while also investigating and deploying on board localisation and sensing strategies. Improvements in orders of magnitude require to be realised to bring the current bounds (-19.38 to +13.48 mm with a mean of 4.41 mm) down to values desirable and desired for accurate NDE measurement and mapping.

Similarly the CUE ASA requires optimisation and adoption of localisation sensing modalities and control systems to improve its positional performance to more consistent levels. Additionally the integration of local range sensors, such as the LRF, to remove the requirement of global tracking systems such as VICON or GPS would further enhance the suitability and applicability of such a platform with

respect to practical deployment. Future work in this area should also include clear understanding and minimisation of turbulence when approaching horizontal or vertical surfaces to perform meaningful NDE measurements. Miniaturisation of platform footprint, while retaining stability, positional performance and NDE sensor lifting capability will also serve to increase the range of available inspection scenarios.

It has been shown that when deploying range estimation sensors, such as the characterised LRF, requires careful consideration and interpretation of the received data. A new material identification and resultant range correction algorithm suite has been proposed and developed, which while offering and highlighting promising results, requires far greater testing and scrutiny for robustness and accuracy. Only with this performed against an extensive suite of material surfaces can quantifiable and confident judgements made on the suitability and performance of the scheme.

The newly presented CAD/CAM based path planning strategy has highlighted the full area coverage and obstacle avoidance benefits of such an approach. However correct *a priori* structure information and coordinate alignment is currently required and therefore adoption of on-board mapping and localisation sensors, such as the LRF, should be adopted for live environment mapping and correction. Only with such a strategy can feedback of the metrological data be utilised to update the current path trajectories. This is an area which requires considerable research and development with respect to map accuracy, filtering and updating.

With respect to the tactile whisking sensor the immediate focus should identify the limitations and then address improving the surface profiling resolution of the sensor

from its current limit of 0.24 mm to a number more similar to current conventional profiling equipment (0.1 mm). Additional research should focus on understanding the effect of whisker shaft profile, in terms of length and area, while also investigating the effect of whisking speed on surface roughness and profile measurement. The suitability of the whisking sensor to environmental conditions and contaminates such as liquids, dust and temperature must be examined, with special interest in its ability to measure NDE properties under these conditions. Additional work would also investigate its applicability and suitability to other NDE inspection situations such as its ability to identify areas of barely visible impact damage (BVID) in composite panels, which traditionally humans are unable to reliably detect. Other avenues of potential application would naturally include the detection of areas of dissimilar paintwork, highlighting corrosion beneath the layers or paint loss. The extension to large arrays of multiple sensor tips to increase coverage and offer greater sensory information is similarly a natural area of future work with particular emphasis on the practicality and miniaturisation of the system.

The above information has dealt with specific future work related to all the presented work and developments however global changes and future focus must be also identified.

A key area of future focus should investigate and asses the feasibility of the integration of all the above bodies of work into one coherent remote automated NDE system. Whether it be wheeled or aerial platforms, full localisation and mapping through methodologies as SLAM should be implemented on data such as that measured from the optimised LRF and other suitable sensors. Data generated in real time will allow path and motion planning, utilising the machine tool derived

algorithms above, to be conducted without prior knowledge of the structure. This will begin to introduce a level of autonomy required to drive forward credible remote NDE inspection.

Finally the development of tactile sensors in detecting greater sensory information when deployed from a fully autonomous NDE platform will provide far greater environmental information in a manner to the animals they were modelled on. These sensors as stated have the potential to realise the autonomous deployment of traditional ultrasonic and magnetic sensors by directly controlling and optimising the initially position uncertain platform. This exciting potential and area will require greater work in both sensor data interpretation and multi-stage control strategy deployment and optimisation.

Only by addressing some of the above challenges along with the more traditional robotic challenges such as SLAM, can NDE sensors be deployed to the points of interest on a structure, independently and autonomously, to allow quantifiable and meaningful NDE inspection to occur.

References

[1]   HSE 'The Health and Safety of Great Britain' Health and Safety Executive 2009, http://www.hse.gov.uk/, Accessed Apr. 2014.

[2]   SEPA 'Protecting Scotland's Environment – A 10 Year Perspective' Scottish Environmental Protection Agency, 2011.

[3]   Ramírez, P. A. P. and Utne, I. B. 'Challenges due to aging plants', Process Safety Progress, vol. 30, issue 2, pp. 196–199, 2011.

[4]   Baacchiocchi, E. and Borghi E., 'Public Investment under Fiscal Constraints', The Institute for Fiscal Studies – Journal of Fiscal Studies, vol. 32, no. 1, 2011.

[5]   British Standards Institution BS EN ISO 17640:2010, Non-destructive testing of welds. Ultrasonic testing. Techniques, testing levels, and assessment, London, BSI, 2011.

[6]   Halmshaw, R., Non-Destructive Testing, 2nd Edition. London: Edward Arnold, 1991.

[7]   British Standards Institution, BS EN ISO 17636-2:2013, Non-destructive testing of welds. Radiographic testing. X- and gamma-ray techniques with digital detectors, London, BSI, 2013.

[8]   UK Research Centre in Non-Destructive Evaluation, www.rcnde.ac.uk, Accessed Apr. 2014.

[9]   Thayer, P., 'RCNDE industrial members' vision for the future requirements for NDE', Insight - Non-Destructive Testing and Condition Monitoring, vol. 54, no. 3, pp. 124-127, Mar. 2012.

[10] Mackenzie, L. D., 'An Intelligent Inspection System for Non-Ferromagnetic Pipes' PhD Thesis, University of Strathclyde, 2011.

[11] MacKenzie, L.D., Pierce, S.G. and Hayward, G., 'Robotic inspection system for non destructive evaluation (NDE) of pipes' Proceedings of the 35th Annual Review of Progress in Quantitative Nondestructive Evaluation, pp. 1687-1694, 2008.

[12] Hancock, P.A. and Chignell, M.H., , 'Mental workload dynamics in adaptive interface design', Systems, Man and Cybernetics, IEEE Transactions on , vol.18, no.4, pp.647-658, Jul. /Aug. 1988.

[13] Farley, J.M. and Babcock, M., 'Best Practice in the Application of NDT – An Update' In World Conference on NDT, 2004.

[14] Aldrin, J. C, Coughlin, C. R., Forsyth, D. S. and Welter, J. T., 'Progress on the Development of Automated Data Analysis Algorithms and Software for Ultrasonic Inspection of Composites' Review of Progress in Quantitative Nondestructive Evaluation (QNDE). Baltimore, Maryland, 2013.

[15] Friedrich, M., Dobie, G., Chan, C.C., Pierce, S.G., Galbraith, Marshall, W. S., and Hayward, G., 'Miniature Mobile Sensor Platforms for Condition Monitoring of Structures'. Sensors Journal, IEEE , vol.9, no.11, pp.1439-1448, Nov. 2009.

[16] Dobie, G., 'Ultrasonic Sensor Platforms for Non-Destructive Evaluation' PhD Thesis, University of Strathclyde, 2010.

[17] Dobie, G., Summan, R., MacLeod, C.N. and Pierce, S.G., 'Visual odometry and image mosaicing for NDE'. NDT and E International, vol. 57, pp. 17-25, 2013

[18]   Summan, R., Pierce, S.G., Dobie, G., Hensman, J. and MacLeod, C.N., 'Practical constraints on real time Bayesian filtering for NDE applications', Mechanical Systems and Signal Processing, vol. 42, issue 1-2, pp. 181-193. 2014.

[19]   Dobie, G., Summan, R., Pierce, S. G., Galbraith, W. and Hayward, G., 'A noncontact ultrasonic platform for structural inspection' Sensors Journal, IEEE , vol.11, no.10, pp. 2458-2468, Oct. 2011.

[20]   Dobie, G., Pierce, S. G. and Hayward, G., 'The feasibility of synthetic aperture guided wave imaging to a mobile sensor platform', NDT and E International, vol. 58. pp. 10-17, 2013.

[21]   Dobie, G., Spencer, A., Burnham, K., Pierce, S. G., Worden, K., Galbraith, W. and Hayward, G. 'Simulation of ultrasonic lamb wave generation, propagation and detection for an air coupled robotic scanner', Ultrasonics, vol. 51, issue 3, pp. 258-269, 2011.

[22]   Friedrich, M., Pierce, S.G., Galbraith, W. and Hayward. G., 'Data fusion in automated robotic inspection systems', Insight-Non-Destructive Testing and Condition Monitoring, vol. 50, no. 2, pp. 88-94, 2008.

[23]   Shu, L., Songling, H., Wei, Z. and Peng, Y., 'Improved immunity to lift-off effect in pulsed eddy current testing with two-stage differential probes' Russian Journal of Non Destructive Testing, vol. 44, issue: 2, pp 138-144, 2008.

[24]   Thrun, S., Burgard, W. and Fox., D., Probabilistic Robotics. MIT Press, Cambridge, MA, 2005.

[25]   Herath, D.C., Kodagoda, S. and Dissanayake, G., 'Simultaneous Localisation and Mapping: A Stereo Vision Based Approach', Intelligent Robots and Systems, IEEE/RSJ International Conference on, pp. 922-927, Oct. 2006.

[26]   Khurshid, J. and Bing-rong, H., 'Military robots - a glimpse from today and tomorrow', Control, Automation, Robotics and Vision Conference, 8th ICARCV, vol.1, pp.771-777, Dec. 2004.

[27]   'U.S. Military Robotics Initiatives', Robotics & Automation Magazine, IEEE , vol.12, no.3, pp.108-109, Sept. 2005.

[28]   Yoshida, K., 'Achievements in space robotics', Robotics & Automation Magazine, IEEE , vol.16, no.4, pp.20-28, Dec. 2009.

[29]   Sallaberger, C., 'Robotics and control R&D in the Canadian Space Station program', Electrical and Computer Engineering, 1996. Canadian Conference on, vol.2, pp. 482-485, May 1996.

[30]   Harris, S., 'Robots are coming [Utopias Manufacturing]', Engineering & Technology, vol.9, no.1, pp.48-50, Feb. 2014.

[31]   Ray, D.D. and Singh, M., 'Development of a force reflecting Tele-robot for remote handling in nuclear installations', Applied Robotics for the Power Industry (CARPI), 1st International Conference on, pp.1-6, Oct. 2010.

[32]   Forlizzi, J., 'How robotic products become social products: An ethnographic study of cleaning in the home', Human-Robot Interaction (HRI), 2nd ACM/IEEE International Conference on , pp.129-136, Mar. 2007.

[33]   Seongsoo, L. and Sukhan, L., 'Embedded Visual SLAM: Applications for Low-Cost Consumer Robots', Robotics & Automation Magazine, IEEE , vol.20, no.4, pp. 83-95, Dec. 2013.

[34]   Youngkak, M., Seungwoo, K., Dongik, O. and Youngwan, C., 'A study on development of home Mess-Cleanup Robot McBot', Advanced Intelligent Mechatronics, IEEE/ASME International Conference on, pp.114-119, July 2008.

[35]   IFR International Federation of Robotics, 'World Robotics 2013 Industrial Robots − Executive Summary', 2013.

[36]   Kavoussi, L.R., Moore, R.G., Adams, J. B. and Partin, A.W., 'Comparison of Robotic Versus Human Laparoscopic Camera Control', The Journal of Urology, vol. 154, issue 6, pp. 2134-2136, Dec.1995.

[37]   Sandler, B.Z., Robotics, Designing the Mechanisms for Automated Machinery, 2nd Edition, Academic Press, San Diego, 1999.

[38]   The Manchester Association of Engineers or MAE http://www.mae.uk.com/Maudsley.PDF, Accessed Apr. 2014.

[39]   McComb, G. 'Robot Builder's Bonanza', 4th Edition, McGraw Hill Professional, 2011.

[40]   Pease, W., 'An automatic machine tool' Scientific American, pp. 101-115, Sep. 1952.

[41]   Minhat, M., Vyatkin,V., Xu, X., Wong, S. and Al- Bayaa, Z, 'A novel open CNC architecture based on STEP-NC data model and IEC 61499 function blocks', Robotics and Computer-Integrated Manufacturing, vol. 25, issue 3, 2009.

[42]   Dragomatz, D. and Mann, S.,'A classified bibliography of literature on NC milling

        path generation', Computer-Aided Design, vol. 29, issue 3, pp. 239-247, Mar. 1997.

[43]   Lund, H.H., 'Modern artificial intelligence for human-robot interaction', Proceedings

        of the IEEE, vol.92, no.11, pp. 1821-1838, Nov. 2004.

[44]   Zhao, Z. and Zheng, J. , 'Artificial intelligence robot brings business opportunities to

        3D virtual world and new model company', Journal of Information and

        Computational Science, vol. 5, no. 6, pp. 2567-2574, Dec. 2008.

[45]   NSpect 210,

        www.diagnosticsonar.com/english/industrial/datasheets/NSpect210%20Brochure.pdf,

        Accessed Apr. 2014.

[46]   RMS2, http://www.silverwingndt.com/downloads/brochures/rms-auto-ut-corrosion-

        mapping.pdf, Accessed Apr. 2014.

[47]   FIRST Laboratory, http://www.strath.ac.uk/eee/research/cue/. Accessed Apr. 2014.

[48]   Cyberhawk, http://www.thecyberhawk.com, Accessed Apr. 2014.

[49]   Marietta NDT, http://www.marietta-ndt.com, Accessed Apr. 2014.

[50]   Phoenix Inspection Systems Limited, http://www.phoenixisl.com/sage, Accessed Apr.

        2014.

[51]   Cooper, I., Nicholson, I., Yan, D., Wright, B., Liaptsis, D. and Mineo, C.,

        'Development of a fast inspection system for complex composite structure-The

        IntACOM project', Proceeding of the 5th International Symposium on NDT in

        Aerospace, Singapore, Nov. 2013.

[52]   Ultrasonic Sciences Ltd., http://www.ndt.net/search/docs.php3?id=15455&content=1, Accessed Apr. 2014.

[53]   High-Performance Composites, Vol. 21, No. 6. Nov.2013.

[54]   KUKA KR5 ARC HW, http://www.kukarobotics.com, Accessed 04/2014.

[55]   Wang, J., Sun, A., Zheng, C. and Wang, J. 'Research on a new crawler type inspection robot for power transmission lines', Applied Robotics for the Power Industry (CARPI), 1st International Conference on, pp.1-5, Oct. 2010.

[56]   Sheng, W., Chen, H. and Xi, N., 'Navigating a Miniature Crawler Robot for Engineered Structure Inspection', Automation Science and Engineering, IEEE Transactions on, vol.5, no.2, pp.368,373, Apr. 2008.

[57]   Packard, G.E., Stokey, R., Christenson, R., Jaffre, F., Purcell, M. and Littlefield, R., 'Hull inspection and confined area search capabilities of REMUS autonomous underwater vehicle', OCEANS, pp. 1-4, Sept. 2010.

[58]   Huerzeler, C., Caprari, G., Zwicker, E. and Marconi, L., 'Applying aerial robotics for inspections of power and petrochemical facilities', Applied Robotics for the Power Industry (CARPI), 2nd International Conference on, pp. 167-172, Sept. 2012.

[59]   Chenghui, N., Pacheco, C., X. and Spenko, M., 'Robots on the Move: Versatility and Complexity in Mobile Robot Locomotion', Robotics & Automation Magazine, IEEE , vol.20, no.4, pp.72-82, Dec. 2013.

[60]   Zheng, H. and Appleton, E., 'Dynamic characteristics of a novel self-drive pipeline pig', Robotics, IEEE Transactions on, vol.21, no.5, pp.781-789, Oct. 2005.

[61]   Kim, H.M., Woo Rho, Y., Ryong Yoo, H., Ho Cho, S., Kyu Kim D., Koo, S.J. and Park, G.S., 'Defect estimation of a crack in underground pipelines by CMFL type NDT system', Electrical Machines and Systems (ICEMS), International Conference on, pp.725-728, Oct. 2013.

[62]   Roslin, N.S., Anuar, A. Jalal, M.F.A and Sahari, K.S.H, 'A Review: Hybrid Locomotion of In-pipe Inspection Robot', Procedia Engineering, vol. 41, pp. 1456-1462, 2012.

[63]   Meinecke, G., Ratmeyer, V. and Renken, J., 'HYBRID-ROV - Development of a new underwater vehicle for high-risk areas', OCEANS, pp. 1-6, Sept. 2011.

[64]   Marsh, L., Copley, J.T., Huvenne, V.A.I. and Tyler, P.A., 'The Isis ROV Facility, Getting the bigger picture: Using precision Remotely Operated Vehicle (ROV) videography to acquire high-definition mosaic images of newly discovered hydrothermal vents in the Southern Ocean', Deep Sea Research Part II: Topical Studies in Oceanography, vol. 92, pp.124-135, Aug. 2013.

[65]   Gros, X.E., Strachan, P. and Lowden, D., 'Fusion of multiprobe NDT data for ROV inspection', OCEANS '95. MTS/IEEE. Challenges of Our Changing Global Environment. Conference Proceedings., vol.3, pp. 2046-2050, Oct. 1995.

[66]   Marinho, C.A., Patusco, C., Carmweini, C., Mesquita, L., Santos, R.W.D, Damasceno, S. and Morikawa, S., 'Petrobras' Developmnets in Underwater Inspection', 18th World Conference on Nondestructive Testing, Durban, South Africa, Apr. 2012.

[67] Jeppesen, L., Dam, J., Olsen, H.O., 'Subsea Automated Ultrasonic Inspection', 3rd MENDT - Middle East Nondestructive Testing Conference & Exhibition, Bahrain, Manama, Nov. 2005.

[68] Mitsuru, O., Masahiro, K., Yutaka K., Yoshiaki, N. and Masahiro, T., 'Advanced Inspection Technologies for Nuclear Power' Plants Hitachi Review, vol. 58. no. 2, pp. 82-87, 2009.

[69] Scoprion, http://www.silverwingndt.com/ultrasonic-testing/scorpion-remote-ut-thickness-measurements, Accessed Apr. 2014.

[70] TriPod, http://www.jireh-industries.com/products/tripod/aag020/, Accessed Apr. 2014.

[71] HR-MP20T, http://www.helicalrobotics.com/HR-MP20T, Accessed Apr. 2014.

[72] Blyth, W.A, Barr, D.R.W. and Hankinson, N., 'An assessment of mecanum wheels for non-destructive testing (NDT) applications' BINDT NDT 2014 Conference, Manchester, 2014.

[73] Ceta, http://www.tecnitestndt.com/wall-crawler/, Accessed Apr. 2014..

[74] Mobile Robot Scanners, http://www.inspection-robotics.com/site/index.cfm?id_art=48114&actMenuItemID=22702&vsprache/EN, Accessed Apr. 2014.

[75] MagBug, http://www.phoenixisl.com/magbug, Accessed Apr. 2014.

[76] Osswald, M. and Iida, F., 'Design and control of a climbing robot based on hot melt adhesion', Robotics and Autonomous Systems, vol. 61, issue 6, pp. 616-625, June 2013.

[77]   Ackerman, J. and Seipel, J., 'Energy Efficiency of Legged Robot Locomotion With

        Elastically Suspended Loads', Robotics, IEEE Transactions on, vol.29, no.2, pp. 321-

        330, Apr. 2013.

[78]   Han, S., Lim, H.S and Lee, J.M., 'An Efficient Localization Scheme for a

        Differential-Driving Mobile Robot Based on RFID System', Industrial Electronics,

        IEEE Transactions on, vol.54, no.6, pp. 3362-3369, Dec. 2007.

[79]   Su, Y. and Swevers, J., 'Finite-time tracking control for robot manipulators with

        actuator saturation', Robotics and Computer-Integrated Manufacturing, vol. 30, issue

        2, pp. 91-98, Apr. 2014.

[80]   Zarrouk, D., Sharf, I. and Shoham, M., 'Analysis of Wormlike Robotic Locomotion

        on Compliant Surfaces', Biomedical Engineering, IEEE Transactions on, vol. 58, no.

        2, pp. 301-309, Feb. 2011.

[81]   Hu, H. and Woo, P.Y., 'Fuzzy supervisory sliding-mode and neural-network control

        for robotic manipulators', Industrial Electronics, IEEE Transactions on , vol. 53, no.

        3, pp. 929-940, June 2006.

[82]   ROBAIR, http://www1.lsbu.ac.uk/esbe/mrndt/robair.shtml, Accessed Apr. 2014.

[83]   FPSO, http://www1.lsbu.ac.uk/esbe/mrndt/fpso.shtml, Accessed Apr. 2014.

[84]   RING, http://www1.lsbu.ac.uk/esbe/mrndt/pipeclimber.shtml, Accessed Apr. 2014.

[85]   Carvalho, A.A, Sagrilo, L.V.S., Silva, I.C., Rebello, J.M.A. and Carneval, R.O., 'On

        the reliability of an automated ultrasonic system for hull inspection in ship-based oil

        production units', Applied Ocean Research, vol. 25, issue 5, pp. 235-241, Oct. 2003.

[86]   Caprari, G., Breitenmoser, A., Fischer, W., Hurzeler, C., Tache, F., Siegwart, R., Schoeneich, P., Rochat, F., Mondada, F. and Moser, R., 'Highly compact robots for inspection of power plants'. In Applied Robotics for the Power Industry (CARPI), 1st International Conference on, pp 1-6, 2010.

[87]   Tache, Fabien. Robot locomotion and localization on 3D complex-shaped structures. PhD thesis, ETH Zurich, 2010.

[88]   Tâche, F., Fischer, W., Caprari, G., Siegwart, R., Moser, R. and Mondada, F., 'Magnebike: A magnetic wheeled robot with high mobility for inspecting complex-shaped structures', Journal of Field Robotics, vol. 26, issue 5, pp. 453-476, 2009.

[89]   White, T.S., Alexander, R., Callow, G., Cooke, A., Harris, S. and Sargent, J., 'A mobile climbing robot for high precision manufacture and inspection of aerostructures' The International Journal of Robotics Research, vol. 24, no. 7 pp. 589-598, 2005.

[90]   Schempf, H., Mutschler, E., Gavaert, A., Skoptsov, G. and Crowley, W., 'Visual and nondestructive evaluation inspection of live gas mains using the ExplorerTM family of pipe robots', Journal of Field Robotics, vol. 27, issue 3, pp. 217-249, 2010

[91]   Schempf, H., 'Neptune: above-ground storage tank inspection robot system', Robotics and Automation, Proceedings IEEE International Conference on, vol. 2, pp.1403-1408, May 1994.

[92]   Gumstix. www.gumstix.com, Accessed Apr. 2014.

[93]   Microchip dsPIC, https://www.microchip.com/pagehandler/en-us/family/16bit/, Accessed Apr. 2014.

[94] ADIS16364, http://www.analog.com/en/mems-sensors/mems-inertial-sensors/adis16364/products/product.html, Accessed Apr. 2014.

[95] Mandow, A., Martinez, J.L., Morales, J., Blanco, J.-L., Garcia-Cerezo, A. and Gonzalez, J., 'Experimental kinematics for wheeled skid-steer mobile robots', Intelligent Robots and Systems, IROS, IEEE/RSJ International Conference on , pp. 1222-1227, 2007.

[96] Silverwing dry coupled wheel transducer, http://www.silverwingndt.com/ultrasonic-testing/scorpion-remote-ut-thickness-measurements, Accessed Apr. 2014.

[97] KNJN SAXO-Q, http://www.knjn.com/FPGA-FX2.html, Accessed Apr. 2014.

[98] Verilog, http://www.altera.co.uk/support/examples/verilog/verilog.html, Accessed Apr. 2014.

[99] http://www.engineeringtoolbox.com/sound-speed-solids-d_713.html, Accessed Apr. 2014.

[100] Hilbert transform, http://www.mathworks.co.uk/help/signal/ref/hilbert.html, Accessed Apr. 2014.

[101] Dobie, G., RSA API Documentation, CUE, University of Strathclyde, 2012.

[102] Jamieson, J., 'Artificial potential Functions' EPSRC ASCL CUE Summer Internship 2012.

[103] Everaerts, J., 'The use of unmanned aerial vehicles(uavs) for remote sensing and mapping', in International Archives of the Photogrammetry, Remote Sensing and Spatial Information Sciences, vol. XXXVII, pp. 1187-1191, 2008.

[104] Mascrenas, D.D. L., 'Mobile Host Wireless Sensor Networks – A New Sensor Network Paradigm for Structural Health Monitoring Applications' PhD Thesis, University of California, San Diego, 2008.

[105] Corke, P., Hrabar, P., Peterson S., Rus, R., Saripalli, D. and Sukhatme, G., 'Autonomous deployment and repair of a sensor network using an unmanned aerial vehicle', Robotics and Automation, Proceedings. ICRA '04, IEEE International Conference on, vol.4, 2004.

[106] Whitworth, C.C., Duller, A.W.G., Jones, D.I. and Earp, G.K., , 'Aerial video inspection of overhead power lines', Power Engineering Journal , vol.15, no.1, pp.25-32, Feb. 2001.

[107] Cyberhawk Innovations, www.tcetoday.com/~/media/Documents/TCE/Articles/2012/854/854cyberhawk.pdf, Accessed Apr. 2014.

[108] Colomina, I., Aigner, I. and Agea E., 'The uVISION project for helicopter-UAV photogrammetry and remote-sensing', In: Proceedings of the VII International Geomatic Week, 2007.

[109] McKerrow, P., 'Modelling the Draganflyer four-rotor helicopter', Robotics and Automation, 2004. Proceedings. ICRA '04. 2004 IEEE International Conference on , vol.4, pp. 3596- 3601 Vol.4, 2004.

[110] Newman, S., The Foundations of Helicopter, Flight Edward Arnold, 1994.

[111] Barnes, C. H. and James, D. N., 'Shorts Aircraft since 1900', Naval Institute Press, 1989.

[112] J. Rubio, JM, Lahoz J.G. and Aguilera D.G., 'Low-cost photogrammetry for cultural heritage', In Proceedings of the CIPA International Symposium,. Camera and Imaging Products Association, 2005.

[113] Zufferey, J. C. and Guaella A., 'Flying Over the Reality Gap: From Simulated to Real Indoor Airships' Autonomous Robots, vol. 21, no. 3, pp. 243-254, 2006.

[114] Filippone A., 'Flight Performance of Fixed and Rotary Wing Aircraft', A Butterworth-Heinemann Title, 2006.

[115] Ratti, J. and Vachtsevanos, G., 'A Biologically-Inspired Micro Aerial Vehicle' Journal of Intelligent & Robotic Systems, vol. 60, no. 1, pp 153-178, 2010.

[116] Conn, A., Burgess, A., Hyde, S. and Chung Seng Ling, R. 'From Natural Flyers to the Mechanical Realization of a Flapping Wing Micro Air Vehicle,' Robotics and Biomimetics, ROBIO '06. IEEE International Conference on, pp.439-444, Dec. 2006.

[117] Groen, M. Bruggeman, M.A., Remes, B., Ruijsink, B., Van Oudheusden, R. and Bijl B.W.H., 'Improving flight performance of the flapping wing MAV DelFly II', International Micro Air Vehicle Conference and Flight Competition, Braunschweig, Germany, 2010.

[118] Bouabdallah, S., Murrieri, P. and Siegwart, R., 'Towards Autonomous Indoor Micro VTOL', Autonomous Robots, vol. 18, no. 2, pp. 171-183, Mar. 2005.

[119] Mian A. A. and Wang D., 'Dynamic Modelling and Nonlinear Control Strategy for an Underactuated Quad Rotor Rotorcraft', Journal of Zhejiang University Science, vol. 9, issue 4, pp. 539-545, 2008.

[120] Hoffman, G. M., Haung, H., Waslander S. L. and Tomlin, C. J 'Quadrotor Helicopter Flight Dynamics and Control: Theory and Experiment' Proc. of the AIAA Guidance, Navigation, and Control Conference, 2007.

[121] Murray, R.M., Li, Z. and Sastry S.S., A Mathematical Introduction to Robotic Manipulation. CRC Press, 1994.

[122] TJ Koo, T., Ma, Y., and Sastry, S., 'Nonlinear control of a helicopter based unmanned aerial vehicle model', UC Berkeley, 2001.

[123] Luukkonen, T., 'Modelling and control of quadcopter', Independent research project in applied mathematics, Espoo, Aug. 2011.

[124] http://www.stemmer-imaging.co.uk/, Accessed Apr. 2014.

[125] Hokuyo URG-4LX, http://www.hokuyo-aut.jp/02sensor/07scanner/urg_04lx_ug01.html, Accessed Apr. 2014.

[126] Draganfly Innovations, http://www.draganfly.com/uav-helicopter/draganflyer-x6/index.php, Accessed Mar. 2011.

[127] Draganfly Innovations, http://www.draganfly.com/uav-helicopter/draganflyer-x8/index.php, Accessed Mar. 2011.

[128] Ascending Technologies, http://www.asctec.de/asctec-pelican-5/, Accessed Mar. 2011.

[129] Bachrach, A., de Winter, A., Ruijie He, Hemann, G., Prentice, S. and Roy, N., 'RANGE - Robust Autonomous Navigation in GPS-denied Environments,' Robotics and Automation (ICRA), IEEE International Conference on, pp.1096-1097, May 2010.

[130] Achtelik, M, Bachrach, A, He, R, Prentice, S, Roy, N., 'Stereo vision and laser odometry for autonomous helicopters in GPS-denied indoor environments', In Proceedings of the SPIE unmanned systems technology XI, vol. 7332. Orlando, FL., 2009.

[131] Ascending Technologies, http://www.asctec.de/uav-applications/research/products/asctec-firefly/, Accessed Apr. 2014.

[132] Ascending Technologies, http://www.asctec.de/asctec-falcon-2/, Accessed 03/2011.

[133] Microdrones, http://www.microdrones.com/, Accessed Mar. 2011.

[134] Danish Aviation Systems, http://www.danishaviationsystems.dk/ , Accessed Mar. 2011.

[135] Mikrokopter, http://www.mikrokopter.de/, Accessed Mar. 2011.

[136] Mikrokopter http://www.mikrokopter.de/ucwiki/en/MK-Okto2/, Accessed Mar. 2011.

[137] Senkul, F. and Altug, E., 'Modeling and control of a novel tilt - Roll rotor quadrotor UAV', Unmanned Aircraft Systems (ICUAS), International Conference on, pp.1071-1076, May 2013

[138] Lee, J., Lee, C. and Kim, D., 'Attitude control of quadrotor with on-board visual feature projection system', Intelligent Robots and Systems (IROS), IEEE/RSJ International Conference on, pp.2426-2431, Nov. 2013.

[139] Sydney, N., Smyth, B. and Paley, D.A., 'Dynamic control of autonomous quadrotor flight in an estimated wind field', Decision and Control (CDC), IEEE 52nd Annual Conference on, pp.3609-3616, Dec. 2013.

[140]   Tian, W.K., Unmanned Air Vehcile (UAV) Ducted Fan Propulsion System Design and Manufacture, National University of Singapore, 2010.

[141]   Cao, J., 'Aerial Vehicle for Inspection', 19.496 Individual Project Report, University of Strathclyde, 2013.

[142]   Robbe-Roxxy 2827/34, http://www.robbe.de/roxxy-bl-outrunner-2827-34.html, Accessed Apr. 2014.

[143]   HobbyKing 40A BlueSeries Brushless Speed Control,www.hobbyking.co.uk, Accessed Apr. 2014.

[144]   OpenPilot CC3D, http://www.openpilot.org/products/openpilot-coptercontrol-platform/, Accessed Apr. 2014.

[145]   Eschmann, C., Boller, C., Kuo, C.-M. and Kuo, C.-H., 'Unmanned Aircraft Systems for Remote Building Inspection and Monitoring', Proc. of the Sixth European Workshop on Structural Health Monitoring, pp. 1179-1186, 2012.

[146]   Remondino, F., Barazzetti, L., Nex, F., Scaioni, M. and Sarazzi, D., UAV photogrammetry for mapping and 3D modelling - Current status and future perspectives', Int. Archives of Photogrammetry, Remote Sensing and Spatial Information Sciences, vol. 38, ISPRS Conference UAV-g, Zurich, Switzerland, 2011.

[147]   Szeliski, R., 'Image alignment and stitching: A tutorial', Foundations and Trends in Computer Graphics and Computer Vision', vol. 2, no. 1, pp.1-104, Dec.2006.

[148]   Nister, D., Naroditsky, O. and Bergen, J., 'Visual odometry, 'Computer Vision and Pattern Recognition, CVPR, Proceedings of the 2004 IEEE Computer Society Conference on, vol.1, pp. 652- 659, July 2004.

[149] Aptina MT9V032 1/3-Inch Wide VGA CMOS Digital Image Sensor Datasheet, 2011.

[150] Texas Instruments OMAP3530 Application Processor Datasheet, 2009.

[151] Haight, J. M. and Caringi, R.,G., 'Automation vs. human intervention: What is the best mix for optimum system performance? A case study', International Journal of Risk Assessment and Management, vol. 7, no. 5, pp. 708-721, 2007.

[152] Hallowell, M.R., Worker Fatigue: 'Managing concerns in rapid renewal highway construction projects', Professional Safety, 2010.

[153] Haight, J. M. and Kecojevic, V., 'Automation vs. Human intervention: What is the best fit for the best performance?', Proc. Safety Prog., vol. 24, issue 1, pp. 45–51, 2005.

[154] Wilkie, J., Johnson, M. A. and Katebi, R., Control Engineering: An Introductory Course. New York: Palgrave Macmillan, 2002.

[155] Summan R., 'Positioning for Mobile NDE Inspection Platforms' PhD Thesis, University of Strathclyde, 2013.

[156] http://www.ptgui.com/, Accessed Apr. 2014..

[157] Lowe, D. G., 'Object recognition from local scale invariant features'. Proceedings of the International Conference on Computer Vision 2, pp. 1150-1157, 1999.

[158] Zhang, Y., Yang, L. and Wang, Z., 'Research on Video Image Stitching Technology Based on SURF', Computational Intelligence and Design (ISCID), Fifth International Symposium on , vol.2, pp. 335-338, Oct. 2012.

[159] Morrison, J. P., Dixon, S. M., Potter, D. G. and Jian, X., 'Lift-off compensation for improved accuracy in ultrasonic lamb wave velocity measurements using

electromagnetic acoustic transducers (EMATs)', Ultrasonics, vol. 44, pp. 1401–1404, Dec. 2006.

[160] Huang, S., Zhao, W., Zhang, Y. and Wang, S., 'Study on the liftoff effect of EMAT', Sens. Actuators A, Phys., vol. 153, no. 2, pp. 218–221, Aug. 2009.

[161] Lee, J. Y., Hwang, J. S., Lee, K. E. and Choi, S. H. 'A Study of leakage magnetic flux detector using hall sensors array', Key Eng. Mater., vols. 306–308, pp. 235–240, Mar. 2006.

[162] Kneip, L., Tache, F., Caprari, G. and Siegwart, R., 'Characterization of the compact Hokuyo URG-04LX 2D laser range scanner', Robotics and Automation, ICRA '09. IEEE International Conference on , pp.1447-1454, May 2009.

[163] Iborra, A., Pastor, J.A., Alvarez, B., Fernandez, E. and Merono, J.M.F., 'Robots in radioactive environments', Robotics & Automation Magazine, IEEE , vol.10, no.4, pp.12-22, Dec. 2003.

[164] Roetenberg, D., Slycke, P.J. and Veltink, P.H., 'Ambulatory Position and Orientation Tracking Fusing Magnetic and Inertial Sensing', Biomedical Engineering, IEEE Transactions on , vol.54, no.5, pp.883-890, May 2007.

[165] Hebert, M., 'Active and passive range sensing for robotics', Robotics and Automation, Proceedings. ICRA '00. IEEE International Conference on , vol.1, pp.102-110 vol.1, 2000.

[166] Curtis, P. and Payeur, P., 'An integrated robotic laser range sensing system for automatic mapping of wide workspaces', Electrical and Computer Engineering, Canadian Conference on, vol.2, pp.1135-1138, May 2004.

[167]   Curtis, P., Yang, E.S. and Payeur, P., 'An Integrated Robotic Multi-Modal Range Sensing System', Instrumentation and Measurement Technology Conference, IMTC, Proceedings of the IEEE , vol.3, pp.1991-1996, May 2005.

[168]   Davison, A.J., 'Real-time simultaneous localisation and mapping with a single camera', Computer Vision, Proceedings. Ninth IEEE International Conference on , vol., no., pp.1403-1410 vol.2, 13-16 Oct. 2003

[169]   Kwok, N. M., Liu, D.K., Fang G. and Dissanayake, G., 'Path planning for bearing-only simultaneous localisation and mapping', Robotics, Automation and Mechatronics, IEEE Conference on, vol. 2, pp. 828-833, Dec. 2004

[170]   Hua, H., Wang, Y. and Yan, D., 'A low-cost dynamic range-finding device based on amplitude-modulated continuous ultrasonic wave', Instrumentation and Measurement, IEEE Transactions on, vol. 51, no. 2, pp. 362-367, Apr. 2002.

[171]   Loianno, G., Lippiello, V. and Siciliano, B., 'Fast localization and 3D mapping using an RGB-D sensor', Advanced Robotics (ICAR), 16th International Conference on, pp. 1-6, Nov. 2013.

[172]   Souza, A.A.S. and Maia, R.S., 'Occupancy-Elevation Grid Mapping from Stereo Vision', Robotics Symposium and Competition (LARS/LARC), Latin American, pp. 49-54, Oct. 2013.

[173]   Smith, P.W., Nandhakumar, N. and Chien, C.-H., 'Object motion and structure recovery for robotic vision using scanning laser range sensors', Robotics and Automation, IEEE Transactions on, vol. 13, no. 1, pp. 74-80, Feb. 1997.

[174] Chen, Y. D. and Ni, J., 'Dynamic calibration and compensation of a 3D laser radar scanning system', Robotics and Automation, IEEE Transactions on, vol. 9, no. 3, pp. 318-323, Jun. 1993.

[175] Adams, M.D., 'Lidar design, use, and calibration concepts for correct environmental detection', Robotics and Automation, IEEE Transactions on, vol.16, no.6, pp.753-761, Dec. 2000.

[176] Okubo Y., Ye E. and Borenstein J., 'Characterization of the Hokuyo URG-04LX laser rangefinder for mobile robot obstacle negotiation', Proc. SPIE 7332, Unmanned Systems Technology XI, Apr. 2009.

[177] Kogut, G., Ahuja, G., Sights, B., Pacis, E.B. and Everett, H.R., 'Sensor Fusion for Intelligent Behaviour on Small Unmanned Ground Vehicles', Proc. SPIE 6561, Unmanned Systems Technology IX, 65611V, May 2007.

[178] Chang, Y., Kuwabara, H. and Yamamoto, Y., 'Novel Application of a Laser Range Finder with Vision System for Wheeled Mobile Robot', ProE. of IEEE/ASME Int. Conf. on Advanced Intelligent Mechatronics, pp. 280-285, 2008.

[179] Zeng, S. and Weng, J., 'Online-learning and Attention-based Approach to Obstacle Avoidance Using a Range Finder', Journal of Intelligent Robot System 50, pp. 219-239, 2007.

[180] Choi, Y., Hong, J. and Park, K., 'Obstacle Avoidance using Active Window and Flexible Vector Field with a Laser Range Finder', Int. Conf. on Control, Automation and Systems, pp. 2123-2128, 2007.

[181]   Ye, E. and Borenstein, J., 'A New Terrain Mapping Method for Mobile Robots Obstacle Negotiation', Proc. SPIE 5083, Unmanned Ground Vehicle Technology V, Sept. 2003.

[182]   Ueda, T., Kawata, H., Tomizawa, T., Ohya, A. and Yuta, S., 'Mobile SOKUKI Sensor System: Accurate Range Data Mapping System with Sensor Motion', Int. Conf. on Autonomous Robots and Agents, pp. 309-314, 2006.

[183]   Sohn, H. and Kim, B., 'A Robust Localization Algorithm for Mobile Robots with Laser Range Finders', ProE. IEEE Int. Conf. on Robotics and Automation, pp. 3545-3550, 2005.

[184]   Lingemann, K., Nüchter, A., Hertzberg, J., Surmann, H., 'High-speed laser localization for mobile robots', Robotics and Autonomous Systems, vol. 51, issue 4, pp. 275-296, June 2005.

[185]   Borges, G. and Aldon, M., 'Line Extraction in 2D Range Images for Mobile Robotics', Journal of Intelligent and Robotic Systems, vol. 40, issue 3. pp. 267-297, 2004.

[186]   Nguyen, V.; Martinelli, A.; Tomatis, N. and Siegwart, R., 'A comparison of line extraction algorithms using 2D laser rangefinder for indoor mobile robotics', Intelligent Robots and Systems, IROS, IEEE/RSJ International Conference on , pp.1929-1934, Aug. 2005.

[187]   Koskinen, M., Kostamovaara, J. T. and Myllylae R.A., 'Comparison of continuous-wave and pulsed time-of-flight laser range-finding techniques', Proc. SPIE 1614, Optics, Illumination, and Image Sensing for Machine Vision VI, Mar. 1992.

[188]   www.sick.com, Apr. 2014.

315

[189] Ye, C. and Borenstein, J., 'Characterization of a 2D laser scanner for mobile robot obstacle negotiation', Robotics and Automation, Proceedings, ICRA '02. IEEE International Conference on , vol. 3, pp. 2512-2518, 2002.

[190] Kawata H., Ohya A., Yuta S., Santosh W. and Mori T., 'Development of ultra-small lightweight optical range sensor system', ProE. IEEE/RSJ Int. Conf. on Intelligent Robots and Systems, Edmonton, pp. 1078-1083, 2005.

[191] www.hokuyo-aut.jp, Accessed Apr. 2014.

[192] Łabęcki, P., Nowicki, M. and Skrzypczyński, P., 'Characterization of a compact laser scanner as a sensor for legged mobile robots', Management and Production Engineering Review, vol. 3, issue 3, pp. 45–52, Oct.2012.

[193] Winkvist, S., Rushforth, E. and Young, K.. 'Towards an autonomous indoor aerial inspection vehicle', Industrial Robot: An International Journal, vol. 40 issue 3, pp.196- 207, 2013.

[194] Pouliot, N., Richard, P. and Montambault, S., 'LineScout power line robot: Characterization of a UTM-30LX LIDAR system for obstacle detection', Intelligent Robots and Systems (IROS), IEEE/RSJ International Conference on, pp.4327-4334, Oct. 2012.

[195] Luo, R.E. and Lai C. C., 'Indoor mobile robot localization using probabilistic multi-sensor fusion', Advanced Robotics and Its Social Impacts, ARSO, IEEE Workshop on, pp. 1-6, Dec. 2007.

[196] Park, C.H., Kim D., You, B.J. and Oh, S.O, 'Characterization of the Hokuyo UBG-04LX-F01 2D laser rangefinder', RO-MAN, IEEE , pp. 385-390, Sept. 2010.

[197] Kawata, H., Miyachi, K., Hara, Y., Ohya, A. and Yuta, S., 'A method for estimation of lightness of objects with intensity data from SOKUIKI sensor', Multisensor Fusion and Integration for Intelligent Systems, MFI, IEEE International Conference on, pp. 661-664, Aug. 2008.

[198] Vocabulaire international de l'éclairage. International lighting vocabulary, International commission on illumination, 3. éd. commune `a la CIE et `a la CEI, Publisher: Paris, Bureau central de la CIE, 1970.

[199] Boeckler, G. K., 'Surface Smoothness and Its Influence on Paint Appearance: How to Measure and Control it', Creative manufacturing engineering program, Society of Manufacturing Engineers, 1992.

[200] http://www.hokuyo-aut.jp/02sensor/07scanner/download/data/URG_SCoku20.pdf Accessed Apr. 2014..

[201] http://www.kuka-robotics.com, Accessed Apr. 2014..

[202] Umeyama, S., 'Least-squares estimation of transformation parameters between two point patterns', Pattern Analysis and Machine Intelligence, IEEE Transactions on , vol. 13, no. 4, pp. 376-380, Apr. 1991.

[203] Kirchner, N., Dikai Liu and Dissanayake, G., 'Surface Type Classification With a Laser Range Finder', Sensors Journal, IEEE , vol. 9, no. 9, pp. 1160-1168, Sept. 2009.

[204] Kirchner , N., Taha, T., Liu, D. and Paul, G., 'Simultaneous material type classification and mapping data acquisition using a laser range finder', Proc. Int. Conf. on Intelligence Technologies: Intelligent Technology in Robotics and Automation, 2007.

[205] J. Hancock, Laser intensity-based obstacle detection and tracking, Doctoral Dissertation, 1999.

[206] Sanmartín, P., Silva, B., and Prieto, B., 'Effect of Surface Finish on Roughness, Color, and Gloss of Ornamental Granites', J. Mater. Civ. Eng., vol. 23, issue 8, pp. 1239-1248, 2011.

[207] Kurisu, M., Muroi, H. and Yokokohji, Y., 'Calibration of laser range finder with a genetic algorithm', Intelligent Robots and Systems, IROS, IEEE/RSJ International Conference on, pp.346-351, 2007.

[208] Ohtani, K., Li L. and Baba, M., 'Laser rangefinder calibration based on Genetic Algorithm', SICE Annual Conference, Proceedings of, pp.1234-1237, Aug. 2012.

[209] Galceran, E. and Carreras, M., 'A survey on coverage path planning for robotics, Robotics and Autonomous Systems', vol. 61, issue 12, pp. 1258-1276, Dec. 2013.

[210] Yasutomi, F., Yamada, M. and Tsukamoto, K., 'Cleaning robot control', in: Proc. Conf. IEEE Int. Robotics and Automation, pp. 1839-1841, 1988.

[211] Atkar, P., Greenfield, A.L., Conner, D.C., Choset, H. and Rizzi, A., 'Uniform coverage of automotive surface patches', The International Journal of Robotics Research, vol. 24, no. 11, pp. 883-898, Nov. 2005.

[212] Hert, S., Tiwari, S. and Lumelsky, V., 'A terrain-covering algorithm for an auv', Autonomous Robots 3, pp. 91-119, 1996.

[213] Gage, D.W., 'Randomized search strategies with imperfect sensors', in: Proc.SPIE, Mobile Robots VIII—Int. Soc. Optical Engineering, Boston, MA, pp. 270-279, 1994.

[214]   Najjaran, H. and Kircanski, N., 'Path planning for a terrain scanner robot', in: Proc.31st Int. Symp. Robotics, Montreal, QC, Canada, pp. 132-137, 2000.

[215]   Acar, E.U., Choset, H., Zhang, Y. and Schervish, M., 'Path planning for robotic demining: robust sensor-based coverage of unstructured environments and probabilistic methods', International Journal of Robotics Research, vol. 22, pp. 441-466, 2003.

[216]   Cao, Z.L., Huang, Y. and Hall, E.L., 'Region filling operations with random obstacle avoidance for mobile robotics', Journal of Robotic Systems, vol. 5, issue 2. pp. 87-102, 1988.

[217]   Bosse, M., Nourani-Vatani, N. and Roberts, J., 'Coverage algorithms for an underactuated car-like vehicle in an uncertain environment', in: Proc. IEEE Int.Robotics and Automation Conf., pp. 698-703, 2007.

[218]   Ollis, M. and Stentz, A., 'First results in vision-based crop line tracking', in: Proc.Conf. IEEE Int. Robotics and Automation, vol. 1, pp. 951-956, 1996.

[219]   Ollis, M. and Stentz, A., 'Vision-based perception for an automated harvester', in:Proc. IEEE/RSJ Int. Intelligent Robots and Systems IROS'97. Conf., Vol. 3, pp. 1838-1844, 1997.

[220]   Farsi, M., Ratcliff, K., Johnson, J.P., Allen, C.R., Karam, K.Z. and Pawson, R., 'Robot Control system for window cleaning', in: Proc. American Control Conf., vol. 1, pp. 994-995, 1994.

[221]   Choset, H., 'Coverage for robotics—a survey of recent results', Annals of Mathematics and Artificial Intelligence, vol. 31, issue 1-4, pp. 113-126, 2001.

[222] Neto, P. and Mendes, N., 'Direct off-line robot programming via a common CAD package', Robotics and Autonomous Systems, vol. 61, issue 8, pp. 896-910, Aug. 2013.

[223] Chan, S.F. and Kwan R., 'Post-processing methodologies for off-line robot programming within computer integrated manufacture', Journal of Materials Processing Technology, vol. 139, issues 1-3, Aug. 2003.

[224] Gadow, R., Candel, A. and Floristán, M., 'Optimized robot trajectory generation for thermal spraying operations and high quality coatings on free-form surfaces', Surface and Coatings Technology, vol. 205, issue 4, pp. 1074-1079, Nov. 2010.

[225] Atkar, P., Greenfield, A, L., Conner, D. C., Choset, H. and Rizzi, A., 'Uniform Coverage of Automotive Surface Patches', The International Journal of Robotics Research, vol. 24, no. 11, pp. 883- 898, Nov. 2005.

[226] Suh, S.-H., Woo, I.-K. and Noh, S.-K., 'Development of an automatic trajectory planning system (ATPS) for spray painting robots', Robotics and Automation, Proceedings, IEEE International Conference on, vol. 3, pp. 1948-1955, Apr. 1991.

[227] Asakawa, N. and Takeuchi, Y., 'Teachingless spray-painting of sculptured surface by an industrial robot', Robotics and Automation, Proceedings, IEEE International Conference on , vol.3, pp. 1875-1879, Apr 1997.

[228] Chen, H., Xi, N., Sheng, W., Song, M. and Chen, Y., 'CAD-Based Automated Robot Trajectory Planning for Spray Painting of Free-Form Surfaces', An International Journal of Industrial Robot, vol. 29, no. 5, pp. 426-433, 2002.

[229] Pan, H.P, Feng, H. and Cao L.G., 'Trajectory Generation for Glazing Spray Gun Based on STL Model', Applied Mechanics and Materials, vol. 487, pp. 617-620. 2014.

[230] Olivieri, P., Birglen, L., Maldague, X. and Mantegh I., 'Coverage path planning for eddy current inspection on complex aeronautical parts', Robotics and Computer-Integrated Manufacturing, vol. 30, issue 3, pp. 305-314, June 2014,

[231] Bangert M. Tech showcase: 'Eddy current today', http://www.qualitymag.com/articles/89905-tech-showcase-eddy-current-today, 2009 , Accessed Apr. 2014.

[232] Sattar, T.P. and Brenner, A.A. 'Robotic system for inspection of test objects with unknown geometry using NDT methods' Industrial Robot: An International Journal, vol. 36, issue. 4, pp. 340–343, 2009.

[233] 'EloScan Technical Data', http://www.rohmann.de/datasheets/special/EloScan_eng.pdf, Accessed Apr. 2014.

[234] Mineo, C., Pierce, S. G., Morozov, M., Nicholson I. P. and Cooper, I., 'Computer-Aided Tool Path Generation for Robotic Non-Destructive Inspection' In proceeding of: 52nd Annual Conference of the British Institute for Non-Destructive Testing, At Telford, UK, Sept. 2013,

[235] ANDSCAN, http://www.andscan.com/ANDSCAN_Web_Site.htm, Accessed 02/14.

[236] Buckley, J.M., Smith, R.A. and Skramstad, J.A. 'Transient eddy currents for aircraft structure inspection –an introduction', Sonatest, Milton Keynes, QinetiQ Ltd, Farnborough, NDT Solutions Inc., New Richmond, WI., 2003,

http://joe.buckley.net/papers/JMB%20200309%20Transient%20Eddy%20currents%2
0introduction.pdf, Accessed Feb. 2014.

[237] Yau, H.T. and Menq, C.H., 'Path planning for automated dimensional inspection using coordinate measuring machines', Robotics and Automation,. Proceedings., IEEE International Conference on , vol. 3, pp. 1934-1939, Apr. 1991.

[238] Englot, B.H. and Franz S. TI 'Three-dimensional coverage planning for an underwater inspection robot' International Journal of Robotics Research, vol. 32 issue: 9-10, pp. 1048-1073, 2013.

[239] Hoff, E.B. and Sarker, B. R., 'An overview of path design and dispatching methods for automated guided vehicles', Integrated Manufacturing Systems, vol. 9 issue. 5, pp. 296-307, 1998.

[240] De Carvalho, R.N., Vidal, H.A., Vieira, P. and Ribeiro, M.I. Complete coverage path planning and guidance for cleaning robots. In: Proceedings of the IEEE international symposium on industrial electronics, ISIE '97, vol. 2, p. 677-682,1997.

[241] Jin, J. and Tang L., 'Coverage path planning on three-dimensional terrain for arable farming' Journal of Field Robotics, vol. 28, issue 3, pp. 424-440, 2011.

[242] Englot, B. and Hover, F., 'Inspection planning for sensor coverage of 3D marine structures', In: IEEE/RSJ International Conference Intelligent Robots and Systems, Taipei, Taiwan, pp. 4412-4417, Oct. 2010.

[243] Englot, B. and Hover, F., 'Planning complex inspection tasks using redundant roadmaps'. In: International Symposium on Robotics Research, Flagstaff, New York, USA, Sept. 2011.

[244] Englot, B. and Hover, F., 'Sampling-based coverage path planning for inspection of complex structures'. In: 22nd International Conference Automated Planning and Scheduling, Sao Paulo, Brazil, pp. 29–37, June 2012.

[245] Donald, B.R., 'Motion Planning with Six Degrees of Freedom', Massachusetts Institute Technology Artificial Intelligence Laboratory, Technical Report AIM-791, 1984.

[246] Brooks, R. A., 'Solving the find path problem by representing free space as generalized cones' A.I Memo No 674, Massachusetts Institute Technology, May 1982.

[247] Kambhampati, S. and Davis, L.S., 'Multiresolution path planning for mobile robots', Robotics and Automation, IEEE Journal of , vol.2, no.3, pp.135-145, Sep. 1986

[248] Sariff, N. and Buniyamin, N., 'An Overview of Autonomous Mobile Robot Path Planning Algorithms', Research and Development, SCOReD 4th Student Conference on, pp.183-188, Jun. 2006.

[249] Babel L., 'Flight path planning for unmanned aerial vehicles with landmark-based visual navigation', Robotics and Autonomous Systems, vol. 62, issue 2, pp 142-150, Feb. 2014.

[250] Barrientos, A., Colorado, J., Cerro, J. d., Martinez, A., Rossi, C., Sanz, D. and Valente, J., 'Aerial remote sensing in agriculture: A practical approach to area coverage and path planning for fleets of mini aerial robots', Journal of Field Robotics, vol. 28, pp. 667-689, 2011.

[251] Murtaza, G., Kanhere, S. and Jha, S., 'Priority-based coverage path planning for Aerial Wireless Sensor Networks', Intelligent Sensors, Sensor Networks and

Information Processing, IEEE Eighth International Conference on, pp.219-224, Apr. 2013.

[252] Fahimi, F., Autonomous Robots Modeling, Path Planning, and Control, Springer US, 2009.

[253] MacLeod, C. N., Pierce, S. G., Morozov, M., Summan, R., Dobie, G. I. , McCubbin, P., McCubbin, C., Dearie, S. and Munro, G., 'Automated Metrology and NDE Measurements for Increased Throughput in Aerospace Component Manufacture', 41st Annual Review of Progress in Quantitative Nondestructive Evaluation, Boise, Idaho, USA, 2014.

[254] Pease W, 'An automatic machine tool' Scientific American, issue Sep., pp. 101-115, 1952.

[255] Thyer, G. E., Computer numerical control of machine tools, Industrial Press, Incorporated, 1988.

[256] Dragomatz, D. and Mann, S., 'A classified bibliography of literature on NC milling path generation', Computer-Aided Design, vol. 29, issue 3, pp. 239-247, Mar. 1997.

[257] CNC Simulator
http://cncsimulator.info/OnlineHelp/OnlineHelp.html?PocketMilling.html, Accessed Feb. 2014.

[258] Xu, X.W., Wang, L. and Rong, Y., 'STEP-NC and function blocks for interoperable manufacturing', Automation Science and Engineering, IEEE Transactions on , vol. 3, no. 3, pp. 297- 308, Jul. 2006.

[259] Mastercam, 2014, http://www.mastercam.com/, Accessed Feb. 2014.

[260] Sandvik Cormorant, http://www2.coromant.sandvik.com/coromant/pdf/metalworking_products_061/tech_d_1.pdf, Accessed Feb. 2014.

[261] Southwestern Industries, http://www.southwesternindustries.com/protoTRAK-CNC/prototrak-smx, Accessed Feb. 2014.

[262] GE RotoArray, https://utprobes.gemcs.com/utprobes/assets/images/rotoArrayProbes/GEIT-20121EN_RotoArray_2301.pdf, Accessed Feb. 2014.

[263] Olympus NDT. OmniScan MX2 , http://www.olympus-ims.com/en/omniscan-mx2, Accessed Feb. 2014.

[264] Carvell, G. E. and Simons, D. J., 'Biometric analyses of vibrissal tactile discrimination in the rat', The Journal of Neuroscience, vol. 10, no. 8, pp. 2638–2648, 1990.

[265] Dehnhardt, G., Mauck, B., Hanke, W. and Bleckmann, H., 'Hydrodynamic trail-following in harbor seals (Phoca vitulina)', Science, vol. 293, no. 5527, pp. 102–104, 2001.

[266] Anjum, F., Turni, H., Mulder, P. G., Burg, J.V.D. and Brecht, M., 'Tactile guidance of prey capture in Etruscan shrews', Proc Natl Acad Sci USA, vol. 103, no. 44, pp. 16544-16549, 2006.

[267] Fox, C., Mitchinson, B., Pearson, M., Pipe, A. and Prescott, T., 'Contact type dependency of texture classification in a whiskered mobile robot', Autonomous Robots, vol. 26, pp.223-239, 2009

[268] Mitchinson, B., Gurney , K. N., Redgrave , P., Melhuish, C., Pipe, A. G., Pearson, M.. Gilhespy, I. and Prescott, T. J. 'Empirically inspired simulated electro-mechanical model of the rat mystacial follicle-sinus complex', Proc. Royal Society of London B: Biological Sciences, vol. 271, no. 1556, pp.2509-2516, 2004.

[269] Prescott, T., Pearson, M., Mitchinson, Sullivan, C. J. and Pipe, A., 'Whisking with robots from rat vibrissae to biomimetic technology for active touch', IEEE Robot. Automation Magazine, vol. 16, no. 3, pp.42-50 2009.

[270] Kleinfeld, D., Ahissar, E. and Diamond, M. E., 'Active sensation: Insights from the rodent vibrissa sensorimotor system' Current Opinion in Neurobiology., vol. 16, no. 4, pp. 435-444, 2006.

[271] Sullivan, J.C., Mitchinson, B., Pearson, M.J., Evans, M., Lepora, N.F., Fox, C.W., Melhuish, C. and Prescott, T.J., 'Tactile Discrimination Using Active Whisker Sensors', Sensors Journal, IEEE , vol. 12, no. 2, pp.3 50-362, Feb. 2012.

[272] Pearson, M. J., Gilhespy, I., Melhuish, C., Mitchinson, B., Nibouche, M., Pipe, A. G., and Prescott, T. J., 'A biomimetic haptic sensor' International Journal of Advanced Robotic Systems, 2, pp. 335-343, 2005.

[273] Pearson, M.J., Mitchinson, B., Sullivan, J.C., Pipe, A.G. and Prescott, T.J., 'Biomimetic vibrissal sensing for robots', Phil. Trans. Royal Society of London B: Biological Sciences,, vol. 366, no.1581, pp. 3085-3096, 2011.

[274] Pearson, M.J., Fox, C., Sullivan, J.C., Prescott, T.J., Pipe, T. and Mitchinson, B., 'Simultaneous localisation and mapping on a multi-degree of freedom biomimetic whiskered robot', Robotics and Automation (ICRA), IEEE International Conference on, pp. 586-592, May 2013.

[275] Evans, M.H., Pearson, M.J., Lepora, N.F., Prescott, T.J. and Fox, C.W., 'Whiskered texture classification with uncertain contact pose geometry', Intelligent Robots and Systems (IROS), IEEE/RSJ International Conference on, pp.7-13, Oct. 2012.

[276] National Physical Laboratory, 'Surface Preparation for Coating', National Physical Laboratory, National Corrosive Service (NCS), 2000.

[277] Surnam, B. Y. R. and Oleti, C. V., 'Using three-dimensional surface roughness parameters in analysis of atmospheric corrosion degradation of carbon steel' Corrosion Engineering, Science and Technology, vol. 47, no. 2, , pp. 96-106, Apr. 2012.

[278] British Standards Institution BS EN ISO 8501-1:2007, Preparation of steel substrates before application of paints and related products – Visual Assessment of Surface Cleanliness - Part 1. Rust grades and preparation grades of uncoated steel substrates and of steel substrates after overall removal of previous coatings, London, BSI, 2007

[279] Xie, D.M., Wang, J. M., Hu, J.M. and Zhang, J.Q., 'Influence of surface roughness on performance of zinc-rich paint coatings' Transactions of Nonferrous Metals Society of China (English Edition), vol. 12, issue 6, pp. 1036-1039, Dec. 2002.

[280] Dagnall, H, Exploring Surface Texture, Rank Taylor Hobson, Leicester, 1980.

[281] British Standards Institution BS EN ISO 8503-1:2012, Preparation of steel substrates before application of paints and related products - Surface roughness characteristics of blast-cleaned steel substrates - Part 1. Specifications and definitions for ISO surface profile comparators for the assessment of abrasive blast-cleaned surfaces, London, BSI, 2012.

[282] Taylor Hobson, http://www.taylor-hobson.com, Accessed Apr. 2014.

[283] Govindan, G., Dillibabu, S., Athi, G. and Thotta, R., 'Fiber-optic sensor to estimate surface roughness of corroded metals' Optica Applicata, vol.39, no.1, pp. 5-11, 2009.

[284] http://www.mitutoyo.co.uk/form-measurement/surface-roughness/178-561-02e, Accessed Apr. 2014.

[285] http://www.mitutoyo.co.uk/form-measurement/surface-roughness/178-544-2, Accessed Apr. 2014.

Appendix A

Key Enabling Technologies

A.1 Facility for Innovation and Research in Structural Testing (FIRST) Laboratory

Through an EPSRC (Engineering and Physical Science Research Council) equipment grant (EP/G038627/1) "New Imaging Systems for Advanced Non-Destructive Evaluation", and support from the Electronic & Electrical Engineering (EEE) department, CUE has developed two bespoke laboratories to house state of the art imaging and positioning systems to assist with NDE research and deployment.

Within the FIRST Laboratory exists the following specialised equipment:

1. **2x KUKA KR5 ARC HW robot positioners.**

2. **VICON MX Giganet motion capture system**

3. **LEICA Absolute Laser Tracker AT901-B**

4. **FARO Quantum 3m & laser line probe V3 Scanner**

5. **DSL Flaw Inspecta Array Controller**

6. **ZETEC Dynaray ZPA-RDT 256/256 PR Array Controller**

7. **Lecoeur Electronique 128 Channel Open System Array Controller**

8. **PVA TePla SAM 300 Acoustic Microscope**

9. **HIRST GM08 Magnetic characterisation system**

A.2   Motion Capture System

One of the positioning systems available within the FIRST laboratory suite is the VICON MX Giganet Motion Capture System (VMCS) [97]. This commercial photogrammetry based optical tracking system utilises multiple high resolution optical cameras and resultant images to track the position of reflective markers within a measurement volume.

Each camera consists of a custom 16 megapixel high resolution global shutter Vicon Avalon image sensor, capable of 120 frames per second at full resolution. Additionally a custom made motion capture lens with low distortion and uniform illumination allows control of aperture and focus. Concentric to the lens, three active Infrared(IR) Light Emitting Diode (LED) circular array rings illuminate the measurement volume and offer continuous or strobe firing options.

The markers consist of retro-reflective tape wrapped around a spherical or hemispherical body, which when illuminated by a suitable source produce a strong reflection, as shown in Figure A.1. Markers range in size from 3 mm to 14 mm diameter and rely on the accurate determination of the centre of the sphere/hemisphere. Through stereo image processing the 3 D.O.F. position of a single marker can be found within the measurement volume through triangulation. By the minimum addition of another two markers an object can be defined and the full 6 D.O.F. positional information of the object measured through the multiple

cameras (Figure A.2). The positional data can be streamed at 120 Hz across a

TCP/IP network through the running of a server on the control unit.

Figure A.1 a) VICON marker b) IR illuminated VICON marker
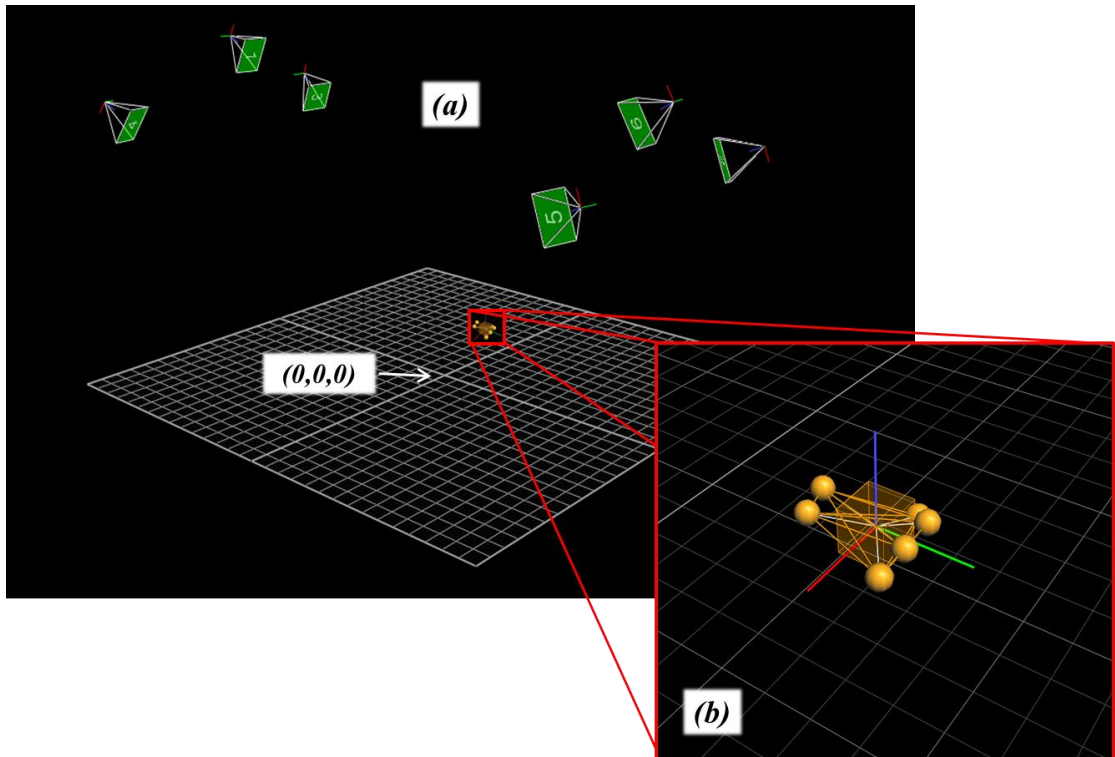
Figure A.2 VMCS virtual world and object [98]

Real time measurement capability is achieved through operation of all cameras at full resolution and sampling frequencies of 120 Hz. The current six camera system can provide full coverage over a measurement volume of 98 m^3, (6.8 x 3.8 x 3.8 m^3) (Figure A.3). Each camera is mechanically fixed to a global supporting rigid frame structure as shown in Figure A.4 and A.5.
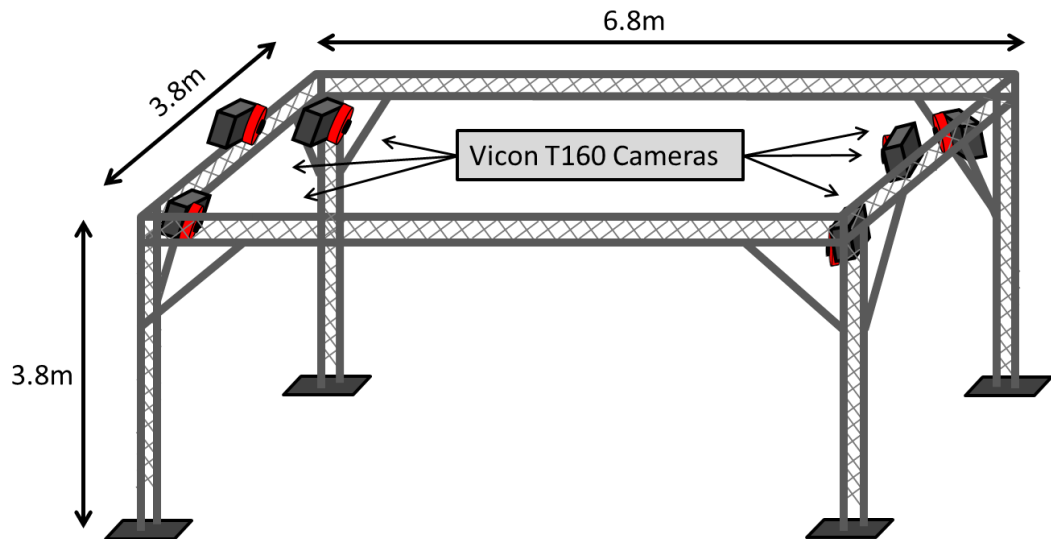
Figure A.3 VCMS measurement volume [98]
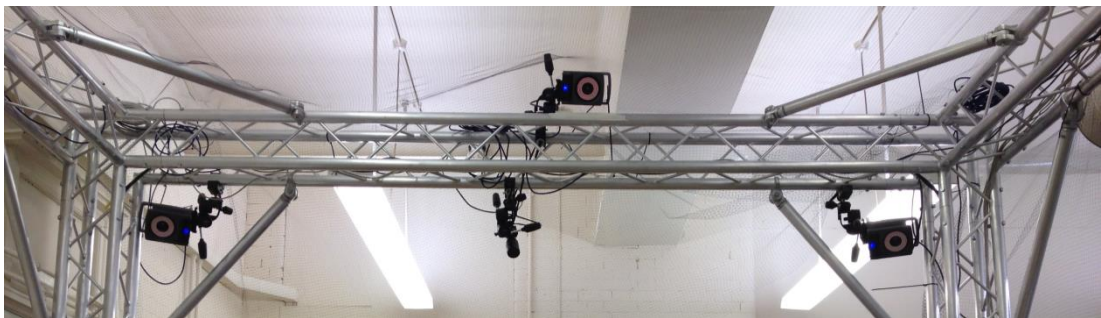
Figure A.4 VCMS camera set-up
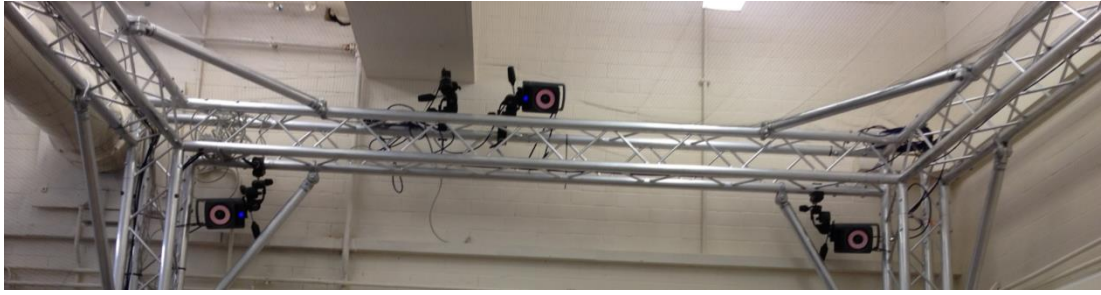
Figure A.5 VCMS camera set-up

Initial trials to ascertain the actual positional accuracy have confirmed the importance and significance of the calibration routine [98], while confirming that the accuracy is a function of:

1. **Number of rays intersecting the target , which in turn is a function of:**

    a. Camera density within the measurement volume

    b. Pose of the object relative to the cameras.

    c. Distance from the measurement camera to the object – as this defines the number of pixels capturing the shape of the target.

2. **Accuracy with which the pose (extrinsic) and optical model (intrinsic) of each measurement camera is known, which in turn is a function of:**

    a. Function of the accuracy of the calibration

    b. Environmental conditions.

    c. Ability of the system to extract the centre of each marker, controlling the accuracy of the whole object.

    d. Resolution of measurement camera and size of targets.

    e. System set-up

All six camera locations were iteratively adjusted on the frame to ensure maximum volume coverage and minimisation of un-imaged areas within the volume. The focus of each lens and camera was manually set to image a spherical marker, located at the volume central point, and correctly display a circular resultant image on the Vicon GUI. Aperture settings were manually adjusted to ensure maximum sensitivity and minimal background noise.

The calibration routine consists of a manual process of sweeping a known fixed dimension calibration wand through the volume, to determine the intrinsic and extrinsic information of the cameras. Two *a priori* wands are available to successfully allow system calibration to be undertaken. Firstly a five marker passive wand (Figure A.6), each of diameter 14mm, and of overall dimension (520 x 320 x 20 mm) defines the calibration object in a manner identical to that of an object desired to be tracked. Secondly an active wand (Figure A.7) with five active LED markers (625 & 780 nm), and of similar dimension, permits imaging and measuring by emitting light at a measurement camera optimised frequency. The key difference exists in the measurement of the marker central point, wherein the passive wand it is the centre of the wrapped spherical bodies that are computed, however it is the LED die emitting area that defines the point within the active wand.

Figure A.6 VICON passive wand

Figure A.7 VICON active wand

The optimisation process undertaken to determine the cameras optical and positional information relies on the quality and quantity of image data collected within the calibration routine. A user set number of frames per camera, ranging from 2000 to 10,000, controls the quantity of resultant point cloud data gathered, while the integrity of the wand and human sweeping motion control the quality of the data. The

recommended process for sweeping the volume, is that of a figure of eight motion throughout the whole volume, whereby the markers are imaged by the individual cameras through a variety of angles and distances. The calibration quality is expressed for each individual camera in image error and measured in pixels.

The quality of the calibration and thus accuracy of the system is a function of the point cloud data and therefore the wand motion as executed by the operator. The calibration quality is measured by image error, a value which is associated with each camera and is expressed in terms of pixels.

A.2.1 Defining Objects

As stated above objects are defined by three of more markers, however typically the position of only one specific point of interest on the object is desired or required. It is not the arbitrary position of the individual markers, which are what are actually measured, but a specific point on the object which is of interest for further processing and control. Such a point could be the turning point of the CUE RSA's which is located at the midpoint between the two drive wheels. The procedure for defining the origin or measurement point of the CUE RSA object is established by aligning individual markers with axes of interest. This was achieved by the structure shown in Figure A.8. Markers 1 and 2 were aligned to the central X axis of the drive wheels while marker 3 was aligned to the centre of the RSA chassis intersecting in a perpendicular fashion with the drive wheel axis giving the X and Y measurement origin. The Z axis origin point can be achieved by placing a single marker on the reference ground surface and removing the radius of the marker.
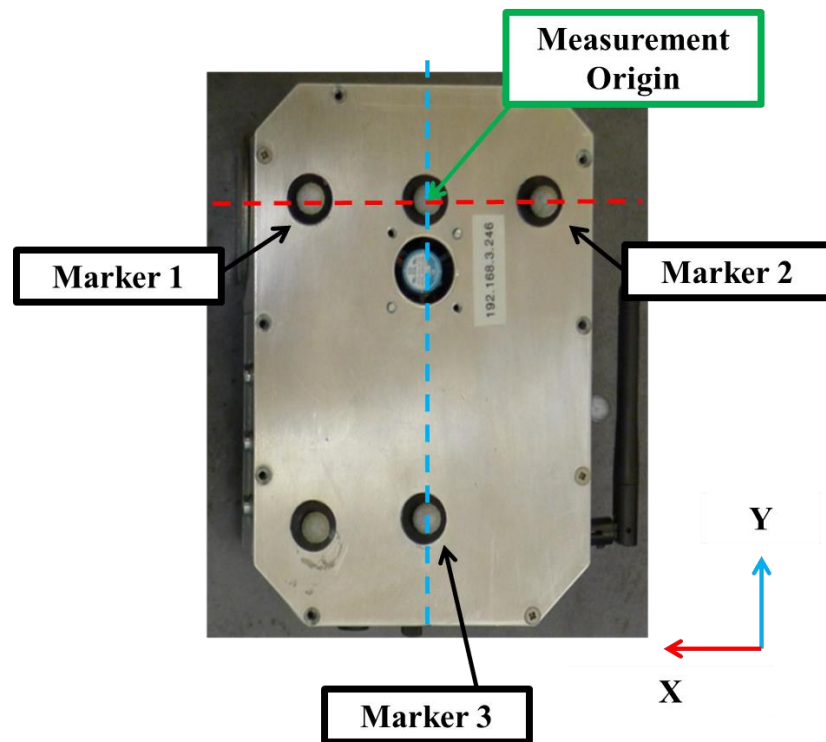
Figure A.8 CUE RSA VCMS Measurement Origin

A.3 Laser Tracker

Another positioning system present within the FIRST laboratory is a Leica AT901 Absolute Tracker [99]. The Leica AT901-B (LAT) (Figure A.8) is a high accuracy laser tracker traditionally deployed in large scale metrology and aligning operations in the manufacturing and aerospace sectors. The device is capable of measuring the absolute 3 D.O.F. position of a Spherically Mounted Reflector (SMR) within a spherical volume of up to 80 m radius, by the return projection of laser beam from the measurement unit to the SMR. By control and measurement of the yaw and pitch of both the laser projection and measurement receiver mirror, located within the tracker head, the system is capable of determining the position of an SMR within the measurement volume with an overall accuracy of $\pm$ 15 μm + 6 μm/m.

The tracker uses both an Absolute Distance Metre (ADM) which measures absolute distances, and a laser Interferometer (IFM) which determines instantaneous relative distances. Once the laser beam is locked on to the SMR the ADM determines the global position of the SMR with respect to the tracker coordinate system, using time of flight measurement to an accuracy of $\pm$ 10 μm/m. However this approach lacks sufficient dynamic capability to provide real time tracking information. The IFM then measures instantaneous relative changes of the SMR through phase interference of the outgoing and incoming electromagnetic waves with an accuracy of $\pm$ 0.2 μm + 0.15 μm/m. When combined within the tracker to form an Absolute Interferometer (AIFM) absolute distances can be measured dynamically with precision and speed [20].

The Tracker utilises "Leica Power Lock" technology which utilises an inbuilt camera to search and locate a reflector within the field of view if it becomes unlocked from the laser beam through lack of continuous line of sight.

The tracker outputs the 3 D.O.F. positional data at a frequency of 1000 Hz across a standard TCP/IP connection protocol, while an external temperature sensor allows for compensation of environmental influences, in turn reducing measurement error.
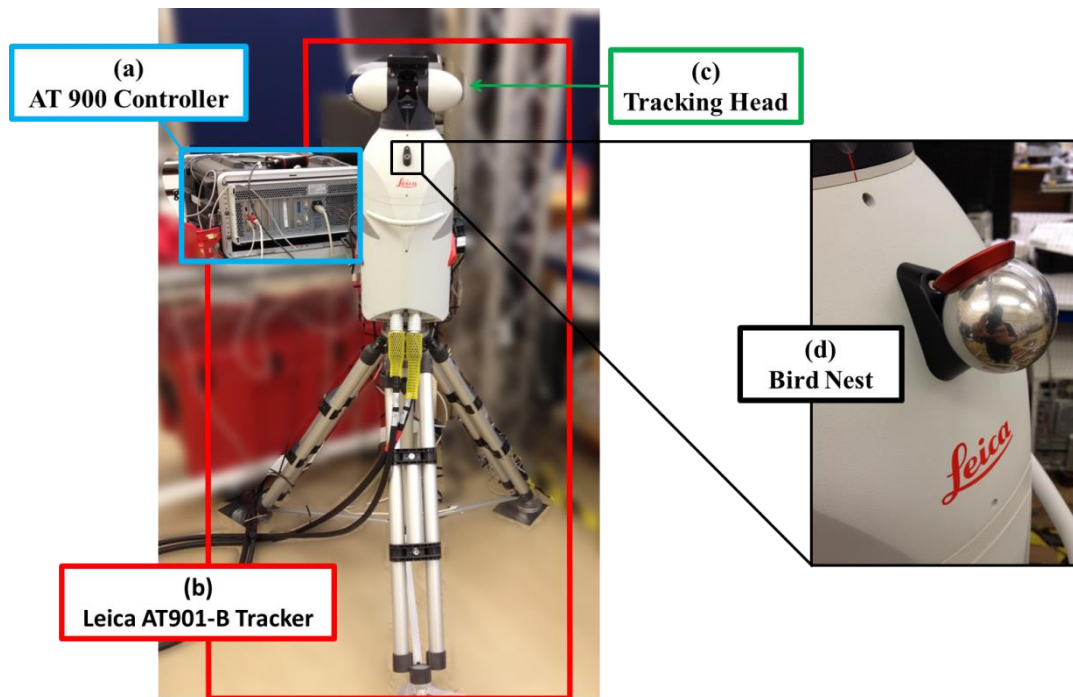
Figure A.9 LEICA AT901-B [98]

Various designs of SMR exist depending on required accuracy, robustness and application. The Red Ring Reflector (RRR) (Figure A.9) consists of a magnetic spherical housing (1.5 or 0.5") with internal air path corner cube mirror arrangement, with $\pm 30°$ acceptance angle, to successfully reflect the incoming the laser beam. The acceptance angle specification is defined by the user removable red ring which when detached can permit far greater entry and exit angles, at the expense of the stated performance accuracy. The RRR optics are centred with an accuracy of $< \pm$ 0.006 mm and giving the RRR the highest accuracy of any Leica reflector. The Tooling Ball Reflector (TBR) is a low cost 0.5" magnetic closed prism reflector with centring optics accuracy of $< \pm 0.01$ mm, intended for robotic or automated applications (Figure A.10).
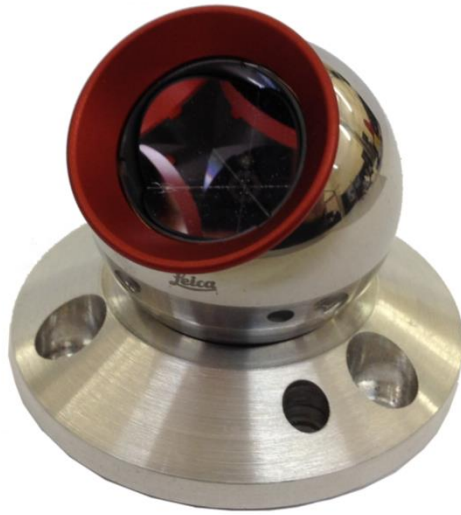
Figure A.10 LEICA 1.5" RRR [99]

Figure A.11 LEICA 0.5" TBR [99]

Appendix B

B.1   500 mm Altitude Flight Data

(a)

(b)

(c)

(d)

(e)

(f)
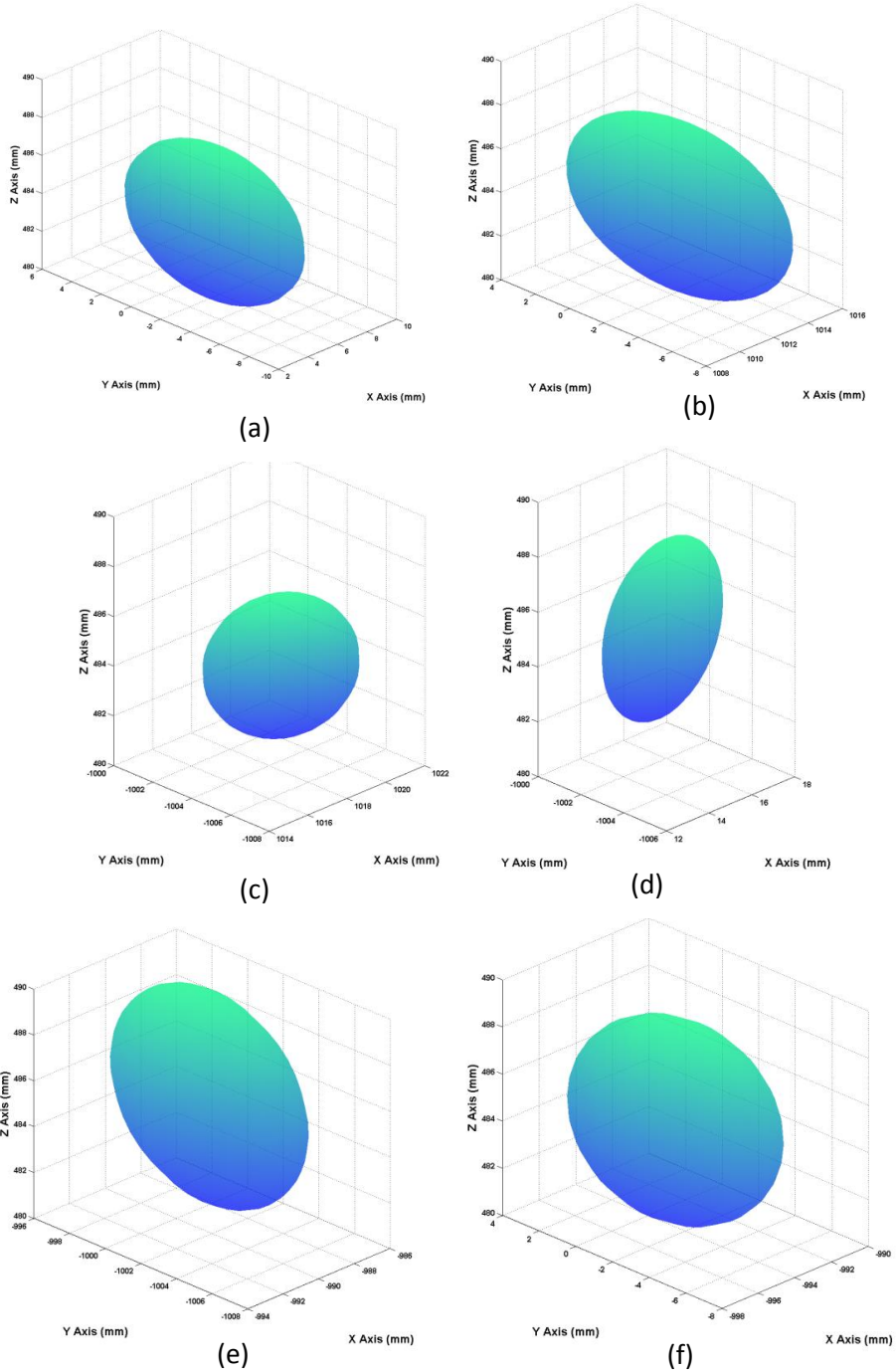
Figure B. 1 CUE ASA Position Error Distribution at Desired Positions (a) 0,0,500, (B) 1000,0,500, (C) 1000,-1000,500, (D) 0,-1000,500, (E) -1000,-1000,500, (F) -1000,0,500
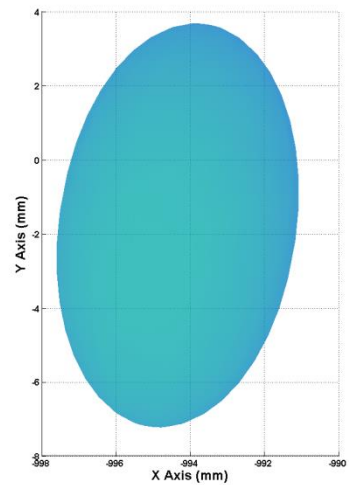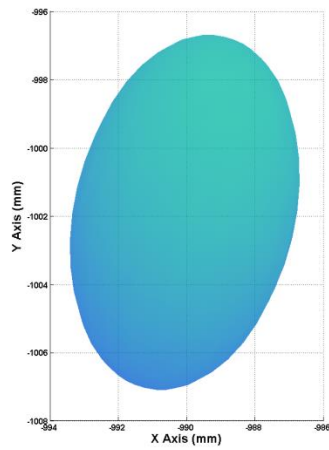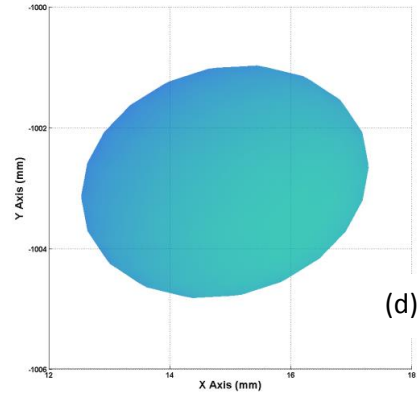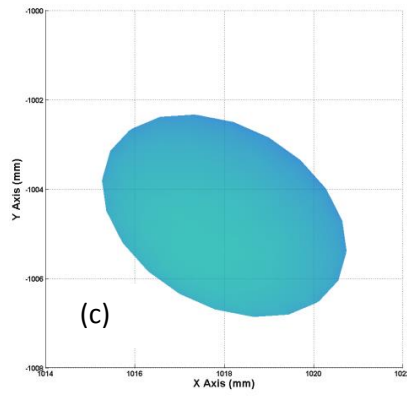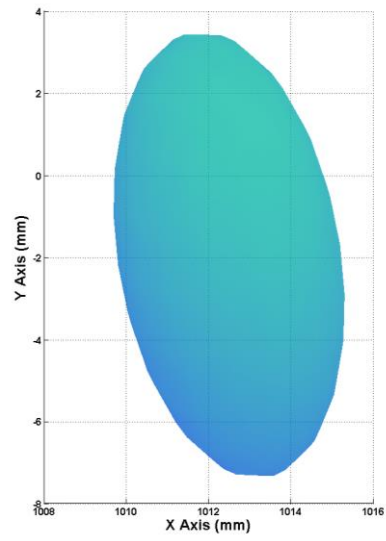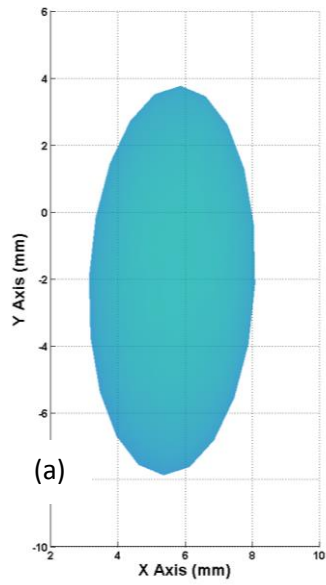
Figure B.2 CUE ASA Position X-Y Plane Error Distribution at Desired Positions (a) 0,0,500, (B) 1000,0,500, (C) 1000,-1000,500, (D) 0,-1000,500, (E) -1000,-1000,500, (F) -1000,0,500
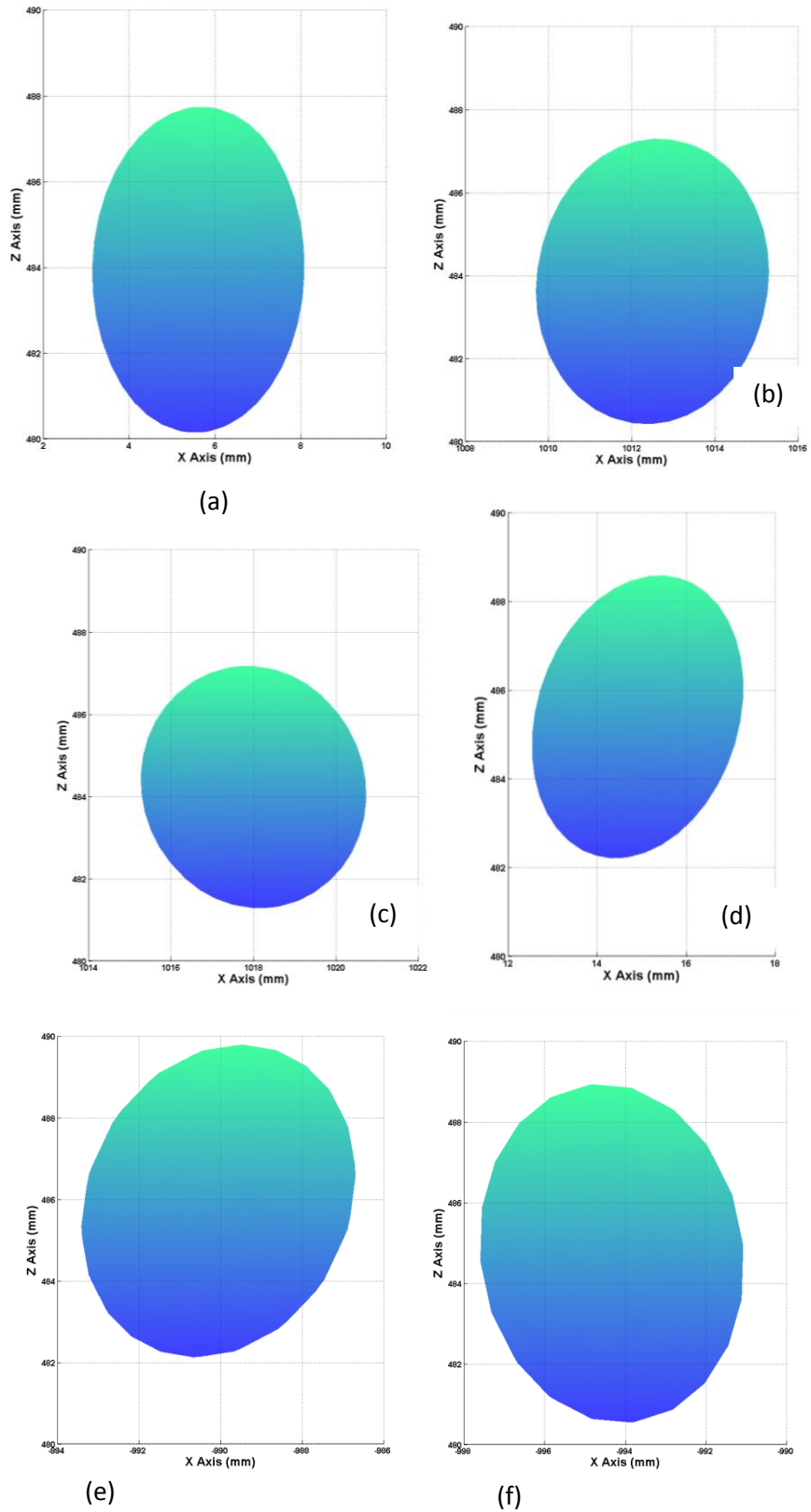
Figure B.3 CUE ASA Position X-Z Plane Error Distribution at Desired Positions (a) 0,0,500, (B) 1000,0,500, (C) 1000,-1000,500, (D) 0,-1000,500, (E) -1000,-1000,500, (F) -1000,0,500

343
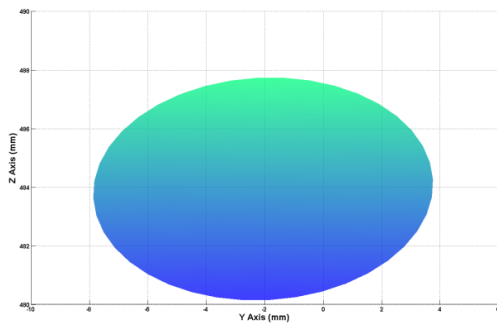
(a)
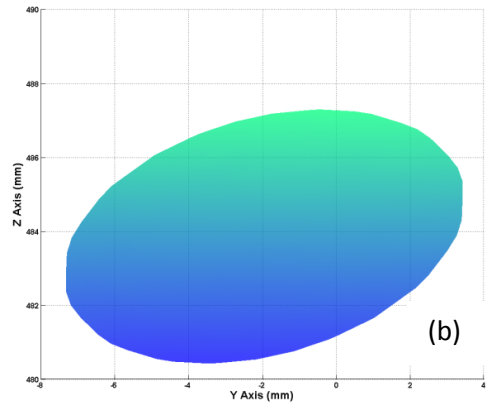
(b)
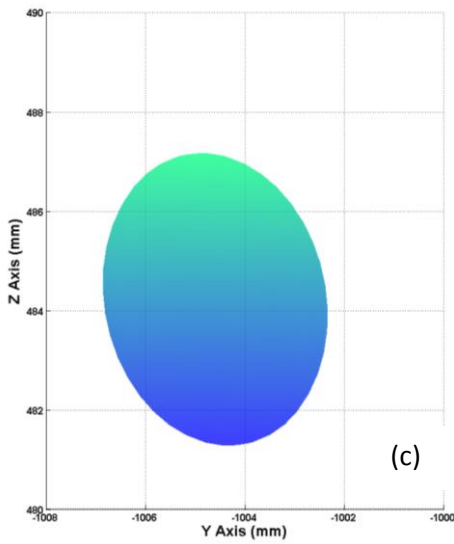
(c)
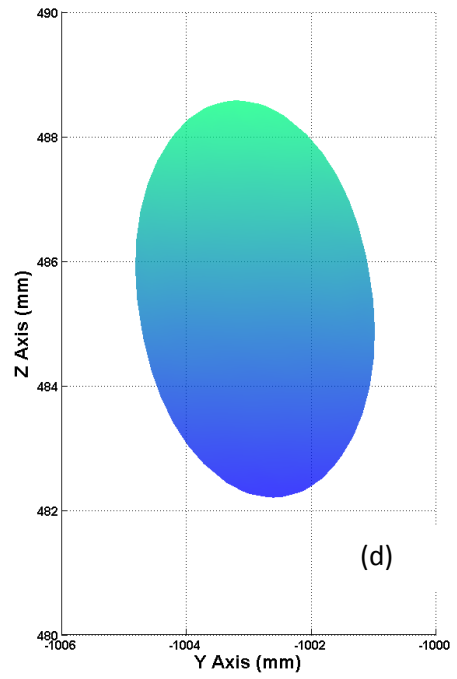
(d)
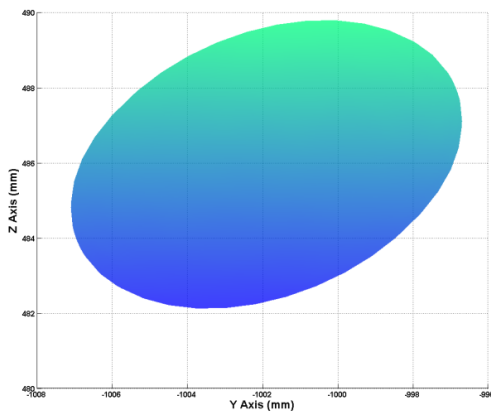
(e)
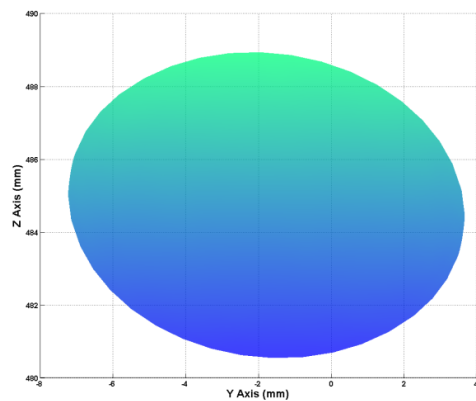
(f)

Figure B.4 CUE ASA Position Y-Z Plane Error Distribution at Desired Positions (a) 0,0,500, (B) 1000,0,500, (C) 1000,-1000,500, (D) 0,-1000,500, (E) -1000,-1000,500, (F) -1000,0,500

B.2 1500 mm Altitude Flight Data
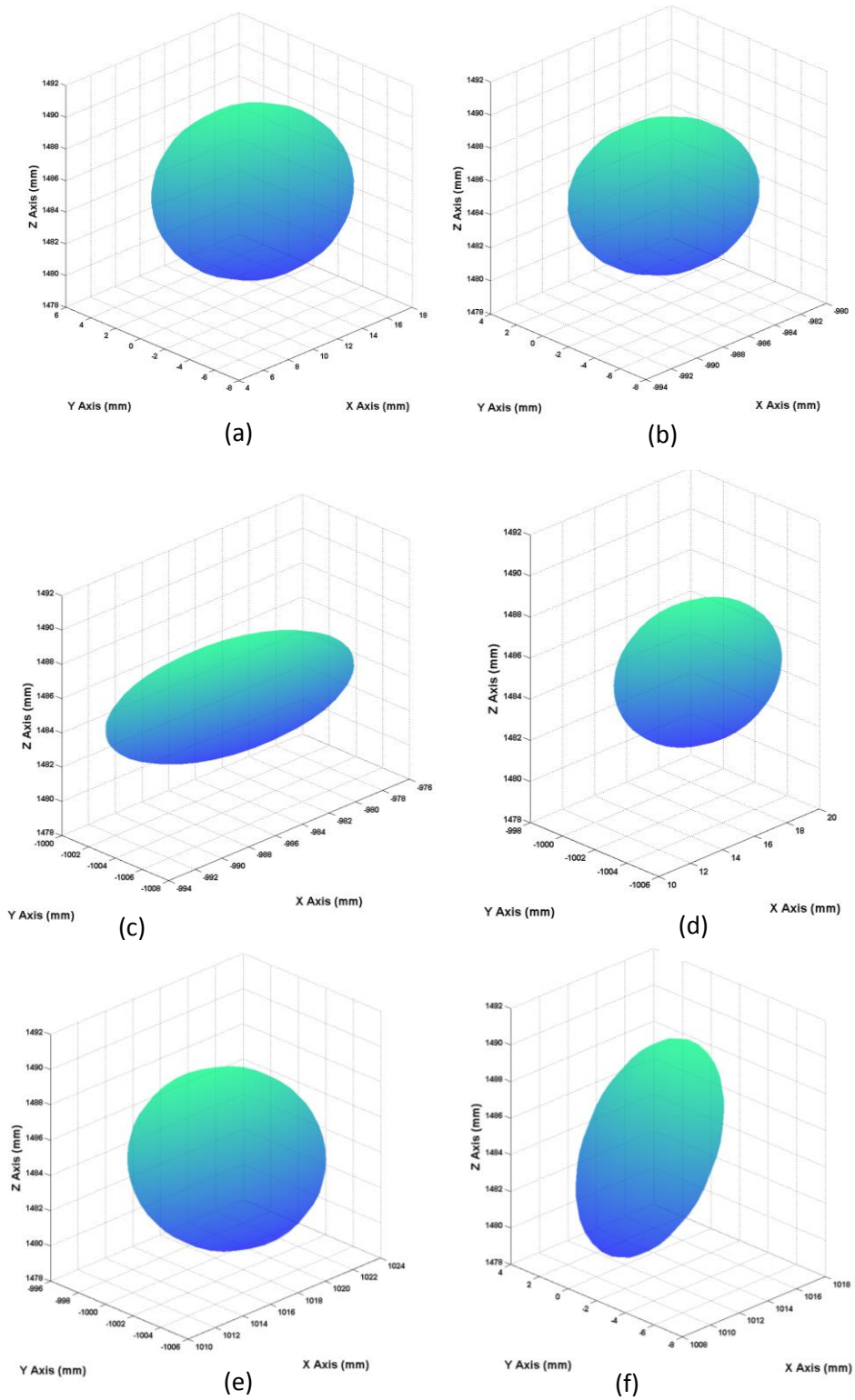
Figure B.5 Figure 2.18 CUE ASA Position Error Distribution at Desired Positions (a) 0,0,1500, (B) 1000,0,1500, (C) 1000,-1000,1500, (D) 0,-1000,1500, (E) -1000,-1000,1500, (F) -1000,0,1500
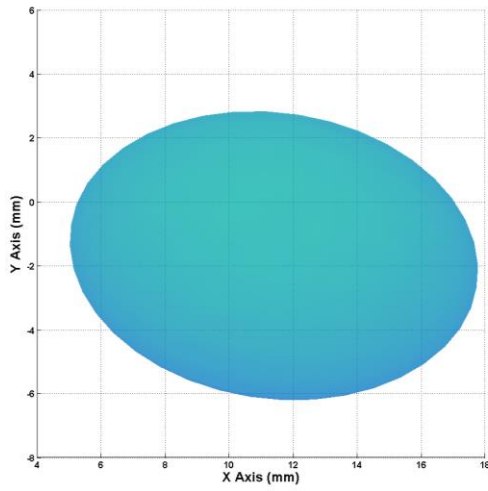
(a)
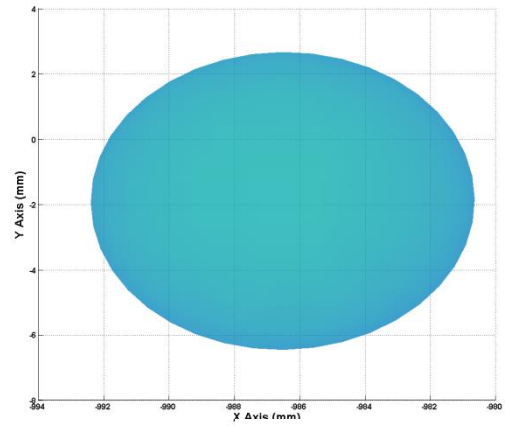
(b)
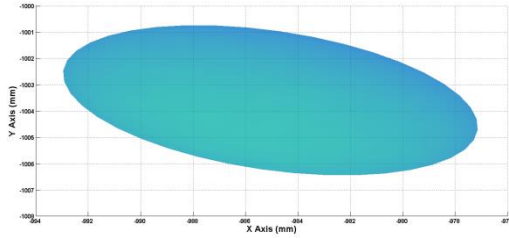
(c)
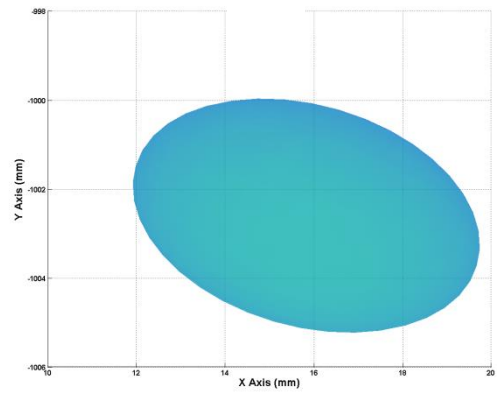
(d)
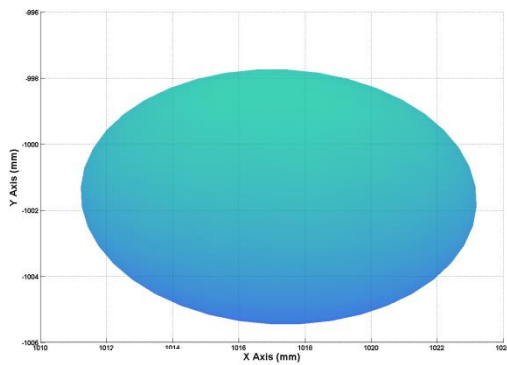
(e)
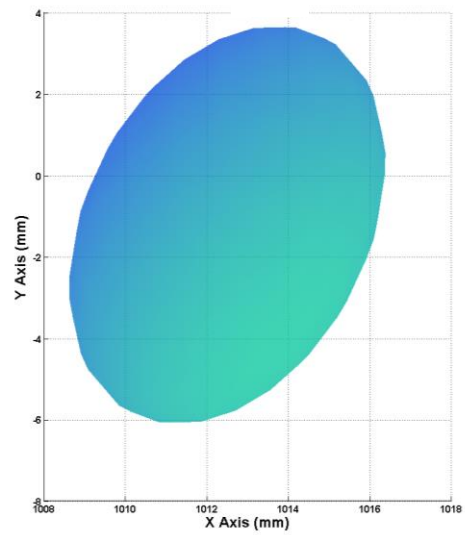
(f)

Figure B.6 CUE ASA Position X-Y Plane Error Distribution at Desired Positions (a) 0,0,1500, (B) 1000,0,1500, (C) 1000,-1000,1500, (D) 0,-1000,1500, (E) -1000,-1000,1500, (F) -1000,0,1500

346
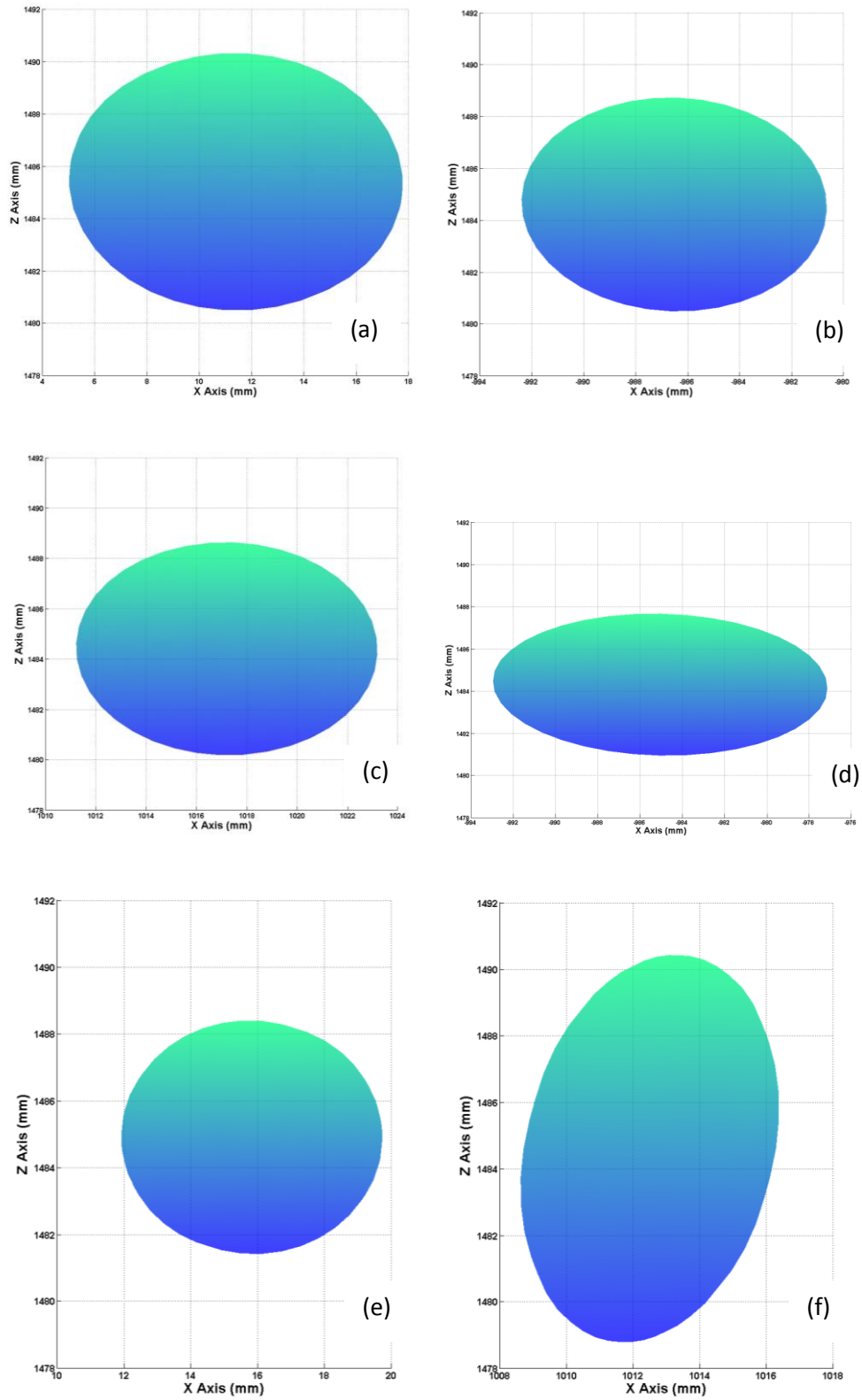
Figure B.7 CUE ASA Position X-Z Plane Error Distribution at Desired Positions (a) 0,0,1500, (B) 1000,0,1500, (C) 1000,-1000,1500, (D) 0,-1000,1500, (E) -1000,-1000,1500, (F) -1000,0,1500
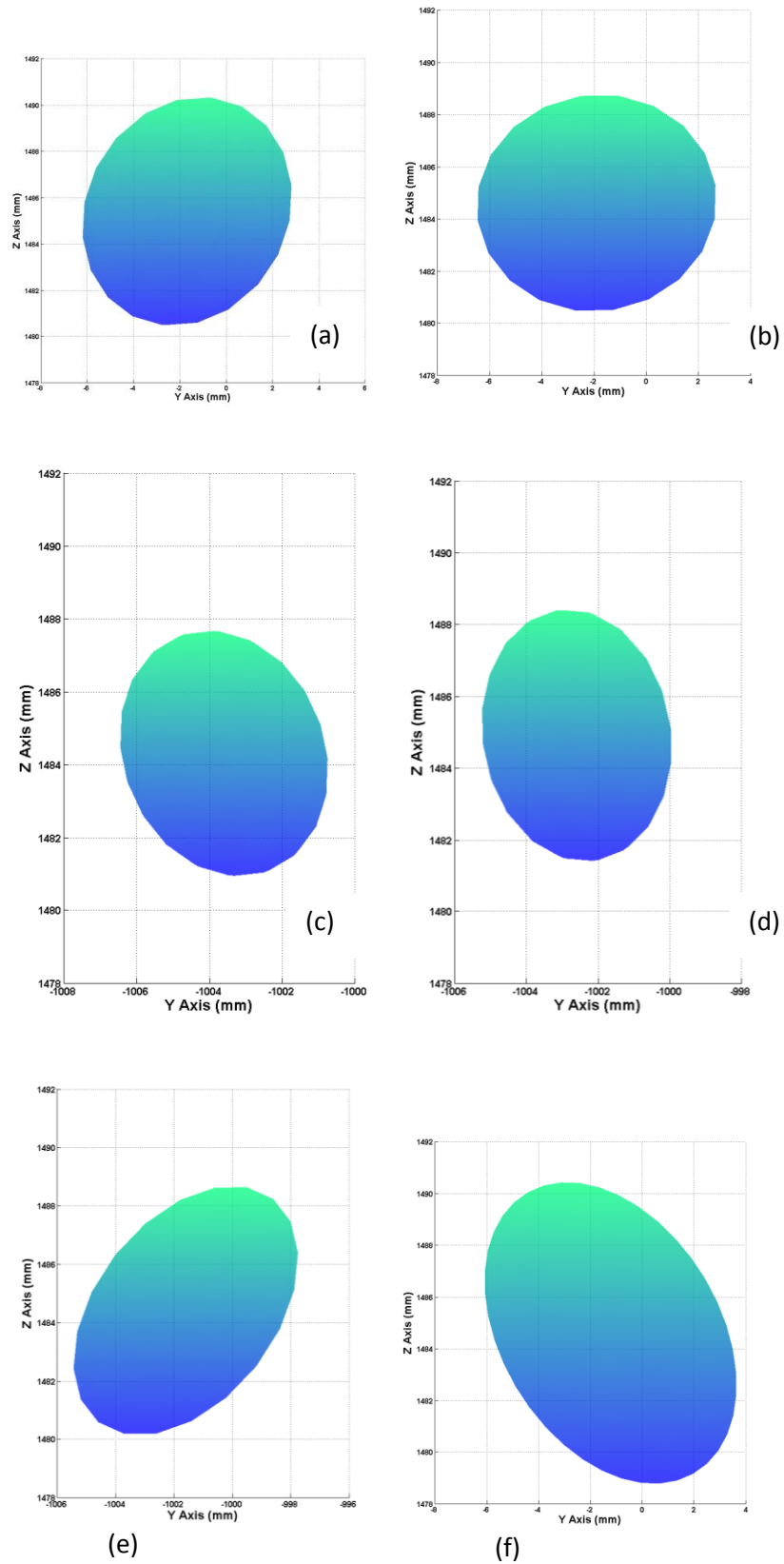
Figure B. 8 CUE ASA Position Y-Z Plane Error Distribution at Desired Positions (a) 0,0,1500, (B) 1000,0,1500, (C) 1000,-1000,1500, (D) 0,-1000,1500, (E) -1000,-1000,1500, (F) -1000,0,1500

Appendix C

C.1   Aluminium Surfaces

Restored Intensity viewed from AB Angle
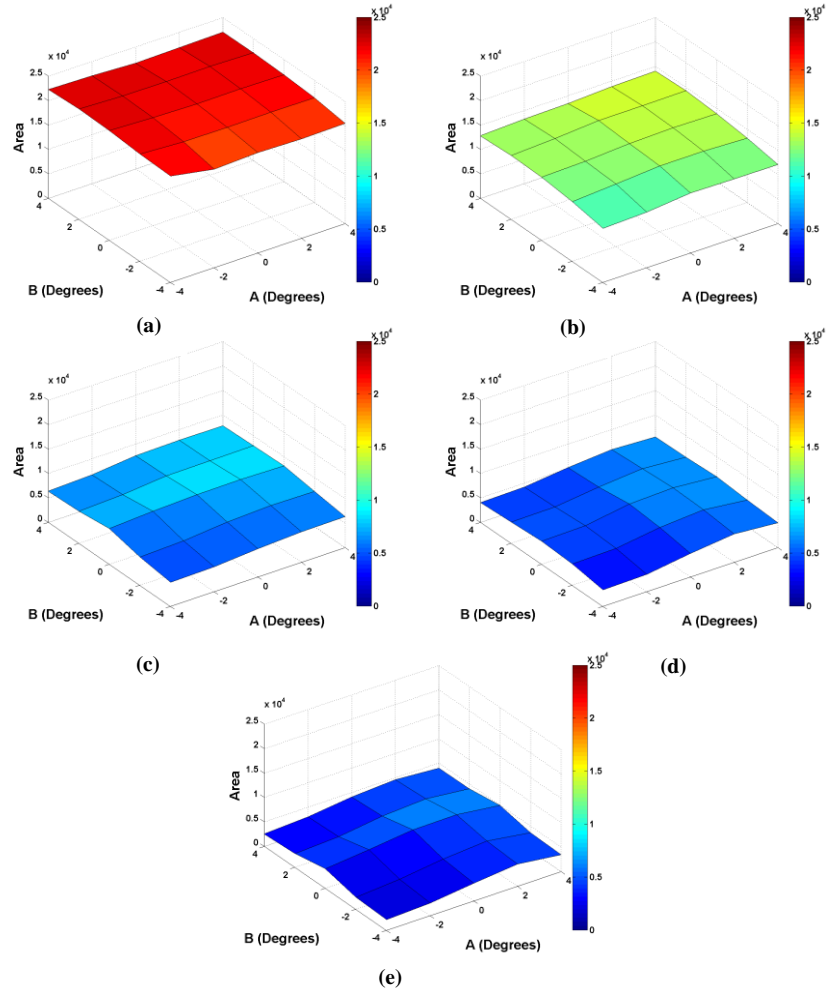
Figure C.1 AB Angle LRF Restored Intensity Area, (a) – Nominal SSD 500 mm, (b) – Nominal SSD 10000 mm, (c) – Nominal SSD 2000 mm, (d) – Nominal SSD 3000 mm, (e) – Nominal SSD 4000 mm (All other plots follow this labelling convention) (Aluminium)

Nominal SSD (mm)	Restored Intensity Area Mean	Restored Intensity Area (AB) Standard Deviation
500	21711.60	674.53
1000	13152.60	885.58
2000	7005.02	977.18
3000	5148.29	901.62
4000	3948.78	1061.31

Table C.1 AB Angle LRF Restored Intensity Area Statistical Performance (Aluminium)

Restored Intensity viewed from AC Angle

(a)

(b)
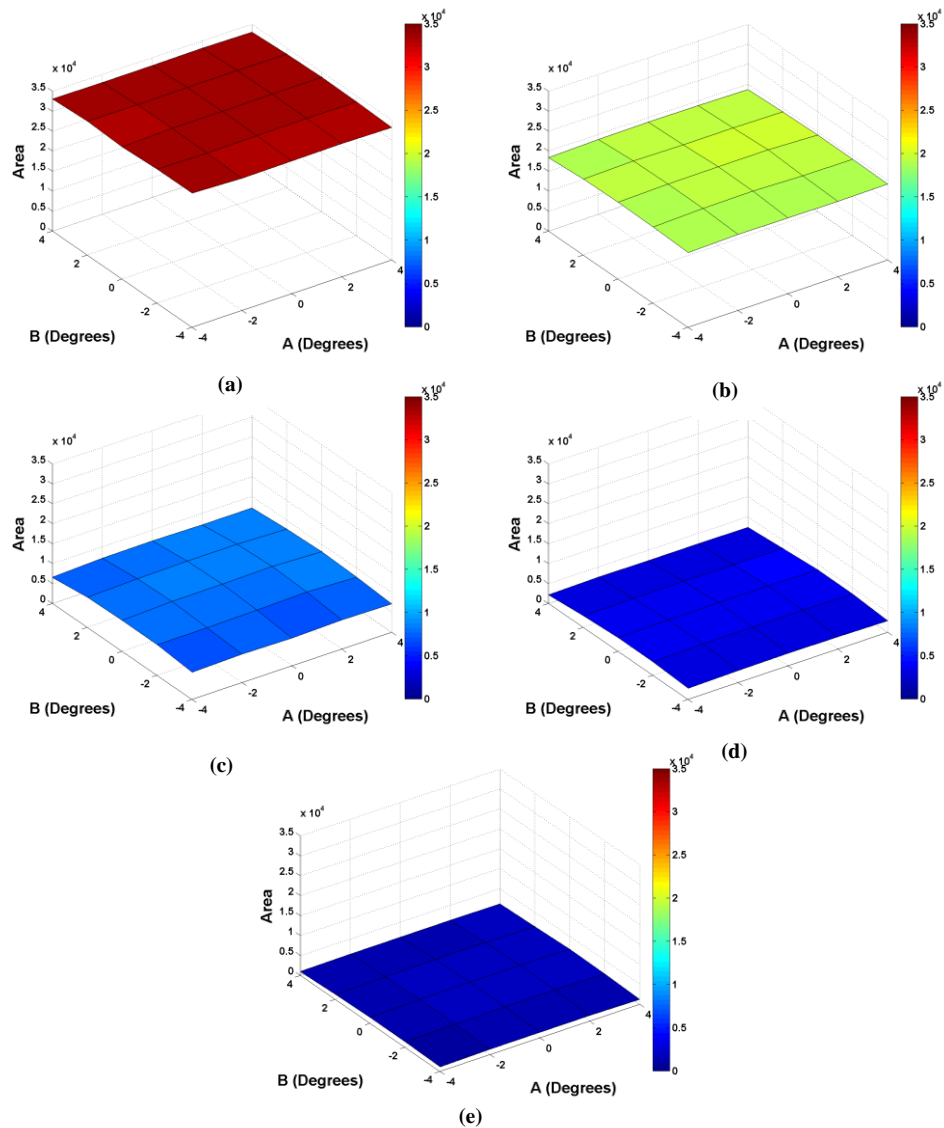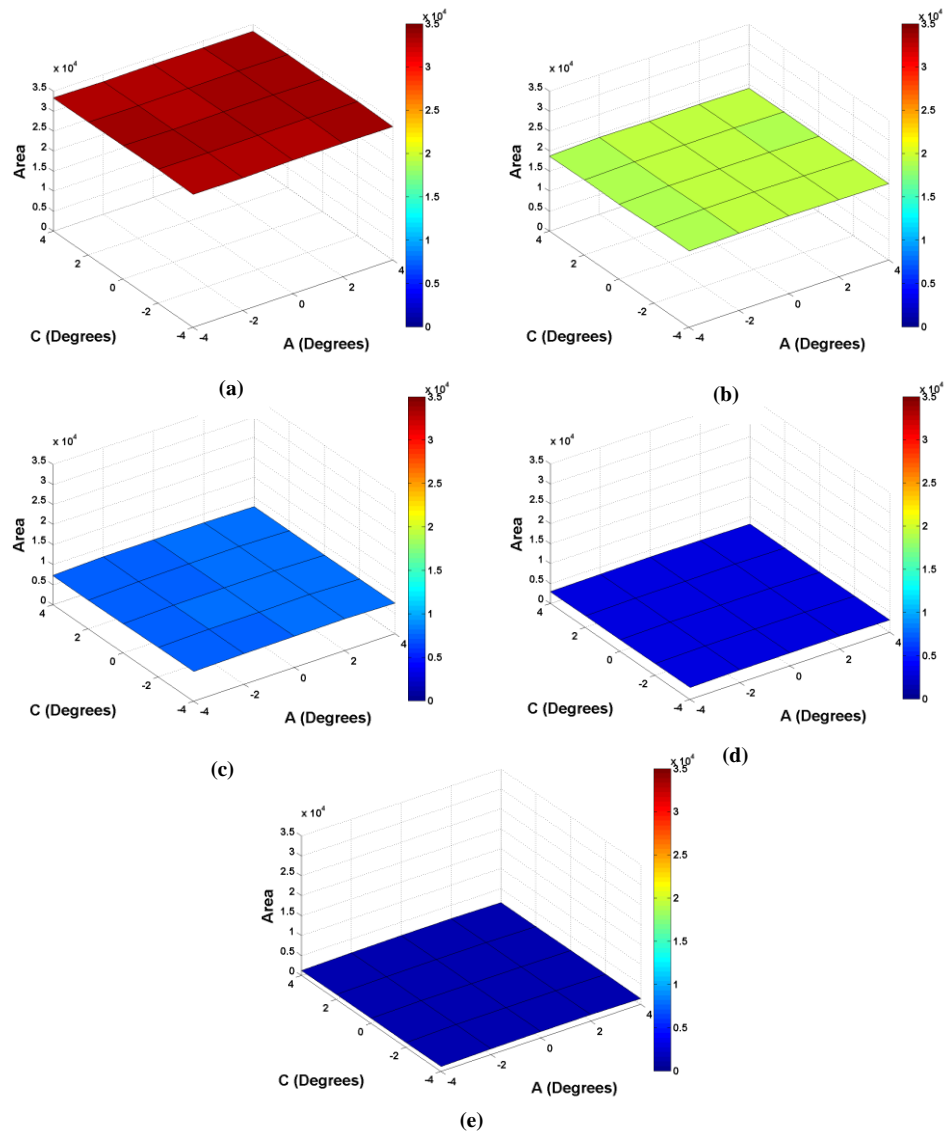
(c)

(d)

(e)
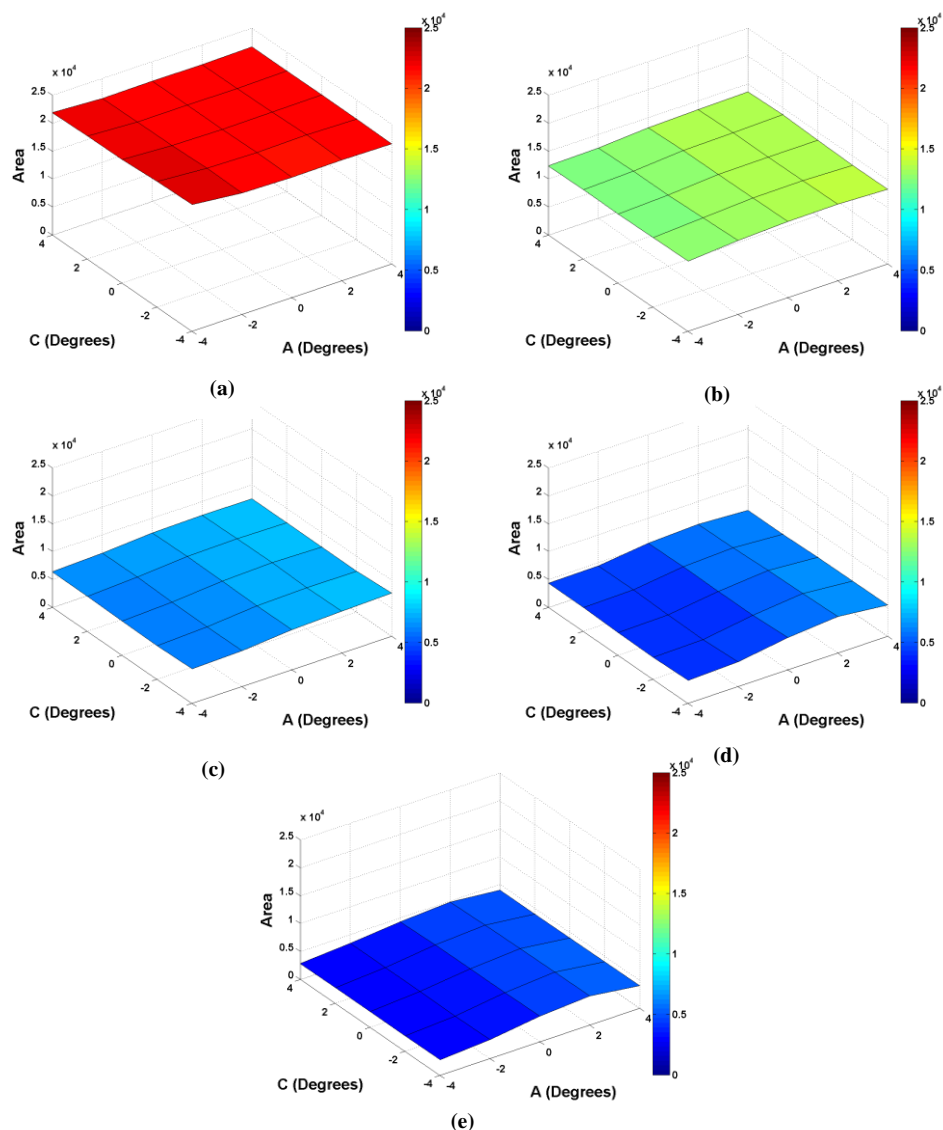
Figure C.2 AC Angle LRF Restored Intensity Area (Aluminium)

Nominal SSD (mm)	Restored Intensity Area Mean	Restored Intensity Area (AC) Standard Deviation
500	21711.60	305.49
1000	13152.60	483.97
2000	7005.02	549.00
3000	5148.29	813.15
4000	3948.78	810.00

Table C.2 AC Angle LRF Restored Intensity Area Statistical Performance (Aluminium)

Restored Intensity viewed from BC Angle

(a)

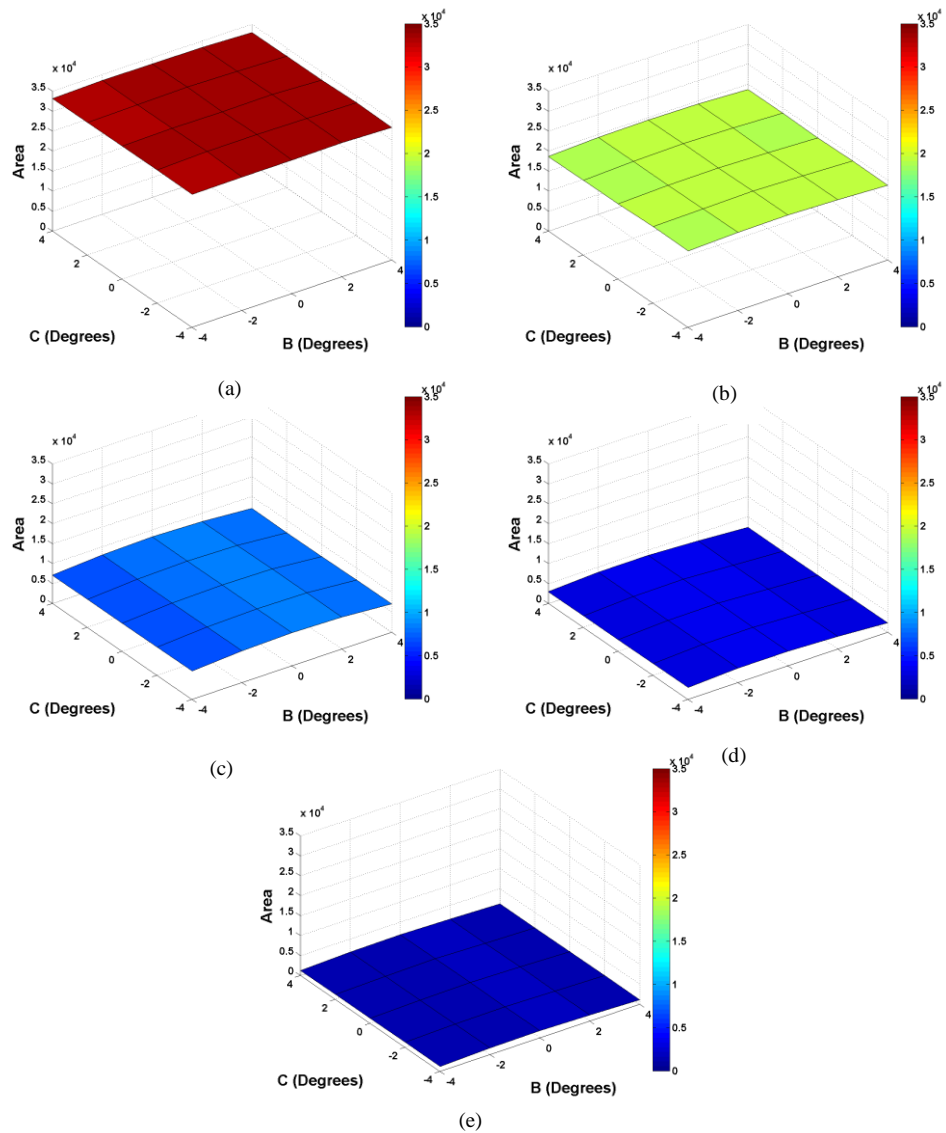(b)

(c)

(d)

(e)
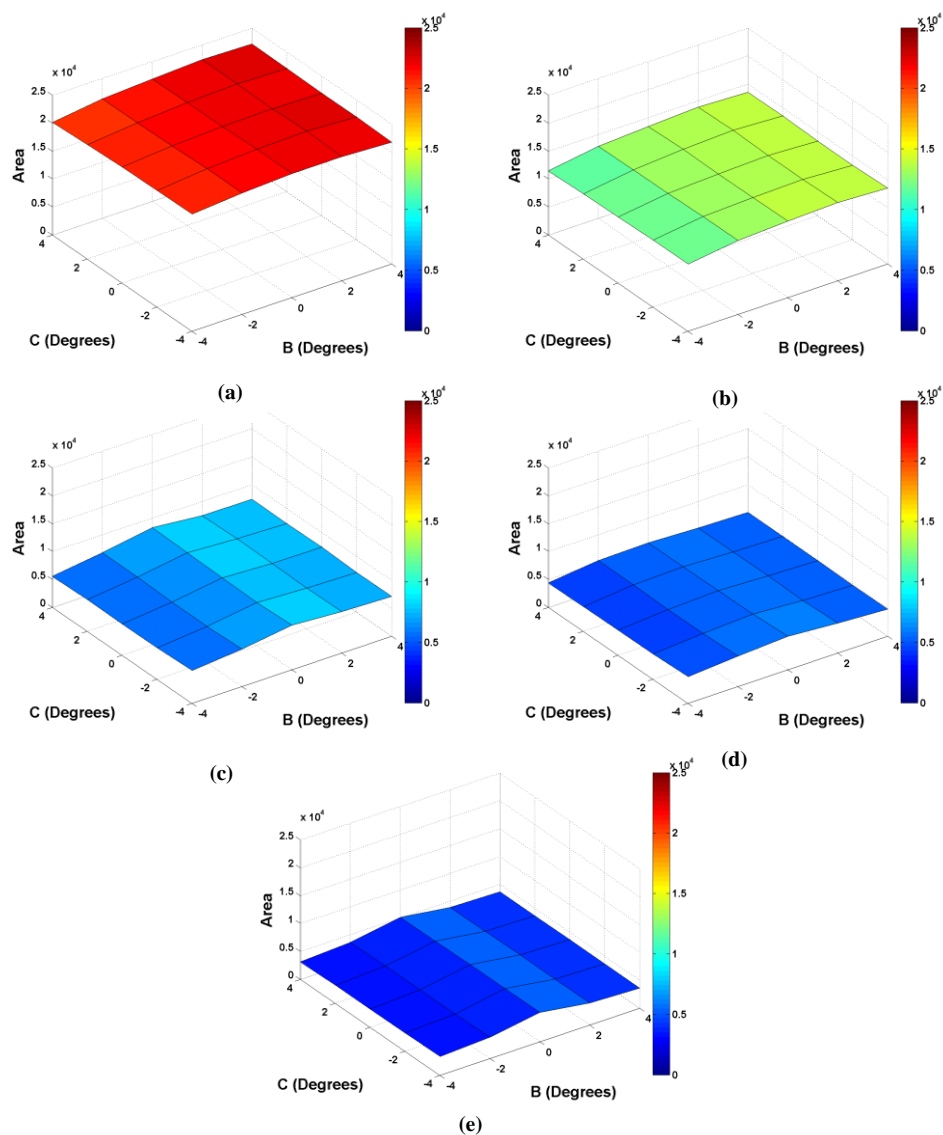
Figure C.3 BC Angle LRF Restored Intensity Area (Aluminium)

Nominal SSD (mm)	Restored Intensity Area Mean	Restored Intensity Area (BC) Standard Deviation
500	21711.60	622.21
1000	13152.60	759.49
2000	7005.02	828.84
3000	5148.29	416.91
4000	3948.78	676.48

Table C.3 BC Angle LRF Restored Intensity Area Statistical Performance (Aluminium)

351

Single Shot Histogram
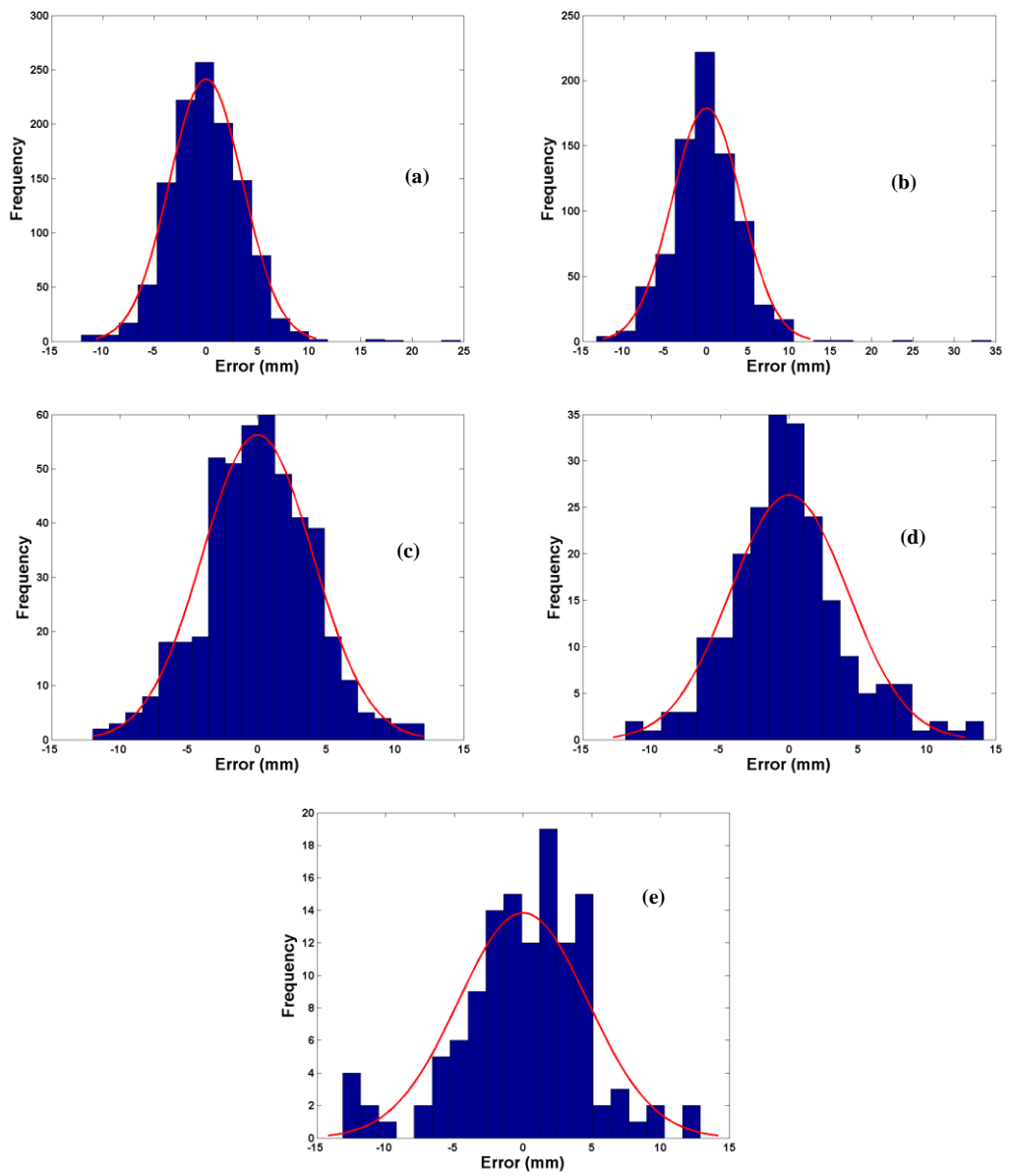
Figure C. 4 LRF Range Data Variation (Aluminium)

C.2 Steel Surfaces

Distance Error viewed from AB Angle

(a)

(b)

(c)

(d)

(e)
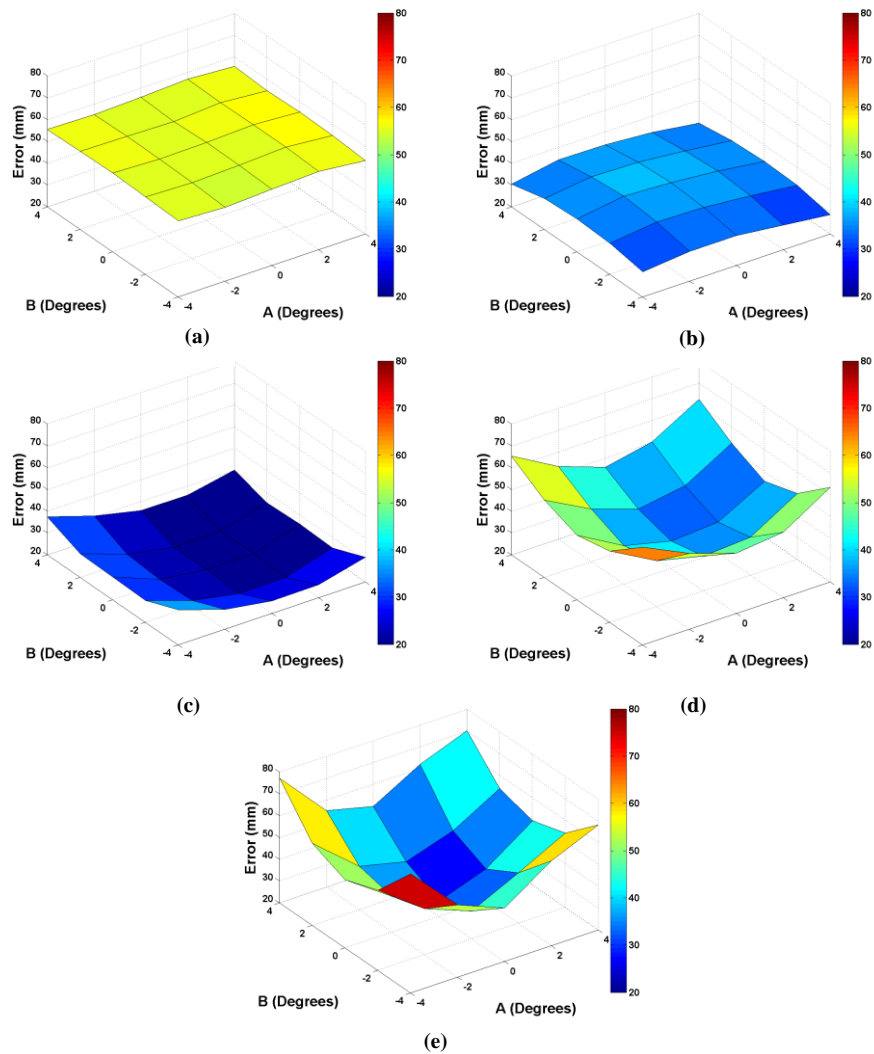
Figure C.5 AB Angle LRF RMSE Mean Error (Steel)

Nominal SSD (mm)	RMSE Mean (mm)	Distance Error (AB) Standard Deviation (mm)
500	55.47	0.82
1000	33.82	2.48
2000	26.00	5.29
3000	48.17	9.74
4000	50.72	13.35

Table C.4 AB Angle LRF RMSE Mean Error (Steel)

353

Distance Error viewed from AC Angle

(a)

(b)

(c)

(d)

(e)

Figure C.6 AC Angle LRF RMSE Mean Error (Steel)

Nominal SSD (mm)	RMSE Mean (mm)	Distance Error (AC) Standard Deviation (mm)
500	55.47	0.77
1000	33.82	1.95
2000	26.00	4.25
3000	48.17	7.10
4000	50.72	9.60

Table C.5 AC Angle LRF RMSE Mean Error (Steel)

Distance Error viewed from BC Angle

(a)

(b)

(c)

(d)

(e)
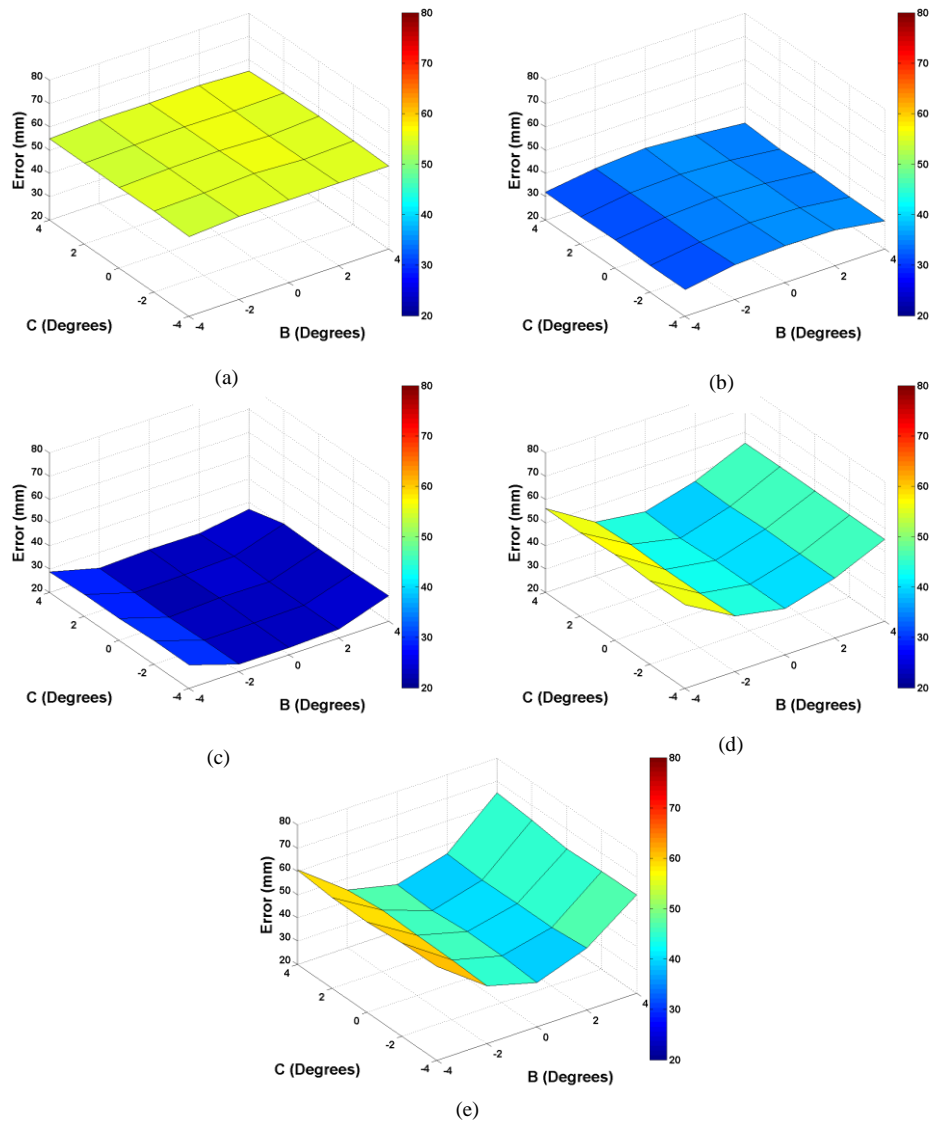
Figure C.7 BC Angle LRF RMSE Mean Error (Steel)

Nominal SSD (mm)	RMSE Mean (mm)	Distance Error (BC) Standard Deviation (mm)
500	55.47	0.57
1000	33.82	1.64
2000	26.00	3.26
3000	48.17	6.66
4000	50.72	9.22

Table C.6 BC Angle LRF RMSE Mean Error (Steel)

355

Restored Intensity viewed from AB Angle

(a)

(b)

(c)

(d)

(e)

Figure C.8 AB Angle LRF Restored Intensity Area (Steel)

Nominal SSD (mm)	Restored Intensity Area Mean	Restored Intensity Area (AB) Standard Deviation
500	33386.10	235.28
1000	19118.80	357.68
2000	7650.40	579.15
3000	3114.57	520.29
4000	1456.78	280.03

Table C.7 AB Angle LRF Restored Intensity Area Statistical Performance (Steel)

Restored Intensity viewed from AC Angle

(a)

(b)

(c)

(d)

(e)

Figure C.9 AC Angle LRF Restored Intensity Area (Steel)

Nominal SSD (mm)	Restored Intensity Area Mean	Restored Intensity Area (AC) Standard Deviation
500	33386.10	137.04
1000	19118.80	187.67
2000	7650.40	219.34
3000	3114.57	116.14
4000	1456.78	128.58

Table C. 8 AC Angle LRF Restored Intensity Area Statistical Performance (Steel)

Restored Intensity viewed from BC Angle

(a)

(b)

(c)

(d)

(e)

Figure C.10 BC Angle LRF Restored Intensity Area (Steel)

Nominal SSD (mm)	Restored Intensity Area Mean	Restored Intensity Area (BC) Standard Deviation
500	33386.10	225.07
1000	19118.80	335.59
2000	7650.40	527.66
3000	3114.57	506.83
4000	1456.78	246.34

Table C. 9 BC Angle LRF Restored Intensity Area Statistical Performance (Steel)

Percentage Rejections viewed from AB Angle

(a)

(b)

(c)

(d)

(e)
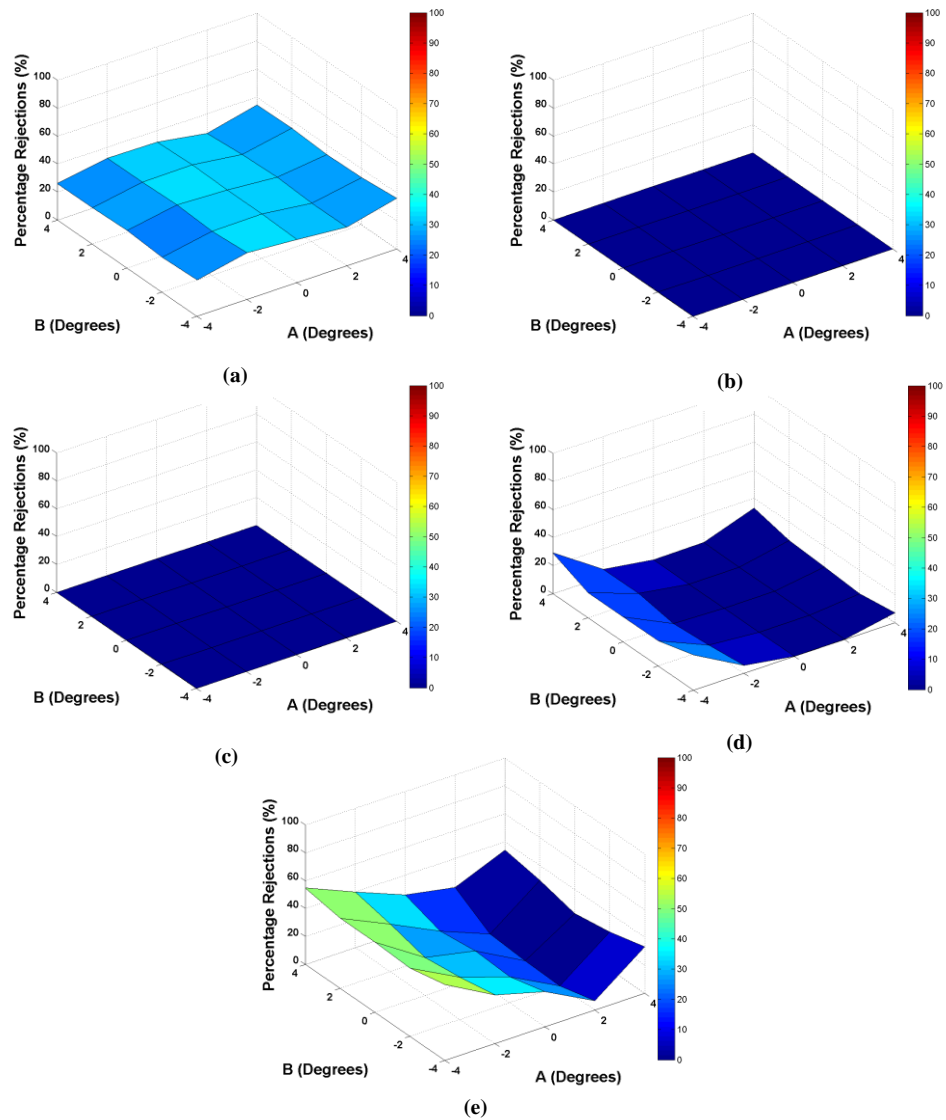
Figure C.11 AB Angle LRF Percentage Rejections (Steel)

Nominal SSD (mm)	Percentage Rejection Mean	Percentage Rejection (AB) Standard Deviation
500	30.47	3.32
1000	0	0
2000	0	0
3000	6.55	8.55
4000	28.33	15.99

Table C.10 AB Angle LRF Percentage Rejection Statistical Performance (Steel)

Percentage Rejections viewed from AC Angle

(a)

(b)

(c)

(d)

(e)
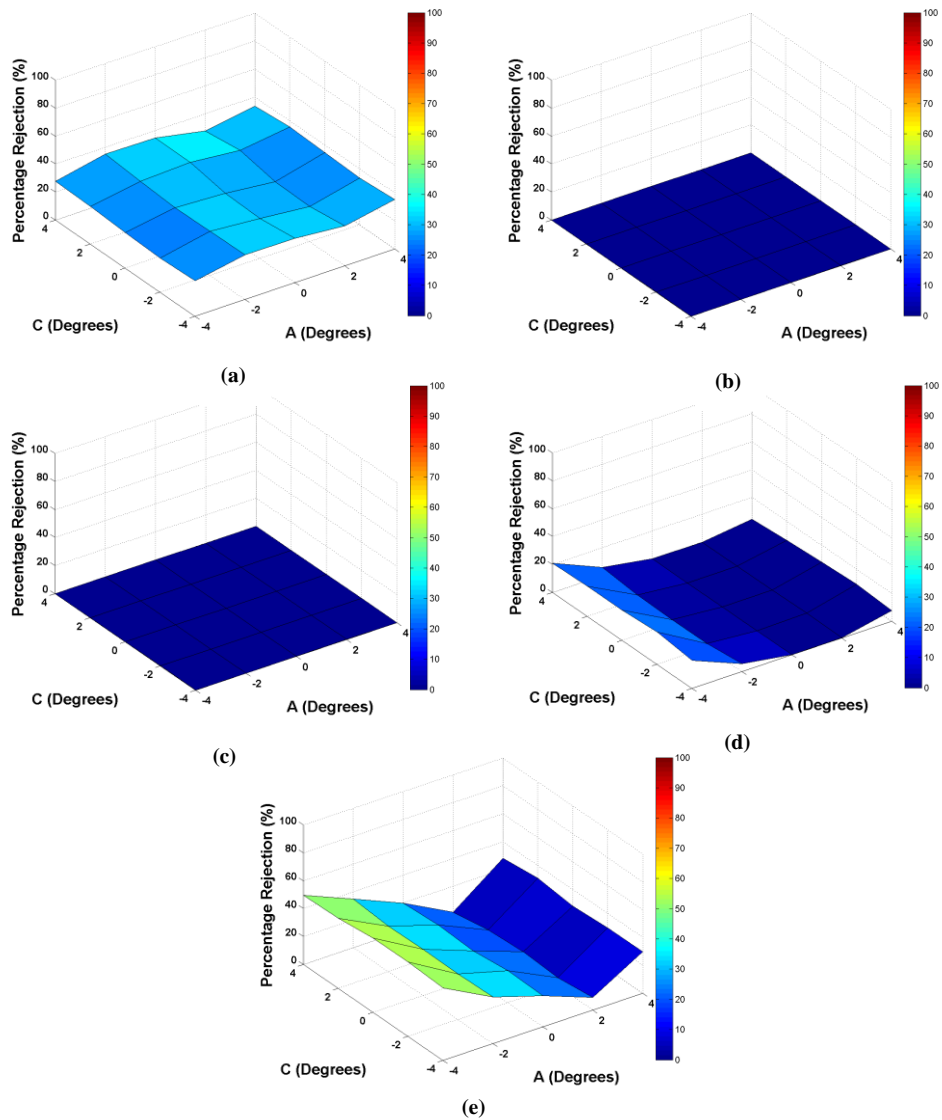
Figure C.12 AC Angle LRF Percentage Rejections (Steel)

Nominal SSD (mm)	Percentage Rejection Mean	Percentage Rejection (AC) Standard Deviation
500	30.47	3.68
1000	0	0
2000	0	0
3000	6.55	8.18
4000	28.33	15.38

Table C.11 AC Angle LRF Percentage Rejection Statistical Performance (Steel)

Percentage Rejections viewed from BC Angle

(a)

(b)

(c)

(d)

(e)
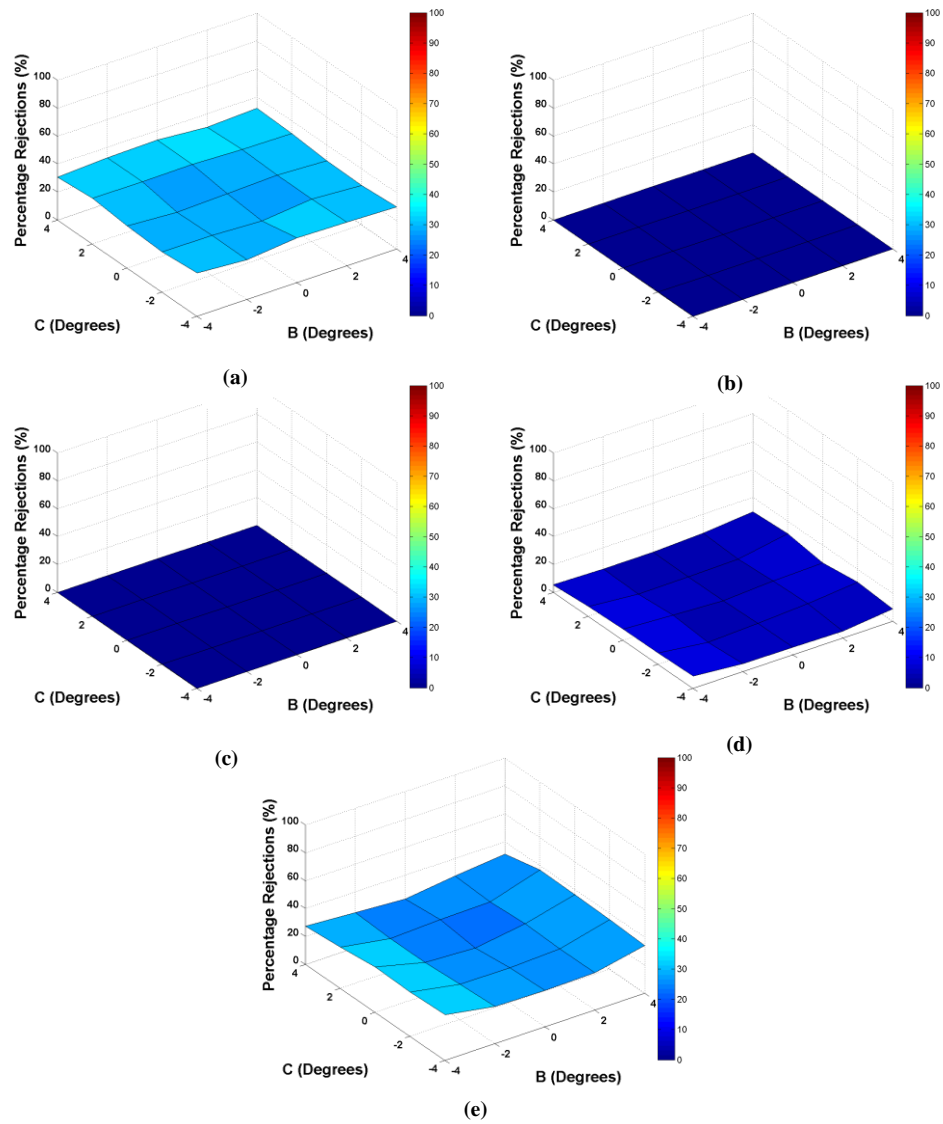
Figure C.13 BC Angle LRF Percentage Rejections (Steel)

Nominal SSD (mm)	Percentage Rejection Mean	Percentage Rejection (BC) Standard Deviation
500	30.47	1.75
1000	0	0
2000	0	0
3000	6.55	2.14
4000	28.33	4.34

Table C.12 BC Angle LRF Percentage Rejection Statistical Performance (Steel)

Valid Measurement Probability
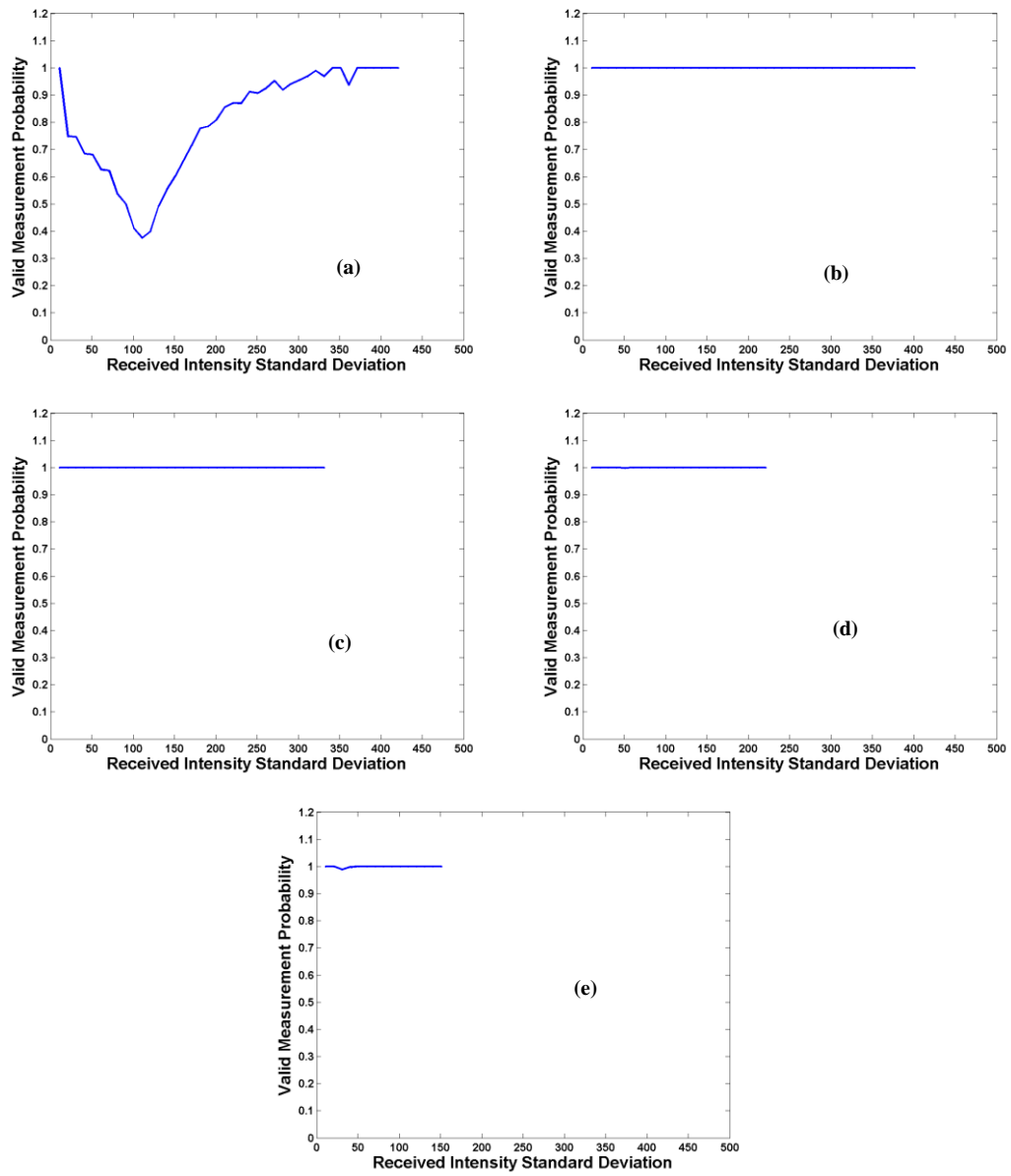
Figure C.14 LRF Range Validity as a function of Received Intensity Standard Deviation (Steel)

Scan Plan View
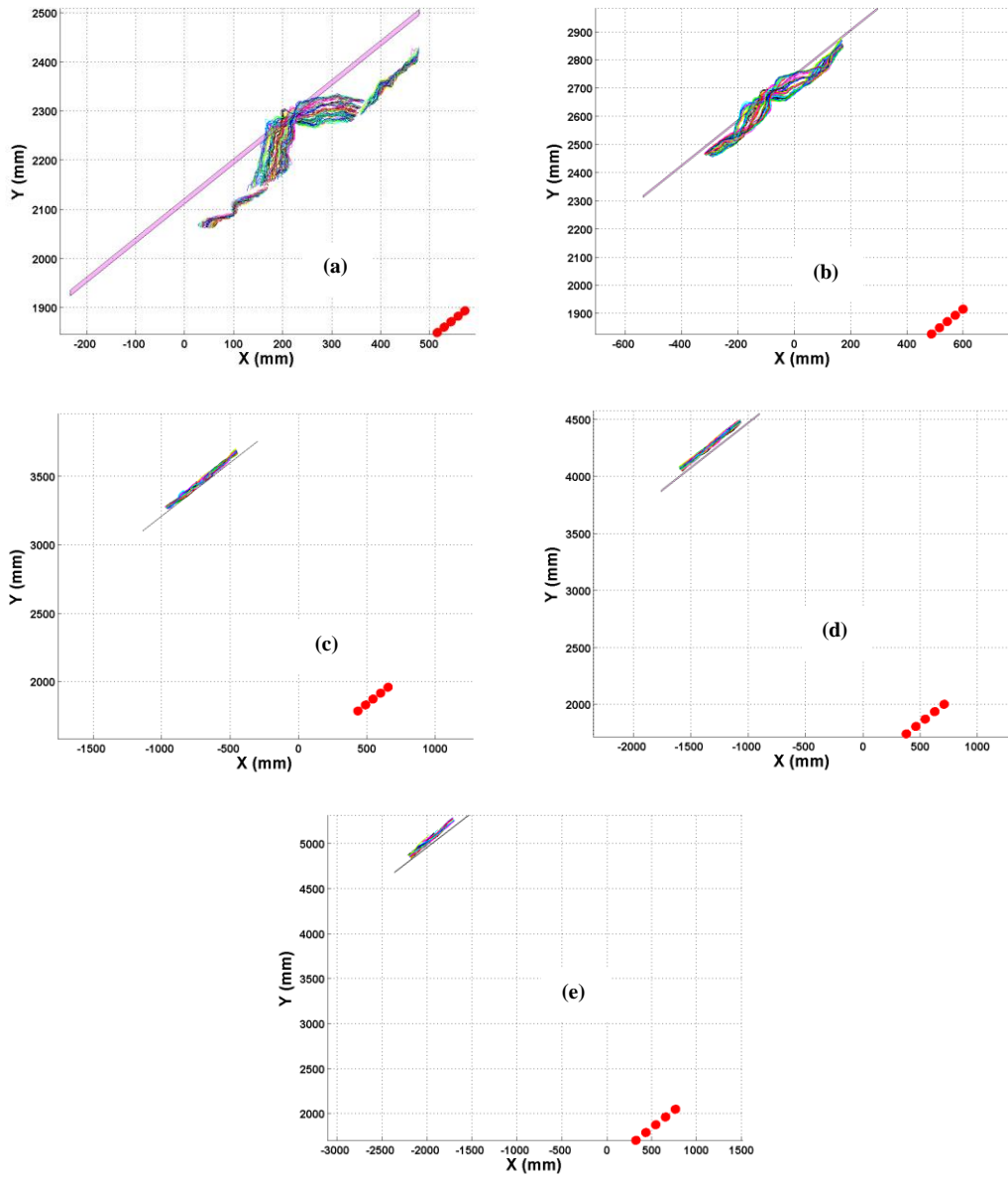
Figure C.15 LRF Scan Plan View (Steel)

Distance Error
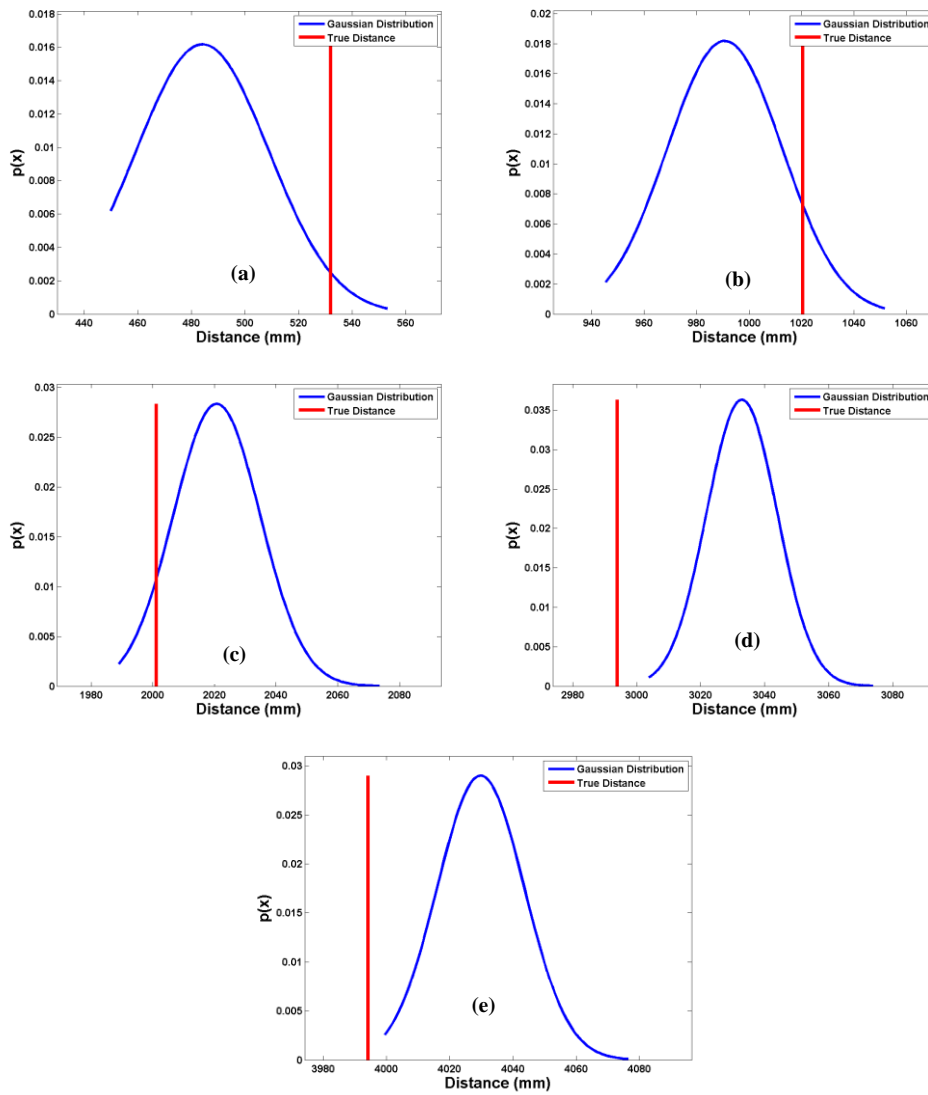
Figure C.16 LRF Distance Error (Steel)

Nominal SSD (mm)	Distance Error Mean (mm)	Distance Error Standard Deviation (mm)	Distance Error Minimum (mm)	Distance Error Max (mm)
500	-47.84	24.66	-81.98	21.10
1000	-29.75	21.95	-75.19	32.29
2000	19.58	14.08	-12.14	72.35
3000	38.95	10.98	9.92	79.94
4000	35.57	13.75	5.32	82.20

Table C.13 LRF Distance Error Statistical Performance

Single Shot Histogram
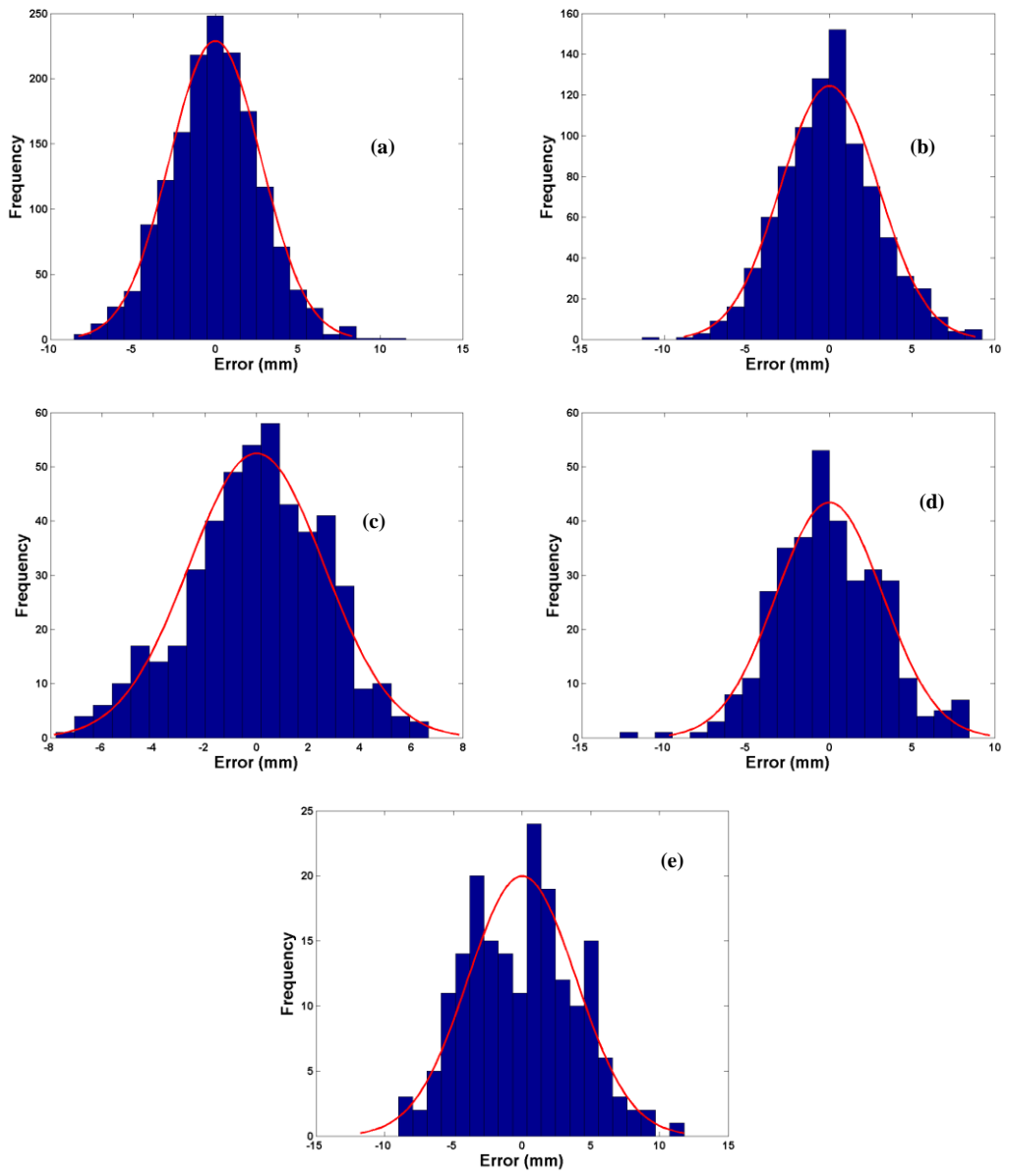
Figure C.17 LRF Range Data Variation (Steel)

C.3 Stainless Steel Surfaces

Distance Error viewed from AB Angle
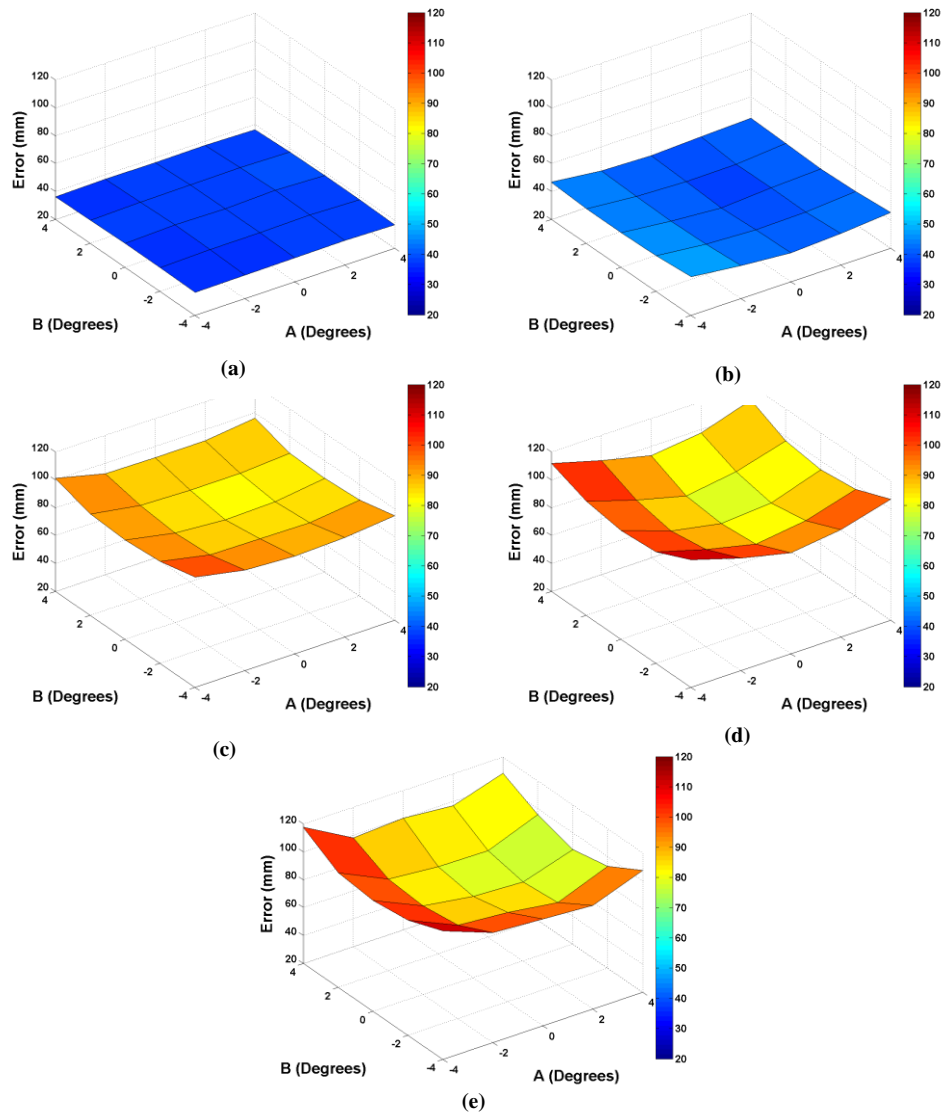
Figure C.18 AB Angle LRF RMSE Mean Error (Stainless Steel)

Nominal SSD (mm)	RMSE Mean (mm)	Distance Error (AB) Standard Deviation (mm)
500	37.37	0.75
1000	42.78	2.26
2000	89.82	4.93
3000	94.92	9.44
4000	94.04	11.06

Table C.14 AB Angle LRF Distance Error Statistical Performance (Stainless Steel)

Distance Error viewed from AC Angle

(a)

(b)

(c)

(d)

(e)
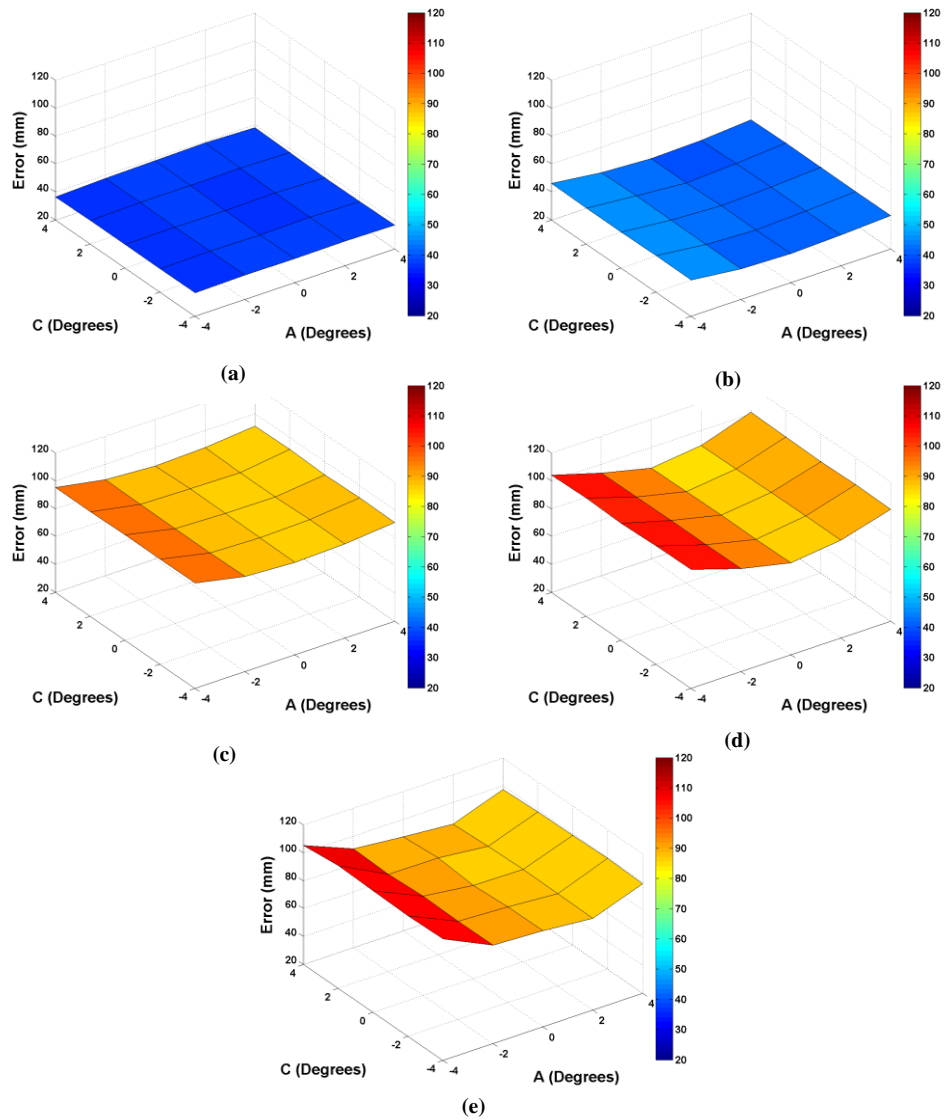
Figure C.19 AC Angle LRF RMSE Mean Error (Stainless Steel)

Nominal SSD (mm)	RMSE Mean (mm)	Distance Error (AC) Standard Deviation (mm)
500	37.37	0.65
1000	42.78	2.02
2000	89.82	3.26
3000	94.92	7.09
4000	94.04	7.88

Table C.15 AC Angle LRF Distance Error Statistical Performance (Stainless Steel)

Distance Error viewed from BC Angle

(a)

(b)

(c)

(d)

(e)
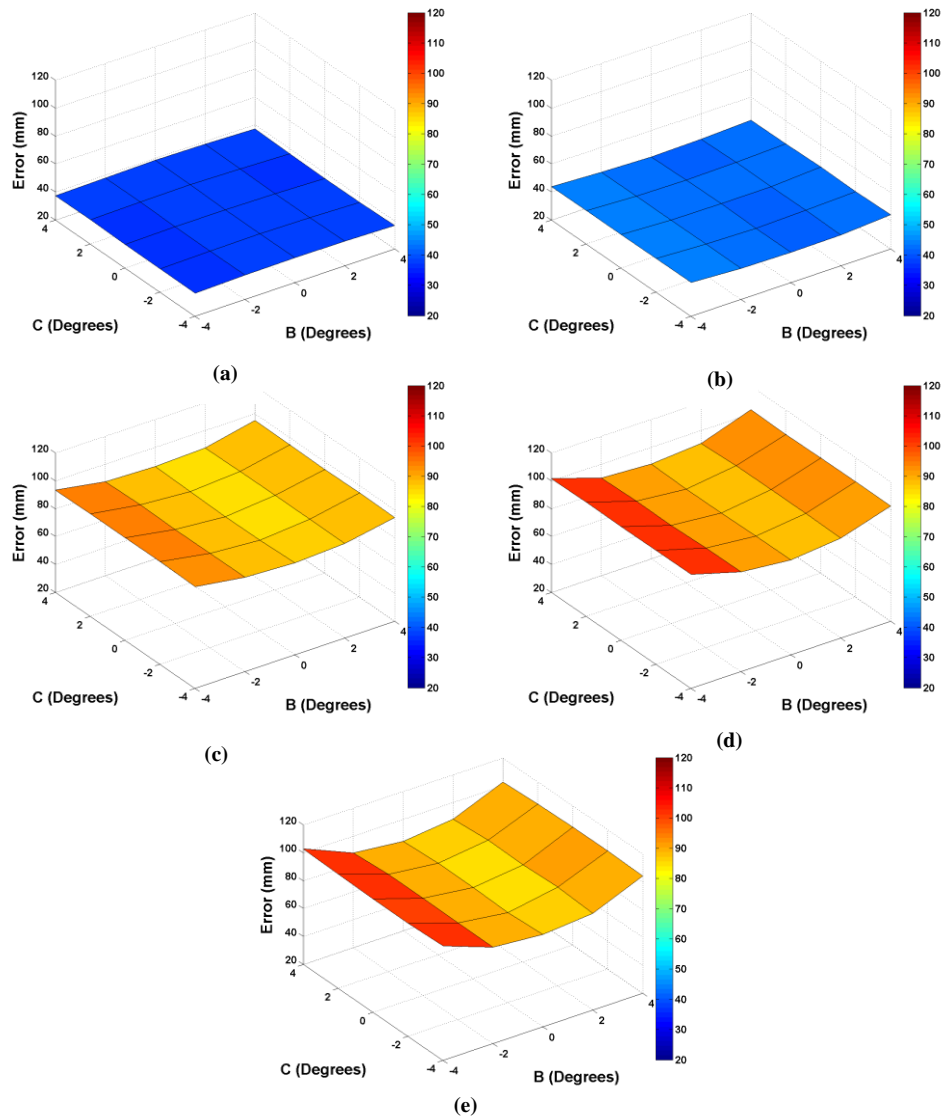
Figure C.20 BC Angle LRF RMSE Mean Error (Stainless Steel)

Nominal SSD (mm)	RMSE Mean (mm)	Distance Error (BC) Standard Deviation (mm)
500	37.37	0.69
1000	42.78	1.03
2000	89.82	3.70
3000	94.92	6.24
4000	94.04	7.73

Table C.16 BC Angle LRF Distance Error Statistical Performance (Stainless Steel)

Restored Intensity viewed from AB Angle

(a)

(b)

(c)

(d)

(e)
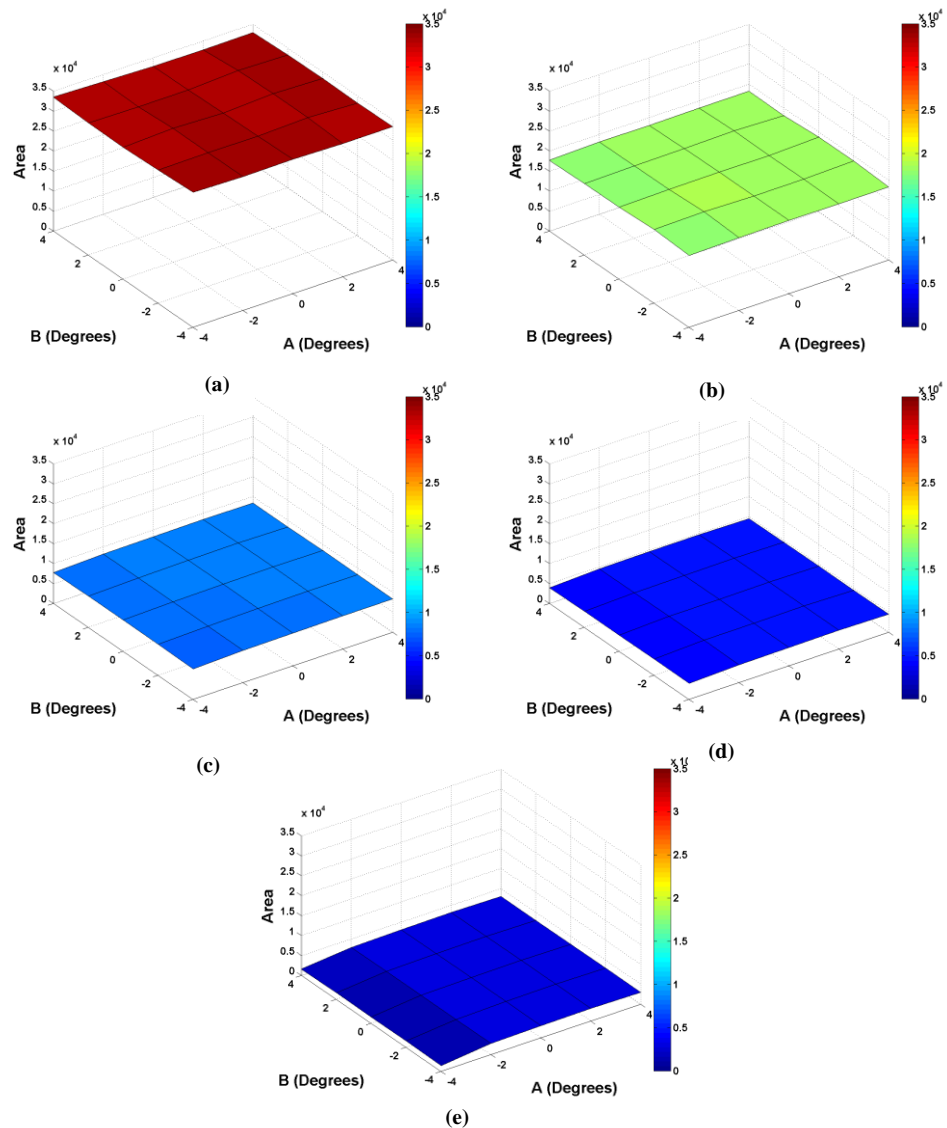
Figure C.21 AB Angle LRF Restored Intensity Area (Stainless Steel)

Nominal SSD (mm)	Restored Intensity Area Mean	Restored Intensity Area (AB) Standard Deviation
500	33313.70	309.88
1000	18262.50	240.53
2000	8230.51	281.82
3000	4469.79	259.41
4000	2722.75	606.80

Table C.17 AB Angle LRF Restored Intensity Area Statistical Performance (Stainless Steel)

Restored Intensity viewed from AC Angle
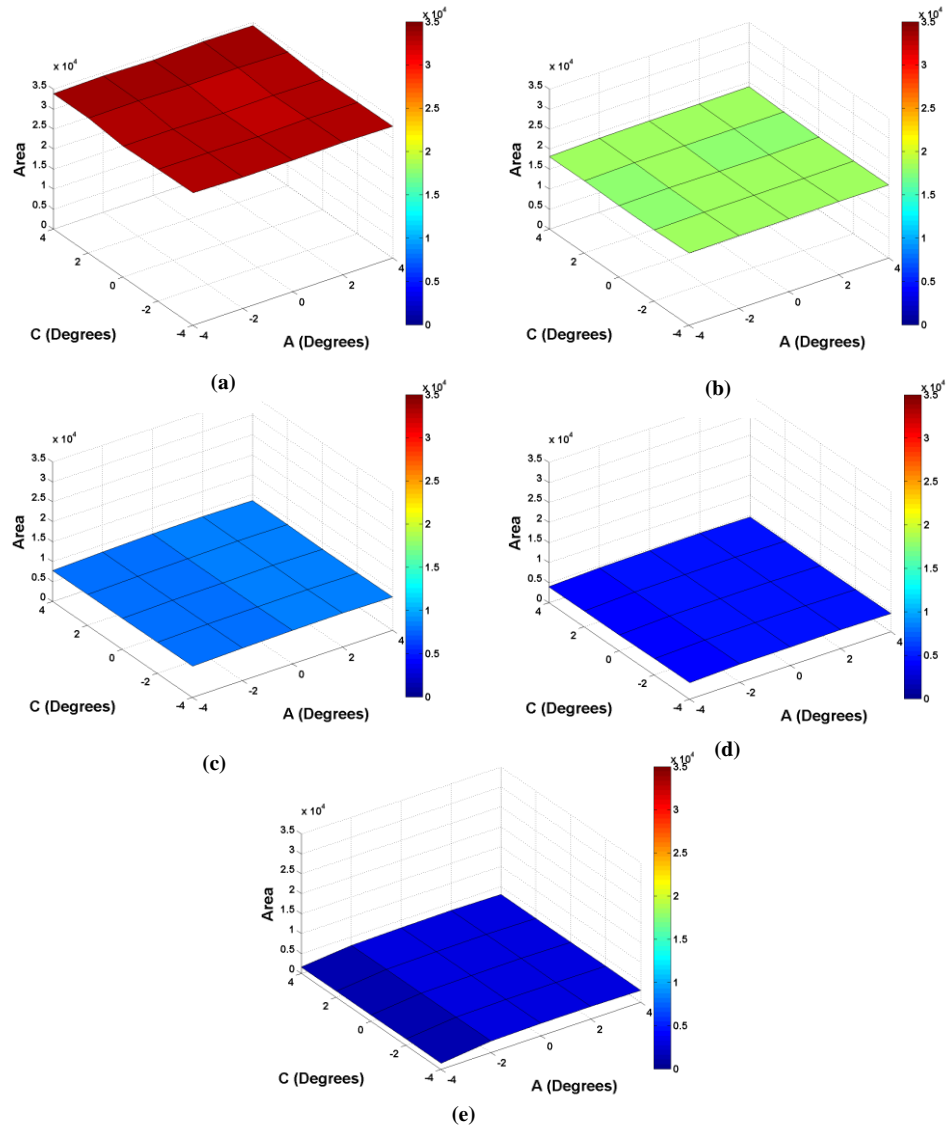
Figure C.22 AC Angle LRF Restored Intensity Area (Stainless Steel)

Nominal SSD (mm)	Restored Intensity Area Mean	Restored Intensity Area (AC) Standard Deviation
500	33313.70	527.45
1000	18262.50	252.61
2000	8230.51	273.67
3000	4469.79	252.37
4000	2722.75	604.66

Table C.18 AC Angle LRF Restored Intensity Area Statistical Performance (Stainless Steel)

Restored Intensity viewed from BC Angle

(a)

(b)

(c)

(d)

(e)
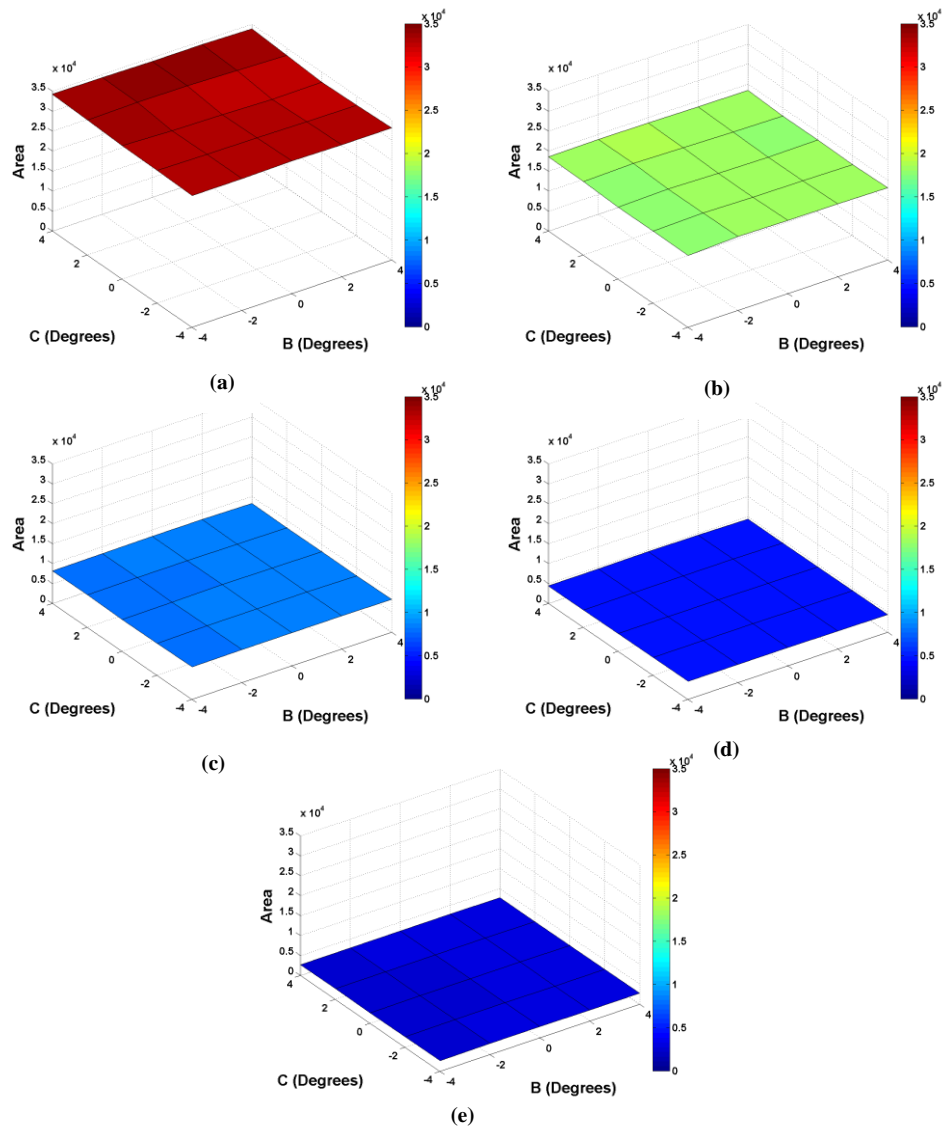
Figure C.23 BC Angle LRF Restored Intensity Area (Stainless Steel)

Nominal SSD (mm)	Restored Intensity Area Mean	Restored Intensity Area (BC) Standard Deviation
500	33313.70	569.78
1000	18262.50	268.38
2000	8230.51	102.55
3000	4469.79	57.79
4000	2722.75	43.12

Table C.19 BC Angle LRF Restored Intensity Area Statistical Performance (Stainless Steel)

Rejected Percentage viewed from AB Angle

(a)

(b)

(c)

(d)

(e)
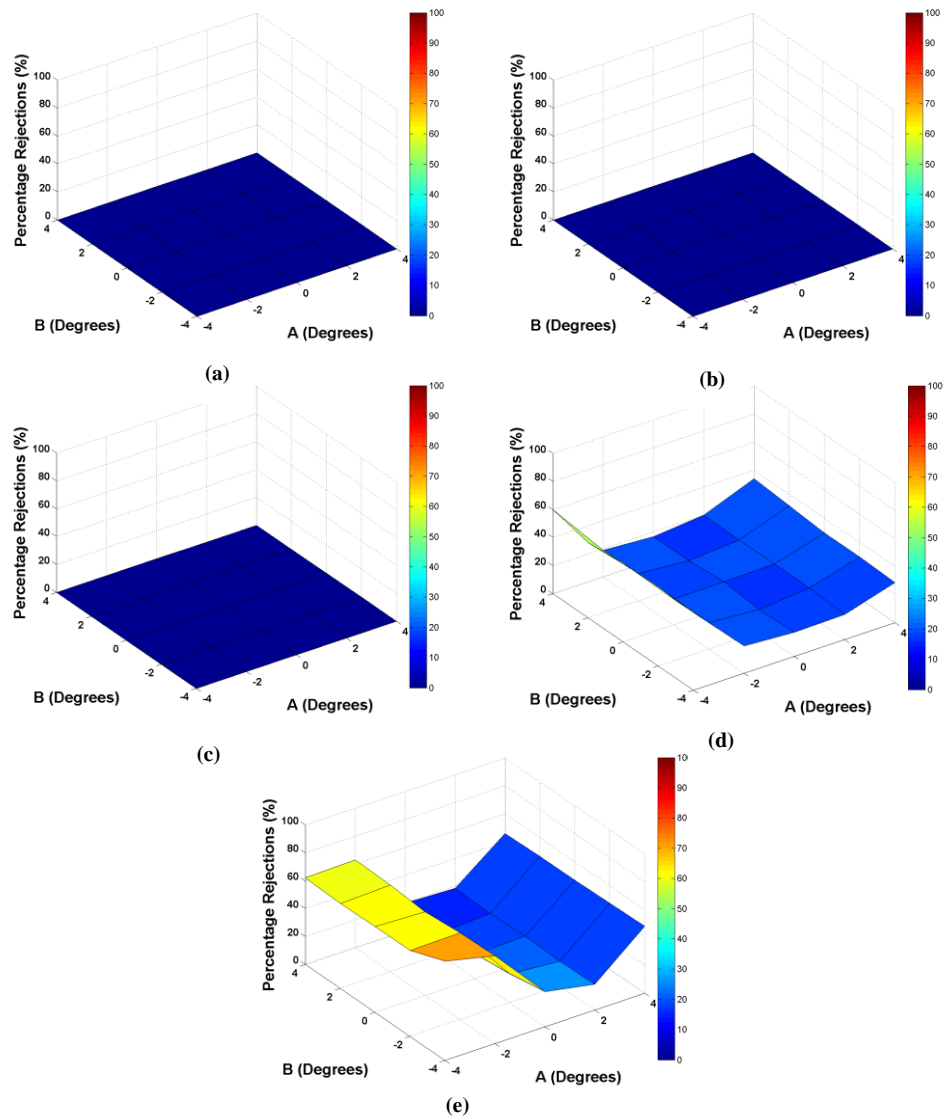
Figure C.24 AB Angle LRF Percentage Rejections (Stainless Steel)

Nominal SSD (mm)	Percentage Rejection Mean	Percentage Rejection (AB) Standard Deviation
500	0	0
1000	0	0
2000	0	0
3000	28.50	15.05
4000	42.10	20.25

Table C.20 AB Angle LRF Percentage Rejection Statistical Performance (Stainless Steel)

Rejected Percentage viewed from AC Angle

(a)

(b)

(c)

(d)

(e)
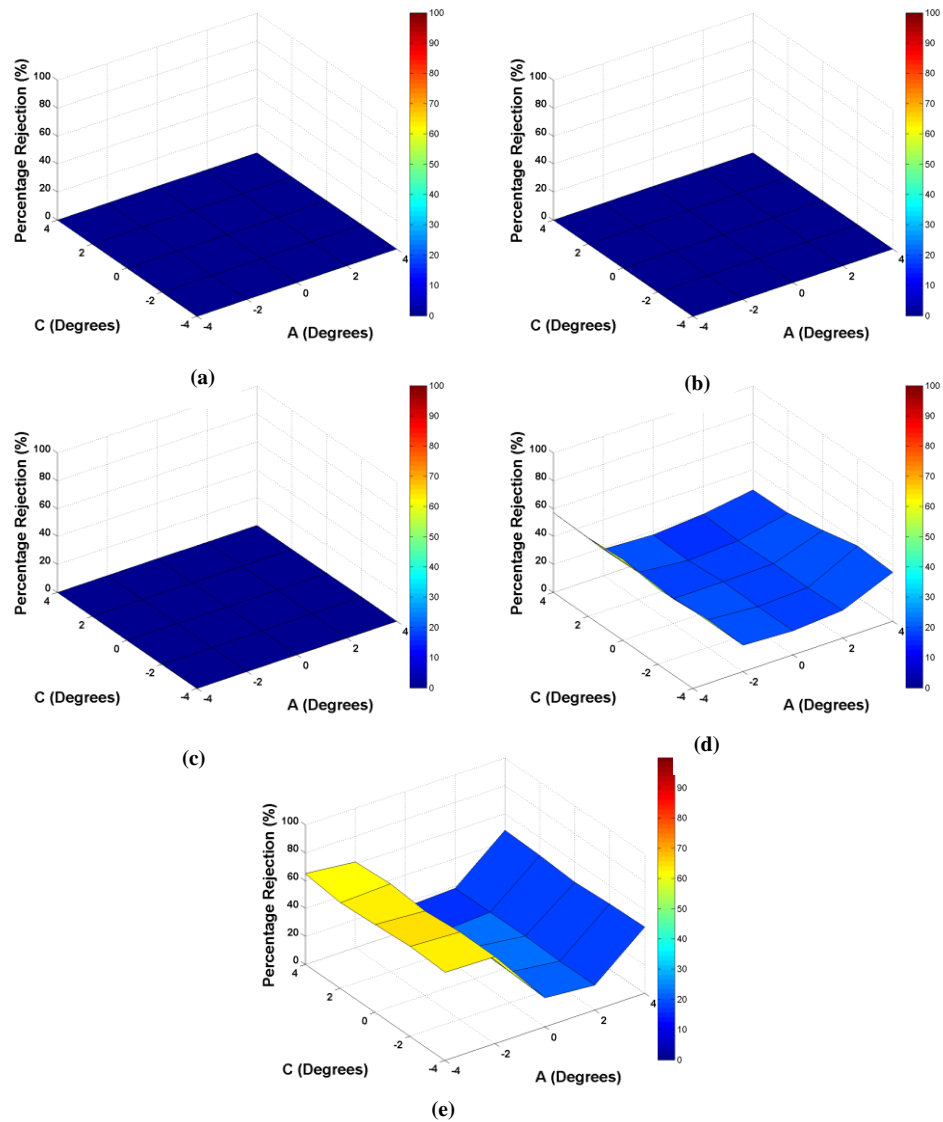
Figure C.25 AC Angle LRF Percentage Rejections (Stainless Steel)

Nominal SSD (mm)	Percentage Rejection Mean	Percentage Rejection (AC) Standard Deviation
500	0	0
1000	0	0
2000	0	0
3000	28.50	15.15
4000	42.10	20.17

Table C.21 AC Angle LRF Percentage Rejection Statistical Performance (Stainless Steel)

Rejected Percentage viewed from BC Angle

(a)

(b)

(c)

(d)

(e)
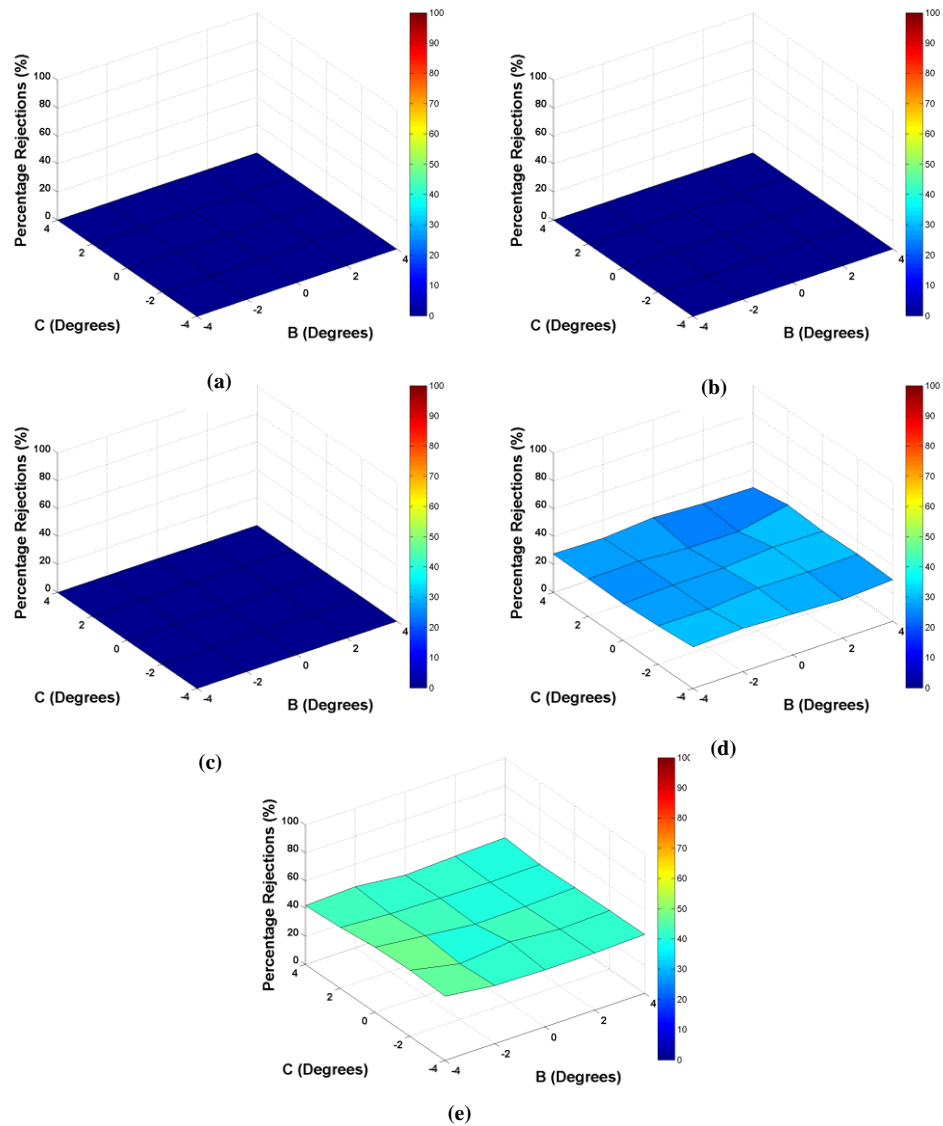
Figure C.26 BC Angle LRF Percentage Rejections (Stainless Steel)

Nominal SSD (mm)	Percentage Rejection Mean	Percentage Rejection (BC) Standard Deviation
500	0	0
1000	0	0
2000	0	0
3000	28.50	1.91
4000	42.10	2.13

Table C.22 BC Angle LRF Percentage Rejection Statistical Performance (Stainless Steel)

Valid Measurement Probability
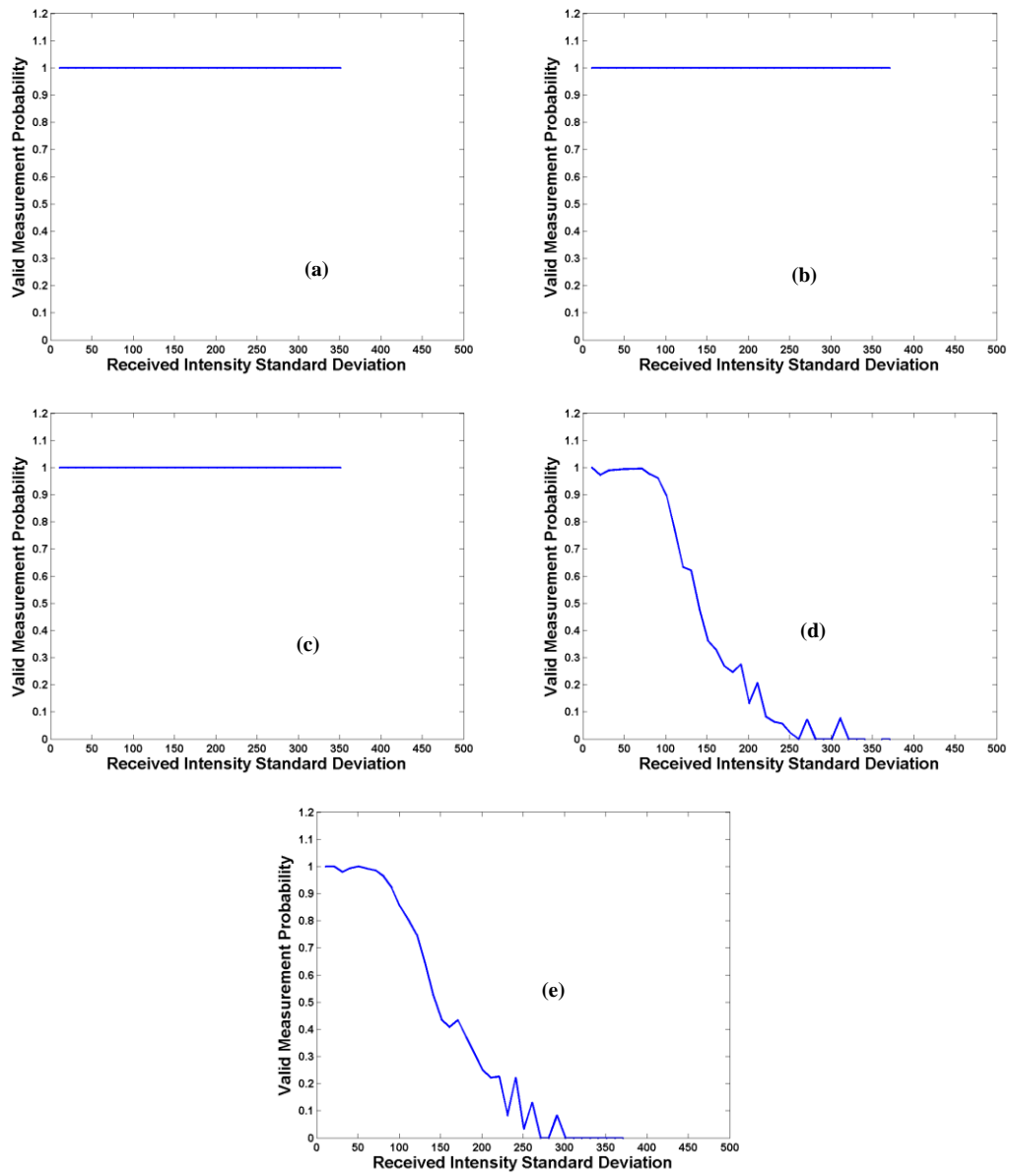
Figure C.27 LRF Range Validity as a function of Received Intensity Standard Deviation (Stainless Steel)

Scan Plan View
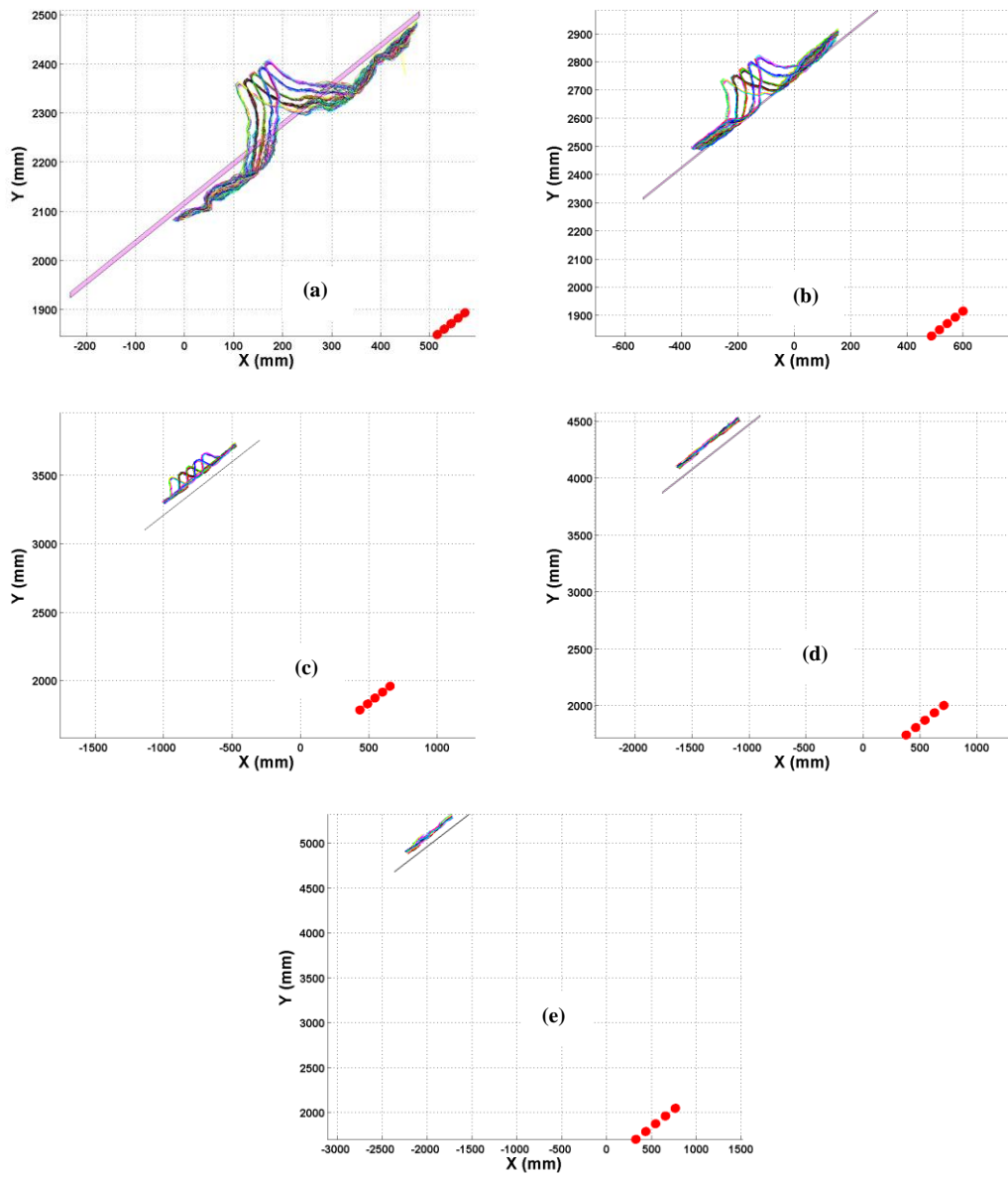
Figure C.28 LRF Scan Plan View (Stainless Steel)

Distance Error
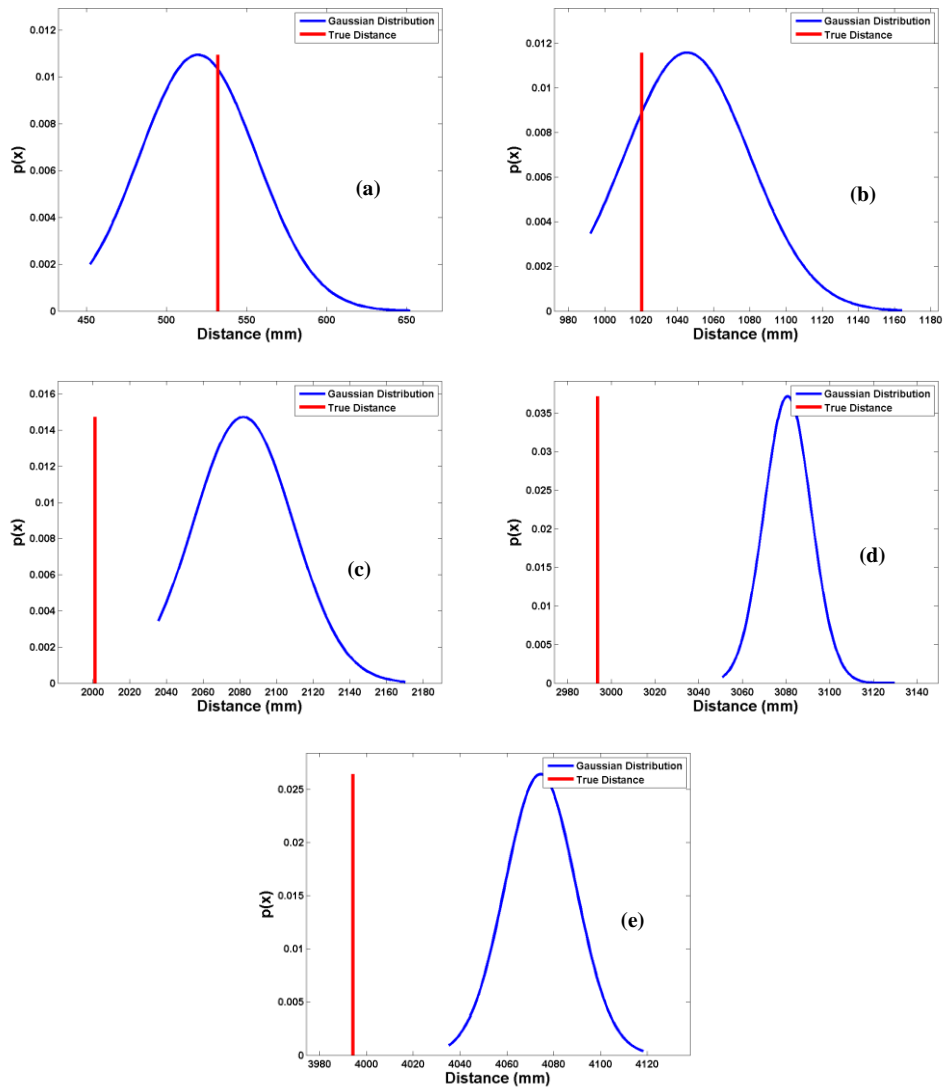
Figure C.29 LRF Distance Error (Stainless Steel)

Nominal SSD (mm)	Distance Error Mean (mm)	Distance Error Standard Deviation (mm)	Distance Error Minimum (mm)	Distance Error Max (mm)
500	-12.37	36.46	-79.52	119.89
1000	24.94	34.41	-28.38	143.51
2000	80.79	27.09	34.67	169.04
3000	86.83	10.72	57.03	135.68
4000	80.04	15.08	41.00	123.96

Table C.23 LRF Distance Error Statistical Performance (Stainless Steel)

Single Shot Histogram
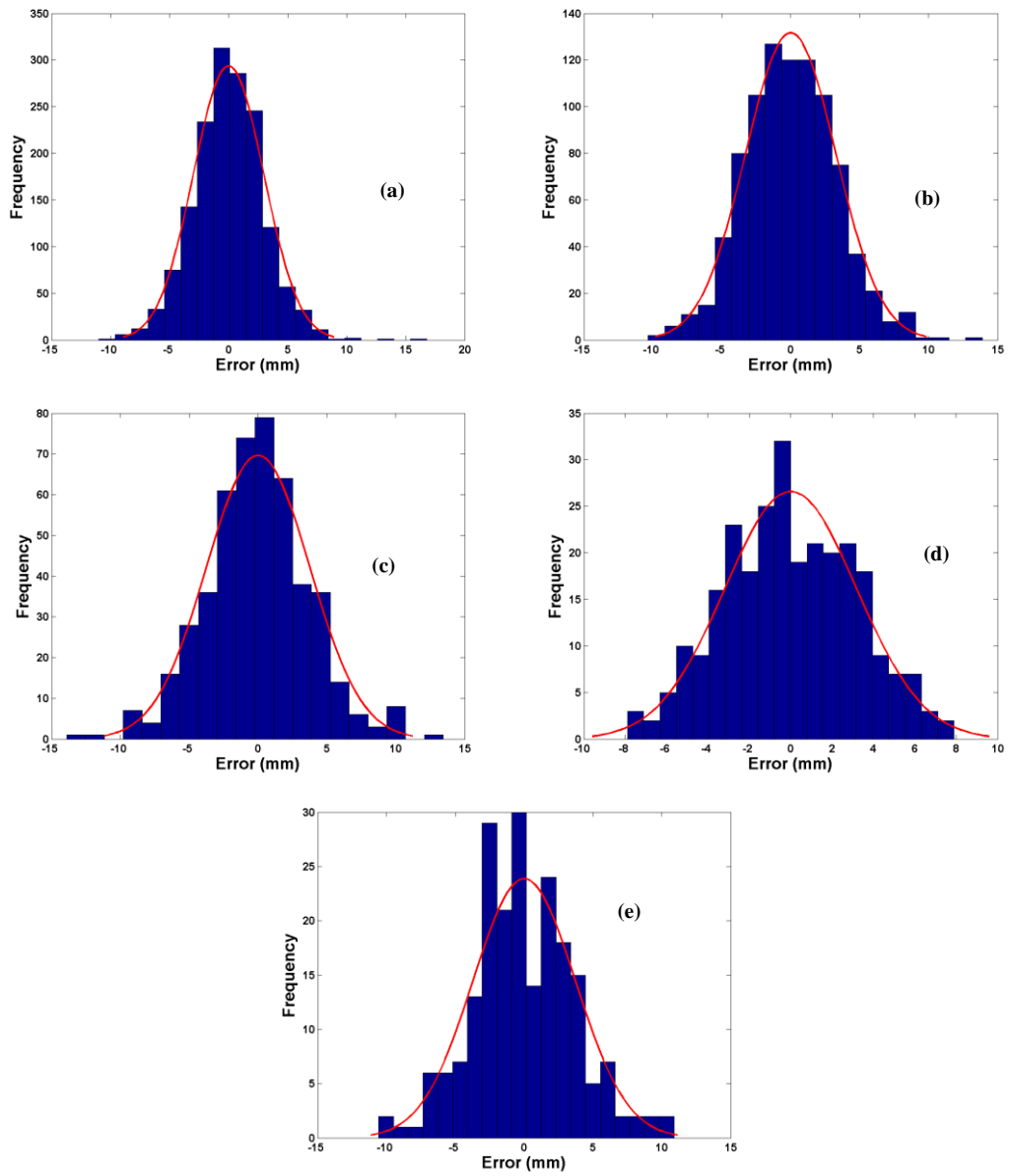
Figure C.30 LRF Range Data Variation (Stainless Steel)

C.4   Concrete Surfaces

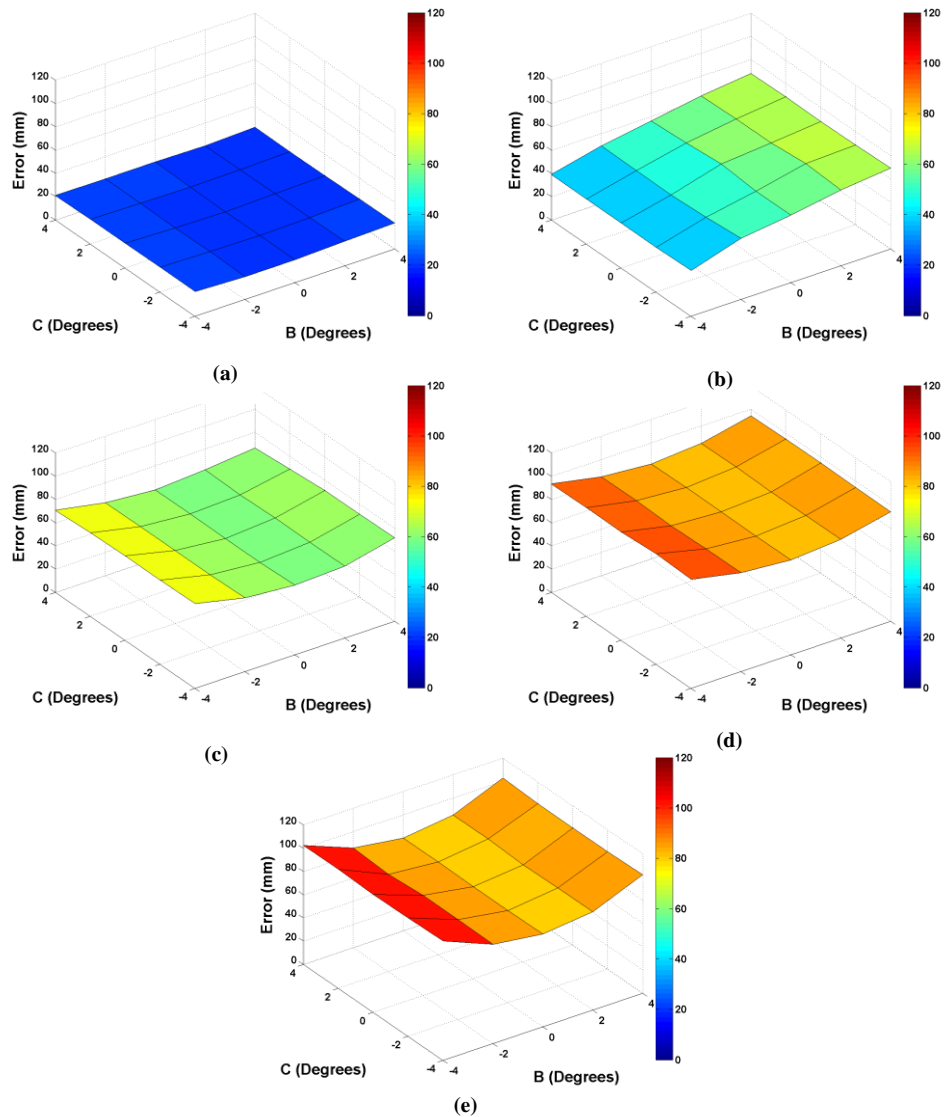## Distance Error viewed from AB Angle

(a)

(b)

(c)

(d)

(e)
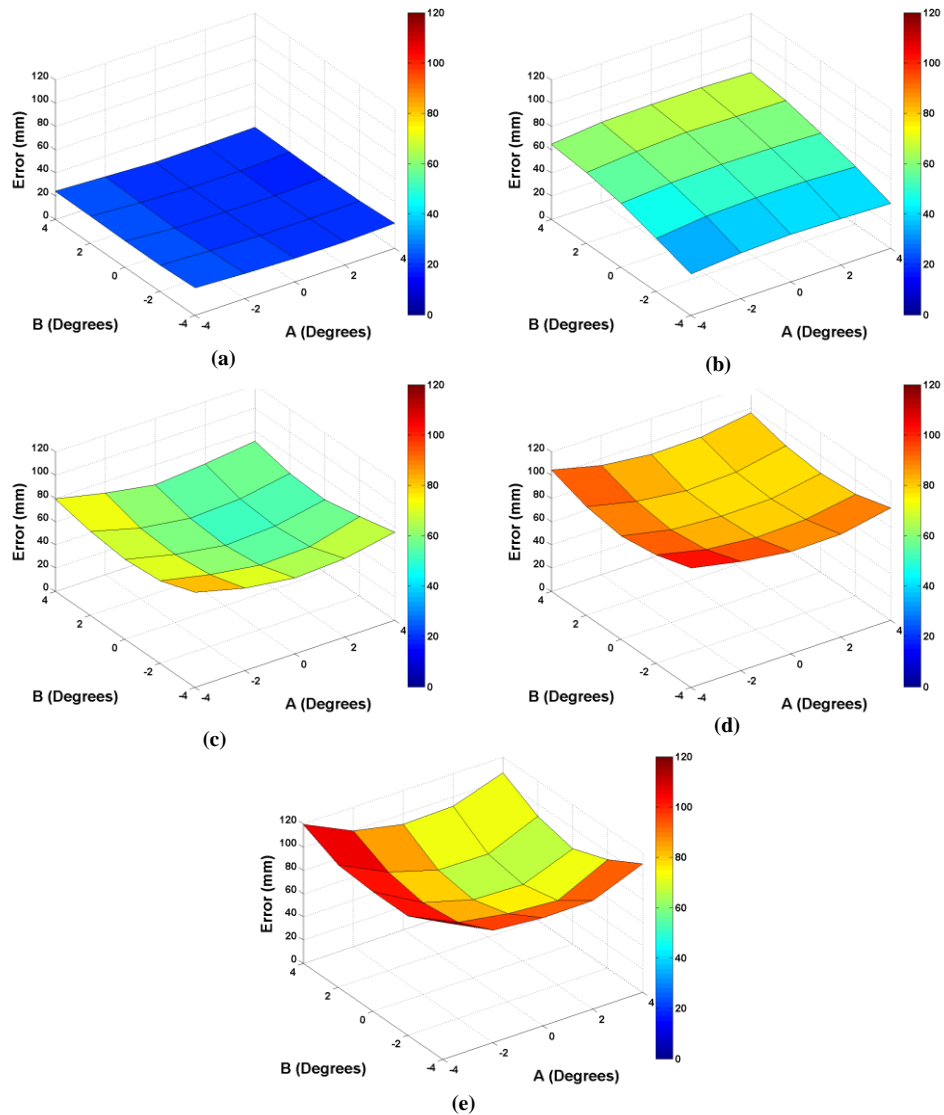
Figure C.31 AB Angle LRF RMSE Mean Error (Concrete)

Nominal SSD (mm)	RMSE Mean (mm)	Distance Error (AB) Standard Deviation (mm)
500	20.80	1.60
1000	55.98	11.12
2000	65.28	7.92
3000	88.00	7.60
4000	90.73	15.22

Table C.24 AB Angle LRF Distance Error Statistical Performance (Concrete)

Distance Error viewed from AC Angle

(a)

(b)

(c)

(d)

(e)
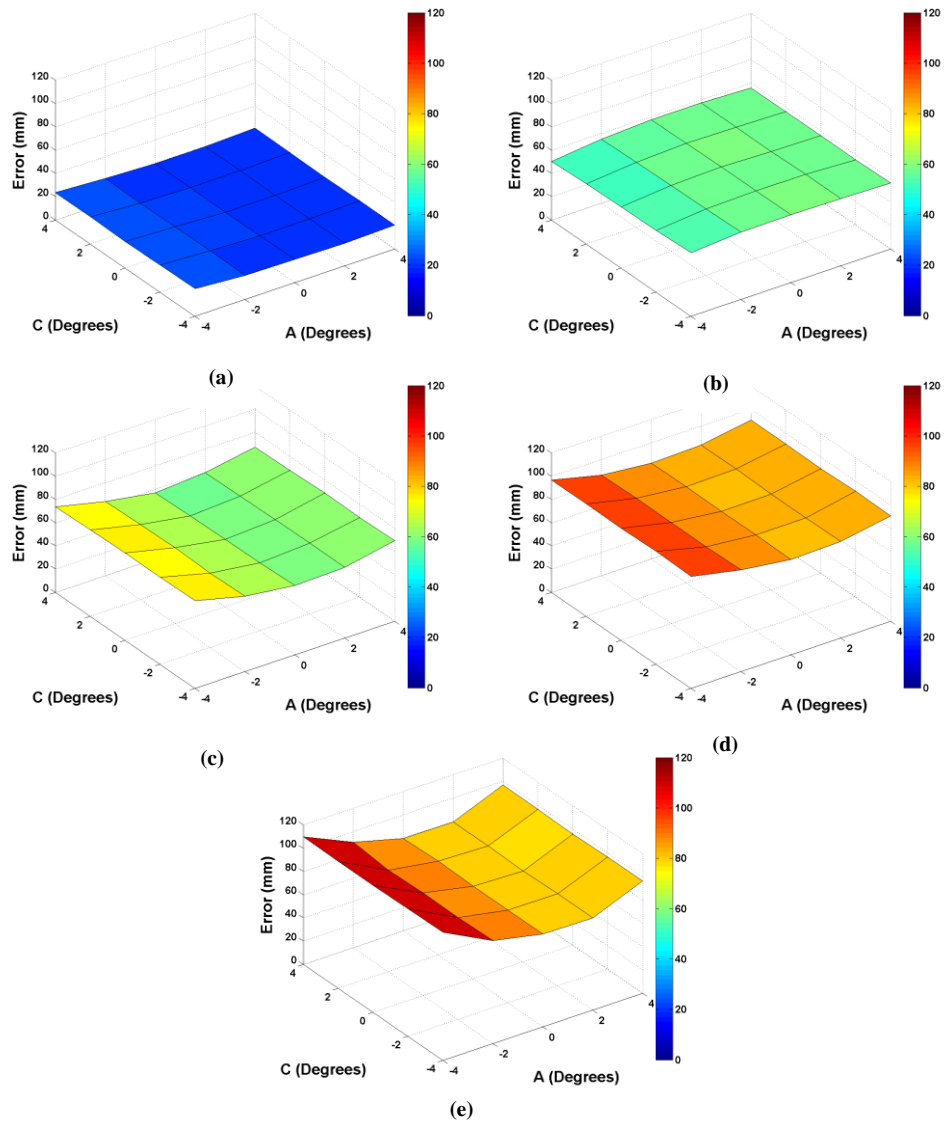
Figure C.32 AC Angle LRF RMSE Mean Error (Concrete)

Nominal SSD (mm)	RMSE Mean (mm)	Distance Error (AC) Standard Deviation (mm)
500	20.80	1.43
1000	55.98	2.10
2000	65.28	6.05
3000	88.00	5.37
4000	90.73	11.65

Table C.25 AC Angle LRF Distance Error Statistical Performance (Concrete)

Distance Error viewed from BC Angle

(a)

(b)

(c)

(d)

(e)

Figure E.33 BC Angle LRF RMSE Mean Error (Concrete)

Nominal SSD (mm)	RMSE Mean (mm)	Distance Error (BC) Standard Deviation (mm)
500	20.80	0.83
1000	55.98	11.00
2000	65.28	5.17
3000	88.00	5.37
4000	90.73	9.60

Table C.26 BC Angle LRF Distance Error Statistical Performance (Concrete)

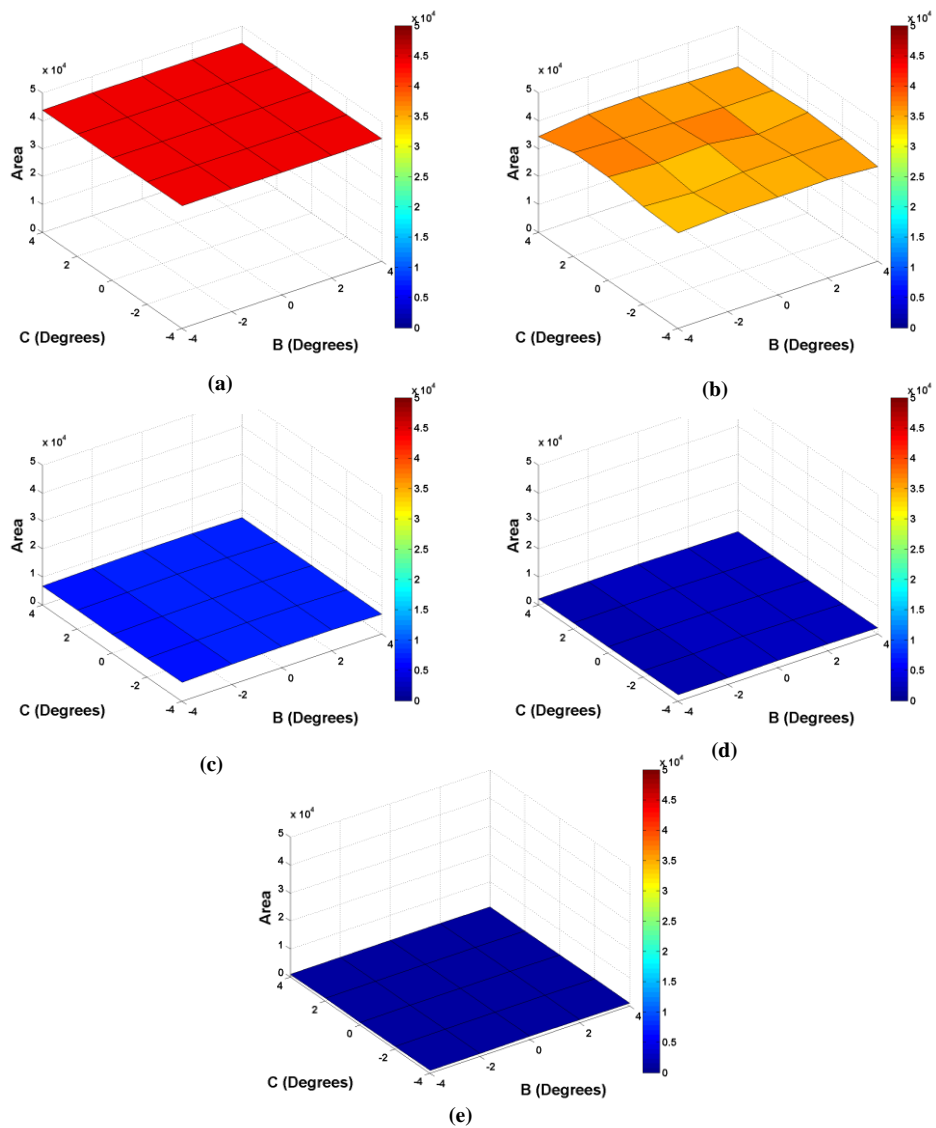**Restored Intensity viewed from AB Angle**

(a)

(b)

(c)

(d)

(e)
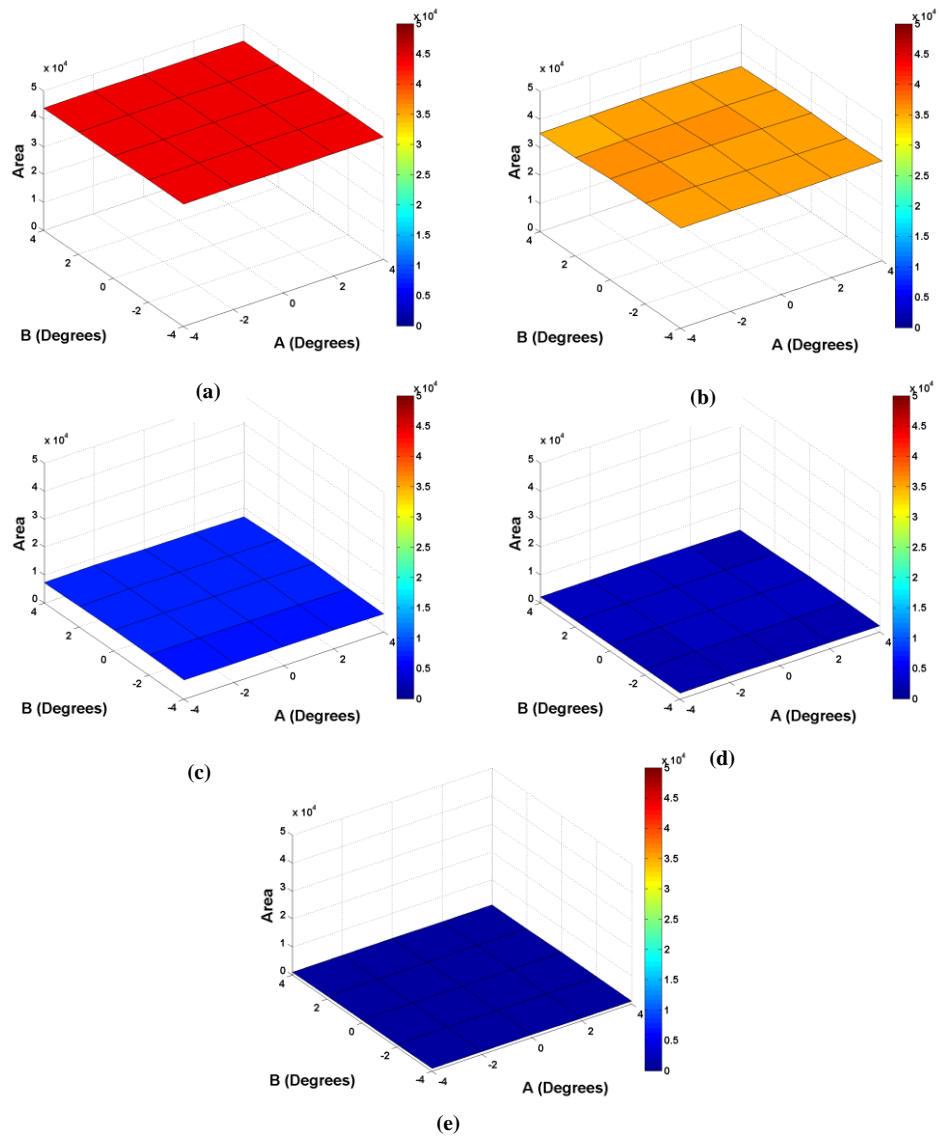
Figure C.34 AB Angle LRF Restored Intensity Area (Concrete)

Nominal SSD (mm)	Restored Intensity Area Mean	Restored Intensity Area (AB) Standard Deviation
500	43928.30	80.58
1000	35525.50	339.05
2000	7214.63	338.96
3000	2339.84	153.12
4000	1068.24	84.46

Table C.27 AB Angle LRF Restored Intensity Area Statistical Performance (Concrete)

Restored Intensity viewed from AC Angle

(a)

(b)

(c)

(d)

(e)
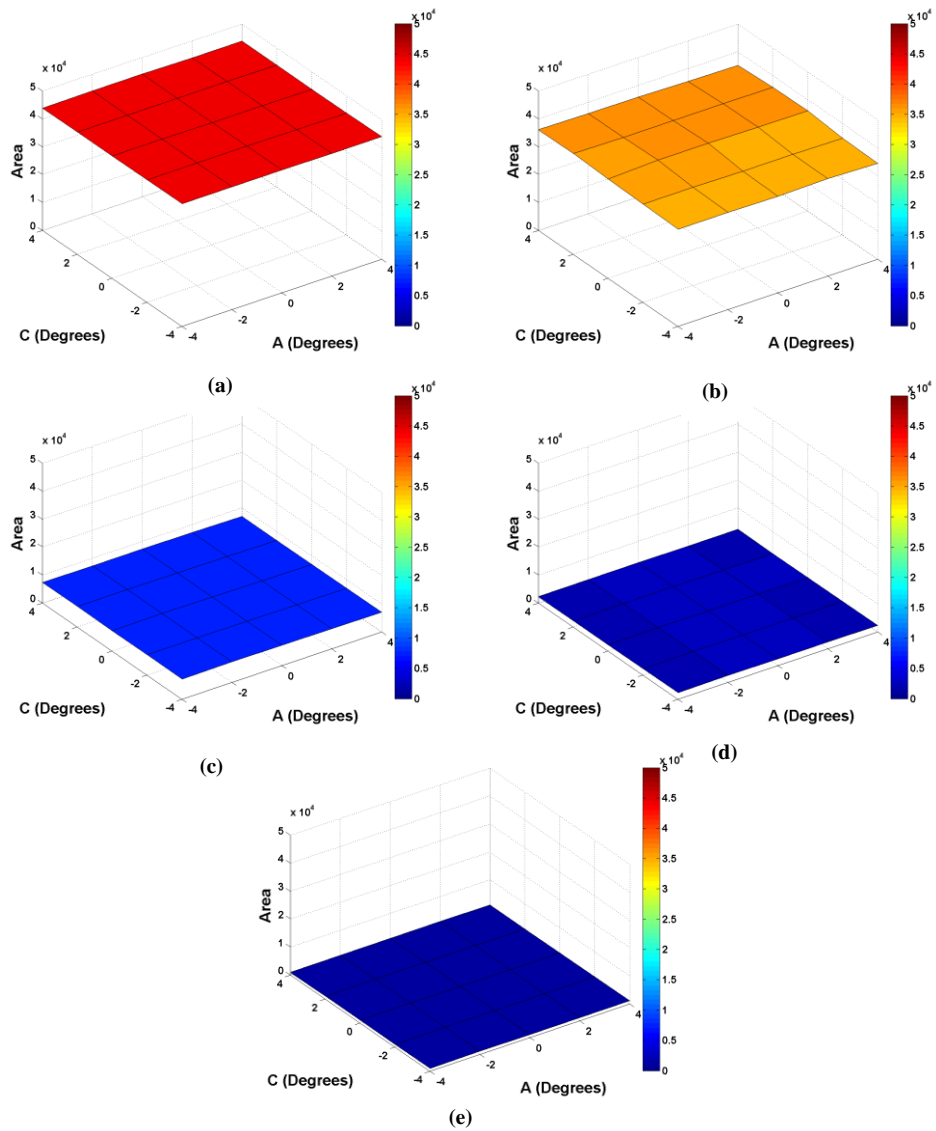
Figure C.35 AC Angle LRF Restored Intensity Area (Concrete)

Nominal SSD (mm)	Restored Intensity Area Mean	Restored Intensity Area (AC) Standard Deviation
500	43928.30	65.15
1000	35525.50	627.52
2000	7214.63	142.72
3000	2339.84	45.59
4000	1068.24	41.65

Table C.28 AC Angle LRF Restored Intensity Area Statistical Performance (Concrete)

Restored Intensity viewed from BC Angle

(a)

(b)

(c)

(d)

(e)

Figure C.36 BC Angle LRF Restored Intensity Area (Concrete)

Nominal SSD (mm)	Restored Intensity Area Mean	Restored Intensity Area (BC) Standard Deviation
500	43928.30	55.81
1000	35525.50	920.51
2000	7214.63	300.69
3000	2339.84	142.13
4000	1068.24	65.37

Table C.29 BC Angle LRF Restored Intensity Area Statistical Performance (Concrete)

Percentage Rejections viewed from AB Angle

(a)

(b)

(c)

(d)

(e)
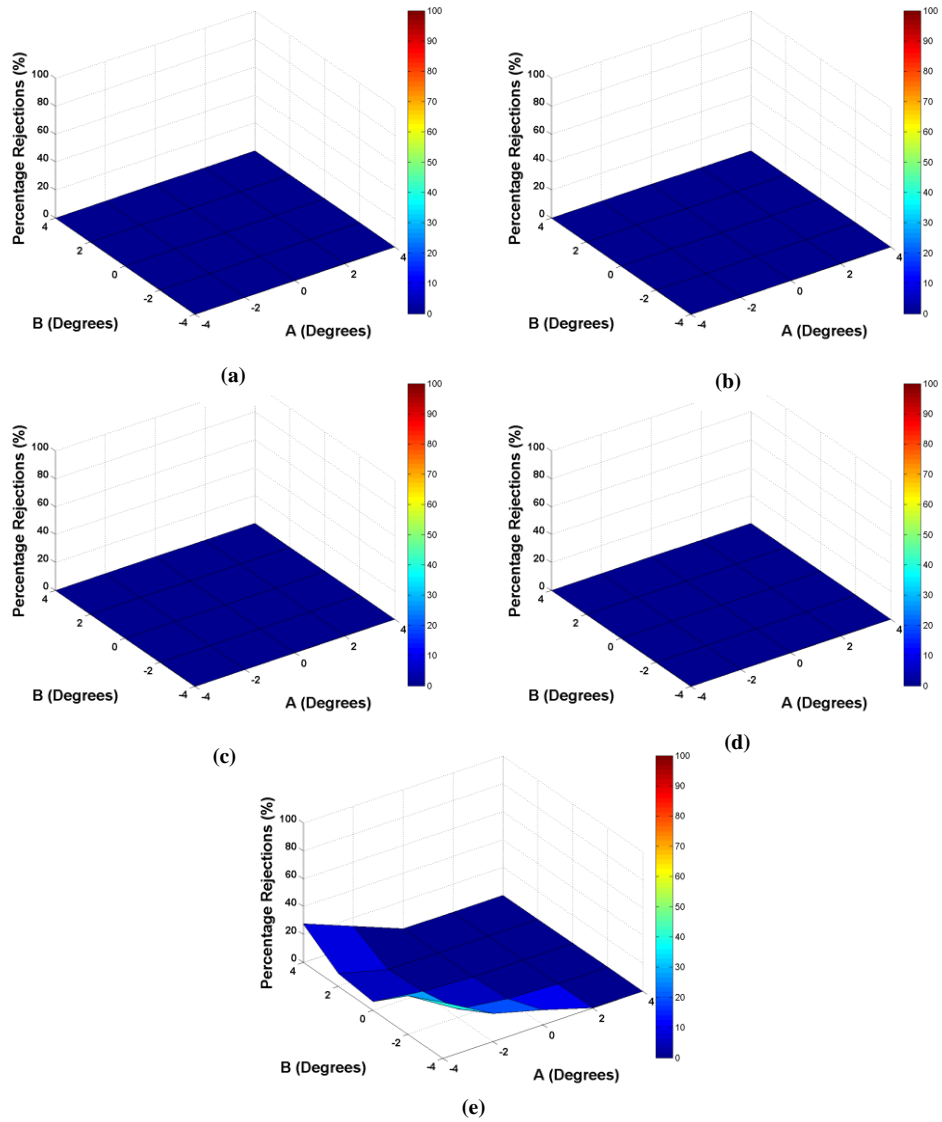
Figure C.37 AB Angle LRF Percentage Rejections (Concrete)

Nominal SSD (mm)	Percentage Rejection Mean	Percentage Rejection (AB) Standard Deviation
500	0	0
1000	0	0
2000	0	0
3000	0	0
4000	6.59	11.04

Table C.30 AB Angle LRF Percentage Rejection Statistical Performance (Concrete)

Percentage Rejections viewed from AC Angle

(a)

(b)

(c)

(d)

(e)
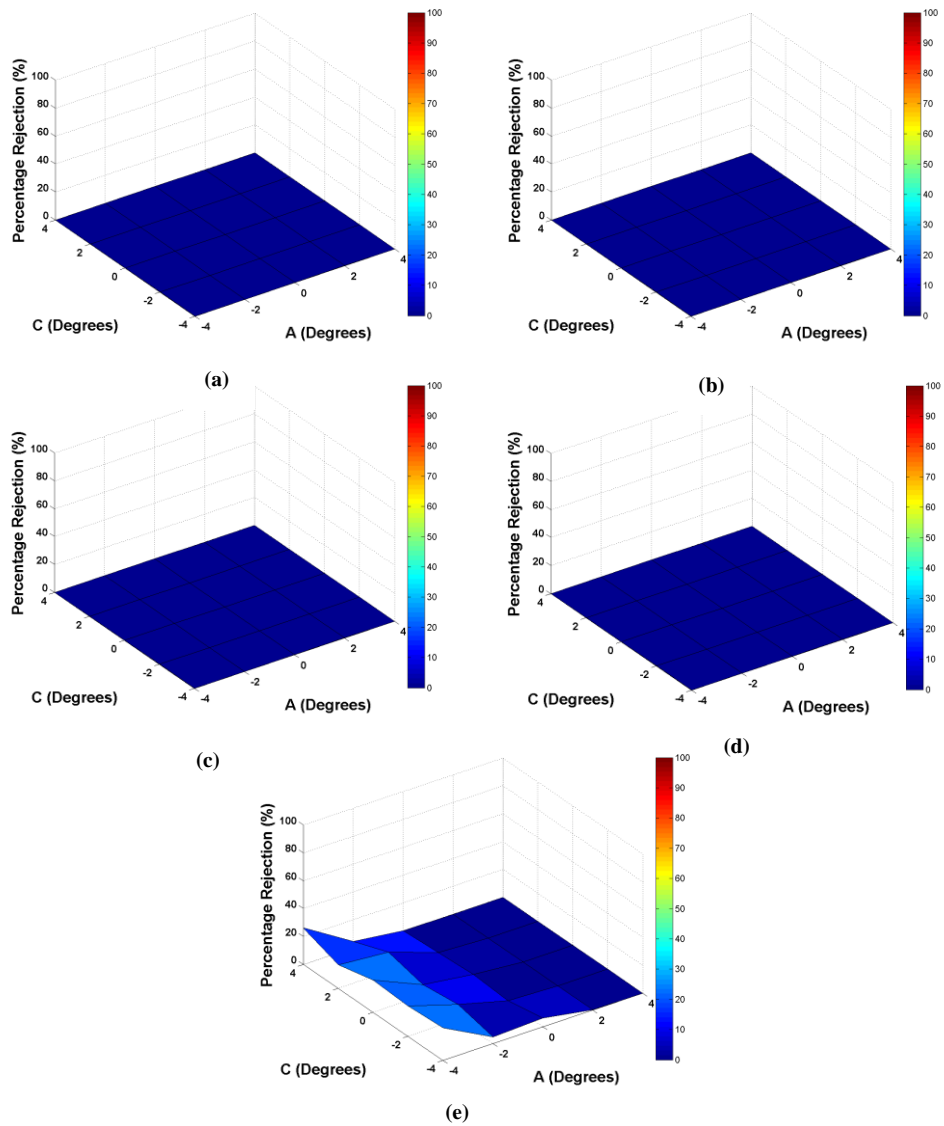
Figure C.38 AC Angle LRF Percentage Rejections (Concrete)

Nominal SSD (mm)	Percentage Rejection Mean	Percentage Rejection (AB) Standard Deviation
500	0	0
1000	0	0
2000	0	0
3000	0	0
4000	6.59	8.84

Table C.31 AC Angle LRF Percentage Rejection Statistical Performance (Concrete)

Percentage Rejections viewed from BC Angle

(a)

(b)

(c)

(d)

(e)
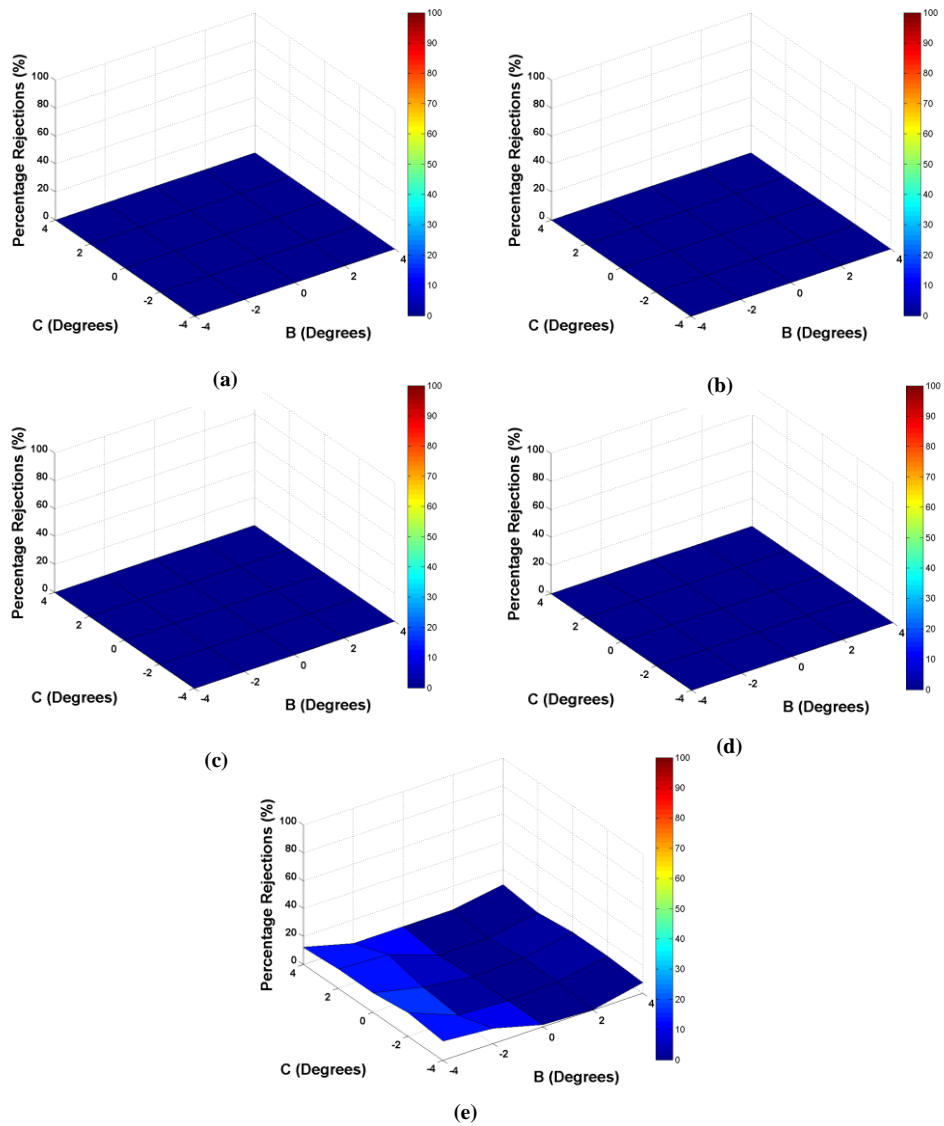
Figure C.39 BC Angle LRF Percentage Rejections (Concrete)

Nominal SSD (mm)	Percentage Rejection Mean	Percentage Rejection (AB) Standard Deviation
500	0	0
1000	0	0
2000	0	0
3000	0	0
4000	6.59	5.21

Table C.32 BC Angle LRF Percentage Rejection Statistical Performance (Concrete)

Valid Measurement Probability
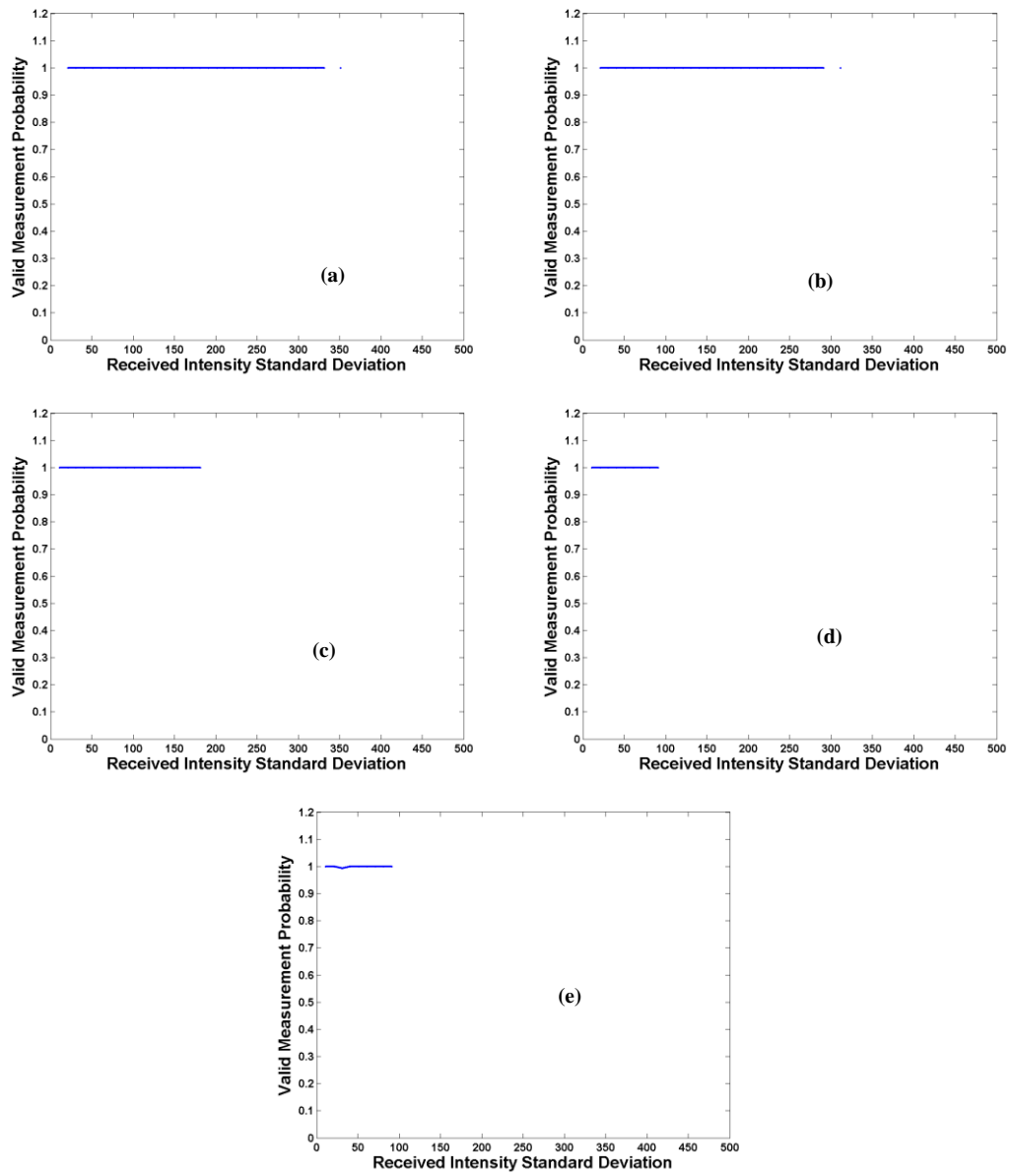
Figure C.40 **LRF Range Validity as a function of Received Intensity Standard Deviation (Concrete)**

Scan Plan View
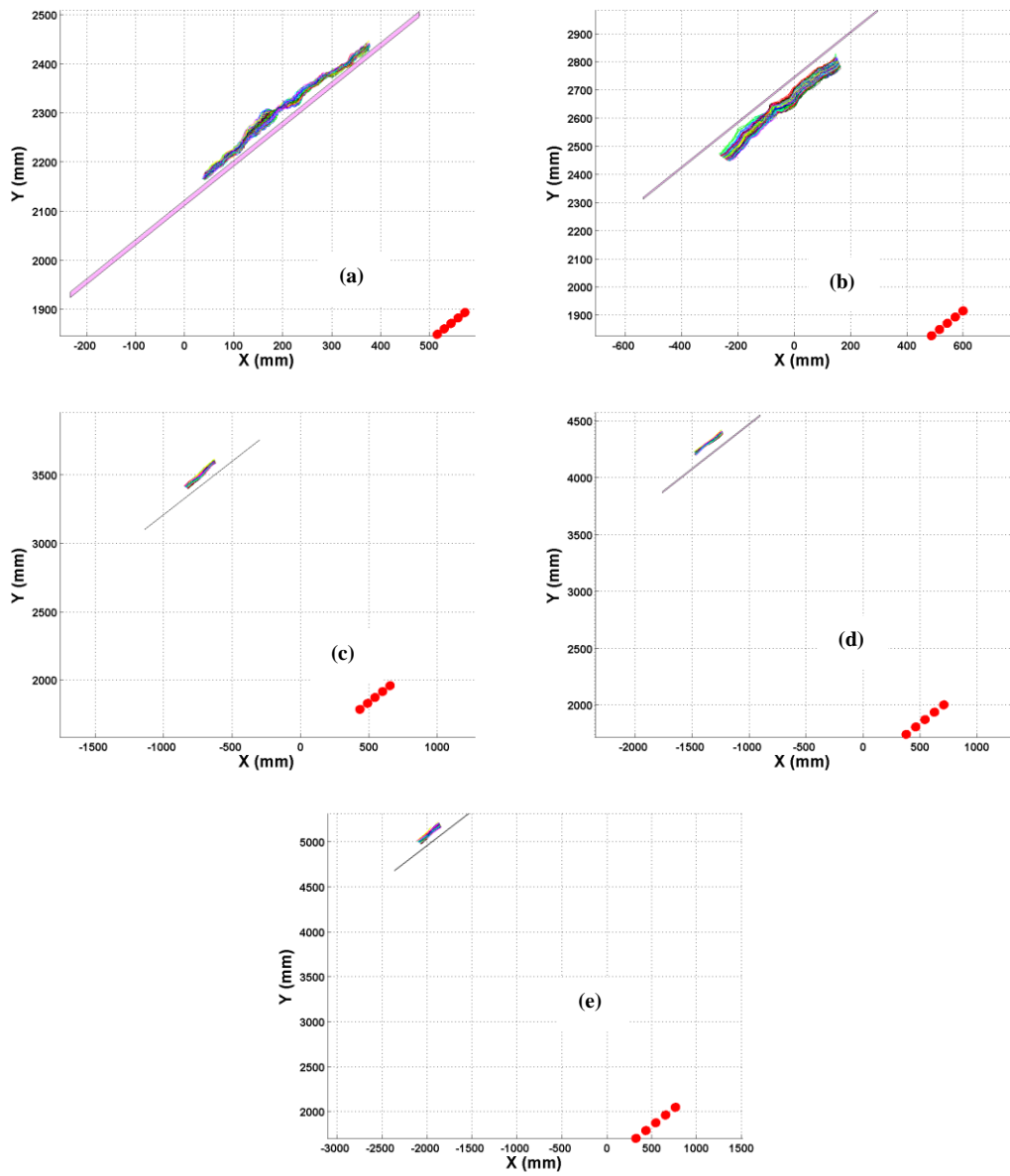
Figure C.41 LRF Scan Plan View (Concrete)

Distance Error
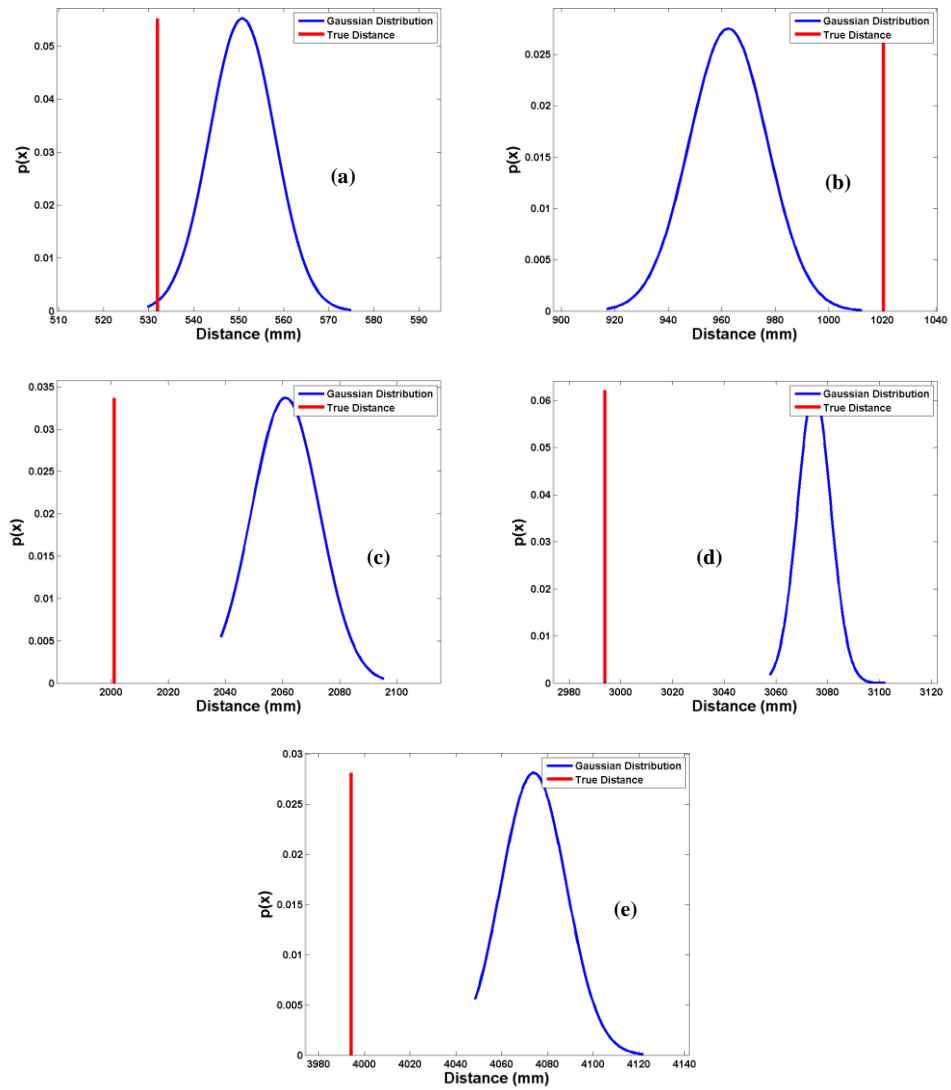
Figure C.42 LRF Distance Error (Concrete)

Nominal SSD (mm)	Distance Error Mean (mm)	Distance Error Standard Deviation (mm)	Distance Error Minimum (mm)	Distance Error Max (mm)
500	18.77	7.22	-2.28	42.88
1000	-57.99	14.49	-103.45	-8.06
2000	59.87	11.84	37.28	94.29
3000	80.85	6.42	63.72	108.29
4000	79.76	14.19	54.25	127.61

Table C.33 LRF Distance Error Statistical Performance (Concrete)

Single Shot Histogram
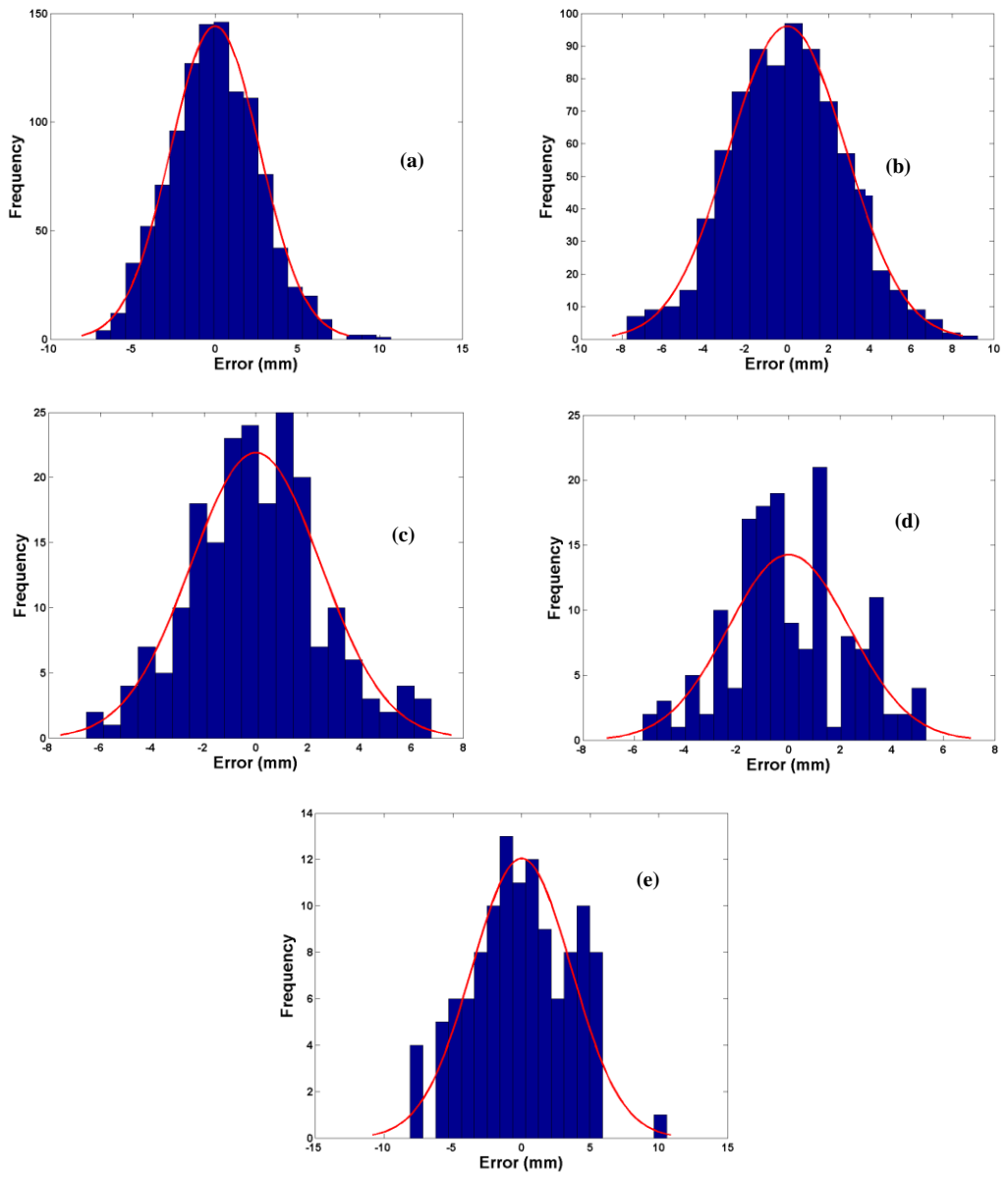
Figure C.43 LRF Range Data Variation (Concrete)

C.5 PVC Surfaces

Distance Error viewed from AB Angle

<div align="center">(a)</div>

<div align="center">(b)</div>

<div align="center">(c)</div>
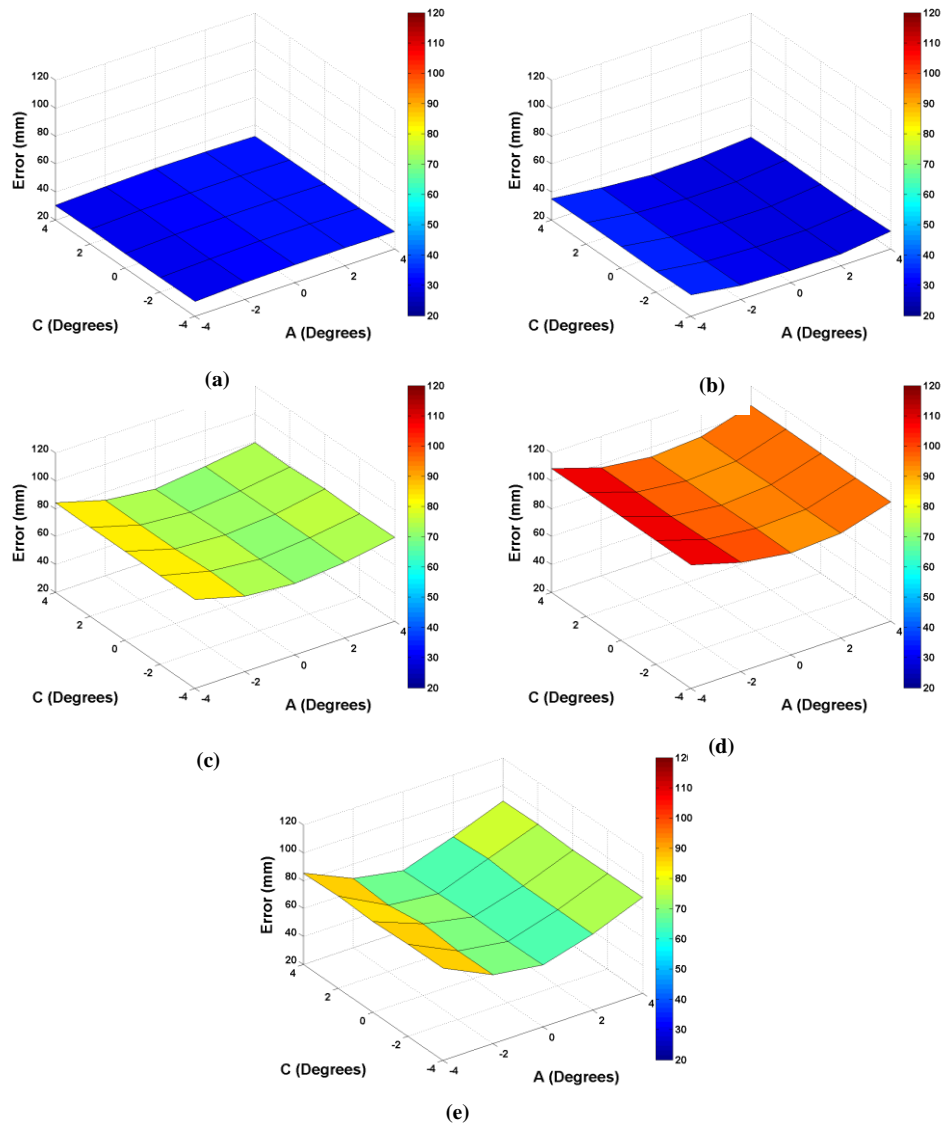
<div align="center">(d)</div>

<div align="center">(e)</div>
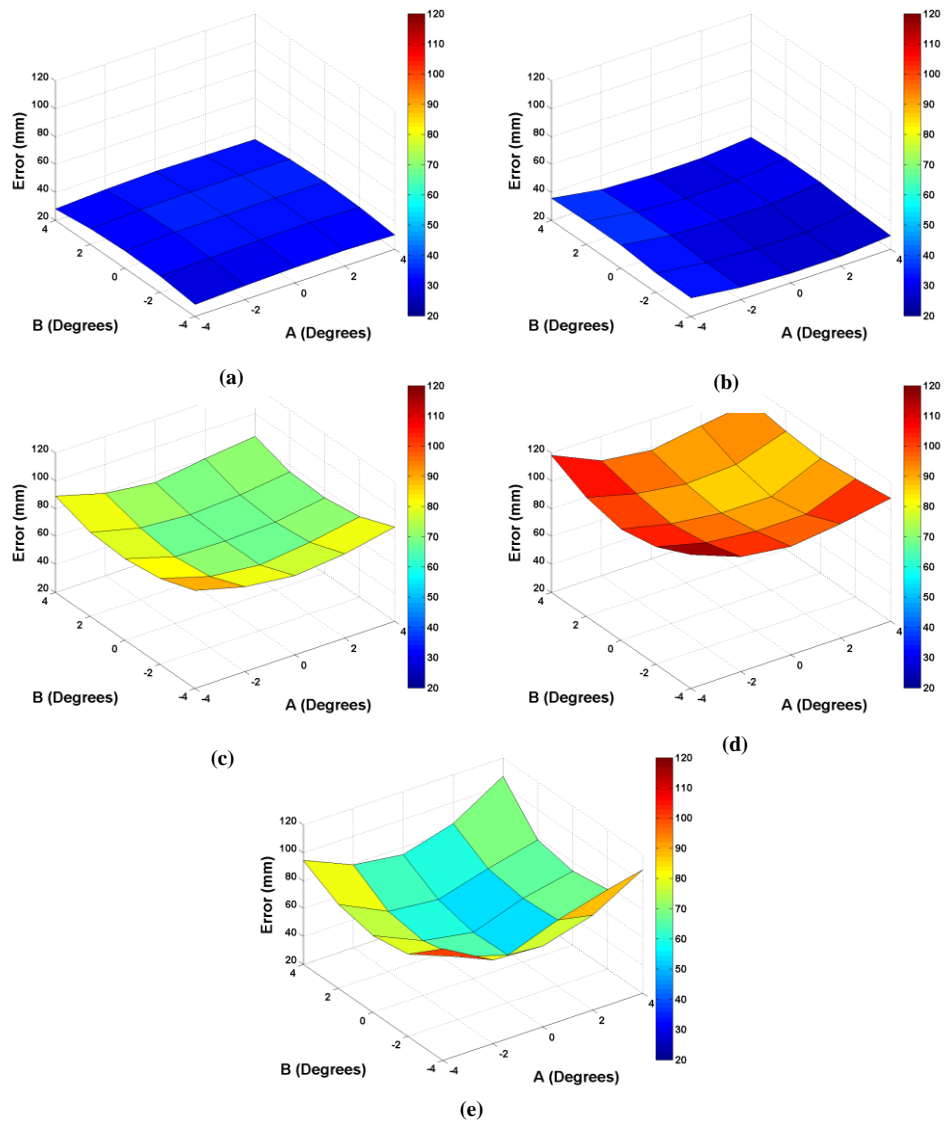
Figure C.44 AB Angle LRF RMSE Mean Error (PVC)

Nominal SSD (mm)	RMSE Mean (mm)	Distance Error (AB) Standard Deviation (mm)
500	31.96	1.83
1000	30.82	2.91
2000	76.62	6.75
3000	100.12	8.11
4000	76.67	14.80

Table C.34 AB Angle LRF Distance Error Statistical Performance (PVC)

Distance Error viewed from AC Angle

(a)

(b)

(c)

(d)

(e)

Figure C.45 AC Angle LRF RMSE Mean Error (PVC)

Nominal SSD (mm)	RMSE Mean (mm)	Distance Error (AC) Standard Deviation (mm)
500	31.96	0.865
1000	30.82	2.59
2000	76.62	4.74
3000	100.12	6.23
4000	76.67	9.69

Table C.35 AC Angle LRF Distance Error Statistical Performance (PVC)
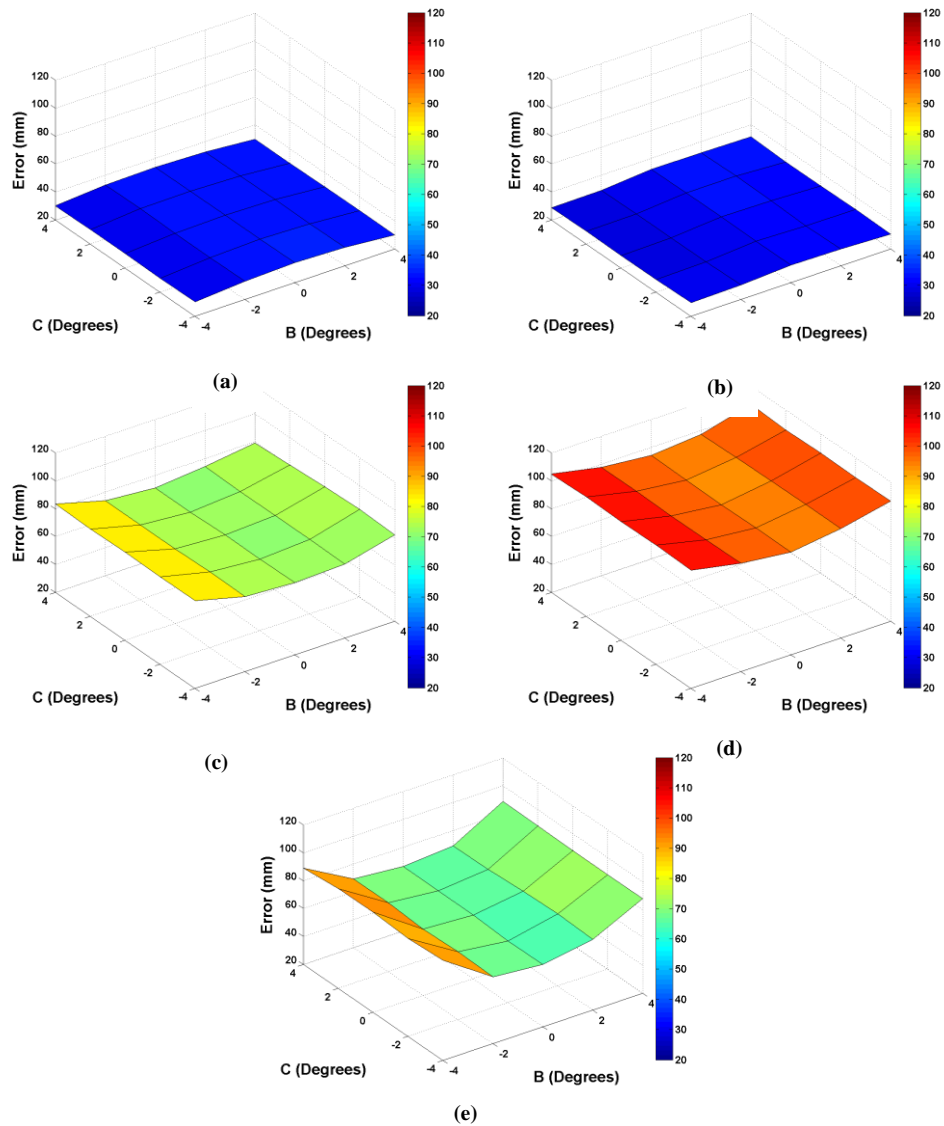
Distance Error viewed from BC Angle

(a)

(b)

(c)

(d)

(e)

Figure C.46 BC Angle LRF RMSE Mean Error (PVC)

Nominal SSD (mm)	RMSE Mean (mm)	Distance Error (BC) Standard Deviation (mm)
500	31.96	1.62
1000	30.82	1.36
2000	76.62	4.82
3000	100.12	4.91
4000	76.67	10.90

Table C.36 BC Angle LRF Distance Error Statistical Performance (PVC)
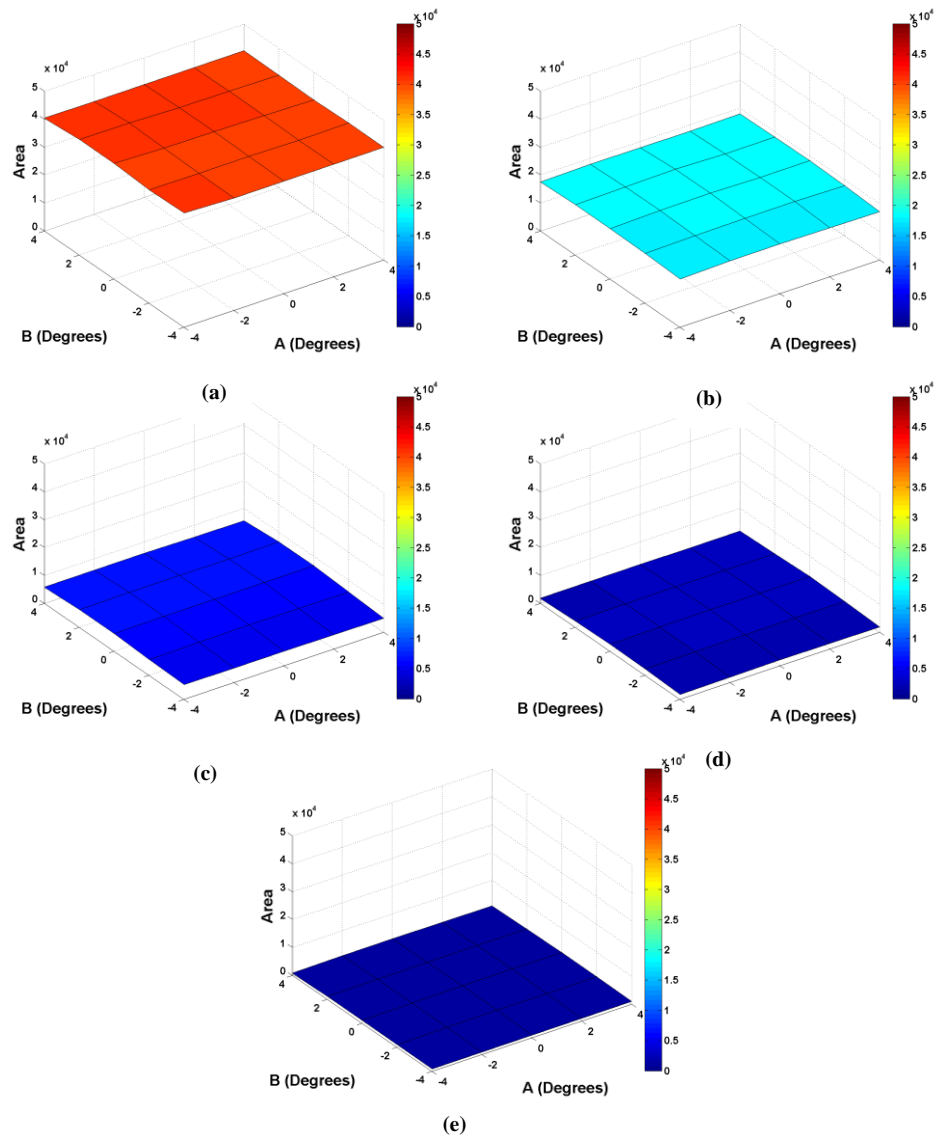
Restored Intensity viewed from AB Angle
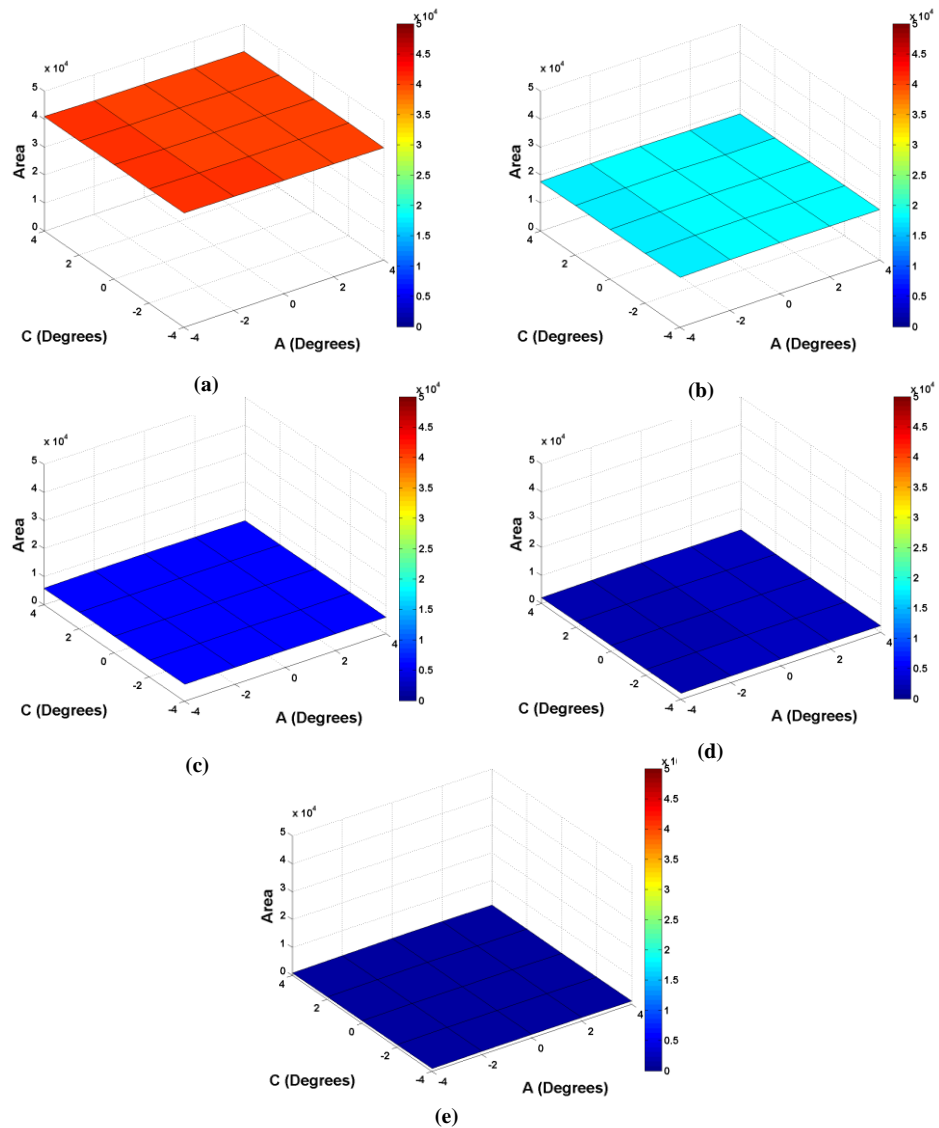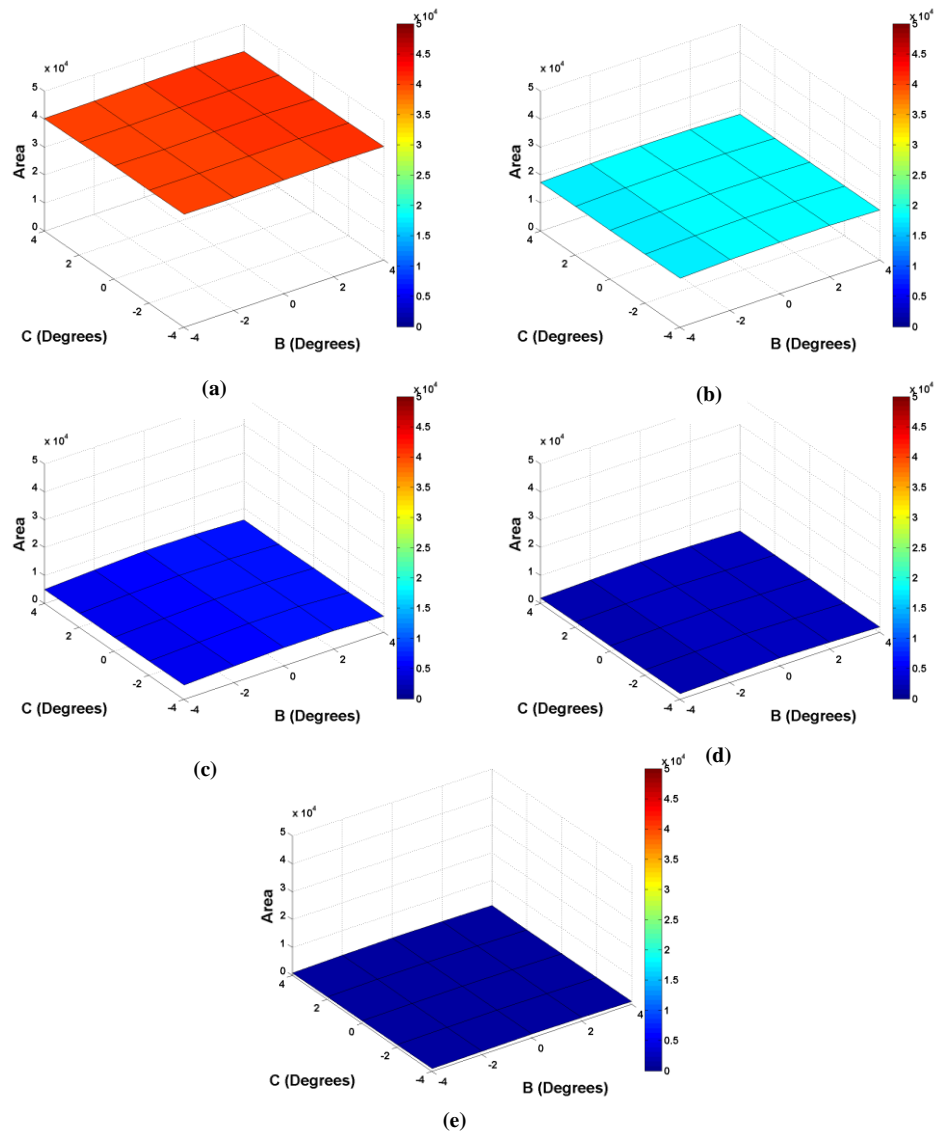

(a)

(b)

(c)

(d)

(e)

Figure C.47 AB Angle LRF Restored Intensity Area (PVC)

Nominal SSD (mm)	Restored Intensity Area Mean	Restored Intensity Area (AB) Standard Deviation
500	40537.00	348.92
1000	17990.60	409.25
2000	5973.49	577.54
3000	2289.70	349.64
4000	1118.19	204.11

Table C.37 AB Angle LRF Restored Intensity Area Statistical Performance (PVC)

Restored Intensity viewed from AC Angle

(a)

(b)

(c)

(d)

(e)

Figure C.48 AC Angle LRF Restored Intensity Area (PVC)

Nominal SSD (mm)	Restored Intensity Area Mean	Restored Intensity Area (AC) Standard Deviation
500	40537.00	221.28
1000	17990.60	184.89
2000	5973.49	72.12
3000	2289.70	103.22
4000	1118.19	110.27

Table C.38 AC Angle LRF Restored Intensity Area Statistical Performance (PVC)

Restored Intensity viewed from BC Angle

(a)

(b)

(c)

(d)

(e)

Figure C.49 AC Angle LRF Restored Intensity Area (PVC)

Nominal SSD (mm)	Restored Intensity Area Mean	Restored Intensity Area (BC) Standard Deviation
500	40537.00	210.52
1000	17990.60	357.49
2000	5973.49	565.80
3000	2289.70	332.63
4000	1118.19	164.41

Table C.39 BC Angle LRF Restored Intensity Area Statistical Performance (PVC)

Percentage Rejections viewed from AB Angle

(a)

(b)

(c)

(d)

(e)
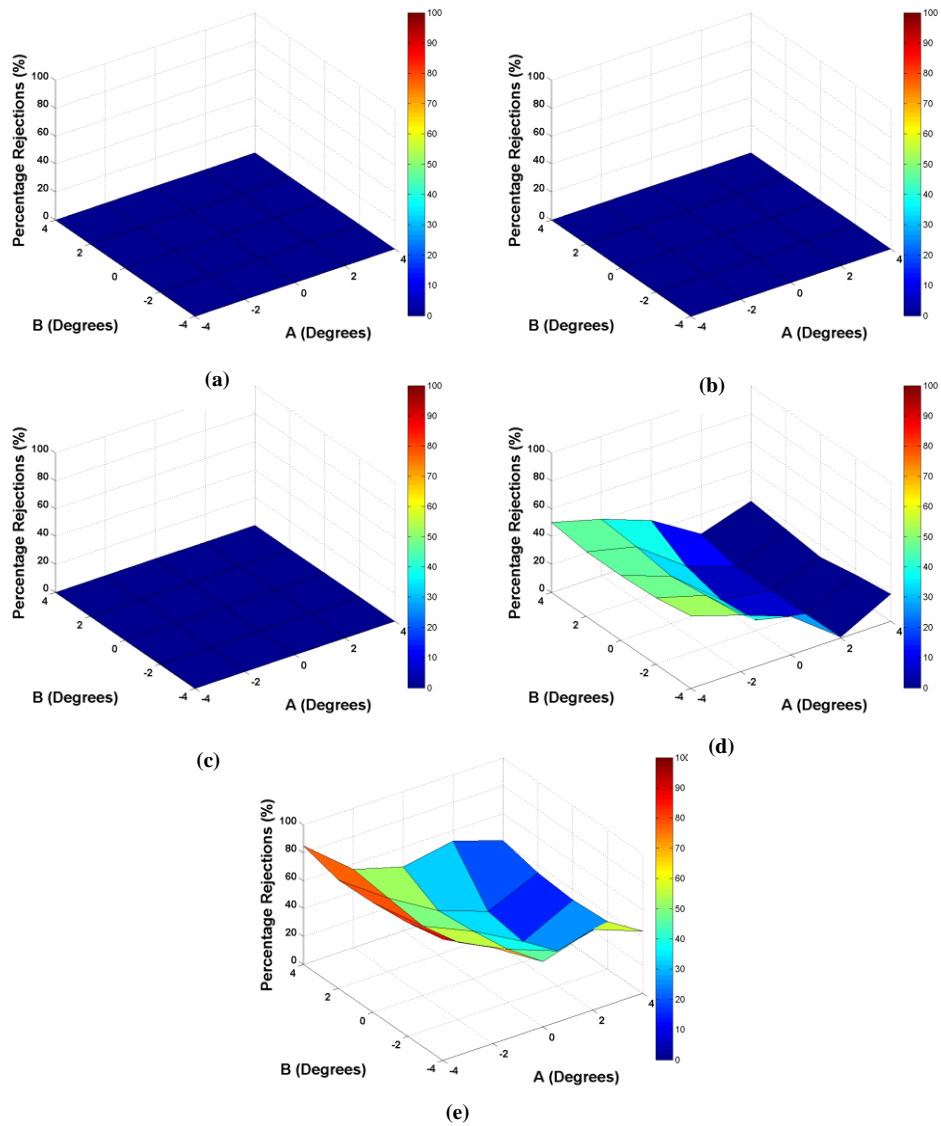
Figure C.50 AB Angle LRF Percentage Rejections (PVC)

Nominal SSD (mm)	Percentage Rejection Mean	Percentage Rejection (AB) Standard Deviation
500	0	0
1000	0	0
2000	0	0
3000	23.91	18.07
4000	49.84	20.52

Table C.40 AB Angle LRF Percentage Rejection Statistical Performance (PVC)
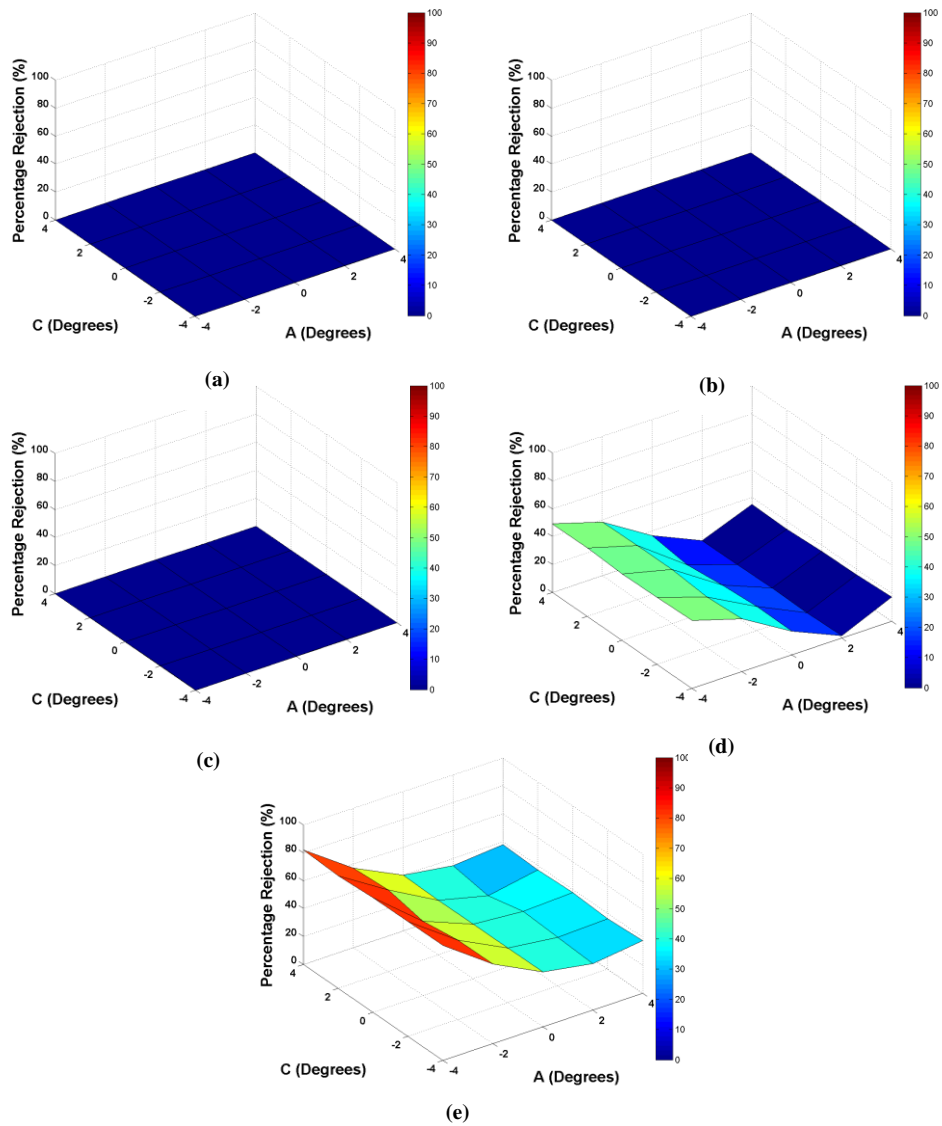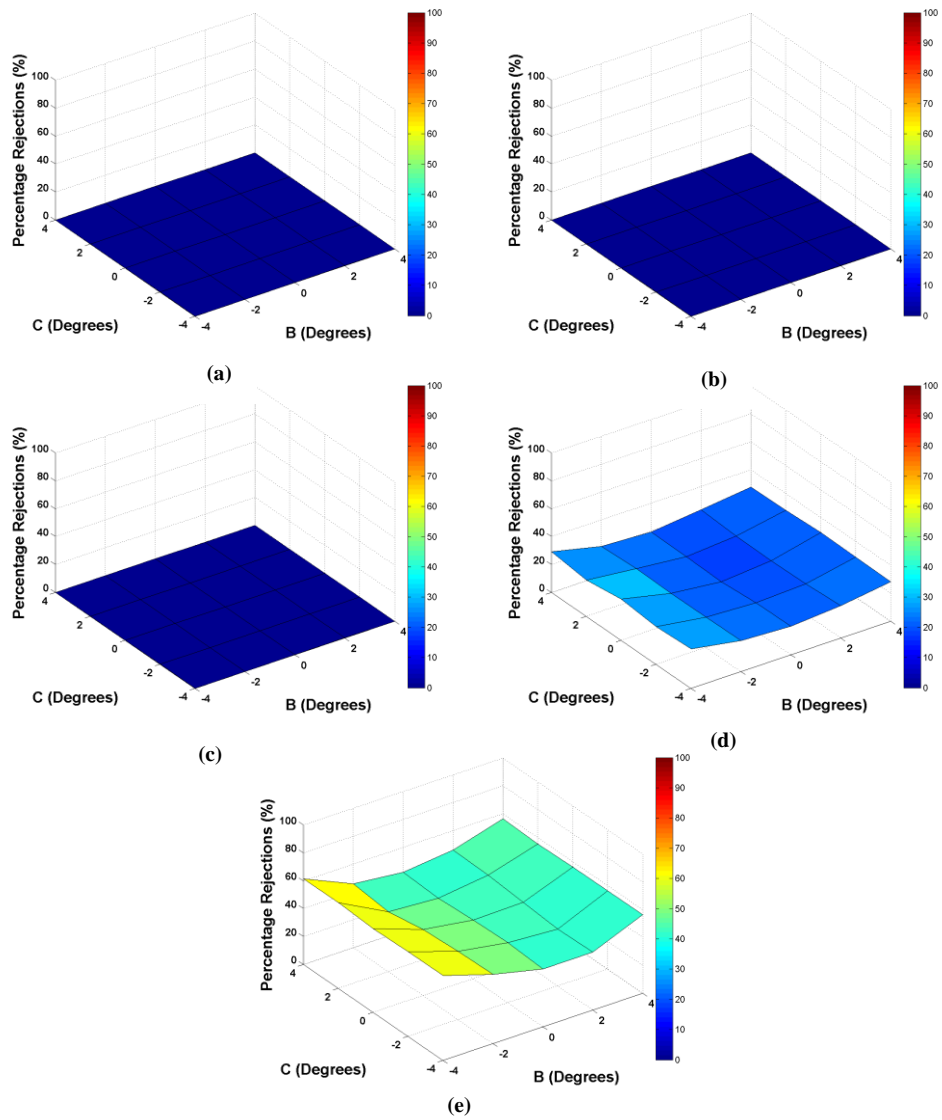
Percentage Rejections viewed from AC Angle

(a)

(b)

(c)

(d)

(e)

Figure C.51 AC Angle LRF Percentage Rejections (PVC)

Nominal SSD (mm)	Percentage Rejection Mean	Percentage Rejection (AC) Standard Deviation
500	0	0
1000	0	0
2000	0	0
3000	23.91	17.40
4000	49.84	18.27

Table C.41 AC Angle LRF Percentage Rejection Statistical Performance (PVC)

Percentage Rejections viewed from BC Angle

(a)

(b)

(c)

(d)

(e)

Figure C.52 BC Angle LRF Percentage Rejections (PVC)

Nominal SSD (mm)	Percentage Rejection Mean	Percentage Rejection (BC) Standard Deviation
500	0	0
1000	0	0
2000	0	0
3000	23.91	3.79
4000	49.84	7.73

Table C.42 BC Angle LRF Percentage Rejection Statistical Performance (PVC)
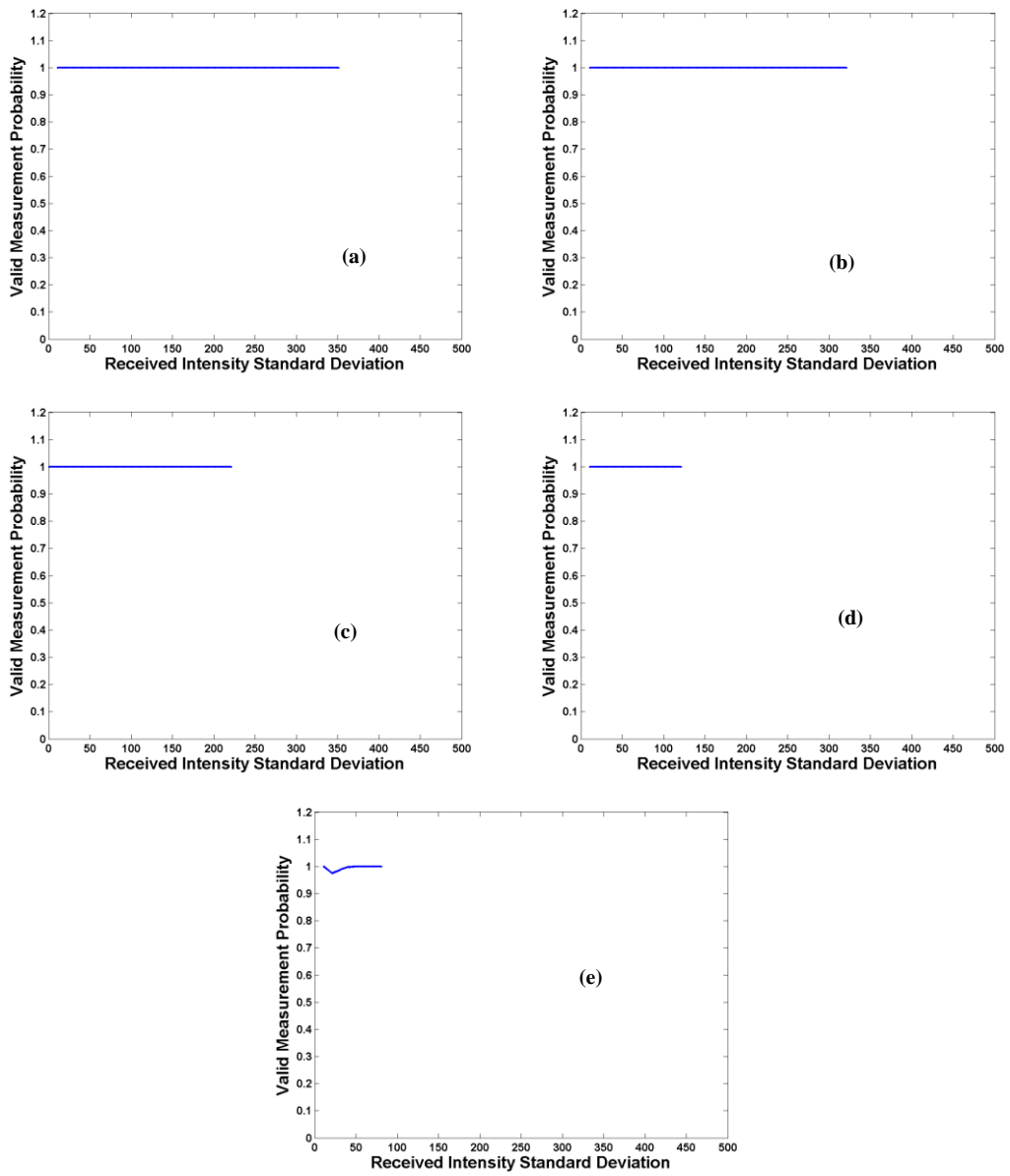
Valid Measurement Probability

Figure C.53 LRF Range Validity as a function of Received Intensity Standard Deviation (PVC)

Scan Plan View
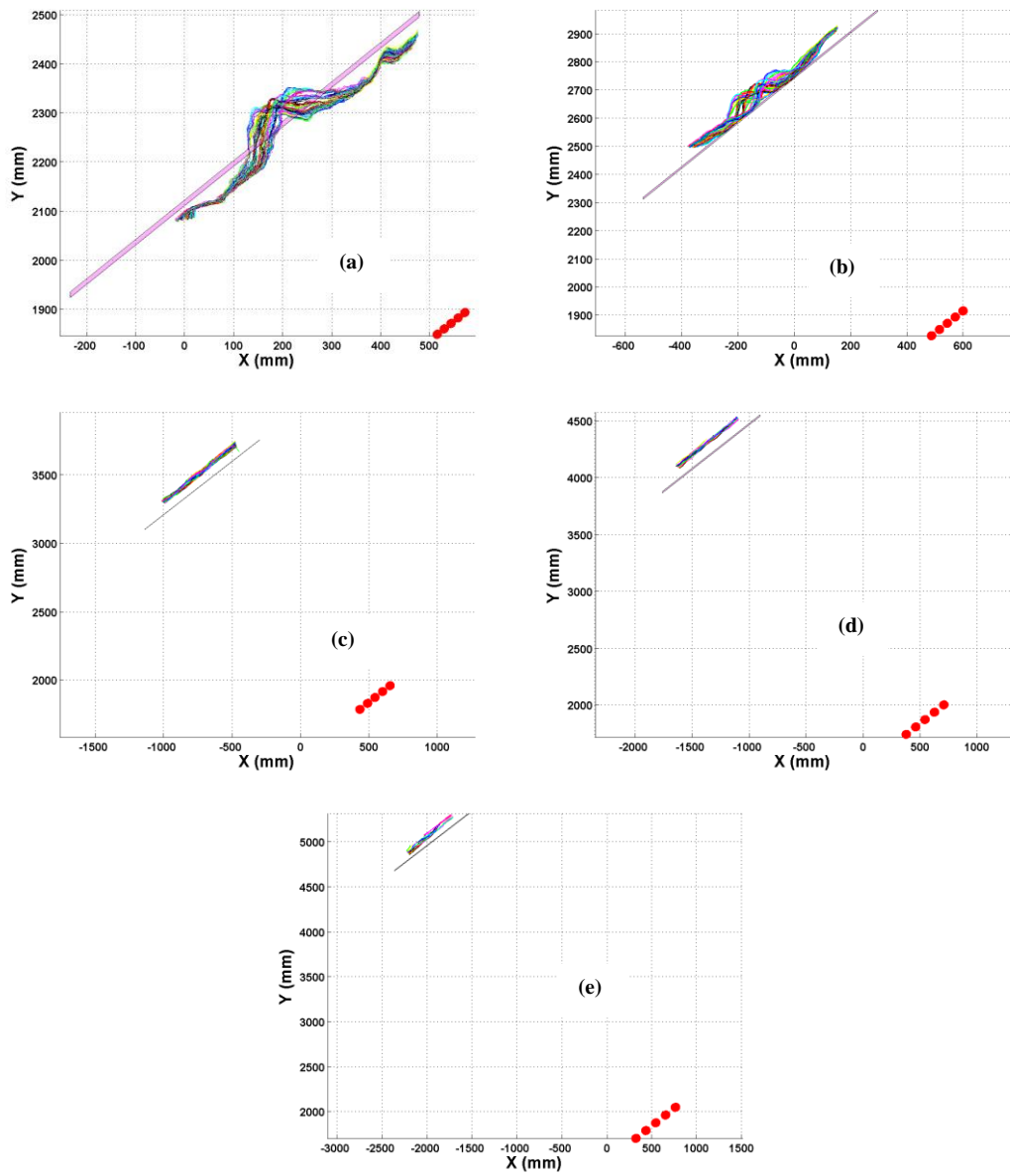
Figure C.54 LRF Scan Plan View (PVC)
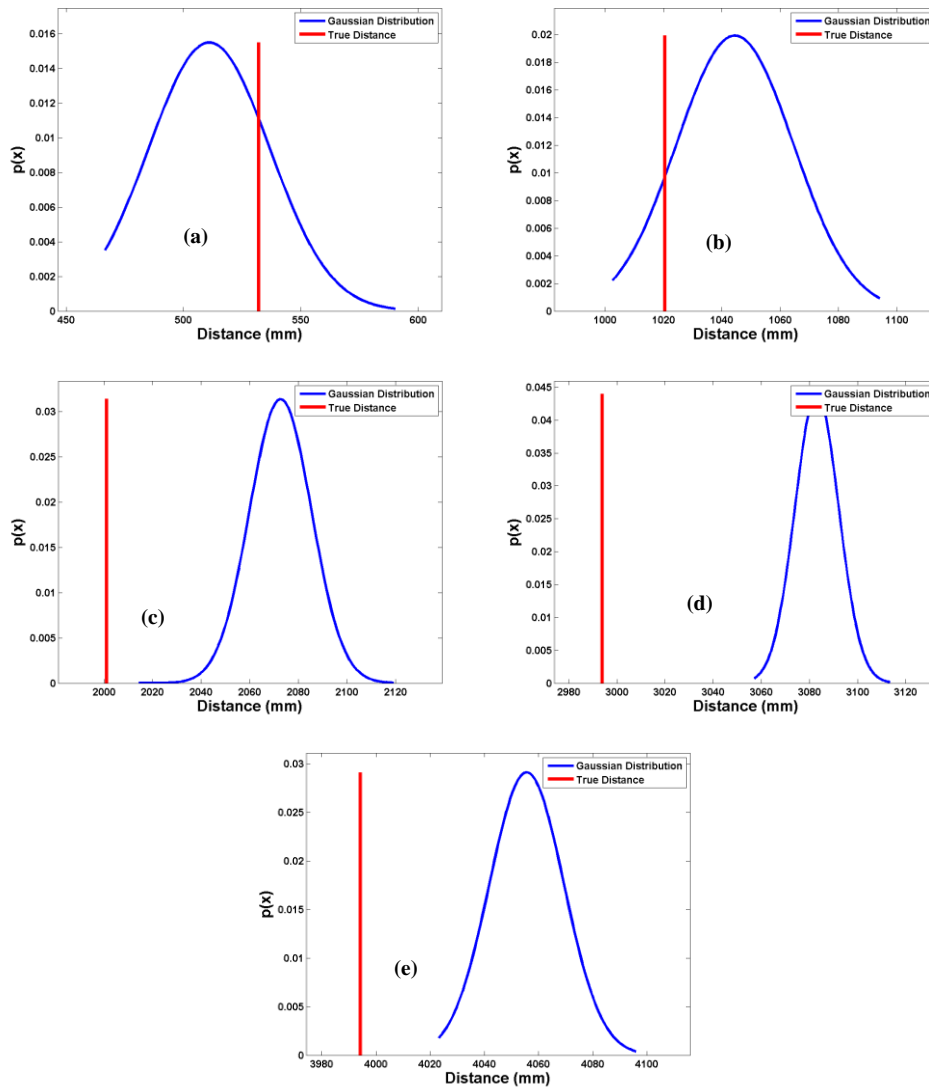
402

Distance Error

Figure C.55 LRF Distance Error (PVC)

Nominal SSD (mm)	Distance Error Mean (mm)	Distance Error Standard Deviation (mm)	Distance Error Minimum (mm)	Distance Error Max (mm)
500	-21.08	25.73	-65.37	58.10
1000	24.00	20.03	-17.93	73.63
2000	71.49	12.70	13.15	117.97
3000	89.12	9.08	63.22	119.45
4000	61.33	13.71	28.94	101.61

Table C.43 LRF Distance Error Statistical Performance (PVC)
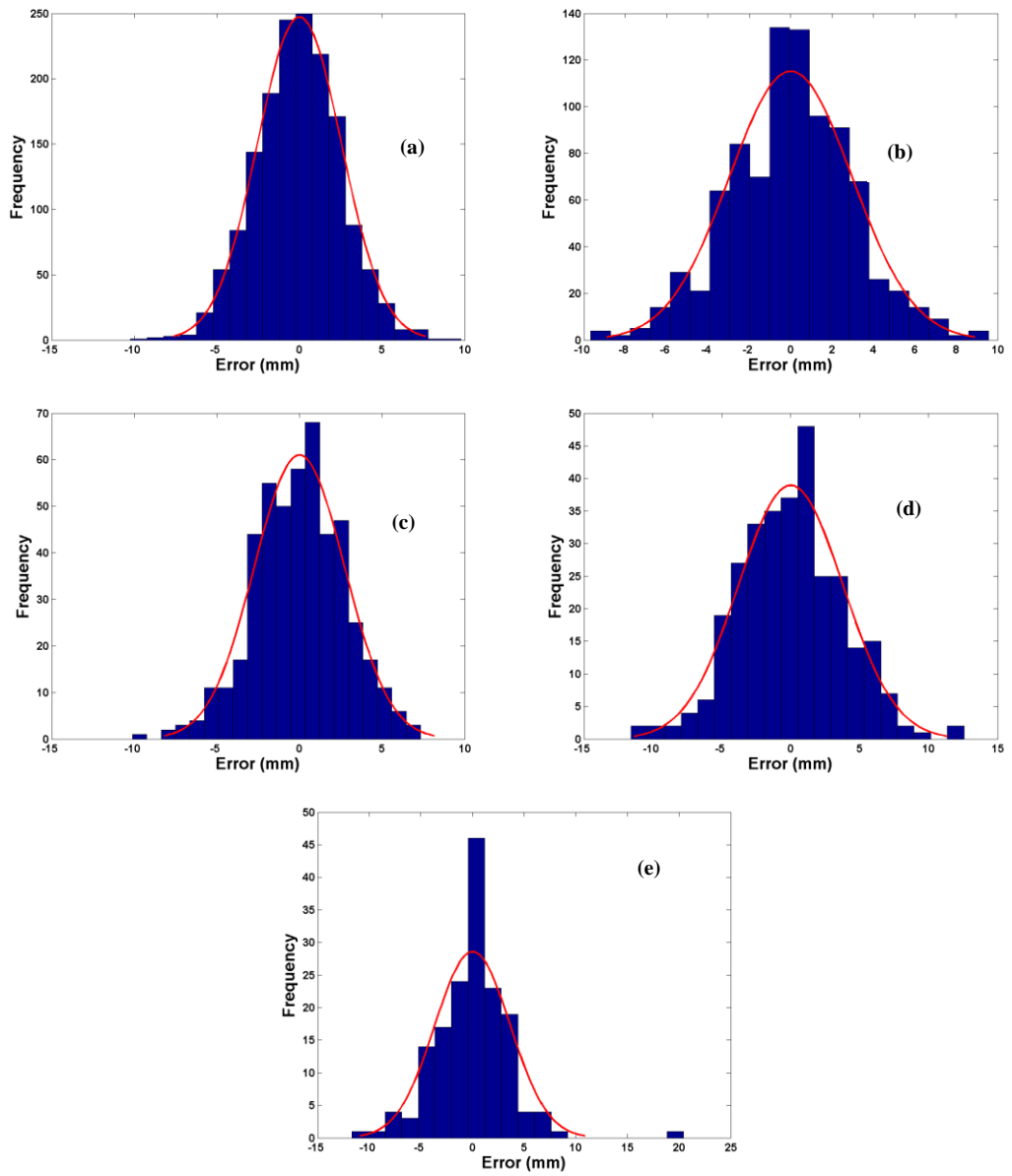
403

Single Shot Histogram

Figure C.56 LRF Range Data Variation (PVC)

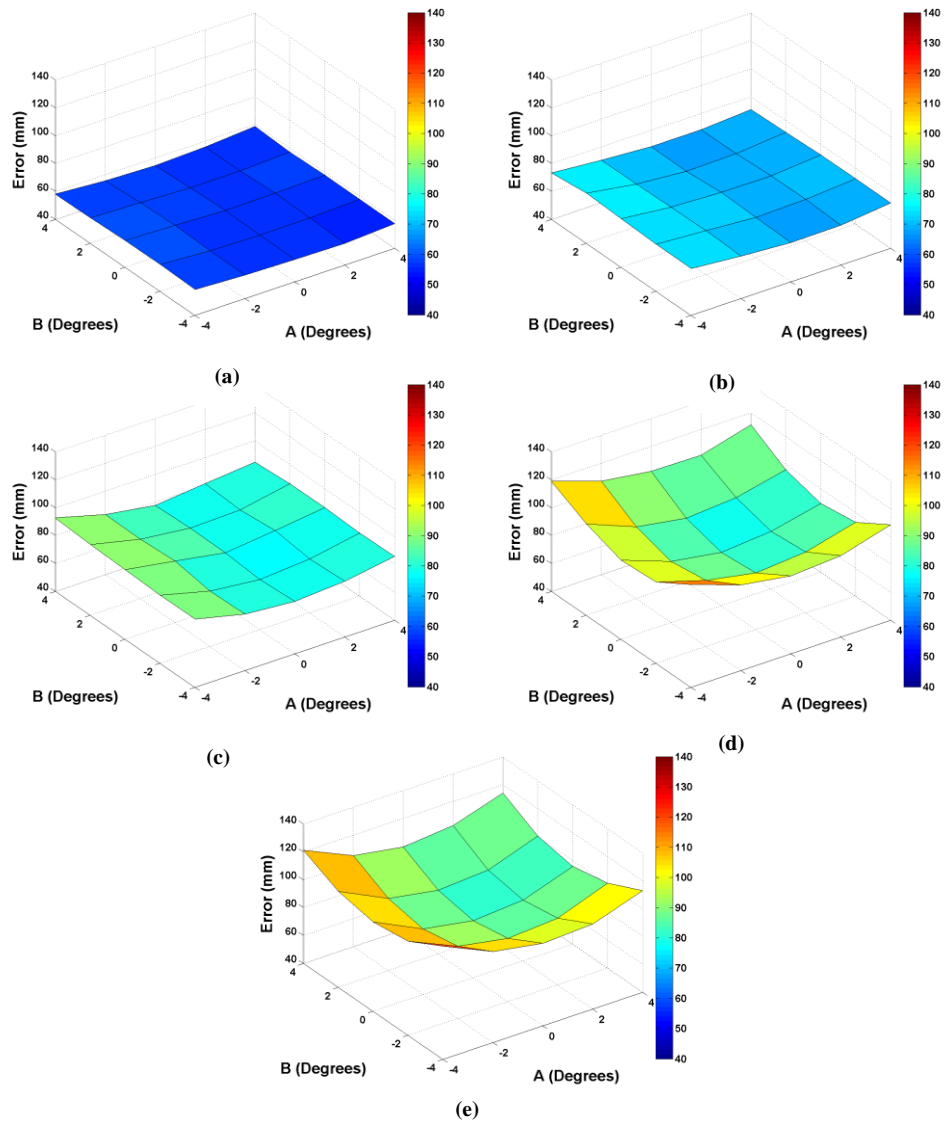# C.6 Wood Surfaces

Distance Error viewed from AB Angle

(a)

(b)

(c)

(d)

(e)

Figure C.57 AB Angle LRF RMSE Mean Error (Wood)

Nominal SSD (mm)	RMSE Mean (mm)	Distance Error (AB) Standard Deviation (mm)
500	57.13	1.26
1000	70.91	2.31
2000	83.18	4.67
3000	95.99	11.05
4000	99.32	11.38

Table C.44 AB Angle LRF Distance Error Statistical Performance (Wood)
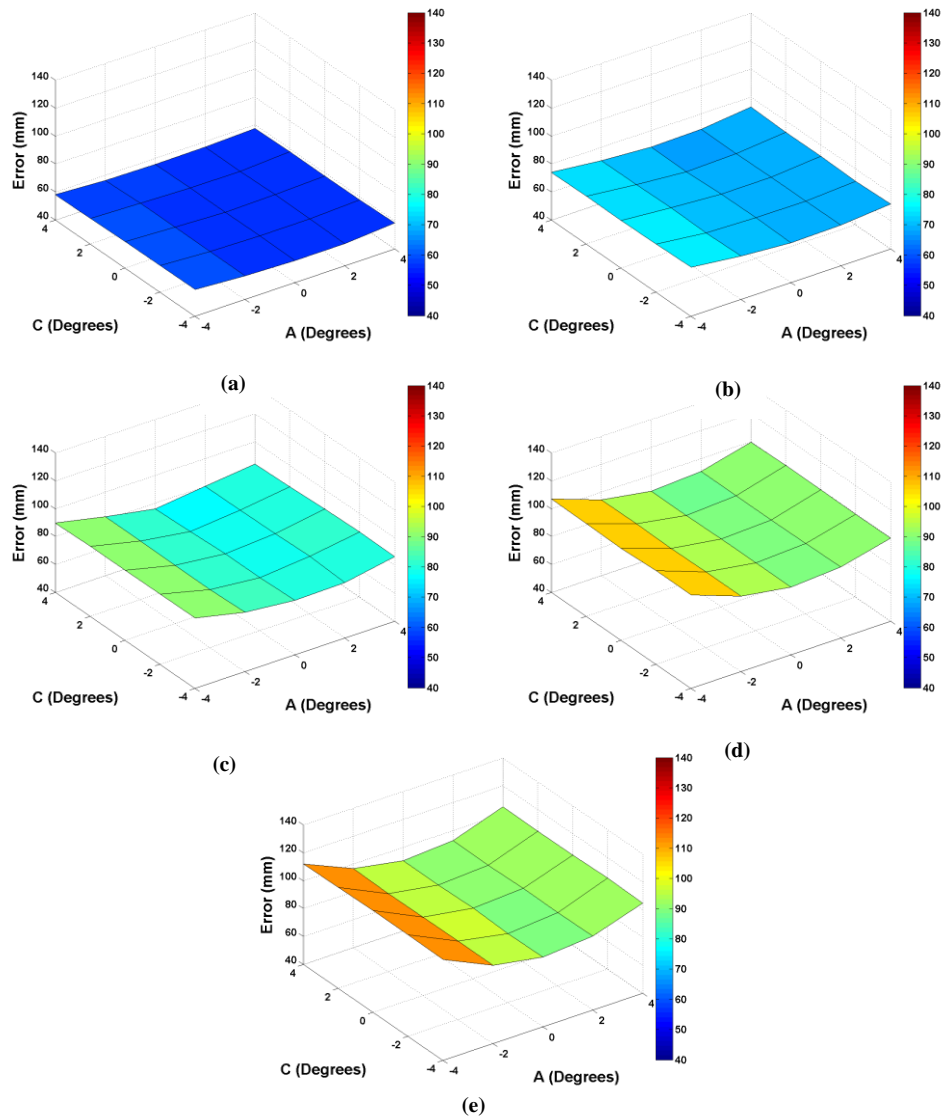
Distance Error viewed from AC Angle

(a)

(b)

(c)

(d)

(e)

Figure C.58 AC Angle LRF RMSE Mean Error (Wood)

Nominal SSD (mm)	RMSE Mean (mm)	Distance Error (AC) Standard Deviation (mm)
500	57.13	1.13
1000	70.91	2.22
2000	83.18	4.57
3000	95.99	6.7
4000	99.32	8.46

Table C.45 AC Angle LRF Distance Error Statistical Performance (Wood)
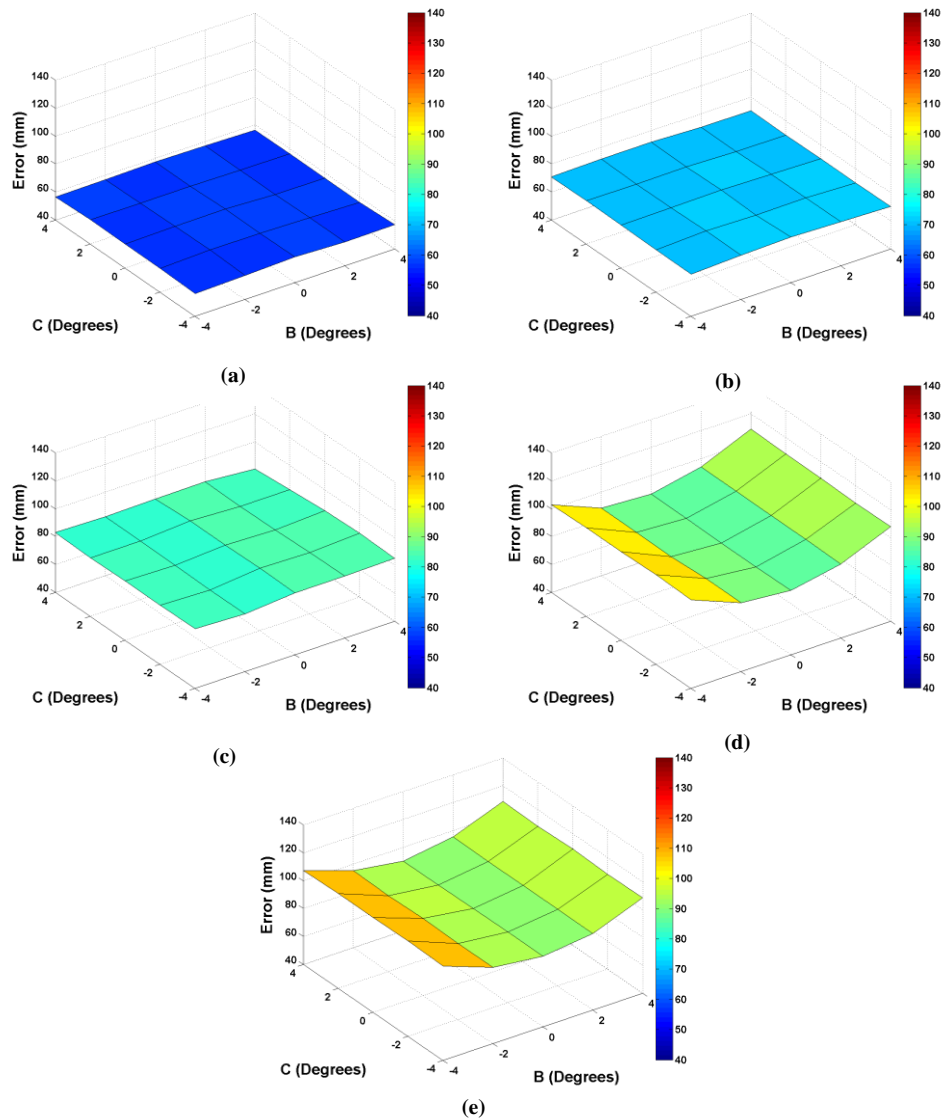
Distance Error viewed from BC Angle

(a)

(b)

(c)

(d)

(e)

Figure C.59 BC Angle LRF RMSE Mean Error (Wood)

Nominal SSD (mm)	RMSE Mean (mm)	Distance Error (BC) Standard Deviation (mm)
500	57.13	0.62
1000	70.91	0.70
2000	83.18	1.35
3000	95.99	8.76
4000	99.32	7.61

Table C.46 BC Angle LRF Distance Error Statistical Performance (Wood)

Restored Intensity viewed from AB Angle
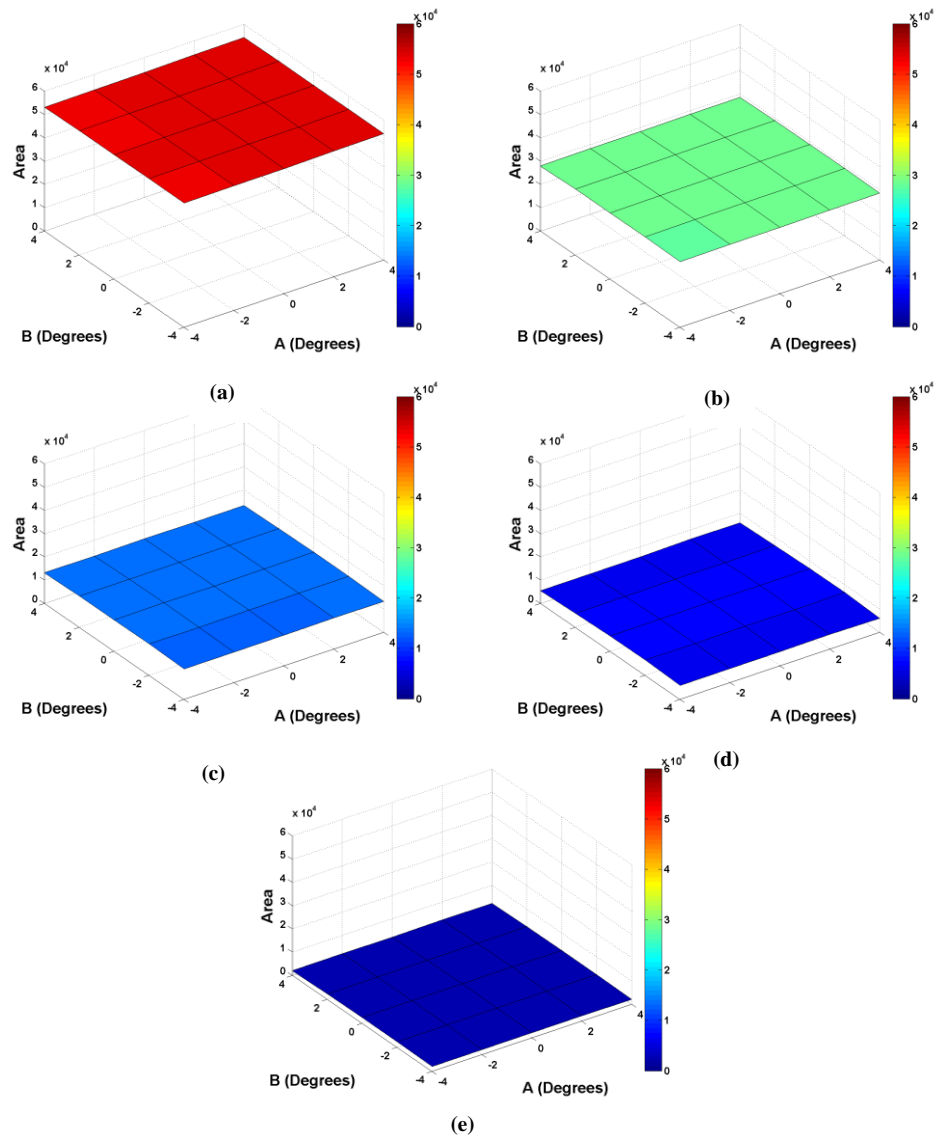

(a)

(b)

(c)

(d)

(e)

Figure C.60 AB Angle LRF Restored Intensity Area (Wood)

Nominal SSD (mm)	Restored Intensity Area Mean	Restored Intensity Area (AB) Standard Deviation
500	53777.7	352.39
1000	28556.5	270.43
2000	13463.4	243.44
3000	6258.85	427.11
4000	2324.02	182.23

Table C.47 AB Angle LRF Restored Intensity Area Statistical Performance (Wood)

408

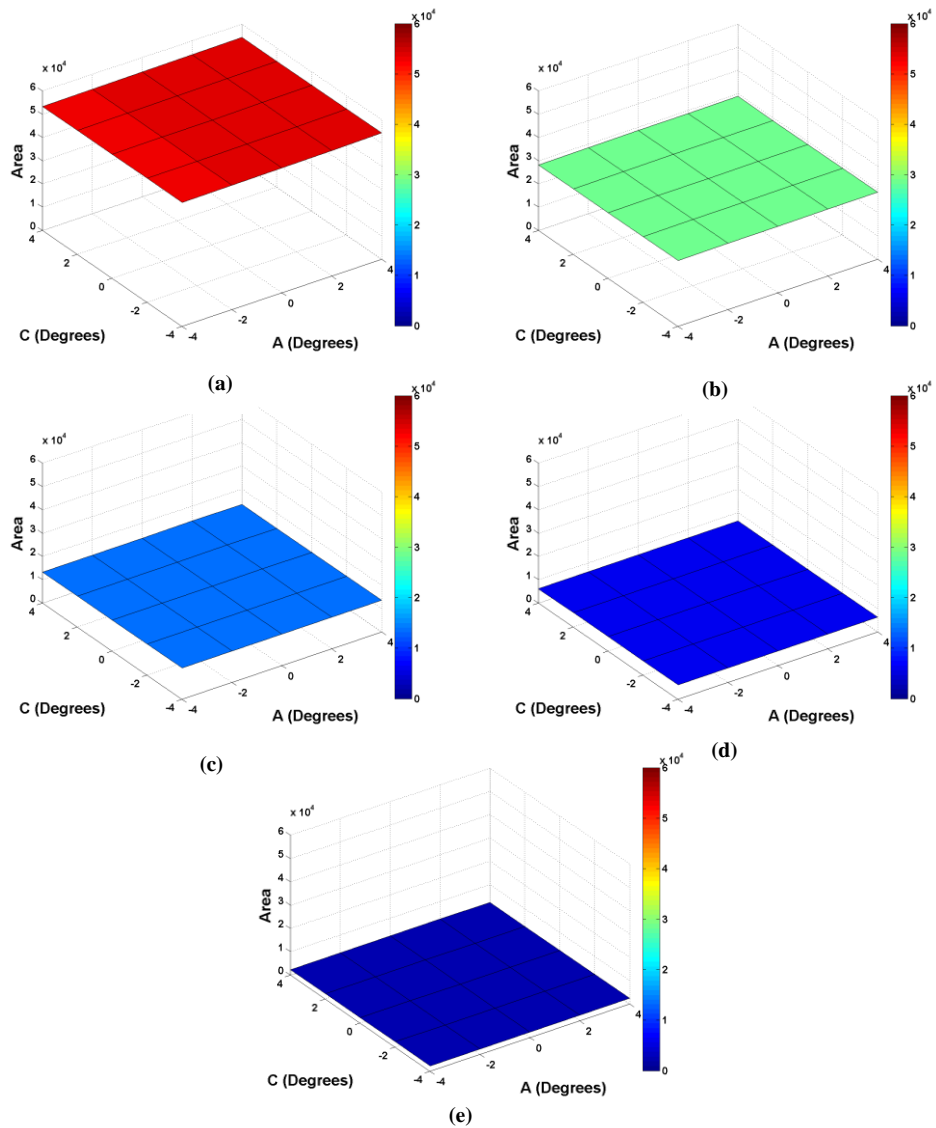# Restored Intensity viewed from AC Angle

(a)

(b)

(c)

(d)

(e)

Figure C.61 AC Angle LRF Restored Intensity Area (Wood)

Nominal SSD (mm)	Restored Intensity Area Mean	Restored Intensity Area (AC) Standard Deviation
500	53777.7	338.19
1000	28556.5	207.42
2000	13463.4	100.76
3000	6258.85	79.38
4000	2324.02	30.40

Table C.48 AC Angle LRF Restored Intensity Area Statistical Performance (Wood)

Restored Intensity viewed from BC Angle
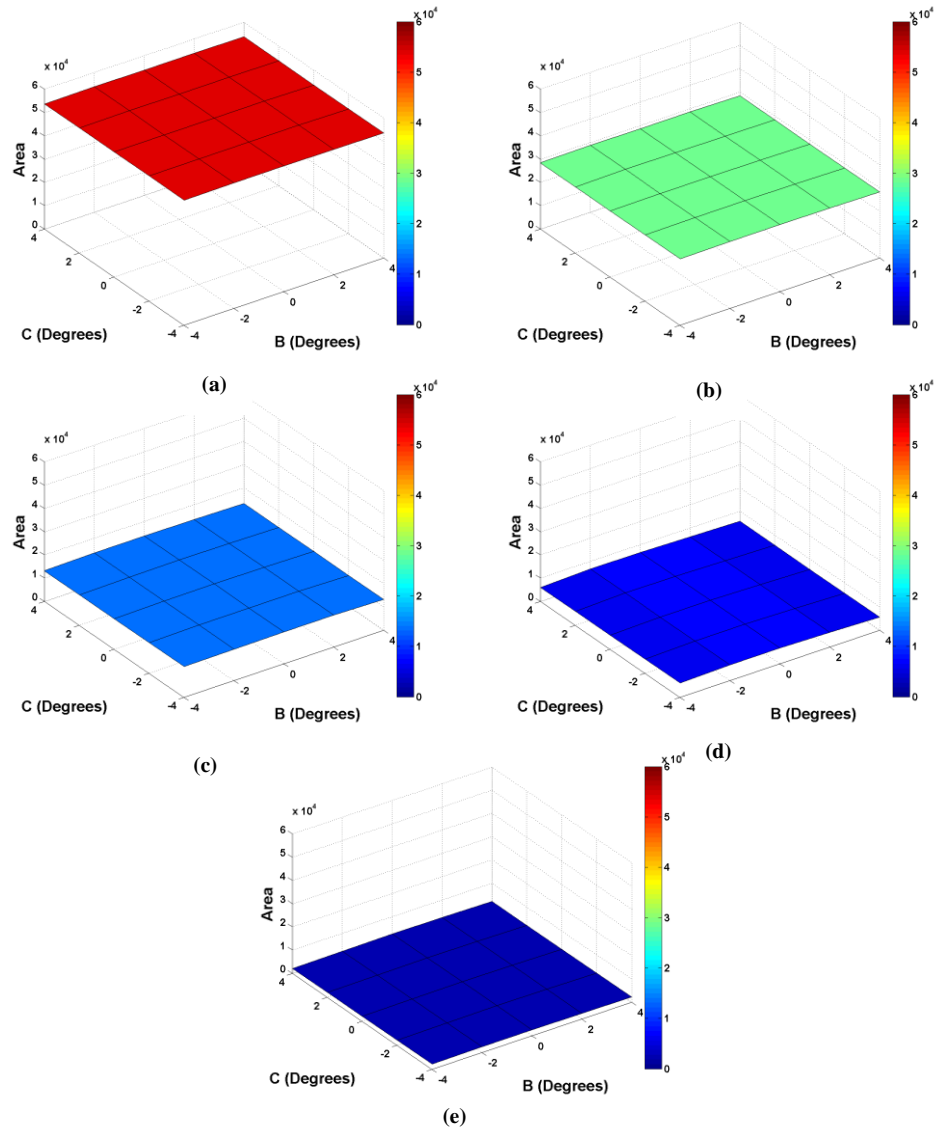

(a)

(b)

(c)

(d)

(e)

Figure C.62 BC Angle LRF Restored Intensity Area (Wood)

Nominal SSD (mm)	Restored Intensity Area Mean	Restored Intensity Area (BC) Standard Deviation
500	53777.7	96.10
1000	28556.5	173.71
2000	13463.4	212.37
3000	6258.85	411.88
4000	2324.02	178.02

Table C.49 BC Angle LRF Restored Intensity Area Statistical Performance (Wood)
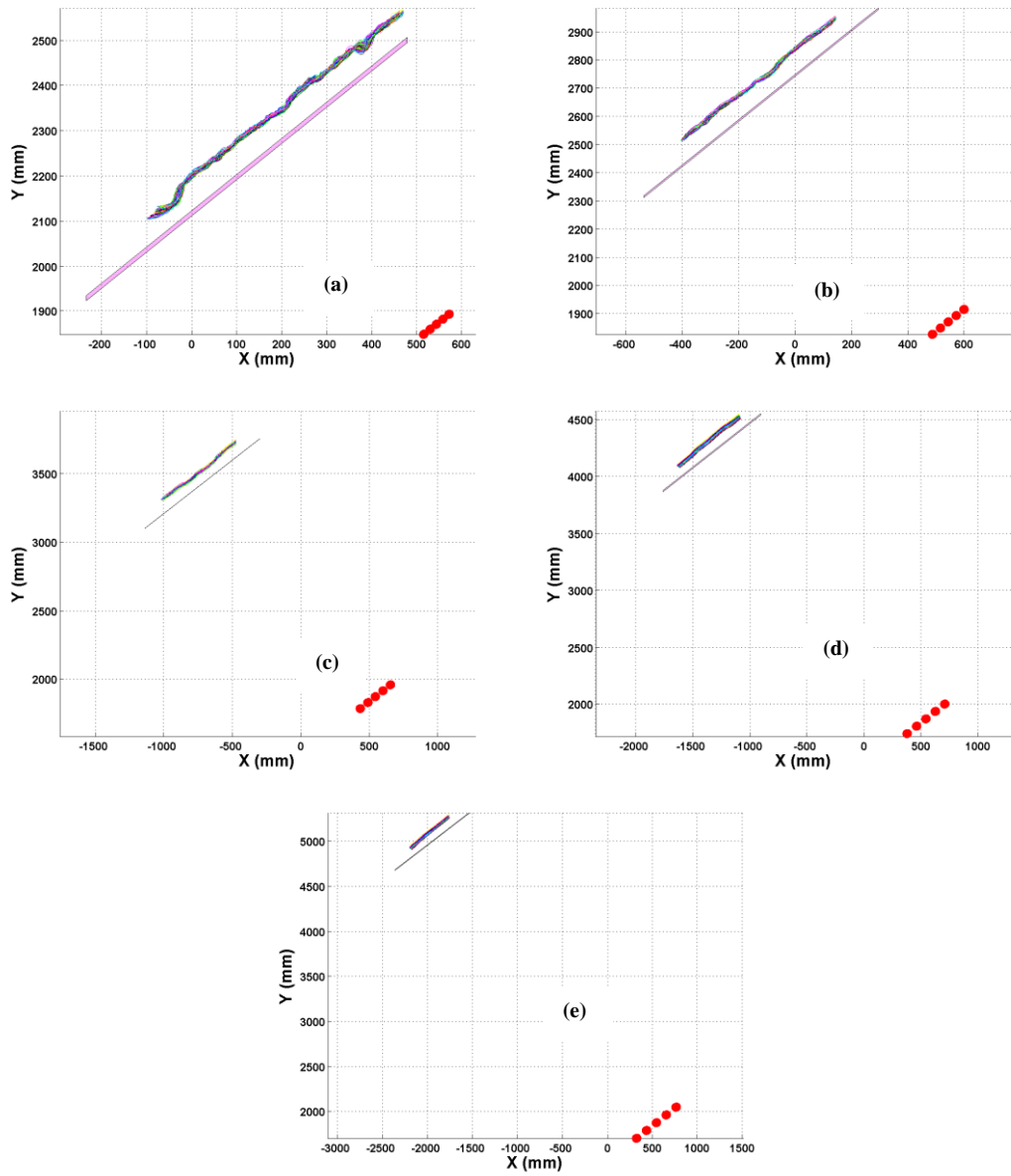
Scan Plan View

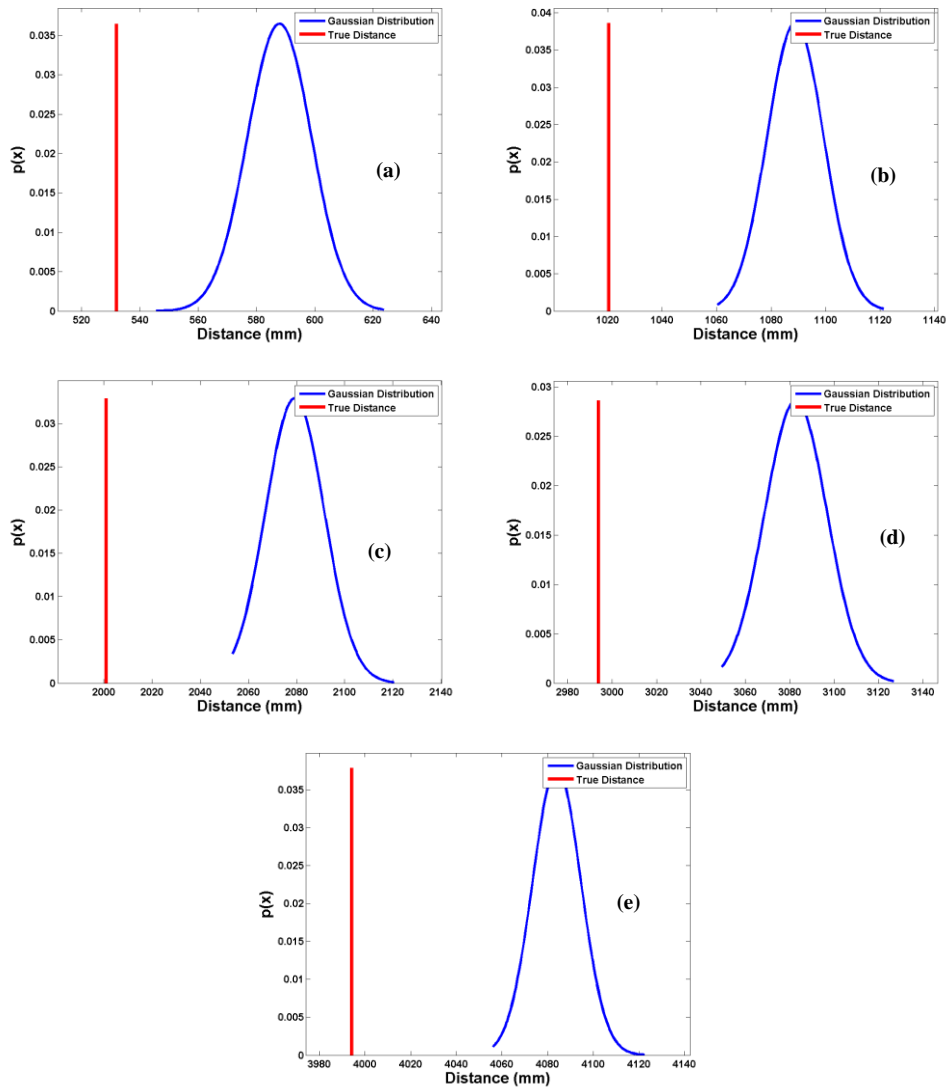**Figure C.63 LRF Scan Plan View (Wood)**

Distnace Error

Figure C.64 LRF Distance Error (Wood)

Nominal SSD (mm)	Distance Error Mean (mm)	Distance Error Standard Deviation (mm)	Distance Error Minimum (mm)	Distance Error Max (mm)
500	55.89	10.94	13.53	91.64
1000	68.47	10.32	39.92	100.79
2000	78.17	12.11	52.40	119.22
3000	88.82	13.95	55.51	132.81
4000	89.78	10.53	61.90	128.16

Table C.50 LRF Distance Error Statistical Performance (Wood)
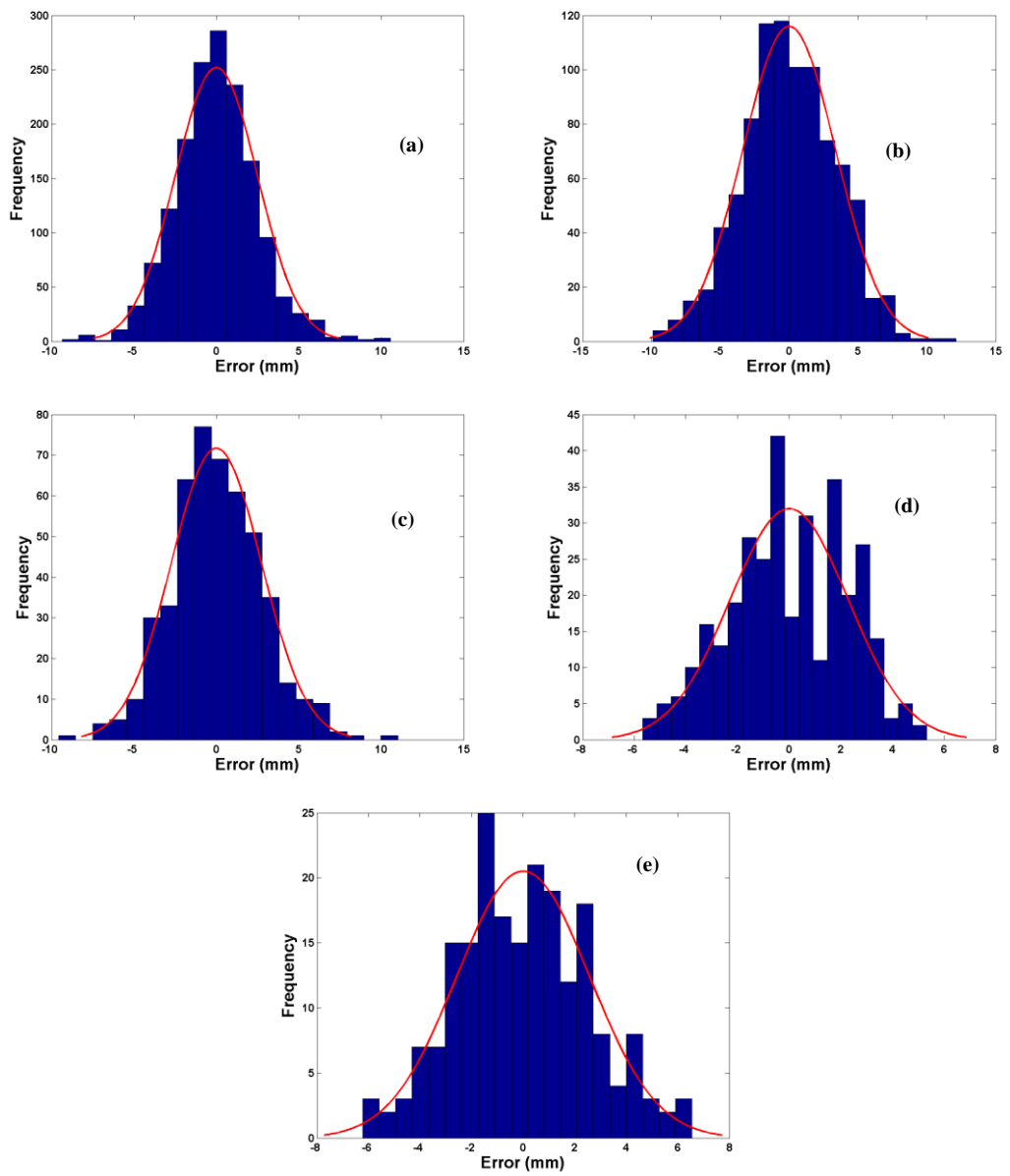
Single Shot Histogram

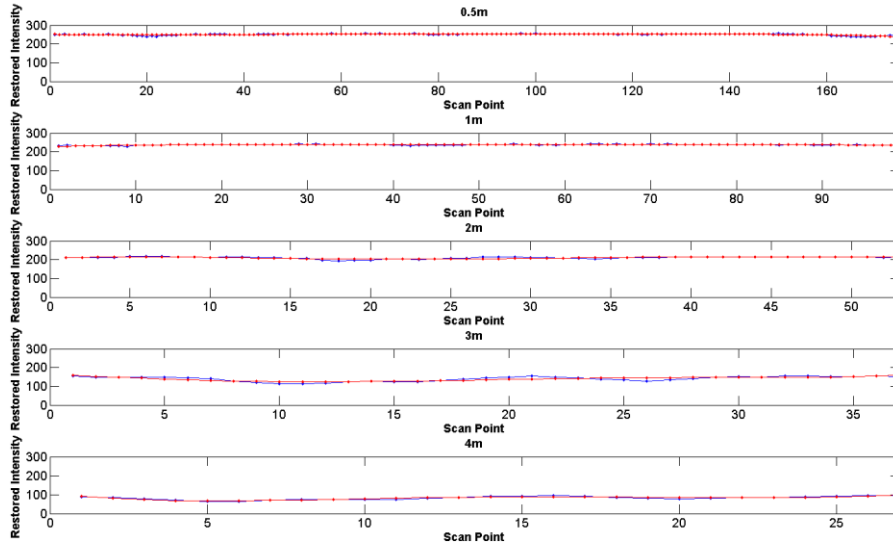**Figure C.65 LRF Range Data Variation (Wood)**

LRF Material Identification

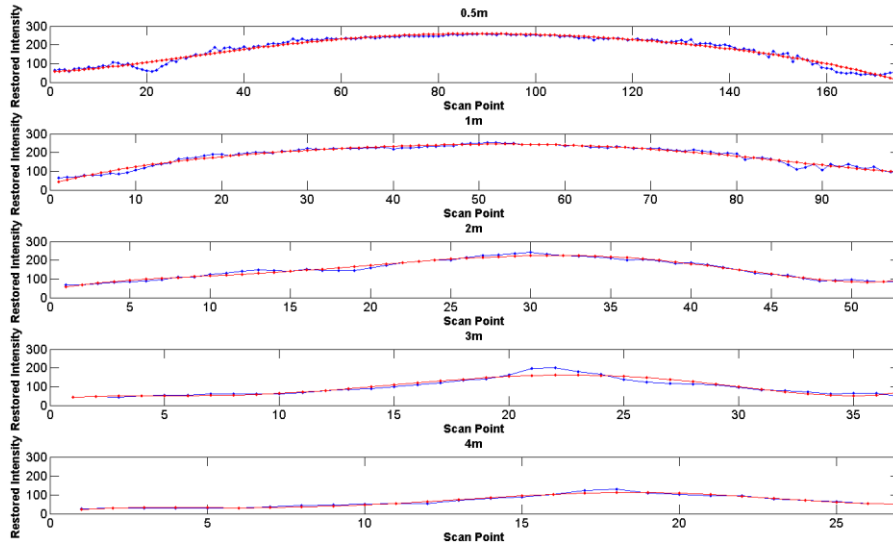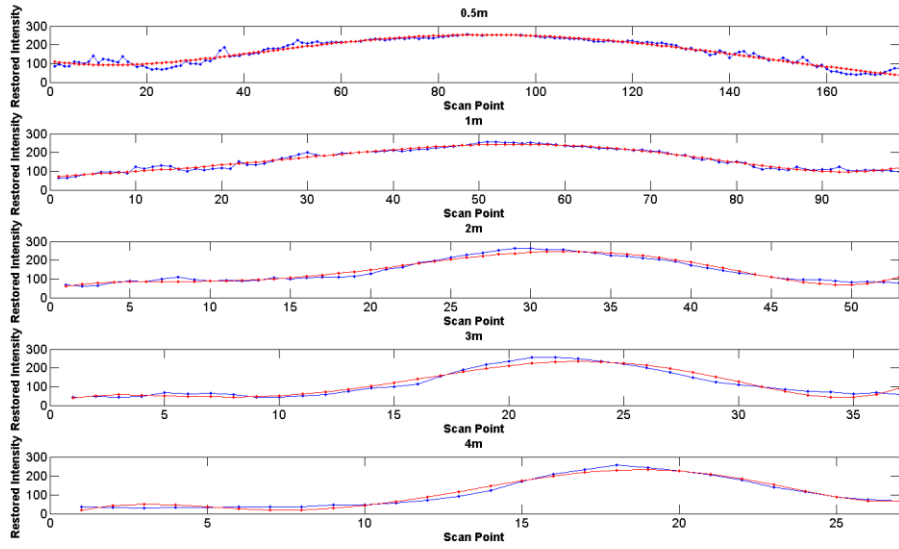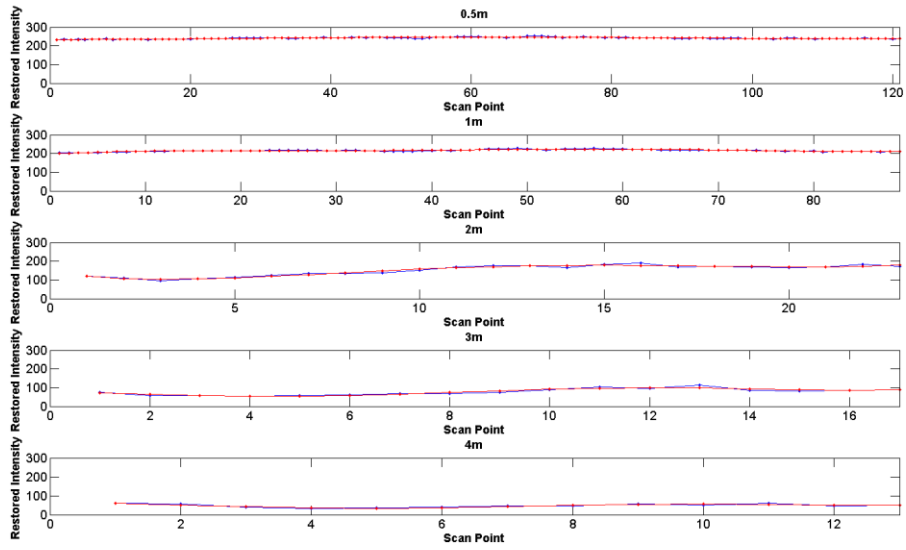**Figure C.66 Paper Surface Restored Intensity Curve Fitting**

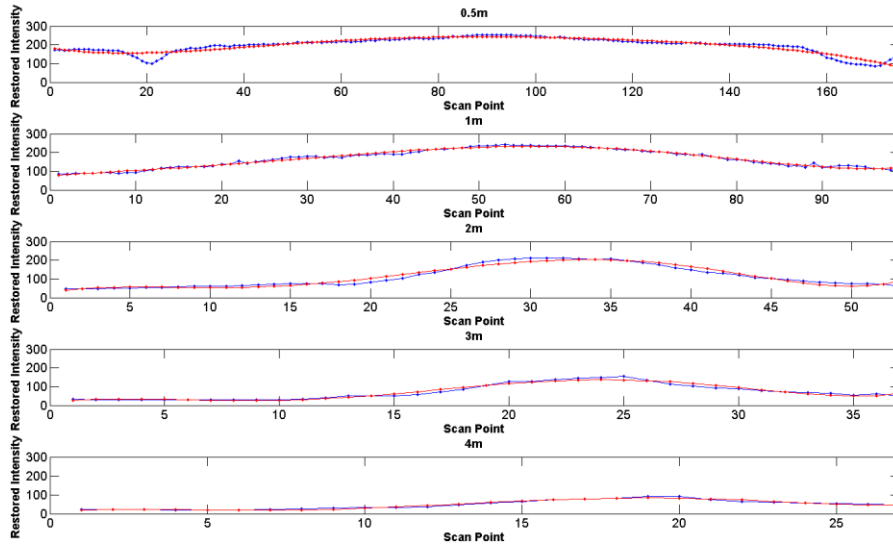**Figure C.67 Steel Surface Restored Intensity Curve Fitting**

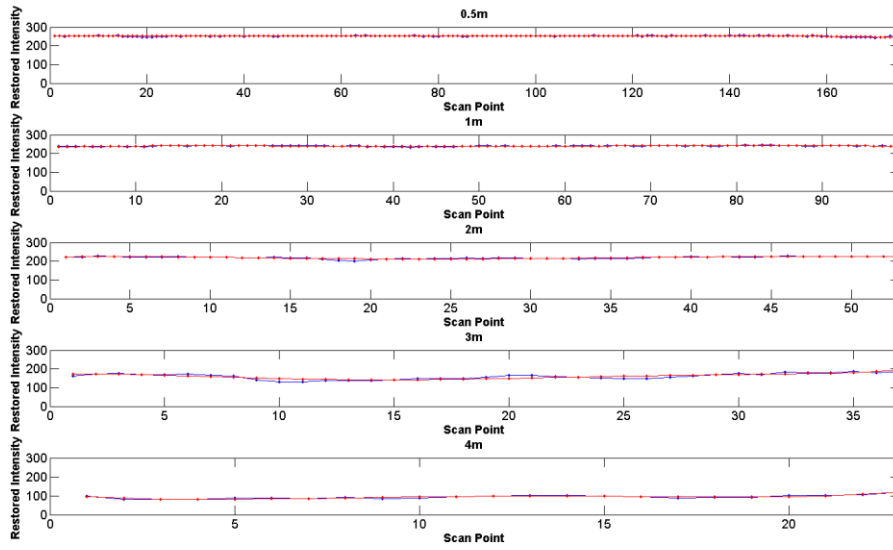**Figure C.68 Stainless Steel Surface Restored Intensity Curve Fitting**

Figure C.69 Concrete Surface Restored Intensity Curve Fitting

Figure C.70 PVC Surface Restored Intensity Curve Fitting

Figure C.71 Wood Surface Restored Intensity Curve Fitting

Material Surface				Paper	
Nominal SSD (mm)	Polynomial Coefficient				
	a	b	c	d	e	f
500	0	0	-0.0003	0.0233	-0.5486	251.8869
1000	0	0	0.0008	-0.0461	1.2015	227.8629
2000	0	-0.0005	0.0270	-0.5896	4.3756	205.6724
3000	0	-0.0017	0.0423	-0.1344	-5.2756	164.0481
4000	0	0.0032	-0.1536	2.7532	-18.1538	106.4176

Table C.51 Paper Surface Curve Fitting Coefficients

Material Surface				Steel	
Nominal SSD (mm)	Polynomial Coefficient				
	a	b	c	d	e	f
500	0	0	-0.0016	0.0938	1.2250	55.5591
1000	0	-0.0001	0.0067	-0.3467	12.1317	30.6012
2000	0	-0.0023	0.0920	-1.5101	15.2413	43.7949
3000	0.0001	-0.0102	0.2723	-2.5439	10.1439	35.2169
4000	0.0004	-0.0271	0.6192	-5.4588	19.6788	7.7137

Table C.52 Steel Surface Curve Fitting Coefficients

Material Surface	Stainless Steel				
Nominal SSD (mm)	Polynomial Coefficient				
	a	b	c	d	e	f
500	0	0	-0.0022	0.1948	-3.8717	114.3579
1000	0	-0.0001	0.0059	-0.0885	3.4207	68.8172
2000	0	-0.0044	0.1749	-2.5855	16.3171	48.2893
3000	0.0003	-0.0248	0.7049	-7.5005	29.8503	16.9453
4000	0.0014	-0.0949	2.2536	-21.0685	74.5784	-37.4461

Table C.53 Stainless Steel Surface Curve Fitting Coefficients

Material Surface	Concrete				
Nominal SSD (mm)	Polynomial Coefficient				
	a	b	c	d	e	f
500	0	0	-0.0001	0.0085	0.0950	233.1032
1000	0	-0.0001	0.0052	-0.1849	2.9773	196.5241
2000	-0.0001	0.0096	-0.3838	5.6861	-25.6822	139.2582
3000	0.0020	-0.0804	1.0423	-4.0446	-1.7024	77.1427
4000	0.0057	-0.1987	2.3356	-10.0632	7.9047	60.3657

Table C.54 Concrete Surface Curve Fitting Coefficients

Material Surface	PVC				
Nominal SSD (mm)	Polynomial Coefficient				
	a	b	c	d	e	f
500	0	0	-0.0024	0.1828	-4.1791	184.8615
1000	0	-0.0001	0.0040	-0.0602	3.0469	76.2741
2000	0.0001	-0.0040	0.1622	-2.4417	14.4696	27.6033
3000	0.0001	-0.0130	0.3826	-4.2248	16.9224	12.5748
4000	0.0003	-0.0206	0.4676	-3.9560	12.1872	11.2875

Table C.55 PVC Surface Curve Fitting Coefficients

Material Surface	Wood				
Nominal SSD (mm)	Polynomial Coefficient				
	a	b	c	d	e	f
500	0	0	-0.0001	0.0098	-0.2553	253.3902
1000	0	0	0.0009	-0.0481	1.0169	234.2304
2000	0	-0.0003	0.0157	-0.3532	2.3338	219.9926
3000	0	-0.0033	0.1107	-1.4248	3.9091	169.3840
4000	0	0.0013	-0.1246	2.2823	-13.1368	104.6747

Table C.56 Wood Surface Curve Fitting Coefficients